

A.Y. Oral
Z.B. Bahsi Oral
M. Ozer *Editors*

2nd International Congress on Energy Efficiency and Energy Related Materials (ENEFM2014)

Proceedings, Oludeniz, Fethiye/Mugla,
Turkey, October 16–19, 2014

Springer Proceedings in Energy

More information about this series at <http://www.springer.com/series/13370>

A.Y. Oral · Z.B. Bahsi Oral · M. Ozer
Editors

2nd International Congress on Energy Efficiency and Energy Related Materials (ENEFM2014)

Proceedings, Oludeniz, Fethiye/Mugla,
Turkey, October 16–19, 2014



Springer

Editors

A.Y. Oral
Department of Materials Science
and Engineering
Gebze Technical University
Gebze, Kocaeli
Turkey

M. Ozer
Department of Physics
İstanbul Kültür University
Bakırköy, İstanbul
Turkey

Z.B. Bahsi Oral
Department of Environmental Engineering
Gebze Technical University
Gebze, Kocaeli
Turkey

ISSN 2352-2534
Springer Proceedings in Energy
ISBN 978-3-319-16900-2
DOI 10.1007/978-3-319-16901-9

ISSN 2352-2542 (electronic)
ISBN 978-3-319-16901-9 (eBook)

Library of Congress Control Number: 2015939822

Springer Cham Heidelberg New York Dordrecht London
© Springer International Publishing Switzerland 2015

This work is subject to copyright. All rights are reserved by the Publisher, whether the whole or part of the material is concerned, specifically the rights of translation, reprinting, reuse of illustrations, recitation, broadcasting, reproduction on microfilms or in any other physical way, and transmission or information storage and retrieval, electronic adaptation, computer software, or by similar or dissimilar methodology now known or hereafter developed.

The use of general descriptive names, registered names, trademarks, service marks, etc. in this publication does not imply, even in the absence of a specific statement, that such names are exempt from the relevant protective laws and regulations and therefore free for general use.

The publisher, the authors and the editors are safe to assume that the advice and information in this book are believed to be true and accurate at the date of publication. Neither the publisher nor the authors or the editors give a warranty, express or implied, with respect to the material contained herein or for any errors or omissions that may have been made.

Printed on acid-free paper

Springer International Publishing AG Switzerland is part of Springer Science+Business Media
(www.springer.com)

Preface

The *2nd International Congress on Energy Efficiency and Energy Related Materials (ENEFM2014)* provided all scientists the opportunity to meet, present their work, discuss, and mutually interact in order to enhance and promote their research work.

This volume, published by Springer, includes selected papers presented at this Congress, held in Oludeniz, Turkey, during October 16–19, 2014.

On behalf of the organizing committee we would like to thank all the plenary and invited speakers for their valuable contribution.

We would also like to thank TURA Tourism for their support in the organization of the Congress as well as the publishers for the quality of this edition.

Gebze, Turkey

A.Y. Oral

Gebze, Turkey

Z.B. Bahsi Oral

Istanbul, Turkey

M. Ozer

Organization

Scientific Committee

Masayuki Yamaguchi, Japan Advanced Institute of Science and Technology, Japan
Scala Fabrizio, The Institute for Research on Combustion (IRC) of the Italian National Council for Research (CNR), Italy

Jiri Klemes, University of Pannonia, Hungary

Taehoon Hong, Yonsei University, Republic of Korea

Doriano Brogioli, Università degli Studi di Milano-Bicocca, Italy

Abd Halim Shamsuddin, Universiti Tenaga Nasional, Malaysia

Mohamed Bououdina, University of Bahrain, Kingdom of Bahrain

Chuanbao Cao, Beijing Institute of Technology, China

Jamal Khatib, University of Wolverhampton, UK

Holger Schlör, Forschungszentrum Jülich, Institute for Energy and Climate Research, Systems Analysis and Technology Evaluation (IEK-STE), Germany

Zuoqian Wang, University of California, Berkeley, USA

Lidija Čuček, University of Maribor, Slovenia

Farzad Jafarkazemi, Islamic Azad University, Iran

Reinhard Haas, Vienna University of Technology, Austria

Beddiah Zaidi, LSC, Badji Mokhtar University, Algeria

Su Huaizhi, Hohai University, China

Cengiz Ozkan, University of California, Riverside, USA

Organizing Committee

Ahmet Yavuz Oral, Gebze Technical University, Turkey

Z. Banu Bahsi Oral, Gebze Technical University, Turkey

M. Alper Sahiner, Seton Hall University, USA

Ersin Kayahan, Kocaeli University, Turkey

Mehmet Ozer, Istanbul Kultur University, Turkey
Dong Ha Kim, Ewha Womans University, Republic of Korea

Conference Organizing Company

Tura Tourism Ltd.



Cumhuriyet Cad. No: 109/A Elmadag—Sisli/Istanbul
E-mail: enefm2014@turaturizm.com
Phone: +90 212 241 27 00
Fax: +90 212 241 29 89
Web: www.turaturizm.com.tr

Contents

Part I General Issues

Reliability Importance Measures of Components for Stand-Alone Hybrid Renewable Energy Microgrid	3
Abubakar Abdulkarim, Sobhy M. Abdelkader and D. John Morrow	

Statistical Analyses of Wind and Solar Energy Resources for the Development of Hybrid Microgrid.	9
Abubakar Abdulkarim, Sobhy M. Abdelkader and D. John Morrow	

Entering the Bio Based Economy—Verification of Demand on Education in the Field of Green Economy	15
Zuzana Palkova	

Hybrid Power System Supply for Electric Vehicles	23
Marian Gaiceanu and Razvan Buhosu	

Part II Wind Energy

Temporal Assessment of Wind Energy Resource in “Adrar” (South of Algeria); Calculation and Modeling of Wind Turbine Noise.	33
M. Benmedjahed, N. Ghellai, Z. Bouzid and A. Chiali	

Part III Solar Energy

Photo-Electro-Thermal Characteristics of Photovoltaic Panels	45
Krzysztof Górecki, Ewa Krac and Janusz Zarębski	

MLP/Levenberg-Marquardt for Prediction Solar Radiation: A Case Study Bejaia City	53
Z. Asradj and R. Alkama	
Modeling of Solar Cell Efficiency Improvement Using Pyramid Grafting in Single Junction Silicon Solar Cell	61
Hamid Heidarzadeh, Mahboubeh Dolatyari, Ghassem Rostami and Ali Rostami	
A Proposal for Intermediate Band Solar Cells with Optimized Transition Energy in Cr Doped 3C-SiC	69
M. Esgandari, H. Heidarzadeh, A. Rostami, G. Rostami and M. Dolatyari	
Comparison the Effect of Size and Inter-dot Spaces in Different Matrix Embedded Silicon Quantum Dots for Photovoltaic Applications	77
Hamid Heidarzadeh, Ghassem Rostami, Mahboubeh Dolatyari and Ali Rostami	
Sand Effect on Photovoltaic Array Efficiency in Algerian Desert	85
S. Semaoui, A. Hadj Arab, S. Bacha, H. Zeraia and E.K. Boudjelthia	
Solar Irradiation on <i>Lawsonia Inermis</i> Sensitized with Red Blood Cells: Effect on Osmotic Fragility	91
Rami Alkhateib, M-Ali Al-Akhras and Duaa J. Al-Khalili	
Part IV Nuclear Energy	
Perspectives of Industrial Separation of Zirconium Isotopes by Laser Assisted Retardation of Condensation Method	99
K.A. Lyakhov and H.J. Lee	
Part V Biofuels and Bioenergy	
Promising Technologies of Biomass Use for Energy Production Purposes	107
V. Zaichenko	
Heterogeneous Cracking of Tars on Surface of Charcoal	117
Valentin Kosov, Vladimir Kosov and Victor Zaichenko	

Part VI Fossil Energy

Investigation of Two-Component Hydrocarbon Mixture Filtration in Porous Media	125
I.L. Maikov, D.A. Molchanov and V.M. Torchinsky	

Part VII Hydropower

Deformation Analysis and Monitoring for Extra High Hydropower of 305 m	135
Huaizhi Su and Meng Yang	
Hydropower Plant Regime Management According to the Market Conditions	141
Hasan H. Coban, Renata Varfolomejeva, Antans Sauhats and Inga Umbrasko	

Part VIII Energy Storage, Conservation and Efficiency

Hydration Behavior of Mg-Ni Mixed Hydroxide Synthesized by Mechano-chemical Method for Chemical Heat Storage	155
Junichi Ryu, Yuki Hara and Yukitaka Kato	
Regenerative AC Drive System Based on the Three Phase Permanent Magnet Synchronous Machine	163
Marian Gaiceanu and Cristian Nichita	
CFD Analysis of Supersonic Ejectors Operating with Mixture of Gases	171
Maziar Shafaei, Mohsen Tavakol and Rouzbeh Riazi	
Integrated Energy-Efficient Hydrogen Production from Low Rank Coal and Its Storage for Transportation	179
Muhammad Aziz, Takuya Oda, Takumi Kurokawa and Takao Kashiwagi	
Ignition of Combustible Gases in Water	187
Vyacheslav Teslenko, Alexey Drozhzhin, Ruslan Medvedev and Igor Batraev	

Method of Assessing Energy Consumption in the Transport of Pallets in Logistics	195
Paweł Zajac	

Part IX Environmental Issues

Adsorption of Methyl Red from Aqueous Solutions by Algerian Bentonite Clay	203
Karima Boudouara, Madani Ghelamallah and Halima Nadia Khemliche	
Is Hospitals Ready for Energy Management and Green Building? Health Managers Opinions in Turkey	211
Meriç Yavuz Çolak and Levent Çolak	
Design of High Sensitive Optical Sensor for Seawater Salinity	219
Ahlam Harhouz and Abdesselam Hocini	
A Fuzzy Inference System to Evaluate the Environmental Effects of Electricity Generation Technologies	227
Fausto Cavallaro	

Part X Carbon Capture and Storage

Molasses Based Activated Carbons as CO₂ Sorbents	237
J. Młodzik, K. Glonek, U. Narkiewicz, A.W. Morawski, R.J. Wróbel and B. Michalkiewicz	

Part XI Bio-Assessment and Toxicology

Influence of the <i>Staphylococcus Aureus</i> Bacteria Cells on the Zeta Potential of Graphene Oxide Modified with Alumina Nanoparticles in Electrolyte and Drinking Water Environment	245
A. Jastrzebska, E. Karwowska and A. Olszyna	

Part XII Air Pollution from Mobile and Stationary Sources

**The State of Art Technique of Pre-ozonation Processes
for Intensification of Emission Control from Stationary Sources** 253
Kinga Skalska

Part XIII Transport of Air Pollutants

**The Energy Performance Model of Mechanical
and Natural Ventilation** 261
Richard Nagy, Danica Košičanová and Jan Lojkovics

Part XIV Environment-Friendly Construction and Development

**How to Refurbish '80s *Brutalist Architecture*, Turning It
into NZEB: The Case Study of the High School "Enrico Fermi"
in Muro Lucano (Potenza, Italy)** 269
Francesco Paolo R. Marino and Filiberto Lembo

**The Environment-Friendly Architecture Come
Through Wooden Architecture** 281
Filiberto Lembo and Francesco Paolo R. Marino

**Energy Efficiency Engineering—Towards an Integrated
Method Framework for Energy-Oriented Product
and Production Development** 291
Pascal Stoffels, Dirk Bähre, Georg Frey and Michael Vielhaber

**Modeling the Air Channel Ventilation in Ansys CFX
of a Romanesque Church** 299
Anna Sedlakova and Ladislav Tazky

Part XV Energy Management Systems

Many Kinds of Energy Source in Our Surroundings at Home 307
Takashi Yoshikawa

Optimizing Residential Energy Consumption in Romania 313
Ion Smeureanu, Francesco Moresino, Marian Dardala,
Adriana Reveiu and Felix Furtuna

Part XVI Materials for Sustainable Energy

Determination of Assessment Scale for Selected Indicators in Slovak Building Environmental Assessment System BEAS.	321
Silvia Vilčeková, Eva Krídlová Burdová and Monika Čuláková	
Effect of Ni Seed Layer for Electroplating ^{63}Ni in Beta Voltaic Battery	327
Y.R. Uhm, B.G. Choi, K.J. Son and D.H. Jeong	
Structural Properties of Polystyrene (PS)/Ferroelectric Barium Stannate Titanate $\text{Ba}(\text{Ti}_{0.9}\text{Sn}_{0.1})\text{O}_3$ Ceramic (BST) Composite	335
M-Ali Al-Akhras, Subhi Saq'an and Zeinab Ghadieh	

Part XVII Materials for Renewable Energy Storage and Conversion

Waynergy Vehicles—An Innovative Pavement Energy Harvest System	343
Francisco Duarte, Adelino Ferreira and João Champalimaud	
Nanostructured TiO_2 Film Deposition by Supersonic Plasma Jet Source for Energetic Application.	349
E.C. Dell'Orto, S. Caldirola, H.E. Roman and C. Riccardi	
A Method for Building a Simple and Applicable Power Inverter	357
Mohamed Abdelati and Georg Frey	

Part XVIII Fuel Cells

Evaluation of Electrocatalytic Activity of Pt-Co/Ti Towards Methanol Oxidation.	371
E. Norkus, Ž. Činčienė, A. Balčiūnaitė, A. Zabielaite, I. Stankevičienė, J. Vaičiūnienė, A. Selskis and L. Tamašauskaitė-Tamašiūnaitė	
The Origin of Electrocatalytic Activity of Gold Nanoparticles Modified Pt-Based Surfaces Towards Formic Acid Oxidation	379
Gumaa A. El-Nagar, Ahmad M. Mohammad, Mohamed S. El-Deab and Bahgat E. El-Anadouli	

The Effect of Humidification Strategies on Efficiency and Durability of Hydrogen Fuel Cells in Automotive Application	389
F. Migliardini, A. Unich and P. Corbo	

Electrocatalytic Activity of NiOx Nanostructured Modified Electrodes Towards Oxidation of Small Organic Molecules	397
Sayed M. El-Refaei, Guma A. El-Nagar, Ahmed M. Mohammad, Mohamed S. El-Deab and B.E. El-Anadouli	

Part XIX Hydrogen Storage

Computational Design of Dual Cation Ammine Metal Borohydrides: $\text{LiTi}(\text{BH}_4)_5(\text{NH}_3)_X$	407
Yusuf Kışlak and Adem Tekin	

Discovery of New Dual Cation Metal Ammine Borohydrides: A Computational Study	413
Samet Demir and Adem Tekin	

Part XX Photovoltaics and Solar Cells

Properties of CdS Deposited by the SILAR Method Using Cd(II) Organic Salt as Precursor	423
L. Tamašauskaitė-Tamašiūnaitė, B. Šimkūnaitė-Stanygienė, G. Grincienė, A. Žielienė, L. Naruškevičius, A. Selskis, V. Jasulaitienė and E. Norkus	

Analysis of the Performance a PV System Based on Empirical Data in a Real World Context	429
Seyed Amin Tabatabaei and Jan Treur	

Efficient Models of Partially Shaded PV Modules for Energy System Design	441
Lukas Exel, Felix Felgner and Georg Frey	

Part XXI Hydrogen Production and Fuel Generation from Renewables (Catalysis)

Modelling and the Analysis of the Power Supply System for the Generator of Hydrogen	451
Krzysztof Górecki, Janusz Zarębski, Paweł Górecki and Sławomir Halbryt	

Conductometric Titration to Analyze Nafion® 117 Conductivity. 459
María José Lavorante and Juan Isidro Franco

**High Thermal Conductivity Structured Bimetallic Catalysts
for Low Temperature Ethanol Steam Reforming.** 467
Vincenzo Palma, Concetta Ruocco, Filomena Castaldo
and Antonio Ricca

**Experimental Investigations on Structured Catalysts
in CH₄ Steam Reforming Intensification.** 473
V. Palma, A. Ricca, E. Meloni, M. Martino, M. Miccio
and P. Ciambelli

Catalysts for the Intensification of the Water Gas Shift Process. 479
V. Palma, D. Pisano, M. Martino, A. Ricca and P. Ciambelli

**Hydrogen Production by Steam Conversion of a Model Biogas
Over the Co-based Supported Catalysts.** 485
S.S. Itkulova, G.D. Zakumbaeva, Y.Y. Nurmakanov,
A.M. Abdullin and A. Ospanova

Nanostructured Co-B Catalysts for Hydrogen Generation. 491
David Richardson and Fernando M.F. Rhen

Part XXII Carbon Dioxide Sequestration and Conversion

**Carbon Dioxide Conversion of Biogas with Producing Syngas
Over the Polymetallic Supported Catalysts.** 499
Y.Y. Nurmakanov, V.S. Yemelyanova, S.S. Itkulova,
G.D. Zakumbaeva and N.N. Nurgaliyev

Part XXIII Materials for Energy Saving

**Effects of Cobalt on the Crystalline Structures
of the Ni-Mn-In Giant Magnetocaloric Heusler Alloys.** 507
Amila Madiligama, P. Ari-Gur, V. Shavrov, V. Koledov,
Y. Ren, S. Calder and A. Kayani

Analysis of the External Magnetic Field Influences on the Measurements Realized with a Single Strip Tester (SST) Using Finite Element Modeling.	515
Veronica Manescu (Paltanea), Gheorghe Paltanea, Dorina Popovici and Gabriel Jiga	

Part XXIV Thermoelectrics

Energy Harvesting from Open Fireplaces	525
Marco Nesarajah and Georg Frey	

Part XXV Energy Saving in Buildings

The Impact of Installing Variable Frequency Drives for Cooling Towers in Kuwait on Energy Consumption.	535
Etidal Al-Bassam	

Solutions of Ground Floor for Energy Efficient Buildings—Economic Evaluation	541
Anna Sedlakova, Pavol Majdlen and Ladislav Tazky	

Analysis of Air Velocity, Moisture and Thermal Regime in a Double-Shell Roof.	547
Martin Kovac and Jaroslav Vojtus	

Simulation of Energy Demand in a Shopping Centre—Case Study	553
Martin Kovac and Katarina Kovacova	

Build-in Transparent Collector Construction	559
Ján Lojkovics, Danica Košičanová, Richard Nagy, Marek Kušnír and Martin Štefanco	

Part XXVI Modeling and Theoretical Aspects in Energy Related Materials

Tensile and Torsional Loads Stress Distribution Along the Drill String for Deep Wells.	567
Lallia Belkacem, Noureddine Abdelbaki, Mohamed Gaceb, Elahmoun Bouali, Hedjaj Ahmed and Mourad Bettayeb	

Computational Screening of Dual Cation Metal Ammine Borohydrides	581
Arash Emdadi, Yusuf Kişiak, Samet Demir and Adem Tekin	
Analysis of Electricity Usage for Domestic Heating Based on an Air-to-Water Heat Pump in a Real World Context	587
Seyed Amin Tabatabaei and Jan Treur	
The Method of Determining Certain Parameters of Energy Absorption in Materials Under Complex Dynamic Excitations	597
Miroslaw Bocian, Krzysztof Jamroziak, Maciej Kulisiewicz and Stanislaw Piesiak	
Erratum to: Tensile and Torsional Loads Stress Distribution Along the Drill String for Deep Wells.	E1
Lallia Belkacem, Noureddine Abdelbaki, Mohamed Gaceb, Elahmoun Bouali, Hedjaj Ahmed and Mourad Bettayeb	

Contributors

Mohamed Abdelati Electrical Engineering Department, IUG, Gaza, Palestine

Noureddine Abdelbaki Laboratory of Petroleum Equipments Reliability and Materials, Faculty of Hydrocarbons and Chemistry Independence Street, University Mohamed Bougara, Boumerdes, Bougara, Algeria

Sobhy M. Abdelkader Energy, Power and Intelligent Control, School of Electronics, Electrical Engineering and Computer Science, Queen's University Belfast, Belfast, UK

Abubakar Abdulkarim Energy, Power and Intelligent Control, School of Electronics, Electrical Engineering and Computer Science, Queen's University Belfast, Belfast, UK

A.M. Abdullin D.V. Sokolsky Institute of Organic Catalysis and Electrochemistry, Almaty, Kazakhstan

Hedjaj Ahmed University Akli Mohand Oulhadj, Bouira, Algeria

M-Ali Al-Akhras Bio-Medical Physics Laboratory, Department of Physics, Jordan University of Science & Technology (JUST), Irbid, Jordan

Etidal Al-Bassam Energy and Building Research Center, Kuwait Institute for Scientific Research, Kuwait City, Kuwait

Duaa J. Al-Khalili Bio-Medical Physics Laboratory, Department of Physics, Jordan University of Science & Technology (JUST), Irbid, Jordan

R. Alkama Laboratory of Electrical Engineering, Faculty of Technology, University of Bejaia, Bejaia, Algeria

Rami Alkhatib Department of Biotechnology and Genetic Engineering, Jordan University of Science & Technology (JUST), Irbid, Jordan

P. Ari-Gur Western Michigan University, Kalamazoo, MI, USA

Z. Asradj Laboratory of Electrical Engineering, Faculty of Technology, University of Bejaia, Bejaia, Algeria

Muhammad Aziz Solutions Research Laboratory, Tokyo Institute of Technology, Tokyo, Japan

S. Bacha Grenoble Electrical Engineering Laboratory, G2Elab, St Martin d'Hères, France

A. Balčiūnaitė Center for Physical Sciences and Technology, Vilnius, Lithuania

Igor Batraev Lavrentyev Institute of Hydrodynamics SB RAS, Novosibirsk, Russia

Lallia Belkacem University Akli Mohand Oulhadj, Bouira, Algeria

M. Benmedjahed Research Unit of Renewable Energies in the Sahara, Adrar, Algeria

Mourad Bettayeb University Akli Mohand Oulhadj, Bouira, Algeria

Miroslaw Bocian Department of Mechanics, Materials Science and Engineering, Wroclaw University of Technology, Wroclaw, Poland

Elahmoun Bouali University Akli Mohand Oulhadj, Bouira, Algeria

E.K. Boudjelthia Centre de Développement des Energies Renouvelables, Algiers, Algeria

Karima Boudouara Laboratoire de Matériaux, Applications et Environnement, Faculté des Sciences et de la Technologie, Université de Mascara, Mascara, Algeria

Z. Bouzid Unit Research in Materials and Renewable Energy, University of Tlemcen, Tlemcen, Algeria

Razvan Buhosu Dunarea de Jos University of Galati, Galati, Romania

Dirk Bähre Saarland University, Saarbruecken, Germany

S. Calder Quantum Condensed Matter Division, Oak Ridge National Lab, Oak Ridge, TN, USA

S. Caldirola Dipartimento di Fisica, Università degli Studi di Milano-Bicocca, Milano, Italy

Filomena Castaldo University of Salerno, Fisciano, SA, Italy

Fausto Cavallaro Department of Economics, Management, Society and Institutions (EGSI), University of Molise, Campobasso, ITALY

João Champalimaud Waydip, Parkurbis, Parque de Ciência e Tecnologia da Covilhã, Covilhã, Portugal

A. Chiali Preparatory School of Science and Technology of Tlemcen, Tlemcen, Algeria

B.G. Choi Human Interface SoC Research Section, Electronics and Telecommunications Research Institute (ETRI), Daejeon, Korea

P. Ciambelli University of Salerno, Fisciano, SA, Italy

Hasan H. Coban Institute of Power Engineering, Riga Technical University, Riga, Latvia

P. Corbo Istituto Motori, National Research Council of Italy, Naples, Italy

Marian Dardala Bucharest University of Economic Studies, Bucharest, Romania

E.C. Dell'Orto Dipartimento di Fisica, Università degli Studi di Milano-Bicocca, Milano, Italy

Samet Demir Informatics Institute, Istanbul Technical University, Istanbul, Turkey

M. Dolatyari Photonics Research Group, School of Engineering Emerging Technology, University of Tabriz, Tabriz, Iran

Alexey Drozhzhin Lavrentyev Institute of Hydrodynamics SB RAS, Novosibirsk, Russia

Francisco Duarte Pavement Mechanics Laboratory, Department of Civil Engineering, University of Coimbra, Coimbra, Portugal

B.E. El-Anadouli Chemistry Department, Faculty of Science, Cairo University, Cairo, Egypt

Mohamed S. El-Deab Chemistry Department, Faculty of Science, Cairo University, Cairo, Egypt; Department of Chemical Engineering, Faculty of Engineering, The British University in Egypt, Cairo, Egypt

Gumaa A. El-Nagar Chemistry Department, Faculty of Science, Cairo University, Cairo, Egypt

Sayed M. El-Refaei Chemistry Department, Faculty of Science, Cairo University, Cairo, Egypt

Arash Emdadi Energy Institute, Istanbul Technical University, Istanbul, Turkey

M. Esgandari Photonics Research Group, School of Engineering Emerging Technology, University of Tabriz, Tabriz, Iran

Lukas Exel Saarland University, Saarbrücken, Germany

Felix Felgner Saarland University, Saarbrücken, Germany

Adelino Ferreira Pavement Mechanics Laboratory, Department of Civil Engineering, University of Coimbra, Coimbra, Portugal

Juan Isidro Franco Departamento de Investigación y Desarrollo de Energías Renovables (CITEDEF-EST), Provincia de Buenos Aires, Argentina

Georg Frey Chair of Automation and Energy Systems, Saarland University, Saarbrücken, Germany

Felix Furtuna Bucharest University of Economic Studies, Bucharest, Romania

Mohamed Gaceb University Akli Mohand Oulhadj, Bouira, Algeria

Marian Gaiceanu Dunarea de Jos University of Galati, Galati, Romania

Zeinab Ghadieh Bio-Medical Physics Laboratory, Department of Physics, Jordan University of Science & Technology (JUST), Irbid, Jordan

Madani Ghelamallah Laboratoire de Matériaux, Applications et Environnement, Faculté des Sciences et de la Technologie, Université de Mascara, Mascara, Algeria

N. Ghellai Unit Research in Materials and Renewable Energy, University of Tlemcen, Tlemcen, Algeria

K. Glonek Institute of Chemical and Environment Engineering, West Pomeranian University of Technology, Szczecin, Poland

G. Grincienė Center for Physical Sciences and Technology, Vilnius, Lithuania

Krzysztof Górecki Department of Marine Electronics, Gdynia Maritime University, Gdynia, Poland

Paweł Górecki Department of Marine Electronics, Gdynia Maritime University, Gdynia, Poland

A. Hadj Arab Centre de Développement des Energies Renouvelables, Algiers, Algeria

Slawomir Halbryt SESCOM S.A, Gdańsk, Poland

Yuki Hara Research Laboratory for Nuclear Reactors, Tokyo Institute of Technology, Meguro, Tokyo, Japan

Ahlam Harhous Electronics Department, University of M'sila, M'sila, Algeria

H. Heidarzadeh Photonic and Nanocrystal Research Lab. (PNRL), Faculty of Electrical and Computer Engineering, University of Tabriz, Tabriz, Iran

Abdesselam Hocini Electronics Department, University of M'sila, M'sila, Algeria

S.S. Itkulova D.V. Sokolsky Institute of Organic Catalysis and Electrochemistry, Almaty, Kazakhstan

Krzysztof Jamroziak General Tadeusz Kosciuszko Military Academy of Land Forces, Wroclaw, Poland

A. Jastrzebska Faculty of Material Science and Engineering, Warsaw University of Technology, Warsaw, Poland

V. Jasulaitienė Center for Physical Sciences and Technology, Vilnius, Lithuania

D.H. Jeong Dongnam Institute of Radiological and Medical Science, Busan, Korea

Gabriel Jiga Politehnica University of Bucharest, Bucharest, Romania

D. John Morrow Energy, Power and Intelligent Control, School of Electronics, Electrical Engineering and Computer Science, Queen's University Belfast, Belfast, UK

E. Karwowska Faculty of Environmental Engineering, Warsaw University of Technology, Warsaw, Poland

Takao Kashiwagi Solutions Research Laboratory, Tokyo Institute of Technology, Tokyo, Japan

Yukitaka Kato Research Laboratory for Nuclear Reactors, Tokyo Institute of Technology, Meguro, Tokyo, Japan

A. Kayani Western Michigan University, Kalamazoo, MI, USA

Halima Nadia Khemliche Laboratoire de Matériaux, Applications et Environnement, Faculté des Sciences et de la Technologie, Université de Mascara, Mascara, Algeria

V. Koledov Kotelnikov Institute of Radio-Engineering and Electronics of RSA, Moscow, Russia

Valentin Kovov Joint Institute for High Temperatures of the Russian Academy of Sciences (JIHT RAS), Moscow, Russia

Vladimir Kovov Joint Institute for High Temperatures of the Russian Academy of Sciences (JIHT RAS), Moscow, Russia

Martin Kovac Department of Architectural Engineering, Faculty of Civil Engineering, Technical University of Kosice, Kosice, Slovak Republic

Katarina Kovacova Department of Architectural Engineering, Faculty of Civil Engineering, Technical University of Kosice, Kosice, Slovak Republic

Danica Košičanová Department of Indoor Technologies and Building Services, Civil Engineering Faculty, Institute of Architectural Engineering, Technical University of Košice, Košice, Slovakia

Ewa Krac Department of Marine Electronics, Gdynia Maritime University, Gdynia, Poland

Eva Krídlová Burdová Faculty of Civil Engineering, Institute of Environmental Engineering, Technical University of Košice, Košice, Slovakia

Maciej Kulisiewicz Department of Mechanics, Materials Science and Engineering, Wroclaw University of Technology, Wroclaw, Poland

Takumi Kurokawa Solutions Research Laboratory, Tokyo Institute of Technology, Tokyo, Japan

Marek Kušnír Department of Indoor Technologies and Building Services, Civil Engineering Faculty, Institute of Architectural Engineering, Technical University of Košice, Košice, Slovakia

Yusuf Kışlak Informatics Institute, Istanbul Technical University, Maslak Istanbul, Turkey

María José Lavorante Departamento de Investigación y Desarrollo de Energías Renovables (CITEDEF-EST), Provincia de Buenos Aires, Argentina

H.J. Lee Institute for Nuclear Science and Technology, Applied Plasma Physics Lab, Department of Nuclear and Energy Engineering, Jeju National University, Jeju-si, South Korea

Filiberto Lembo School of Engineering, Basilicata University, Potenza, Italy

Ján Lojkovics Department of Indoor Technologies and Building Services, Civil Engineering Faculty, Institute of Architectural Engineering, Technical University of Košice, Košice, Slovakia

K.A. Lyakhov Institute for Nuclear Science and Technology, Applied Plasma Physics Lab, Department of Nuclear and Energy Engineering, Jeju National University, Jeju-si, South Korea

Amila Madiligama Western Michigan University, Kalamazoo, MI, USA

I.L. Maikov Joint Institute for High Temperatures of Russian Academy of Sciences (JIHT RAS), Moscow, Russian Federation

Pavol Majdlen Civil Engineering Faculty, Institute of Architectural Engineering, Technical University of Košice, Košice, Slovakia

Veronica Manescu (Paltanea) Politehnica University of Bucharest, Bucharest, Romania

Francesco Paolo R. Marino School of Engineering, Basilicata University, Potenza, Italy

M. Martino University of Salerno, Fisciano, SA, Italy

Ruslan Medvedev Lavrentyev Institute of Hydrodynamics SB RAS, Novosibirsk, Russia

E. Meloni University of Salerno, Fisciano, SA, Italy

M. Miccio University of Salerno, Fisciano, SA, Italy

B. Michalkiewicz Institute of Chemical and Environment Engineering, West Pomeranian University of Technology, Szczecin, Poland

F. Migliardini Istituto Motori, National Research Council of Italy, Naples, Italy

Ahmad M. Mohammad Chemistry Department, Faculty of Science, Cairo University, Cairo, Egypt

D.A. Molchanov Joint Institute for High Temperatures of Russian Academy of Sciences (JIHT RAS), Moscow, Russian Federation

A.W. Morawski Institute of Chemical and Environment Engineering, West Pomeranian University of Technology, Szczecin, Poland

Francesco Moresino Haute Ecole de Gestion de Genève, Geneva, Switzerland

J. Młodzik Institute of Chemical and Environment Engineering, West Pomeranian University of Technology, Szczecin, Poland

Richard Nagy Department of Indoor Technologies and Building Services, Civil Engineering Faculty, Institute of Architectural Engineering, Technical University of Košice, Košice, Slovakia

U. Narkiewicz Institute of Chemical and Environment Engineering, West Pomeranian University of Technology, Szczecin, Poland

L. Naruškevičius Center for Physical Sciences and Technology, Vilnius, Lithuania

Marco Nesarajah Chair of Automation and Energy Systems, Saarland University, Saarbrücken, Germany

Cristian Nichita University of Le Havre, Le Havre Cedex, France

E. Norkus Center for Physical Sciences and Technology, Vilnius, Lithuania

N.N. Nurgaliyev D.V. Sokolsky Institute of Organic Catalysis and Electrochemistry, Almaty, Kazakhstan

Y.Y. Nurmakanov D.V. Sokolsky Institute of Organic Catalysis and Electrochemistry, Almaty, Kazakhstan

Takuya Oda Solutions Research Laboratory, Tokyo Institute of Technology, Tokyo, Japan

A. Olszyna Faculty of Material Science and Engineering, Warsaw University of Technology, Warsaw, Poland

A. Ospanova D.V. Sokolsky Institute of Organic Catalysis and Electrochemistry, Almaty, Kazakhstan

Zuzana Palkova Slovak University of Agriculture in Nitra, Nitra, Slovak Republic

V. Palma University of Salerno, Fisciano, SA, Italy

Gheorghe Paltanea Politehnica University of Bucharest, Bucharest, Romania

Stanislaw Piesiak The Lower Silesian University of Entrepreneurship and Technology, Polkowice, Poland

D. Pisano University of Salerno, Fisciano, SA, Italy

Dorina Popovici Politehnica University of Bucharest, Bucharest, Romania

Y. Ren Advanced Photon Source, Argonne National Laboratory, Argonne, IL, USA

Adriana Reveiu Bucharest University of Economic Studies, Bucharest, Romania

Fernando M.F. Rhen Department of Physics and Energy, Materials and Surface Science Institute, University of Limerick, Limerick, Ireland

Rouzbeh Riazi Faculty of New Science and Technologies, Tehran, Iran

A. Ricca University of Salerno, Fisciano, SA, Italy

C. Riccardi Dipartimento di Fisica, Università degli Studi di Milano-Bicocca, Milano, Italy

David Richardson Department of Physics and Energy, Materials and Surface Science Institute, University of Limerick, Limerick, Ireland

H.E. Roman Dipartimento di Fisica, Università degli Studi di Milano-Bicocca, Milano, Italy

A. Rostami Photonic and Nanocrystal Research Lab. (PNRL), Faculty of Electrical and Computer Engineering, University of Tabriz, Tabriz, Iran; Photonics Research Group, School of Engineering Emerging Technology, University of Tabriz, Tabriz, Iran

G. Rostami Photonics Research Group, School of Engineering Emerging Technology, University of Tabriz, Tabriz, Iran

Concetta Ruocco University of Salerno, Fisciano, SA, Italy

Junichi Ryu Research Laboratory for Nuclear Reactors, Tokyo Institute of Technology, Meguro, Tokyo, Japan

Subhi Saq'an Bio-Medical Physics Laboratory, Department of Physics, Jordan University of Science & Technology (JUST), Irbid, Jordan

Antans Sauhats Institute of Power Engineering, Riga Technical University, Riga, Latvia

Anna Sedlakova Civil Engineering Faculty, Institute of Architectural Engineering, Technical University of Košice, Košice, Slovakia

A. Selskis Center for Physical Sciences and Technology, Vilnius, Lithuania

S. Semaoui Centre de Développement des Energies Renouvelables, Algiers, Algeria

Maziar Shafaei Faculty of New Science and Technologies, Tehran, Iran

V. Shavrov Kotelnikov Institute of Radio-Engineering and Electronics of RSA, Moscow, Russia

Kinga Skalska Faculty of Process and Environmental Engineering, Lodz University of Technology, Lodz, Poland

Ion Smeureanu Bucharest University of Economic Studies, Bucharest, Romania

K.J. Son Radioisotope Research Division, Korea Atomic Energy Research Institute (KAERI), Daejeon, Korea

I. Stankevičienė Center for Physical Sciences and Technology, Vilnius, Lithuania

Pascal Stoffels ZeMA gGmbH, Saarbruecken, Germany

Huaizhi Su State Key Laboratory of Hydrology-Water Resources and Hydraulic Engineering, Hohai University, Nanjing, China

Seyed Amin Tabatabaei Agent Systems Research Group, Department of Computer Science, VU University Amsterdam, Amsterdam, The Netherlands

L. Tamašauskaitė-Tamašiūnaitė Center for Physical Sciences and Technology, Vilnius, Lithuania

Mohsen Tavakol Faculty of New Science and Technologies, Tehran, Iran

Ladislav Tazky Civil Engineering Faculty, Institute of Architectural Engineering, Technical University of Košice, Košice, Slovakia

Adem Tekin Informatics Institute, Istanbul Technical University, Maslak Istanbul, Turkey

Vyacheslav Teslenko Lavrentyev Institute of Hydrodynamics SB RAS, Novosibirsk, Russia

V.M. Torchinsky Joint Institute for High Temperatures of Russian Academy of Sciences (JIHT RAS), Moscow, Russian Federation

Jan Treur Agent Systems Research Group, Department of Computer Science, VU University Amsterdam, Amsterdam, The Netherlands

Y.R. Uhm Radioisotope Research Division, Korea Atomic Energy Research Institute (KAERI), Daejeon, Korea

Inga Umbrasko Institute of Power Engineering, Riga Technical University, Riga, Latvia

A. Unich Dipartimento di Ingegneria Industriale e dell'informazione, Second University of Naples, Aversa CE, Italy

J. Vaičiūnienė Center for Physical Sciences and Technology, Vilnius, Lithuania

Renata Varfolomejeva Institute of Power Engineering, Riga Technical University, Riga, Latvia

Michael Vielhaber Saarland University, Saarbruecken, Germany

Silvia Vilčeková Faculty of Civil Engineering, Institute of Environmental Engineering, Technical University of Košice, Košice, Slovakia

Jaroslav Vojtus Department of Architectural Engineering, Faculty of Civil Engineering, Technical University of Kosice, Kosice, Slovak Republic

R.J. Wróbel Institute of Chemical and Environment Engineering, West Pomeranian University of Technology, Szczecin, Poland

Meng Yang College of Water Conservancy and Hydropower Engineering, Hohai University, Nanjing, China

V.S. Yemelyanova Research Institute of New Chemical Technologies and Materials, Almaty, Kazakhstan

Takashi Yoshikawa Kindai University Technical College, Nabari-shi, Japan

A. Zabielaite Center for Physical Sciences and Technology, Vilnius, Lithuania

V. Zaichenko Joint Institute for High Temperature, Russian Academy of Sciences (JIHT RAS), Moscow, Russian Federation

Pawel Zajac Wrocław University of Technology, Wrocław, Poland

G.D. Zakumbaeva D.V. Sokolsky Institute of Organic Catalysis and Electrochemistry, Almaty, Kazakhstan

Janusz Zarębski Department of Marine Electronics, Gdynia Maritime University, Gdynia, Poland

H. Zeraia Centre de Développement des Energies Renouvelables, Algiers, Algeria

Levent Çolak Engineering Faculty, Mechanical Engineering Department, Başkent University, Baglica Campus, Ankara, Turkey

Meriç Yavuz Çolak Faculty of Health Sciences, Department of Healthcare Management, Başkent University, Baglica Campus, Ankara, Turkey

Ž. Činčienė Center for Physical Sciences and Technology, Vilnius, Lithuania

Monika Čuláková Faculty of Civil Engineering, Institute of Environmental Engineering, Technical University of Košice, Košice, Slovakia

B. Šimkūnaitė-Stanygienė Center for Physical Sciences and Technology, Vilnius, Lithuania

Martin Štefanco Department of Indoor Technologies and Building Services, Civil Engineering Faculty, Institute of Architectural Engineering, Technical University of Košice, Košice, Slovakia

A. Žielienė Center for Physical Sciences and Technology, Vilnius, Lithuania

Part I

General Issues

Reliability Importance Measures of Components for Stand-Alone Hybrid Renewable Energy Microgrid

Abubakar Abdulkarim, Sobhy M. Abdelkader and D. John Morrow

Abstract This paper presents the results of a new approach on the reliability analyses of standalone hybrid microgrid based on components importance measures. The microgrid presented consists of wind, photovoltaic, diesel generator and energy storage systems for supplying an isolated load. Reliability models of the customers connected to the Microgrid with the mentioned components have been model using a new approach based on reliability block diagram algebra. Different microgrid design structures and component measures on the reliability of load points were examined on a standard low voltage benchmark microgrid. Finally, other novel approaches on how to rank components that make up standalone microgrid were investigated for reliability. The results show the possibility of modeling and reliability analyses of standalone microgrid using the proposed technique. Additionally, this paper presents results of the contribution of components to the system reliability based on the structure of microgrid. The work could be used in identifying direction, priority, upgrading and suggest the most efficient way to operate and maintain a microgrid.

1 Introduction

In the field of reliability evaluation of standalone microgrid, the reliability is usually evaluated from the point of demand and supply [1]. Other factors that may influence the reliability of standalone microgrid were not given the expected attention or no attention is given.

These factors include the reliability of non-electric components, the network structure and the type of fault. Hence the need to revisit the reliability of microgrid based on these factors. Some recent works in this field includes the influence of protection system systems and operating conditions on the reliability of microgrid

A. Abdulkarim (✉) · S.M. Abdelkader · D. John Morrow
Energy, Power and Intelligent Control, School of Electronics, Electrical Engineering
and Computer Science, Queen's University Belfast, Belfast, UK
e-mail: abdulkarim02@qub.ac.uk

[1]. Another effort [2] analyzed the reliability of microgrid considering load and generation. Model for the analysis of microgrid consisting of both wind and pv system has been developed in [3]. The influence of repair rate on the reliability analysis of microgrid has been carried out [4]. Other efforts include the investigation of the impact of distributed generation on the reliability of microgrid [5]. However, previous studies have failed to study the impact of components on the reliability of microgrid and the impact of network structure [6]. In this work, the influences of some selected components on the microgrid reliability are researched using reliability measure of components importance on different microgrid designs.

2 Components Importance Analyses

The most widely measure in the power industry to carried out the analyses are Barbiums and Components Importance. Barbiums importance measure defined the maximum loss in system reliability when a particular component i transit from the perfect function to the condition of certain failure. Therefore, the index could be used to estimate the probability of a component being responsible for system failure at time t [7]. The mathematical expression is given in (1), that is

$$I_i^B = \frac{\partial R_s(t)}{\partial R_i(t)} = R_s(t; R_i(t) = 1) - R_s(t; R_i(t) = 0) \quad (1)$$

where, I_i^B = Birnbahum importance of components i , R_s = system reliability at time t and $R_i(t)$ = reliability of components i at $t = t$.

Another proposed measure of importance that is an extension of equation (1) is called Component Importance (CI) measure. The measure is use to determine the probability that a component was responsible for system failure at time t . Therefore, this measure uses the components unreliability $F_i(t)$ and system unreliability $F_s(t)$ that were not considered in (1), the expression for the determination of CI is defined in (2).

$$I_i^{CI} \times \frac{F_i(t)}{F_s(t)} = [R_s(t; R_i(t) = 1) - R_s(t; R_i(t) = 0)] \times \frac{F_i(t)}{F_s(t)} \quad (2)$$

Other measures used to quantitatively evaluate the impacts of particular component on the system reliability includes network reliability achievement worth (NRAW) and network reliability reduction worth (NRRW) as defined in [8]. Therefore, NRAW can be define as the ratio of the actual system reliability when component i is in perfect condition ($R_i(t) = 1$) to the actual system reliability $R_s(t)$. However in order to quantify the maximum possible increase in the system reliability, the expression defined in (3) is used.

$$NRAW_i = \frac{R_s(t; R_i(t) = 1)}{R_s(t)} \quad (3)$$

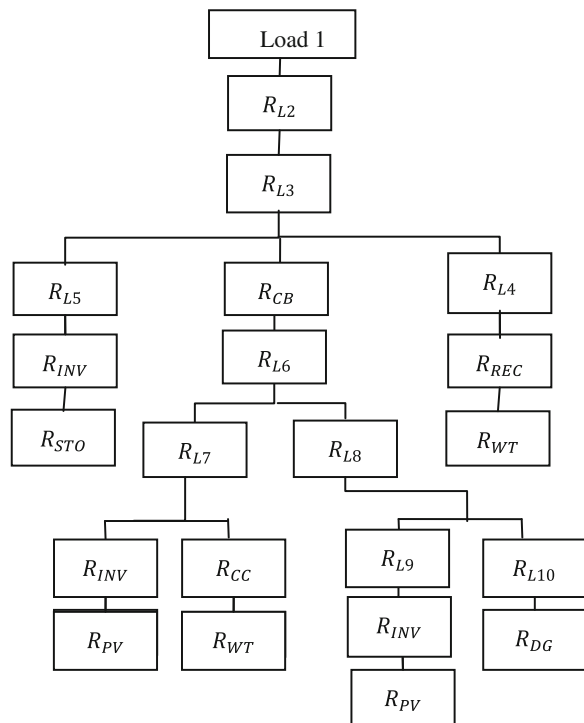
On the other hand NRRW defines an index for measuring the damage caused to the systems reliability by a component i , the mathematical relation is as given by

$$NRRW_i = \frac{R_s(t)}{R_s(t; R_i(t) = 0)} \quad (4)$$

3 Reliability Block Diagram of Standalone Benchmark Microgrid

The study is based on the assumption that a low voltage microgrid is running on island mode for a period of time t . The microgrid consist of loads points 1–5 connected to the points of generation through AC bus and consists of sources such as photovoltaic, wind turbine, storage system and a diesel generator. The details parameters of this network can be found in [9, 10]. The reliability block diagram for load 1 is as shown in Fig. 1, from the reliability block diagram, the reliability model of each load points was derived based on the concept of reliability block diagram theorems. Having obtained the reliability expression, the standard failure rates in the standard Military Handbook were used in simulating the reliability model of the

Fig. 1 Reliability block diagram of load point 1



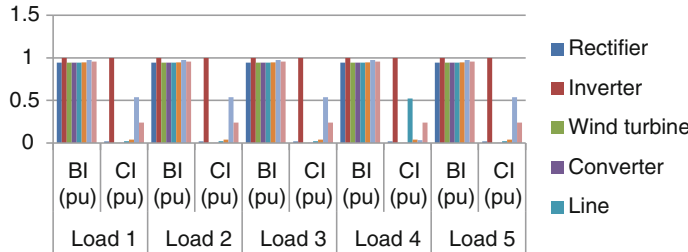


Fig. 2 Reliability measures (BI and CI) for load points 1–5

Table 1 Measures (RAW and RRW) for different network structure

Comp.	DC		AC		AC-DC	
	RAW	RRW	RAW	RRW	RAW	RRW
INV	1.0605632	∞	1.0000004	1.0000864	1.001878	1.030547
STO	1.0000003	0.9999797	1.0000001	1.0000049	1.0000001	1.000006
WT	1	0.9999948	1	1.0001434	1	1.000002
CONV	1.0000001	1.0000628	1.0000002	1.0001434	1	1.000019
LN	1.0014111	∞	1.0014114	∞	1.0015769	∞
PV	1.0000002	0.9999372	1	1.0000059	1	1.000019
DG	1.0000001	0.9999956	1.0000004	1.0000111	1.0018866	1.061469

load 1. The simulation was run for a period of 1 year and the results are presented in Fig. 2. Components importance analyses process of load 2–5 is the same with load 1 and the result of the analysis is presented in Table 1. The procedure is applied on different configuration of hybrid microgrid system; three most common configurations were compared for reliability. This includes DC couple [11], AC coupling [12] and AC-DC coupling microgrid [13]. The results of the analysis are presented in Table 1.

4 Conclusion

The work has proposed the application of components importance metrics namely Birnbaum, Criticality Importance, reliability achievement worth and reliability reduction worth in the reliability study of microgrid structure. As indicated by the result, the most important component is inverter. The components ranked second and third are diesel generator and the storage unit. The least important components are wind turbine and rectifier units, it should be noted that this trend is uniform throughout the analyses. The results obtained from the analyses have indicated that, the location of the load on isolated microgrid does not affect the rank contribution of the component to the system reliability. It can be seen that the components that

makes up microgrid have different level of importance with respect to the system reliability. It has been observed that inverter unit has the highest BI measure and CI. Other measure evaluated at system level includes RAW and RRW, the result obtained indicated the rank of component based on these measure depend on the type of microgrid coupling.

References

1. X. Xu, J. Mitra, T. Wang, L. Mu, Evaluation of operational reliability of a microgrid using a short-term outage model. *IEEE Trans. Power Syst.* **29**(5), 2239–2247 (2014)
2. M. Ghahderijani, S. Barakati, S. Tavakoli, *Reliability evaluation of stand-alone hybrid microgrid using Sequential Monte Carlo simulation*. In Renewable Energy and Distributed Generation (ICREDG), Second Iranian Conference on, Tehran (2012)
3. H. Wei, H. Zijun, F. Li, T. Hongliang, Z. Li, *Reliability evaluation of Microgrid with PV-WG hybrid system*. In Electric Utility Deregulation and Restructuring and Power Technologies (DRPT), 4th International Conference on, Weihai, Shandong (2011)
4. M. Theristis, I. Papazoglou, Markovian reliability analysis of standalone photovoltaic systems incorporating repairs. *IEEE J. Photovoltaics* **4**(1), 414–422 (2014)
5. S. Kennedy, *Reliability evaluation of islanded microgrids with stochastic distributed generation*. In Power & Energy Society General Meeting. PES '09. IEEE, Calgary, AB (2009)
6. L. Qiao, A summary of optimal methods for the planning. *J. Energy Power Eng., Sci. Res.* **5**, 992–998 (2013)
7. W. Wang, J. Loman, P. Vassiliou, *Reliability importance of components in a complex system*. In Reliability and Maintainability, Annual Symposium—RAMS, IEEE (2004)
8. M. Anthony, R. Arno, N. Dowling, R. Schuerger, Reliability analysis for power to fire pump using fault tree and RBD. *IEEE Trans. Ind. Appl.* **49**(2), 997–1003 (2013)
9. Z. Li, Y. Yuan, F. Li, *Evaluating the reliability of islanded microgrid in an emergency mode*. In Universities Power Engineering Conference (UPEC), 45th International, Cardiff, Wales (2010)
10. P. Stavros, H. Nikos, S. Kai, *A Benchmark low voltage microgrid network*. In Power systems with dispersed generation: technologies, impact on development, operation and performance. Athens, Greece (2005)
11. L. Saeed, T. Farid Lotfi, G. Mohammad, Optimal design of a hybrid solar—wind-diesel power system for rural electrification using imperialist competitive algorithm. *Int. J. Renew. Energy Res. IJRER* **3**(2), 403–411 (2013)
12. S.M. Sayeef, *Optimisation of component sizes for a hybrid remote area power supply system*. In Proceedings of the 19th Australasian Universities Power Engineering Conference, Australia (2009)
13. J. Fatemeh, H.R. Gholam, *Optimum design of a hybrid renewable energy system*. In Renewable Energy—Trends and Applications, Iran, Majid Nayeripour and Mostafa Kheshti (2011), pp. 231–250. ISBN 978-953-307-939-4

Statistical Analyses of Wind and Solar Energy Resources for the Development of Hybrid Microgrid

Abubakar Abdulkarim, Sobhy M. Abdelkader and D. John Morrow

Abstract In this paper, a procedure for the statistical analyses of wind and solar energy resources are investigated in order to determine the accurate frequency distribution for the development of hybrid microgrid. The frequency distributions used for wind speed data analysis include Weibull, Rayleigh and Gamma distribution functions. On the other hand the frequency distributions used for the analysis of solar radiation data include Weibull, Logistics, lognormal, Beta and Gamma functions. The performance of the probability distributions used in the wind speed analyses are based on the error evaluations between the predicted and the theoretical wind power densities of the site. Similarly, the performance of the probability distribution functions used in the solar radiation data were judged based on Kolmogorov-Smirnov, Anderson-Darling and Chi-Square tests. The goodness of fit tests (GOF) results of the wind speed analyses show that Weibull distribution performed better compared to Rayleigh and Gamma distributions. On the other hand Beta distribution fitted the solar radiation data better than all other distributions models.

1 Introduction

Solar and wind energy are non-dispatchable sources, site dependant, pollution free and therefore act as one of the leading potential sources of alternative energy. However, the factors that judge the possibility of utilizing these sources of energy are the solar and wind energy potentials of the site under consideration.

To accurately assess the renewable energy potentials of any site for production of electrical energy, historical records of the wind speed or solar radiation data are analysed. This acts as the preliminary step in siting the hybrid energy system.

A. Abdulkarim (✉) · S.M. Abdelkader · D. John Morrow
Energy, Power and Intelligent Control, School of Electronics, Electrical Engineering
and Computer Science, Queen's University Belfast, Belfast, UK
e-mail: abdulkarim02@qub.ac.uk

The factors to be analyse if available all includes wind speed and its prevailing direction, turbulence intensity, wind distribution, solar radiation, scale and shape parameters and class etc. In order to use the historical record of the site, it is recommended that a data for at least 30 year period should be used. Some of the drawback of the historical approach includes difficulty in getting accurate data, time consuming, technical challenges and very expensive. This results in some researchers into analyses with data for a period between 1 and 5 years. This may not accurately result in an optimum performance of the system under consideration. Recently, the statistical methods are gaining popularity. Some of the reasons leading to the popularity of the statistical methods include economics, time and possibility of predicting the behaviour of the system with less error to mention just a few. Therefore, in this work, the feasibility study of the site under consideration for hybrid microgrid application is conducted by statistical judgments.

Recently efforts been made in analysing the renewable energy potentials of a particular site include the statistical analysis of wind speed data [1] and Turkey [2]. In some site such as Pakistan [3] Weibull distribution was not suitable for them. Wind energy potentials of India [4] and in [5], the wind energy potential of Penjwen region, Iraq has been investigated using Weibull distribution model. On the other hand, the application of statistical analysis of solar radiation data in Taiwan has been considered in [6]. Others include the solar energy variations in some sites in Nigeria [7] and fitting Weibull distribution to Ultraviolet radiation data in Kuwait [8]. It can be observed that literature for the assessments of both wind and solar energy potentials of a particular site is very limited. Therefore, the paper demonstrated the applications of some statistical models to fit the wind and solar energy data of the sites under consideration for the development of hybrid renewable energy system. Most of the research effort focused on the use of Weibull distribution. It has been established that, the probability distribution function for predicting the behaviour of wind and solar resources may be different from one site to another. In this work the mentioned probability distributions are employed to fit both solar and wind energy of a particular site separately. This is because the design of hybrid renewable energy systems is based on the performance of individual system [9]. The mathematical or statistical judgments used are based on some factors such as accuracy in fitting the available data from the site.

2 Determination of the Mean Wind Speed of the Sites

The analysis starts from the determination of the mean wind speed and acts as important parameter in power generation from wind energy. Therefore, the mean wind speeds for the two sites were obtained from the data collected for a period of 1 year. The data involved the sample of wind and solar radiation at 5 min interval. The rmc velocity was used in the analysis in order not under estimate the wind energy potentials of the sites as in (1). The average wind power density can be

defined as the annual average power per unit area as defines in [10]. The expression for the power used in the analysis is given in (2).

$$v_{rmc} = \sqrt[3]{\frac{1}{N} \sum_{i=1}^N v_i^3} \quad (1)$$

where v_i is the wind speed observation at i th time, v_{rmc} is the root means square cube wind speed and N is the number of wind speed data points.

$$\overline{P_w} = \frac{1}{2} \rho \sum_{i=1}^N P(v_i) \cdot v_i^3 \quad (2)$$

where $\overline{P_w}$ the average wind is power density at the given site, and ρ is the observed air density if available. The air density is assumed to be $1.225 \text{ (kg/m}^3\text{)}$.

3 Probability Density Functions for Wind Speed Data

3.1 Weibull Distribution

Weibull distribution is one of the most widely used probability distribution in the statistical analysis of experimental data. The most important property of this distribution is that it has no specific shape [11]. The sites average power densities can be determine based on shape and scale parameters [12]. The Weibull average wind power density is calculated using (3).

$$WPD_w = \frac{1}{2} \times \rho \times c^3 \Gamma\left(1 + \frac{3}{k}\right) \quad (3)$$

3.2 Rayleigh Distribution

The second proposed probability distribution used in the analysis is called Rayleigh distribution and its probability density function is given in [13]. The Rayleigh probability density function is also defined in [13]. The Raleigh wind power density can be defined in terms of c and k parameters as in (4).

$$WPD_R = \frac{3}{\pi} \times \rho \times c^3 \sqrt{\frac{\pi}{4}} \quad (4)$$

3.3 Gamma Distributions

The Gamma has similar properties to those of Weibull distribution that is; it is a two parameter distribution with shape α and scale β parameter defined in [12]. Similarly, the wind power density of gamma function in term of c and k parameter can be define as

$$WDP_{Gam} = \frac{1}{2} \rho \times c^3 [k(k+1)(k+2)] \quad (5)$$

3.4 Goodness of Fits

In this work, the performance of the models used in predicting the wind power densities of the sites were investigated by evaluating the error between the actual and the predicted powers of different probability density functions as in [5]. Comparison is made by quantifying the errors evaluated such that the closer the error to 0 %, the more accurate the model is in predicting the wind power density of the site.

3.5 Application of the Procedure

Applying the procedure above on a data for both Northern Ireland and Nigeria, the results of the analyses are presented in Table 1. On the whole Weibull distribution fits best in all the sites followed by Gamma distribution; Rayleigh has the least fitting compliance. This has further confirmed that when modelling wind speed for power generation, Weibull distribution could be regarded as the most preferred approach.

4 Analyses of Solar Radiation

In this section, the solar radiation data was analysed by fitting three more distributions. These includes Lognormal distribution in [6], Beta Distribution and Logistic as defined as [3]. On the other hand, solar radiation goodness of fits used in the proposed tests includes Kolmogorov-Smirnov, Anderson-Darling and Chi-Square tests [14]. Application of the procedure presented for the analysis of solar radiation

Table 1 Annual average errors of site in Belfast, UK and Abuja, Nigeria

Parameter		Weibull		Rayleigh		Gamma	
		WPD	Error	WPD	Error	WPD	Error
Ave.	Bel.	194.2	0.02	342.1	0.73	208.2	0.07
	Nig.	173.7	0.03	306.2	0.84	178.7	0.10

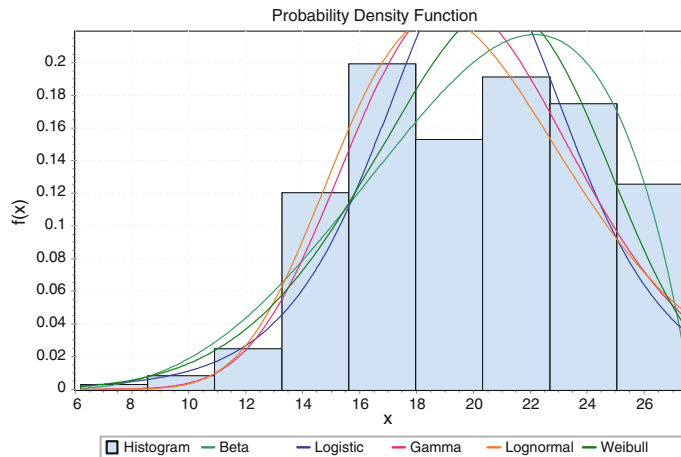


Fig. 1 Average solar radiation Abuja, Nigeria

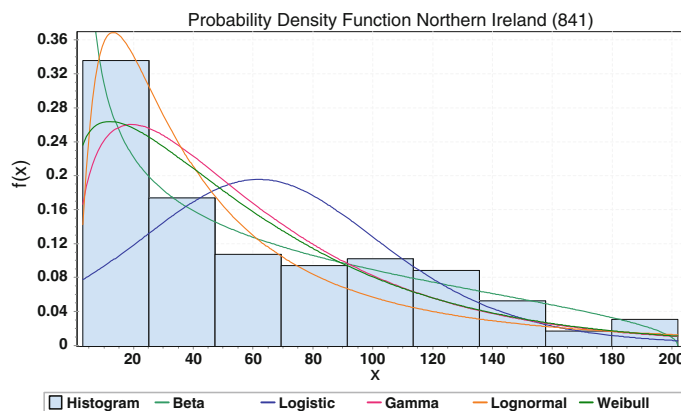


Fig. 2 Average solar radiation Belfast, United Kingdom

data were applied to the solar radiation data for the sites under consideration. The results obtained are presented in Figs. 1 and 2 for Abuja, Nigeria and Belfast, United Kingdom in that order.

5 Conclusion

In this paper, throughout the study, Weibull distribution performed better follow by Gamma and Rayleigh ranked lowest in predicting the average wind power densities of the two sites. The analysis of solar radiation data indicated the good performance

of Beta compared to Gamma, Logistic, Lognormal and Weibull distributions in that order for both Nigeria and Northern Ireland. The findings in this paper can be further use in the areas that are having similar meteorological conditions with the study areas.

References

1. A. Zaharim, A.M. Razali, R.Z. Abidin, K. Sopian, Fitting of statistical distributions to wind speed data in Malaysia. *Eur. J. Sci. Res.* **26**(1), (2009)
2. N.C. Ali, A statistical analysis of wind power density based on the Weibull and Rayleigh models at the southern region of Turkey. *Renew. Energy* **29**, 593–604 (2003)
3. A. Kamran, A.K. Alamgir, A. Sajjad, D.M.K. Amjad, K. Umair, Statistical analysis of wind speed data in Pakistan. *World Appl. Sci. J.* **18**(11), 1533–1539 (2012)
4. V.W. Atul, P. Thatkar, R.K. Dase, T.V. Tandale, Modified anderson darling test for wind speed data. *Int. J. Comput. Sci. Emerg. Technol.* **2**(2), 2044–6004 (2011)
5. S. Ahmed, H. Ohammed, A statistical analysis of wind power density based on the Weibull and Raleigh models of Penjwen region Sulaimani-Iraq. *JJMIE* **6**(2), 135–140 (2012)
6. T.P. Chang, Investigation on frequency distribution of global radiation using different probability density functions. *Int. J. Appl. Sci. Eng.* **8**(2), 99–107 (2010)
7. C.O. Osueke, P. Uzendu, I.D. Ogbonna, Study and evaluation of solar enegry variation in Nigeria. *IJETAE* **3**(6), 501–505 (2013)
8. M. Ghitany, N.F. ElNashar, Fitting Weibull distribution to ultraviolet solar radiation data. *Int. J. Sustain. Energy Taylor Francis* **24**(4), 167–173 (2005)
9. G. Tina, S. Gagliano, *Probability analysis of weather data for energy assessments of hybrid solar/wind power system*. In 4th International Conference on Energy, Environment Ecosystems and Sustainable Development, Algarve, Portugal (2008)
10. M. Patel, *Wind and Solar Power System, Design, Analysis and Operations*, 2nd edn. (CRC Press, Taylor Francis, USA, 2006)
11. R. Billinton, R.N. Allen, *Reliability Evaluation of Engimneering Systemes Concepst and Techniques* (Plenum, New York, 1993)
12. O. Olaope, K. Folly, Statistical analysis of the wind resources at darling for energy production. *Int. J. Renew. Energy Res.* **2**, 250–261 (2012)
13. S. Ahmed, Comparative study of four methods for Weibull parameters for Halabja, Iraq. *Int. J. Phys. Sci.* **8**, 186–192 (2013)
14. R. Kollu, S. Rayapudi, S. Narasimham, K.M. Pakkurthi, Mixture probability distribution functions to model wind speed distributions. *IJEEE* **3**(27), 1–10 (2012)

Entering the Bio Based Economy—Verification of Demand on Education in the Field of Green Economy

Zuzana Palkova

Abstract So far worldwide economy was oil-based. Oil and other examples of fossil energy were used for fuel, for heating, for the production of a wide range of products like plastics, medicines, food additives, etc. This oil-based economy has many consequences—global warming due to a growing production of carbon dioxide, limited quantities of oil, dependency on unstable countries and/or governments. These consequences have led to a search for alternatives for oil in many sectors:

- renewable energy, like wind and solar energy,
- bio-fuel, like bio-diesel and bio-gas,
- production of raw materials for further processing, like fibres and dyes,
- additives, alternatives for plastics, etc.

From this point of view, global climate changes, the greenhouse gas emissions and reduced sources of traditional fossil fuels are one of the most serious environmental problems of present time. This fact was the starting point for Directive 2009/28/EC, which defined two objectives in the area of RES, the mandatory 20 % share of RES in gross final energy consumption in the European Community and the mandatory 10 % share of RES in transport, which all Member States must achieve by 2020. In 2011 was the share of renewable energy sources in total energy production in the European Union 13 % (http://epp.eurostat.ec.europa.eu/portal/page/portal/statistics/search_database). The article presents general state in the Bio Based Economy (Green Economy or BBE) and a way how to increase the attractiveness and accessibility of vocational education and training for employees in green economy in the selected European countries.

Z. Palkova (✉)

Slovak University of Agriculture in Nitra, Tr. A. Hlinku 2,
949 76 Nitra, Slovak Republic

e-mail: Zuzana.Palkova@uniag.sk

1 Introduction

The bio-based economy can and should be to the 21st century what the fossil-based economy was to the 20th century. Agriculture will be core to the bio-based economy, providing source materials for commodity items, e.g. liquid fuels and value-added products such as chemicals and materials [1]. Biomass may be produced in a great number of countries. Preservation of biodiversity is a necessary prerequisite for such a sustainable use of biomass. New applications of biomass may be helpful to develop the economic strength of developing nations, whilst reducing CO₂ emissions [2].

In the present time, the research is going on to find new applications in BBE. As example is Slovak University of Agriculture in Nitra. Since 2013 the Slovak University of Agriculture in Nitra builds the research centre AgroBioTech focused on the area of Agrobiology, biotechnology and technological processes like as using of stem cells within the bioenergy conversion of biomass into second-generation of biofuels [3].

The survey aimed the general state in the Bio Based Economy and related education—quantitative and foremost qualitative—in the agro/processing sector in selected European countries—Poland, Slovakia, Cyprus, Bulgaria and Romania [4].

Actual state of Bio Based Economy in partners countries: Bio-based resources are renewable, widely distributed, available locally, moldable, anisotropic, hydroscopic, recyclable, versatile, non-abrasive, porous, viscoelastic, easily available in many forms, biodegradable, combustible, compostable, and reactive [5].

For all economies, and Bio Based as well, crucial role play primary energy sources. From this point of view, the situation in investigated countries are rather different—Poland has the biggest sources of coal and water energy while in Slovakia is on a first place the nuclear energy followed by water energy. Cyprus mainly uses the solar energy, probably thanks to its geographical location (Table 1).

According to the EU Directive 2009/28/EC the renewable energies are: wind, solar, aerothermal, geothermal, hydrothermal and ocean energy, hydropower,

Table 1 Primary energy sources (2012) [6–8]

Table 1.	Poland	Slovakia	Cyprus	Bulgaria	Romania
Coal (Mtoe)	154,320	567.4	—	167.4	7,151.2
Petroleum products (Mtoe)	25.89	10.7	2.39	89.5	9,001.6
Hydropower (MW)	970,128	1,622	—	0.3932	—
Natural gas	12.83	127.2	—	140.3	10,883
Nuclear (Mtoe)		4,047.5	—	234	3,942.3
Biomass/Biogas (MW)	162,241/986,872	118	20.297	—	—
Solar (MW)	1,900	480	66.330	0.070	6.5
Wind (MW)	3,389.541	5	15.951	0.0894	2,000

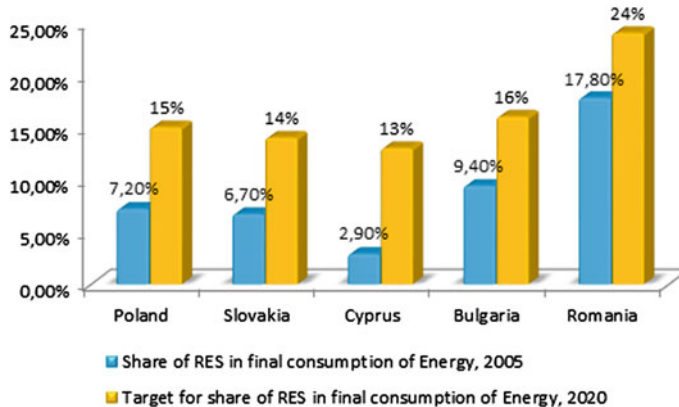


Fig. 1 Mandatory national targets for share of RES in final consumption of energy

biomass, landfill gas, sewage treatment plant gas and biogases [9]. This directive required EU Member States to have submitted national renewable energy action plans by 30 June 2010 and national overall targets for the share of energy from renewable sources in gross final consumption of energy in 2020 (Fig. 1).

In terms of renewable energy sources usage, all partner countries in compliance with the EU Regulation No. 2009/28/EC have adopted national action plans defining total share of renewable energy sources in the country energy mix for 2020—Bulgaria 16 %, Poland 15 %, Slovakia 14 %, Cyprus 13 % and Romania 24 % [10].

According to the latest “The state of renewable energies in Europe 2013” report [11], Poland has the biggest share on the wind energy. Bulgaria most used photovoltaic panels within the OnGrid system with annual growth by almost 400 % for 2012, Slovakia is on the second place with 517.2 MWp. In terms of the OnGrid installations, Poland has the highest cumulated capacity with the 100 % annual growth in 2011 and 2012. There is also a similar situation in the heat and warm water production through thermo solar panels—Poland and Cyprus have the largest area of installed square meters and the highest power, too.

In Bulgaria and Romania there is the highest installed capacity of water energy involving only hydroelectric power stations with maximum 10 MW power. Using the geothermal energy—Romania, Slovakia and Poland. In a case of Bulgaria it’s going on insignificant number of MWth.

Feed-in tariffs exist in all of the investigated countries. These systems are characterized by a specific price, normally set for a period of around 7 years, but for these countries is most typical 15–20 years period. The level of feed-in-tariff is rather similar across all of them (around 10 % of differences), but the scale of supported technologies is rather different.

2 Research and Results

During our research we realized survey and interview with the aim to bridge the gap between the theoretical aspects of interest about the aspects of bio based economy and its exploitation in agrosector and training needs.

The survey was an action aimed at finding some information on whether managers and employees in agrosector have interest, knowledge and skills about the principles of BBE and what are the most important BBE topics for them.

The survey was sent to 300 respondents representing different area of agriculture. The return on the survey was approximately 85 % of the number sent out, which allowed for suitable analysis of the results and the responses were anonymous.

From activities of farms involved in the survey, the combined production dominates—61 % in Bulgaria, 80 % in Slovakia and 50 % in Poland. Plant production is the priority in Romania—80 % while the animal production (33 %) prevails in Cyprus.

Concerning the farm area, large disproportions were found out. In Slovakia, large farms (84 %) over 1000 ha dominate while in Poland (80 %) and in Cyprus (50 %) most farms are smaller than 10 ha. In Bulgaria and Romania there are middle farms with area from 10 to 1000 ha.

Information about the existence of the BBE knowledge was a first question within the “training” block. Most respondents—60 % in Poland, 89 % in Slovakia, 97 % in Cyprus, 53 % in Bulgaria and 97 % in Romania, informed that they have this knowledge even if at the different qualitative level (Fig. 2).

More than 85 % of respondents in more or less each country think that it is important for the organisation to have employees with BBE knowledge and experiences—100 % in Romania, 97 % in Cyprus, 93 % in Poland, 76 % in Slovakia and 64 % in Bulgaria (Fig. 3).

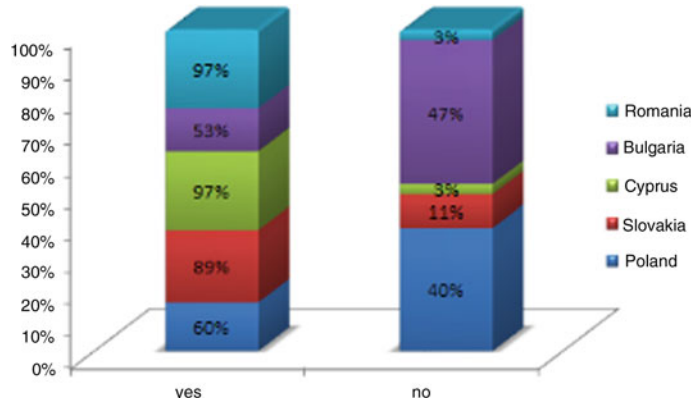


Fig. 2 Do you have knowledge about BBE?

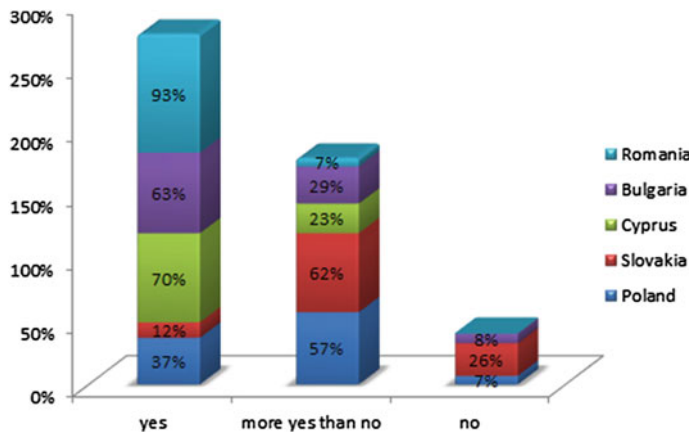


Fig. 3 Do you think a training course about BBE would be of value to your organisation?

Almost 90 % of all respondents appreciate the usefulness of the online training in the relevant topics. On the contrary, 26 % of sceptical Slovak respondents don't consider the online training to be useful.

Allowing a multiple answer in the field of questions dedicated to biomass and biogas usage, using biomass and biogas for energy production was marked most—100 % in Slovakia and 97 % in Romania. Heat production and waste handling was the next following alternative. Using biomass and biogas is the least expected for motor vehicles propulsion—13 % in Poland and Romania (Fig. 4).

There is generally an interest about small biogas stations—just 7 % of respondents in Cyprus and 1 % in Poland are interested in big biogas stations.

Results of survey in particular highlighted the positive impact of the renewable energy sources exploitation, such as diversification of primary energy sources, increase of energy self-sufficiency of the institution or, in the case of biomass, more efficient waste management in agricultural production.

As the biggest problem in all partner countries was identified inadequate legislation and bureaucracy by the authorities as well as by the owners of energy distribution networks. Respondents indicated as more negative reluctance to go to the farm owners demanding investment activities without the strong support of national, respectively local governments or the European Commission.

As one of the reasons for this fact has been cited lack of good practices—functional and cost-effective installation and lacks clear information about the latest technologies.

From the educational activities point of view respondents highlighted the needs of formal and informal education about Bio Based Economy, especially in the field of renewable energies, with emphasis on the current, brief and accurate information, supported by case studies and examples of good practice. Suitable forms of education were mentioned in particular e-learning courses supported by “live” case

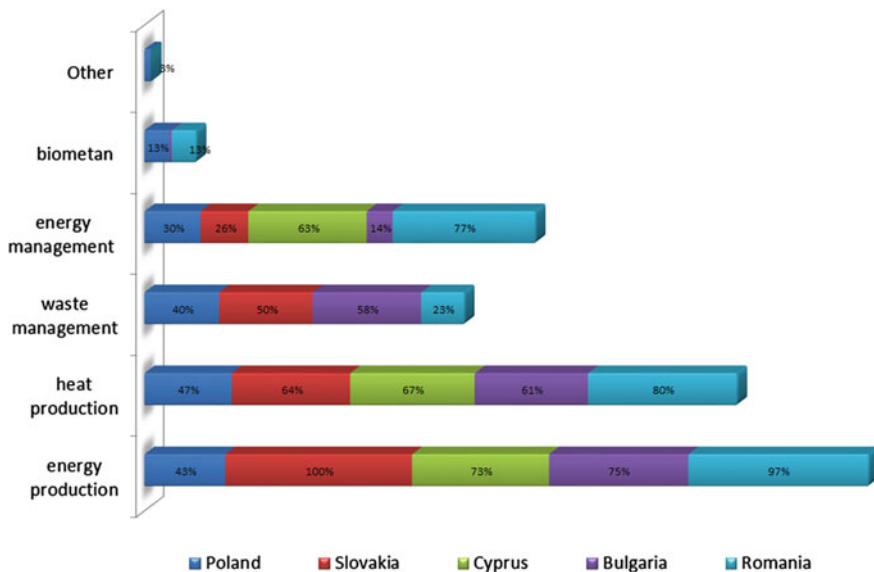


Fig. 4 What do you expect to using biomass/biogas from agricultural production?

studies and presentations of examples of good practice. The participation of lecturers with international experience is highly appreciated.

As appropriate for the field of education have been identified topics from biomass and biogas, waste management, which consider as a priority by respondents in all countries. In Romania and Cyprus, because of their climatic conditions, were also interested in wind and solar power.

Problematic factors of education and practical implementation of the acquired knowledge, respondents identified primarily lack of time and lack of really valuable training courses/activities. Moreover, respondents emphasized the necessity to support these educational activities.

3 Conclusion

The objective of this article is to present current state of the art in terms of understanding and using the Bio Based Economy in selected EU countries—Poland, Slovakia, Cyprus, Bulgaria and Romania. Individual partner countries are different in area of the territory and in number of inhabitants but also in the GDP rate and in climate conditions involving all climate zones within Europe.

Documents passed by the European Commission concerning general characteristics of using the RES, the electricity production from the RES, heating and

cooling, using biofuels and water energy, are the basis for national legislations in the field of using the RES and BBE in all investigated countries.

In terms of understanding the Bio Based Economy, on the basis of the results of our research, seems to be proved that the respondents have an open mind towards environmental conscious, and follow the renewable energy sources.

From the educational activities point of view, the survey confirmed the needs of formal and informal education in the field of Bio Based Economy, with emphasis on the current, brief and accurate information, supported by case studies and examples of good practice. Suitable forms of education were mentioned in particular e-learning courses supported by “live” case studies and presentations of examples of good practice.

As appropriate for the field of education have been identified topics from biomass and biogas, waste management, which consider as a priority by respondents in all countries. In Romania and Cyprus, because of their climatic conditions, were also interested in wind and solar power.

Acknowledgments This research has been founded with support from the European Commission. The content of this document does not necessarily reflect the view or legislation of the European Commission. Neither the European Commission nor the project partners or any person acting on behalf of the Commission is responsible for the use that might be made of the information in this document.

References

1. R.W.F. Hardy, The bio-based economy. Trends in new crops and new uses, pp. 11–16 (ASHS Press, Alexandria, 2002)
2. J. Sanders, D. Van der Hoeven, Opportunities for a bio-based economy in the Netherlands. *Energies* **1**, 105–119 (2008)
3. <http://agrobiotech.uniag.sk>
4. <http://www.rubigas.eu>
5. R.M. Rowell, in *The state of art and future development of bio-based composite science and technology towards the 21st century*, ed. by Y.S. Hadi. Proceedings: The Fourth Pacific Rim Bio-Based Composite Symposium (Bogor, Indonesia, 1998)
6. http://epp.eurostat.ec.europa.eu/portal/page/portal/statistics/search_database
7. <http://www.erec.org/media/publications/roadmap-2020.html>
8. http://europa.eu/legislation_summaries/energy/index_en.htm
9. http://ec.europa.eu/energy/renewables/reports/reports_en.htm
10. http://ec.europa.eu/energy/renewables/action_plan_en.htm
11. http://www.energies-renouvelables.org/observer/stat_baro/barobilan/barobilan13-gb.pdf

Hybrid Power System Supply for Electric Vehicles

Marian Gaiceanu and Razvan Buhosu

Abstract In this paper a hybrid power system for electric vehicles is proposed. The power system combines two complementary technologies: fuel cells and one storage element (supercapacitor). The objective of this paper is to maintain a high level of reliability with minimal cost through optimal design of a hybrid electric vehicle system. For this reason, it is presented the optimum design method of a hybrid power generation system. The primary objective of this study was to propose a strategy for the control of an electric vehicle powered by a source consisting of a fuel cell main source and the auxiliary power supercapacitor. The fuel cell supply is made by using the electrolysis of water. Modelling and control design of the hybrid system is validated by using the Matlab/Simulink software environment.

1 Introduction

Renewable energy resources exploitation conducts to the reduction of the greenhouse gases emissions in the atmosphere [1–3]. Technical achievements in the fuel cells were attained by NASA to power the Gemini Program in 1963 (PEMFC stacks manufactured by General Electric), and the Apollo in 1968. The first electric tractor based on fuel cells was made in the United States (containing a 15 kW AFC) in 1960. The objective of this paper is to describe an autonomous hybrid-system that maintains a high level of reliability with minimal cost through optimal design of the component. Through the numerical simulation and appropriate design, optimal sizes of the various components of the hybrid system have been determined [4].

M. Gaiceanu (✉) · R. Buhosu

Dunarea de Jos University of Galati, 47 Domneasca Street, Galati, Romania
e-mail: marian.gaiceanu@ugal.ro

R. Buhosu
e-mail: razvan.buhosu@ugal.ro

2 Numerical Simulation of the Hybrid Power System Supply for Electric Vehicle

There are different kinds of fuel cell supply systems. In general, the fuel cell supply system consists of a reformer, hydrogen storage, stack and a static power converter to deliver the required electrical energy to the consumers. In order to obtain a constant DC link voltage with an increased value, the unidirectional boost power converter has been used (Fig. 1). The common DC link of the hybrid power system consists of the output of the boost power converter connected to the output of the reversible buck boost converter (Fig. 2).

Fuel Cell mathematical model: Voltage /current characteristic of a fuel cell can be expressed by [2]:

$$v_f = E - A \cdot \ln\left(\frac{i_f + i_n}{i_0}\right) - R_m(i_f + i_n) + B \cdot \ln\left(1 - \frac{i_f + i_n}{i_L}\right) \quad (1)$$

where E is the reversible power without loss of fuel cell; i_f , i_0 and i_L display the output current, exchange current and current limiter. Also, A and B are the slope of the Tafel line and the mass transfer constant, i_n is the internal current, and R_m is the internal membrane and contact resistances ($E = 27$ V, $A = 1.35$ V, $B = 1.19$ V, $R_m = 0.045$ Ω , $i_0 = 6.54 \times 10^{-3}$ A, $i_n = 230 \times 10^{-3}$ A, $i_L = 100$ A).

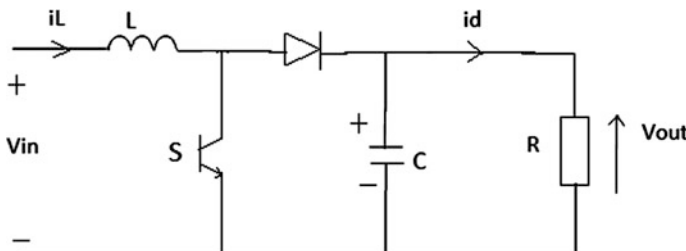


Fig. 1 Basic schematics of the boost converter

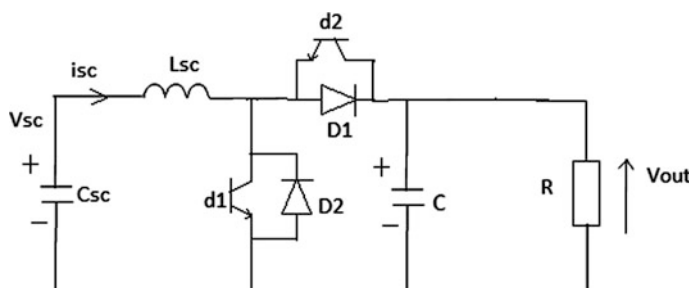


Fig. 2 Reversible buck /boost converter

The electrolyser mathematical model: The electrolysis is a way to obtain hydrogen from water. The electrolysis is the reverse process of the fuel cell. Mathematical model of the electrolyser consists of:

$$n_{H_2} = \frac{\eta_F \cdot n_n \cdot i_e}{2F}, \quad \eta_F = 96.5 \times \left[e^{\frac{0.09}{i_e} - \frac{75.5}{i_e^2}} \right] \quad (2)$$

n_{H_2} = Hydrogen production rate, mol s⁻¹;

η_{H_2} = Faraday's efficiency;

n_c = the number of electrolyser cells in series;

i_e = electrolyser current [A];

F = Faraday constant [C kmol⁻¹];

By using the equation (2), the Simulink model of the electrolyser could be done.

DC-DC unidirectional power converter: In order to eliminate the consequences of the load fluctuations and source variability, static power converters correlated with an adequate battery or supercapacitors are used. In order to connect fuel cell to the load, the unidirectional boost power converter is used (adaptation of the voltage level $V_{fc} = 12.5$ V to $V_{load} = 42$ VDC).

$$\begin{cases} L \frac{di_L}{dt} = V_{in} - (1 - d)V_{out} - ri_L \\ C \frac{dV_{out}}{dt} = (1 - d)i_L - \frac{V_{out}}{R} \end{cases} \quad (3)$$

where r is the internal resistance of the inductance L .

Fuel cell hybrid vehicle system: Proton Exchange Membrane Fuel Cell has been considered in this paper. The hybrid system consists of a DC link, unidirectional DC-DC boost power converter, and current controlled by a PI controller associated with a conventional PWM, a storage device (supercapacitor) connected to the DC link through a 2 quadrants DC-DC converter, current controlled by a hysteresis regulator.

Supercapacitor mathematical model and the associated power converter: Buck /boost reversible power converter is connected between the supercapacitor and the DC link (Fig. 3). The circuit is described by the following equations:

$$\begin{cases} C \frac{dV_{out}}{dt} = (1 - u)i_{sc} - \frac{V_{out}}{R} \\ L_{sc} \frac{di_{sc}}{dt} = V_{sc} - (1 - u)V_{out} - r_{sc} \cdot i_{sc} \\ V_{sc} = -\frac{1}{C_{sc}} \int i_{sc} + V_{sc0} \end{cases} \quad (4)$$

Control strategy: Control is achieved by conventional voltage control of the DC link voltage, and of the load current.

Proportional integral regulator has been involved (v_{busREF} DC link voltage) for the DC link voltage control. The voltage loop (Fig. 4) uses the energy stored in the

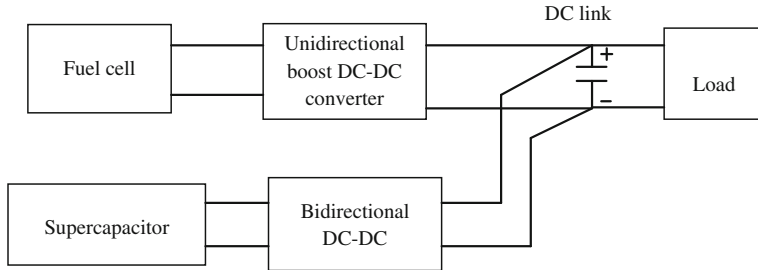


Fig. 3 Hybrid system structure

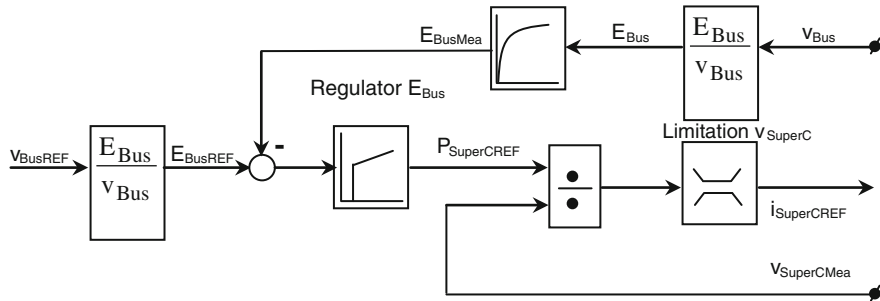


Fig. 4 DC link voltage control loop

DC link and the power supplied by the storage element as the control variables. This change of variable allows to the linear systems theory to be applied.

The term $E_{\text{Bus}}/v_{\text{Bus}}$ is the function that allows the calculation of stored energy in the DC link [2]. The PI controller generates a reference power $P_{\text{superCREF}}$ which is divided by the supercapacitor voltage. The generated reference current of the supercapacitor $i_{\text{superCREF}}$ is delivered to the current loop. The proportional regulator with limited amplitude range $[0, i_{\text{fcRated}}]$, and a limited gradient of growth (in order to respect the constraints associated with the fuel cell operation) is inserted to control the supercapacitor voltage (Fig. 5).

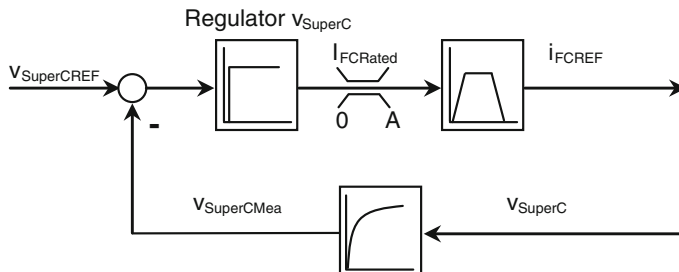


Fig. 5 Supercapacitor voltage control loop

Simulation results: In Fig. 6 the output voltage, V_{out} , and the load current are shown. For a sudden change of the load, at $t = 2.5$ s (step current from 5 to 15 A), the output voltage of the hybrid system decreases up to 2 V and the adequate control eliminates fastly the perturbation, by maintaining the constant output voltage (42 V).

In Fig. 7 the power comparisons during on the charging and discharging process of the supercapacitor is shown. During the $[0, 2.5]$ s time interval, the load power, P_{load} , is lower than of the fuel cell power source, P_{fc} , the power P_{sc} has the negative

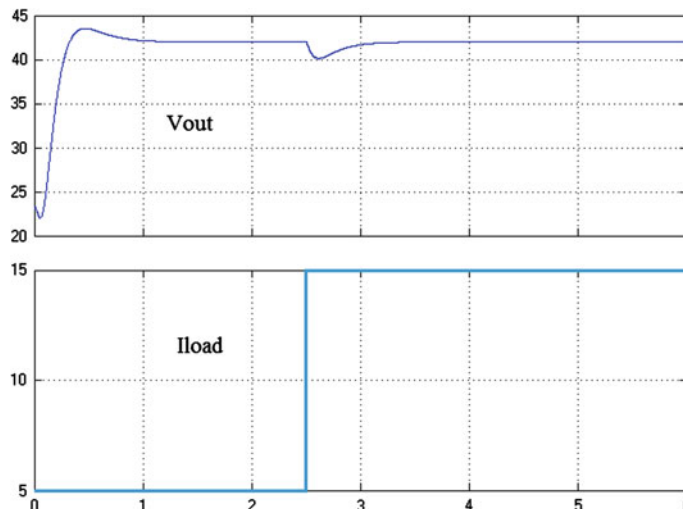


Fig. 6 The output voltage of the hybrid system and the load current

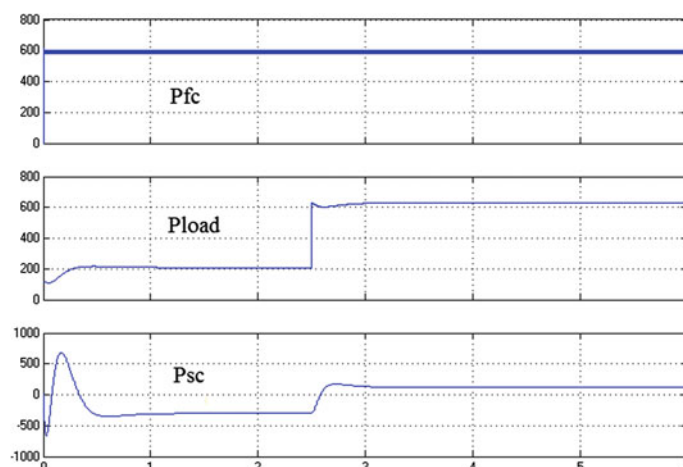


Fig. 7 The charging and discharging process of the supercapacitor: power comparisons

value. Therefore, the supercapacitor is charging. At $t = 2.5$ s, a step load power is applied and the load power becomes higher than of the fuel cell power supply. During this period of time, the supercapacitor is discharging.

From Fig. 8 the following remark could be obtained: even if the supercapacitor voltage increases, the output voltage of the hybrid system remains at the constant value. In Fig. 9 it could be noticed that the supercapacitor is charging during no-load, and continues to charge during the load power reversal (regenerating).

The supercapacitor current control performances are shown in Fig. 10. The feedback current of the supercapacitor is tracking the reference during all the operating regimes, while the fuel cell delivers the constant current.

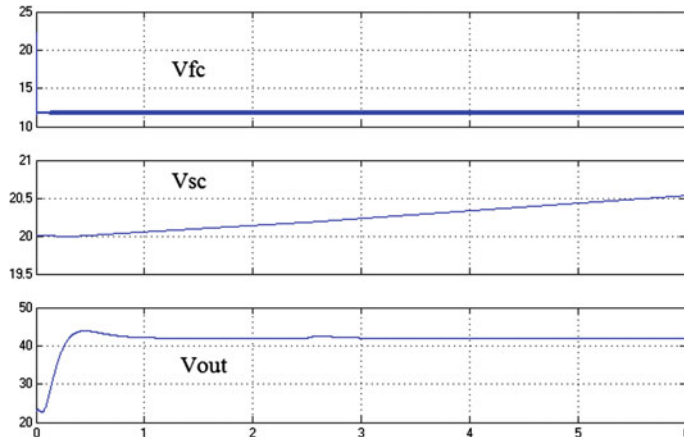


Fig. 8 Relationship between the voltages of the hybrid power system

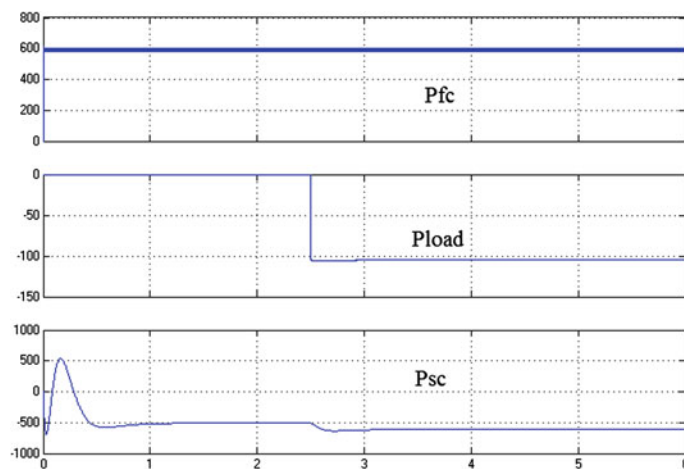


Fig. 9 The charging process of the supercapacitor

In Fig. 11 the charging and discharging processes of the supercapacitor are shown. During the charging process the supercapacitor current decreases, while the supercapacitor voltage increases. The discharging process is the opposite of the charging one. At the same time, the current control of the supercapacitor is shown.

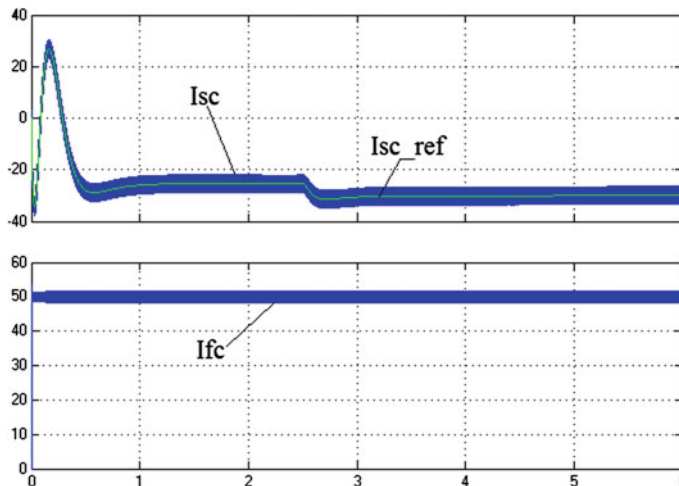


Fig. 10 The current control of the supercapacitor and the fuel cell current

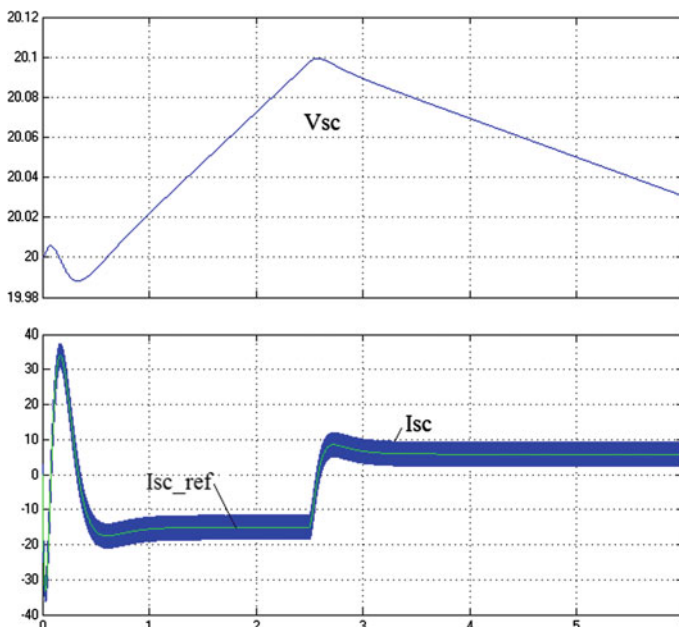


Fig. 11 The charging and discharging process of the supercapacitor

3 Conclusions

The hybrid system to supply an electric vehicle is shown in this paper. The PEMFC mathematical model of the fuel cells has been taken into account. Through a PI control, the unidirectional boost power converter increases the voltage to the rated power of the DC motor of the electric vehicle. The supercapacitor charging and discharging processes are assured by a bidirectional buck-boost power converter. The hybrid power system is implemented in Matlab Simulink and adequate numerical results are provided.

Acknowledgments This work was supported by a grant of the Romanian National Authority for Scientific Research, CNDI-UEFISCDI, project number PN-II-PT-PCCA-2011-3.2-1680.

References

1. P. Tritschler, Optimisation de l'architecture électrique et gestion d'énergie pour un système à pile à combustible embarquée dédié à l'application agricole, Docteur de l'Université de Grenoble France, 22 Oct. 2010
2. A. Payman, *Energy control of supercapacitor/fuel cell hybrid power source* (Institut National Polytechnique de Lorraine (INPL), Vandoeuvre-lès-Nancy, France, 2007)
3. P. Barrade, A. Rufer, in *The use of supercapacitors for energy storage in traction systems*. Proceedings of IEEE Vehicular Power and Propulsion Symposium, (VPP), Paris, France, 6–8 Oct 2004
4. A. Mustafa, Al-Refai, *Matlab/Simulink Simulation of Solar Energy Storage System*. World Acad. Sci. Eng. Technol. Int. J. Electr. Robot. Electron. Commun. Eng. **8**(2), 304–309 (2014)

Part II

Wind Energy

Temporal Assessment of Wind Energy Resource in “Adrar” (South of Algeria); Calculation and Modeling of Wind Turbine Noise

M. Benmedjahed, N. Ghellai, Z. Bouzid and A. Chiali

Abstract The objective of this work is to evaluate the wind resource on the site of Adrar in southern Algeria. The hourly data used in this study span a period of 5 years. The considered parameters are the speed and direction of wind. For this purpose, the most energetic and frequent speed as well as the Weibull parameters to plot the wind rose were evaluated. Treatment focuses on coverage, the average monthly rate, annual average speed and average speeds by sector and their frequencies, to optimize site selection for future wind farm. The southern site “Adrar” is favorable for large ZWD (zone of wind development), why it was decided to investigate the possibility to set up a wind farm of 9 MW consisting of twelve wind turbines VERGNET GEV HP with nominal power of 800 KW. Next, the noise was calculated and modeled. The obtained results are $k = 2.06$ and $C = 7.4$ m/s for the Weibull parameters at ten meters above the ground with an average wind speed of 6.5 m/s. Our simulation of the noise propagation for the wind farm shows that noise level is estimated around 38 dB (A) at a distance of 220 m from the nearest turbine. We can conclude that these noise levels have no effect on health and comply with the Algerian standard.

1 Introduction

In Algeria, the objectives established by the join-stock company NEAL (NEW Energy Algeria), focused on raising renewable energy production to 1400 MW in 2030 and 7500 MW at the beginning of 2050. The Electricity production will be

M. Benmedjahed

Research Unit of Renewable Energies in the Sahara, Adrar, Algeria

N. Ghellai (✉) · Z. Bouzid

Unit Research in Materials and Renewable Energy, University of Tlemcen, Tlemcen, Algeria
e-mail: na_ghellai@yahoo.fr

A. Chiali

Preparatory School of Science and Technology of Tlemcen, Tlemcen, Algeria

obtained from solar power plants, which use exclusively solar energy, or hybrid power plants that can also use other renewable or conventional sources, preferably natural gas [1].

Harnessing the wind is one of the cleanest and most sustainable ways to generate electricity. Wind energy produces no toxic or greenhouse gas emissions. Wind energy is one of the most abundant energy and increasingly cost-competitive energy resources, makes it a viable alternative to fossil fuels that harm our health and threaten the environment. In 2012, wind installations worldwide have increased by 10 % compared to 2011 [2].

The first Algerian works on wind energy potential were published by Said and al [3] in 1984, followed by Hammouche in 1990 [4], Kasbadji in 2000 [5], Chellali [6], Boudia [7] and Benmedjahed in 2013 [8].

The energy available in the wind varies as the cube of wind speed, so an understanding of the characteristics of the wind resource is critical to all aspects of wind energy exploitation, from the identification of suitable sites and prediction of the economic viability of wind farm project.

The present study focuses on the processing and simulation of hourly data, collected during 5 years, for determining various wind parameters. Wind potential, its direction and frequency are assessed by plotting the wind rose, in order to select the appropriate site for future wind turbines. Finally, after the evaluation of wind power, the environmental impact of wind turbines was evaluated. For this purpose, the ISO 9613-2 calculation model is used in the case where octave data are available; otherwise some calculation formulas based on Matlab are developed.

2 Site Description and Wind Data Analysis

In this study, meteorological data from Adrar (27.88°N, 0.28°W and altitude of 263 m), located in the south of Algeria, were used to evaluate the wind potential. The measurements were performed, at a height of 10 m above ground with a time interval of 3 h for each recording for 5 years.

2.1 Weibull Distribution

The Weibull law is used to characterize the frequency distribution of wind speeds over time [9, 10]. His probability density function is:

$$f(v) = \left(\frac{k}{C}\right) \left(\frac{v}{C}\right)^{k-1} \exp\left[-\left(\frac{v}{C}\right)^k\right] \quad (1)$$

where k is the dimensionless shape parameter and C is the scale parameter (m/s).

2.2 The Wind Rose

The wind rose is like a navigational compass that divides the horizon into angular sectors. For each sector, are exhibited [11]:

- The wind frequency, the percentage of time that the wind blows in this sector,
- The average wind speed multiplied by its frequency,
- The power available in the wind.

2.3 Extrapolation of the Weibull Parameters

If the wind distribution is desired at some height other than the anemometer level, different relations can adjust the Weibull parameters to any desired height. For this, we use the model of Justus [12], to extrapolate the weibull parameters k_1 and C_1 at point Z_1 towards level Z_2 expressed by:

$$k_2 = k_1 \left(\frac{1 - 0.0881 \log(z_1/10)}{1 - 0.0881 \log(z_2/10)} \right) \quad \text{and} \quad C_2 = C_1 \left(\frac{z_2}{z_1} \right)^n \quad (2)$$

With $n = (0.370 - 0.0881 \log(C_1)) / (1 - 0.0881 \log(z_1/10))$

2.4 Wind Power

The effective power extracted by a wind turbine is:

$$P_{\text{eff}} = C_e P_{\text{wind}} = C_e \frac{1}{2} \rho S v^3 \quad (3)$$

ρ is the density of air at sea level (kg/m^3), S is the pipe section or area swept by the rotor (m^2), v is the wind speed (m/s) and C_e the efficiency coefficient of the wind turbine.

3 Estimation of the Generated Energy and the Capacity Factor

The histogram method is used to estimate the energy generated by a wind turbine. The superposition of the energy response curve (KW) and the frequency histogram give [13]:

$$E = \sum_{i=1}^n P_i(v_i) f_i(V_i) \times N \quad (4)$$

N : number of hours per year

$P(v_i)$ and $f(v_i)$, respectively, effective power and probability at speed v_i

The capacity factor is defined as the ratio of the actual energy produced E in a period of time, if the turbine operates at its rated power P_N , for 1 year.

$$CF = \frac{E}{P_N \times 8760} \quad (5)$$

4 Placement of Wind Turbines

To produce a large amount of energy, a wind farm must be installed as shown in Fig. 1 with D_T the diameter of the rotor [8, 14]. We use in this model VERGNET GEV HP wind turbine [13].

5 Calculation Models to Estimate the Noise Level

Noise of wind farm turbine is perceived as one of the more significant environmental impacts. Usually, in order to measure the wind turbine noise, the level of the weighted acoustic power is calculated as an average level at 500 Hz. The impact of noise is calculated according to the international standard ISO 9613-2, as follows [15–18]:

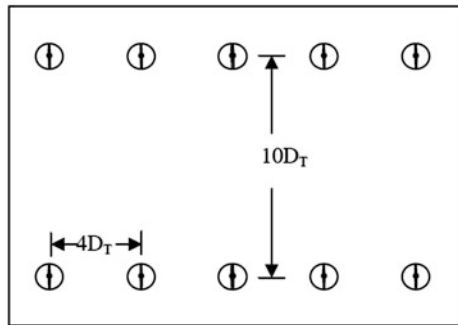
$$L_{AT}(DW) = L_{WA} + D_c - A - C_{met} \quad (6)$$

L_{AW} : is the level of weighted acoustic power of the noise source and $D_c = D_\Omega$ is the correction made in order to take into consideration the directivity of the source (without directivity = 0 dB). D_Ω : represents the reflection on the floor:

$$D_\Omega = 10 \log \left[1 + \frac{d_p^2 + (h_s - h_r)^2}{d_p^2 + (h_s + h_r)^2} \right] \quad (7)$$

h_s and h_r are, respectively, the height of source above the ground and the height of point of noise impact. d_p : distance between noise source and point of impact,

Fig. 1 Placement of wind turbines



projected on the ground (m), is calculated from the coordinates (x, y) of the source (index s) to the point of impact (index r):

$$d_p = \sqrt{(x_s - x_r)^2 + (y_s - y_r)^2} \quad (8)$$

A: attenuation during noise propagation between the source (the wind turbine nacelle) and the point of impact. The total attenuation is given by:

$$A = A_{div} + A_{atm} + A_{grd} + A_{scr} + A_{var} \quad (9)$$

$A_{div} = 10 \log(d) + 11$ is the attenuation due to spatial propagation with d distance between source and point of impact (m).

$A_{atm} = \alpha d / 1000$ is the attenuation due to atmospheric absorption with α the absorption coefficient of air which is equal to 1.9 dB/km in the most favorable sound propagation conditions (temperature of 10 °C and relative humidity of 70 %).

A_{grd} is the attenuation of ground.

$$A_{grd} = 4.8 - \left[\left(\frac{2h_m}{d} \right) \left(17 + \frac{300}{d} \right) \right] \geq 0 \quad (10)$$

h_m : average height (m) of noise path above the ground and d is the distance from the source to receiver (in meters). If no digital model of ground is found, then the average height can be calculated as follows:

$$h_m = \frac{h_s + h_r}{2} \quad (11)$$

The average height is calculated as: $h_m = \frac{F}{d}$

F is the vertical surface, between the wind turbine and the point of noise impact. A_{scr} : attenuation due to absorption (soundproof barrier). Generally, when there is no sound protection $A_{scr} = 0$.

A_{var} : various attenuations (vegetation, construction, industry). Generally these attenuations are not taken in the calculations, $A_{var} = 0$.

C_{met} : weather correction. This is done as follows:

$$C_{met} = \begin{cases} 0 & \text{if } d_p < 10(h_s + h_r) \\ C_0 \left[1 - \frac{10(h_s + h_r)}{d_p} \right] & \text{if } d_p > 10(h_s + h_r) \end{cases} \quad (12)$$

6 Results and Interpretations

From the hourly data measured for five years (from 2006 to 2010) at 10 m above the ground, the Weibull parameters were calculated ($k = 2.06$ and $C = 7.4$ m/s) with an average wind speed of 6.5 m/s. The value of the shape factor k shows that the distribution is stable (Fig. 2).

The value of k for the month of July is the maximum (Table 1), which shows that the distribution is more stable. For the other months it varies from 2.43 to 2.89 indicating that the distribution is fairly stable throughout the year. The analysis of C shows that the windiest months are April and May.

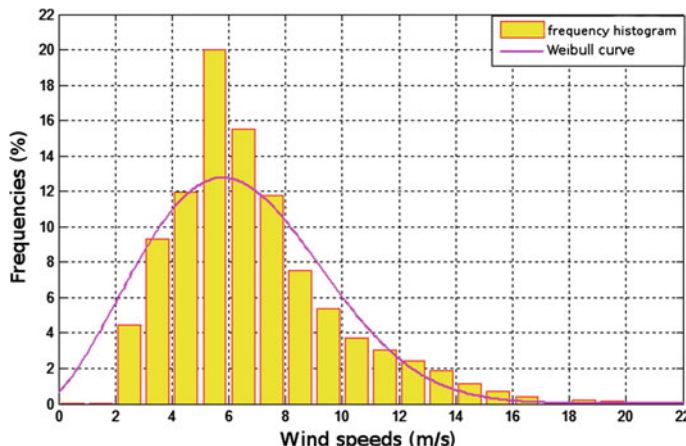


Fig. 2 Wind speeds frequency and Weibull distribution at 10 m

Table 1 Weibull parameters and monthly average speeds at 10 m above ground

Month	C (m/s)	k	v (m/s)	Month	C (m/s)	k	v (m/s)
January	7.2	2.69	6.4	July	8.6	2.93	7.6
February	7.8	2.43	6.9	August	7.6	2.60	6.7
March	8.3	2.61	7.4	September	7.4	2.77	6.6
April	8.7	2.65	7.7	October	7.7	2.69	6.8
May	8.7	2.79	7.7	November	7.2	2.97	6.4
June	7.7	2.89	6.8	December	7.0	2.79	6.2

Table 2 Weibull parameters and average annual rate by sector at 10 m above ground

Sector	C (m/s)	k	v (m/s)	Sector	C (m/s)	k	v (m/s)
N	6.8	2.47	6.1	S	7.5	2.72	6.6
NNE	7.3	2.89	6.5	SSW	7.6	2.61	6.7
NE	7.5	3.13	6.7	SW	7.7	2.57	6.9
ENE	8.5	2.99	7.6	WSW	7.9	2.33	7.0
E	8.5	2.94	7.6	W	8.1	2.39	7.2
ESE	8.0	2.76	7.1	WNW	6.7	0.23	5.9
SE	8.0	2.84	7.1	NW	6.3	2.51	5.6
SSE	8.2	2.62	7.2	NNW	6.3	2.86	5.6

The parameters of Weibull and the annual average speed v for the frequency distribution by sector at 10 m are calculated and shown in the Table 2 (N for North, E for East, W for West and S for South).

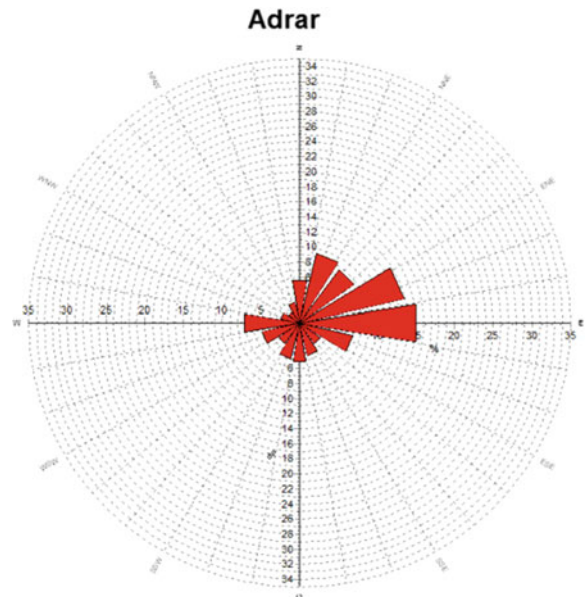
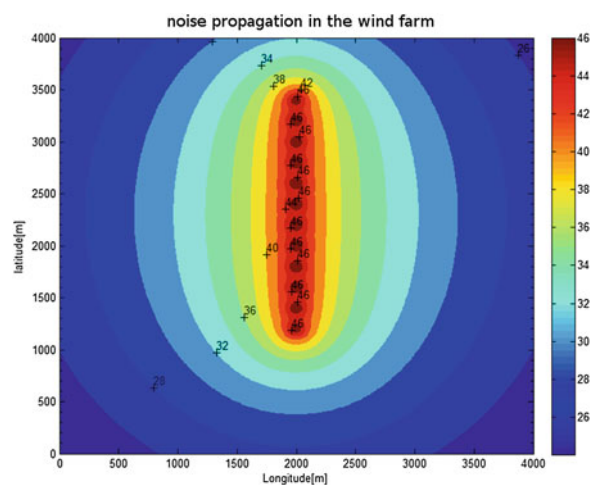
The value of the form factor k for the West North West sector is 0.23, which shows that the distribution is dispersed. For the other sectors it varies between 2.47 and 3.13 indicating that the distribution is stable.

Analysis of scale factors C shows that the windiest areas are East North East and the East sector. For other sectors C varies from 6.3 to 8.2 m/s.

Statistical analysis of the data allowed us to plot the wind rose (Fig. 3). The results show that the dominant wind direction is East (15 % of the frequencies).

Our wind farm is composed of a single row of 12 wind turbines. The distance between each turbine is 248 m from North to South. Matlab software was used to calculate the noise generated by the wind turbine under the conditions encountered on our site (flat ground) and the results are exhibited in Fig. 4.

This wind turbine produces noise of magnitude 103 dB (A) (as given by the manufacturer). According to our calculations, by using the method ISO 9613-2, the noise level is approximately 38 dB (A) to 250 m of nearest wind turbine and will be 31 dB (A) at a distance of 100 m.

Fig. 3 Annual wind rose**Fig. 4** Noise propagation

7 Conclusion

This study focused on the evaluation of acoustic impacts of a wind farm in the area of Adrar. For this purpose, the ISO 9613-2 calculation model was used; otherwise, some calculation formulas based on Matlab was developed. The obtained results show that:

- The noise level is approximately 38 dB (A) to 250 m of the nearest wind turbine of the park and at distance of 100 m, the noise level will be 31 dB (A).
- The noise level of a wind (38 dB) corresponds to the noise of a quiet house, have not an effect on health and are in conformity with the Algerian standard. The sound level emitted by this source will decrease with the distance. This decrease depends on dimensions (point source, surface, linear) and the acoustic characteristics (directivity) of the source. The first cause of attenuation of the sound is the geometrical diffusion, it is also easiest to predict.
- Absorption is caused by traditional physical processes coupled with absorption due to energy of rotation of the molecules in the air. Whatever is the nature and the composition of the ground between the source and the receiver, homogeneous or discontinuous, their respective influence on the attenuation of the sound wave along the field of propagation is important.

References

1. T. Hasni, *Former president of NEAL « Développement des Energies Renouvelables en Algérie »* (National Conference on Renewable Energies and Sustainable Development, Laghouat, Algeria, 2006)
2. A.B. Stambouli, Promotion of renewable energies in Algeria: strategies and perspectives. Renew. Sustain. Energy Rev. **15**, 1169–1181 (2011)
3. M. Said, A. Ibrahim, Energy in the Arab World. Energy, **9–3**, 217–238 (1984)
4. R. Hammouche, *Atlas des vents de l’Algérie*. ONM Office des Publications Universitaires (OPU), Algiers (1990)
5. N. Kasbadji Merzouk, Wind energy potential in Algeria. Renew. Energy **21**, 553–562 (2000)
6. F. Chellali, A. Khellaf, A. Belouhrani, Application of time–frequency representation in the study of the cyclical behavior of wind speed in Algeria: wavelet transform. Stochast. Environ. Res. Risk Assess. **24**(8), 1233–1239 (2010)
7. S.M. Boudia, A. Benmansour, N. Ghellai, M. Benmedjahed, M.A. TabetHellal, Monthly and seasonal assessment of wind energy potential in Mechria Region, occidental highlands of Algeria. Int. J. Green Energy **9**(3), 243–255 (2012)
8. M. Benmedjahed, *Choix du site et optimisation du dimensionnement d’une installation éolienne dans le nord algérien et son impact sonore sur l’environnement*, Doctoral thesis, University of Tlemcen (2013)
9. G. Boroumand Jazi, B. Rismanchi, R. Saidur, Technical characteristic analysis of wind energy conversion systems for sustainable development. Energy Convers. Manage. **69**, 87–94 (2013)

10. A.S. Ahmed, Wind energy as a potential generation source at Ras Benas. Egypt. Renew. Sustain. Energy Rev. **14**, 2167–2173 (2010)
11. S. Mathew, *Wind Energy Fundamentals. Resource Analysis and Economics* (Springer, Berlin, 2006)
12. C.G. Justus, W.R. Hargraves, A. Mikhail, D. Graber, Methods for estimating wind speed frequency distributions. J Appl. Meteorol. **17**, 350–353 (1977)
13. NORDEX EnergyGmbH Modifications techniques réservées
14. B. Yousef, G. Aymeric, Collecte, organisation, traitement, analyse de mesures éoliennes et modélisation énergétique. Thèse doctorat, Université Tecnica Federico Santa Maria, UTFSM, Valparaso, Chili, 2005
15. ISO 3741, Acoustics—Determination of sound power levels of noise sources, Precision methods for broad-band sources in reverberation rooms (1988)
16. ISO 1996-1, Acoustics—Description and measurement of environmental noise, Part 7: Basic quantities and procedures (1982)
17. ISO 1996-2, Acoustics—Description and measurement of environmental noise, Part 2: Acquisition of data pertinent to land use (1987)
18. ISO 1996-3, Acoustics—Description and measurement of environmental noise, Part 3: Application to noise limits (1987)

Part III

Solar Energy

Photo-Electro-Thermal Characteristics of Photovoltaic Panels

Krzysztof Górecki, Ewa Krac and Janusz Zarębski

Abstract In the paper the measuring-set elaborated by the authors designed to characterize photovoltaic panels is presented. The mechanical construction and the electrical network of this set are shown and described. The simple method of calculating photo-electro-thermal characteristics of the photovoltaic panel with the use of SPICE software is proposed. Some results of measurements and calculations of characteristics of the selected photovoltaic panel are presented and discussed.

1 Introduction

Photovoltaic panels are important structural parts of solar power stations and autonomous photovoltaic systems [1]. Characteristics of these devices depend both on power density and the spectrum of radiation on their surface, as well as on temperature and on resistance of the circuit being a load of these panels. For self-heating phenomena, appearing with the temperature rise of the panel as a result of the exchange of the dissipated electrical energy into heat, and the phenomena of absorption of infrared radiation causing also the temperature rise of this panel, one can speak about the interaction of electric, optical and thermal phenomena in the considered device, which decides about the shape of characteristics of the considered panel in the real conditions of its operation. Therefore, the characteristics obtained under these conditions can be called photo-electro-thermal characteristics.

In order to obtain such characteristics the realization of measurements in the conditions which make possible the simultaneous control of optical, electric and thermal parameters of the examined panel or the realization of computer simulations with the use of the model taking into account all the mentioned phenomena, is

K. Górecki (✉) · E. Krac · J. Zarębski

Department of Marine Electronics, Gdynia Maritime University, Gdynia, Poland
e-mail: k.gorecki@we.am.gdynia.pl

indispensable. In the paper, the constructed by the authors measuring set to measure photo-electro-thermal characteristics of photovoltaic panels and the elaborated by the authors method of calculating of nonisothermal characteristics of photovoltaic panels with the use of SPICE software are presented.

Characteristics of the selected photovoltaic panels are measured by means of the constructed set and calculated with the use of SPICE software.

2 Description of the Measurement Set

The block diagram of the measuring set worked out by the authors is shown in Fig. 1. This set consists of 2 parts:

- (a) The measuring chamber, along with the measured panel and light sources,
- (b) The control position, containing the system of the control of illuminance and the network to measure the voltage and the current of the panel.

The measuring-chamber is the light-tight room of the dimensions $2.65 \times 1.4 \times 2.5$ m. In the ceiling of this room there are 32 halogenous lamps of regulated illuminance and regulated on-time. The distance between each lamp is equal to 30 cm. Illuminance is regulated by means of a classical thyristor power regulator. In the chamber there is also a meter of illuminance. It is used to measure the distribution of power density of radiation on the surface of the examined panel. The temperature of the panel is measured by means of the thermo-hunter Optex ST-3. The examined panel is situated on the table of the regulated depression angle. The dimensions of this table are $500 \times 1500 \times 1000$ mm.

Terminals of the examined panel are connected with the control position including the voltmeter, the ammeter, the load resistor and, in the case of the

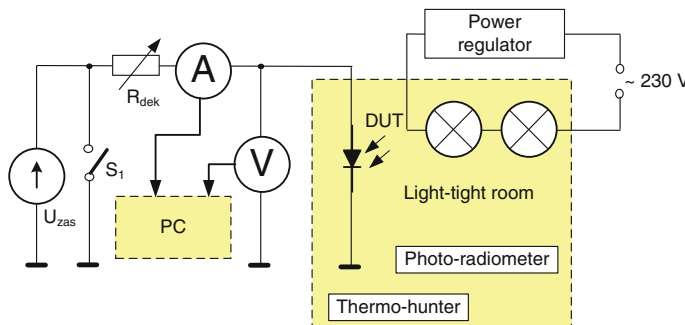
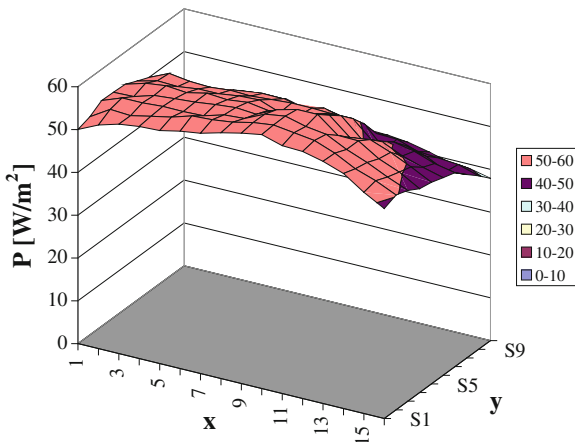


Fig. 1 The block diagram of the measurement set to measure characteristics of photovoltaic panels

Fig. 2 The measured distribution of power density of radiation on the surface of the panel



measurement of dark characteristics—the source of the supply voltage. To measure the voltage and the current the multimeters APPA 207 equipped with the USB interface which make possible transmission of the measurement results to the computer, are used. The recorded results of measurements are used to draw current-voltage characteristics of the panel at different conditions of lighting and the power supply.

The aim is to obtain the lighting conditions of the examined panel close to the day lighting, so that the distribution of power density of radiation on the surface of this panel could be uniform, and the spectrum of this radiation could be close to the spectrum of the sunshine.

In Fig. 2 the measured distribution of power density of radiation on the surface of the photovoltaic panel is presented. This distribution was measured by means of the photoradiometer HD 2302.0 LightMaster by Delta OHM with the probe LP 471 RAD. During the measurements, in the place of the panel the plywood with holes for the probe situated in nodes of the net of the side 10 cm is put.

As it is visible, the obtained distribution of power density of radiation is practically uniform. The obtained differences between the values of this parameter do not exceed $\pm 5\%$ in the centre of the panel and $\pm 10\%$ at its edges.

Halogenous lamps are used as the sources of radiation. The spectrum of these lamps is shown in Fig. 3. The measurement was performed with the spectrometer USB 2000 by Ocean Optics.

As one can notice in Fig. 3, the spectrum of radiations of both lamps are close to each other. The shapes of the obtained spectrum for the daylight and for halogenous lamps are similar, whereas the energy of radiation of halogenous lamps is concentrated within the range of higher wavelengths, attaining the maximum at $\lambda \approx 620$ nm. Also, the higher level of infrared radiation is visible.

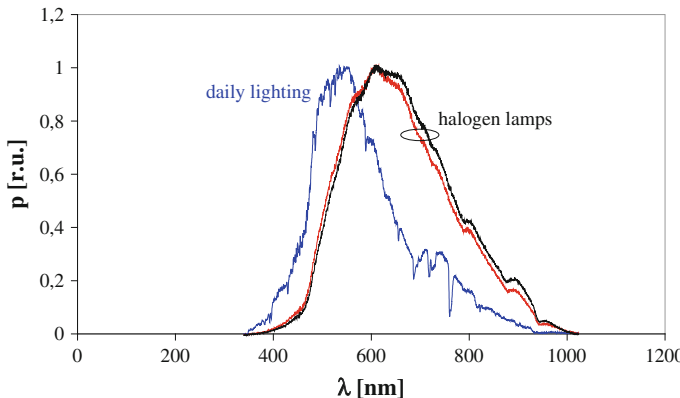


Fig. 3 The measured distribution of radiation of the used halogenous lamps

3 Examined Panel and the Method of Calculating Its Characteristics

By means of the measuring set described in the previous section dark characteristic of the photovoltaic panel MK-240 by Solar-Energy is measured and its bright characteristics at the selected values of power density of radiation on the surface of the panel is also measured. This panel has dimensions $1000 \times 1681 \times 50$ mm and contains 60 solar cells made of poly-crystalline silicon coated with preservative layers of foil and glass of the thickness 3.2 mm. The maximum electric power, which can be received from the panel amounts up to 240 W, and its watt-hour efficiency attains 16.4 %. The value of the occlusal current amounts up to 8.54 A, and the voltage of the opened panel -37.1 V [4].

Characteristics of the considered panel are measured at the steady-state with thermal phenomena taken into account. These characteristics are also calculated by means of SPICE software, using the model of the solar cell presented in the paper [2]. In calculations, the values of parameters of the poly-crystalline solar cell given in the paper [3] are used.

The image of the structure of the panel would demand copying the structure of the model of the solar cell, described in the paper [2], 60 times, but as a result the model of the panel would be unjustifiably complicated. This could cause problems with the convergence of calculations or, to considerable degree, lengthen the time of these calculations. In order to avoid the mentioned problems, the performance of calculations for a single solar cell is proposed for scaling the value of selected elements of the application circuit and then scaling the obtained results is indispensable.

While calculating the characteristics of the lighted up panel one ought to leave without scaling the value of the parameter describing the power density of radiation, and load resistance of the panel should be divided by the number of solar cells

contained in the panel ($k = 60$). Obtained value of the voltage on the panel should be multiplied by k .

In turn, while calculating the dark characteristic the value of voltage biasing the panel and series resistance connected serially with this source should be divided by k . While calculating both the considered characteristics the value of the internal temperature T_j of the solar cell (equal to the temperature of the panel) can be calculated using the following formula

$$T_j = T_a + R_{th} \cdot k \cdot u \cdot i \quad (1)$$

where T_a is the ambient temperature, R_{th} —the thermal resistance of the panel, whereas i and u denote the values of the current and voltage on the panel, respectively.

4 Results of Calculations and Measurements

Figure 4 presents the calculated (lines) and measured (points) dc characteristics of the lighted up panel for two mean values of power density on its surfaces equal to 49.7 and 81.7 W/m^2 , respectively.

As it is visible, the good agreement between the calculated and measured characteristics of the panel is obtained. An increase in the value of power density of radiation causes an increase in the value of the voltage on the panel at the small load current and an increase in the occlusal current. However, for the low value of power density of radiation, the opening voltage and the occlusal current are smaller than their values given by the producer. As a result of lighting up the panel and absorption of infrared radiation from light sources by the panel, its temperature increases from 19 to 27 °C.

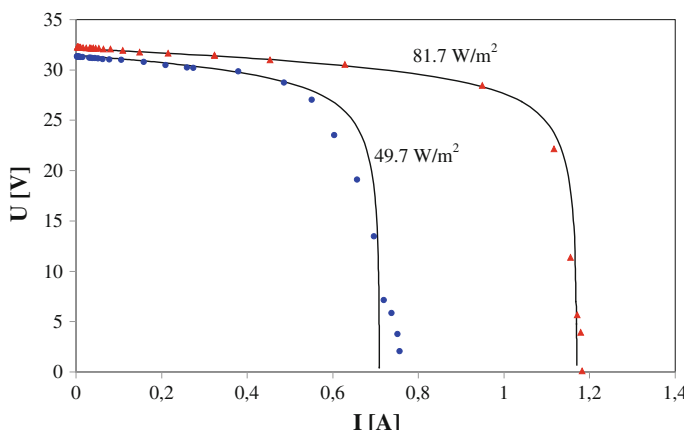
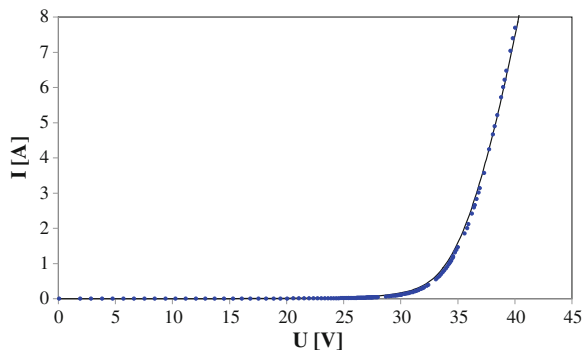


Fig. 4 The calculated and measured dc characteristics of the lighted up panel

Fig. 5 The measured and calculated dark characteristic of the tested panel



In Fig. 5 the calculated (lines) and measured (points) dark characteristics of the examined panel at the forward biased junctions of solar cells are presented.

As it is visible, also on the dark characteristic of the panel, the good agreement between the results of calculations and measurement is obtained. During the measurements the ambient temperature was 19 °C, and as a result of self-heating the temperature of the panel grew to 31.6 °C at the current $I = 8$ A. This means that thermal resistance of the examined panel amounts only just to 0.039 K/W. For large sizes of the examined panel the set-up time of its thermal state is long and exceeds 1 h.

Of course, the value of the temperature of the panel at the normal biasing is equal to the sum of the ambient temperature and an increase of the temperature due to absorption of the optical radiation and self-heating.

5 Conclusions

In the paper the constructed by the authors measuring set to measure characteristics of photovoltaic panels is presented. The results of measurements of characteristics of this set are shown, in particular the obtained spectral characteristics of the applied light sources and distribution of power density of radiation on the surface of the panel.

The effective method of calculating electrothermal characteristics of the photovoltaic panel based on the electrothermal model of the solar cell, from the paper [2], is presented also. This method simplifies the computer analysis of panels in an essential manner. The results of measurements of electrothermal characteristics of the chosen panels, obtained with the use of the presented measuring set, and the results of calculations of these characteristics obtained with the use of the proposed computational method show the good agreement. This testifies to the usefulness of the presented measuring set and the computational method, which can be used in research of photovoltaic systems, particularly their electric-thermal-optical characteristics.

Acknowledgments The Authors thank PVE Poland for financing the construction of the measuring set and Solar-Energy Poland for giving the photovoltaic panel.

References

1. M.H. Rashid, *Power Electronic Handbook* (Academic Press, Elsevier, 2007)
2. K. Górecki, P. Górecki, K. Paduch, Modelling solar cells with thermal phenomena taken into account. *J. Phys: Conf. Ser.* **494**, 012007 (2014). doi:[10.1088/1742-6596/494/1/012007](https://doi.org/10.1088/1742-6596/494/1/012007)
3. K. Górecki, E. Krac, Badanie wpływu temperatury na charakterystyki fotoogniw. *Elektronika* **9**, 95–98 (2014)
4. Solar-Energie fur Jedermann. Solar-energy Ltd. www.solar-energy.pl

MLP/Levenberg-Marquardt for Prediction Solar Radiation: A Case Study Bejaia City

Z. Asradj and R. Alkama

Abstract In order to model the global solar radiation based on meteorological parameters for the Bejaia site, we established a database of more than 26,000 points obtained by recording every 8 min of illumination and meteorological parameters (sunshine hours, ambient temperature, air pressure, relative humidity and rainfall). Empirical models have been developed using several parameters and, recently, prognostic and prediction models based on artificial intelligence techniques such as neural networks. The daily averages were used to test NN models with 5 parameters and the relationship with the coefficient of the highest correlation was chosen. Two thirds were used to establish the model and one third for validation. We compared its performance with four models in the literature (Angstrom-Prescott, Bahel, Newland and Abdalla).

1 Introduction

Solar energy is the most ancient source of energy; it is the basic element for almost all fossil and renewable types. Solar energy is freely available and could be easily harnessed to reduce our reliance on hydrocarbon-based energy by both, passive and active designs. Precise solar radiation estimation tools are critical in the design of solar systems [1].

While solar energy data are recognized as very important, their acquisition is not easy. The measurement of solar radiation requires the use of expensive equipment, and in developing countries there are not always adequate facilities to mount viable

Z. Asradj (✉) · R. Alkama

Laboratory of Electrical Engineering, Faculty of Technology,
University of Bejaia, Bejaia, Algeria
e-mail: zahirasradj@yahoo.fr

monitoring programs. Therefore, there have been several attempts to estimate solar radiation through the use of meteorological and physical parameters [2].

Several empirical models have been developed to calculate global solar radiation using various parameters, the relative sunshine duration is the most commonly used.

In 1924 Angstrom used a linear relationship between global radiation and sunshine duration; a modified version of this correlation, proposed by Prescott in 1940, has been the most convenient and widely used for estimating global solar radiation; this is known as the Angstrom-Prescott equation [3]. Falayi et al. [4] developed, for Nigeria, multilinear regression equations to predict the relationship between global solar radiation with different weather parameters.

A simple and fast physically based method for the estimation of global solar radiation using meteorological satellite data was presented for Wloczyk and Richter [5].

Fortin et al. [6] developed a long-utilized linear approach based on latitude and daily temperature range. In addition, estimations of daily radiation resulting from an Angstrom-Prescott relationship have adequate accuracy at a monthly scale, but are not accurate at a daily scale [7].

Recently, prognostic and prediction models based on artificial intelligence techniques such as neural networks (NN) have been developed. These models can handle a large number of data, predict the contribution of these in the outcome and provide prompt and adequate predictions [8]. Using neural networks, Bocco et al. [9] made models to estimate solar radiation at Córdoba (Argentina), Mohandes et al. [10] for Saudi Arabia and Fortin et al. [6] for Canada.

Within this methodology, the multilayer perceptron is probably the most commonly used algorithm with the architecture of neural networks because of its capacity to tolerate information that is incomplete, inaccurate or contaminated with noise [11].

The aim of this work was to develop linear models and neural networks to estimate daily global solar radiation from commonly observed meteorological data and compare the overall efficiency of these models and networks in an application to a region of BEJAIA site.

2 Data Base

In the present work, meteorological station Oregon Scientific was used for the meteorological parameters (ambient temperature, air pressure, relative humidity and rainfall) and global solar radiation data of the corresponding periods were recorded by Data logger TARCOM. The registrations make themselves every 8 min during all year 2010. After the deletion of the data of the night, close to 26,000 data are exploitable. Sunshine hours, is the time during which the solar radiation is superior to 120 W/m^2 . To calculate it, we add 8 min every time the solar radiation is superior

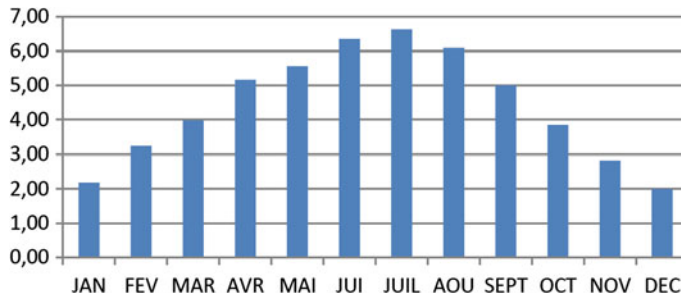


Fig. 1 Irradiation ($\text{kWh}/\text{m}^2/\text{d}$) in Bejaia City during 2010

to 120 W/m^2 while supposing that it keeps this value during all the interval of 8 min. We divided this data base in two intervals.

The first interval contains the daily values of the months February, March, May, June, August, September, November and December. This interval is used to develop some models. The second interval contains the daily values of the months of January, April, July and October, in order to value the performances of the models gotten.

The daily extraterrestrial radiation on a horizontal surface was calculated from the following equation [12]:

$$H_0 = I_{cs}(1 + 0.0333\cos(360n/365)) (\cos\varphi \cos\delta \sin\omega_s + \pi\omega_s/180 \sin\varphi \sin\delta) \quad (1)$$

where I_{cs} is the solar constant ($=1373 \text{ W/m}^2$), φ is the latitude of the site ($36.817.\pi/180$ rad), δ is the solar declination (rad), ω_s is sunrise hour angle and n is the number of the day of year starting from the first of January. Solar declination and sunrise hour angle can be computed by (2)–(3), respectively [13]:

$$\delta = 23.45 \sin[360(284 + n)/365] \quad (2)$$

$$\omega_s = \cos^{-1}(-\tan\varphi \tan\delta) \quad (3)$$

The Fig. 1 shows the solar radiation during the year 2010 in Bejaia.

3 Neural Networks Models

3.1 Neural Networks

A neural network (NN) model, multilayer perceptron, was used to estimate the incident solar radiation. This procedure is a mathematical model that performs a computational simulation of the behavior of neurons in the human brain by replicating, on a small scale, the brain's patterns in order to produce results from the

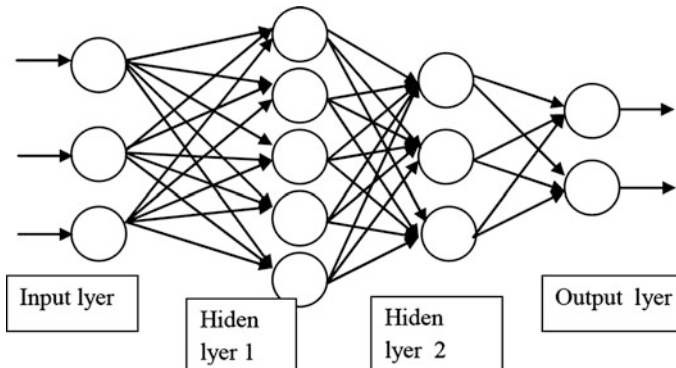


Fig. 2 Schematic map of a multilayer perceptron artificial neural network

events perceived, i.e. it is a model based on learning a set of training data. The main characteristic of NN is their capacity for learning by example. This means that by using a NN there is no need to program how the output is obtained, given certain input; the NN will learn the existing input-output relationship by means of a learning algorithm. This learning will materialize in the network's topology and in the value of its connections. Once the NN has learnt to carry out the desired function, input values for which the output is unknown can be entered, and the NN will calculate the output.

The NN are composed of a number of interconnected processing elements which are joined by weighted connections. The training algorithm adjusts the connection weights through an iterative procedure in which the error is minimized [13]. The amount of training data required for successful classification increases exponentially with increased dimensionality of the input data [14]. The Multilayer Perceptron (Fig. 2) is a fully connected multilayer feed forward supervised learning network with symmetric hyperbolic tangent activation functions, trained by the Levenberg-Marquardt backpropagation algorithm to minimize a quadratic error.

3.2 Learning Algorithm

The neural network is trained using Levenberg-Marquardt backpropagation algorithm. It is a network training function that updates weight and bias values according to Levenberg-Marquardt optimization. It is often the fastest backpropagation algorithm for training moderate-sized feedforward neural networks (up to several hundred weights), although it does require more memory than other algorithms.

Like the quasi-Newton methods, the Levenberg- Marquardt algorithm was designed to approach second order training speed without having to compute the Hessian matrix. When the performance function has the form of squares sum (as is

typical in training feedforward networks), then the Hessian matrix can be approximated as

$$H = J^T J \quad (4)$$

and the gradient can be computed as

$$g = J^T e. \quad (5)$$

where J is the Jacobian matrix that contains first derivatives of the network errors with respect to the weights and biases, and e is a vector of network errors. The Jacobian matrix can be computed through a standard backpropagation technique that is much less complex than computing the Hessian matrix.

The Levenberg-Marquardt algorithm uses this approximation to the Hessian matrix in the following Newton-like update [15]:

$$X_{k+1} = x_k - [J^T J + \mu I]^{-1} J^T e \quad (6)$$

When the scalar μ is zero, this is just Newton's method, using the approximate Hessian matrix. When μ is large, this becomes gradient descent with a small step size. Newton's method is faster and more accurate near an error minimum, so the aim is to shift toward Newton's method as quickly as possible. Thus, μ is decreased after each successful step (reduction in performance function) and is increased only when a tentative step would increase the performance function. In this way, the performance function is always reduced at each of iteration of the algorithm.

Training stops when any of these conditions occurs:

- The maximum number of epochs (repetitions) is reached.
- The maximum amount of time is exceeded.
- Performance is minimized to the goal.
- The performance gradient falls below the minimum gradient.
- μ exceeds the maximum μ_u .

Validation error failed to decrease for six iterations (validation stop).

4 Estimation Methods

The objective of this work was to develop some statistical relations to estimate the global solar radiation H by applying multiple linear regressions to various parameters, such as S/S_0 , T , P , RH and W , and compare them with neuronal model.

The size of the input layer that receives the information from various parameters that affect the radiation is the number of variables (05 parameters) and the output layer has one neuron which indicates the predicted total daily solar radiation. The number of neurons in the hidden layer and the number of hidden layers are selected during the training process.

We are going to compare his performances to four models of the literature: Angstrom-Prescott, Bahel, Newland and Abdalla.

Angstrom-Prescott model [16, 17]:

$$H/H_0 = a + b(S/S_0) \quad (7)$$

With: $a = 8.01589 \cdot 10^{-2}$; $b = 0.7092$

Bahel model: Bahel developed a worldwide correlation based on bright sunshine hours and global radiation data of 48 stations around the world, with varied meteorological conditions and a wide distribution of geographic locations:

$$H/H_0 = a + b(S/S_0) + c(S/S_0)^2 + d(S/S_0)^3 \quad (8)$$

With: $a = 0.16$; $b = 0.87$; $c = -0.16$; $d = 0.34$.

Newland model: Newland include a logarithmic term.

$$H/H_0 = a + b(S/S_0) + \log(S/S_0) \quad (9)$$

With: $a = 0.34$; $b = -0.4$; $c = 0.17$

Abdalla model: Abdalla modified the Gopinathan model for Bahrain

$$H/H_0 = a + b(S/S_0) + cT + dRH \quad (10)$$

With: $a = 0.5289$; $b = 0.459$; $c = 4.073 \cdot 10^{-3}$; $d = -6.481 \cdot 10^{-3}$.

To compare solar radiation estimation equations, the most widely used statistical indicators are the root mean square error (RMSE). Low values of RMSE are desirable.

$$RMSE = \sqrt{\frac{\sum_{i=1}^N (H_{i,m} - H_{i,c})^2}{N}} \quad (11)$$

where N is the measurements number, $H_{i,c}$ and $H_{i,m}$ are the calculated and measured values of global solar radiation in the day i , respectively.

5 Results and Discussion

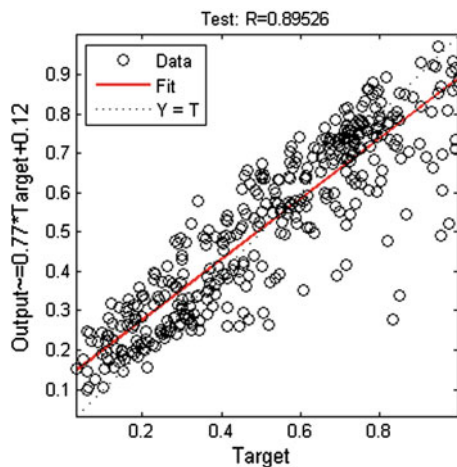
Table 1 shows the calculated RMSE and the correlation coefficient R between MNN model and the regression models.

The correlation coefficients increase with the number of parameters that is taken in account in the models, while the RMSE values decrease. The MNN present the best results compared to other models in literature (Table 1). The models Angstrom-Prescott and Newland underestimate the global solar radiation. The models Abdalla

Table 1 The calculated RMSE and R between MNN model and others models

Models	RMSE	R
Angstrom–prescott	16.5420	0.8116
Bahel	7.6889	0.8556
Newland	18.5387	-0.5007
Abedalah	15.4016	0.8942
MNN	0.0150	0.8952

Fig. 3 Scatter plots of relationships between measured and estimated solar radiations



and Bahel overestimate the global radiation. Figure 3 shows the relationship between measured and estimated solar radiation using NN model.

To confirm the results found, we traced the regression line for all test data (Fig. 3). A prediction will be considered satisfactory when the coefficient of correlation and regression line slope are particularly close to unity (0.895), and the ordinate the closer to zero origin.

We found that the correlation coefficients and slopes of the regression lines are close to unity and intercept is close to zero.

6 Conclusion

After confronting the measured values and those estimated by the models in the literature and the proposed one, we noted that this last, driven to better results ($R = 0.8952$, $RMSE = 0.0150 \text{ MJ/m}^2/\text{j}$). This is explained by the fact that this model considers five meteorological parameters (sunshine hours, ambient temperature, air pressure, relative humidity and rainfall). Solar radiation can be adequately estimated by linear models and neural networks from values of meteorological variables of routine use; even NN produced better estimates (Fig. 3). Neural

networks are an efficient methodology to estimate daily solar radiation, using a reduced number of meteorological parameters. They allowed, principally, reproduce the solar radiation evolution patterns for BEJAIA city (Algeria).

References

1. M.A. AbdulAzeez, Artificial neural network estimation of global solar radiation using meteorological parameters in gusau, nigeria. *Arch. Appl. Sci. Res.* **3**(2), 586–595 (2011)
2. I. Togrul, H. Togrul, Global solar radiation ver Turkey: comparison of predicted and measured data. *Renew. Energy* **25**(1), 55–67 (2002)
3. G. Podestá, L. Núñez, C. Villanueva, M. Skanski, Estimating daily solar radiation in the Argentine Pampas. *Agric. For. Meteorol.* **123**, 41–53 (2004)
4. E.O. Falayi, J.O. Adepitinan, A.B. Rabiu, Empirical models for the correlation of global solar radiation with meteorological data for Iseyin, Nigeria. *Int. J. Phys. Sci.* **3**(9), 210–216 (2008)
5. C. Wloczyk, R. Richter, Estimation of incident solar radiation on the ground from multispectral satellite sensor imagery. *Int. J. Remote Sens.* **27**, 1253–1259 (2006)
6. J. Fortin, F. Ancil, L. Parent, M. Bolinder, Comparison of empirical daily surface incoming solar radiation models. *Agric. For. Meteorol.* **148**, 1332–1340 (2008)
7. C. Ceballos, M. Botino, y R. Righini, Radiación solar en Argentina estimada por satélite: algunas características espaciales y temporales. In IX Congreso Argentino de Meteorología, Buenos Aires, Argentina. Octubre 2005. Ed. Universidad Nacional de Buenos Aires, Buenos Aires, Argentina (2005)
8. S. Al-Alawi, H. Al-Hinai, An ANN-based approach for predicting global radiation in locations with no direct measurement instrumentation. *Renew. Energy* **14**, 199–204 (1998)
9. M. Bocco, G. Ovando, S. Sayago, Development and evaluation of neural network models to estimate daily solar radiation at Córdoba. Argentina. *Pesquisa Agropecuaria Brasileira* **41**(2), 179–184 (2006)
10. M. Mohandes, S. Rehman, T. Halawani, Estimation of global solar radiation using artificial neural networks. *Renew. Energy* **14**, 179–184 (1998)
11. J.F. Mas, J.J. Flores, The application of artificial neural networks to the analysis of remotely sensed data. *Int. J. Remote Sens.* **29**, 617–663 (2008)
12. M.T.Y. Tadros, Uses of sunshine duration to estimate the global solar radiation over eight meteorological stations in Egypt. *Renew. Energy* **21**, 231–246 (2000)
13. D. Ashish, G. Hoogenboom, R.W. McClendon, Land-use classification of grey-scale aerial images using probabilistic neural networks. *Trans. ASAE* **47**, 1813–1819 (2004)
14. B. Dixon, N. Candade, Multispectral land-use classification using neural networks and support vector machines: one or the other, or both. *Int. J. Remote Sens.* **29**, 1185–1206 (2008)
15. M.T. Hagan, M. Menhaj, Training feed-forward networks with the Marquardt algorithm. *IEEE Trans. Neural Networks* **5**(6), 989–993 (1994)
16. A. Angstrom, Solar and terrestrial radiation. *Quart. J. Roy. Meteor. Soc.* 121–126 (1924)
17. J.A. Prescott, Evaporation from a water surface in relation to solar radiation. *Trans. Roy. Soc. Aus.* **64**, 114–118 (1940)

Modeling of Solar Cell Efficiency Improvement Using Pyramid Grating in Single Junction Silicon Solar Cell

Hamid Heidarzadeh, Mahboubeh Dolatyari, Ghassem Rostami and Ali Rostami

Abstract In order to manipulate light in more effective ways than conventional optical materials to convert extra and cheap electrical energy from the sunlight we focused on surface and backside of solar cells. At first this paper concentrate on solar cell performance enhancement by introducing pyramids at the top of the wafer based crystalline silicon solar cells. The optimization of used pyramids as well as their height and width were performed. The efficiency of 24.45 % has been obtained for a cell (thickness of 50 μm) with surface pyramids, while efficiency of 19.53 % has been obtained for flat surface cell. Simulation results show improvement of performance when pyramids are used. Then we will focus on thickness reduction by manipulating the backside of the cell. Reducing the overall cost per watt is thus one of the major goals of this paper. As the thickness of the absorbing region is reduced, however, the absorption significantly decreases at energies close to the electronic bandgap of the semiconductor. This is particularly a problem for thin-film silicon cells. Devices based on crystalline silicon have poor absorption near the bandgap. Light trapping schemes are thus needed to enhance light absorption. In this paper light trapping is achieved using a micron-sized pyramidal surface texture and backside filters that causes scattering of light into the solar cell over a large angular range, thereby enhance the effective light path length. So this paper investigated the use of antireflection coating and back reflectors to improve thin film solar cell performances. Finally, efficiency of upper than 24 % is obtained for 8 μm thin film silicon cell with rear side filter.

H. Heidarzadeh · A. Rostami

Photonic and Nanocrystal Research Lab. (PNRL), Faculty of Electrical and Computer Engineering, University of Tabriz, Tabriz 5166614761, Iran

M. Dolatyari (✉) · G. Rostami · A. Rostami

School of Engineering-Emerging Technologies, University of Tabriz,
Tabriz 5166614761, Iran

e-mail: m.dolatyari@tabrizu.ac.ir; mdolatyari@gmail.com

G. Rostami

e-mail: rostami@tabrizu.ac.ir

1 Introduction

Energy that achieved from the sun is one of the most promising energy sources to replace with fossil fuels. Solar energy is pollution free, and most abundant energy sources with an energy flux at the earth's surface. Achievable energy from sun is several thousand times larger than worldwide power consumption. Today a number of different photovoltaic technologies exist. Longest production history and largest share of production of solar cells are based on silicon wafers, with a market share of 85 % in 2010, and thin-film solar cells which made up the remaining 15 % in 2010 [1]. We focused on two types of optical losses in this work (1) reflection from the front surface and (2) transmission from the rear side [2, 3]. First type prevents light from entering the solar cell and low absorption for shorter wavelengths is due to front side reflection. Second type makes poor absorption for longer wavelengths. There are many advantages for silicon as a solar cell material [4, 5]. So, High energy conversion efficiency achievement for silicon based solar cell is more important. Low cost cells with higher conversion efficiency are the main target of photovoltaic industry. Low energy photons need longer travelling length to absorb in silicon. The light which is not absorbed is either lost and passes straight the absorber. Therefore, as solar cells are made increasingly thinner, the optical losses due to poor light absorption becomes more and more important. The main focus has traditionally been to reduce the front-surface reflectance because the solar cells have been sufficiently thick to absorb most of the light and less light passes the absorber. In thick silicon wafer-based solar cell, surface texturing (with or without an anti-reflection coating) can be used to minimize reflection [6, 7]. Any "roughening" of the surface reduces reflection by increasing the chances of reflected light bouncing back onto the surface, rather than out to the surrounding air. In this kind cells the rear side reflection are not more important. For decreasing the production cost it is necessary to use less material and hence thin film solar cell. Light trapping is critical to achieve thin film solar cell with high conversion efficiency. Here we propose ultra-thin silicon cell with an appropriate backside filter. In the other hand, improving light absorption can be obtained by light trapping that increase path length of light inside the photo active material as long as possible. These structures are mainly applied to get light into the solar cell, but they also serve the purpose of scattering and thereby increasing the path length and thus absorption of light within the cells. Efficient light trapping is necessary for reduction of cell thickness without degrading the efficiency.

The paper is organized as follows: Sect. 2 explains the device design and simulation methodology and the principles of the light trapping techniques. This section includes the use of pyramid grating in surface of wafer based solar cell and pyramid grating in rear side of thin film solar cell. In Sect. 3, the simulation results of mentioned structure are presented. At the end of the section, the efficiency comparison of the thin and thick cells with pyramid structures will be discussed. Finally, the paper is closed by a brief conclusion in Sect. 4.

2 Device Design and Simulation Methodology

As we mentioned this work present the application of pyramid grating in thick (wafer-based) solar cell and thin film solar cell (light trapping). For first case, the pyramid grating can be used to minimize reflection of light from top surface. The typical sizes of the pyramids are in the range of 1–10 μm , depending on etching time and concentration [8]. The pyramid structures are more suitable for reducing front-side reflectance because the light reflected at the first bounce will always get a second chance of entry as it hits the pyramid wall on the opposite side, as shown in Fig. 1a. For second case, the use of combined pyramid grating and distributed Bragg reflector (DBR) can yield a high efficiency thin film. If light passes from a high refractive index medium to a low refractive index medium, there is the possibility of total internal reflection. Using total internal reflection, light can be trapped inside the cell and make multiple passes through the cell, thus allowing even a thin solar cell to maintain a high optical path length. The structures are used for this kind a cell in order to light-trapping is shown in Fig. 1b.

The incident wave is assumed to have transverse electric (TE) polarization. For the TE polarization due to 2D simulation it is needed to solve for electrical field (E_z). The electrical field may be obtained by the solution of Helmholtz equation that is given as:

$$\nabla^2 E_z(x, y) + \omega^2 \mu \epsilon E_z(x, y) = 0 \quad (1)$$

where, μ and ϵ are permeability and permittivity of materials, respectively. The total power absorbed within the cell with the volume of V can be calculated by:

$$A(\lambda) = \frac{1}{2} \int_V \omega \epsilon_2 |E(x, y, \lambda)| dV \quad (2)$$

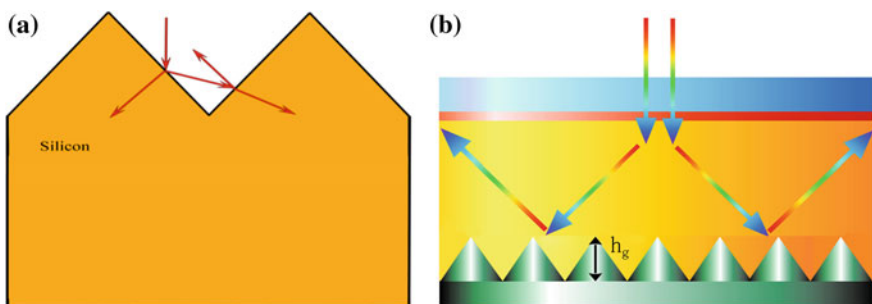


Fig. 1 **a** Light incident on a cell will have at least two chances of transmission into the Si and with an antireflection coating this structure may yield a very low front-side reflection. **b** Light diffracted by a back side grating increases the path length inside the absorbing solar cell material

where the integral is evaluated over the entire material volume V in the x–y plane, ϵ_2 is the imaginary part of the permittivity and ω is the angular frequency, respectively.

In our simulation, we considered the frequency dependence of the silicon refractive index from [9]. The frequency-dependent absorption of Si plays a key role in the calculation of performance parameters of the solar cell. For the complex refractive index we used the data related to SiO_2 [10].

We used the AM1.5 as the incident spectrum. Once the light enters into the solar cell from top side, it propagates through the solar cell. The total photocurrent that collected by the electrodes is computed from the following integral [11]:

$$J_{SC} = e \int_{\lambda_{\min}}^{\lambda_{\max}} A(\lambda) S(\lambda) d\lambda \quad (3)$$

where incident photon flux $S(\lambda)$ is derived from the AM1.5 standard solar spectrum, $A(\lambda)$ is photon absorption inside the absorber and e is an electron charge. The open circuit voltage is the maximum voltage available from a solar cell and can be obtained by the following equation [12]:

$$V_{OC} = \frac{KT}{e} \ln\left(\frac{J_{ph}}{J_0} + 1\right) \quad (4)$$

where J_{ph} is light generation current, J_0 is dark saturation current and KT/e is thermal voltage. The efficiency of a solar cell is determined as the fraction of incident power which is converted to electricity and is defined as [13, 14]:

$$\eta = \frac{J_{ph} V_{OC} FF}{P_{in}} \quad (5)$$

where V_{OC} is open circuit voltage, J_{ph} is total photo current density, FF is the fill factor and P_{in} is the incident input power solar spectrum ($P_{in} = 100 \text{ mW/cm}^2$ for AM1.5).

3 Results and Discussion

We simulated both of thick wafer based solar cell with surface pyramid and thin silicon solar cell with back side grating to compare the results of them. At first we have focused on pyramid geometries at the surface of 50 μm silicon solar cell as shown in Fig. 1a. This work demonstrates solar cell performance increase by introducing pyramids at the top of the cell. Whether or not pyramids are used as well as their geometries was optimized in this work. Figure 2a shows the efficiency of 50 μm silicon solar cell with a pyramid surface as a function of pyramid period

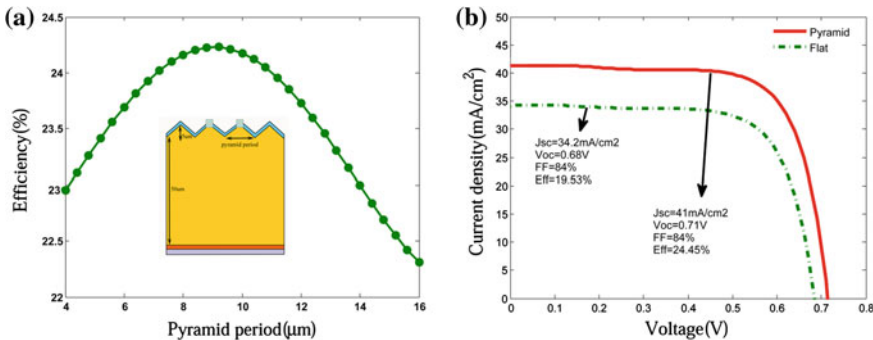


Fig. 2 **a** Efficiency as a function of pyramid periods, **b** comparison current-voltage characteristics of a cell with flat surface and pyramid surface

for a pyramid height of 5 μm . The surface texturing increases the efficiency because it minimizes reflection. As we discussed in above in a textured surface, the reflected light can strike the silicon surface again and thus reduce the reflection to air. Voltage-current characteristic curve of a cell without and with pyramids with a period of 10 μm and a height of 5 μm are depicted in Fig. 2b. Simulation results confirmed this fact that improvement of cell performance occurs when pyramids are used. The short circuit current, open circuit voltage, fill factor and efficiency of 34.2 mA/cm^2 , 0.68 V, 84 % and 19.53 % are obtained for a cell with flat surface while these values are 41 mA/cm^2 , 0.71 V, 84 % and 24.45 % for a cell with pyramid surface.

The Simulation results show performance of thick silicon cells are improved when pyramids are used. The main problem of these cells is their relatively thick thicknesses. Thin film crystalline silicon solar cells have an active layer of only several micrometers thick. It is expected that they are a promising candidate for further cost reduction while maintaining the advantages thick wafer based solar cell. In the other hand decreasing the thickness of silicon solar cells is a most promising ways for reducing the production cost of them per watt. However, the efficiency of thin film silicon cells critically depends on optical absorption in the silicon layer since silicon has low absorption coefficient in the red and near-infrared (IR) wavelength ranges due to its indirect bandgap nature. To address this problem, we propose a backside pyramid grating with a DBR as a light trapping structure. Optical path inside the absorber can be increased by use of backside side filters (see Fig. 3a). We optimize the structure by scanning pyramid height. The efficiency as function of pyramid height is depicted in Fig. 3b. As shown in this figure maximum efficiency of up to 24 % has been achieved for pyramid height of 0.2 μm . Figure 3c also show the efficiency as function of number of SiO_2/Si multilayer DBR. As a result, if we use pyramid grating with some multilayer structures in the backside of cell which scatters light into the absorber due to refraction at the backside then the wafer can be made proportionally thinner without sacrificing efficiency.

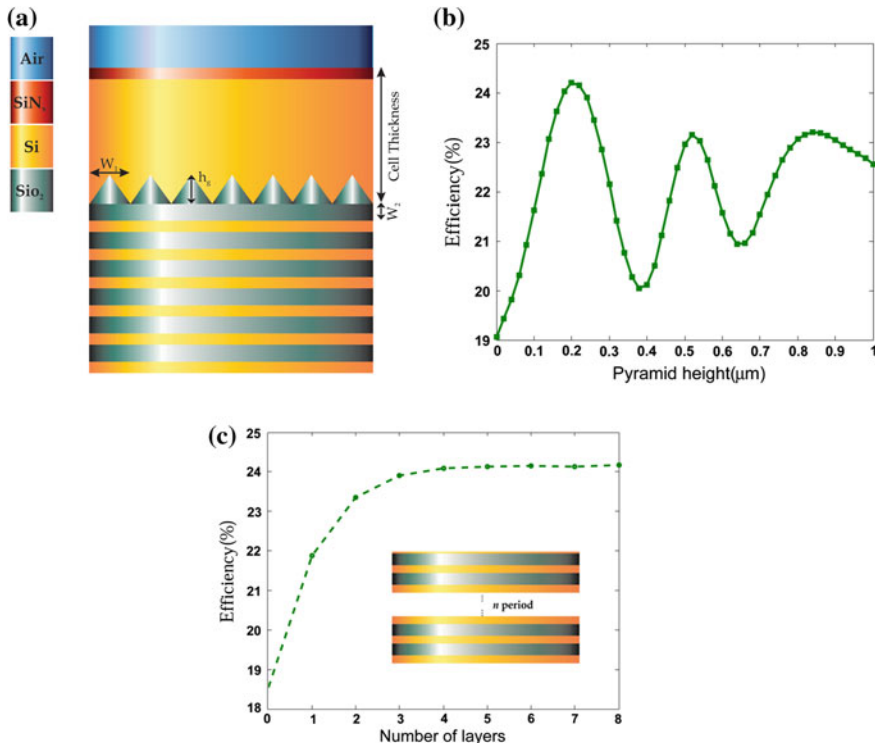


Fig. 3 **a** Schematic diagram of the crystalline silicon solar cell with a back reflector, **b** efficiency versus the pyramid height for cell thicknesses of 8 μm , **c** efficiency versus the number of the layers

Table 1 Summary of introduced cell efficiencies

	Thickness (μm)	Pyramid height	Efficiency (%)
Thick wafer with flat surface	50	—	19.53
Thick wafer with pyramid surface	50	5 μm	24.45
Thin film cell	8	0.2 μm	24.2

Table 1 summarizes obtained cell efficiencies for both mentioned structures. As we can see, for thick wafer based solar cell efficiency of up to 24 % has been achieved for cell thickness of 50 μm , which is relatively larger efficiency of conventional cells with thickness of 50 μm . Also, efficiency as large as 24 % are obtained for thin film cells with 8 μm thickness and pyramid gratings.

4 Conclusion

We have optimized and compared the conversion efficiency potential of cells with pyramid structure at surface of thick silicon solar cell and cell with pyramid grating at backside of thin silicon solar cell. A simulated result of a cell with 50 μm thickness with a surface pyramid length of around 10 μm gives efficiency of higher than 24 %. Analysis of the backside filter revealed that we can make high efficiency cell with thickness of lower than 10 μm . Poor absorption of silicon makes light trapping as an important issue. For a cell with thickness of 8 μm (with a pyramid grating) the efficiency of upper than 24 % are obtained.

References

1. https://energypedia.info/wiki/Solar_Cells_and_Modules
2. O. Semonin, J.M. Luther, M.C. Beard, Multiple exciton generation in a quantum dot solar cell. *SPIE (International Society for Optics and Photonics) Newsroom* (2012)
3. B. Richards, Enhancing the performance of silicon solar cells via the application of passive luminescence conversion layers. *Sol. Energy Mater. Sol. Cells* **90**, 2329–2337 (2006)
4. C. Becker, D. Amkreutz, T. Sontheimer, V. Preidel, D. Lockau, J. Haschke et al., Polycrystalline silicon thin-film solar cells: status and perspectives. *Sol. Energy Mater. Sol. Cells* **119**, 112–123 (2013)
5. S. Kim, J.H. Lee, M.T. Swihart, J.-C. Lee, J.Y. Kim, Silicon nanoparticle size-dependent open circuit voltage in an organic–inorganic hybrid solar cell. *Curr. Appl. Phys.* **14**, 127–131 (2014)
6. F. Toor, H.M. Branz, M.R. Page, K.M. Jones, H.-C. Yuan, Multi-scale surface texture to improve blue response of nanoporous black silicon solar cells. *Appl. Phys. Lett.* **99**, 103501 (2011)
7. F. Wang, H. Yu, J. Li, S. Wong, X.W. Sun, X. Wang et al., Design guideline of high efficiency crystalline Si thin film solar cell with nanohole array textured surface. *J. Appl. Phys.* **109**, 084306 (2011)
8. Y. Han, X. Yu, D. Wang, D. Yang, Formation of various pyramidal structures on monocrystalline silicon surface and their influence on the solar cells. *J. Nanomaterials* **2013**, 7 (2013)
9. http://snap.lbl.gov/ccdweb/ccd_data.html
10. I. Malitson, Interspecimen comparison of the refractive index of fused silica. *JOSA* **55**, 1205–1208 (1965)
11. J. Nelson, *The physics of Solar Cells*, vol. 57 (World Scientific, 2003)
12. S.M. Sze, K.K. Ng, *Physics of Semiconductor Devices* (Wiley, New York, 2006)
13. H. Heidarzadeh, H. Baghban, H. Rasooli, M. Dolatyari, A. Rostami, A new proposal for Si tandem solar cell: significant efficiency enhancement in 3C–SiC/Si. *Optik-Int. J. Light Electron Opt.* **125**, 1292–1296 (2014)
14. M.A. Green, Third generation photovoltaics: ultra-high conversion efficiency at low cost. *Prog. Photovoltaics Res. Appl.* **9**, 123–135 (2001)

A Proposal for Intermediate Band Solar Cells with Optimized Transition Energy in Cr Doped 3C-SiC

M. Esgandari, H. Heidarzadeh, A. Rostami, G. Rostami and M. Dolatyari

Abstract The Intermediate Band Solar Cell (IBSC) is a new concept proposed to better match the solar spectrum by absorbing sub-bandgap energy photons. One approach to implement this idea is to form an intermediate band (IB) with creating metallic intermediate band inside the host semiconductor. Excellent electronic properties of 3C-SiC such as high electron mobility and saturated electron drift velocity and its suitable band gap makes it an important alternative material for light harvesting technologies instead of conventional semiconductors like silicon. In this paper, the electronic band structure along with density of states calculated by the density functional theory (DFT). Main goal of this paper is proposing a new materials in the field of photovoltaic with intermediate band in the appropriate position. However our theoretical analysis show Cr is appropriate doping for 3C-SiC. In the other hand we demonstrated that our material choice is more advantageous in order to approach to efficiency of near 60 %.

1 Introduction

Intermediate band solar cells have been considered as an interesting researches topic in recent years [1, 2]. They are expected to be a suitable solution for production of high efficiency solar cells. IBSCs are formed through the addition of a narrow band of states in the middle of the bandgap of a main semiconductor. So, they are characterized by three band states (valance band, conduction band and intermediate band). In most works, intermediate band is created by two basic

M. Esgandari · A. Rostami · G. Rostami · M. Dolatyari
Photonics Research Group, School of Engineering Emerging Technology,
University of Tabriz, Tabriz 5166614761, Iran

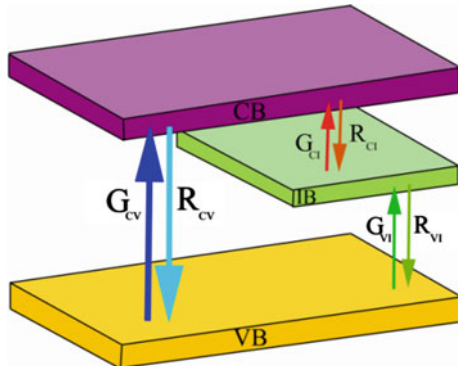
H. Heidarzadeh · A. Rostami (✉)
Photonic and Nanocrystal Research Lab. (PNRL), Faculty of Electrical and Computer
Engineering, University of Tabriz, Tabriz 5166614761, Iran
e-mail: rostami@tabrizu.ac.ir

strategies [3, 4]. The first is based on the use of quantum dots, the IB arising from the confined energy levels of the electrons in the dots. The second approach is based on the creation of intermediate bands by the doping of an appropriate impurity into a bulk semiconductor. 3d transition metals are considered as an appropriate impurity for intermediate band creation. In the intermediate band solar cell with metal doping an intermediate narrow metallic band is placed in the traditional forbidden bandgap which extends the absorption spectrum [5, 6]. This generates extra electron-hole pairs and thus increases the current without decreasing the output voltage and therefore increases the quantum efficiency. Substitution of transition metal atoms in 3C-SiC may give rise to a new type of high-efficiency photovoltaic materials based on silicon component. Numerous ab initio quantum calculations have been performed in the quest to realize IB materials [5, 7]. Wahñón and Tablero [5] published Ab initio electronic structure calculations for metallic intermediate band formation in photovoltaic materials in 2002. In 2006 Palacios et al. [8] introduced Energetics of formation of TiGa₃As₄ and TiGa₃P₄ intermediate band materials. The same authors [6] reported Transition metal-substituted indium thiospinels as novel intermediate-band materials: Prediction and understanding of their electronic properties in 2008. In 2012 Antonio Luque, Antonio Martí and Colin Stanley [3] reported a comprehensive article in nature photonics with the topic of understanding intermediate-band solar cells.

Conventional materials that have been used in single junction solar cells fabrication have some problems. Low band gap single junction solar cells produce high current density but their voltage is low. This is in contrast for high band gap materials. Shockley and Queisser [9] showed that the maximum theoretical efficiency of a single junction solar cell is limit to 40.7 % for full concentration. However the maximum conversion limitation for these solar cells is low. In the intermediate band solar cells a high band gap material has been used that yield a high open circuit voltage. The IB is designed to be partially filled to permit the absorption of low-energy photons to pass the electrons from the VB to the partially filled IB and from the IB to the CB to support both high voltage and high photocurrent by absorbing sub-band gap photons. In order to best understand of the device performances the band diagram of intermediate band solar cells is depicted in Fig. 1.

The limiting efficiency of an IBSC for full concentration and at room temperature is 63.2 %. Optimized absorption energy is placed in 0.7 eV up to valance band or below the conduction band with the main band gap of 1.9 eV, [1] significantly overcoming the Shockley-Queisser limit [9]. 3C-SiC is a wide-band gap semiconductor that is a compound of silicon and carbon. It is an intrinsic semiconductor with a band gap of about 2.3 eV at 25 °C [10, 11]. 3C-SiC is a promising material for photovoltaic application [12, 13], especially, intermediate band solar cell because of its band energy that is near to optimum value of IBSCs [14]. Also it has high mobility due to its lower density of interface states compared to other polytypes [15]. Here we describe a comprehensive study on electronic and optical properties of Cr doped 3C-SiC. They are studied with density functional theory to survey a new candidate of intermediate band (IB) material. The result shows that

Fig. 1 Band diagram of the intermediate band solar cells

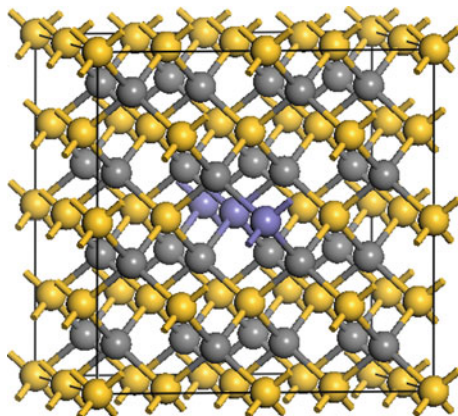


the sub-band formed in the 3C-SiC and some bands are completely isolated from the CB and the VB. The absorption coefficient calculation for proposed materials were performed and it is greatly improved by the induction of the IB compared to the 3C-SiC host semiconductor.

2 Simulation Methodology

For the past 30 years density functional theory has been the dominant method for the quantum mechanical simulation of periodic systems [16]. In recent years it has also been adopted by quantum chemists. In our proposed material, for determining the electronic properties of Cr doped 3C-SiC, the electronic band structures along with the density of states (DOS) are calculated. Calculations are based on DFT using one of the three non-local gradient-corrected exchange-correlation functionals (generalized gradient approximation-Perdew-Burke-Ernzerhof parametrization, GGA-PBE). Despite its approximations, this theory is one of the few that allows the study of large systems such as crystalline solids and allows us to obtain realistic results for many electron systems. However, LDA and GGA approximations have the problem of underestimating the band gaps. Nevertheless, some methods to avoid this inconvenience have been proposed [17, 18]. Plane-wave DFT method has been developed, along with a plane-wave quantum mechanics. These methods are very powerful but they require thousands of plane waves to correctly compute the bands. In our case, the KS equations are solved using the CASTEP code [19–21]. CASTEP is a commercial (and academic) software package which uses density functional theory with a plane wave basis set to calculate the electronic properties of crystalline solids, surfaces, molecules, liquids and amorphous materials from first principles. We analyzed the electronic properties of a material derived from 3C-SiC doped semiconductor where Cr atoms are substituted by some of 3C-SiC atoms that were shown in Fig. 2. 3C-SiC is semiconductor with the

Fig. 2 Simulated supercell structure of Cr doped 3C-SiC



lattice parameters of $a = 4.3596 \text{ \AA}$, and $\alpha = 90^\circ$ and the symmetry group of $T_d^2\text{-}F43\text{ m}$.

Theoretical calculations using the detailed balance model [22–24] show that the conversion efficiency of this photovoltaic device can overcome 60 and 70 % for one and two forbidden band, respectively. So in the end of this work we used detailed balance model to achieve maximum efficiency of silicon carbide based intermediate band solar cell as a function of sub-band energies.

3 Simulation Results and Discussion

The electronic properties are obtained by using the above mentioned methodology for evaluation of Cr doped 3C-SiC to show intermediate band formation. The IB principally arise as a consequence of the interaction between the crystalline potential and spin interaction with transitions metal d orbitals. The main goal of this work is to show an IB formation within the forbidden band energy of 3C-SiC. Towards this end, we calculated band structure, density of states, and optical absorption coefficient of Cr doped and un-doped 3C-SiC.

3.1 Band Structure of Proposed Material

Band structure calculation is an important topic in theoretical solid state physics. In this section we obtained the band structure of proposed materials. At first, we obtained the band structure of 3C-SiC with and without transition metal doping. The calculated energy-band structures for 3C-SiC without and with Cr are given in Fig. 3a, b, respectively. The obtained curves show it is possible to form intermediate band in 3C-SiC. Cr has an obvious effect on the band structure of 3C-SiC and

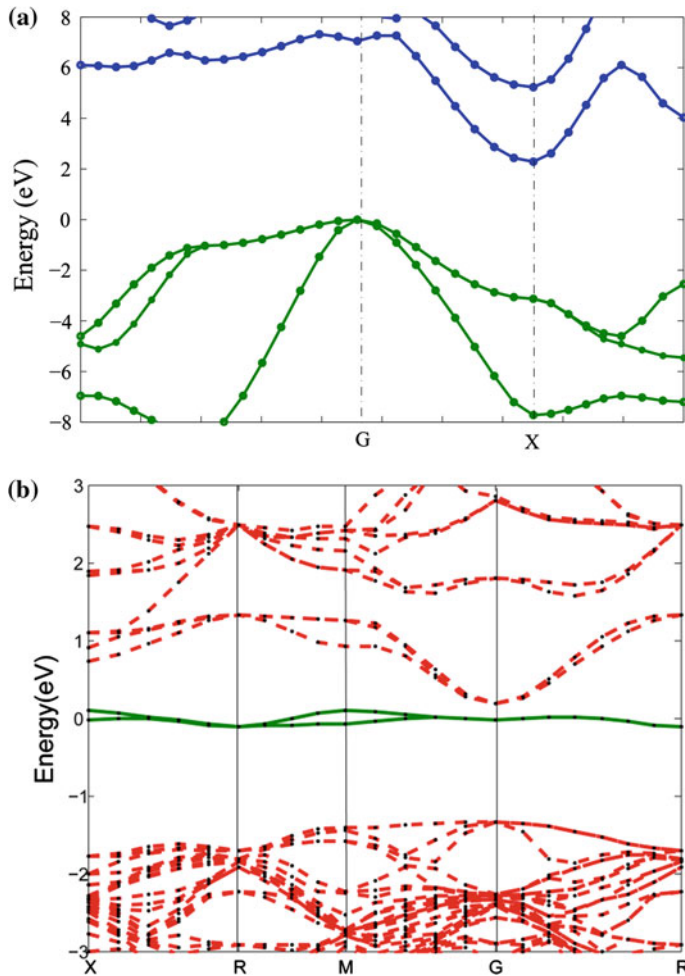


Fig. 3 **a** The band structures of intrinsic 3C-SiC and **b** the band structures of Cr doped 3C-SiC

formed IB present sub-gap absorption for low energies. This absorption is responsible for the efficiency increase in solar cells based on these materials.

3.2 Density of State Calculation

In this section we calculated the DOS of 3C-SiC with and without Cr substitution. Figure 4a, b shows DOSs for 3C-SiC without and with Cr, respectively. Where the creation of intermediate density of states by mentioned ions are clear. In the Cr doped system 3d electron orbital mainly form IB and this appears in DOS. In

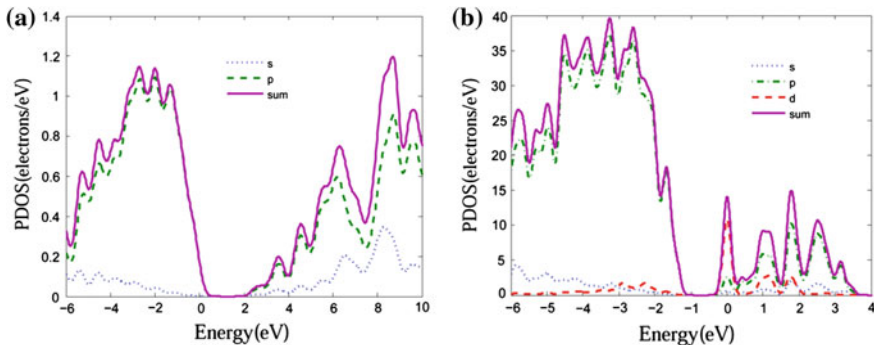


Fig. 4 **a** The density of state of intrinsic 3C-SiC and **b** the density of state of Cr doped 3C-SiC

Cr-doped 3C-SiC, the IB mainly originates from Cr 3d orbitals and the poor contribution of p orbitals. The conduction band is mainly formed from p electrons.

3.3 Optical Absorption Coefficient

We present with first-principles calculations, optical properties of new Cr-substituted in 3C-SiC compounds presenting a narrow half-filled intermediate band isolated from the VB and the CB of the host semiconductor. Figure 5 depict the optical absorption coefficient for proposed materials. The computed optical absorption of Cr doped compound compared to the corresponding undoped semiconductor predicts a significant absorption below the band gap of the parent semiconductor and an enhancement of the optical absorption in the whole energy range of the visible region. Moreover, introducing these systems can be developed more efficient novel optoelectronic devices.

4 Efficiency Potential of Proposed Materials

The energetic position of the intermediate band will strongly influence the power conversion efficiency of the solar cell. Calculations of the efficiency versus energetic position of intermediate band for 3C-SiC with band gap of 2.2 eV are shown in Fig. 6 as a dashed line. It has maximum value of 59 % at 0.8 eV up to valance band or 1.4 eV below the conduction band for 1000 sun concentration under AM1.5 spectrum irradiance.

Fig. 5 The calculated optical absorption coefficient for undoped 3C-SiC and Cr doped 3C-SiC

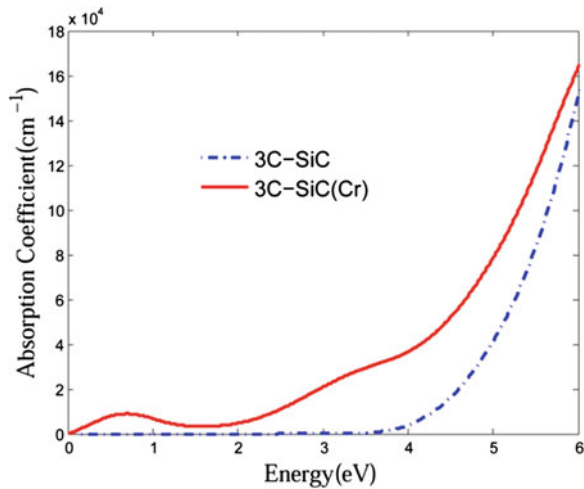
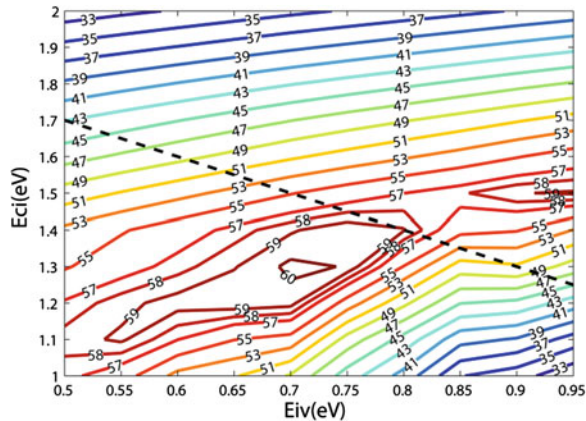


Fig. 6 Efficiency versus intermediate band energy level, efficiencies for 3C-SiC is along the *dashed line* indicated in these figures



5 Conclusions

The new intermediate band materials based on Cr doped 3C-SiC for high efficiency solar cell application were introduced in this article. Evaluation of band structure, DOS, and optical properties were performed for proposed materials. Development of new intermediate band materials based on 3C-SiC doped with the Cr opens new promising horizons in high efficiency solar cells. The simulation also shows 3C-SiC is an interesting candidate for intermediate band solar with efficiency near 60 %.

References

1. A. Luque, A. Martí, Phys. Rev. Lett. **78**, 5014 (1997)
2. A. Luque, A. Martí, C. Stanley, Nat. Photonics **6**, 146 (2012)
3. A. Luque, P. Linares, E. Antolín, I. Ramiro, C. Farmer, E. Hernández, I. Tobías, C. Stanley, A. Martí, J. Appl. Phys. **111**, 044502 (2012)
4. W. Wang, A.S. Lin, J.D. Phillips, Appl. Phys. Lett. **95**, 011103 (2009)
5. P. Wahnón, C. Tablero, Phys. Rev. B **65**, 165115 (2002)
6. P. Palacios, I. Aguilera, K. Sánchez, J. Conesa, P. Wahnón, Phys. Rev. Lett. **101**, 046403 (2008)
7. A. Martí, C. Tablero, E. Antolín, A. Luque, R. Campion, S. Novikov, C. Foxon, Sol. Energy Mater. Sol. Cells **93**, 641 (2009)
8. P. Palacios, P. Wahnón, S. Pizzinato, J.C. Conesa, J. Chem. Phys. **124**, 014711 (2006)
9. W. Shockley, H.J. Queisser, J. Appl. Phys. **32**, 510 (1961)
10. K. Karch, P. Pavone, W. Windl, O. Schütt, D. Strauch, Phys. Rev. B **50**, 17054 (1994)
11. G.L. Harris, *Properties of Silicon Carbide* (IET, 1995)
12. H. Heidarzadeh, H. Baghban, H. Rasooli, M. Dolatyari, A. Rostami, Optik-Int. J. Light Electron Opt. **125**, 1292 (2014)
13. A. Rostami, H. Heidarzadeh, H. Baghban, M. Dolatyari, H. Rasooli, J. Optoelectron. Adv. Mater **15**, 1 (2013)
14. H. Heidarzadeh, A. Rostami, M. Dolatyari, G. Rostami, *Effect of Dopant Concentrations on Conversion Efficiency of SiC-Based Intermediate Band Solar Cells*, International Congress on Energy Efficiency and Energy Related Materials (ENEFM2013) (Springer, 2014), p. 119
15. B. Gupta, M. Notarianni, N. Mishra, M. Shafiei, F. Iacopi, N. Motta, Carbon **68**, 563 (2014)
16. A.D. Becke, J. Chem. Phys. **140**, 18A301 (2014)
17. J. Fernández, C. Tablero, P. Wahnón, Int. J. Quantum Chem. **91**, 157 (2003)
18. P. Palacios, K. Sánchez, J. Conesa, J. Fernández, P. Wahnón, Thin Solid Films **515**, 6280 (2007)
19. V. Milman, K. Refson, S. Clark, C. Pickard, J. Yates, S.-P. Gao, P. Hasnip, M. Probert, A. Perlov, M. Segall, J. Mol. Struct. (Thoechem) **954**, 22 (2010)
20. S.J. Clark, M.D. Segall, C.J. Pickard, P.J. Hasnip, M.I. Probert, K. Refson, M.C. Payne, Z. Kristallogr. **220**, 567 (2005)
21. D. Hamann, M. Schlüter, C. Chiang, Phys. Rev. Lett. **43**, 1494 (1979)
22. T. Nozawa, Y. Arakawa, Appl. Phys. Lett. **98**, 171108 (2011)
23. L. Cuadra, A. Martí, A. Luque, Electron Devices. IEEE Trans. **51**, 1002 (2004)
24. A.S. Brown, M.A. Green, R.P. Corkish, Physica E: Low-dimensional Syst Nanostruct **14**, 121 (2002)

Comparison the Effect of Size and Inter-dot Spaces in Different Matrix Embedded Silicon Quantum Dots for Photovoltaic Applications

Hamid Heidarzadeh, Ghassem Rostami, Mahboubeh Dolatyari and Ali Rostami

Abstract The quantum dot solar cell concept is proposed as a scheme to optimize the efficiency of standard solar cells. The two most significant power loss mechanisms in single band gap solar cells are the inability to absorb photons with energy less than the band gap (transparency loss), and thermalisation of photon energy exceeding the band gap (thermalisation loss). There are several approaches for tackling these losses for instance tandem cell with increasing the number of band gaps or intermediate band solar cell by creating energy level inside the forbidden band of host materials. Quantum confined nanostructures of silicon with barriers of SiO_2 or SiC can potentially fill these criteria and allow designing of tandem cell or intermediate band solar cell with increased absorption given by direct band gap of such quantum confined systems. In this work, the comparison of solar cell is done based on tunneling probability between QDs which depends on dot size, type of matrices (SiO_2 or SiC) and thickness of barrier layer. The simulation results indicate that the chosen of SiC as dielectric matrix for silicon quantum dots could improve the tunneling rates, which provides an efficiency improvement in silicon, based nanostructure solar cells.

1 Introduction

Recently, renewable energy demand rises to record 2.7 % of global consumption and the demand of solar cells has been growing rapidly because of social interest for clean energy. Improving the energy conversion efficiency of solar cells is one of the

H. Heidarzadeh · A. Rostami

Photonic and Nanocrystal Research Lab. (PNRL), Faculty of Electrical and Computer Engineering, University of Tabriz, Tabriz 5166614761, Iran

G. Rostami (✉) · M. Dolatyari · A. Rostami

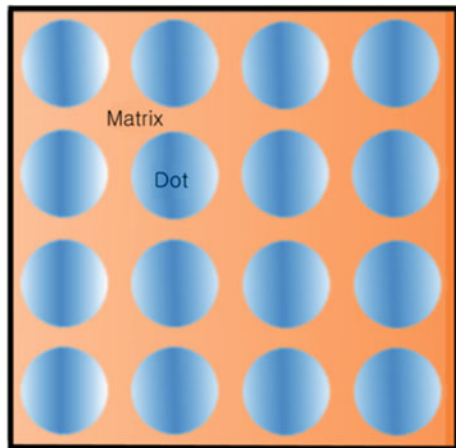
School of Engineering-Emerging Technologies, University of Tabriz, Tabriz 5166614761, Iran

e-mail: gh.rostami@tabrizu.ac.ir

main challenges in this field. The main problem of photovoltaic modules are their rather high production and energy cost. By developing the nano technology it is expected to develop high efficiency thin film solar cell [1]. Third generation solar cells are the alternative type of the promising devices, which aims to achieve high-efficiency devices with low cost in comparison with expensive first generation solar cells and low-efficiency second generation solar cells [2, 3]. One of the prominent types is silicon-based third generation solar cells. These cells benefit from thin film processes and abundant, nontoxic materials [4]. To gain efficiencies more than Shockley and Queisser limit for a standard solar cells and overcome the loss mechanisms in these cells, different methods have been proposed [5–7]. The two kind of significant losses in single junction solar cells are inability to absorb photons with energy less than the band gap and thermalization of photon energy exceeding the band gap [8]. Tandem solar cell and intermediate band solar cell concepts are well established as two ways of improving solar cell performance [5, 9, 10]. It is well known that more photons can be absorbed in tandem cells with more junctions. A difficulty in using the tandem cell approach to improve silicon cells performance is that there are no obvious candidates for suitable high-band gap cells to use with silicon that would not, to some extent, compromise the reliability and stability expected from silicon devices, or depend upon toxic or scarce elements [10, 11]. One of the approaches is using the quantum confinement effect of silicon quantum dots embedded in a dielectric matrix to engineer the energy band gap of solar cell material [12, 13]. Using intermediate band technique is another way that significantly improves the efficiency of single junction solar cells. The idea of intermediate band is to create a semiconductor with a band of levels contained entirely inside the band gap between the valence and conduction bands [14]. In a super-lattice structure (quantum dots arrays) the wave function can be diffuses into neighboring QDs. They couple with each other to broaden the discrete quantum levels to form finite-width mini-bands [14–16]. Mini-bands formation is a key parameter in QD solar cell. In this condition two-photon absorption can be done that satisfies photo-generation carrier transport. These levels will allow the material to absorb lower-energy photons while still getting a large voltage, exceeding the efficiency of all simple semiconductor designs [14].

In the quantum dot based photovoltaic materials, optical and electrical properties can be tuned and controlled simply by changing the size of the QDs because of quantum confinement effect. Energy band structure is one of the important features that can be control by QDs sizes to obtain the optimum band structure. In order to realize the “all-silicon” tandem solar cell concept or intermediate band solar cell, there are several aspects that need to be established. First of all, certain features of silicon quantum dots including dot size and inter-dot space must be controlled. The broad objective of this paper is detailed study of silicon based quantum dots materials in order to determine the material requirements to realize high-efficiency solar cells. For reach to this aim we simulated a 2D simulation of 4×4 quantum dots arrays as depicted in Fig. 1. The optimization of dot size and inter dot spaces has been done for silicon dioxide and silicon carbide matrixes.

Fig. 1 Schematic of simulated silicon quantum *dot* embedded in different matrixes



2 Results and Discussion

One way to realize quantum dot solar cell is to create intermediate bands. The dependence of optical properties on particle size of quantum dots can be used in order to designing effective and efficient solar cell. First the theoretical calculation from 1D simulation of Schrodinger equation has been done. The size dependence of energy band structure for conduction band is plotted as a function of the quantum dot size in Fig. 2a, b for SiO_2 and SiC matrixes, respectively.

In the next, Schrodinger equation has been solved in the slowly varying envelope approximation in two dimensions for a periodical silicon quantum arrays embedded in SiO_2 and SiC matrixes. Multi-level IBSCs can be achieve from the use of these structures. The quantum confinement effect in crystalline silicon QDs leads to the splitting of the energy levels and the coupling among the QDs forms the mini-bands. Figure 3 depicts the energy levels and wave function of 4×4 crystalline silicon QDs embedded in SiC for dot diameters of 4 nm and inter-dot distance of 2 nm. There are three eigenvalues inside the conduction band at 0.1136, 0.282 and 0.472 eV energy levels. Energy levels and corresponding wave functions for quantum dot arrays with dot diameters of 6 nm and inter dot distance of 2 nm are shown in Fig. 4a, b, respectively.

Effect of quantum dot size and inter dot distances from each other on conduction band and overlap of wave functions in SiO_2 matrixes are calculated in this part of paper. Figure 5a, b shows the energy band structure and wave function of silicon quantum dot arrays in a SiO_2 matrix for 4 nm diameter QDs and 0.5 nm inter dot spacing, respectively. There is a reasonable overlap of the wave functions between dots. Figure 5c, d shows same information for 4 nm diameter QDs with 2 nm inter dot spacing. There are less overlapping between wave functions. So, spacing between dots very powerfully influence on mini-band formation or localization of quantum dot states. Our simulation results suggest that QDs distance must be not

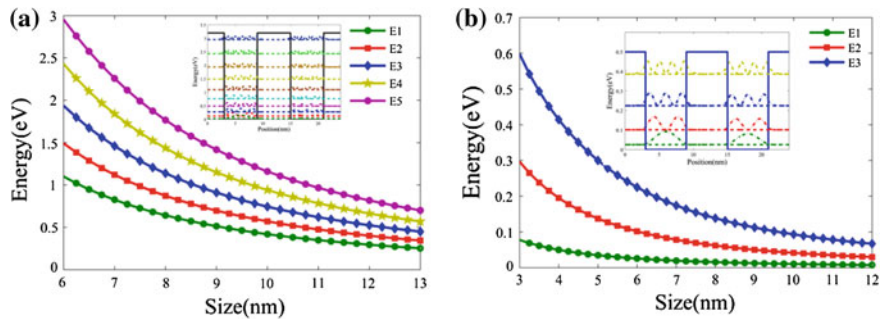


Fig. 2 Calculated mini band formation in conduction band of silicon quantum *dots* embedded in **a** SiO₂ matrix and **b** SiC matrix

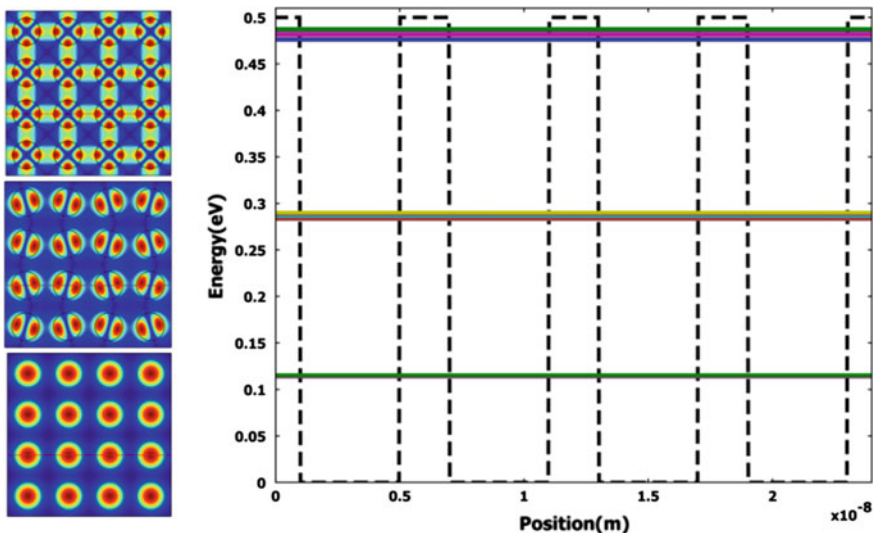


Fig. 3 The schematic conduction band structures and distribution of their relative 2D wavefunctions for a system with 4 × 4 silicon QD embedded in SiC with diameters of 4 nm

more than 1–2 nm, for a reasonable overlap of the wave-function in SiO₂ while they could be separated by more than 6 nm of SiC. However, the charge transport between dots can be significantly increased by using alternative layers with a lower barrier height, ΔE .

Calculated 2D wave-function cross section of silicon quantum dots with 4 nm diameter in SiC matrix are shown in Fig. 6a, b for 2 and 8 nm inter dot spacing, respectively. Using these results it can be seen that Eigen functions for dots with 2 nm inter dot spaces has more overlapping while there are less overlapping for QDs with 8 nm inter dot spaces.

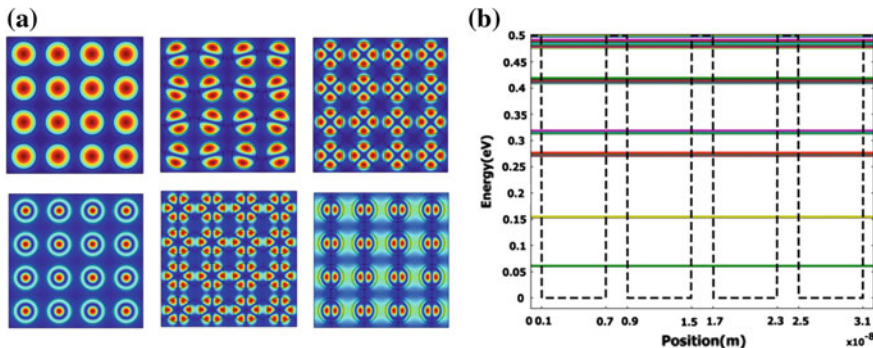


Fig. 4 Energy levels and corresponding wave functions for quantum *dot* arrays with dot diameters of 6 nm **a** schematic of system and 2D wave function **b** energy levels

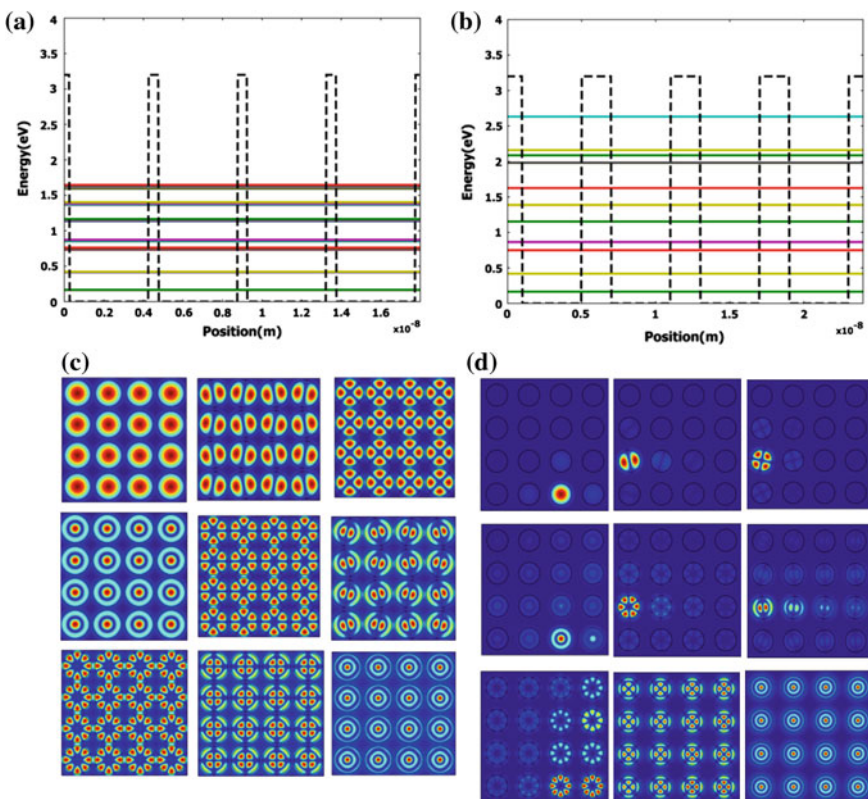


Fig. 5 Calculated miniband above the Si band gap for a superlattice of Si quantum dots in SiO_2 and related wave function, **a, b** 4 nm diameters with 0.5 nm separated Si quantum dots, **c, d** 4 nm Si quantum *dots* diameter with 2 nm spacing in SiO_2 matrices, respectively

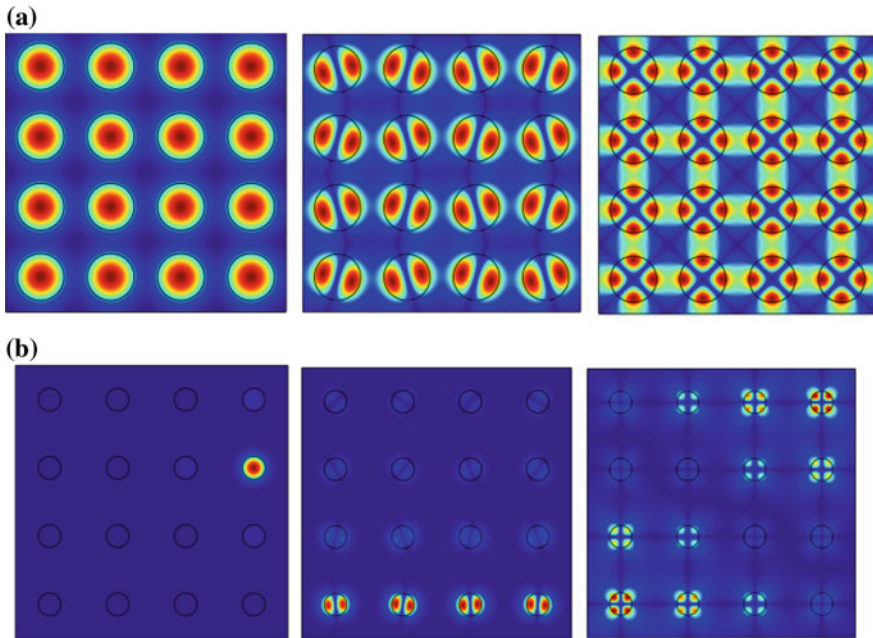


Fig. 6 Eigen functions of three Eigen values (first state in each mini bands) inside the barrier which are from *left to right* for E_1 , E_2 , and E_3 , respectively, for silicon QDs with 4 nm diameter with **a** 2 nm inter *dot* spaces and **b** 8 nm inter *dot* spaces

Governing of the quantum states is a possible way to enhance the intraband transitions. One possible solution is formation of a miniband, such that the wave functions of the QDs have overlapping. Because of the reduction in the wave function overlapping by inter dot spaces of QDs, it appears that possible solution could be employing a structure with an ultrahigh density of QDs, or a structure with lower barrier matrix material. Quantum confined nanostructures of silicon with barriers of SiO_2 or SiC can potentially create these mini-bands. Hence, small confinement barriers will increase the tunneling probability. However, appropriate distance of QD leads to formation of extended mini-bands instead of localized quantum dot states. This makes such structures suitable for photovoltaic application in the form of intermediate band solar cell or middle or top cell of tandem solar cell.

3 Conclusion

We demonstrated the formation of intermediate electronic bands through host band of silicon carbide and silicon dioxide. In order to enhance the intraband transitions one possible solution is formation of a miniband, such that the wave functions of the QDs have overlapping. It showed that spacing between dots very powerfully

influence on mini-band formation or localization of quantum dot states. QDs distance must be not more than 1–2 nm for silicon QDs in SiO_2 matrix while it can be upper than 6 nm for SiC matrix. We conclude that transport in SiC best done and degrees of freedom for quantum-dot spacing is large in compared to SiO_2 .

References

1. P.V. Kamat, G.C. Schatz, J. Phys. Chem. C **113**, 15473 (2009)
2. R. King, N. Karam, J. Ermer, N. Haddad, P. Colter, T. Isshiki, H. Yoon, H. Cotal, D. Joslin, D. Krut, *Next-generation, High-efficiency III-V Multijunction Solar Cells*. Photovoltaic Specialists Conference, 2000. Conference Record of the Twenty-Eighth IEEE (IEEE, 2000), p. 998
3. A. Martí, A. Luque, *Next Generation Photovoltaics: High Efficiency Through Full Spectrum Utilization* (CRC Press, 2010)
4. G. Conibeer, M. Green, R. Corkish, Y. Cho, E.-C. Cho, C.-W. Jiang, T. Fangsuwannarak, E. Pink, Y. Huang, T. Puzzer, Thin Solid Films **511**, 654 (2006)
5. A. Luque, A. Martí, Phys. Rev. Lett. **78**, 5014 (1997)
6. M.C. Hanna, Z. Lu, A.J. Nozik, *Hot Carrier Solar Cells, Future Generation Photovoltaic Technologies* (AIP Publishing, 2008), p. 309
7. A.J. Nozik, M.C. Beard, J.M. Luther, M. Law, R.J. Ellingson, J.C. Johnson, Chem. Rev. **110**, 6873 (2010)
8. O. Semonin, J.M. Luther, M.C. Beard, *SPIE (International Society for Optics and Photonics) Newsroom* (2012)
9. S. Yoshida, *Tandem Solar Cell* (Google Patents, 1991)
10. G. Conibeer, Mater. Today **10**, 42 (2007)
11. N. Espinosa, F.C. Krebs, Sol. Energy Mater. Sol. Cells **120**, 692 (2014)
12. J. Wu, Z.M. Wang, *Quantum Dot Solar Cells* (Springer, 2014)
13. Y. Okada, K. Yoshida, Y. Shoji, *Nanotechnology: Concepts, Methodologies, Tools, and Applications* (2014), p. 406
14. A. Luque, A. Martí, C. Stanley, Nat. Photonics **6**, 146 (2012)
15. T.-W. Kim, C.-H. Cho, B.-H. Kim, S.-J. Park, Appl. Phys. Lett. **88**, 123102 (2006)
16. Y.-H. So, A. Gentle, S. Huang, G. Conibeer, M.A. Green, J. Appl. Phys. **109**, 064302 (2011)

Sand Effect on Photovoltaic Array Efficiency in Algerian Desert

S. Semaoui, A. Hadj Arab, S. Bacha, H. Zeraia and E.K. Boudjelthia

Abstract The Algerian energy strategy recommends an increase of renewable energies contribution. The objective is to reach a renewable energies contribution for electricity production of 5 % by year 2015 and 40 % by year 2030, through photovoltaic (PV), solar thermal and wind generators. In this sense, the insertion of a PV system has an impact on social development, economy and environment on desert regions. However, the southern Algerian regions are generally characterized by frequent sandstorms. This natural phenomenon causes the dust accumulation on PV panels. Consequently, this may reduce the efficiency of PV array. The objective of this research is to study the effects of the dirt accumulation on the performance of a PV array in a desert region of Algeria (for our case Ghardaia site, $32^{\circ}29'N$, $3^{\circ}40'E$, 450 m). The experiments have been conducted on the effect of the dust particle accumulation on the PV modules. The tests were performed with the PVPM2540C in natural conditions to determine the current/voltage characteristics and see the resulting efficiency. It was found in this study, that the dust accumulation on the PV array surface for a period of several months can significantly reduce the PV array efficiency with an average power loss of about 4.38 %.

1 Introduction

Such as example, the Algerian energy strategy recommends an increase of renewable energies contribution. The objective is to reach a renewable energies contribution for electricity production of 40 % by year 2030, through the photovoltaic, solar thermal and wind generators. The Algerian desert presents over 80 %

S. Semaoui (✉) · A. Hadj Arab · H. Zeraia · E.K. Boudjelthia
Centre de Développement des Energies Renouvelables, BP 62 Route de l'Observatoire
Bouzaréah, 16340 Algiers, Algeria
e-mail: smsemaoui@yahoo.fr

S. Bacha
Grenoble Electrical Engineering Laboratory, G2Elab, 38402 St Martin d'Hères, France

of the country area. This is considered as one of the regions in the world that receive a great portion of solar radiation, especially in summer time with an average of 3000 sunshine hours per year [1]. One of the most promising applications of solar energy in Algeria would be PV system. This is the direct conversion of sunlight to electricity. It is an attractive alternative to conventional sources of electricity for many reasons. In this sense, the insertion of a PV system has an impact on development, economy and environment of country and it can be installed anywhere. However, sandstorm, low frequency and intensity of rain in Algerian desert region provoke the dust accumulation on PV modules and affect their performance. When foreign particles fall on PV modules, they interfere with illumination quality by both absorbing and scattering light, which consequently cause degradation in the efficiency of PV modules. This study can be of great importance to PV solar system designers in Algeria and all other countries with similar weather conditions of sandstorms. The dust accumulated on the PV module surface decreases the transmittance of irradiance and consequently decreases the useful energy received by the modules. To investigate the effect of dust on the transparent cover of solar sensor, Elminir et al. [2] performed measurements on several sensor and concluded that dirt accumulated on glass inclined of an angle of 0° at 90° from horizontal in Egypt causes a reduction in the corresponding transmittance by approximately 52.54 at 12.38 %, respectively. Al-Hasan [3] investigated the effect of the amount of accumulated dust on the efficiency of a PV module in the Kuwait climate (latitude 30°). A linear relation has been proposed to correlate the degradation in efficiency to the amount of sand dust accumulated on the module surface. This relation can help PV system designers to reliably predict the effect of sand dust accumulation on PV module efficiency under real environmental conditions. Another study has been carried out by Jiang et al. [4], to investigate the output degradation of different types of PV modules with different surface materials caused by airborne dust pollution experimentally. It is a series of experiments under controlled conditions were designed and conducted. The results indicated that dust pollution has a significant impact on PV module output. With dust deposition density increasing from 0 to 22 g m^{-2} , the corresponding reduction of PV output efficiency grew from 0 to 26 %. The reduction of efficiency has a linear relationship with the dust deposition density, and the difference caused by cell types was not obvious. A tilt angle is one of the important factors that determine the performance of PV panels. In an experiment carried out in Roorkee by Grag [5] discovered that gather dust on a glass plate titled at 45° decrease transmittance by an average of 8 % after an exposure period of 10 days. Hegazy [6] studied dust deposition on glass plate with different tilt angles as well as measured the transmittance of the plate under different weather conditions. It was found that degradation in solar transmittance depend on the tilt angle. Also, the work by Sayigh et al. [7] of dust deposition on a tilted glass plate located in Kuwait city were found to reduce the transmittance of the plate from 64 to 17 % for tilt angles ranging from 0° to 60° respectively after 38 days of exposure to the environment. Cano [8] has studied the effect of tilt angle of PV modules on deposition of soiling in Arizona State. This study shows that during the period of January through March 2011 there was an average loss due to soiling of

approximately 2.02 % for 0° tilt angle. Modules at tilt angles 23° and 33° also have some irradiance losses but do not come close to the module at 0° tilt angle. Tilt angle 23° has approximately 1.05 % monthly irradiance loss, and 33° tilt angle has an irradiance loss of approximately 0.96 %. The soiling effect is present at any tilt angle, but the magnitude is evident, the flatter the solar module is placed the more energy it will lose. Zorrilla-Casanova et al. [9] are worked on the measurements of radiation losses produced by the accumulation of dust. The experiment has been carried out at the roof of the PV Laboratory of the University of Malaga (36.7°N, 4.5°W, 50 m) in the south of Spain. Their results show that the mean of the daily energy loss along a year caused by dust deposited on the surface of the PV module is around 4.4 %. In long periods without rain, daily energy losses can be higher than 20 %. In addition, the irradiance losses are not constant throughout the day and are strongly dependent on the sunlight incident angle. When has studied as a function of solar time, the irradiance losses are symmetric with respect noon, where they reach the minimum value. The authors have also proposed a simple theoretical model that, taking into account the percentage of dirty surface and the diffuse/direct radiation ratio, accounts for the qualitative behavior of the irradiance losses during the day. Recently, Ndiaye et al. [10] investigated the effect of dust on the performance of PV modules. This work has highlighted the impact of dust on the current-voltage and power-voltage characteristics of PV modules with the advent of the mismatch effect. The maximum power (P_{max}), the maximum current (I_{max}), the short-circuit current (I_{sc}) and the fill factor are the most affected performance characteristics by the dust deposits on the PV modules surface. P_{max} output loss can be from 18 to 78 % respectively for the polycrystalline module (pc-Si) and monocrystalline module (mc-Si). I_{max} loss can vary from 23 to 80 % for respectively pc-Si and mc-Si modules. However, the maximum voltage output (V_{max}) and the open-circuit voltage (V_{oc}) are not affected by dust accumulation for both technologies studied. This work presents measurements of power losses produced by the accumulation of dust on PV array. The experiment has been carried out at the roof of the PV Laboratory of the Research Unit of Ghardaia in the south of Algeria. The unit is located close of an industrial area surrounded by an open desert space. A national road with heavy traffic flow is very close to the unit. At the time of the measurements, a mine of rock not very far from the unit is in full activity, which has increased the amount of dust particles present in atmospheric air.

2 Experimentation Description

This study focuses in Ghardaia region, at 600 km south of the capital Algiers. This region takes profit from a climate that is arid. Indeed, it is ranked in the third climatic zone [11]. This region is characterized by exceptional sunlight. The database of solar radiation components is available (Global measured on a horizontal plane and global on a titled plane to the latitude of the site), in addition to temperature. These parameters are recorded on a daily basis, with an interval of five

minutes. During the winter season, 62 % of days have values between 2330 and 4660 (Wh/m²). During spring and autumn, 46 % of days have a value higher than 5800 (Wh/m²). In the summer season, 72 % of days have a value between 6990 and 8155 (Wh/m²) [12]. A data acquisition system was installed in order to ensure the data collection of the various climatic parameters. For irradiation measurement, a CM11 Pyranometer type with a sensitivity equal to 4.57×10^{-6} V/Wm⁻² was used. The experimental I-V characteristics of PV array was measured by the PVPM2540C with the calibrated PV cell. The PV array includes 20 PV modules arranged in 10 parallel groups of 2 modules in series. Total module area is 7.49 m². The array consists of mono-crystalline modules (I-50). The array DC output at STC (1000 W/m², 25 °C) was 1 kW_p. The modules are titled 32° from horizontal plane and oriented to south. This slope was chosen according to the optimization done for different fixed slopes, each one during a whole year [13].

3 Results and Discussion

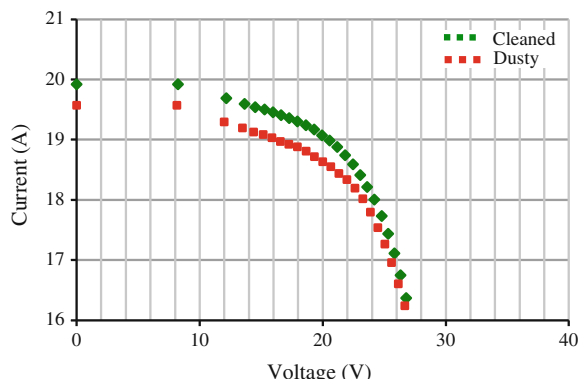
The experimental I-V characteristics of PV array with and without dust on surface are illustrated in Fig. 1, for a cell temperature of 58 °C and an irradiance of 608 W/m² at 10h00. This figure shows the effect of dust on the short circuit current.

Figure 2 shows that the effect of dust is very low at noon. The experimental I-V characteristics of dusty and cleaned PV array are illustrated for a cell temperature respectively of 65.5 and 64.6 °C with an irradiance of 934 W/m² at 13h00.

The curve that describes the dependence of losses on the angle of incidence has a very specific shape (Fig. 3). The loss has a minimum around solar noon, and then increases with the elevation of the incidence angle up to a maximum value, and then decreases for larger values of incidence angle.

Daily evolution of power losses due to dust effect the 22/07/2010 is shown in Fig. 3. This is a clear sky summer day, more than 2 months after the last rains; as consequence, dust level deposited on the PV generator surface causing an average

Fig. 1 Example of experimental I-V with and without dust at 10h00



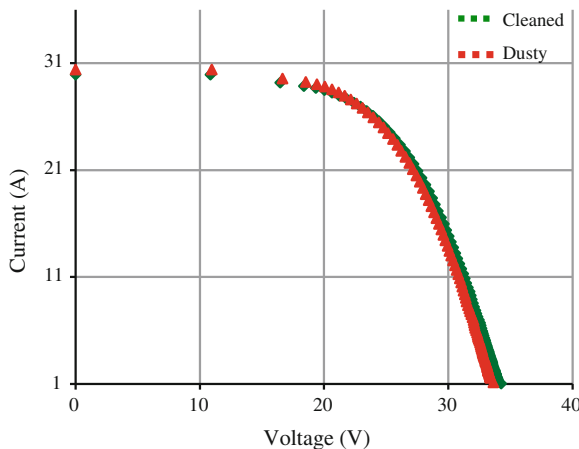


Fig. 2 Example of experimental I-V with and without dust at 13h00

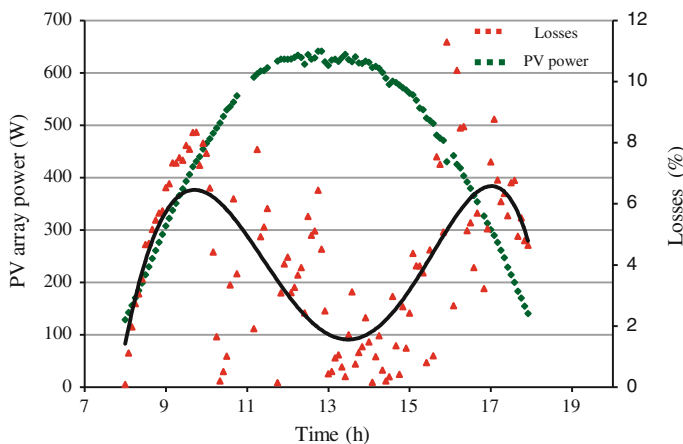


Fig. 3 Daily evolution of power losses

daily loss of 4.384 % with a minimum of 0.082 % and maximum of 8.76 %. These power losses represent the fraction of irradiance that the PV array will not receive. When PV modules are clean, losses are approximately constant during the day. As dust is deposited on the module surface, the behavior of the losses is not constant throughout the day in clear sky days, becoming dependent on the angle of incidence.

4 Conclusion

In this work we have studied in general the energy losses due to accumulated dust on the surface of photovoltaic modules. First, the results about the dust effect on electrical parameters of PV generator have been presented. The relative losses of parameters I_{sc} are around of 1.75 %. Secondly, the results of the dust effect on irradiance losses have been presented at through the power losses of PV array along the day. These losses depend of the incidence angle of irradiance on tilted plane. The mean value of these losses is about 4.38 %.

References

1. Algerian Ministry of Energy and Mines, *Renewable Energy and Energy Efficiency Program* (SATINFO Algeria, 2011)
2. H.K. Eliminir, A.E. Ghitas, R.H. Hamid, F.E. Hussainy, M.M. Beheary, K.M. Abdel-Moneim, Effect of dust on the transparent cover of solar collectors. *Energ. Convers. Manage.* **47**(3), 192–203 (2006)
3. A.Y. Al-Hasan, A new correlation for direct beam solar radiation received by photovoltaic panel with sand and dust accumulated on its surface. *Sol. Energy* **63**(3), 23–33 (1998)
4. H. Jiang, L. Lu, K. Sun, Experimental investigation of the impact of airborne dust deposition on the performance of solar photovoltaic (PV) modules. *Atmos. Environ.* **45**(4), 299–304 (2011)
5. H.P. Garg, Effect of dirt on transparent covers in flat-plate solar energy collectors. *Sol. Energy* **15**(4), 299–302 (1973)
6. A.A. Hegazy, Effect of dust accumulation on solar transmittance through glass covers of plate-type collectors. *Renew. Energy* **22**, 525–540 (2001)
7. A.A.M. Sayigh, S. Al-Jandal, H. Ahmed, *Dust Effect on Solar Flat Surfaces Devices in Kuwait*. Proceedings of the Workshop on the Physics of Non-conventional Energy Sources and Materials Science for Energy, Italy, 1985, pp. 353–367
8. J. Cano, *Photovoltaic Modules: Effect of Tilt Angle on Soiling*. Theses, Arizona State University, 2011
9. J. Zorrilla-Casanova, M. Piliougine, J. Carretero, P. Bernaola, P. Carpena, L. Mora-López, M. Sidrach-de-Cardona, *Analysis of Dust Losses in Photovoltaic Modules*, World Renewable Energy Congress, Linköping, Sweden, 8–13 May 2011
10. A. Ndiaye, C. M. F. Kébé1, P. A. Ndiaye, A. Charki, A. Kobi, V. Sambou, Impact of dust on the photovoltaic (PV) modules characteristics after an exposition year in Sahelian environment: the case of Senegal. *Int. J. Phys. Sci.* **8**, 21, 1166–1173 (2013)
11. A. Hadj Arab, B. Ait Driss, R. Amimeur, E. Lorenzo, Photovoltaic systems sizing for Algeria. *Sol. Energy* **2**, 99–104 (1995)
12. K. Gairaa, S. Benkaciali, Analysis of solar radiation measurements at Ghardaïa area, south Algeria. *Energy Procedia* **6**, 122–129 (2011)
13. S. Semaoui, A. Hadj Arab, S. Bacha, B. Azoui, *Performance Evaluation of a Photovoltaic System with Battery Storage in Ghardaïa Site (South Algeria)*. In: 9th International Multi-Conference on Systems, Signals and Devices, IEEE, Chemnitz, Germany, 20–23 March 2012

Solar Irradiation on *Lawsonia Inermis* Sensitized with Red Blood Cells: Effect on Osmotic Fragility

Rami Alkhatib, M-Ali Al-Akhras and Duaa J. Al-Khalili

Abstract *Lawsonia Inermis*, known as Henna, is a widely used product for cosmetic and medicinal purposes in many countries. It is native to tropical and subtropical regions of Africa, southern Asia, and northern Australia. Although Henna is widely used; it has been shown to cause oxidative hemolysis, especially in people with glucose-6-phosphate dehydrogenase deficiency. The objective of this study was to determine whether henna is light sensitive or not and to examine the effect of henna seed extract and henna powder on osmotic fragility of blood cells. Henna seeds were extracted using a microwave-assisted extraction method. The effect of henna seed and powder was tested on red blood cells (RBCs) with three different NaCl concentrations. Henna seed extraction increased hemolysis rate, meanwhile, henna powder did not affect hemolysis even at high NaCl concentration. This suggests that henna powder is not sensitive to sunlight. Our results suggest that the seed extraction of *Lawsonia inermis* could be potentially used as a protective agent as well as a sunscreen substitute.

1 Introduction

Lawsonia inermis which is commonly known in the Middle East as Henna is native to tropical and subtropical regions of Africa, southern Asia, and northern Australasia in semi-arid zones [1, 2]. Henna leaves, flower, seeds, stem bark and roots have been found to exhibit antioxidant, antidiabetic, hepatoprotective,

R. Alkhatib (✉)

Department of Biotechnology and Genetic Engineering,
Jordan University of Science & Technology (JUST), P.O. Box 3030, Irbid 22110, Jordan
e-mail: rqalkhatib@just.edu.jo

M. Al-Akhras · D.J. Al-Khalili

Bio-Medical Physics Laboratory, Department of Physics,
Jordan University of Science & Technology (JUST), P.O. Box 3030, Irbid 22110, Jordan
e-mail: alakmoh@just.edu.jo

hypoglycemic, antimicrobial, anticancer and wound healing properties [3]. The plant constituents are made up of mannite, tannic acid, mucilage and gallic acid, but the main constituent is 2-hydroxynaphthoquinone Henna (lawsone), known to be the major bioactive constituent, dried powdered leaves of contain about 0.5–1.5 % lawsone [4]. Henna is universally used in cosmetic and medicine. It was reported that the pharaohs in Egypt used henna to treat skin diseases and it was used for mummification in form of oilmen and to rejuvenate the mummy by coloring the hair [5]. Henna leaves have been used in India to treat wounds, ulcers, mouth ulcers, bruises, sprains, swelling, burns, and stomach pain caused by childbirth, sore throats, gonorrhea, and obesity, to promote menstruation and to induce abortion. Fruit oil is a folk remedy used in disorders causing hardening of the liver and diaphragm, and an ointment made from young fruit is used to prevent itching [6, 7].

It has been reported that henna can cause critical condition (life threatening) to G6PD (Glucose-6-phosphate dehydrogenase)-deficiency patient's which is an X-linked recessive hereditary disease featuring non-immune hemolytic anemia [8]. It also causes acute hemolytic anemia; the abnormal breakdown of red blood cells either in the blood vessels (intravascular hemolysis) or elsewhere in the body (extravascular) [9]. It has been reported that Lawsone increases the oxygen affinity of blood at levels as low as 1 mM of the compound but with little change in the characteristics of normal blood at this concentration [10]. However, at high concentrations, Lawsone can deplete Glutathione (GSH) and increase methemoglobin in the blood [11].

The osmotic fragility is a common test used to diagnose different types of anemia. The physical properties of anemia are depending on the shape of red blood cells (RBC), surface area including the functioning state of the RBC membrane. An increased osmotic fragility is found in hemolytic anemia, hereditary spherocytosis (auto-hemolytic anemia) and whenever spherocytes are found. Membrane abnormality increases the permeability to sodium. This causes water to move into the RBC decreasing the mean corpuscular hemoglobin concentration. A measure of RBC resistance to hemolysis by osmotic stress depends primarily on the volume of the cell, the surface area, and the cell's membrane function. As the concentration of NaCl decreases, cells take on water to produce osmotic equilibrium and RBC swelling up until critical volume then hemolysis occurs [12].

The objective of the study was to determine the effects of henna seed and henna leaf powder on osmotic fragility of blood in the presence and absence of solar irradiation.

2 Materials and Methods

2.1 Sample Preparation

Fresh human blood samples were donated by healthy volunteers (Jordan University of Science and Technology). Blood samples were mixed with phosphate buffer saline (PBS), (pH = 7.4).

2.2 Plant Extraction

Henna seeds were extracted using a microwave-assisted extraction method as described in the protocol of Archives of Pharmacal Research [12]. Briefly, In this method, extraction was based on the selective heating of the matrix that contains the target extract when the matrix is immersed in a solvent such as ethanol and water. Mixtures were then irradiated with microwave with output power of the 300 W. The extract was finally filtered through gauze and evaporated under vacuum at 40 °C using a rotary evaporator. The extract was dissolved in phosphate buffered saline (PBS, P4417), purchased from Sigma/USA (P4417 Sigma, USA).

2.3 Materials and Samples Preparation

0.5 g of Henna seeds powder was added to 12 ml of PBS and left in a shaker for 48 h and then sonicated for 2 h. The solution finally filtered to get henna seeds solution of 28.5 mg/ml concentration. RBCs were obtained from healthy human blood by repeated centrifugation at 4000 rpm. The cells were suspended in 7.4 pH phosphate buffered saline until the supernatant was clear. The previous amounts of henna seed solution and PBS were added to RBCs and incubated for 30 min with continuous shaking for 15 min. The NaCl solutions were made in three different concentrations (0 % (tap water), 0.9 and 5 %). After incubation, 2.5 ml of NaCl solution was added to 0.5 ml of RBCs mixed with henna seed extract to get 3 ml as total volume. As soon as the RBCs and henna seeds were added to the solution, the optical density (OD) was recorded using Shimadzu UV-VIS spectrophotometer/Japan. The optical density (OD) of 14 μ l of RBCs diluted in 3 ml PBS at 680 nm was approximately 2 cm^{-1} which correspond to 7.86×10^6 cells/mm³ erythrocytes concentration as measured by using haemocytometer.

2.4 Spectrophotometry

Samples were incubated for 10 min at 37 °C with or without light followed by the spectrophotometric measurements of the optical density (560 nm).

2.5 Photosensitivity

The concentration of henna leaf powder in this experiment is (5.43 mg/ml). 0.5 ml of henna solution with 1 ml of RBCs were mixed then 1.5 ml of PBS buffer was

added. Then, the first replicate (total of 3 samples), Sample A, B and C was exposed to sun light for (10, 20, 30) seconds respectively, as for the second replicates were placed in a dark box, but all sample were placed outside.

3 Results and Discussion

Figure 1 showed the normal hemolysis of RBC with out the presence of henna seeds extracts. The t_{50} for 5 % of NaCl concentration was over 80 min. Meanwhile, the hemolysis of RBC in the presence of henna seeds extracts at the same NaCl concentration was faster of about 2.5 folds ($t_{50} = 30$ min). The optical density of the samples at 0 % NaCl (Isotonic) increases with increasing the seeds extracts, while in both cases 0.9 and 5 % (Hypotonic, and Hypertonic) respectively did not show any significant effects at concentration below 2.85, meanwhile the optical density at higher concentration (4.27) declined (Table 1). This suggests that at higher concentration of the henna seeds could have higher impact of RBC's hemolysis.

Fig. 1 Hemolysis % of RBC in 5 % NaCl concentrations with and without henna seed extract

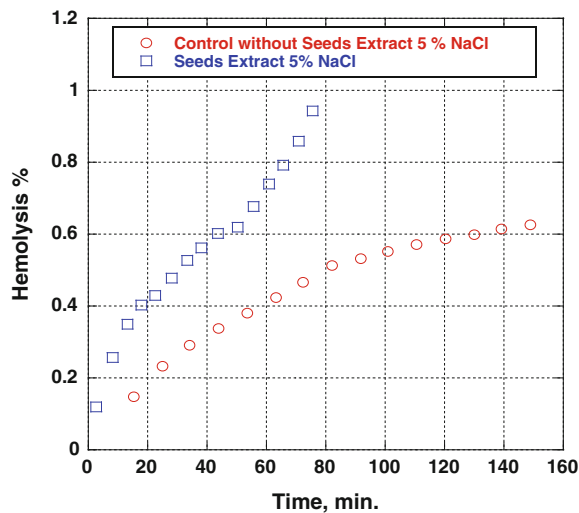


Table 1 OD readings with different henna extract concentrations mixed with different NaCl concentrations

NaCl (%)	Henna seeds concentration (mg/ml)								
	0.000	0.285	0.570	0.855	1.425	1.995	2.280	2.850	4.272
0	0.045	0.103	0.190	0.374	1.620	2.000	2.100	2.140	1.520
0.9	1.850	1.840	1.830	1.850	1.890	1.857	1.824	1.840	1.524
5	2.050	2.700	2.200	2.180	2.190	2.030	1.930	1.840	1.610

Furthermore, it has been suggested by Mcmillan et al. [11] that Henna which contain an active compound Lawsone (2-Hydroxy-1,4-nephthoquinone), which structurally similar to menadione (2-methyl-1,4-nephthoquinone) which is known to induce oxidative injury within red blood cells.

The Photosensitivity test showed that henna leaves and seeds extracts of 4 mg/ml concentration did not induce hemolysis for over 200 min (data not shown).

4 Conclusion

Henna seed extraction has shown to induce hemolysis in a faster rate than control (NaCl with RBC's), and it was more effective at higher concentration greater than 2.85 mg/ml. On the other hand, henna powder did not induce hemolysis even at high concentration. In addition to above finding, henna powder is not sensitive to sunlight; meanwhile, henna seed extract was light sensitive (data not shown). The seed extraction of *Lawsonia inermis* could be potentially used as a protective agent as well as a sunscreen substitute.

Acknowledgments This work was supported by a grant from the Deanship of Scientific Research at Jordan University of Science and Technology (JUST) No. 7/2014.

References

1. M.S. Lavhate, S.H. Mishra, A review: nutritional and therapeutic potential of *Ailanthus excelsa*. *Pharmacog. Re.* **1**, 105–113 (2007)
2. Abdelraouf, A. Amany, A. Nedaa, Antibacterial, antifungal and synergistic effect of *Lawsonia inermis*, *Punicagranatum* and *Hibiscus sabdariffa*. *Ann. Alquds Med.* (7), 33–41 (2011)
3. R. Hema, S. Kumaravel, N. Gomathi, Gas chromatography mass spectroscopic analysis of *Lawsonia inermis* Leaves. *NY Sci. J.* **3**(12), 99–101 (2010)
4. P. Arun, K.G. Purushotham, J. Jayarami, V. Kumari, In vitro Antibacterial activity and Flavonoid contents of *Lawsonia inermis* (Henna). *Int. J. Pharm. Technol. Res.* **2**(2), 1178–1181 (2010)
5. F.R. Gallo, G. Multari, G. Palazzino, G. Pagliuca, M.M. Zadeh, P.N. Biapa, M. Nicoletti, Henna through the centuries: a quick HPTLC analysis proposal to check henna identity. *Rev. Bras Farmacogn.* **24**, 133–140 (2014)
6. K. Reddy, Folk medicine from Chittoor District Andhra Pradesh, India used in the treatment of jaundice. *International Journal Crude Drug Research.* **26**(3), 137–140 (1988)
7. K. Chetty, *Flowering Plants of Chittoor*, 1st edn. (Andhra Pradesh, 2008)
8. I. Perinet, E. Lioson, L. Tichadou, M. Glaizal, L. de Haro, Hemolytic anemia after voluntary ingestion of henna (*Lawsonia inermis*) decoction by a young girl with G6PD deficiency. *Med. Trop. (Mars.)* **71**(3), 292–294 (2011)
9. A. Vander, J. Sherman, D. Luciano, E. Widmaier, H. Raff, H. Strang, *Human Physiology—the Mechanism of Body Function*, 8th edn. (McGraw-Hill Education, 2001), pp. 132–144
10. H. Chang, S.E. Suzuka, Lawsone (2-OH-1,4-naphthoquinone) derived from the henna plant increases the oxygen affinity of sickle cell blood. *Biochem. Biophys. Res. Commun.* **107**(2), 602–608 (1982)

11. D. McMillan, S. Sarvate, J. Oatis, J. Jollow, Role of oxidant stress in Lawsone-induced hemolytic anemis. *Toxicol. Sci.* **82**, 647–655 (2004)
12. Archives of Pharmacal Research, *Natural Medicines Comprehensive Database* (2001), pp. 431–436. www.naturaldatabase.com

Part IV

Nuclear Energy

Perspectives of Industrial Separation of Zirconium Isotopes by Laser Assisted Retardation of Condensation Method

K.A. Lyakhov and H.J. Lee

Abstract Modern researches indicate many possible ways of isotopically enriched materials applications in different spheres of human activity. In particular, zirconium isotope enriched materials can be used in nuclear industry in order to save fuel. Therefore, the problem of finding cheaper ways of zirconium isotope separation arises. In this paper we focus on this issue by proposing optimal design of industrial facility for zirconium isotope separation by laser assisted retardation of condensation (SILARC) method. Optimal parameters for this facility were found from the optimization criterion based on the transport model for rarefied gas flow dynamics in external laser field specifically tuned for selective excitation of target isotopes, Eerkens (Laser Part Beams 23:225, 2005). Because product cut and enrichment factor corresponding to the optimal conditions are rather small, isotopes should be recovered iteratively. By developing appropriate model for gas flow separation we have found the optimal values of laser intensity, gas flow temperature, nozzle throat area, and number of nozzles.

1 Introduction

Natural zirconium is comprised of five isotopes with atomic weights 90, 91, 92, 94, and 96, the abundance of which is 51.5, 11.2, 17.1, 17.4, and 2.8 %, respectively. Zirconium is commonly used for forming fuel cladding, pressure tubing and other components of nuclear reactors. Zirconium is useful for such applications because of its relatively low neutron capture cross-section. The neutron capture cross-section of natural zirconium is dominated by the ^{91}Zr . The fuel economy of a nuclear reactor can be greatly improved by using ^{91}Zr depleted zirconium in place of natural

K.A. Lyakhov (✉) · H.J. Lee

Institute for Nuclear Science and Technology, Applied Plasma Physics Lab,
Department of Nuclear and Energy Engineering, Jeju National University,
Araill-dong 1, Jeju-si 690-756, South Korea
e-mail: lyakhov2000@yahoo.com

zirconium. Reduction of ^{91}Zr in natural zirconium is cheaper than separation of ^{90}Zr \$80 (in contrast to \$115USD), but fuel cost saving is higher (estimation is 7 % in contrast to 5 % for 4 loops PWR). The use of ^{91}Zr depleted (or $^{90}\text{Zr}/^{94}\text{Zr}$ enriched) zirconium not only allows improved fuel efficiency, but also allows the use of thicker pressure in calandria tubes by reducing tube sag and increasing safety margins. As a result, a substantial saving in the costs of re-tubing reactors can be realized. In view of future fusion power market great benefits are expected for the uses of enriched or depleted zirconium isotopes. Very small isotopic shift for Zr isotopes ($\sim 1.5 \text{ cm}^{-1}$) and relatively low energy consumption make the method of isotope separation by laser assisted retarded condensation (SILARC) economically promising. Zirconium tetra-tert-butoxide molecule $\text{Zr}[\text{OC}(\text{CH}_3)_3]_4$ can be chosen due to relatively small boiling temperature (at $T_b = 80 \text{ }^\circ\text{C}$ it has vapor pressure 3 Torr), and, therefore, less vaporization heat required [1]. In this paper we analyze theoretical performance of industrial setup, which principle of operation is based on the SILARC method [2], subject to efficiency of electricity consumption. This method is one of the variety of Molecular Laser Isotope Separation (MLIS) methods, where isotopes harvesting is based upon well-established mass separation effect in overcooled supersonic gas flow: light species escape the gas flow core at higher rate than heavy ones. The larger mass difference the more separation effect is pronounced. In order to produce sufficient mass difference, gas flow should be irradiated by laser photons of energy specifically tuned to excitation of specific isotope. Photons absorption and re-absorption in gas flow takes place repeatedly. For effective enrichment the rate of this process should exceed rate of excitation loss caused by collisions in the gas flow. Formation of van der Waals clusters, which is the onset of condensation in free jets, can be schematically represented as following. If gas flow temperature is still higher than temperature T_b corresponding to carrier and target gas molecule binding energy, selectively excited molecules form transient states (dimers) with carrier gas molecules ${}^i\text{Q:CG}$ that decompose rapidly as $\text{Q+CG} \rightarrow {}^* \text{Q:CG} \rightarrow \text{Q+CG}$, where in our case $\text{Q} = \text{Zr}[\text{OC}(\text{CH}_3)_3]_4$, and index i corresponds to target isotopomer. However, with decreasing gas flow temperature, and/or increasing the number of collisions (pressure), probability of bound state formation also increases $T < T_b$: ${}^i\text{Q+CG} + \varepsilon_L \rightarrow {}^i\text{Q:CG} \rightarrow {}^i\text{Q+CG} + \Delta E_c$; ${}^j\text{Q+CG} \rightarrow {}^j\text{Q:CG}$, where $\varepsilon_L = h\nu_L$ is photon energy required to excite given vibrational state and ΔE_c is energy release due to condensation. Viability of this method was originally demonstrated on the example of sulfur isotopes separation in SF_6 target gas mixed with argon [3, 4].

2 Basic Parameters

In order to calculate enrichment factor and product cut from the transport model given in [5] one need to know Lennard-Jones potential parameters. They can be found from experimental data on viscosity and surface tension [6] at given temperature by the method given in [7]. Laser excitation rate of Q molecules by

selective photoabsorption is: $k_A = \varphi_L \sigma_A$, s^{-1} per molecule, where photon flux density is $\varphi_L = \frac{5.035 \times 10^{22} I_L \left(\frac{w}{cm^2} \right)}{\varepsilon_L (cm^{-1})}$ where $I_L = I_p / (\pi R^2)$, I_L is laser intensity, R_L is the laser beam radius, and laser photon energy ε_L corresponds to absorption band of Q in gaseous state $\nu_L = 1011 \text{ cm}^{-1}$ [1], which can be excited by specifically tuned CO₂ laser. Resonant value of Q (in liquid state) photoabsorption cross section σ_A can be extracted from spectral line corresponding to $\nu_L = 1002 \text{ cm}^{-1}$, [8].

3 Operational Principles

In this section we discuss operational principles of the industrial setup for isotopes separation. The principal scheme of multi-nozzle separation chamber for industrial setup is shown in the Fig. 1.

In the beginning of operation, the mixing tank is occupied only by carrier gas, while Q , having natural isotopic abundance, is stored in the target gas feed chamber. Then, Q is injected into the mixing tank, where it is mixed with carrier gas at some optimal molar fraction μ , so that the total pressure is of optimal level P_0 . In order to minimize significant, nearly resonant, vibrational energy transfer between selectively excited isotopes in the collisional region of the free jet [9], target gas molecules have to be substantially diluted inside the carrier gas. On the other hand, apparently, this molar fraction should not be too much small in order to have still economically justified production rate. From the mixing tank gas expands continuously into separation chamber, where it is irradiated by many times reflected laser beam. It is

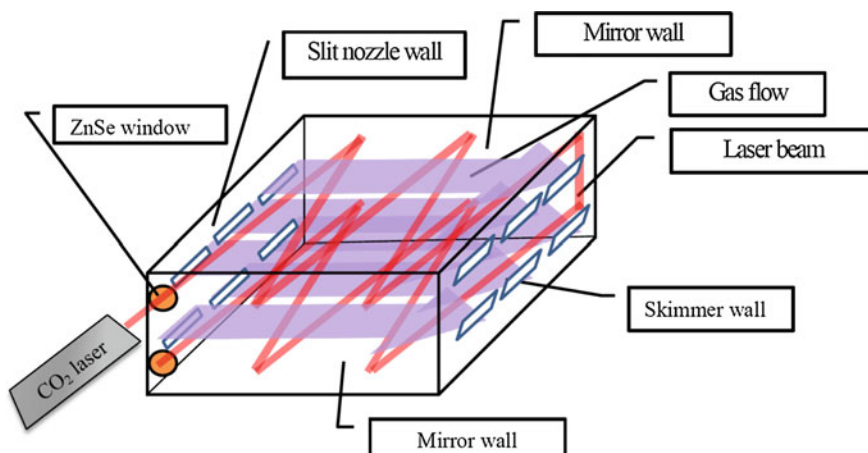


Fig. 1 Multi-nozzle industrial scale separation chamber

reasonable to assume that the core of the produced supersonic gas flow remains isentropic over distance between mixing tank and skimmer chamber, because of rather weak interaction between gas flow and surrounding gas due to low pressures of both gases. According to the model in [5], optimal gas flow temperature and pressure depend on the mass of carrier gas molecules: the heavier this mass the larger production rate (carrier gas binding energy is also important factor as follows from the same model). However, carrier gas molecules should not be too large, because gas flow cooling of polyatomic molecules is much less effective than monatomic molecules (this is also one of reasons why only a small amount of polyatomic molecules can be injected into an carrier gas). Skimmer blade divides the gas flow onto two parts corresponding to rim and tail gases. For perfectly expanded gas flow produced by the slit nozzle orientation of the small and large sides of its cross section stays the same as at the nozzle outlet over the large distance between nozzle and skimmer, while for under-expanded gas flow they change their orientation periodically with subsequent relaxation to the distribution equivalent to the produced by the coaxial source [10]. This feature is definitely not desirable if gas flow is irradiated cross-wise. Therefore, ambient gas pressure in the discharge chamber should match the pressure at the nozzle outlet (condition of perfect expansion), and skimmer inlet should be of wedge-like shape with inlet dimensions corresponding to the velocity profile inside the gas flow at this distance. We assume that tail gas sub-flow is represented by unexcited molecules that reside mainly in the gas flow core, which can be represented as a rectangular parallelepiped occupying the space between cross sections of the nozzle outlet and the skimmer chamber inlet. Rim gas part of the gas flow is represented by excited molecules that are target isotope enriched and constitute the part of the flow outside this parallelepiped. This outside part belongs to the zone of gas flow mixing with ambient gas. These two parts of the gas flow are evacuated separately by vacuum pumps having different pumping speeds. Outlets of the vacuum pumps, evacuating target isotope enriched gas flow periphery, are connected to the mixing tank for further gas recycling. After completing certain number of cycles required to achieve required enrichment level valve between product cold trap and vacuum pump outlet opens and enriched gas is captured in it. In order to maintain Q molar fraction in the gas flow after each iteration on the same level, background gas in the separation cell should has the same components ($Q+Ar$) as the gas in the mixing tank mixed at the same molar fraction. In order to compensate pressure loss in the mixing tank caused by gas expansion, carrier gas and Q enriched by target isotopes on previous cycle should be continuously pumped back inside the mixing tank. Tail gas sub-flow is evacuated by another vacuum pump through the cold trap, where it is separated from Q . Schematic of circulation of rim and tail gases is shown in the Fig. 2.

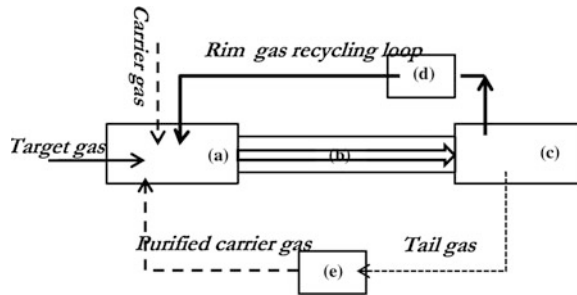


Fig. 2 Recycling scheme: solid arrow corresponds to target isotope enriched (rim) gas circulation, dashed arrow corresponds to carrier gas circulation; **a** mixing tank; **b** irradiation partition of separation cell; **c** skimmer partition of separation cell; **d** cold trap for tails; **e** cold trap for product

4 Global Minimum of Isotope Separation Energy as Optimization Criterion

Efficacy of isotope separation is conditioned by energy consumption and isotope separation rates. The objective function, which takes into account both characteristics, and the minimum of which corresponds to the requirement to produce the largest amount of isotopes over shortest period of time but by lowest energy expenses, can be introduced as instantaneous energy expenses per isotope separation ε : $\frac{dE_{tot}}{dt} = \varepsilon \frac{dQ_p}{dt}$ where $\frac{dE_{tot}}{dt}$ is electricity consumption rate, and $\frac{dQ_p}{dt}$ is isotope production rate. Apparently, electricity consumption rate remains constant over all processing time. We estimate it as: $\frac{dE_{tot}}{dt} \approx W_{vac;A} + W_{vac;B} + W_{las}$, where W_{las} is laser pumping speed, $W_{vac;A}$ and $W_{vac;B}$ are motor rating of vacuum pumps evacuating rim and tail gases respectively. Isotope production rate decreases cycle by cycle due to mixing of enriched and recycled rim gas with fresh gas having natural isotope abundance in the mixing tank in order to keep Q molar fraction in the gas flow on the same level. Therefore, the objective function should be constrained as:

$\varepsilon \geq \underline{\varepsilon} = \frac{dE_{tot}}{dt} / \frac{d\overline{Q_p}}{dt}$, $i = \overline{1, N_c}$, where $\underline{N_c} = \log_{\beta}(\frac{c_0}{x})$ is the lower limit for number of recyclings to perform in order to achieve desired enrichment level c_0 , where $\beta = \beta(x)$. The upper limit for isotope separation rate for each iteration is assumed constant $\frac{dQ_p}{dt} \approx \frac{Q_p}{T_{tot}}$, where $\underline{T_{tot}} = \underline{N_c} t_{tr}$ is the lower limit for total processing time, and $Q_p = c_0 \mu \theta Q_{ftr}$ is the number of isotopomers in rim gas after final recycling.

Therefore, the lower limit for objective function is given by $\underline{\varepsilon} = \frac{N_c \frac{dE_{tot}}{dt}}{c_0 \mu \theta Q_p}$. Since, we need to find the minimum of objective function we are interested only in its lower: $\min_Q \underline{\varepsilon}$, where $Q = \{I_{CW}, T_{opt}, P_0, \mu, A_t, N_{nozz}\}$ where N_{nozz} is number of nozzles.

5 Conclusion

Rarefied gas flow dynamics (its expansion and dimerization) in external specifically tuned laser field, corresponding to SILARC method, is treated within the transport model developed previously by Jeff Eerkens. By developing appropriate model for gas flow separation by skimmer blades, we have found the optimal values for laser intensity, gas flow temperature, and nozzle throat area in prospective experimental setup. Related optimization criterion is based on minimization of isotope separation energy averaged over total processing time. It was shown that larger nozzle throughput does not necessarily lead to higher production rate (larger product cut). Optimal nozzle profile was calculated. Upscaling to industrial scale facility can be implemented straightforwardly by applying the same optimization criterion with additional free parameter which is number of nozzles.

Acknowledgments This work was supported by Priority Research Centers Program through the National Research Foundation of Korea (NRF) funded by Ministry of Education, Science and Technology (2010-0020077).

References

1. Y. Okada, S. Kato, S. Satooka, K. Takeuchi, Spectrochim. Acta Part A Mol. Biomol. Spectrosc. **46**, 643 (1990)
2. J.W. Eerkens, Nucl. Sci. Eng. **150**, 1 (2005)
3. J.M. Zellweger, Phys. Rev. Lett. **52**(7), 522 (1984)
4. V. den Bergh, Laser und Optoelectronik **3**, 263 (1985)
5. J.W. Eerkens, Laser Part. Beams **23**, 225 (2005)
6. D.C. Bradley, R.C. Mehrotra, D.P. Gaur, *Metal Alkoxides* (Academic Press Inc., London, 1978)
7. J.W. Eerkens, Chem. Phys. **293**, 112 (2003)
8. C.T. Lynch, K.S. Mazdiyasni, J.S. Smith, W.J. Crawford, Anal. Chem. **36**, 2332 (1964)
9. J.W. Eerkens, Chem. Phys. Lett. **430**, 271 (2006)
10. G.N. Abramovich, Bulltinies of USSR academy of science. Fluid Mechanics **1**, 54 (1983)

Part V
Biofuels and Bioenergy

Promising Technologies of Biomass Use for Energy Production Purposes

V. Zaichenko

Abstract The new technologies of biomass processing developed in the Joint Institute for High Temperature, Russian Academy of Sciences (JIHT RAS) are described in this paper. The first one connected with production energy gas with enhanced calorific value from biomass and another with improving consumer properties of biomass granulated fuel.

1 Introduction

Progress is always connected with additional burden upon the environment. Improvement of life standard is always connected with an increase of energy consumption and in its turn with worsening of world ecological situation. Energy consumption is constantly increasing. Now we are trying to replace part of organic fossil fuel by renewable energy sources whose use does not lead to environmental pollutions. The main way to solve this problem is to develop new methods and processes of clean energy production. Among new energy production methods whose usage allows minimizing negative man-caused affect of fuel-energy complex on the environment due to replacement of fossil fuels bioenergetics has the greatest prospects.

As it is well known biomass (wood and agricultural waste, peat and so on) consists of approximately 50 % of carbon. This carbon is one of the main sources of carbon dioxide emission to the atmosphere due to its rotting. For example if a tree dies in the forest and rots, some amount of CO₂ will be emitted. The same amount of CO₂ is formed during burning this wood. In this case the natural balance of CO₂ is not changed. But if we extract fossil fuel and also burn it the balance is changed.

V. Zaichenko (✉)

Joint Institute for High Temperature, Russian Academy of Sciences (JIHT RAS),
Moscow, Russian Federation
e-mail: zaitch@oivtran.ru

In the world there are huge resources of biomass which can be used as power fuel. To a great extent it concerns Russia as well. In Russia about 23 % of the world's resources of wood and approximately 47 % from world's peat resources are concentrated. Peat reserves in the country exceed total reserves of oil and natural gas and concede in amount only to coal reserves. Now possible processes of energy productions from biomass are investigated in various scientific institutions all over the world. The main problem is the creation of technologies of biomass power use which economically would be competitive with existing technologies. It is hard to imagine the use new in energetic processes if they are not economically justified.

The main task today is the development of new technologies of power production from a biomass which should provide competitiveness of created technologies with existing ones, based on the use of fossil fuels. The transition from traditional fossil fuel to the local power energy source may be considered as the new direction of energy development. It is a big and a very complicated problem important for all countries and cooperation of scientists from various countries is necessary for successful decision of this problem.

The paper presents the description of the investigation directed at new power technologies creation based on local fuels which is carried out at the Joint Institute for High Temperature Russian Academy of Sciences from Moscow. The developed methods of biomass use for energy purposes may be divided into two groups: receiving power gas for further use as fuel in electricity producing equipment and improving the consumption properties of biomass fuel.

2 Power Gas Production from Biomass

The first direction of our investigation is the creation of local construction of gas piston power plants. We designed an investigation stand for working out domestically produced improving gas piston power plants characteristics and parameters of their operations [1]. But gas piston power plants are widely-spread now in the world. The development of distributed energy is growing rapidly. Distributed energy in many cases has more profitable economic characteristics compared with centralized system. The main equipment for electricity production in the distributed energy system includes a gas turbine and gas piston installations. It is usually considered that gas turbine installations are more profitable with capacity of over 3 MW, at smaller capacities gas-piston installation are more profitable. The photo of JIHT stand for working out the regime parameters of gas-piston installation is presented on the Fig. 1. But these installations are operated on natural gas. The main task for developing distributed energy now is creation of power production installations operated on gas fuel produced from biomass, namely wood and agricultural waste, peat and vital activity waste of different types.

It is a rather complicated problem. Processes of energy gas production from biomass have been known for more than a 100 years. There are gasification and pyrolysis processes. Both processes provide the production of energy gases with



Fig. 1 General view of JIHT PAS experimental complex for working out regime parameters of gas piston installations which use natural gas and thermal processing of biomass products as a fuel

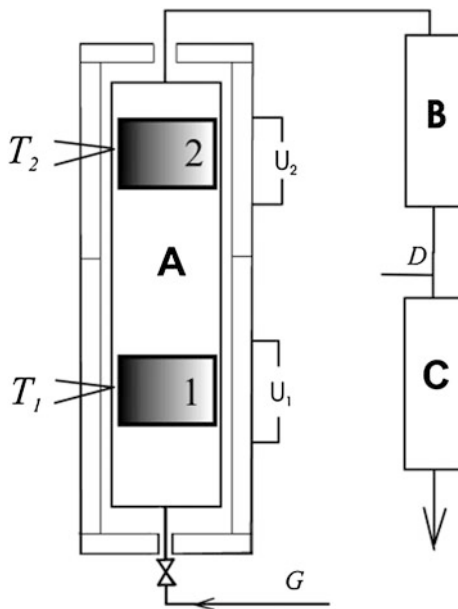
some content of liquid phase consisting of high-molecular hydrocarbons. It is not possible to use this gas as fuel in gas piston installations without purification. Purification of these gases from liquid phase and its further utilization of the liquid phase produced in process demands additional expenses. As a result, the use of gases from biomass as fuel received with traditional technologies such as gasification and pyrolysis becomes unprofitable and is used in practice. For this purpose it is necessary to develop a new technology of thermal biomass conversion which will provide dry energy gas production. This gas can have acceptable calorific value for contemporary energy equipment.

Today we do not have the technologies meeting these requirements in practice. Our main task is to create such technologies, which are we are engaged in.

At the first stage of the technology which is under development at our Institute we carry out the pyrolysis of biomass with formation of gas, liquid and solid products. In the picture we can see the reactionary space in which biomass pyrolysis is carried out [2, 3]. It is shown by Fig. 2. The gas phase of pyrolysis reactions consists of condensate and non-condensate parts. In its turn the condensate phase of pyrolysis consists of a set of high-molecular connections C_nH_m and pyroligneous liquor in the form of steam. At temperatures of pyrolysis $T_1 = 400\text{--}900\text{ }^{\circ}\text{C}$ all liquid products of reaction are in a steam phase.

Gaseous products of the pyrolysis reaction, consisting of condensed and non-condensed parts at temperatures of about $1000\text{ }^{\circ}\text{C}$ are blown through the firm carbon phase formed at pyrolysis, carried out at the first stage of the process (in the scheme it is reactionary space 2, temperature T_2).

Fig. 2 Experimental installation scheme



B and C are devices for measurement of volume and composition of gaseous reactions products. The pyrolytic liquor which is part of gaseous pyrolysis products interacts with the solid phase of pyrolysis reaction products in the carbon form which leads to formation of hydrogen and carbon oxide according to the following reaction



The high-molecular compounds which are part of the condensed pyrolysis phase, decomposed into hydrogen and carbon during the blowing through high-temperature carbon bed according to the following reaction



Carbon formed in the process of thermal decomposition of high molecular compounds during the interaction with pyrolytic liquor (water steam) simultaneously with carbon formed during the biomass pyrolysis turns into hydrogen and carbon oxide too. Thus, conversion of liquid and firm products of reaction into hydrogen and carbon oxide provides wasteless processing of biomass with the production of hydrogen and carbon oxide.

The both stages of the given process (first stage—biomass pyrolysis and the second—thermal decomposition of high molecular compounds and interaction of solid phase with pyrolytic liquor) are carried out in one device.

Table 1 Composition and calorific value of gas mixtures obtained from peat pellets under developed technology

T ₂ (°C)	Volume fractions of combustible components			Calorific value (MJ/m ³)		Volume (m ³ /kg)	Conversion efficiency
	H ₂	CO	C _n H _m	Q _B	Q _H		
850	0.40	0.27	0.08	11.7	10.6	0.76	0.42
950	0.43	0.40	0.02	11.3	10.4	1.1	0.60
1000	0.49	0.41	0.01	11.7	10.6	1.39	0.78
Traditional pyrolysis	0.23	0.19	0.13	10.4	9.6	0.29	0.15

Table 1 shows the dependence on the temperature of gas reaction products received due to peat processing in the zone where thermal decomposition of liquid and gaseous reactions products take place. The reaction products composition for peat traditional pyrolysis is shown here for comparison.

Similar results were received for agricultural and wood waste. We can see from these tables that content of hydrogen and carbon oxides in the reaction products received by technology under development are near 90 %. While in traditional pyrolysis these figures are about 42 % for peat pellets. The basic advantage of our technology is high degree of conversion of processed biomass into power gas. In existing technologies of pyrolysis this parameter does not exceed 0.18, in the technology under consideration it is approximately 0.75–0.80.

Quantity of produced gases in this process—is 1.4 m³ per kg of initial product, and calorific value is about 11.5 MJ/m³. The structure of the received gas mix is carbon oxide and hydrogen.

It is interesting to note that the mix of gases produced by the given biomass thermal conversion technology is ideal for synthesis of liquid fuels. Now at the first stage of our work we are planning to use the given technology for gas fuel production for gas pistol and gas turbine installations. Further we are going to develop a technology of producing synthetic motor fuel from biomass based on developed approaches.

Power plant with capacity of 50 kW was designed on the basis of experimental data mentioned above, it is shown in Fig. 3.

3 Improving the Consumer Properties of Biomass Fuel (Torrefacation)

So, from economic and ecological point of view it is profitable to involve local fuels such as agricultural and wood waste, peat and vital waste of different origin in power production. Earlier our results connected with the creation energy gas production technology from biomass were presented. Another task is connected with



Fig. 3 The power station for production of electrical energy from biomass with capacity 50 kW

the production of heat energy from local fuels. For this purpose it is necessary to have fuel from biomass in some standard form with definite set of thermo technical characteristics. Widely used biofuel in the form of wood waste pellet does not completely meet existing requirements in the energy field.

The main problem which must be solved for the wide use of biomass as fuel is the improvement of its consumer properties. Pellets have rather low combustion heat and high level of hygroscopicity. It is necessary to maintain special conditions for pellets transportation and storage. During contact with atmospheric air pellet humidity increases and when it reaches 24–26 %, pellets lose shape and are disintegrate. Now we are trying to develop a technology aimed at improving pellet consumer properties. It means enhancing their calorific value and decreasing the ability to absorb water. The use of the technology under development will lead to an essential reduction of expenses for storage and transportation pellet fuel. It concerns not only wood waste pellets whose production is widely developed in the world, but pellet production from other kinds of biomass including agricultural waste.



Fig. 4 The experimental facility for working out the regime parameters biomass fuel consumer properties improving process

Improving the consumer properties of biomass fuel is achieved in the process of heating it up to temperature 250–2700 °C. This process has received the name “torrefaction”. The main problem of torrefaction is spontaneous biomass temperature increase up to 700–8000 °C at heating it up to temperature 240–2700 °C. It is the main problem why this technology is not used for practical purposes. Now a lot of research organizations are trying to find appropriate decisions of practical implementation of torrefaction by economically justified ways. We are also trying to find a solution to the problems which hinder the industrial application of this process. We have created a pilot plant with a capacity 50–70 kg per hour. Now we can see this facility in Fig. 4.

The decrease of water absorption possibility depends on heating temperature for straw and wood pellet is shown in the Fig. 5. It is evident that torrefaction leads to considerable decrease of hydrophobic properties. The dependence of specific calorific value on torrefaction temperature is presented in Fig. 6. Heating up to temperature 2700 °C leads to increasing specific calorific value up to 30 % for different types of biomass.

Now we have carried out fulfilled the first phase of work connected with the creation of new technology, and developed technical decision requires confirmation. For this purpose it is necessary to create a pilot facility and to pass to industrial production of the given installations.

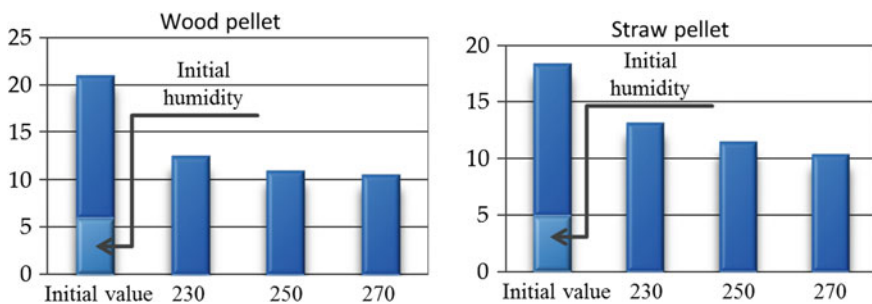


Fig. 5 Dependence of hydrophobic properties on torrefaction temperature

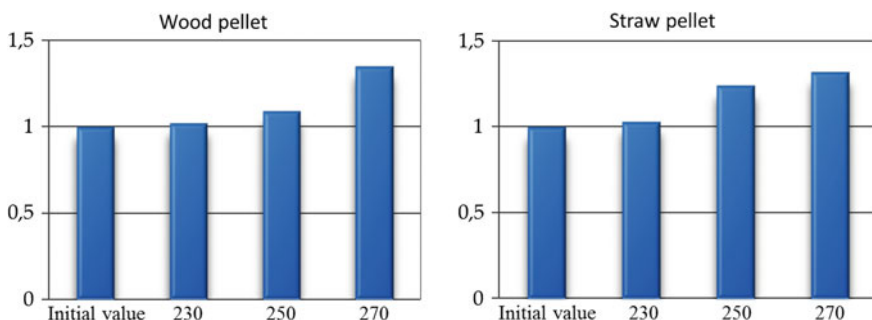


Fig. 6 Dependence of specific calorific value on torrefaction temperature

First we investigate the possibility of torrefaction of wood waste and peat. After that we investigate the process of processing of rice and sunflower husk and other sorts of agricultural waste including straw. The use of this technology will, from our point of view, help to solve the main problems connected with energy use of biomass fuels. The special direction of our investigation is the creation of technologies of utilizations of vital waste of different origin including chicken litter.

4 Conclusions

The article presents new technologies of processing biomass. These are the technology of production of energy gas with enhanced calorific value without liquid phase and the technology improving consumer properties of granulated fuel from biomass. Optimization of these technologies and their further industrial implementation gives the possibility to solve the main problems connected with biomass utilization as a fuel. It is a very big and complicated task whose decision is important for a lot of countries. Cooperation of scientists and engineers of various countries is necessary for a successful decision of the given problem.

References

1. L.B. Direktor, V.M. Zaichenko, A.V. Markov, V.A. Suslov, Result of Bench test of a gas-piston mini cogeneration station constructed on the basis of a YaMZ-240 engine. *Therm. Eng.* **55**(11), 967–970 (2008)
2. V.M. Batenin, A.V. Bessmertnykh, V.M. Zaichenko, V.F. Kosov, V.A. Sinel'shchikov, Thermal methods of reprocessing wood and peat for power engineering purposes. *Thermal Eng.* **57**(11), 946–952 (2010)
3. V.M. Batenin, V.M. Zaichenko, V.F. Kosov, V.A. Sinel'shchikov, Pyrolytic conversion of biomass to gaseous fuel. *Doklady Chem.* **446**(Part 1), 196–199 (2012)

Heterogeneous Cracking of Tars on Surface of Charcoal

Valentin Kosov, Vladimir Kosov and Victor Zaichenko

Abstract One of the most urgent problems of biomass gasification is cleaning of the product gas from pyrolysis tars and carbon dioxide. Joint Institute for High Temperatures of the Russian Academy of Sciences suggests the gas cleaning technology based on the heterogeneous cracking of pyrolysis tars on surface of charcoal. For the practical implementation of this method it is important to know efficiency of the hot charcoal filter for pyrolysis liquid products cracking. There are two cracking processes take place: homogeneous cracking in volume and heterogeneous cracking on the surface of porous charcoal matrix. In this paper the results of experimental determination of the efficiency of heterogeneous of pyrolysis tar cracking depending of the hot charcoal filter parameters are presented.

1 Introduction

Being renewable, biomass is considered to be one of major potential energy sources in the future [1]. Combustion, pyrolysis and gasification are three main thermo-chemical methods used for biomass conversion into energy. Traditionally, combustion is used for heat; pyrolysis converts biomass into bio-oil and gasification is the way to convert biomass into fuel gas.

Gasification is very attractive method for power generation because produced gas can be easily stored, transported and utilized in different power facilities [2]. Different methods of gasification have different advantages and disadvantages, but common problem for all methods is cleaning the gas from tars. The presence of tars in the gas prevents its using in diesel engines and turbines. These tars can cause several problems, such as condensing in the cold spots and plugging the lines, forming coke and plugging the filters. Moreover, these tars contain significant

V. Kosov (✉) · V. Kosov · V. Zaichenko

Joint Institute for High Temperatures of the Russian Academy of Sciences (JIHT RAS),
Izhorskaya str. 13, 125412 Moscow, Russia
e-mail: kosov@ihed.ras.ru

amounts of energy contained in biomass. Conversion of tars into synthesis gas allows increasing gasification efficiency by solving two tasks: cleaning the produced gas and increasing its volume.

Tars can be converted by catalytic (heterogeneous) and non-catalytic (homogeneous) cracking processes. Catalytic cracking is based on the capacity of catalysts to decompose hydrocarbons into carbon monoxide, hydrogen, and lower hydrocarbons. Typically dolomites, alkali metals, and nickel are used as catalysts [3]. Along with these materials, biomass char was noticed to have a good catalytic activity. The economical attractiveness of biomass char for the tar cracking comes from its low cost and availability.

For several years, in the Joint Institute for High Temperatures of Russian Academy of Sciences, the two-stage technology of biomass gasification has been developing [4]. The technology is based on pyrolysis of biomass as the first stage. The second stage is high-temperature conversion of liquid fraction of the pyrolysis on the surface of charcoal. Such way the charcoal is used as catalyst for cracking of liquid fraction of the pyrolysis. For the practical implement of this method it is important to know effectiveness of the charcoal catalyst for pyrolysis products cracking.

The paper [5] described an attempt to estimate decomposition degree of liquid pyrolysis products by measuring volume fraction of carbon dioxide in output gas. It was shown that using the charcoal filter is equal to the initial weight of the biomass is possible to achieve a high degree of decomposition of the pyrolysis products. Further increase in coal mass filter does not significantly increase the degree of decomposition.

However, the experiments were not considered processes of tars volumetric decomposition in the cracking chamber. Additional experiments with increased sample weight of initial biomass for the same reactor size were necessary to be carried out.

This paper describes experiments to determine the effectiveness of heterogeneous cracking in comparison with homogeneous cracking and optimal size of charcoal filter.

2 Experimental

The experimental set-up (Fig. 1) consisted of a high-temperature two-chamber fixed-bed reactor and a system of extraction and analysis of gas and vapor forming as a result of heating an initial raw material.

The reactor was a stainless steel tube with an inside diameter of about 37 mm, which was placed within two-section furnace with independent heaters for each section. The chambers were 300 mm length each. Raw material was placed into the chamber 1. There were series of experiments with different amount of char placed and different temperatures in the chamber 2. Pyrolysis process was explored when chamber 2 was empty and its temperature was 20 °C.

To explore homogeneous and heterogeneous cracking, the chamber 1 was heated up to temperature 1000 °C that was held further at the constant level. After that the

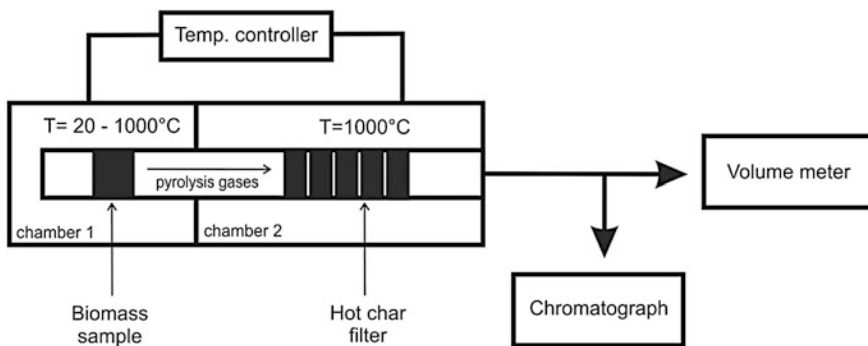


Fig. 1 Scheme of the experimental reactor

Table 1 Properties of softwood pellets (dry material, wt%)

Moisture	8.3
Ash	1.4
Volatiles	84.6
C	47
H	6
N	0.2
O	44

temperature of the bottom chamber was raised at the rate 10 °C/min. Process of homogeneous cracking was explored with empty chamber 2. To explore heterogeneous cracking, char obtained by pyrolysis of the same raw material was placed in the chamber 2 and heated up to 1000 °C.

Gases formed during pyrolysis of initial raw material passed through the porous carbon bed in the chamber 2. As a result of homogeneous and heterogeneous chemical reactions in the high-temperature zone, the pyrolysis gases decomposed into synthesis gas, which came into the volume meter (eudiometer). The samples of the gas were chromatographed.

Softwood pellets were used as a raw material for pyrolysis. Carbonized softwood pellets were used as the hot char filter. The properties of the pellets are shown in Table 1.

3 Results and Discussion

The results of measurements of the volume gas produced per 1 kg of softwood pellets during pyrolysis and two types of tars cracking are shown in Fig. 2.

From these data it follows that heterogeneous cracking of pyrolysis tars on the surface of coal is more effective than homogeneous cracking in volume of the

Fig. 2 Gas yield per 1 kg of raw material during pyrolysis of softwood pellets and two types of tars cracking

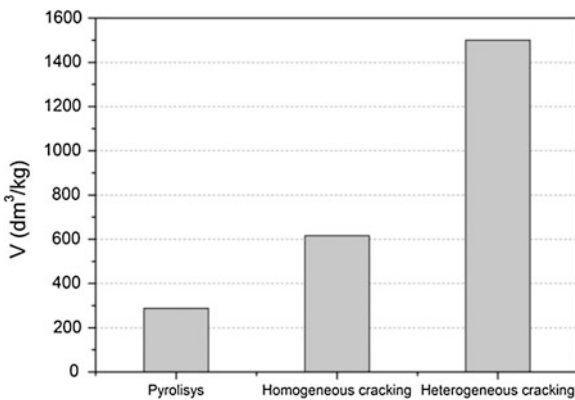
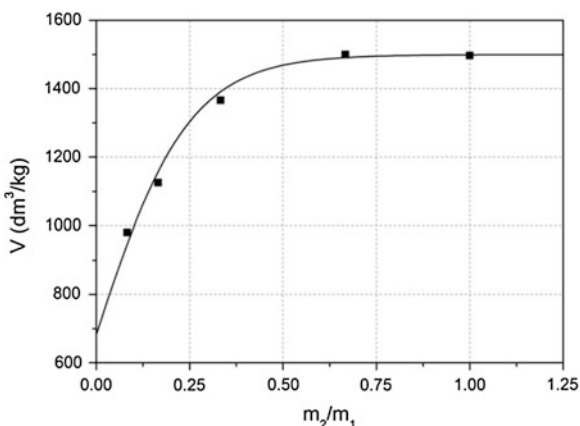


Fig. 3 Gas yield per 1 kg of raw material during pyrolysis and subsequent cracking of tars at different mass ratio



reactor and allows receiving the maximum volume of synthesis gas in the same reactor.

During the experiments, the optimal ratio of the mass of the initial biomass (m_1) and mass of the coal in chamber 2 (m_2) was determined. The results are presented in Fig. 3.

From these data it follows that at a mass of coal in the chamber 2 at half the weight of processed biomass, the amount of the product gas becomes close to the maximum, indicating the complete decomposition of pyrolysis tars. This is confirmed by the data on the composition of the synthesis gas produced at different quantities of coal in the chamber 2, as it is shown in Table 2.

For the mass ratio greater than 0.5 synthesis gas composition becomes constant, that indicating complete tar decomposition.

Thus, using the charcoal filter is equal to one half of initial weight of the biomass may be considered as optimal to achieve the maximum degree of decomposition of the pyrolysis products. Further increase in coal mass filter does not increase the degree of decomposition and volume of the gas.

Table 2 Composition of the synthesis gas produced at different coal/biomass mass ratio

m_2/m_1	H ₂ (%)	CO (%)	CO ₂ (%)	CH ₄ (%)	N ₂ (%)
pyrolysis	32.6	22.4	24.1	16.3	4.6
0.00	43.7	36.2	10.3	7.9	1.9
0.08	46.8	38.7	6.6	6.1	1.8
0.17	49.4	40.7	4.9	4.1	0.9
0.33	50.2	42.4	3.1	2.5	1.8
0.67	53.2	43.6	0.9	1.2	1.1
1.00	54.4	43.6	0.3	0.9	0.8

4 Conclusions

The data obtained show the possibility of experimental determination of parameters of carbon filter to achieve the desired characteristics of the gas produced two-step conversion of biomass. The method takes into account the processes of heterogeneous and homogeneous pyrolysis, which allows significantly specify the parameters of the carbon filter for the two-stage gasification process.

Further work involves determining the mass balance of the two-stage gasification process that will assess the accuracy of the data.

References

1. M. Demirbes, M. Balat, Recent advances on the production and utilization trends of bio-fuels: a global perspective. *Energy Convers. Manag.* **47**, 2371–2381 (2006)
2. A. Kumar, D.D. Jones, M.A. Hanna, Thermochemical biomass gasification: a review of the current status of the technology. *Energies* **2**, 556–581 (2009)
3. D. Sutton, B. Kelleher, J.R.H. Ross, Review of literature on catalysts for biomass gasification. *Fuel Process. Technol.* **73**, 155–173 (2001)
4. V.V. Kosov, V.F. Kosov, V.A. Sinelshchikov, V.M. Zaichenko, *The two-stage technology of biomass conversion into synthesis gas*, in *Materials and processes for energy: communicating current research and technological developments* (Formatex Research Center, Spain, 2013), pp. 393–398
5. A.Y. Oral et al. (eds.), International congress on energy efficiency and energy related materials (ENEFM2013). *Springer Proceedings in Physics*, **155**, 371–376 (2014)

Part VI

Fossil Energy

Investigation of Two-Component Hydrocarbon Mixture Filtration in Porous Media

I.L. Maikov, D.A. Molchanov and V.M. Torchinsky

Abstract Natural-gas condensate is valuable raw for chemical and oil industries. In the process of gas-condensate reservoir exploitation, one has to deal with a product which changes its composition all the time. This is due to retrograde condensation phenomenon of reservoir hydrocarbon mixture during reservoir pressure decrease. With appearance of such condensate within reservoir porous space, fluid flowrate decreases and even ultimate extinction of filtration process takes place. A mathematical model is developed, which describes one-dimension filtration of two-component hydrocarbon mixture in porous media. Methane-n-butane mixture appears as model mixture for being a close approximation of real gas-condensate reservoir hydrocarbon mixture. Structurally, the model consists of two parts, namely, the hydrodynamic part, which describes the process of two-phase filtration in a porous medium in the Darcy law approximation, and the thermodynamic part, within which the equations of state for mixture are used to calculate the compressibility coefficients of the mixture and the parameters of phase equilibrium of the system in the vapor and liquid phases. The results of mathematical modeling are in good agreement with experimental research of filtration processes of methane-n-butane binary hydrocarbon mixture. Possibility of gas-condensate plug (each of dynamic and static) formation is shown. Wave impact on an active reservoir could be a way to increase production rate.

1 Introduction

Gas-condensate reservoir exploitation experience shows that one of the causes for diminished performance is the significant saturation of the porous medium of the bottom-hole area by retrograde condensate.

I.L. Maikov · D.A. Molchanov (✉) · V.M. Torchinsky

Joint Institute for High Temperatures of Russian Academy of Sciences (JIHT RAS),
Moscow, Russian Federation

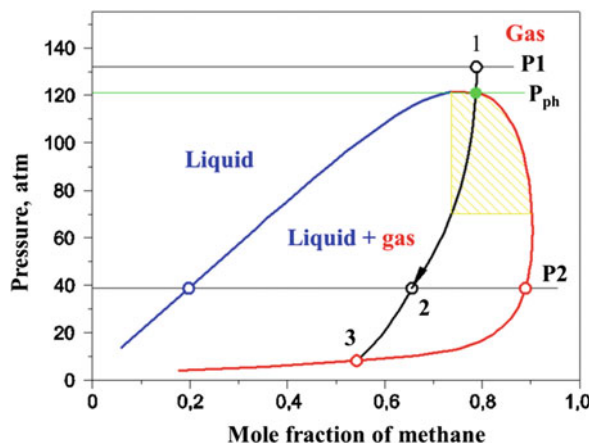
e-mail: dmitriy.molchanov13@gmail.com

The gas-condensate system behavior in the reservoir being not only nearby the wellhead but also at a significant distance from it is determined by many factors: initial mixture composition, temperature, reservoir pressure, pressure gradient, reservoir rock properties. Phase viscosity, interfacial tension, interfacial angle, reservoir structure affect filtration processes. It is practically impossible to take account of the influence of these factors on filtration characteristics in a full-scale experiment, moreover a set of essential experimental studies, including PVT-characteristics study, mixture viscosity of variable composition, surface properties, hydrodynamics process characteristics, etc., is huge. In this regard it seems reasonable to implement the processes which occur during a gas-condensate reservoir exploitation in experimental physical and mathematical models. This complex approach makes it possible to identify the main physical processes affecting filtration mixtures and to evaluate them numerically, to simulate the processes on a physical model, and ultimately to develop impact methods on gas-condensate system in order to improve the efficiency of reservoir exploitation.

2 Reservoir Mixture Features

Gas-condensate is a complex mixture of methane and other members of its series. The phase-diagram of such a mixture contains a so-called “retrograde area”, i.e. an area in which there is a possibility of fluid formation with pressure decrease (Fig. 1). Under gas-condensate production from active reservoir, pressure decrease and temperature changes nearby a bottom-hole. A gas-condensate mixture into the bottom-hole area is partially condensed with retrograde liquid formation (condensate “plug”) that fills the porous medium and prevents gas phase discharge [1].

Fig. 1 Phase diagram of binary methane-n-butane mixture



Model mixture was determined by the following specification:

- (1) Presence of methane as a main component
- (2) Presence of a sufficiently broad retrograde area at the phase diagram for the provision of significant condensate amount
- (3) Not too high pressure for dew point (15 MPa)
- (4) Realizable temperature range (300–400 K) in the experimental study, availability of mixture components.

Methane-n-butane mixture was chosen for simulation as the most suitable.

3 Mathematical Model

Non-stationary processes occurring with two-phase hydrocarbon mixture filtration in a porous reservoir were simulated in the one-dimensional approximation under isothermal and phase equilibrium conditions (i.e. the characteristic phase transition times are significantly smaller than hydrodynamic times). The structure of the mathematical model consists of two parts—the hydrodynamic one describes two-phase filtration process in a porous medium in the Darcy's law approximation, and thermodynamic one enables calculation of compressibility factors and system phase equilibrium by means of state equations for a mixture of the vapor and liquid phases [2].

Use of generalized four-coefficient cubic Van der Waals equation developed for natural oil-gas-condensate mixtures under the pressure of 100 MPa and temperature of 200 °C was made for vapor and liquid phase properties calculation of the binary mixture:

$$p = \frac{RT}{v - b} - \frac{a}{(v + c) \cdot (v + d)} \quad (1)$$

The filtration equations under the assumption of chemical components neutrality in the one-dimensional case are the mass-conservation equations for each component used in divergence form in terms of mass densities:

$$m \frac{\partial}{\partial t} \left(\sum_j c_{ij} \rho_j s_j \right) + \frac{\partial}{\partial x} \left(\sum_j c_{ij} \rho_j U_j \right) \quad (2)$$

where m —the porosity, $i = \text{CH}_4, \text{C}_4\text{H}_{10}$, $j = 1$ (gas), 2 (liquid), c_{ij} —the mass percentage of the i -component in the j th phase of the two-phase mixture, ρ_j —density of the j th phase, s_j —the volume percentage of the j th phase in the mixture, U_j —velocity of the j th phase, t —time, x —coordinate.

Momentum conservation equations take the form of Darcy's law:

$$U_j = -k \frac{f_j(s_j)}{\mu_j} \frac{\partial P}{\partial x} \quad (3)$$

where k —the absolute permeability, μ_j —dynamic viscosity of the j th phase, P —pressure, f_j —relative phase permeability of the j th phase. Phase pressures are assumed to be equal.

Let us write the equation of state for gas and liquid phases which are expressed in terms of compressibility factors:

$$P = \frac{\rho_j z_j R T}{m_j} \quad (4)$$

where m_j —the molar mass of the j th phase; z_j —compressibility factors of the j th phase; R —gas constant; T —mixture temperature.

The equilibrium concentrations of the components in both phases depend on the pressure and satisfy following condition:

$$\sum_i c_{ij} = 1 \quad (5)$$

These concentrations are connected by the conditions of thermodynamic equilibrium—the chemical potentials are equal. The volume percentage of each phase are related by the following correspondence:

$$\sum_j s_j = 1 \quad (6)$$

Hydrodynamic equations obtained are supplemented by boundary and initial conditions. In particular, pressure conditions are as follows:

$$\begin{aligned} P(x, t = 0) &= P_1 \\ P(x = 0, t) &= P_1 \\ P(x = L, t) &= P_2 \end{aligned} \quad (7)$$

Thus above equation system describes evolution of the two-component two-phase mixture. The mixture is assumed to be in local thermodynamic equilibrium. Since the process is isothermal this system describes temporal and space changes of pore pressure and concentration of each component in the mixture.

4 Numerical Simulation

In hydrocarbon mixtures filtration simulation the following values of initial parameters was given: initial methane mole percentage was 0.75, pressure gradient was 45 atm over a length of 3 m. The dependence of non-dimensional flow rate of

Fig. 2 Gas (1) and liquid (2) outlet flow rate dependence (in relative units) for model mixture

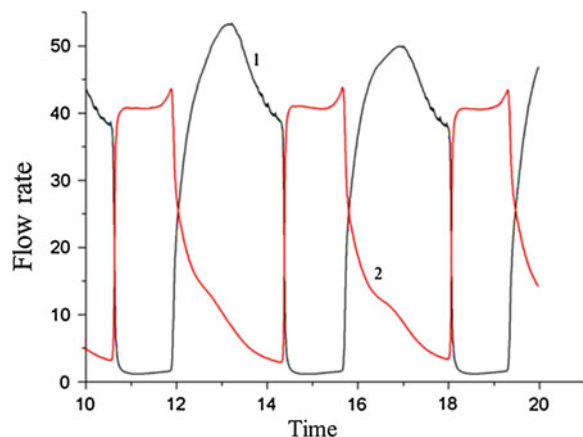
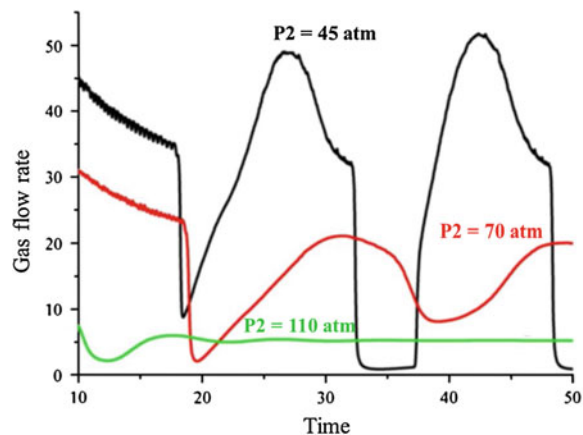


Fig. 3 Gas flow rate dependence (in relative units) for different outlet pressures
 P_2 : 1–45 atm, 2–70 atm, 3–110 atm ($P_1 = 125$ atm)



gas and liquid phases at the outlet of experimental stretch ($x = L$) on non-dimensional time is shown in Fig. 2. As the figure shows, the solution is periodic. Primarily such behavior is associated with relative permeability dependencies. They are characteristic curves for hydrocarbon mixtures, which comprise sections where phase permeability equals to 0. Thus the phase velocity is also equals to 0 in this case, therefore, the phase does not sweep.

Filtration simulation of methane-n-butane mixture was also conducted under various pressure gradients on the model stretch. The solution is aperiodic in the case of large values of P_2 (Fig. 3, curve 3). Small pressure gradient ($P_1 - P_2$) leads to low phase velocities, and area with considerable relative phase velocities fails to be formed because formation time for this area is greater than residence time of the gas phase in the reservoir model. Similar behavior is shown by liquid phase flow rate.

5 Physical Simulation

A pipe made of stainless steel and filled pre-washed quartz sand was used as a one-dimensional reservoir model. Inner pipe diameter was 8 mm, pipe length was 3 m, sand fraction was 0.09–0.125 mm. A mixture containing 75 % vol. methane was filtered through an experimental stretch at a temperature of 286 K. Inlet pressure was $P_{in} = 120$ atm, outlet pressure was $P_{out} = 60$ atm. These pressures were held constant while the experiment was running. Mixture flow rate was stabilized and reached 75 % of initial flow rate at the 450th second. Outlet mixture composition jumped to the n-butane proportion increase indicating the gas-condensate plug formation.

Oscillation appeared after 600th second and natural period of the system was about 10–20 s. The results of the gas-condensate plug formation experiment are shown in Fig. 4. The plug can move (if pressure gradient is sufficiently great) or stand still depending on the filtration conditions.

Also experiments were carried out with three-component mixture of methane, propane and butane under the same conditions (component concentration, pressure and temperature). Natural period of the system was determined, followed by the wave generator running. The impact amplitude was related with generator frequency and ranged from 30 to 10 atm. Mixture flow rate before wave impacts conducted with different frequencies was compared with mixture flow rate after these impacts. The natural period of the system ranged from 10 to 40 s for the chosen experimental conditions.

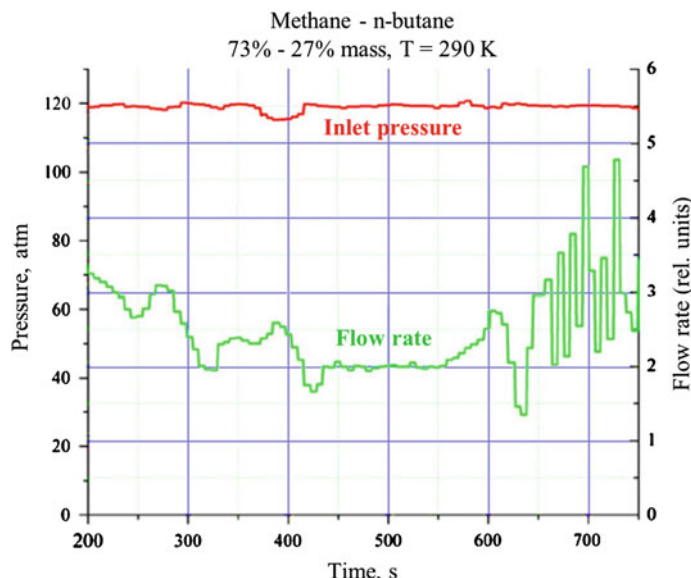


Fig. 4 Gas-condensate plug formation

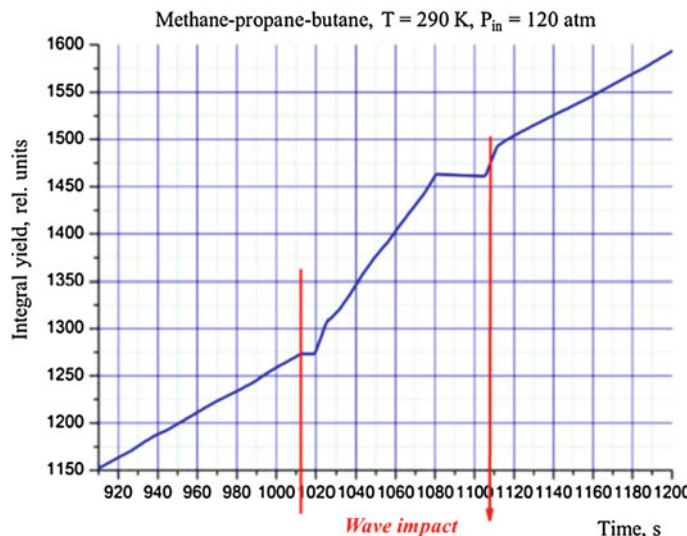


Fig. 5 Wave impact results with period of 6 s

Periods of 60, 40 and 6 s were chosen for wave impact. The results are shown in Fig. 5. Wave impacts with period of 60 and 40 s caused no changes in the integral flow rate which are out of true. Impact with period of 6 s caused an increase of flow rate by 2.5 times during the impact and an increase of integral mixture yield by 30 %.

6 Conclusions

Technologies of wave impact on multiphase systems can be used for intensification of technological processes in gas-condensate production, gas flow rate and reservoir permeability increase. Wave (acoustic) impact on the reservoir bottom-hole area can be used in order to overcome or reduce filtration resistance. Reservoir permeability can be changed with the use of wave impact, and thus gas and condensate production can be increased.

References

1. I.L. Maikov, V.M. Torchinsky, V.M. Zaichenko, Features of hydrocarbon mixtures filtration in a porous medium. *High Temp.* **51**(6), 776–784 (2013)
2. V.M. Zaichenko, I.L. Maikov, V.M. Torchinskii, E.E. Shpil'rain, Simulation of processes of filtration of hydrocarbons in a gas-condensate stratum. *High Temp.* **47**(5), 669–674 (2010)

Part VII

Hydropower

Deformation Analysis and Monitoring for Extra High Hydropower of 305 m

Huaizhi Su and Meng Yang

Abstract The engineering scale and construction difficulty are beyond imagination. Many technical indicators have exceeded the current specification. Firstly, the denatured state of the dam in active service was analyzed and summarized based on 1:1 prototype test parameters. Secondly, load set and load effect set were combined and the influence factors were determined by deterministic function and physical inference method. The coefficient of each factor was calculated by the measured data. An extra high arch dam deformation monitoring statistic model was finally established. Load effect set can be defined under a group of load set. It can be used to determine the working condition of the structure and monitor buildings. Thirdly, three-dimensional nonlinear finite element model was established and the incremental step difference algorithm was used by considering the weight of the dam and the outside water load. This will accurately simulate the state of the arch dam deformation. This article provides a meaningful reference for the exploration of similar projects in future.

1 Introduction

It is a key hydropower station in Yalong river. This concrete hyperbolic arch dam is the highest in the world with the height of 305 m, the crest width of 16.0 m, the bottom thickness of 63.0 m and the thickness-height ratio of 0.207. The normal water level is 1880 m and dead water level is 1800 m. The floor plan is shown in Fig. 1. There is no ready-made standard for safety monitoring of deformation,

H. Su (✉)

State Key Laboratory of Hydrology-Water Resources and Hydraulic Engineering,
Hohai University, Nanjing 210098, China
e-mail: suhz@163.com

M. Yang

College of Water Conservancy and Hydropower Engineering, Hohai University,
Nanjing 210098, China

seepage and stress. Therefore, a specialized study must be conducted for safety monitoring indicators of deformation, seepage and stress according to the actual situation [1, 2]. Monitoring indicators of the first impoundment must be proposed firstly for the construction cycle.

2 Prototype Data Research

Prototype monitoring is a 1:1 model test as the most reliable application mean [3, 4]. Water pressure is the most direct factor as the largest weight proportion factor among these external influence factors. Deformation is analyzed during water-level uplift period from November 30th to December 7th, 2012. A radial deformation measured data of a typical dam section of 9# was analyzed emphatically and shown in the second one of Fig. 1. with the water level rising from 1648.37 to 1706.76 m. The maximal downstream and upstream displacements are 0.47 and 0.82 mm respectively. The magnitude of the radial displacement change is small. Downstream radial displacement happens at a low elevation and upstream displacement appears in a high altitude. The change value at the low elevation is smaller than that at the high altitude. The radial displacement increases at the beginning and decreases later with the altitude for the same vertical line at the same time. Then, it increases negatively and decreases at last. The maximally radial displacement of downstream and upstream was at the 1664 and 1640 m elevation respectively. For different time in the same height at a low elevation, the maximal value occurred at the end of water-level uplift period at different times. In contrast, for the same height at a high elevation, the radial displacement gradually changed from downstream to upstream with the increase of water level. The whole deformation rule of the radial displacement was

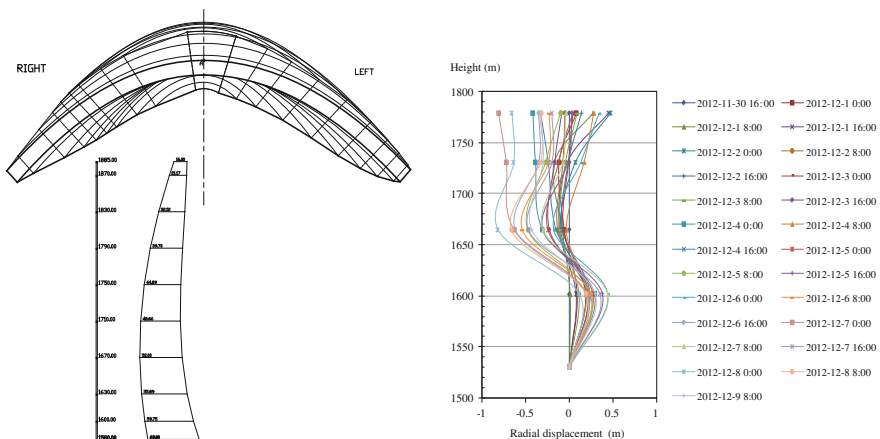


Fig. 1 Layout plan of the hydroelectric power station and radial displacement deflection chart of 9# dam section during water-level uplift period

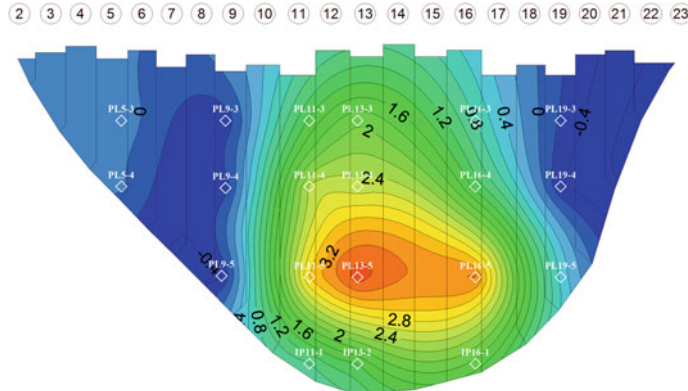


Fig. 2 Radial displacement contour map on December 9th, 2012

shown in Fig. 2. The radial displacement got the maximal downstream value at the 1664 m elevation all the time and the deformation value of the high elevation is larger. The radial displacement decreases around the dam, even appears displacement toward upstream on both sides of the dam.

3 Analysis of the Deformation Monitoring

There is no reliable reference and study for the deformation monitoring for so high arch dam under complex and changeable deformation regularity [5]. The paper builds a stepwise regression model based on the practical operation needs of the arch dam [6]. For the arch dam, the water pressure distribution on the beam presents non-linear variation because of a two-direction effort of horizontal arch and cantilever beam. It can be expressed as

$$\delta_H = \sum_{i=1}^{4(5)} a_{1i} H^i \quad (1)$$

where, δ_H presents deformation value and H is water level.

During the water storage period, dam deformation was greatly influenced by water factor. The monitoring point of PL13-5 was selected for fitting analysis and formulating monitoring indicators. PL13-5 was located at 1664 m elevation in 13# dam section. The measured-fitting process was shown in Fig. 3. The correlation coefficient of R is 0.96. The monitoring indicator of $2S$ can be obtained from the result of stepwise regression based on the (1), and the value is $[-0.40, 0.40]$. The prediction of radial displacement for PL13-5 is $\delta_{1760} = 13.913$ mm for the future water level of 1760 m.

Fig. 3 Radial displacement of the measured-fitting process of PL13-5

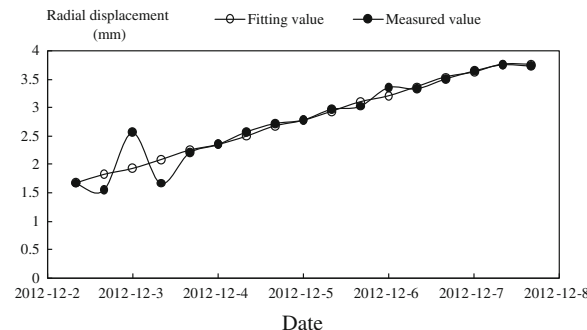


Table 1 The radial displacement calculated value with 1760 m upstream water level

Measuring point	Elevation (m)	Radial formation (mm)	Measuring point	Elevation (m)	Radial formation (mm)
PL13-5	1664	13.16	PL9-5	1664	3.87
PL13-4	1730	14.17	PL16-5	1664	9.17
PL13-3	1778	12.26	PL19-5	1664	2.02

This article also carried out the finite element method to analyze and study the deformation regular. The weight was taken as the initial load and water load was added in the second step increment. The difference, between latter deformation and former result, was corresponding to vertical measured data of the dam deformation. The downstream radial deformation rule is: The biggest value happened in the central dam, which is the largest for the corresponding monitoring point of 13# dam section. In the height direction, the deformation of PL13-4 of 13# dam section at the 1730 m elevation, is the largest with the value of 14.17 mm. Radial deformation of the whole dam body is toward downstream. The deformation around PL13-4 decreases gradually. The minimum value happens at inverted plumb measuring point of 9# dam section with the value of 0.50 mm. Table 1 shows the radial displacement calculated value when the upstream water level reaches 1760 m. The biggest radial displacement occurred in the 13# dam section. The displacement monitoring indicators are PL13-3 (12.78 mm), PL13-4 (14.63 mm) and PL13-5 (13.56 mm) for the water level of 1760 m.

Acknowledgments This research was partially supported by the Jiangsu Natural Science Foundation (SN: BK2012036), the National Natural Science Foundation of China (SN: 51179066, 41323001, 51139001), the Specialized Research Fund for the Doctoral Program of Higher Education of China (SN: 20130094110010), Non-profit Industry Financial Program of MWR (SN: 201301061, 201201038), Jiangsu Province “333 High-Level Personnel Training Project” (SN: BRA2011179), Scientific Innovation Research Scheme for Jiangsu University Graduate (SN: CXLX13_246).

References

1. H.Z. Su, Z.P. Wen, J. Hu, Z.R. Wu, Evaluation model for service life of dam based on time-varying risk probability. *Sci. China Series E: Technol. Sci.* **52**, 1966–1973 (2009)
2. D.H. Zhong, Y.F. Sun, M.C. Li, Dam break threshold value and risk probability assessment for an earth dam. *Nat. Hazards* **1**, 129–147 (2011)
3. H. Chen, *Dike Engineering Safety Evaluation Method Research* (Hohai university, 2004)
4. A.I.H. Malkawi, W.F. Hassan, F.A. Abdulla, Uncertainty and reliability analysis applied to slope stability. *Struct. Saf.* **22**(2), 161–187 (2000)
5. F. Silva, T.W. Lambe, W.A. Marr, Probability and risk of slope failure. *J. Geotech. Geoenviron. Eng.* **134**(12), 1691–1699 (2008)
6. H.Z. Su, J. Hu, Z.P. Wen, Optimization of reinforcement strategies for dangerous dams considering time-average system failure probability and benefit-cost ratio using a life quality index. *Nat. Hazards* **65**, 799–817 (2013)

Hydropower Plant Regime Management According to the Market Conditions

Hasan H. Coban, Renata Varfolomejeva, Antans Sauhats
and Inga Umbrasko

Abstract The dimensions and significance of the modern systems prove the necessity to change principles of the systems management. In order to decrease carbon dioxide (CO_2) emissions, fight climate change, not adhere to fuel resources and increase energy security while decreasing its dependences on foreign countries, many country governments took actions to exploit its domestic resources and raise the renewable energies in the electricity production, that is why renewable energy is a key issue in today's world and may continue to play a globally essential role in the future. Turkey has a large renewable energy potential it is still on a development process and has relevant natural hydropower potential, which is about 1.1 % of the worldwide and 13.75 % of the European potential. The main purpose of this work is to develop optimal short-term planning models for price taker hydropower producer working in the existing regimes. Those models have to deal with the huge level of uncertainty which is the water power introduces into the power system. Hydropower stations (20 MW or less) operation effectiveness under the conditions of market relations is defined by means of income value that is determined during the calculation period. This income can be obtained in the regime providing as large as possible HPP electric energy production with particular water consumption within a considered period. The value of these incomes can be calculated in accordance with pre-set market prices for electric energy within the calculated period. This paper addresses optimization techniques, model applications, and operational issues. Our goal was devoted to the problem of small HPP control regimes optimization. The task of a small HPP operation regime is solved for the maximum income within the cases of the known variation of prices at the market. An optimization tool known as generalized reduced gradient method for nonlinear optimization tasks is used to plan hydropower production under uncertainties. The developed forecasting and optimization technics are established on optimization of the Cobanli HPP in Turkey considering hydropower production and flood control. Optimization of powerhouse regimes operation rules provides optimal solutions that have a larger hydropower

H.H. Coban (✉) · R. Varfolomejeva · A. Sauhats · I. Umbrasko
Institute of Power Engineering, Riga Technical University, Azenes iela 12/1,
Riga 1048, Latvia
e-mail: hasanas.coban@gmail.com

potential compared to the present regulations. It's concluded that real-time optimization in normal flow situations provide solutions that trades-off the immediate and the future value of hydropower production. We developed a model for hydropower plant scheduling under market and fixed electricity price and water inflow rates for to achieve greatest economic benefit.

1 Introduction

The increasing of power consumption, developing the sizes of power systems, complexity and importance of power systems, limited resources, increasing of the prices for the resources, influence of random and uncertain factors, climate change everything brings top importance to the problems connected with power engineering, the consequence of the problem became a reason of power systems restructuring at the international level, market conditions and mechanisms application in the power systems development and operation management. These tasks are very difficult for realization as power systems are one of the most complicated artificial issues existing as a result of human activities. The dimensions of the modern systems prove the necessity to change principles of the systems management. Energy consumption is increasing day by day, also fuel resources is limited and climate changes; because of these 3 factor renewable energy is a key issue in today's world and may continue to play a globally essential role in the future. Turkey has a large renewable energy potential and the participation of private sector in the energy field started a new era on the production of energy from renewable sources. Turkey has an overall natural hydropower potential of 430 TWh, which is about 1.1 % of the worldwide and 13.75 % of the European potential. However, only about 30 % (130 TWh) of the potential is deemed to be economically feasible [1].

Renewable energy is still on a development process. Although there are the legal reforms and regulations to support the process, the system has not been completely settled. The development rate is still below the expectations and there is also a considerable level of non-utilized potential. In the area of renewable energy, the incentives are main driving force as explained in detail. Renewable energy sources (RES) are promoted through different support schemes. In Turkey also there are some support scheme for the attraction RES financing and construction. Also according to the results of the study on feed-in tariffs, the prices applicable to renewable energy resources (RES) oriented energy production are not functional especially for hydropower and wind power plants

In 2010 the Law on Renewable Energy in Turkey was revised by Law 6094. According to this revision, Feed in Tariff values rearranged in dollar-cent terms and these values are specified as resource based [2].

Electricity produced under renewable energy certification can be sold through day-ahead market (Market Financial Reconciliation Centre) or RES support

mechanism (feed-in tariff). RES support mechanism is applicable for 10 years after start of production [3].

The renewable energy generation facilities using mechanical or electro-mechanical components manufactured in Turkey are eligible for a domestic components incentive. With that; you can get additional support amounts for companies with facilitates that use locally produced equipments and components. Hydro power plants (HPP) potential in Turkey is used partial, because is not taken into account the HPP regime management considering market price schedule. For example, the generated power changes chart for several time intervals of SHPP and market price schedule are shown at the Fig. 1 (Table 1).

We can see that price schedule is very complicated for generation plan development. That's why appropriate algorithms on software tools are needed. These tasks are topical in many countries. Large numbers of papers are devoted to solve this problem. For example:

Authors of the [6] article used discrete dynamic programming for the solving sequential decision problems. It is presented an explicit stochastic optimization model based on dynamic programming for the hydropower reservoir by using only the inflow volumes. Their decisions allows to tracing several optimal storage guide curves, which are useful to help decision maker in current operation. But in our optimization task we are using the generalized reduced gradient method for non-linear optimization task solving, because this method not depends on discretization size and provides much accurate optimization result [7, 8].

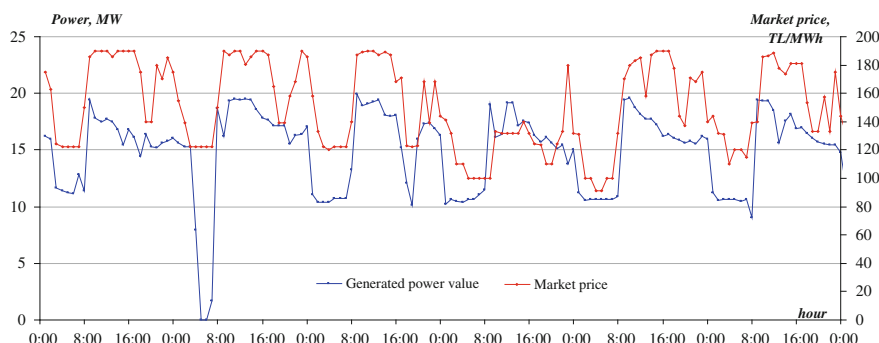


Fig. 1 Cobanli HPP generated power according market price schedule

Table 1 RES support mechanism prices with respect to type of production [4, 5]

Type of production facility based on renewable energy resources	Prices applicable (\$ct/kWh)
a. Hydroelectric production facility	7.3
b. Turbine ^a	1.3
c. Generator and power electronics ^a	1.0

^aLocally produced equipments and components; domestic contribution supplement

Authors of the [9] article applied optimization system to one of biggest Brazilian power plant. The method was proposed for the short-term hydro scheduling problem, considering inflow water. This method allows an efficient consideration of the nonlinear relationship between power generation, water discharge, and reservoir. The results are highly able in that model satisfies demand and produces more energy. It is similar to our optimization task of gaining increasing income of HPP under the known water inflow and price forecast of electricity prices and under conditions of market relations. The HPP operating options are compared with market and fixed price of water resources amount. The obtained results prove the feasibility of the use opportunities of HPP working system for the optimization of our regime by the income amount.

Authors of the [10] article optimization principle was; first is value of the water in the pool, forecasted price of electricity, net head and incoming flow. How the water would be optimally discharged, but only the income obtained by draining the pool to the minimum level as quickly as possible. Second was Revenue. The third was switching cost. According to the optimization genetic algorithm-based and the steepest ascent-based optimization algorithms were tested with different price data and inflow values. The comparison between linear and nonlinear optimization methods shows that the water discharge changes more quickly from the less value to the high value with the linear optimization method than with the offered nonlinear optimization method, thus ignoring the pool's capacity. The water discharge and with the hydroelectric power generation go to follow the form of the electricity price. The aim of the analysis was obtaining the hydro units efficiency and to determine the short term regimes behavior.

In the planning, unstorables nature of electricity and the seasonal variations in demand must be taken into agenda. Also, water can be stored and a hydropower producer can decide separately for each daily and hourly how much electricity to produce or to save for the future when the prices are higher. This means that today's decision is not only placed on the current price but also on the future forecasts. There are concerns in price forecasts, which mean that one cannot trust them completely. Additionally inflows and reservoir water levels affect the production planning. When the inflows are large, power plants are able to produce larger amounts of electricity. When the inflows are small and prices are low, it is acceptable to save water for later use.

Short-term planning determines how much power is generated, at what time, and at which price. We can call the day-ahead phase which can be divided into two phases: to create different pricing scenarios and compare the optimization model against the pricing scenarios and to create a bid to PMUM. The planning time is horizon a week. The most important bid is the one which covers the following day. Short time planning is set to cover 7 days because the dictate includes a daily period [11].

The producers of electricity main task are to get the maximum income from the electricity production and participation in the market. From the Fig. 1 is seen that power distributed not the best this fact decreases available income amount. Firstly producers have to choose the mode power plant management. There are two

possibilities: work on granted prices regime or participate in market strive to adapt generation to maximize revenue. The choice of mode is needed to kind of optimization task selection. In both cases the obligatory energy purchase must be guaranteed by the law. If first mode selected producers have to maximize generated energy quantity. In opposite case producers will strive maximize the planning period revenues. Choice of regime and kind of the optimization task statement have to be made on water inflow and electricity prices prediction base shown in Fig. 2. According to existing power market organization rules; all market players give to the market operator energy bids propositions. At fixed day time power tender occur. The hourly energy prices become known (for 24 h time horizontal). If the work on the base of generated price is chooses. But in opposite case the power plant operator can state and solve optimization task. In today's technology HPP can use special microcontrollers which could react to delivered signal and open the turbine flap in time then the electricity market price high for the production maximal power value. Depicted in Fig. 2 structure include water and prices prediction blocks. For this task solutions are devoted large number of papers. Part of them is based on artificial neural network (ANN) usage [12]. Authors of these paper also use ANN. Structure of this ANN described in previous article and it is out of frames of this paper. The goal of this paper is to propose the operational algorithm supported by feed in tariff

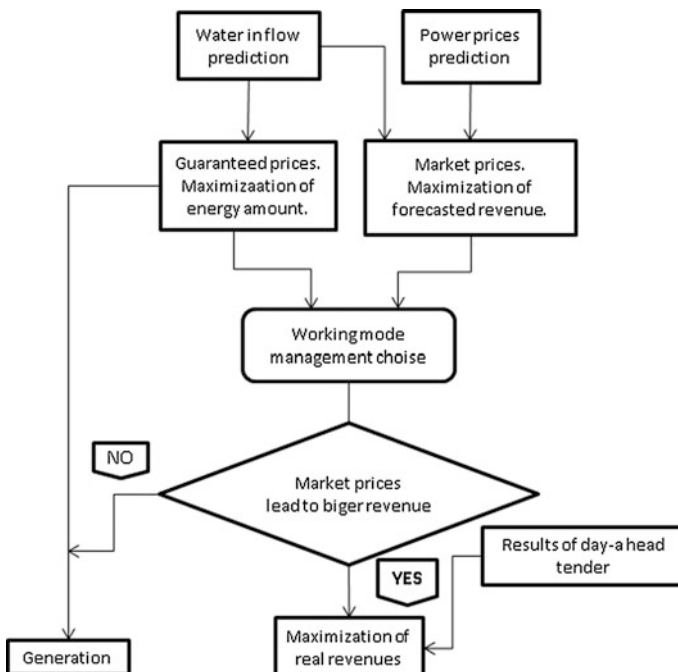


Fig. 2 Structure of HPP regime operation

in HPP. The day a-head operation planning is formulated as result of choice of mode of management. We are proposed the methodology of HPP regime management with taking into account price schedule.

2 Optimization Task Statement

Small hydro power plants have got limited water resource that is why some time period it could work at maximum power and store water in period than water inflow is less. Our methodology of regulation process of SHPP is based on its working regime regulation at hours when market price is high by exhausting the water through the turbine and at other periods of time when price is less SHPP uses less water than inflow and fill up the reservoir before dam. In that way we could consume water than it is benefit and store that at other sides. The time interval from the process optimization beginning with the set start point of reservoir drawdown to the next drawdown period after its filling up the water is called a regulation cycle.

The small capacity of water reservoir (without opportunity of long regulation) does not allow using regular changes in seasonal water inflow. According to this condition planned drawdown and filling up of water reservoir with small capacity can be made only in connection with regular changes of the total electrical load in the power system, which has the daily and weekly periodicity.

The change of water pressure on SHPP is caused by the change of water level in upstream and downstream. This is due to the water use through the turbines of SHPP. Hence, the change of the water level should be restricted by H_{\max} from the top and by H_{\min} from the bottom.

The main criteria of our optimization task is the income maximization, in market conditions the optimization problem can be formulated as follows

$$\begin{aligned} I(P_1, P_2, \dots, P_j) &= \arg \max \sum_{j=1}^J I_j(c_j, P_{SHPP_j}) \\ &= \max \sum_{j=1}^J c_j \cdot (9.81 \cdot \eta_{turb} \cdot \eta_G \cdot Q_j \cdot H_j) \end{aligned} \quad (1)$$

where P_{SHPP} —SHPP generated power, kW;

P_j —power generated at j -time interval;

C_j —market price at the time period j , TL/kWh;

Q_j —water flow through the turbine, m^3/s ;

H_j —difference between water levels at the SHPP, m;

η_{HA} —efficiency factor of hydro unit in relative units: $\eta_{HA} = \eta_{turb} \cdot \eta_G$, where η_{turb} —turbine efficiency factor in relative units; η_G —generator efficiency factor in relative units [13–16].

It is required to determine the SHPP operating schedule by providing maximum income for the regulation cycle $T = 24$ h.

First expression is feasible in condition of considering water level limitations and condition of use of the set amount of water W_J in water reservoir

$$\sum_{j=1}^J Q_j \cdot \Delta t_j = W_J \quad (2)$$

where $I_j(c_j, P_j)$ —income from sale of electricity, that is produced on SHPP during the time interval Δt_j by known market price c_j , €;

T —the regulation cycle duration $T = \sum_{j=1}^J \Delta t_j$

Q_j —the water flow through the SHPP flap during the time interval, m^3/s ;

W_J —the set amount of water that could be passed through the SHPP flap per regulation cycle (day, week and etc.).

The time interval equals to $\Delta t_j = 1$ h at the daily regulation cycle of SHPP. The power generation on SHPP during to the j th interval Δt_j is defined as: $P_j \cdot \Delta t_j$. At the known natural inflow (the natural inflow of the river, due to which the reservoir is filled up) Q_{flow} , the used water flow in each time interval of regulation is determined by value Q_j that depends of the usage of water reservoir capacity (m^3).

3 Case Study

The operability of developed optimization algorithm is illustrated on the example of Cobanli HPP regime optimizations. The powerhouse and reservoir is a multipurpose project built on Cobanli river in Sivas city; Northern Turkey. The powerhouse started to produce electricity in March 2013. This project was conceived for hydropower, with other purposes being flood control. The catchment area of reservoir up to the dam site is about 690 km^2 .

There are 3 Francis type turbines at the Cobanli power house with $2 \times 7.66 \text{ MW} + 1 \times 3.71 \text{ MW}$ power capacity. Length of the penstock is 230 m. The capacity of pool is 1393 m^3 . The Cobanli HPP main data which allows its regulation is given: the net head is 125.81 m; nominal capacity is 19.03 MW; the year average water inflow into the reservoir is $6.8 \text{ m}^3/\text{s}$. Due to the regulations of the environmental protection in Turkey the minimal range of the water in the river should not be less than 20 % at the current time.

In our offered methodology of HPP optimization task realization we assume that prices are predicted without errors and naturel water inflow is constant value for all 24 h regular period and it is equal to $13 \text{ m}^3/\text{s}$. Figure 3 clarifies the power changes results of algorithm of work control of Cobanli depending on market price changes at the end of each hour of the 24 h period. In this paper we compared the results of realistic energy production and offered optimization at the same market condition.

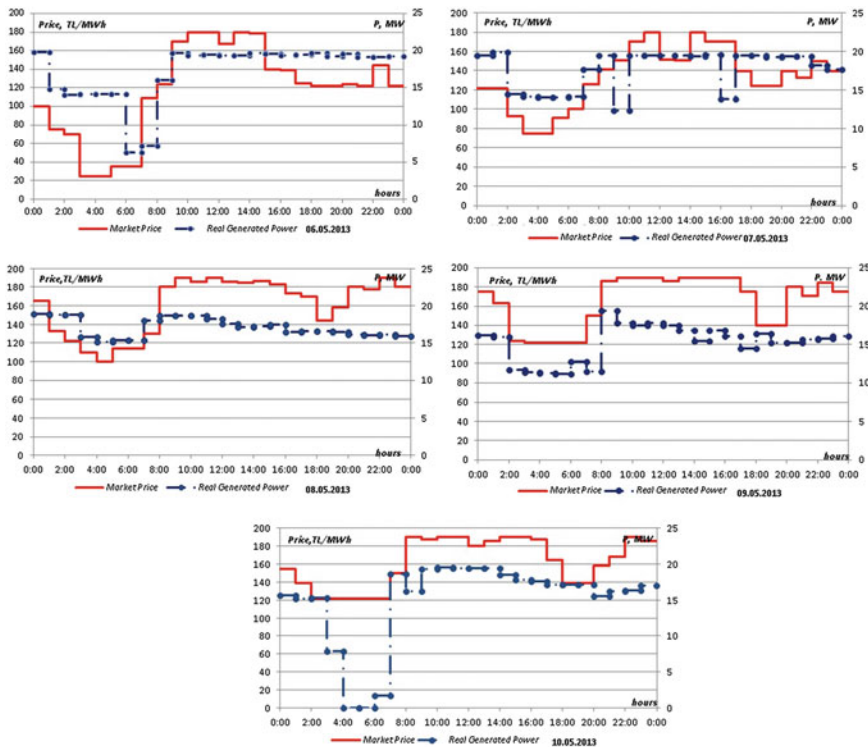


Fig. 3 Cobanli HPP generated power according market price schedule (06–10.05.2013)

The realistic data energy productions are shown at Fig. 3. It is seen that power level not decreases till minimal because of not effective regime planning from expert side.

The results of our optimization are to show the similarity of production of power for 24 h, with more accurate regime planning to have the greatest regular economic benefit (Figs. 4, 5).

Coming by results Figs. 4, 5 provide a conclusion this HPP collect the water before dam in the case when the prices at the market are less and take advantage of the water when market price becomes higher, as well as limitations for the maximum power. Optimizing the operating mode of HPP with the generalized reduced gradient method, income was fewer amounts, but after our optimization we saw that income became bigger. In offered case it provides the opportunity to power producer to maximize their economic benefit at condition of limited resource.

During these 5 days (06–10.05.2013) we saw that; if could work with fixed price our income would be 111340EUR and if could have locally produced equipments and components revenue would be 138146EUR. In Cobanli HPP operators worked by market prices and the income was 129447EUR. But according to our optimization model with market price; they could get 127605EUR and 101717EUR by fixed price tariff with foreign produced equipment by inflow rate $13 \text{ m}^3/\text{s}$. We advise to operators that they have to measure water inflow hourly.

Fig. 4 Cobanli HPP optimized power according to market price schedule (06–10.05.2013)

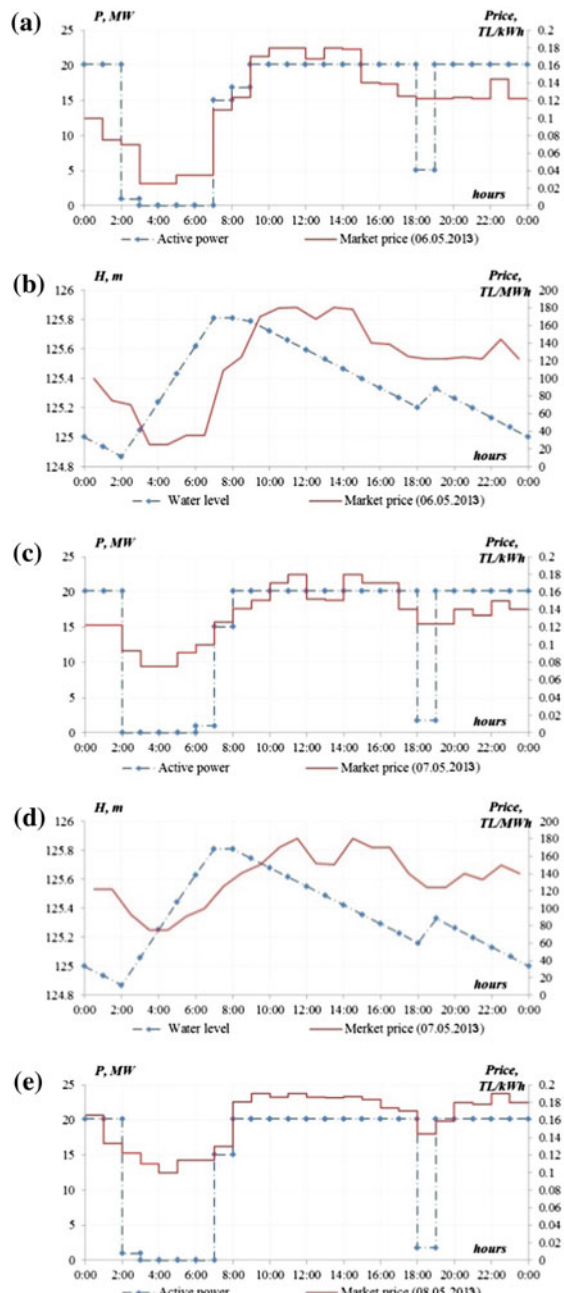
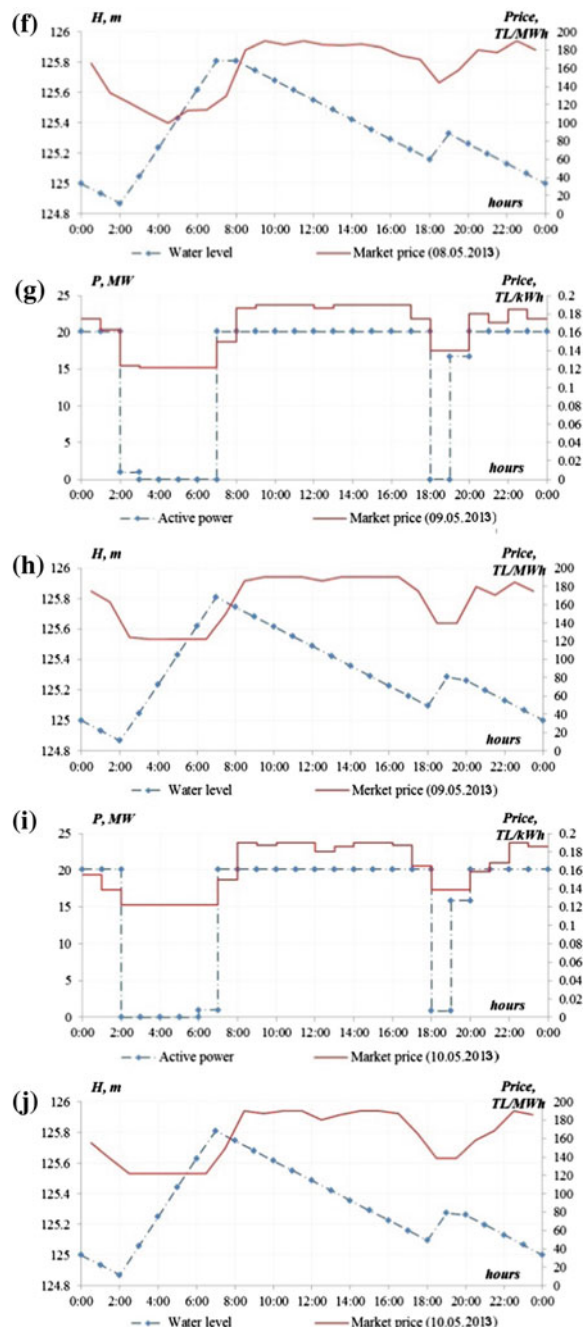


Fig. 4 (continued)



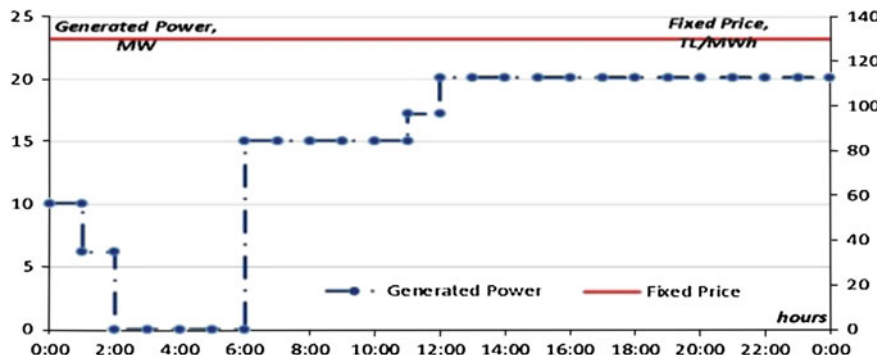


Fig. 5 Cobanli HPP generated power by feed-in tariff (06–10.05.2013)

4 Conclusion

Real time optimization is done using calculations real-time experiments. In this case discharge through turbines and the number of gates at reservoir and spillways to open at 24 h intervals in the forecast period are optimized. The real-time operation depends on the forecasting. If no critical reservoir inflow and flooding at Cobanli HPP are forecasted, the reservoir is operated considering hydropower production only. In this case two objective functions are defined that measure the immediate and the future value of the hydropower production. In our optimization, the trade-off between these two objectives is found, providing optimal solutions for the decision maker. For the optimization of Cobanli HPP generators regimes the prognosis for time considerably exceeding 24 hours is taken into account. The maximal effect for power system from the operation of the HPPs can be obtained in the conduct of their regime relative to the schedule of the market price change. This paper shows that HPP producers can get more income if they work in right water consumption level and on right power range.

Acknowledgments Development of this paper has been co-financed by the European Social Fund within the project “Exploration and Solving of Energy Systems’ Strategic Development and Management Technically-Economic Problems”, project agreement No. 2013/0011/IDP/1.1.1.2.0/13/APIA/VIAA/028.

References

1. Turkish Electricity Transmission Corporation, www.teias.gov.tr
2. EMRA Electricity Market Report, Ankara Turkey (2011)
3. Turkish law on utilization of renewable energy sources. Law No: 5346
4. Electricity regulation in Turkey, <http://uk.practicallaw.com/0-523-5654>

5. Eastern Marmara region renewable energy report, Izmir Province Renewable Energy Sector Analysis. Izmir Turkey (2012)
6. Y. Zheng, X. Fu, J. Wei, Evaluation of power generation efficiency of cascade hydropower plants: a case study. *Energies* **6**, 1165–1177 (2013)
7. R. Varfolomejeva, I. Umbras̄ko, A. Mahn̄itko, in *Algorithm of smart control system operation of small hydropower plant*. No: 12th International Conference on Environment and Electrical Engineering (EEEIC 2013), IEEE, Poland, Wroclaw, pp. 330–334, 5–8 May 2013
8. A. Mahn̄itko, J. Gerhards, R. Varfolomejeva, I. Umbras̄ko, O. Linkevics, Development opportunities of the small hydroenergetics in latvia and smart operating system for small-scale hydropower plants. Nr.31, 2013, 10.-17.ipp. ISSN 14077345
9. T. Mariot, L. Barros, Large-scale hydropower system optimization. *J. Water Resour. Plann. Manage.* **129**(3), 178–188 (2003)
10. R. Tiainen, T. Lindh, J. Ahola, M. Niemelä, V. Särkimäki, Energy price-based control strategy of a small-scale Head-dependent hydroelectric power plant
11. Market Financial Reconciliation Center (PMUM), www.pmum.gov.tr
12. R. Varfolomejeva, M. Bočkarjova, A. Sauhats, I. Umbrasko, H. Coban, Reconsideration of supporting scheme for renewable energy producers. 4ISEBE, Mexico, Sept. 2014
13. V.M.Gornstejn, The most profitable operating regimes of hydro power plant in the power systems, p. 248. Gosenergoizdat, Moscow (1959) (in Russian)
14. J. Gerhards, A. Mahn̄itko, The power system régime optimization. Riga Technical University, Riga (2005) (in Latvian)
15. L.P. Mikhailov, B.N. Feldman, T.K. Markanova et al., Small hydroenergetic, p. 184. Gosenergoizdat, Moscow (1989) (in Russian)
16. M. Grigoriu, M. Popescu, in *Hydropower preventive monitoring action plan*. Proceedings of 5th International Conference on Energy and Environment, UK, pp. 265–270 (2010)

Part VIII

Energy Storage, Conservation

and Efficiency

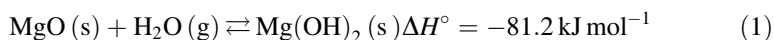
Hydration Behavior of Mg-Ni Mixed Hydroxide Synthesized by Mechano-chemical Method for Chemical Heat Storage

Junichi Ryu, Yuki Hara and Yukitaka Kato

Abstract The hydration behavior of Mg-Ni mixed hydroxides synthesized by mechano-chemical method was studied to develop a new material for chemical heat storage. It was demonstrated that the hydration conversion of Mg-Ni mixed hydroxides synthesized by mechano-chemical method were higher than that of samples synthesized by co-precipitation method as conventional method. It can be explained by the difference of particle size of samples.

1 Introduction

The application of heat storage technologies to waste heat from industrial processes can contribute to energy saving. Chemical heat storage technologies are particularly interesting in view of their heat storage capacity. In recent years, different technologies for chemical heat storage and chemical heat pumping have been widely studied for their role in reducing energy consumption [1–7]. A chemical heat pump system based on the reaction between magnesium oxide and water vapor has been reported by our group [8].



In this reaction system, the dehydration of magnesium hydroxide, the heat storage operation, would proceed at about 265 °C thermodynamically; however, for practical applications, temperature should be above 350 °C. Therefore, this system has to be modified for application to heat utilization below 300 °C at which a large

J. Ryu (✉) · Y. Hara · Y. Kato

Research Laboratory for Nuclear Reactors, Tokyo Institute of Technology,
2-12-1-N1-22, O-Okayama, Meguro, Tokyo 152-8550, Japan
e-mail: cyliu@nr.titech.ac.jp

amount of waste heat is emitted from the garbage-disposal facilities, the petro-chemical plant, the co-generation system, the vehicle engine, and so on. In our previous work, two new materials for chemical heat storage below 300 °C were proposed. The mixed hydroxide of Mg-Ni and Mg-Co showed higher hydration reactivity at 110 °C with 57.8 kPa of water vapor than the authentic oxide after heat storage operation at 280 °C [9, 10]. However, these samples require saturated water vapor at 85 °C for the heat output operation. Hence, it is necessary to develop new materials with higher reactivity for heat storage operation and heat output operation. In this work, $\text{Mg(OH)}_2\text{-Ni(OH)}_2$ mixed hydroxides as new material for chemical heat storage were synthesized by mechano-chemical method. Reactivity for dehydration and hydration of these materials were investigated by thermo-gravimetric method.

2 Experimental Method

2.1 Sample Preparation

The composite of $\text{Mg(OH)}_2\text{-Ni(OH)}_2$ were synthesized by mechano-chemical method with planetary ball mill (P-7, Fritch Japan Co. Ltd.). The mixture of Mg(OH)_2 and Ni(OH)_2 with prescribed molar ratio were mixed in Zirconia pot and grinded for several hours with 400 rpm of rotation speed as mechano-chemical treatment. The progress of solid phase reaction of the mixture was observed by FT-IR method (FT/4200; JASCO Co. Ltd.).

2.2 Reaction Test

The reactivity between the prepared sample and the water vapor was measured by a thermo gravimetric (TG) method, using a thermobalance (TGD9600; ULVAC Riko Co. Ltd.). The sample was charged into a cell of the balance in hydroxide state. The cell was heated up to the targeted dehydration temperature at 300 °C with 20 °C min^{-1} of temperature increasing rate, and kept at that temperature for 30 min with 100 mL min^{-1} of Ar flow, as heat storage operation. Before the dehydration, the sample was dried at 120 °C for 10 min for removing any physically adsorbed water. In this process, physically adsorbed water and water vapor produced by thermal decomposition of sample were removed immediately with Ar flow. The dehydrated sample in the balance was cooled down to 110 °C with 100 mL min^{-1} of Ar flow, and the water vapor ($P_{\text{H}_2\text{O}} = 57.8 \text{ kPa}$) carried with the Ar flow was induced in the balance for hydration for 80 min, as heat output operation. This vapor pressure

corresponds to saturated water vapor pressure at 85 °C. After the hydration operation, the vapor supply was stopped and dry Ar gas was supplied at the same hydration temperature for 20 min to remove physically adsorbed water on the sample, and the second dehydration operation was carried out by heating up the sample to the original dehydration temperature.

2.3 Reactivity Evaluation

The sample forms a mixture of oxide and hydroxide during the reaction. The mole fraction of hydroxide in the mixture of Mg-based mixed hydroxide and mixed oxide, X is determined as

$$X = \left(1 + \frac{\Delta w / M_{\text{H}_2\text{O}}}{w_{\text{ini}} / M_{\text{hydroxide}}} \right) \times 100 \quad (2)$$

Here, Δw is the weight change in the sample; $M_{\text{H}_2\text{O}}$ is molecular weight of water; $M_{\text{hydroxide}}$ is molecular weight of hydroxide, and w_{ini} is the initial sample weight. For Mg-based samples, $X = 100$ or 0 % would imply that the sample is a pure hydroxide or pure oxide, respectively. The value of hydration conversion, ΔX_1 , was calculated from the change of X during hydration process as heat output operation [9].

3 Results and Discussion

3.1 Formation of Mg-Ni Mixed Hydroxide with Mechano-chemical Treatment

The IR spectra for the mixture of $\text{Mg}(\text{OH})_2$ and $\text{Ni}(\text{OH})_2$ with 5:5 of molar ratio are shown in Fig. 1. Before the mechano-chemical treatment (a), two absorption peaks of OH groups of $\text{Mg}(\text{OH})_2$ and $\text{Ni}(\text{OH})_2$ are available at 3697 and 3638 cm^{-1} , respectively. With the passage of mechano-chemical treatment time (b)–(e), a peak at 3638 cm^{-1} become weak and finally disappeared after 20 h treatment (e). On the other hand, a peak at 3697 cm^{-1} moved to lower wavenumber, and finally appeared at 3675 cm^{-1} . These results suggests that the mixed hydroxide of $\text{Mg}(\text{OH})_2$ and $\text{Ni}(\text{OH})_2$, such as $\text{Mg}_{0.5}\text{Ni}_{0.5}(\text{OH})_2$ was synthesized by mechano-chemical treatment. Figure 2 shows the relationship of mechano-chemical treatment time and the peak shift of OH group in the mixture of $\text{Mg}(\text{OH})_2$ and $\text{Ni}(\text{OH})_2$ with different molar ratio. The wave number of OH groups for $\text{Mg}(\text{OH})_2$ were changed with

Fig. 1 IR spectra for the mixture of $\text{Mg}(\text{OH})_2$ and $\text{Ni}(\text{OH})_2$ before mechano-chemical treatment **a**, and after mechanochemical treatment; **b** 4 h, **c** 8 h, **d** 12 h, **e** 20 h

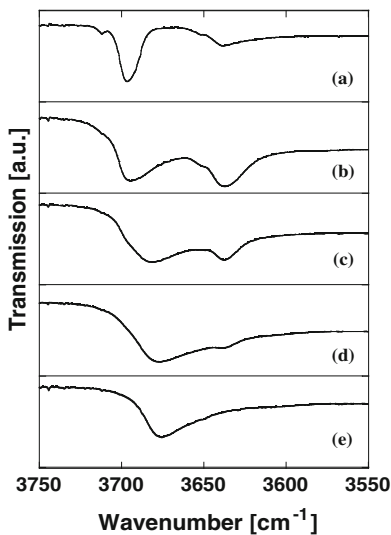
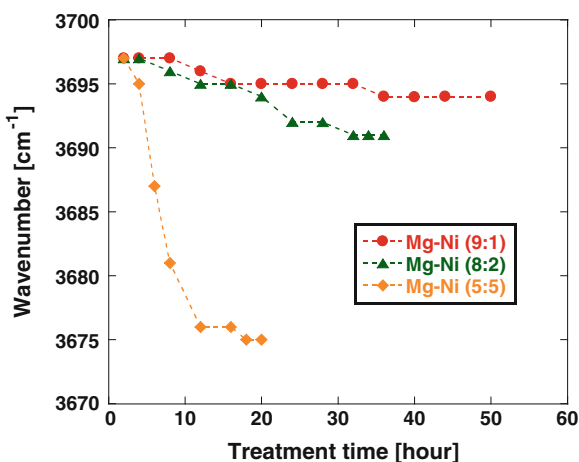


Fig. 2 Relationship of mechano-chemical treatment time and the peak shift of OH group in the mixture of $\text{Mg}(\text{OH})_2$ and $\text{Ni}(\text{OH})_2$



mechano-chemical treatment and these were terminated within 50 h treatment. In addition, the peak shift of OH groups for $\text{Mg}(\text{OH})_2$ become larger with increase of Ni content in the mixture. These results suggests that the final product for the mixture of $\text{Mg}(\text{OH})_2$ and $\text{Ni}(\text{OH})_2$ with $x:y$ ($x + y = 10$) of molar ratio by mechano-chemical treatment were the mixed hydroxide of $\text{Mg}_{0.1x}\text{Ni}_{0.1y}(\text{OH})_2$ ($x + y = 10$). In this work, a sample synthesized by mechano-chemical treatment denoted as “Mg-Ni ($x:y$)”.

3.2 Hydration Behavior of Samples

The hydration behavior of Mg-Ni (9:1) and $Mg_{0.9}Ni_{0.1}(OH)_2$ prepared by co-precipitation method [9] under the reaction temperature of 110 °C and vapor pressure of 57.8 kPa, after dehydration at 300 °C for 30 min, are shown in Fig. 3. The values of hydration conversion, ΔX_1 , for Mg-Ni (9:1) and $Mg_{0.9}Ni_{0.1}(OH)_2$ were 39.5 and 16.3 %, respectively. This indicates that the hydration reactivity of Mg-Ni (9:1) was higher than $Mg_{0.9}Ni_{0.1}(OH)_2$.

Figure 4 shows the hydration conversion of Mg-Ni Mixed Hydroxides prepared by mechano-chemical method and co-precipitation method. The hydration conversion of samples prepared by mechano-chemical method was higher than samples prepared by co-precipitation method between samples with same molar ratio.

Fig. 3 Hydration behavior of Mg-Ni (9:1) and $Mg_{0.9}Ni_{0.1}(OH)_2$

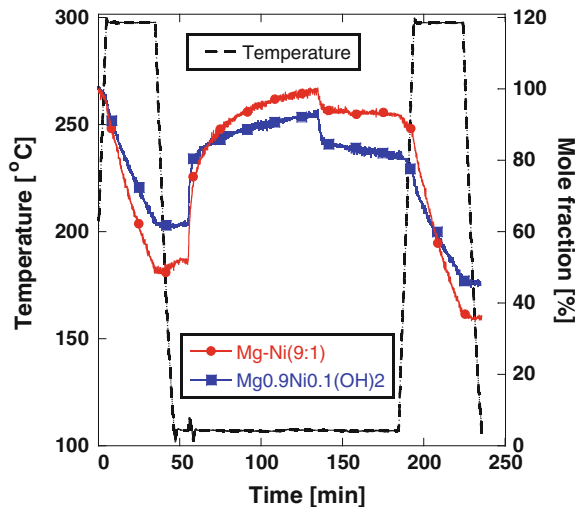
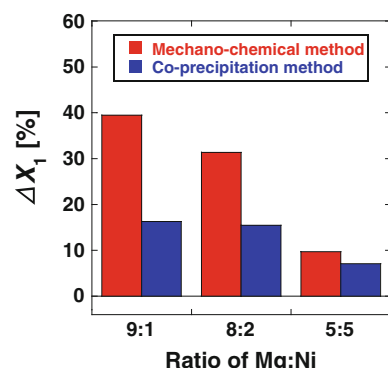


Fig. 4 Comparison of hydration conversion between samples prepared by mechano-chemical method and co-precipitation method with various molar ratio



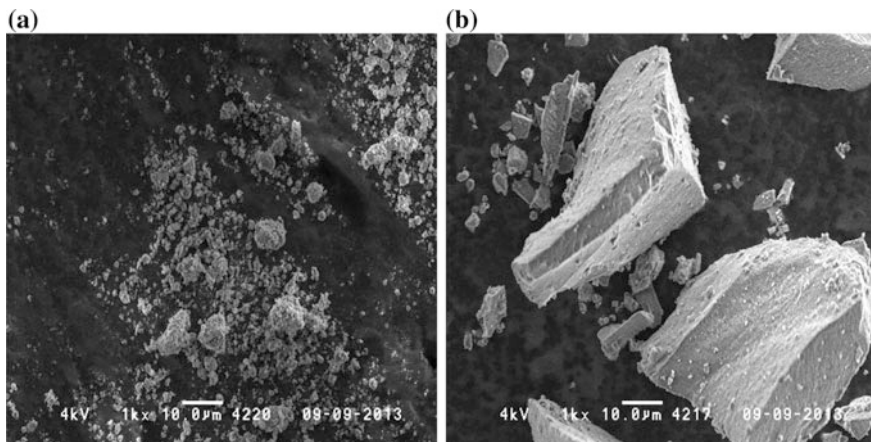


Fig. 5 SEM image of **a** Mg-Ni (9:1) prepared by mechano-chemical method, and **b** $Mg_{0.9}Ni_{0.1}(OH)_2$ prepared by co-precipitation method

3.3 Morphology of Samples

The SEM image of Mg-Ni (9:1) and $Mg_{0.9}Ni_{0.1}(OH)_2$ are shown in Fig. 5. The particle size of Mg-Ni (9:1) was smaller than 10 μm , and that was quite smaller than $Mg_{0.9}Ni_{0.1}(OH)_2$. These results suggest that the difference of hydration reactivity for Mg-Ni (9:1) and $Mg_{0.9}Ni_{0.1}(OH)_2$ shown in Figs. 3 and 4 were due to the difference of particle size of these samples.

4 Conclusion

Mg-Ni mixed hydroxides were synthesized by mechano-chemical method, and evaluated the hydration reactivity as new material for chemical heat storage. Hydration conversion of Mg-Ni (9:1) prepared by mechano-chemical method was 39.5 % at the hydration temperature of 110 $^{\circ}C$ and vapor pressure of 57.8 kPa, after dehydration at 300 $^{\circ}C$. This value was higher than $Mg_{0.9}Ni_{0.1}(OH)_2$ prepared by co-precipitation method. It is suggested that the difference of hydration reactivity between both samples was due to the difference of particle size of samples. The heat output performance and the sample stability against multiple reaction should be studied further.

Acknowledgments This work was partially supported by the Industrial Technology Research Grant Program from New Energy and Industrial Technology Development Organization (NEDO), Japan, the research grant from Tanikawa Foundation and the JSPS KAKENHI Grant Number 24656577.

References

1. Y. Aristov, Challenging offers of material science for adsorption heat transformation: A review. *Appl. Therm. Eng.* **50**, 1610–1618 (2013)
2. R.E. Critoph, Y. Zhong, Review of trends in solid sorption refrigeration and heat pumping technology, *Proc. Inst. Mech. Eng. Part E-J. Process Mech. Eng.* **219**(E3), 285–300 (2005)
3. L. Gordeeva, A. Grekova, T. Krieger, Y. Aristov, Composites “binary salts in porous matrix” for adsorption heat transformation. *Appl. Therm. Eng.* **50**, 1633–1638 (2013)
4. J.H. Lee, H. Ogura, Reaction characteristics of various gypsum as chemical heat pump materials. *Appl. Therm. Eng.* **50**, 1557–1563 (2013)
5. A. Shkatulov, J. Ryu, Y. Kato, Y. Aristov, Composite material “Mg(OH)₂/vermiculite”: a promising new candidate for storage of middle temperature heat. *Energy* **44**, 1028–1034 (2012)
6. L.W. Wang, R.Z. Wang, R.G. Oliveira, A review on adsorption working pairs for refrigeration. *Renew. Sust. Energ. Rev.* **13**, 518–534 (2009)
7. J. Xu, R.Z. Wang, Y. Li, A review of available technologies for seasonal thermal energy storage. *Sol. Energy* **103**, 610–638 (2014)
8. Y. Kato, N. Yamashita, K. Kobayashi, Y. Yoshizawa, Kinetic study of the hydration of magnesium oxide for a chemical heat pump. *Appl. Therm. Eng.* **16**, 853–862 (1996)
9. J. Ryu, R. Takahashi, N. Hirao, Y. Kato, Effect of transition metal mixing on reactivities of magnesium oxide for chemical heat pump. *J. Chem. Eng. Jpn.* **40**, 1281–1286 (2007)
10. Y. Kato, R. Takahashi, T. Sekiguchi, J. Ryu, Study on medium-temperature chemical heat storage using mixed hydroxides. *Int. J. Refrig* **32**, 661–666 (2009)

Regenerative AC Drive System Based on the Three Phase Permanent Magnet Synchronous Machine

Marian Gaiceanu and Cristian Nichita

Abstract The permanent magnet synchronous machine becomes an attractive solution in the transport area providing higher power density than the induction machine. Surface permanent synchronous machine is controlled by using the field oriented control. Therefore, the maximum torque is easily obtained by setting at zero value the longitudinal stator current component, i_{sd}^* . The frequently dynamic regimes of the permanent magnet synchronous machine (PMSM) decrease significantly the overall efficiency of the drive system. Taking into account that during braking or reversing period the actual drive system dissipates the energy by using a brake resistor in DC link side, the authors of this paper have proposed a regenerative drive system. In this way the energy during the dynamic regimes is recovered and delivered into the utility network. Moreover, the power quality is taken into consideration by including an adequate control in order to obtain unity power factor. The topology of the proposed power converter consists of a series AC-DC active power converter, DC link capacitor and the DC-AC power inverter. By introducing a feedforward reference of the transversal stator current (i_{sq}^*) the power balance control is achieved. As a result, the speed response of the control loops is increased, lowering the DC link capacitor value. The maximum 5 % total harmonic distortion (THD) value of the input current is attained by an appropriate design of the boost inductor. By using the DC link voltage control accompanied by an appropriate design of the DC link capacitor, the DC voltage ripple is decreased under the maximum limits. The regenerative PMSM drive is developed in the Matlab/Simulink environment software and the performances in motoring and regenerating operation modes are shown.

M. Gaiceanu (✉)

Dunarea de Jos University of Galati, 47 Domneasca Street, Galati, Romania
e-mail: marian.gaiceanu@ugal.ro

C. Nichita

University of Le Havre, 25, Rue Philippe Lebon, 76058 Le Havre Cedex, France
e-mail: nichitac@univ-lehavre.fr

1 Introduction

The regenerative drive system is a challenge to the modern AC drive in order to transform the mechanical energy into the electrical one, and to send it back to the electrical network instead of dissipating through braking resistor, like into conventional drive systems [1]. The manufacturers of the power converters (ABB, Siemens, Rockwell Automation, Mitsubishi, Gefran, and Toshiba) pay attention to product the regenerative drives for different kinds of electric machines.

Different types of the PMSM drive topology have been developed [2, 3]. One solution to assure a fast control response to load variation is the load feedforward control [4]. The regenerative AC-AC power converters are used in elevators, crane, centrifuge, wind turbine drive systems.

The paper is structured in six sections: the first—introduction, the second includes the proposed topology of the regenerative PMSM drive system, the third section describes the mathematical model of the active front side power converter, the fourth section shows the mathematical model of the permanent magnet synchronous motor, the fifth Section presents the Matlab/Simulink simulated results, and the last section for concluding remarks.

2 The Topology of the Regenerative PMSM Drive System

The structure of the back to back power converter control system is represented in Fig. 1. The detailed mathematical model of the grid converter is shown in Fig. 2.

The structure of the control is in cascaded manner, with the internal current loop and dc link external voltage loop.

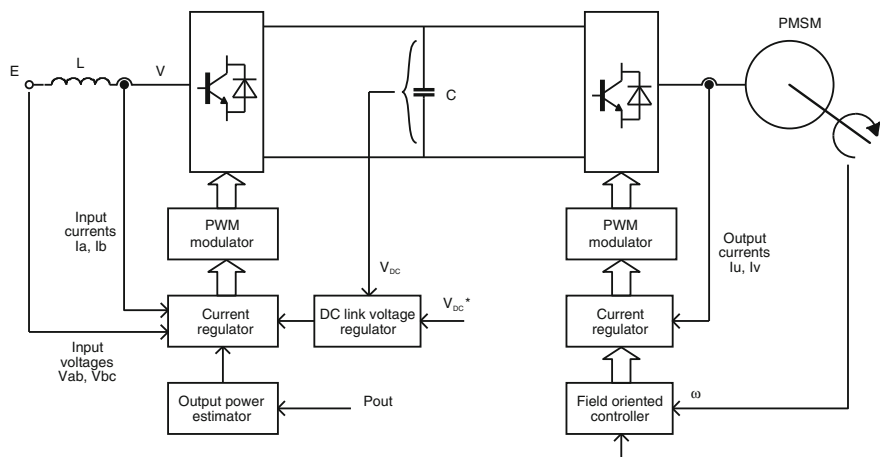


Fig. 1 Block diagram of the complete control system of the quasi sinusoidal AC-AC converter

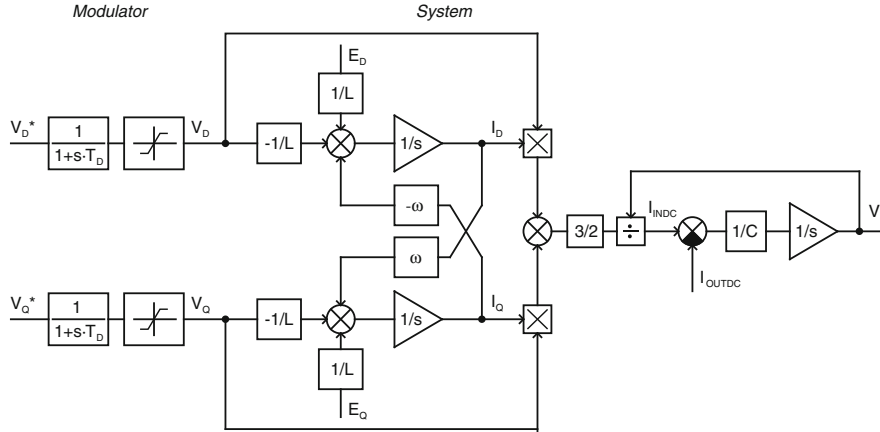


Fig. 2 The control block diagram of the AC-DC converter in d - q coordinates with direct compensation of disturbance E_D and E_Q

3 The Mathematical Model of the AC-DC Power Converter

The main vectorial first-order equation which describes the decoupled mathematical model of the grid power converter is [5]:

$$\vec{E} = L \cdot \frac{d\vec{I}}{dt} + \vec{V} \quad (1)$$

where E is the main voltage vector, L is the line inductance, V is the power converter input voltage, I —the line current vector. Taken into account that in steady state the DC link input power equals the AC input power of the AC-DC supply power converter [4] the DC link capacitor voltage is as follows:

$$\frac{dV_{dc}}{dt} = \frac{3}{2} \cdot \frac{V_D \cdot I_D + V_Q \cdot I_Q}{C \cdot V_{dc}} - \frac{I_{outdc}}{C} \quad (2)$$

where E_Q and E_D are the q - d supply voltage components, I_D and I_Q are the d - q line current components. The real PWM modulator system introduces a delay time due to the IGBT dead time, T_D , which is approximately equal to half of the switching frequency T_s (Fig. 2). There are two current loops: one of them assures the unity power factor operation and the other controls the load current. In order to impose a unity factor the current reference, I_D^* , is set to zero. In such case the current vector I lies on the q axis, i.e. in phase with the vector E . The Proportional Integral controller has been used. The proportional-integral DC voltage controller with the power feedforward component has been implemented [4].

4 Mathematical Model of the Permanent Magnet Synchronous Motor

Matlab-Simulink model of the permanent magnet synchronous motor is obtained by integrating the following state equations:

$$\begin{bmatrix} \frac{di_{sd}}{dt} \\ \frac{di_{sq}}{dt} \end{bmatrix} = \begin{bmatrix} \frac{1}{L_{sd}} & 0 \\ 0 & \frac{1}{L_{sq}} \end{bmatrix} \left\{ \begin{bmatrix} u_{sd} \\ u_{sq} \end{bmatrix} - \begin{bmatrix} R_s & L_{sq}P\Omega_r \\ L_{sd}P\Omega_r & R_s \end{bmatrix} \begin{bmatrix} i_{sd} \\ i_{sq} \end{bmatrix} - \begin{bmatrix} 0 \\ K_T\Omega_r \end{bmatrix} \right\} \quad (3)$$

where: R_s —stator resistance; L_{sd} —equivalent d axis inductance; L_{sq} —equivalent q axis inductance; P —number of the pole pairs; Ω_r —angular velocity of the rotor; K_T —electromotive force constant.

The electromagnetic torque is as follows:

$$T_e = K_T i_{sq} + P(L_{sd} - L_{sq}) i_{sd} i_{sq} \quad (4)$$

Permanent magnet synchronous motors were imposed in applications requiring high static and dynamic performance, especially in electric drives (such as aviation) due to their very good power/weight ratio.

The equation of the rotational movement is described by:

$$T_e = T_L + J \frac{d\omega}{dt} + K\omega \quad (5)$$

where: T_L —load torque; J —total combined moment of inertia reduced to the PMSM rotor; K —viscous force coefficient.

The strategy used in vector control synchronous motor is to maintain the reactive current at zero value, through the d axis, $i_d = 0$, and to control the active current component for torque and speed control.

By maintaining $i_d = 0$, maximum torque is developed by the PMSM. Different control strategies can be addressed: maintaining constant power factor or constant supply of the stator voltage, and constant speed. These types of control lead to more complicated command structure than the proposed maximum torque, because they involve non-linear relationship between current and torque.

5 Simulation Results

The $S_n = 22$ kVA rated apparent power of the front end power converter has been considered. The parameters of the input line inductance are $R_{in} = 0.001 \Omega$, $L_{in} = 2.1$ mH. At the output of the active front end power converter there is a DC-link capacitor of $C = 1565 \mu\text{F}$. The PMSM acts as load of the regenerative drive and

has the following data: $P_n = 4$ kW, $n_N = 2000$ rpm rated speed, $T_L = 19$ Nm rated load torque. The implemented Matlab/Simulink regenerative PMSM drive system is shown in Fig. 3. The adequate numerical simulation results are presented in Figs. 4, 5, 6, 7, 8 and 9.

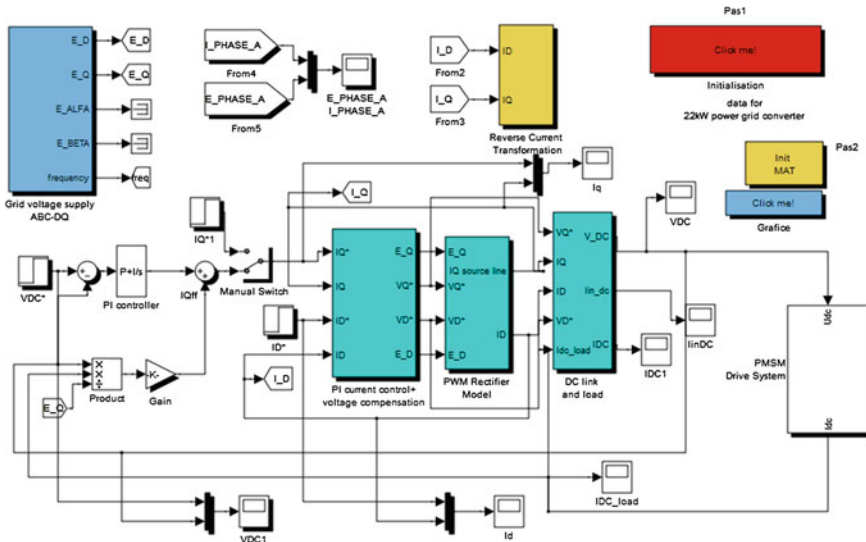


Fig. 3 Simulink model of the PMSM drive system with PI power feedforward DC link voltage controller

Fig. 4 Comparison between speed reference and the feedback speed

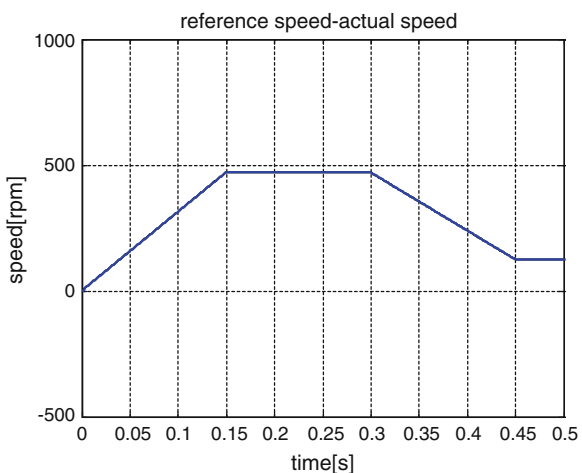


Fig. 5 Electromagnetic torque and load torque comparison

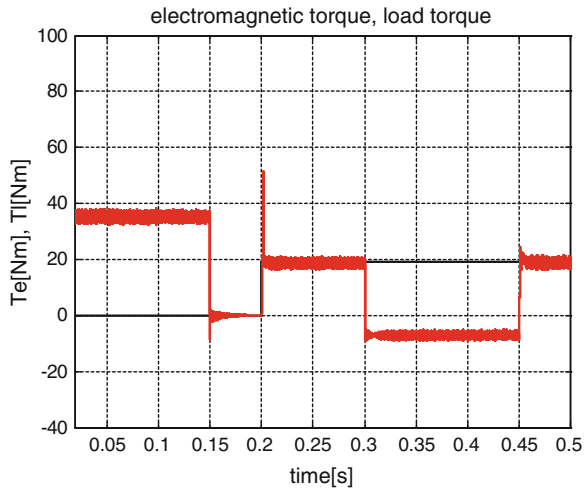
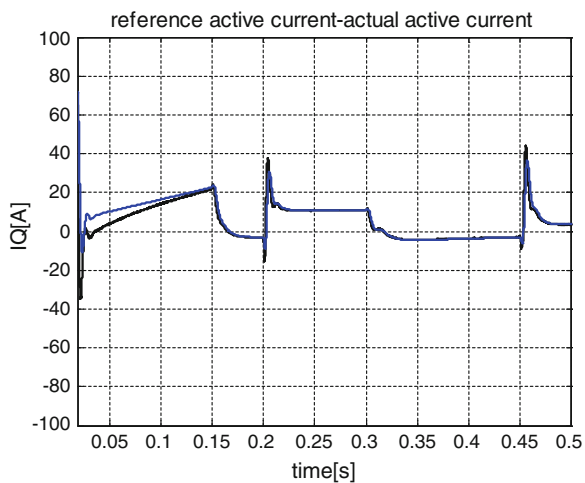


Fig. 6 Active current controller: the reference and the feedback



The feedback speed overlaps the reference speed from starting, breaking to steady state regime (Fig. 4).

In Fig. 5 at starting, the electrical machine develops the maximum torque during transient. At steady state, the electromagnetic torque equals the load torque. During the braking interval [0.2, 0.45] s, the electromagnetic torque becomes negative; therefore, the PMSM machine operates as generator.

Fig. 7 Reactive current controller: the reference and the feedback

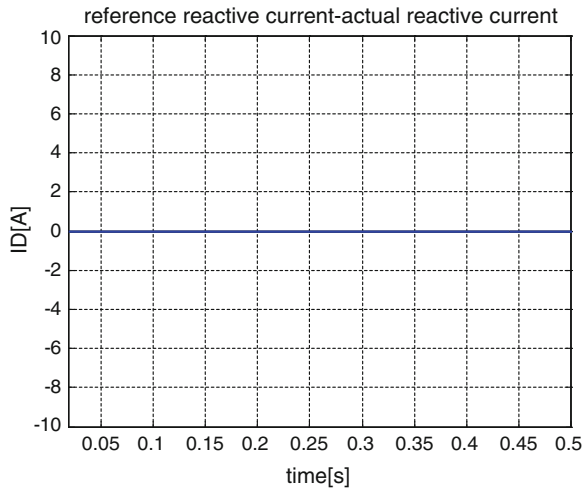
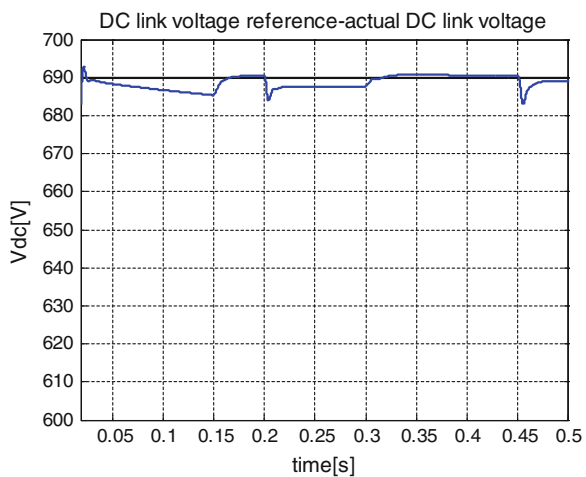


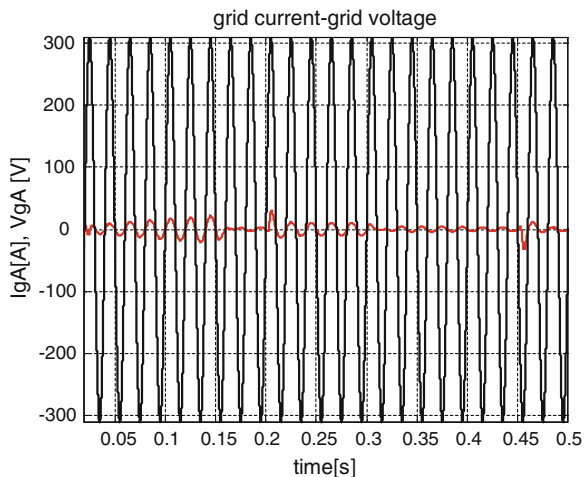
Fig. 8 DC link voltage, V_{DC} (V)



In Figs. 6 and 7 the performances of the current controllers of the grid power converter are shown. For both cases, during the dynamic test, the feedback active and reactive currents follow the references.

During the regenerating intervals, the active currents have negative values, the DC link overvoltage occurs (Fig. 8), the reactive currents are maintained at zero values (Fig. 7); therefore, the unity power factor is obtained (Fig. 9).

Fig. 9 Unity power factor in any operating conditions



6 Conclusion

The regenerative AC drive system based on the PMSM is presented in this paper. A complete methodology of the control design of the back to back power converter is delivered. The proposed topology assures power quality performances for the front end power rectifier; the numerical simulation results show a unity power factor operation in any dynamic regimes. Moreover, during the regeneration, the load current decreases, therefore, an increasing efficiency is obtained.

Acknowledgments This work was supported by a grant of the Romanian National Authority for Scientific Research, CNDI-UEFISCDI, and project number PN-II-PT-PCCA-2011-3.2-1680.

References

1. A. Maamoun, Y.M. Alsayed, A. Shaltout, Space-vector PWM inverter feeding a permanent-magnet synchronous motor. *World Acad. Sci., Eng. Technol.* **4**(2010-05-27), 517–521
2. W. Guo, C.-W. Zhang, Fuzzy PI speed controller optimal design for PMSM drives, advances in computer, communication, control and automation. *Lect. Notes Electr. Eng.* **121**, 565–571 (2012)
3. M.T. Elsayed, O.A. Mahgoub, S.A. Zaid, Simulation study of Conventional Control versus MTPA-Based for PMSM Control, in *Proceedings of the 14th international middle east power systems conference (MEPCON'10)*, Cairo University, Egypt, 19–21 Dec 2010
4. M. Gaiceanu, G. Fetecau, Grid connected wind turbine-fuel cell power system having power quality issues, EPQU'07 Barcelona, pp. 7–13, 2007. ISBN 978-84-690-9441-9
5. S.N. Vukosavic, Mathematical model of synchronous machine. *Electr. Mach. Power Electron. Power Syst.* **2013**, 545–569 (2012)

CFD Analysis of Supersonic Ejectors Operating with Mixture of Gases

Maziar Shafaee, Mohsen Tavakol and Rouzbeh Riazi

Abstract The purpose of this paper is to evaluate the performance of the ejector using two different streams of fluids. To investigate the ejector performance, different operating conditions were applied to ejector. The value of motive and suction pressure were considered to be constant while discharge pressure of ejector was changed continuously. Motive flow was considered to be saturated steam while Suction flow is composed of air and steam. In this mixture, the mass fraction of air and steam changed in the range of 0–1. Ejector performance curves are extracted for different mass fractions of air and steam. The resulted performance curves indicate that the variation of mass fraction of species that were present in the suction flow mixture had significant effect on the performance of ejector. Results showed that as the mass fraction of air in suction flow was increased, the ejector entertainment ratio was increased as well. Also can observed that the variation of mass fraction of suction flow don't have significant effect on break point of ejector performance curves.

1 Introduction

Ejectors are attractive because of their widespread use along with their simplicity. Ejectors operate with compressible or incompressible fluids, and have many applications in various disciplines such as refrigeration, aerospace, water desalination and petroleum industries [1]. In water desalination industry, the ejectors are used to compress the vapor, which is known as Thermal Vapor Compressing (TVC) process. One of the particular applications of the TVC is in Multi-Effect Desalination (MED) units. The low pressure steam during the desalination operation is accumulated in the last stage of evaporators. The main purpose of using the

M. Shafaee (✉) · M. Tavakol · R. Riazi

Faculty of New Science and Technologies, North Karegar Ave., Tehran, Iran
e-mail: mshafaee@ut.ac.ir

M. Tavakol
e-mail: m.tavakol@ut.ac.ir

TVC in desalination units is to return this redundant steam into the evaporators which have higher pressure levels [2].

Theoretical work on ejectors was started by Keenan and Neumann [3]. Their studies led to the first analytical model of ejectors. Constant-area mixing model and constant-pressure mixing model, proposed by Keenan, provided a proper framework for ejector studies. Because of the immense complexities of flow in ejectors, analytical models are not capable of providing sufficient information about the processes happening in the ejector. In 1974, Hedges and Hill [4] were the first to benefit from the results of CFD studies regarding the simulation of flow in the ejectors. They developed a finite-difference scheme for simulation of flow in the ejectors. Sriveerakul et al. [5] used fluent CFD software to simulate the flow inside a steam ejector. They validated their numerical results with the experimental test data. In their research, steam was used as the working fluid with the assumptions of perfect gas and isentropic flow in the ejector. Hemidi et al. [6] used different turbulence models to predict ejector entrainment ratio. Simulation results of different turbulence models, with consideration of the experimental data, were also compared with each other to specify the more accurate models. In their investigation, deviation from experimental data was less than 10 % for the $k-\epsilon$ model, whereas this deviation was increased for the $k-\omega$ -sst turbulence model.

Yang et al. [7] compared the results regarding the three models of Standard, RNG and Realizable k -epsilon with the experimental data of Sriveerakul et al. [5], and stated that the realizable k -epsilon model demonstrated more accurate results compared with the experimental data.

Chen et al. [8] mentioned that regarding the ejectors used in refrigeration systems, one of the key parameters of performance is working fluid. The choice of the appropriate working fluid plays an important role on the design of ejectors.

2 Operating Principles of Steam Ejectors

2.1 Ejector Unit

A typical ejector is composed of two main compartments, one converging-diverging nozzle (primary nozzle) that is surrounded by another that named casing. As shown in Fig. 1, exterior nozzle includes three sections, a mixing chamber, a throat and a diffuser. The primary flow (motive flow) coming from the boiler, enters the ejector at high temperature and high pressure. Since the primary nozzle is a converging-diverging one, static pressure of motive flow converts into velocity and then accelerates by expanding through the nozzle to supersonic velocity. This supersonic speed causes strong shear layers between high velocity flow and surroundings. On the other hand, a very low pressure region forms at the Nozzle Exit Plane (NXP) and, consequently, in the mixing chamber. These two phenomena cause suction of the “secondary fluid” into the mixing chamber. The motive flow

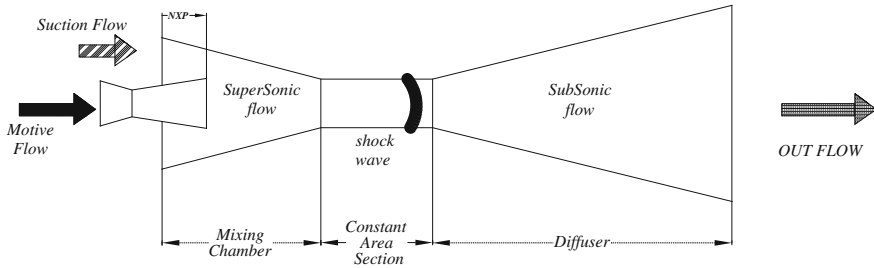


Fig. 1 Schematic of a conventional ejector

expands and forms a converging duct, and the secondary flow accelerates in the duct until it reaches $M = 1$ (i.e., double choked flow). The mixing process is considered to start at this location. By the end of the mixing chamber, the two streams are completely mixed. In an ideal case, due to the high pressure at the diffuser exit, a shock wave takes place somewhere between the end of the constant area section and the beginning of the diffuser. This causes a major compression flow. The mixed fluid leaves the subsonic diffuser at a middle pressure between the primary and secondary flow pressures.

2.2 Ejector Performance

The Entrainment Ratio (ER) and Compression Ratio (CR) are two main characteristics of each ejector used to evaluate the ejector performance. The former is non-dimensional mass flow rate, and the latter is non-dimensional pressure. These two parameters are defined as Eqs. (1) and (2). In Eqs. (1) and (2) \dot{m}_{mot} and \dot{m}_{suc} are the primary and secondary mass flow rates respectively. The terms (p_{dis}) and (p_{suc}) are pressure values at the discharge and the suction boundaries, respectively.

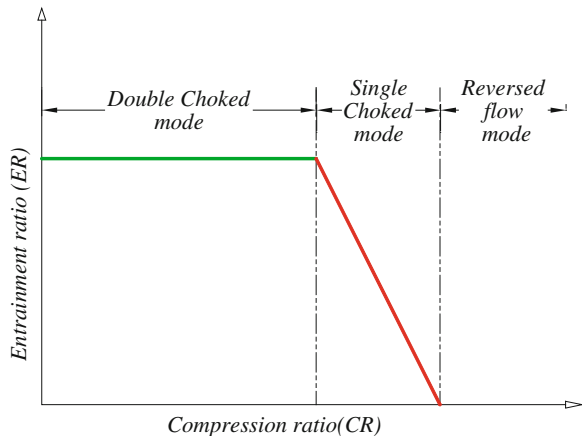
$$ER = \frac{\dot{m}_{suc}}{\dot{m}_{mot}} \quad (1)$$

$$CR = \frac{p_{dis}}{p_{suc}} \quad (2)$$

Figure 2 describes the effect of (CR) on (ER), whereas 3 regions are recognizable in this figure: the double choked flow, the single choked flow and the reversed flow regions. If backpressure (p_{dis}) is less than the critical pressure (p_{dis}^*) , (ER) remains constant because of choking of the secondary fluid in the aerodynamic throat (double-choked flow).

Increase of the back pressure beyond the critical pressure (p_{dis}^*) , causes the secondary fluid not to reach $(M = 1)$, and it remains un-choked (only the primary

Fig. 2 Ejector performance curve



stream is choked in the primary nozzle, i.e. flow is single choked). A sudden drop of secondary mass flow rate is realizable in this mode. A further increase in ejector back pressure causes the flow to return back into the ejector and the suction chamber. This operational condition is known as the reverse flow mode.

3 Model Descriptions

3.1 Numerical Procedure

Commercial CFD software (Fluent 6.3) is utilized to study the flow behavior within an ejector in steady state condition. For all equations, convective terms are discretized using a second-order upwind scheme. The fluid flow inside the ejector is considered to be axisymmetric [9]. The boundary conditions for inlet and outlet of flow are considered as pressure-type. Since the flow in ejector is in high speed condition, the heat transfer across the walls was assumed to be negligible. The realizable k-epsilon model is selected to calculate turbulence effect in ejector flow field. To calculate flow near the wall, a logarithmic function, “standard wall function”, is used.

Since two different gases are assumed as the working flow in this study (i.e., pure air and water vapor), conservation equations for the above-mentioned gas species were solved using (3), (4).

$$\sum_{i=1}^N (mf) = 1 \quad (3)$$

$$mf = \frac{m_i}{m_{tot}} \quad (4)$$

In these equations, (mf) is the mass fraction of each species present in working flow and N is the total number of species.

3.2 Working Fluid Properties

Air and steam are used as working fluids with the assumption of ideal gas behavior to relate pressure to density. This assumption may cause some deviations from the experimental results. However, the result is still accurate because the effects of this assumption on the overall characteristic parameters are lower than 5 % for motive flow and 2.3 % for suction flow as reported by Cardemil and Colle [10].

3.3 Ejector Geometry

The ejector geometry was selected based on the experimental work of Sriveerakul [5]. The following specification (Table 1) was considered as the geometrical parameters of ejector in this study.

3.4 Validation of CFD Results

The experimental data in the study of Sriveerakul et al. [5] is used to validate the CFD results. The ejector used in their experiment [5] is modeled under the same operating conditions. The simulation incorporates vapor stream as motive fluid the comparison of results reveals that the numerical modeling accurately simulates different operating conditions.

4 Results and Discussion

After initial validation, the analysis was extended to the condition where the secondary inlet stream would include both the air and steam. Figure 3 shows the distribution of air and steam in ejector for the case where steam is considered as

Table 1 Ejector geometrical parameters [5]

Ejector's geometry	Dimension (mm)
Throat length (L)	95
Primary nozzle throat	2
Primary nozzle exit diameter	8
Mixing chamber inlet diameter (Z)	24

motive fluid and pure air would be as the secondary fluid. In this figure, blue regions correspond to water vapor and red color indicates presence of air stream.

As can be seen in the Fig. 3, the mixing of two fluids starts at the converging-diverging nozzle exit plane, and the mixture becomes uniform at the end of the constant area section. Along the center line of ejector, a supersonic core can be observed. This core is composed of pure water vapor. Gradually the supersonic core is broken up and water vapor is mixed with surrounding air. At last a homogeneous mixture of air and vapor leave ejector.

Numerical simulation was carried out for operating condition of (360 kPa) for motive pressure and (1.2 kPa) for suction pressure. To obtain the ejector performance in this operating condition; the outlet pressure is continuously reduced. Then, the mass fraction of air at suction inlet is varied in the range of 0–1, and thereby the effect of air suction is investigated. The resulting performance curve is shown in Fig. 4.

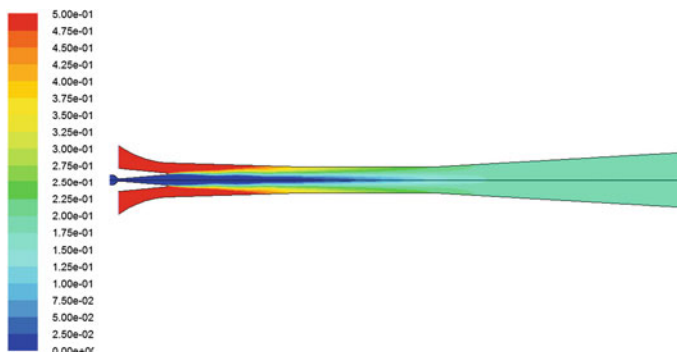
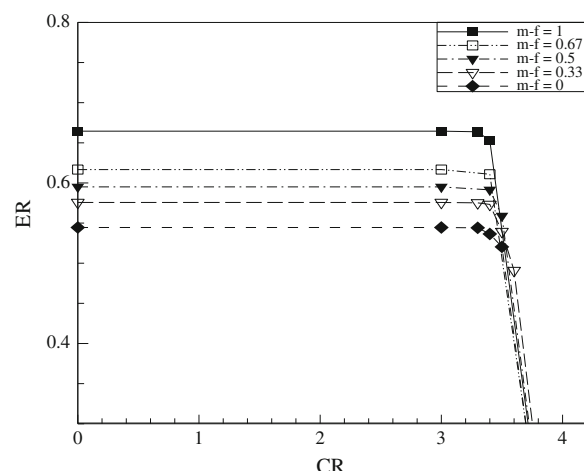


Fig. 3 Species contour for air mass fraction of (0.5)

Fig. 4 Ejector performance curve for low pressure motive flow



As can be seen in Fig. 4, the ejector performance is constantly changing by variation in mass fraction of air in a specific operating condition. For all levels of motive flow, as the mass fraction of air in suction flow is increased, the ejector entrainment ratio increases as well.

5 Conclusions

This paper mainly deals with the aspect of ejector functions which have received little attention so far. In this regard, the ejector performance was numerically studied under the condition of two different gas streams with variable mass fractions. With the convenience of numerical simulation, various conditions for two perfect gas streams of air and steam were investigated. Initially, the numerical solution is carried out for the ejector used pure steam as working fluid of motive and suction flow. After the validation of initial case with experimental data, suction flow changed from pure steam to a mixture of steam and air. By considering all feasible variations of mass fraction of air and steam in the mixture by the range of zero to one, the ejector performance is analyzed. Results indicated that the mass fraction of air had obvious impact on the Entrainment Ratio (ER) of ejector. Also can be concluded that the break point of ejector performance curve, don't influenced by variations of mass fraction of species that are present in suction flow.

References

1. D.W. Sun, I.W. Eames, Recent developments in the design theories and applications of ejectors—a review. *J. Inst. Energy* **68**, 65–79 (1995)
2. N. Sharifi, M. Boroomand, An investigation of thermo-compressor design by analysis and experiment: part 1 validation of the numerical method. *Energy Convers. Manag.* **69**, 217–227 (2013)
3. J.H. Keenan, E.P. Neumann, A simple air ejector. *J. Appl. Mech., Trans. ASME* **64**, A75–A81 (1942)
4. K.R. Hedges, P.G. Hill, Compressible flow ejectors Part I—development of a finite-difference flow model. *J. Fluids Eng., Trans. ASME* **96**, 272–281 (1974)
5. T. Sriveerakul, S. Aphornratana, K. Chunnanond, Performance prediction of steam ejector using computational fluid dynamics: part 1, validation of the CFD results. *Int. J. Therm. Sci.* **46**, 812–822 (2007)
6. A. Hemidi, F. Henry, S. Leclaire, J.M. Seynhaeve, Y. Bartosiewicz, CFD analysis of a supersonic air ejector. Part I: experimental validation of single phase and two-phase operation, *applied thermal engineering* **29**, 1523–1531 (2009)
7. X. Yang, X. Long, X. Yao, Numerical investigation on the mixing process in a steam ejector with different nozzle structures. *Int. J. Therm. Sci.* **56**, 95–106 (2012)
8. X. Chen, S. Omer, M. Worall, S. Riffat, Recent developments in ejector refrigeration technologies. *Renew. Sustain. Energy Rev.* **19**, 629–651 (2013)

9. K. Pianthong, W. Sheehanam, M. Behnia, T. Sriveerakul, S. Aphornratana, Investigation and improvement of ejector refrigeration system using computational fluid dynamics technique. *Energy Convers. Manag.* **48**, 2556–2564 (2007)
10. J.M. Cardemil, S. Colle, A general model for evaluation of vapor ejectors performance for application in refrigeration. *Energy Convers. Manag.* **64**, 79–86 (2012)

Integrated Energy-Efficient Hydrogen Production from Low Rank Coal and Its Storage for Transportation

Muhammad Aziz, Takuya Oda, Takumi Kurokawa
and Takao Kashiwagi

Abstract An integrated system for hydrogen production from low rank coal and its storage is developed based on exergy recovery and process integration technologies to achieve high total energy efficiency. The integrated system consists of drying, gasification, chemical looping, and hydrogenation. In term of energy analysis, exergy recovery technology basically recirculates the energy/heat involved in a single process minimizing the exergy destruction in the process. Unfortunately, not all of the energy/heat involved in a single process can be recirculated thoroughly. Hence, a combination with process integration is performed to enhance the minimization of exergy destruction in the overall integrated system. In this study, the energy efficiency is evaluated. The proposed integrated system shows a very high energy efficiency during conversion of low rank coal to hydrogen which is ready for transportation.

1 Introduction

Hydrogen is considered as secondary energy source suitable to store the energy due to its advantages: cleanliness, abundance, high versatility and efficiency, high variety of fuels and production technologies, etc. [1, 2]. Hydrogen has high flexibility in wide applications including reciprocating combustion engine, fuel cells, and combustion for combined cycle system. Unfortunately, utilization of hydrogen still faces some challenging problems which are needed to be tackled down including its production, storage and transportation [3, 4]. Currently, hydrogen is produced from natural gas (close to 50 %), oil reforming (about 30 %), coal gasification (18 %), water electrolysis (3.9 %), etc. [3]. The trend of decarbonization of fossil fuels also increases due to environmental concern [5]. Among the

M. Aziz (✉) · T. Oda · T. Kurokawa · T. Kashiwagi
Solutions Research Laboratory, Tokyo Institute of Technology, Tokyo 152-8550, Japan
e-mail: maziz@ssr.titech.ac.jp

available fossil fuels, low rank coal (LRC) has relatively larger reserve compared to other fossil fuels including oil and natural gas.

LRC is advantageous due to its low mining cost, low sulfur content, high volatile matter, etc. Unfortunately, it is also disadvantageous because of relatively low calorific value, high moisture content, high risk of spontaneous combustion, and high moisture re-adsorption [6, 7]. These lead to some difficulties during its storage, transportation and utilization. Recently, the trend to convert and decarbonize LRC to secondary energy resources, including hydrogen, increases. The conversion of LRC to hydrogen is considered as one of the best option to utilize LRC effectively in terms of storage, transportation and environment. Currently, hydrogen production from coal is considered as the most economical way until other resources including renewable energy can produce it with lower price.

Unfortunately, hydrogen has problem in its storage and transportation. Although it has high energy density by weight (33 kWh per 1 kg of hydrogen), it is poor in energy density by volume compared to hydrocarbons (3 Wh per 1 l of gaseous hydrogen). Among the available hydrogen storage, liquid organic hydrogen carrier (LOHC) seems promising due to its high safety, reversibility, higher storage capacity, and longer storage time [8]. In LOHC, the hydrogen stored not in its molecular form, but it is covalently bound to LOHC through hydrogenation. Among various LOHC, toluene (C_7H_8)–methylcyclohexane (MCH, C_7H_{14}) cycle is considered as one of the well-established and promising hydrogen carrier as they are inexpensive, stable, and easy to storage and transport. Furthermore, a successful large-scale demonstration test has been conducted in Japan by Chiyoda Corp. [9].

Some studies on hydrogen production from LRC can be found in the literatures including their integration. For example, Minutillo and Perna [10] have proposed an integrated system covering coal hydrogasification, power generation, and electrolysis to produce synthetic natural gas storage. Unfortunately, the integrated system was designed based on simple process integration, hence, the overall integrated system still generates large amount of exergy destruction. To the best knowledge of the authors, no study concerns about the total integration of LRC conversion to hydrogen including drying, gasification, chemical looping, and storage in LOHC with very minimum total exergy destruction. Hence, the objective of this study is proposing an integrated energy-efficient hydrogen production and its storage from LRC with minimum exergy destruction.

2 Proposed Integrated System and Calculation

To achieve high overall energy efficiency, an integrated system for hydrogen production from LRC and its storage was developed employing the principles of exergy recovery and process integration. The integrated system consists of some modules: drying, gasification, chemical looping, and hydrogenation. The combination of exergy recovery and process integration technologies is adopted with the objective of exergy destruction minimization throughout the integrated system.

Figure 1 shows the basic principles of exergy recovery technology. The exergy recovery is conducted in each single process through exergy elevation and heat coupling to recirculate efficiently the energy/heat involved in a process. The exergy of cold stream is initially elevated to facilitate an effective heat coupling among hot and cold streams. Furthermore, an effective heat coupling among hot and cold streams is performed in consideration of heat type and amount to achieve the largest amount of heat exchange. The amount of exergy elevation depends strongly to the performance of heat coupling. This exergy recovery concept is significantly different to conventional energy/heat recovery technology without which only recovers a small part of energy/heat because of unequal amount and type.

Figure 2 shows the basic process flow diagram of the integrated system of hydrogen production from LRC and its storage. In this study, to evaluate the effect of the exergy recovery and process integration applied in each process in terms of energy efficiency, the overall system is divided into three main modules: drying and gasification, chemical looping, and hydrogenation. Figure 3 shows the developed three modules based on exergy recovery.

The as-mined LRC flows initially to drying module for moisture removal as well as increasing its calorific value. A fluidized bed dryer is adopted as the evaporator. Compressor is utilized to elevate the exergy rate of the evaporated steam to

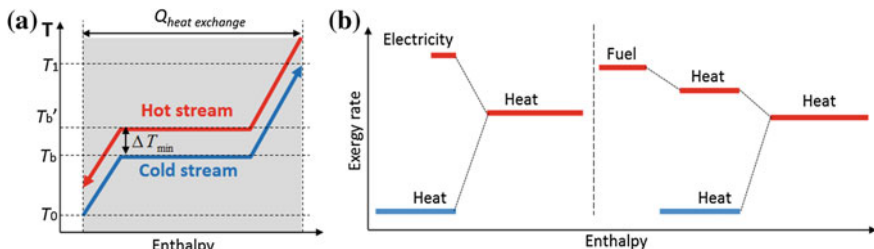


Fig. 1 Principle of exergy recovery technology: **a** exergy elevation and heat coupling to minimize the exergy destruction, **b** two examples of the way to elevate the exergy of the stream

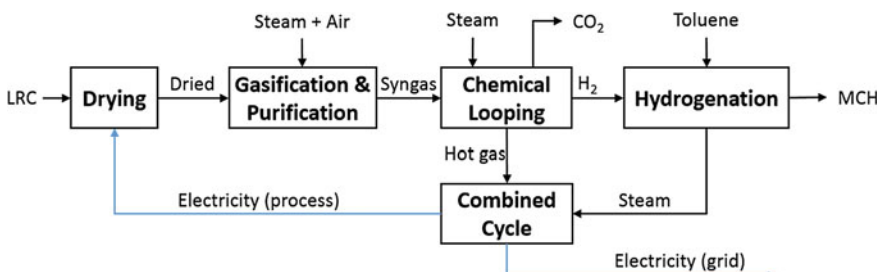


Fig. 2 Basic process flow diagram of proposed integrated-system for hydrogen production from LRC and its storage

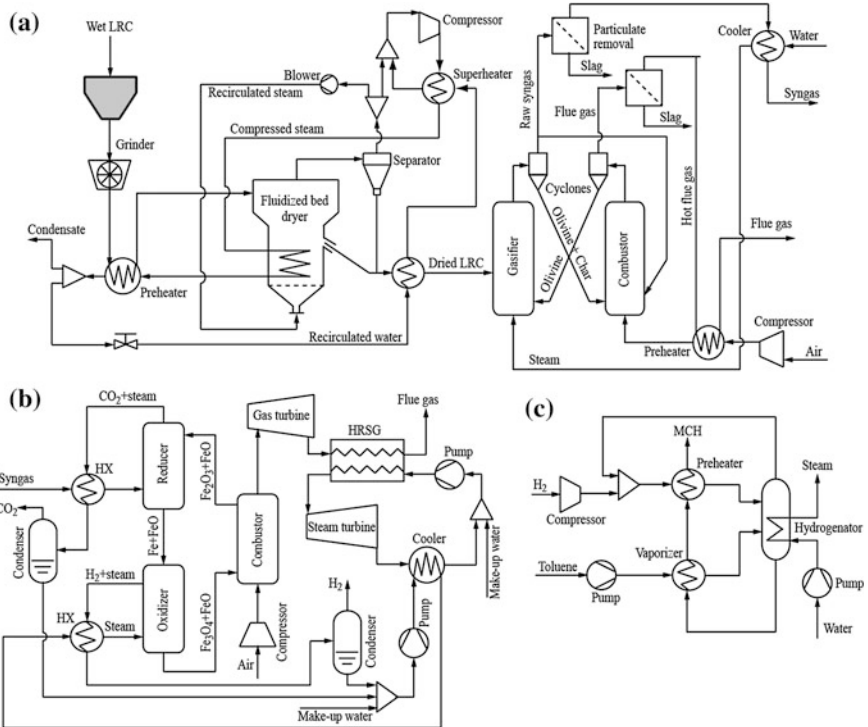
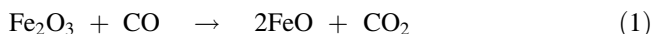
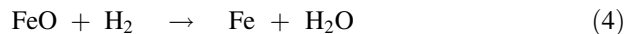


Fig. 3 Developed modules based on exergy recovery and process integration: **a** drying and gasification module, **b** chemical looping module, and **c** hydrogenation module

facilitate effective heat recirculation. The dried LRC flows to the gasification module for conversion to syngas which subsequently will be cleaned to earn pure syngas. A dual circulating fluidized bed type of gasifier is adopted due to its higher carbon conversion efficiency and conversion rate. The hot dried LRC is fed directly to the first reactor where the pyrolysis and gasification take place at certain temperature. The unreacted char leaves together with inert material (olivine, silica sand, etc.) to the second reactor for combustion. Furthermore, the inert material will be recirculated back to the first reactor transporting the heat earned in char combustion to provide the required heat for pyrolysis and gasification.

The cleaned syngas then flows to the chemical looping module consisting of three main reactors: reducer, oxidizer, and combustor. Initially, the following reactions occur inside the reducer which usually operates under 750–900 °C.





CO_2 is leaving the reducer which further cooled down and compressed for sequestration. The remainders are going to oxidizer where the oxidation reactions occur producing high purity hydrogen. The reaction is endothermic with operating temperature of 500–750 °C. The following reactions occur inside the oxidizer



Finally, the remaining gases is flowing to the combustor to oxidize the Fe_3O_4 to become Fe_2O_6 , as well as providing the heat for reduction process. The following reaction occurs in the combustor.



As the reaction in combustor is exothermic, a relatively high temperature hot gas is exhausted ($T > 1000$ °C, $P > 2.5$ MPa) which can be utilized for power generation employing combined cycle. On the other hand, the produced H_2 is fed to hydrogenation to react with toluene producing MCH. As the reaction is exothermic, the produced heat is recovered for steam generation as the additional steam for steam turbine. The theoretical gravimetric and volumetric hydrogen contents of MCH are 6.2 and 47 %, respectively. The hydrogenation reaction occurs as follows:



Table 1 shows the properties of used LRC and produced syngas from gasification. Process calculation is conducted using a steady-state process simulator ProII ver. 9.2 (Invensys Corp.). The minimum temperature approach in heat exchangers is 10 °C. In addition, heat loss is neglected and the materials flow in plug flow mode.

Table 1 Properties of LRC and produced syngas from gasification

Component	Value
Ultimate analysis (wt%)	C: 65.53; H: 3.75; N: 0.84; O: 25.22; S: 0.38; Cl: 0.05; Ash: 4.23
Proximate analysis (wt%)	Moisture: 50; Volatile matter: 25.9; Fixed carbon: 24.1
LCR heating value (MJ kg^{-1})	24.31
Produced syngas ($\text{Nm}^3 \text{kg}_{\text{fuel-daf}}^{-1}$)	H_2 : 0.820; CO: 0.486; CO_2 : 0.255; CH_4 : 0.063; C_2H_4 : 0.011; C_2H_6 : 0.001

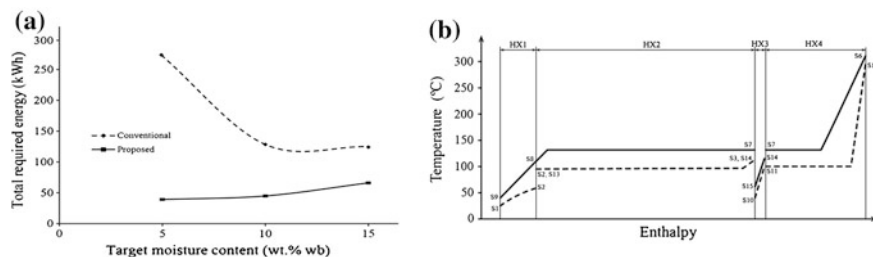


Fig. 4 **a** Total energy consumption of proposed and conventional drying processes (flow rate 100 t h^{-1}), **b** T-H diagram of the proposed drying module (target moisture content 10 wt% wb)

3 Results and Discussion

As a preliminary study, the performance of developed drying module is evaluated in term of energy efficiency. The comparison to the drying process employing conventional heat recovery technology has been performed. Figure 4 shows the total energy consumption of proposed drying module to the conventional drying with heat recovery in different target moisture content. The proposed drying module shows significant lower energy consumption (higher energy efficiency) up to 1/6. Furthermore, from T-H diagram it is clear that almost the heat can be recovered effectively leading to small exergy destruction (hot and cold streams are almost parallel to each other). It is believed that the application of exergy recovery and process integration technologies can improve the energy efficiency of overall integrated system for hydrogen production and its storage.

Acknowledgments This research is conducted under collaboration research project with Mitsubishi Corporation, Japan. Funding for this research was partly provided by Mitsubishi Corporation, Japan.

References

1. T.N. Veziroglu, S. Sahin, 21st Century's energy: hydrogen energy system. *Energy Convers. Manage.* **49**, 1820–1831 (2008)
2. R. Chaubey, S. Sahu, O.O. James, S. Maity, A review on development of industrial processes and emerging techniques for production of hydrogen from renewable and sustainable sources. *Renew. Sustain. Energy Rev.* **23**, 443–462 (2013)
3. I. Dincer, Green methods for hydrogen production. *Int. J. Hydrogen Energy* **37**, 1954–1971 (2012)
4. M.F. Orhan, I. Dincer, M.A. Rosen, M. Kanoglu, Integrated hydrogen production options based on renewable and nuclear energy sources. *Renew. Sustain. Energy Rev.* **16**, 6059–6082 (2012)
5. S. Dunn, Hydrogen futures: toward a sustainable energy system. *Int. J. Hydrogen Energy* **27**, 235–264 (2002)

6. M. Aziz, Y. Kansha, A. Tsutsumi, Self-heat recuperative fluidized bed drying of brown coal. *Chem. Eng. Process.* **50**, 944–951 (2011)
7. M. Aziz, T. Oda, T. Kashiwagi, Energy-efficient low rank coal drying based on enhanced vapor recompression technology. *Drying Technol.* **32**, 1621–1631 (2014)
8. D. Teichmann, W. Arlt, P. Wasserscheid, Liquid organic hydrogen carriers as an efficient vector for the transport and storage of renewable energy. *Int. J. Hydrogen Energy* **37**, 18118–18132 (2012)
9. Y. Okada, M. Shimura, Development of large-scale H₂ storage and transportation technology with liquid organic hydrogen carrier (LOHC), in *The 21st Joint GCC-Japan Environment Symposium*, Doha, Qatar, 5–6 Feb 2013
10. A. Minutillo, A. Perna, Renewable energy storage system via coal hydrogasification with co-production of electricity and synthetic natural gas. *Int. J. Hydrogen Energy* **39**, 5793–5803 (2014)

Ignition of Combustible Gases in Water

Vyacheslav Teslenko, Alexey Drozhzhin, Ruslan Medvedev
and Igor Batraev

Abstract The possibilities of reducing the energy consumption in transformation of chemical energy into heat and mechanical ones due to fundamental change of technologies of fuel combustion are considered by using the methods of combustion of gases being under development.

1 Introduction

The method of gas combustion directly in water with separate supply of combustible gas and oxidizer by using linear slot injectors for direct heating of heat carrier was realized in [1, 2]. A separate method of injection is necessary primarily for safety. The mixture of combustible gases in water was formed by injection of two bubbles (combustible gas and oxygen) in a dynamical regime in the form of quasi-cylindrical bubble. Cyclic regimes of combustion of acetylene, hydrogen, and propane are performed with frequency up to 2.5 Hz.

This work deals with the possibilities to apply the methods of pulse combustion of hydrocarbons and hydrogen in water to develop technologies of direct transformation of chemical energy of hydrocarbons into kinetic energy of the body immersed into a liquid (open system). This will make it possible to avoid losses

V. Teslenko (✉) · A. Drozhzhin · R. Medvedev · I. Batraev
Lavrentyev Institute of Hydrodynamics SB RAS, Novosibirsk, Russia
e-mail: teslenko@hydro.nsc.ru

A. Drozhzhin
e-mail: drozh@hydro.nsc.ru

R. Medvedev
e-mail: ruslan@hydro.nsc.ru

I. Batraev
e-mail: ibatraev@gmail.com

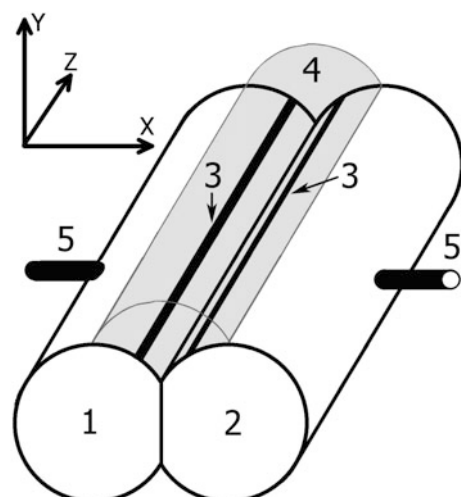
during the momentum transfer from engine to the mover. Moreover, the development of pulsing movers based on the combustion of hydrocarbons on the thrust wall directly in water is in the planning stage.

2 Experimental Set-Up

The scheme of device is presented in Fig. 1. In cylinders 1 and 2 the slots 3 were cut. Each slot is 70 mm long and 0.2 mm wide. Oxygen was injected from one slot and combustible gas was injected from another one. Gases were supplied to the slots through inlet tubes 5. The flow rate of gases was controlled by changing the cross-sectional area of nozzles and time of opening the valves (gas injection time) mounted in gas-supply system. During the process of injection of gases from slots, two quasi-cylindrical bubbles were formed. Then coalescence with mixing of supplied gases and forming of one bubble 4 took place (in Fig. 1, it is shown in grey color). Near the slots of cylinders 1 and 2, isolated conductors were mounted. Between the ends of conductors, a spark discharge was generated. A spark discharge initiated combustion inside the bubble 4. The combustion of mixture in a bubble was performed with specified time intervals from the moment of gas supply commencement.

The investigations of hydrodynamic processes in separate supply of two gases through the slot injectors were performed in Plexiglas cuvette with dimensions of $280 \times 280 \times 500$ mm. Calorimetric investigations were carried out in five-liter polycarbonate bottle. The time of gas supply through tubes 5 varied in the intervals 3, 5, and 8 ms. The initiation of combustible mixture in bubbles was performed by a spark discharge with energy up to 4 J. The delay time of mixture combustion after

Fig. 1 The scheme of linear-slot injector for gas combustion in water in separate supply of gases into water. 1, 2 Copper cylinders; 3 slots; 4 quasi-cylindrical bubble with combustible mixture (it is shown in grey color); 5 tubes for separate gas supply



gas supply commencement was 10, 15, 18, 20, 25, 30, 35, 40 ms. The moment of opening the gas valves was taken as the origin of time.

This work presents the results for lean hydrogen-oxygen ratio and rich ratios of acetylene and propane with oxygen. In all cases the deviation of stoichiometric compositions was so that it had no influence on the stability of combustion.

All necessary parameters, including flow rate, cyclicity of supply of gas and spark discharges and time between them were specified by using the automated system of multifunctional pulse detonation system CCDS-2000 developed in Lavrentyev Institute of Hydrodynamics SB RAS. Figure 2 demonstrates a principal scheme of the set-up with functions of automated gas supply through a slot injector.

For more detailed investigations of hydrodynamic processes in combustion of gases in water, the experiments were performed with gases mixed beforehand. The bubble was placed in horizontal plane into cylindrical (30–70 mm long) or circular (30–60 mm in diameter) groove on the metal wall that correspond to the scheme shown in Fig. 1 if the set-up is turned through 180°. Initiation of combustible mixture in bubbles was performed by a spark discharge of energy up to 4 J.

A high-speed record of gas combustion in bubbles and dynamics of expansion of bubbles after gas mixture combustion was taken. The record was taken in both front and sidewise projections. Measurements of force pulses $F(t)$ acting on the wall were made synchronously. Registration of force pulses on the wall was carried out with digital oscilloscope TDS-210 by using lead-zirconate-titanate piezometers (with diameter of 40 mm and height 15 mm) and emitter follower with constant time component $\theta \approx 10$ s.

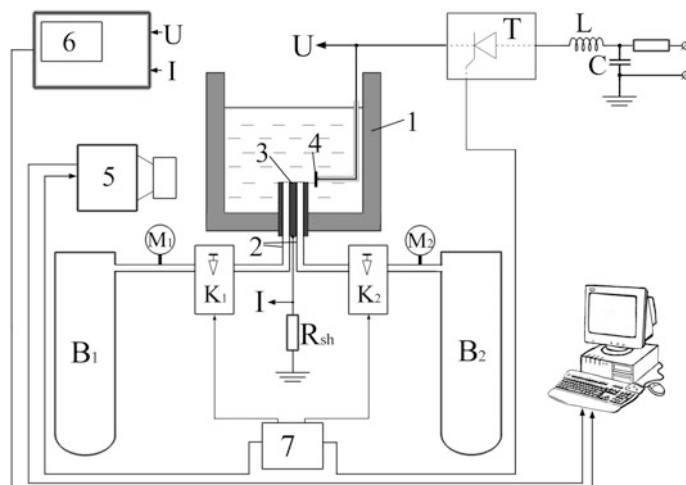


Fig. 2 Principal scheme of the experimental set-up: 1 Plexiglas or polycarbonate cuvette; 2 inlet gas tubes; 3 injection device for combustion of gas fuels in water (Fig. 1); 4 electrode for initiation of combustion; 5 high-speed video camera; 6 oscilloscope; 7 control panel; B_1 , B_2 gas bottles; M_1 , M_2 manometers; K_1 , K_2 valves of speed gas supply into water; T electronic switchboard

3 Experimental Results

Figure 3 presents the example of shadow recording of the processes of injection and dynamic mixing of gases in water, initiation and expansion of quasi-cylindrical bubble. The record is taken along Z-axis (Fig. 1).

Figure 3 clearly demonstrates that it is necessary to divide formally the process of cyclic gas combustion in water into 3 main stages:

- (1) injecting gases into water until the bubble becomes of required size with specified gas proportion;
- (2) initiation of gas combustion in a bubble with specified delay;
- (3) expansion of the bubble after gas combustion with subsequent pulsations and disintegration.

According to results of high-speed recordings of hydrodynamic processes, the velocity of propagation of light fronts was estimated. In the case of acetylene and oxygen injection into water (injection time is 3 ms, initiation time is in 15 ms), visible velocity of light fronts was within the interval of 200–400 m/s. For propane, visible velocity of light fronts was 60–100 m/s.

Table 1 presents the results of calorimetric measurements of burnt-gas heat transfer in 3 L volume of water for experiments with gas injection time of 8 ms and ignition time at 15 ms. The error of experimental measurements was 8–22 %. The error of gas flow rate was 15 %. The cyclic regime was provided with frequency 2.5 Hz (http://www.swsl.newmail.ru/video/MVI_1779.flv.html). Experiments were carried out in series from 400 up to 1990 combustion cycles.

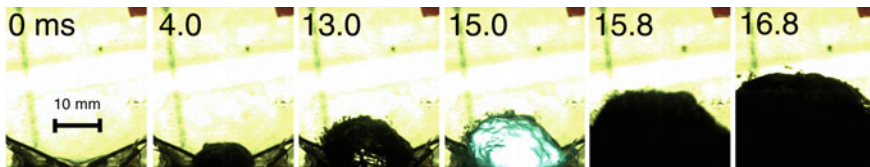


Fig. 3 The example of shadow record of injection, initiation and expansion of quasi-cylindrical bubble. The speed of recording is 5000 frames per second

Table 1 The results of calorimetric measurements of burnt-gas heat transfer in 3 L volume of water for experiments with gas injection time of 8 ms and ignition time at 15 ms

Gas	Heat value of combustible gases (J/cm ³), reference data	Volume of injected combustible gas for one cycle (cm ³)	Volume of injected oxygen for one cycle (cm ³)	Burnt-gas heat transfer in 3 L volume of water (J/cm ³)
Acetylene	56.9	5.1	8	17–25
Hydrogen	10.8	12.6	8	9.3
Propane	93.4	3.55	10.44	21

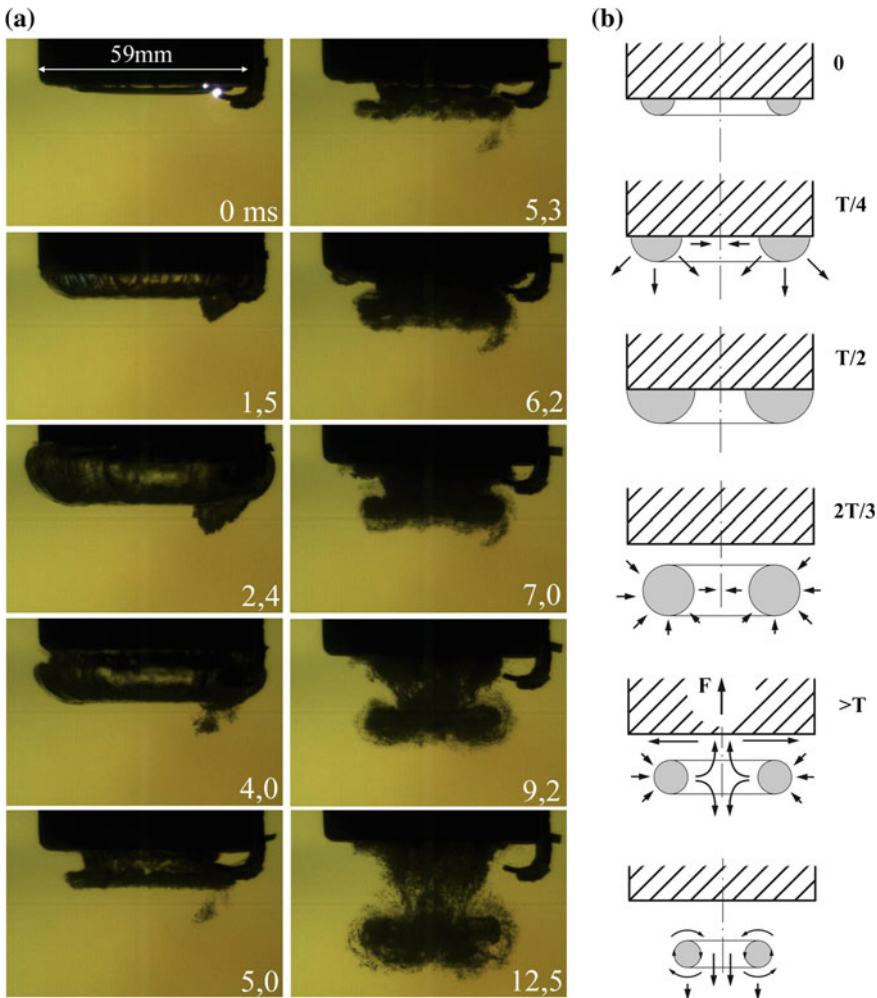
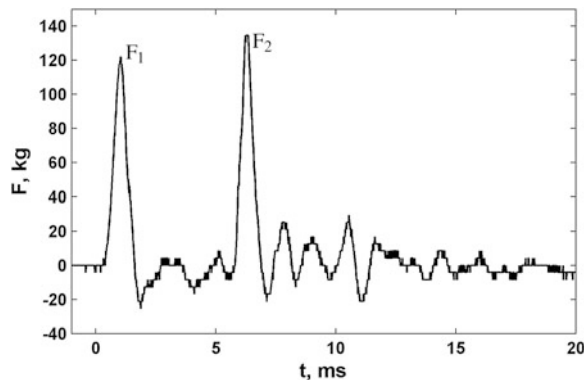


Fig. 4 Frames of shadow recording (a) and corresponding schematic pattern (b) of hydrodynamic processes during the gas combustion in a circular bubble with diameter of 40 mm on the end of the cylinder 59 mm in diameter

Figure 4a presents separate frames of shadow recording of hydrodynamic processes during combustion of stoichiometric propane-oxygen mixture in a circular bubble with diameter of 40 mm and volume 3 cm^3 located on the end of the cylinder 59 mm in diameter. Figure 4b presents corresponding schematic pattern of hydrodynamic processes near the end of the cylinder, where T is the period of bubble pulsation.

It is seen from the experiment that the bubble collapses in the direction to the cylinder axis and forms opposite jet flow along the axis. On the record, at stages

Fig. 5 Oscillogram of pulses of force F caused by bubble expansion and collapse



$t > T$, the liquid flow directed from the cylinder is seen in the form of jet flow forming a circular vortex consisting of small bubbles. The jet that is directed to the cylinder can be found in the form of lateral flowing of bubble sheet over the cylinder end and the motion of cylinder if it is not fixed (Fig. 4a).

Figure 5 shows the oscillogram of pulses of force F acting on the fixed cylinder during combustion of stoichiometric propane-oxygen mixture 2 cm^3 by volume. On this oscillogram, two main pulses are shown. The first pulse (F_1) corresponds to the process of bubble expansion caused by gas combustion and the second pulse (F_2) corresponds to the moment of collapse of the formed bubble. It is seen that the second pulse is commensurable with the first one. Here, $P_1 = \int F_1 dt = 0.077 \text{ kg s}$, $P_2 = \int F_2 dt = 0.075 \text{ kg s}$.

4 Analysis of Experimental Results

Both for dynamic mixing of combustible gas and oxygen [1] and for the mixture made beforehand, visible velocity of combustion front in bubbles did not succeed 400 m/s. Thus, we deal with deflagration mechanism of gas combustion in a bubble.

The observed dynamics of jet flows in a liquid in expanding and pulsing of a bubble near the rigid wall is qualitatively similar to the processes of jet flows described in monograph [3] for cases of bubble pulsations caused by explosions of condensed explosives near the free surface of a liquid. It is necessary to note the following difference taking place in explosions of condensed explosives and those of gases in water: in the second case, the detonation processes of explosion source are absent. Hence, energy redistribution between kinetic energy of liquid caused by gas bubble expansion and shock wave energy will occur in favor of the bubble.

From the results of synchronous registration of hydrodynamic processes and measurements of force acting on the cylinder end it follows that the first pulse corresponds to the process of bubble expansion and the second one corresponds to bubble collapse and forming of two axial flows of liquid bordering to inner

boundary of toroidal bubble. Note that in cases of closing of a toroidal bubble on the axis, the tore becomes an oblate ellipsoid and the process pattern remains unchanged except for that the liquid bordering to the outer perimeter of ex-tore is focused to the axis. This process qualitatively corresponds to cumulation processes.

5 Conclusions

1. It is shown experimentally that combustion of gases in water near the rigid wall makes it possible to transform chemical energy of burnt gas mixture into mechanical energy due to force pulses caused by expansion of gas combustion products in water and bubble collapse. Here, due to forming of axial liquid flows during the bubble collapse near the wall, an additional secondary force pulse commensurable with the first one is provided.
2. By using the considered methods of gas combustion on a rigid wall, it is possible to exclude energy losses in a complex chain of existing technologies of transformation of chemical energy into mechanical one (compression ignition engine, gear reduction, propeller) by changing the methods of combustion of fuels for water movers with direct pulse combustion of gases in water.

Acknowledgments This work is supported by the Russian Foundation for Basic Research (projects Nos. 13-08-00838, 12-08-31087).

References

1. V.S. Teslenko, V.L. Manzhaley, R.N. Medvedev, A.P. Drozhzhin, Burning of hydrocarbon fuels directly in a water-based heat carrier. *Combus. Explos. Shock Waves* **46**(4), 486–489 (2010). <http://www.swsl.newmail.ru/publ/fgv2010.pdf>
2. V.S. Teslenko, A.P. Drozhzhin, V.I. Manzhaley, R.N. Medvedev, V.Y. Ulianitsky, Combustion of gas fuels directly in heat carrier. *Modern Sci.* **10**(2), 64–67 (2012). http://www.swsl.newmail.ru/publ/teslenko_Alushta2012.pdf
3. V.K. Kedrinskii, *Hydrodynamics of Explosion. Experiment and Models* (Springer, Berlin, 2000), 434 p

Method of Assessing Energy Consumption in the Transport of Pallets in Logistics

Pawel Zajac

Abstract The assessment of the energy consumption by the processes in logistic warehouse systems is discussed. The energy consumption problem occurs in many branches of economy. For example, the ODEX indicator has been developed for the power industry in the EU. However, there is no such an indicator for logistic warehouse systems. This paper presents the state-of-the-art in the latter field and the author's own model of determining the energy consumption of servicing a pallet in a warehouse.

1 Introduction

The notion of energy consumption is associated with zero-energy buildings, hybrid vehicles, thermal performance improvement and carbon dioxide emissions, for which CO₂ emission limits (European Union Allowances) are set. Large objects (e.g. buses, lorries), which move at quite high speeds (up to 150 km/h), are readily analyzed since rough calculations show that considerable amounts of energy can be recovered and there is great potential for carbon dioxide emission reduction in such cases [1].

The conditions in warehouses are quite different: first of all, the speed of a load of, e.g., 1500 kg amounts to maximally 15 km/h and the load on a pallet can be a source of a small amount of thermal energy or CO₂ emission.

However, there is one very important reason for taking up this subject: there are hundreds of thousands of such load units.

Having carried out literature surveys based on such electronic publication catalogues as: EBSCO, COMPENDEX, PROQUEST, Baztech and e-Journals [2, 3],

P. Zajac (✉)
Wroclaw University of Technology, 27 Wybrzeze Wyspianskiego St,
50-370 Wroclaw, Poland
e-mail: pawel.zajac@pwr.edu.pl

the author formulated the questions: is there any proper energy consumption for the servicing of a pallet in a warehouse? When is the energy consumption still proper? And at what energy consumption level should one intervene?

2 Model of Energy Consumption Assessment

Figure 1 shows a formal model for assessing the energy consumption of a logistic warehouse system.

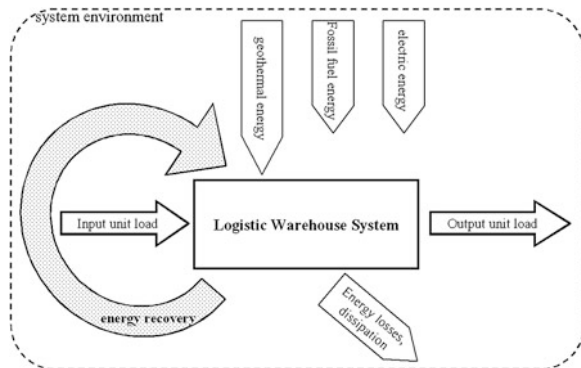
A computing model, consisting of the partial models of the material handling equipment, is presented below. The model is based on the assumption that a load unit received is characterized by a certain energy consumption and that the successive handling-transport and storage processes, in which the unit is transferred in the logistic warehouse system owing to the energy supplied to the drives of the servicing equipment, add up to a change in the energy consumption of the passage through the logistic warehouse system [4].

It is assumed that the energy is equal to the work which needs to be performed in order to relocate the pallet:

$$E_E = E_P + E_S + E_Z + E_C + E_W \quad (1)$$

where: E_P is the energy needed to lift the pallet, E_S —the energy used up by the lifting of the empty fork carriage, E_Z —the energy needed to transport the pallet, E_C —the energy needed for the travel of the forklift truck without load, E_W —the energy used up by the forking processes. The potential energy is calculated from the generally known relation for potential energy while the kinetic energy is determined on the basis of the driving characteristics of the conveyors and the vehicles.

Fig. 1 Model of logistic warehouse system energy consumption



Since no equation for forklift truck motion could be found in the literature on the subject, it was derived for the purposes of this study. The equation is as follows:

$$F = m \cdot a + m \cdot g \cdot \mu \quad (2)$$

where $\mu = f(\text{mat1}, \text{mat2})$, and so one can write relation (3).

$$F(V) = m \cdot a + W_t \quad (3)$$

where: $m \cdot a$ are forces of inertia, $W_t = f_t \cdot Q$ —resistances to motion, f_t —a coefficient of rolling resistance, $F(V)$ —a driving force. The resistances to motion can be divided into primary and secondary resistances. The former include: rolling resistance, damping in the suspension, toe-in resistance and aerodynamic resistance, while the secondary resistances include: grade resistance, turn resistance, starting resistance and towing resistance. Thus the equation of motion assumes the form:

$$\xi \cdot m \cdot \frac{dV}{dt} + W_{r.coal} = F_N(V) \quad (4)$$

where: ξ is the coefficient of the rotating masses. Then the possibilities of energy recovery and its short-term storage or conversion into other forms of energy are taken into account. The following boundary conditions stem from the organization of equipment work in the warehouse: data on devices 1, 2, ..., m, docks (entry-exit gates for load units) 1, 2, 3, ..., s and storage places (rack slot/intermediate storage area) 1, 2, 3, ..., k. The warehousing process consists of: the acceptance-into-storage process, storage, groupage and release. The model assumes that groupage is performed on pallet units. Thus the following stages through which the load unit goes from the moment of its positioning near the handling dock, through its storage and release from the warehouse can be distinguished: picking the pallet (i), transporting the pallet (j), putting the pallet on the storage place (l). In special cases, a change of the transporting device takes place between stages i, j, l. Each of the stages is carried out by a device, i.e. the storage of the pallet (the relocation of the load unit in the transport-warehouse system) can be represented by three symbols (i, j, l) and the number of the device carrying out the storage.

Storage consists of the following operations: o_1 —the travel of the empty forklift truck from the stand-by place to the load unit, o_2 —forking, o_3 —the delivery of the pallet to PP_1 , o_4 —the return of the empty forklift truck to M (its stand-by point), o_5 —reloading, o_6 —transport from PP_1 to PP_2 , o_7 —reloading, o_8 —the delivery of the pallet to the rack, o_9 —forking, o_{10} —the return of the empty forklift truck to its stand-by point M. For each of the devices the energy demand in the vertical and in

the horizontal is given and it is written in the form of matrix **ZE** with dimensions $m \times 2$, defined as follows:

$$ZE = \begin{bmatrix} 1 & [ze_{11} \quad ze_{12}] \\ 2 & [ze_{21} \quad ze_{22}] \\ . & [. \quad .] \\ . & [. \quad .] \\ m & [ze_{m1} \quad ze_{m2}] \end{bmatrix} \quad (5)$$

Unloading (bringing the load unit into the warehouse) comprises a set of n pallets situated in a selected dock. For each pallet its mass and warehouse storage address are specified, which is written in transport parameters matrix **PT** with $n \times 5$ dimensions, where

$$PT = \begin{bmatrix} 1 & [pt_{11} \quad pt_{12} \quad pt_{13} \quad pt_{14} \quad pt_{15}] \\ 2 & [pt_{21} \quad \dots \quad \dots \quad . \quad pt_{25}] \\ 3 & [. \quad . \quad . \quad . \quad .] \\ . & [. \quad . \quad . \quad . \quad .] \\ n & [pt_{n1} \quad . \quad . \quad . \quad pt_{n5}] \end{bmatrix} \quad (6)$$

Considering the possible change of the device between stages, an unloading technology should be defined for each pallet (load unit). Then one gets a $m \times m$, matrix comprising three numbers, each of which is a number of the device carrying out the particular unloading stage (i, j, k), e.g. (3, 5, 1). This means that for the given pallet the first stage is carried out by device no. 3, the second stage by device no. 5 and the third stage by device no. 1. The set of the technologies for the whole set of pallets forms matrix **T**:

$$T = \begin{bmatrix} t_{11} & t_{12} & t_{13} \\ t_{21} & t_{22} & t_{23} \\ t_{n1} & t_{n2} & t_{n3} \end{bmatrix} \quad (7)$$

Number 1 in matrix **Z** shows that reloading from a device to device J is possible and is equal to the specific energy consumption by this operation while 0 means that there is no passage.

Having defined technology **T**, one can determine the operating specific energy consumption for each pallet on the basis of $n \times 10$ matrix **O** where an element of this matrix is defined as: $O_{ij} = 1$ —the specific energy consumption for performing operation j of a task and $O_{ij} = 0$ if operation j is not carried out. Matrix **O** is determined on the basis matrices **ZE**, **Z** and **T**.

In order to obtain the energy consumption for each operation, the matrix elements must be adjusted to take into account the distance, the load and the height. Correction coefficients are determined on the basis of matrix **PT**. As a result, matrix **WK** with $n \times 10$ dimensions, defined as a matrix of coefficients correcting the energy consumption for each operation performed on each pallet, is obtained. By performing

the “truncated” (positional) multiplication of matrix WK and matrix O one gets matrix E, whose elements represent the energy consumption for each operation performed on each pallet. The truncated multiplication is defined as follows:

$$WK_{n \times 10} \otimes O_{n \times 10} = E_{n \times 10} \quad (8)$$

where:

$$e_{ij} = WK_{ij} \cdot O_{ij} \quad (9)$$

The total energy consumption is:

$$E_C = \sum_{i=1}^n \sum_{j=1}^{10} e_{ij} \quad (10)$$

The energy of the passage of the load unit through the warehouse can be presented in the form of a map of the energy consumption by the passage of the load unit through the warehouse. The map shows the supplied energy, the consumed energy and the energy recovered in the logistic system, which means that for any logistic warehouse system one can determine the proper energy consumption and magnitude of energy recovery.

For the defined operating conditions of any warehouse in the logistic warehouse system one can determine such equipment operating parameters that the energy consumption by the warehouse will be the lowest. However, there occur such system operation states, e.g. an unforeseen acceptance of goods into the warehouse, when the energy consumption factor is not important.

Then computations verifying the energy consumption assessment model for the system shown in Fig. 2 were performed. The relocation energy consumption by the forklift truck <http://www.jungheinrich.com/en/fork-lift-trucks-at-a-glance/counterbalance-trucks/efg-425425k430430ks30/> amounted to 50625 J.

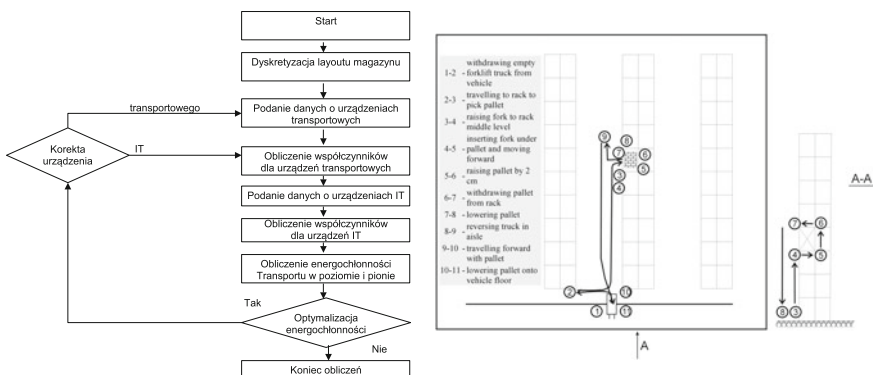


Fig. 2 Exemplary warehouse process

3 Conclusions

The computations have indicated that it is possible to determine the energy consumption by the passage of a pallet through a warehouse. The main conclusions are:

1. The energy consumption by the passage of a load unit through a logistic warehouse system can be determined using the method presented in this paper.
2. For the assumed logistic warehouse system operation criteria the energy consumption model makes it possible to determine such operating parameters of machines and transport-storage equipment at which the energy consumption by the passage of the load unit will be minimal.

The energy consumption of the logistic warehouse system, mentioned in conclusions 1 and 2, is not constant in the whole lifetime of a warehouse system, changing with the degradation of the warehouse machines and equipment.

References

1. Logistics Cost and Service, 2007, Establish, Inc. Herbert W Davis & Company, http://www.establishinc.com/pdfs/2007_CSCMP_Presentation.pdf. Accessed on-line 30 June 2013)
2. P. Zajac, The idea of the model of evaluation of logistics warehouse systems with taking their energy consumption under consideration. *Arch. Civil Mech. Eng.* **11**(2), 479–492 (2011)
3. P. Zajac, in *Production Engineering Innovations and Technologies of the Future*, ed. by C. Edward. Can the Raising of Energy Consumption of Information Interchange be a Factor that Reduces the Total Energy Consumption of Logistic Warehouse System? (2011), pp. 79–89
4. A. Bujak, P. Zajac, in *Communications in Computer and Information Science*, vol. 329, ed. by J. Mikulski (ed.) Can the Increasing of Energy Consumption of Information Interchange be a Factor that Reduces the Total Energy Consumption of a Logistic Warehouse System? Springer, cop., Heidelberg, 2012), pp. 199–210, ISSN 1865-0929

Part IX

Environmental Issues

Adsorption of Methyl Red from Aqueous Solutions by Algerian Bentonite Clay

Karima Boudouara, Madani Ghelamallah
and Halima Nadia Khemliche

Abstract In order to removal methyl red from aqueous solutions using adsorption method, Algerian bentonite-type clay from Mostaganem region (MBC) has been first acid-activated then employed as adsorbent. The influence of several parameters (kinetics, contact time, sorbent amount and pH) on the adsorption capacity was evaluated and discussed. The results indicated that the adsorption was favourable at lower pH. The adsorption isotherm was well described by the Freundlich model and showed high MR adsorption with high correlation coefficient ($R^2 = 0.985$). The adsorption capacity of MBC found to be 2.0 mg g^{-1} . It was seen that pseudo-second order equation describes the adsorption kinetics. The results indicated that this bentonite-type clay is favourable to be used as an economical adsorbent for the removal of methyl red dye.

1 Introduction

Several industries use dyes such as textiles, plastic, paper and cosmetics [1]. Some of the dyes are toxic, carcinogenic, reported to have connections with different respiratory disorders worldwide and induces pollution to the environment [2]. The toxicity of dyes leads to the necessity of treatment. The adsorption in aqueous solutions has been found to be an efficient and economical process for removing the pollutants as the dyes [3]. Studies on the use of bentonite in removing dye pollutants from wastewater have been gaining more attention because of the low-cost of the materials involved and their high specific area, and a variety of surface and structural properties [4, 5]. In the present study, the removal of an anionic dye,

K. Boudouara · M. Ghelamallah (✉) · H.N. Khemliche
Laboratoire de Matériaux, Applications et Environnement, Faculté des Sciences et de la
Technologie, Université de Mascara, BP 305 Route de Mamounia, 29000 Mascara, Algeria
e-mail: gh_madani@hotmail.com

methyl red, from an aqueous solution has been studied by Bentonite Clay. Adsorption properties for the removal of MO from aqueous solution under varied experimental conditions were also investigated.

2 Experimental

Methyl red (MR) was obtained from Merck. The sample of bentonite-type clay was obtained from deposit of Mzila (Mostaganem region), (MBC) and underwent an acid-activation. Methyl red dye ($C_{15}H_{15}N_3O_2$) stock solution, 33 mg/L, is diluted in mixture of distilled water and ethanol (3:1). Successive dilutions were prepared in the range of initial concentrations 2–12 mg/L. The absorbance value is measured at 520 nm with Sedico (VIS-7220G) UV/Visible Spectrophotometer. The adsorption of MR on MBC was studied for different parameters, including adsorbent dose (0.025–1.25 g/L), solution pH (0.5–4), initial MR concentration (2–12 mg/L), temperature (30–50 °C) and contact time were assessed. In each adsorption experiment, 20 mL of dye solution of known concentration was added to 0.02 g of the clay and the initial pH of the MR solutions was adjusted by adding HCl or NaOH solutions. The mixture is agitated for 30 min. The adsorption percentage (R) and adsorption capacity values at equilibrium and t time (q_e and q_t mg g⁻¹) were calculated using the following equations:

$$R\% = ((C_0 - C_e)/C_0) \times 100 \quad (1)$$

$$Q_e = (C_0 - C_e/m) \times V \quad (2)$$

$$Q_t = (C_0 - C_t/m) \times V \quad (3)$$

where C_0 , C_e and C_t (mg L⁻¹) are the MR dye concentrations at initial, equilibrium and t time, respectively, V(L) is the solution volume and m(g) is the mass of used adsorbent.

3 Results and Discussion

3.1 Effect of Initial pH on the Adsorption

The experiments were conducted at MR initial concentration of 20 ppm and 1 g L⁻¹ of MBC. pH of solutions was changed in the range of 0.5–4. In this study, the maximum dye removal (close to 98 %) was observed in the pH range 1.6–3.2, probably due to the protonation of functional groups on MBC adsorbent [6] (Fig. 1).

Fig. 1 Effect of pH on the removal of MR ($C_0 = 4$ ppm, $m_{MBC} = 1$ g L^{-1} at room temperature)

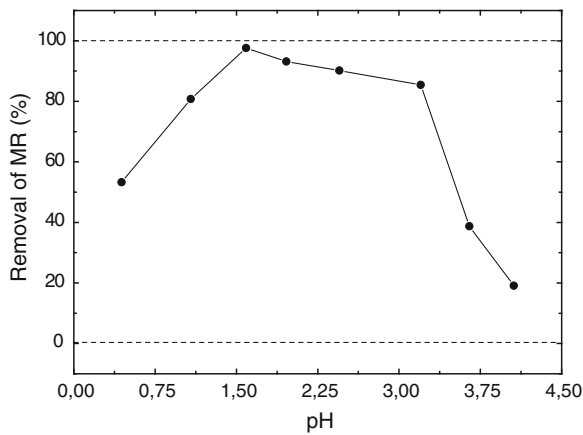
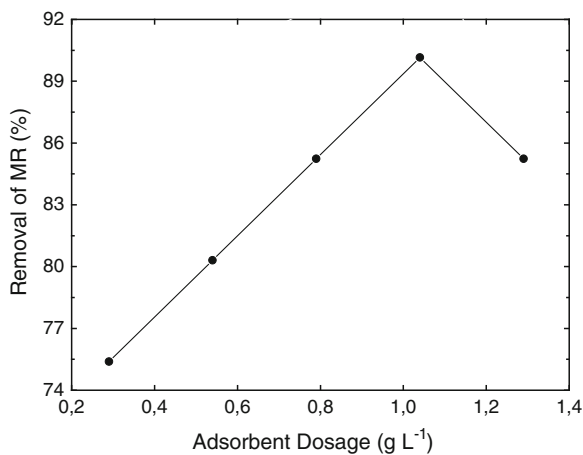


Fig. 2 Effect of adsorbent dosage on the removal of MR ($C_0 = 4$ ppm; contact time = 30 min)



3.2 Effect of Adsorbent Dosage

In order to find the optimum amount of adsorbent for maximizing the interactions between MR molecules and adsorption sites of adsorbent in the solution, various amounts of MBC ($0.25\text{--}1.25$ g L^{-1}) were added to 20 mL of dye solution (4 ppm) and shake for 30 min. It demonstrates in Fig. 2 that even though, the removal efficiency is high, already with strong amount of adsorbent. The efficiency clearly elevated to 90 % for MBC dosage of 1 g L^{-1} . The increase in removal efficiency with adsorbent dosage is due to the availability of larger surface area and greater number of free adsorption sites [7].

3.3 Effect of Contact Time on the Adsorption and the Kinetic Studies

The effect of contact time on MR adsorption was investigated in solutions containing fixed adsorbent amounts (1 g L^{-1}) at initial concentration of MR (4 ppm). As it can be seen in Fig. 3, that the adsorption kinetic curve appears rapid rising and then it stabilizes. So that, the optimal equilibrium adsorption times is 16 min for MR initial concentrations of 4 ppm. The rapid adsorption of MR in the first minutes can be attributed to the availability of a large number of vacant surface sites of fresh MBC.

In order to determine the kinetic parameters of MR adsorption on the MBC, the kinetic models including the pseudo-first-order, pseudo-second-order were applied to fit the experimental data. Calculated results of the fits are listed in Table 1.

The linear form of the pseudo-first order rate equation is given as [8]:

$$\ln (q_e - q_t) = \ln q_e - K_1 t \quad (4)$$

where k_1 is pseudo-first order rate constant and its value was calculated from the slope of the linear plot of $\ln (q_e - q_t)$ versus time. The experimental data were also tested by the pseudo-second order kinetic model which the linear form is shown as (5) [4]:

$$t/q_t = (1/K_2) q_e^2 + (1/q_e) t \quad (5)$$

Fig. 3 Effect of contact time on the MR adsorption on the MBC (MBC amounts = 1 g L^{-1})

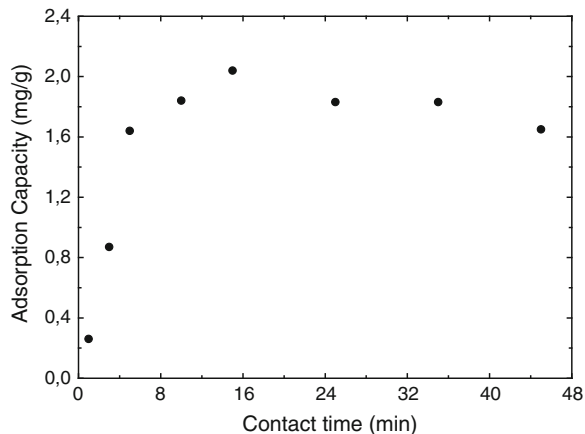


Table 1 Adsorption kinetics parameters for MR adsorption on MBC at ambient temperature

Pseudo-first-order		Pseudo-second-order	
$K_1 (\text{min}^{-1})$	R^2	$K_2 (\text{min}^{-1})$	R^2
0.2511	0.961	0.3020	0.985

where k_2 (g mg⁻¹ min⁻¹) is the second-order rate constant. According to the regression coefficient values ($R^2 > 0.985$) in the Table 1, it clearly shows that MR adsorption data on the MBC were successfully described by pseudo-second order model.

3.4 Isothermal Studies of the Adsorption

The Freundlich isotherm model was employed to simulate the experiment data. Figure 4 shows the adsorption isotherms of the MR on MBC at different temperatures. It can be seen that when the equilibrium concentration of MR increases, the amount adsorbed increases. According to the classification of Giles et al. [9], the experimental isotherms obtained are of type S. It is also clear that the adsorbed amount of MR has been affected by the temperature. The logarithmic equation form of the Freundlich isotherm is given by the following equation [10]:

$$\ln q_e = \ln K_f + (1/n) \ln c_e \quad (6)$$

where K_F (L mg⁻¹) and n are Freundlich constants. K_F is the adsorption capacity of the adsorbent and n gives an indication of how favorable is the adsorption process.

Fig. 4 The isotherms of MR adsorption on Bentonite at different temperature (Effect of initial concentrations on the adsorption of MR on MBC)

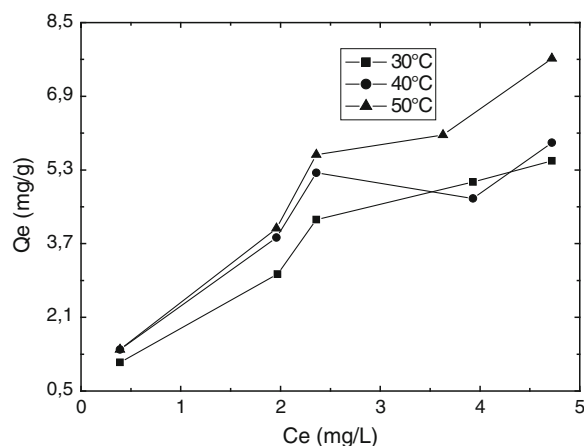


Table 2 Freundlich adsorption isothermal constants, correlation coefficients and the adsorption capacities of MBC for MR

T(K)	K _F	n	1/n	R ²
293	1.454	1.483	0.6740	0.984
313	2.189	1.726	0.5793	0.940
323	2.862	1.659	0.6027	0.991

Table 3 Adsorption thermodynamics parameters for MR adsorption on MBC at different initial MR concentration

C ₀ (mg/L)	ΔH (kJ/mol)	ΔS (J/mol K)	ΔG (kJ/mol)			R ²
			303 K	313 K	323 K	
2	40.49	137.06	-1.04	-2.41	-3.78	0.998
6	28.49	94.75	-0.23	-1.17	-2.12	0.951
8	34.84	115.70	-0.22	-1.38	-2.54	0.967
10	33.16	105.89	-1.08	-0.02	-1.04	0.975
12	24.83	80.04	-0.58	0.22	-1.02	0.951

In the examined cases, the value of n settled between 1 and 2 (Table 2) thus showing a difficult adsorption characteristics. The isotherm constants and correlation coefficients listed in Table 2 showed better fitting of experimental data for Frendlich model.

3.5 Thermodynamic Studies of the Adsorption

Thermodynamic parameters for the adsorption of MR are shown in Table 3. The values such as change in enthalpy ($ΔH^\circ$), entropy ($ΔS^\circ$) and free energy ($ΔG^\circ$) were determined using the following Van't Hoff equations [11, 12]:

$$ΔG = ΔH - TΔS \quad (7)$$

$$ΔG = - RT \ln K_d \quad (8)$$

The values of the standard enthalpy were found in the range of 24.83–40.49 kJ/mol and were all positive. This suggests that the adsorption reaction of methyl red is physical in nature. The positive value of $ΔS^\circ$ shows and its positive value correspond to an increase in adsorbed species degree of freedom at the solid/solution interface of the whole adsorption process. The negative $ΔG^\circ$ suggests spontaneity and feasibility of the adsorption process for adsorbent.

4 Conclusion

In this work, the Mostaganem bentonite clay was prepared by acidic activation and a comprehensive study was conducted on its adsorption capacity for the removal of dye pollutant (Methyl Red) from aqueous solution. MR adsorption onto the MBC was found to be optimal in the wide pH range of 1.6–3.2 and the optimum adsorbent amount of 1 g L⁻¹ was determined. At only 16 min, 2.0 mg g⁻¹ was required. The adsorption kinetics of MR on the MBC can be described by

the pseudo-second-order model. Moreover, the equilibrium data were analyzed by the Freundlich model, which provided the best fit to the experimental data with high correlation coefficient ($R^2 = 0.985$). In addition, various thermodynamic parameters such as changes in enthalpy, entropy, and the Gibbs free energy were calculated, showing spontaneity of the adsorption.

References

1. D. Pokhrel, T. Viraraghavan, *Sci. Total Environ.* **333**, 37–58 (2004)
2. Y. Badr, M.G. Abdul El-Wahed, M.A. Mahmoud, *J Hazard. Mater.* **154**, 245–53 (2008)
3. M.M. Doğan, Y. Özdemir, M. Alkan, *Dyes Pigment.* **75**, 701–13 (2007)
4. E. Repo, J.K. Warchał, A. Bhatnagar, A. Mudhoo, M. Sillanpää, *Water Res.* **47**, 4812–4832 (2013)
5. G. Crini, P.M. Badot, *Prog. Polym. Sci.* **33**, 399–447 (2008)
6. R. Tumlos, J. Ting, E. Osorio, L. Rosario, H. Ramos, A. Ulano, H. Lee, G. Regalado, *Surf. Coat. Technol.* **205**, S425–S429 (2011)
7. B. Tanhaei, A. Ayati, M. Lahtinen, M. Sillanpää, *Chem. Eng. J.* **259**, 1–10 (2015)
8. M.N. Sepehr, V. Sivasankar, M. Zarrabi, M.S. Kumar, *Chem. Eng. J.* **228**, 192–204 (2013)
9. C.H. Giles, T.H. MacEwan, S.N. Nakhwa, D. Smith, *J. Chem. Soc.* **786**, 3973–3993 (1960)
10. Y. Li, K. Sui, R. Liu, X. Zhao, Y. Zhang, H. Liang, Y. Xia, *Energy Proc.* **16**, 863–868 (2012)
11. Y. Ren, H.A. Abbood, F. He, H. Peng, K. Huang, *Chem. Eng. J.* **226**, 300–311 (2013)
12. R. Jiang, Y.-Q. Fu, H.-Y. Zhu, J. Yao, L. Xiao, *J. Appl. Polym. Sci.* **125**, E540–E549 (2012)

Is Hospitals Ready for Energy Management and Green Building? Health Managers Opinions in Turkey

Meriç Yavuz Çolak and Levent Çolak

Abstract Hospitals are of special interest for health promotion and the hospital sector is one of the biggest entrepreneurs in Turkey. Hospitals could be a strong partner for public health issues and also hospital sector has a heavy consumption of material and energy and a huge production of waste and carbon dioxide. This study summarizes research findings concerning knowledge, attitudes and behavior relevant to energy and environmental subjects of health managers. A survey was conducted with 47 decision-makers in nine leader private hospital in Turkey. Survey examines what the healthcare leaders are thinking about the energy management, green hospitals and what healthcare organizations are doing in response to rising energy costs, what factors are motivating efficiency improvements, how many organizations are planning to make investments, what payback they expect on energy efficiency investments, and what technologies and practices they have been implementing in their facilities. Energy performance monitoring is doing in 50 % of hospitals and in 40 % of hospitals there is a budget for energy. There are energy mangers in 45 % of hospitals. Only 18 % of healthcare leaders are defining the hospitals as environmentally friendly and just 2 % of hospitals have Leed certificate. Only the 2 % of hospitals are using just cogeneration systems and are not using the other renewable energy resources. According to 30 % of healthcare leaders the most importance of energy management using in hospitals is decreasing the costs and the second importance is the safety to global warming. Energy efficiency is getting more attention among healthcare facility leaders. They were very or fairly concerned about climate change, they are paying attention to energy management in hospitals and most of them are thinking that energy efficiency and the usage of renewable energy resources in hospitals are very important.

M.Y. Çolak (✉)

Faculty of Health Sciences, Department of Healthcare Management,
Başkent University, Baglica Campus, Ankara, Turkey
e-mail: meric@baskent.edu.tr

L. Çolak

Engineering Faculty, Mechanical Engineering Department,
Başkent University, Baglica Campus, Ankara, Turkey
e-mail: lcolak@baskent.edu.tr

1 Introduction

Hospitals are of special interest for health promotion and the hospital sector is one of the biggest entrepreneurs in Turkey. Hospitals could be a strong partner for public health issues and also hospital sector has a heavy consumption of material and energy and a huge production of waste and carbon dioxide. Recent advances in health and health sector together with the increases in service quality were introduced competition environment in hospital sector in Turkey. Patients were become conscious and were getting more challenged.

In Turkey, according to 2012 statistics, the number of hospitals are 1483 and 134 of these are included in general hospital category. Health expenditures are getting a significant change in recent years. Health expenditures are shown a 21 % increase. The hospital bills are taking the highest expense in public health expenditures. The budget for health in 2014 is 75 billion TL and the budget for health expenditures were increased to quintuple in last 2 years. The 15 % of current budget were given to health. In front of health investments, the number of hospitals and new health buildings is 610 between 2003 and 2012 and new 40 hospital and new buildings are added in 2013. These numbers are 1522 and 71 respectively for primary health institutions. Totally 111 health facility investments were made in 2013. In 2011, 500 million TL is paid for public hospital's energy consumption.

Changes in health politics and payment systems and possible financial crisis risk were produced the necessity of the hospital investments more conscious and sensitive to environment planning. The environmentally friendly hospitals were obligated for operation costs. It is impossible for hospitals stand off from this consciousness.

When one thinks in terms of health sector, especially in hospital system, energy is intensely used. Hospitals are more complex buildings that different services given from medical devices used in diagnosis to patient care services and to devices used for heating. Energy usage is in high level in hospitals due to the necessity of continuously giving service in 7 days and 24 h [1]. Different energy types must be used at the same time in hospitals. Hospitals need huge energy consumption due to the non-stop functions [2]. The heavily energy used areas in hospitals are; medical devices and other devices (33 %), lighting (17 %) and air conditioning (50 %) systems. If we look at the distribution of other energy used areas in total areas; hot water systems (26.8 %), personnel devices (6 %), kitchen services (5.6 %), and cooling systems (2.6 %) [3]. The 91 % of energy used in hospitals is gained from electric energy, 6 % from gases and 3 % from fuel oil [4]. The electricity and gas consumption per bed is 5000 TL in a year in health institutions.

Energy demand is increasing depending on the increasing demand to modern technological buildings in health sector. It is stated that in Holland hospitals have 44 % and in Germany have 20 % energy saving potentials and in 1 year without sacrificing service quality and without an additional special budget, hospitals can provide 10 % energy saving with simple energy saving measures [5].

Decreasing the ecological effects of health systems, protection of resources, pollution prevention and environment management systems applications are very important for green hospitals when preventing the people health at the same time. In green hospitals, patients were discharged averagely 2.5 days early [6]. Green hospitals are economically precious and preventing the investment buildings. They court to hospital managers in terms of costs. Especially they have preventive properties to hospital infections for personnel and patients, they decrease the health risks. It is determined that green buildings can save 50–70 % energy in energy saving. Some of these buildings named as ZEB (zero energy building) are buildings that produce own energy from renewable energy resources [7]. Healthier Hospitals Initiative Corporation was assisted to a lot of hospitals in decreasing the environmental footprint of them in USA in 2 years. In Europe, there is also Global Green and Healthy Hospitals Network organization carrying out similar activities. It is introduced in the report published by commonwealth fund that hospitals can ensure economic saving when they achieving significant decrease in footprint. According to report, all hospitals in USA can save 5.4 billion dollar in 5 years by taking simple protections.

In Turkey, studies for energy tracking system were started by Ministry of Health. Energy Efficiency Project in Health was started with corporation of Ministry of Health, Ministry of Environment and Urban Planning and Ministry of Energy and Natural Resources with the purpose of reducing the costs to minimum and with the purpose of increasing the “energy friendly hospitals”. In public hospitals 10 % decrease in energy consumption were purposed [8].

In addition, the difficulty of cost management and the necessity of starting to energy efficiency studies from awareness education programs in hospitals were introduced in project report. Changing energy composition in health institutions and researching the alternative renewable energy resources usage areas and opportunities, taking energy usage precautions, monitoring energy consumption and costs, monitoring the efficiencies of devices that consume energy, giving a place to green hospital concept, creating awareness for efficient usage of energy, extending the energy consciousness, the necessity of energy manager in hospitals, the necessity of studies for energy identity card that will be mandatory in 2017, the necessity of studies to decrease the costs of medical wastes, collecting the datas related to energy consumption and economically usage of resources were also introduced in the project. According to energy regulations issued in 2012, energy manager in hospitals and energy identity card for hospitals and necessity of energy consumption declarations of hospitals are obligated. In Turkey, only the 27 hospitals have energy identity card. 7 of them is in the old hospital category and old hospitals having energy identity card constitute the 0.44 % of all buildings that have energy identity card and new hospitals constitute the 0.09 % of new buildings that have energy identity card. The minority of old and new hospital buildings is quite remarkable.

2 Research

In this study, the importance of energy, energy efficiency, energy management and alternative energy resources usage in hospitals and management of these resources were introduced. The study is intended for giving the current situation of hospitals, healthcare manager's opinions and attitudes towards these subjects in hospitals. The opinions of healthcare manager's significance to energy, energy management and related topics, whether or not they are aware of the importance current energy resources with regard to costs, positive and negative aspects of the legal practice or financial incentives were given in the study.

A survey was conducted with 47 decision-makers in nine leader private hospital in Turkey. Survey examines what the healthcare leaders are thinking about the energy management, green hospitals and what healthcare organizations are doing in response to rising energy costs, what factors are motivating efficiency improvements, how many organizations are planning to make investments, what payback they expect on energy efficiency investments, and what technologies and practices they have been implementing in their facilities.

The questions aimed at putting the opinions of healthcare manager's about the importance of energy subjects in hospitals, the role of energy subjects in decision making, energy applications in terms of costs, service quality, and image of hospitals, the effects of government promotion, current legal applications, the energy investments applicable in hospitals and the budget for these applications, financial return of energy investments, planning the energy applications, advantages and the barriers, current energy applications in hospitals, hospital's personnel awareness and whether or not hospitals are environmentally friendly hospitals and whether or not hospitals were taken the required documents are introduced.

3 Results

Energy performance monitoring is going in 50 % of hospitals and there is a budget for energy in 40 % of hospitals. There are energy managers in 45 % of hospitals. 21 % of hospitals are getting advisory services. Only 18 % of healthcare leaders are defining the hospitals as environmentally friendly and just 2 of hospitals have Leed certificate. Most of the managers are aware of energy efficiency, energy saving and usage of renewable energy resources in hospitals and they also think that these subjects will be an important issues for their hospitals after 2 years but they defined that these subjects as not important as expected in their hospitals now (Table 1).

Almost half of the managers were indicated that energy investments in their hospital are not different from the previous years. Unfortunately only the 2 of hospitals are using just cogeneration systems and the others are not using the other renewable energy resources. According to health managers, the most three important reason for the necessity of energy efficiency implementations in hospitals

Table 1 Opinions about energy practices, energy management in hospitals

Opinions	Very important (%)
What is the importance of energy efficiency and energy management applications in your hospital?	48.9
What is the importance of energy management after 2 years in your hospital?	87.3
According to you what is the importance of energy efficiency, energy saving and usage of renewable energy resources in hospitals?	83.0

Table 2 Opinions about the importance of energy management in hospitals

Basic 3 reason	%
Reducing/controlling the costs	61.7
Avoiding the global warming	29.8
Catching the good applications and standards in hospital sector	29.8

Table 3 Opinions about the important factors in decision making related with energy efficiency in hospitals

The most important factors	%
Reducing the energy costs	93.6
Climatic changes	89.2
Trademark of hospitals	83.0

are Reducing/controlling the costs, avoiding the global warming and catching the good applications and standards in hospital sector (Table 2).

According to health managers, reducing the energy costs, climatic changes and the trademark of hospitals in population are the three most important factors in taking decisions related with energy efficiency in hospitals (Table 3). Only 36 % of health managers are thinking that energy efficiency applications and energy management decrease both the costs with 50 % and prevent the environment with 50 % at the same time. All most all of the managers stated that, enforcements are a possible state for reducing the carbon emission and toward energy efficiency in health sector especially in hospitals in 2 years. Setting up renewable energy systems and improving the energy efficiency in buildings took the first two strategies according to the managers for reducing the carbon output in hospitals and using energy in efficient way.

Health managers in general have not opinion about how much the budget has to be used for energy efficiency in hospitals but 24 % of them indicated that 10–14 % of operating budget and 17 % of them stated that 1–4 % of capital budget has to be reserved for energy efficiency in hospitals. In next 1 year, hospitals expecting energy investments are 22 % and most of the managers have not an idea for these investments. In a similar way they don't have knowledge of the financial return of the investments in hospitals. The most important barriers in application of energy management and energy efficiency in hospitals are the lack of technical competent

person and then the being hospitals unaware of these subjects and then the lack of hospital decision makers knowledge. Inadequacy of the government investments for these activities is another barrier according to health managers.

According to health managers smart building technologies then lighting technologies and then photovoltaic power generation is the most important strategies for reducing the hospital costs in hospitals in next 10 years. All most half of the managers stated that, treatment costs can be reduced by energy efficiency and energy management. According to 45 % of managers, hospitals are ready for energy management and energy efficiency implementation. But at the same time they indicated that they don't have a sufficient knowledge about energy management. They think that the energy prices will be increased by 7 or more percentage and hospitals will be in a competition environment in future. They stated that, the most five important reason for energy efficiency and energy management in hospitals are; reducing the operating cost, recovering the quality of hospital inside environment for patients and their families and employees, cost-benefit gain, overlapping with hospital mission and decreasing the treatment costs. The most motivating factor for energy management and energy efficiency in hospitals are decreasing the energy costs, global warming and legal issues according to health managers. In last 2 years and intended in 5 years the most applied energy efficiency application in hospitals are using the adjustable heat controlled systems in heating and ventilating systems, using sensor-fitted or time adjusted lighting systems in free areas or unused areas, changing the inadequate and ineffectual devices without waiting the normal economic life. According to 30 % of healthcare leaders the most importance of energy management using in hospitals is decreasing the costs and the second importance is the safety to global warming.

4 Conclusion and Future Work

Energy efficiency is getting more attention among healthcare facility leaders. They were very or fairly concerned about climate change, they are paying attention to energy management in hospitals and most of them are thinking that energy efficiency and the usage of renewable energy resources in hospitals are very important. Generating energy politics special for health sector and starting incentives by Ministry and especially raising awareness, doing studies that introduce the importance of these subjects have to be made. Energy resources must be used in hospitals in an efficient way. With developing technology, integration of background knowledge in energy sector to health sector has to be considered by health managers and managers have to look the ways of applying these technologies in their hospitals. Minimization of costs is very important to get a strong structure in health sector. But at the same time when reducing the costs and controlling the energy costs and using in efficient way, setting and managing systems not affecting

the safety and comfort of patients. Without a capital investment, efficient energy management is impossible and finally modernization of low cost investments and high costs investments are very important in health sector [9].

References

1. CEE1, Commercial building performance healthcare facilities. Sector fact sheet. www.cee1.org. Erişim Tarihi: 05.05.2014
2. U. Weisz, W. Haas, J.M. Pelikan, H. Schmied, Sustainable hospitals: a socio-ecological approach. *GAIA* **20**(3), 191–198 (2013)
3. Energy Consumption Platts, Managing energy costs in hospitals (2004). www.cee1.org/com/bldgs/hc-fs.pdf
4. USAID, *Energy Efficiency in Hospitals Best Practice Guide* (USAID, 2009)
5. EIA, IEO, International energy outlook (2008). www.eia.doe.gov/oiaf/ieo/index. Erişim Tarihi: 20.04.2014
6. O.C. Yonar, Yeşil Binalar Yaşam Konforunu Arttırıyor (2011). www.yesilbina.com/haber/10/Yesil-binalar-yasam-konforunu-artiriyor. Erişim Tarihi: 13.04.2013
7. WHO, Healthy hospitals, healthy planet, healthy people (2008). http://www.who.int/globalchange/publications/climatefootprint_report.pdf
8. Sağlık Bakanlığı, Sağlıklı Enerji Verimliliği Çalıştayı Sonuç Raporu, 13–14 Haziran 2012, Ankara
9. C. Boffa, *Management in Hospitals* (National Research Council Italy, 1989). www.ecbx.org. Erişim Tarihi: 06.05.2014

Design of High Sensitive Optical Sensor for Seawater Salinity

Ahlaam Harhouz and Abdesselam Hocini

Abstract A novel optical sensor was designed for the measurement of salinity in seawater. The principle is to measure the refractive index variation of seawater that corresponds to the change in salinity. The sensor based on the two-dimensional photonic crystal (PhC) microcavity coupled to two waveguide. We have used the FDTD method to simulate the sensor in 2D PhC with triangular lattice of air holes. The influence of the geometrical parameter and refractive index on transmission are studied, and an enhancement in sensitivity in 2D PhC is achieved which proves the ability of the structure to produce salinity sensor using PhC.

1 Introduction

During recent years integrated optical sensors have been used extensively in sensitive (bio) chemical analysis. And the Optical sensing mechanisms receive considerable attention in the areas of industrial process control, military, environmental monitoring, and medical diagnostics... [1, 2].

Monitoring of water quality is a major factor in protecting public health, besides high-quality freshwater is also a key input in agriculture and many industrial processes. Salinity (S) is among the most fundamental parameters for oceanic, marine environment monitoring, seasonal climate prediction, mariculture, and solar engineering, which is essential to climate models, therefore, measurement of such parameters for chemical oceanography has become increasingly attracted to optics sensors community [3, 4]. Salinity sensors play an important role in manufacturing process control and protection of ecosystems. Among the optical sensing mechanism, is to detect the effective refractive index of the resonator that is changed due

A. Harhouz · A. Hocini (✉)

Electronics Department, University of M'sila, PO. Box. 166 Ichebilia Road M'sila, M'sila, Algeria

e-mail: hocini74@yahoo.fr

to analytes binding on it. In order to enhance the sensitivity of detection, one of the most straightforward ways to detect the sensing signal is the resonant wavelength detection/shift and intensity variation. On the other hand, PhCs structure provided a good solution to enable extremist small ring resonator with ultra low bending loss owing to the excellent light confinement [5]. Sensors based on PhC waveguides incorporating with microcavities [6, 7] having high sensitivity, easy extension to sensor arrays, various choices of materials and capability of parallel measurement.

In this work, a novel Optical sensor for seawater salinity proposed. It is formed by two waveguide and one microcavity in a PhC with a triangular lattice of air holes. The sensing principle is based on the shift of resonance wavelength λ_0 , which occurs due to change in refractive index (RI) of the sensor when the PhC's air holes are full of seawater. The RI seawater is from $n = 1.33300$ to $n = 1.34031$ corresponds to the change in salinity from $S = 0\%$ to 40% (g/l) over the temperature $20\text{ }^{\circ}\text{C}$ [3].

The sensor is formed by enlarging the dimension of holes localized at each side of waveguide in order to achieve further improvement in sensitivity. The properties of the sensor are simulated using the (FDTD) algorithm (RSoft Photonic Suite).

2 Theory and Principle

PhC are periodic dielectric material with the capability to control and manipulate light propagation. The periodicity can be formed by etching holes in a dielectric material that provides the photonic band gap, a range of frequency over which propagation is strictly forbidden [8–10]. PhCs with defects in the periodic lattice can thus be exploited to control the propagation of light forming a waveguide and cavity. By varying the local RI, the effective RI of the slab and the RI contrast between the holes and the slab region are changed. Since it is known that the wavelengths of transmission depend directly on the effective index of the slab [11], thus the device can be used as a sensor by detecting the output transmission spectrum. With the presence of analyte, the effective RI changes and hence causes a shift in the of resonance wavelength λ_0 of the output spectrum.

The transmission spectra of resonant mode peak wavelengths under different RI are calculated by FDTD method [12]. The results provide a theoretical basis for the two-dimensional photonic crystals sensor design. FDTD method is a time-domain electromagnetic field numerical computation method. In this approach, the finite difference is applied to the two Maxwell's curl equations in time- and space-domain. So, we can compute electric and magnetic field at each space location and each time step, which can get the wave scattering and propagating process in the designed sensor. The electric and magnetic fields are evaluated at different grid points in leapfrog and staggered grid forms. As the capacity limitations of computer, we can only calculate the electromagnetic field in a limited region. In order to simulate the electromagnetic wave propagating in open domain,

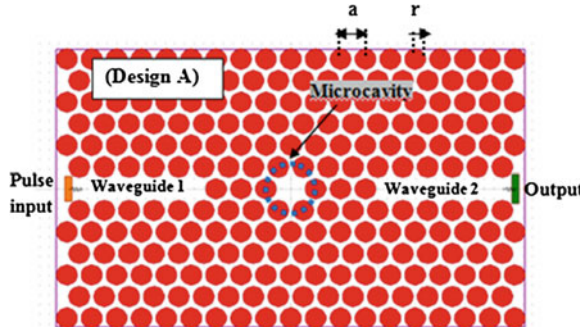


Fig. 1 Layout drawing of the sensor, the structure consists of waveguide. 1 Microcavity, and waveguide. 2 Pulsed light is launched from the *left* (arrow) and the output is measured at the *right* (time monitor)

the absorbing boundary conditions must be given. In this paper, we use Berenger's perfect matched layer (PML) as the absorbing boundary conditions [13].

A 2D triangular lattice of 19×13 PhC structure in a silicon (Si) wafer is considered for designing the sensor. The radius of the air holes is $r = 0.19 \mu\text{m}$ and the distance between any two nearest holes is $a = 0.47 \mu\text{m}$. The index profile of silicon slab ($n_{\text{Si}} = 3.42$) and air ($n_{\text{air}} = 1$)). Utilizing the triangular PhCs is practically important since they have a large transverse electric band gap and it is expected to serve a good platform for photonic integrated circuits and ultra-compact optical sensors [14]. A preliminary analysis of dispersion diagram showing normalized frequency versus the wave vector for transverse magnetic (TM) modes of the 2D photonic crystal. It has been calculated along the Γ -K-M- Γ edge for the Brillouin zone by employing a 2D plane wave expansion (PWE) method. The regular PhC structure exhibits a large band gap between 1135 and 1860 nm for TM polarization; the device also shows smaller bands gaps for TE polarization.

As a first step, we proposed the structure of the sensor's design in the Fig. 1. It is formed with two waveguides couplers and one microcavity. The waveguides are obtained by removing one row of air holes in the Γ K direction. They are used to couple light in and out of the PhC microcavity. A simple microcavity was formed by removing one hole in the center of PhC structure, it is separated from the input and output waveguides by three holes of the PhC.

3 Results and Discussions

For estimating functionality of the structure, a sample, for example water, is supposed to be in contact with the sensor. In simulation, it is carried out by changing the RI of the holes from 1 (air) to 1.33 (water). This leads to a shift in the output

Fig. 2 Transmission of the sensor versus the RI ranging from 1 to 1.33485 (design A)

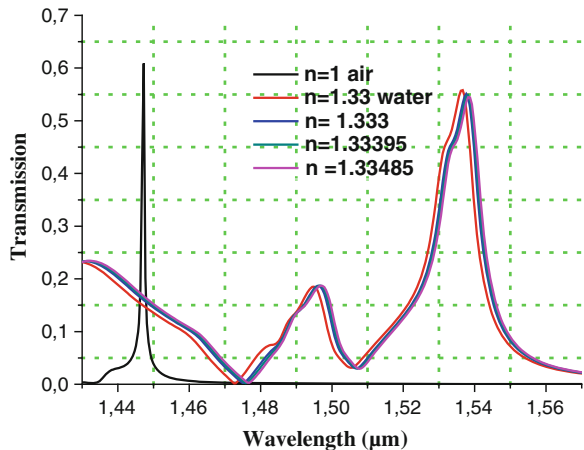


Table 1 Refractive index, resonant wavelength, and transmission for the sensor (design A)

Refractive index	Resonant wavelength (μm)	Transmission
1.00000	1.447245	0.6090046
1.33000	1.536646	0.5581615
1.33300	1.537668	0.5511807
1.33395	1.538179	0.5482122
1.33485	1.538179	0.5482122

transmission spectrum that corresponds to the change in the RI. The transmission spectrum of the PhC sensor is obtained using the Finite-Difference Time Domain (FDTD) method is shown in Fig. 2.

Refractive index of air holes, resonant wavelength, and transmission for the sensor at 20 °C are tabulated in Table 1. It clearly shows that the resonant wavelength increases while increasing the refractive index for all air holes. However, the transmission decreases. And two refractive index (1.33395 and 1.33485) have the same resonant wavelength 1.538179 μm. so with this structure, our sensor can't detect a change of $\Delta n = 0.0009$.

The sensor is sensitive to the change of RI in the air hole and it can be optimized to realize high sensitivity, wide measurement range [15, 16]. By change the size of the air holes localized at each side of the line defect ($r' = 0.2 \mu\text{m}$, green colored). The second proposed design (Design B) is shown in Fig. 3.

Figure 4 shows the output spectrum of the sensor with respect to salinity of seawater ranging from 0 to 40 %. The resonant wavelength and transmission of the sensor with 0 % of salinity are 1.418406 μm, 0.5455746 respectively. It is observed that, approximately, 1.03 % reduction in transmission for every 5 % increasing salinity and 435–436 pm shift in resonant wavelength (Fig. 5).

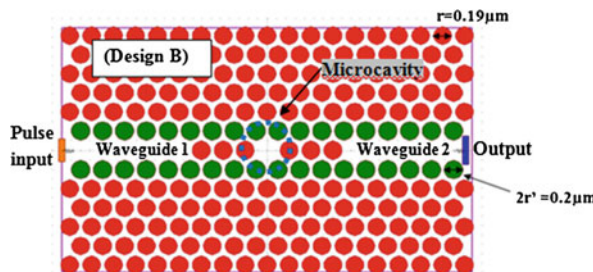


Fig. 3 Layout drawing of the sensor based on 2D PhC using triangular lattice of air holes

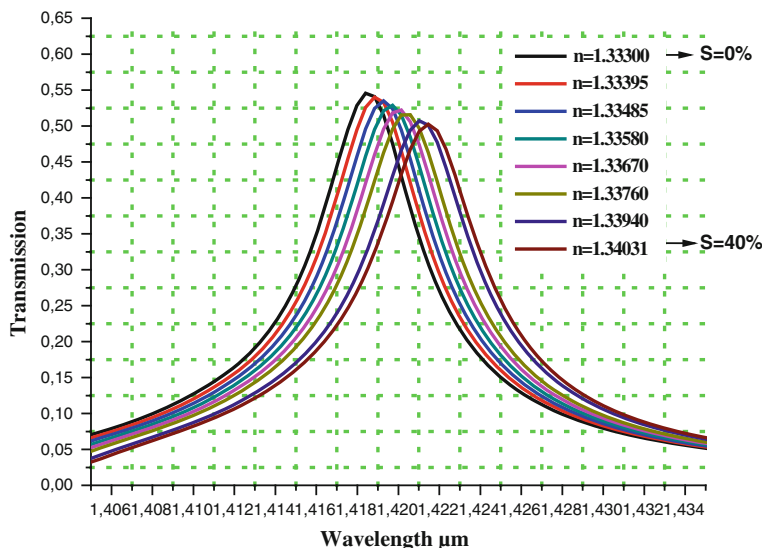


Fig. 4 Transmission of the sensor (design B) versus the RI ranging from 1.333 to 1.34031 corresponds to the change in salinity from 0 to 40 % (g/l)

The level of salinity with its refractive index, resonant wavelength, sensitivity and transmission for the sensor at 20 °C are given in Table 2.

The precise simulation results showed that, the sensitivity of sensor can reach 452.36 nm/RIU with a detection limit of 0.00095 RIU.

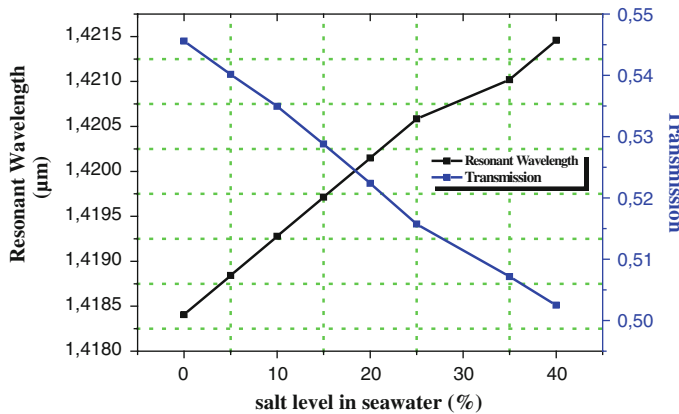


Fig. 5 The resonant wavelength and the transmission of the sensor (design B) with the various in salt level of seawater

Table 2 The salinity with refractive index of seawater, resonant wavelength, transmission and sensitivity for the sensor (Design B) at 20 °C

Salt level (%)	Refractive index (RIU)	Resonant wavelength (μm)	Transmission	Sensitivity ($S = \Delta\lambda_0/\Delta n$) (nm/RIU) $\Delta n = n - n_0$ $n_0 = 1.333$	Δn (RIU)
0	1.333	1.41841	0.54557		—
5	1.33395	1.41884	0.54014	452.36	0.00095
10	1.33485	1.41928	0.53494	470.27	0.00185
15	1.3358	1.41971	0.52879	505.15	0.0028
20	1.3367	1.42015	0.52236	470.27	0.0037
25	1.3376	1.42058	0.51573	471.73	0.0046
35	1.3394	1.42102	0.50717	407.81	0.0064
40	1.34031	1.42146	0.50248	417.23	0.00731

4 Conclusion

A PhC sensor is proposed and designed for sensing the salinity of seawater. The capability of the proposed sensor for sensing the salinity is between 0 and 40 % (g/l). The structure formed by two waveguides and one microcavity in 2D PhC with a triangular lattice of air holes. The defect-line is modified and optimized for achieving the highest possible sensitivity, by change the size of the air holes localized at each side of the line defect. The principle of detection is based on the measurement of resonant wavelength λ_0 to change in RI corresponds to the change

in salinity of seawater, which leads to a shift in the output transmission spectrum. The sensitivity of sensor can reach 452.36 nm/RIU with a detection limit of 0.00095 RIU.

References

1. D. Clerc, W. Lukosz, Integrated optical output grating coupler as biochemical sensor. *Sens. Actuators B* **19**, 581(1994)
2. IUPAC, Compendium of Chemical Terminology, 2nd edn. (Blackwell Scientific Publications, Oxford, 1997)
3. S. Robinson, R. Nakkeeran, Photonic Crystal based Sensor for Sensing the Salinity of Seawater. *IEEE-International Conference on Advances in Engineering, Science and Management* March 30, 31 (2012)
4. Y. Zhao, Y.B. Liao, Novel optical fiber sensor for simultaneous undersea temperature and salinity measurement. *Sens. Actuators B Chem.* **86**(1), 63–67 (2002)
5. Z. Qiang, W. Zhou, R.A. Soref, Optical add-drop filters based on photonic crystal ring resonators. *Opt. Expr.* **15**, 1823–1831 (2007)
6. J.D. Joannopoulos, et al., *Photonic crystals: Molding the Flow of Light*, 2nd edn. (Princeton University Press, 2011), 304 p
7. S. Mandal et al., Nanoscale optofluidic sensor arrays. *Opt. Expr.* **16**, 1623 (2008)
8. T. BaBa, Slow light in photonic crystals. *Nat. Photonics* **2**, 465–473 (2008)
9. S.Y. Lin, E. Chow, S.G. Johnson, J.D. Joannopoulos, Demonstration of highly efficient waveguiding in a photonic crystal slab at the 1.5- μ m wavelength. *Opt. Lett.* **25**(17), 1297–1299 (2000)
10. A. Vlasov, M. Boyle, H. Hamann, J. McNab, Active control of slow light on a chip with photonic crystal waveguides. *Nature* **438**, 65–69 (2005)
11. T. Hasek, H. Kurt, D.S. Citrin, M. Koch, Photonic crystals for fluid sensing in the subterahertz range. *Appl. Phys. Lett.* **89**, 173508-1–173508-3 (2006)
12. G. Benqing, *FDTD Method* (Publishing House of China National Defence Industry, 1995)
13. I.P. Berenger, A perfectly Matched Layer for the absorption of electromagnetic waves. *J. Comput. Phys.* **114**, 185 (1994)
14. A. Kahlouche, A. Hocini, D. Khedrouche, Band-gap properties of 2D photonic crystal made by silica matrix doped with magnetic nanoparticles. *J. Comput. Electron.* **13**(2), 490–495 (2014)
15. A. Harhous, A. Hocini, Design of high-sensitive biosensor based on cavity-waveguides coupling in 2D photonic crystal. *J. Electromagnetic Wave. Appl.* **29**(5), 659–667 (2015)
16. H.S. Dutta, S. Pal, Design of a highly sensitive photonic crystal waveguide platform for refractive index based biosensing. *Opt. Quantum Electron.* **45**, 907–917 (2013)

A Fuzzy Inference System to Evaluate the Environmental Effects of Electricity Generation Technologies

Fausto Cavallaro

Abstract Power plants activity can have positive and negative effects on the population, which must be taken into account. In many cases various kinds of power generation systems can have a significant adverse impact on the environment, increasing health risks and reducing the standard of living of local communities. In this paper a methodology based on fuzzy-sets is proposed to assess the impact on a local scale of the sustainability of the most important electricity power production technologies.

1 Introduction

Power plants have provided the energy required for the economic and technological development over last decade. At the same time the environmental effects of electricity generation are significant because the modern economy uses large amounts of electrical power. So power plant activity can have positive and negative effects on the population, which must be taken into account. In many cases various kinds of power generation systems—due to the release of air pollutants, radioactivity, water and soil contamination (oil spills)—can have a significant adverse impact on the environment, increasing health risks and reducing the standard of living of local communities. For these reasons we absolutely cannot ignore the environmental effects of electricity production processes. In the literature there are interesting papers which shed light on the important relationship between electricity

F. Cavallaro (✉)

Department of Economics, Management, Society and Institutions (EGSI),
University of Molise, Via De Sanctis, Campobasso 86100, ITALY
e-mail: cavallaro@unimol.it

production processes and ecological and human health modifications [1–5]. Unfortunately, in many cases the amount of information used in the assessment models is affected by uncertainty. A first source of uncertainty comes from the variability of the data, due to the non-deterministic nature of the social and natural facts. Another type of uncertainty is the imprecision that appears when observing or measuring the values of a variable due to both the measuring instrument and the observer undertaking the task [6]. Fuzzy-set based methods have proved their ability to deal with uncertainty in environmental topics.

In this paper a methodology based on fuzzy-sets is proposed to assess the pressure on the environment of the most important electricity power production technologies. This paper is organized as follows: Sect. 2 describes the fuzzy inference approach, Sect. 3 contains the application of the model and finally the conclusion is made in Sect. 4.

2 The Fuzzy Inference System (FIS)

The fuzzy inference system employing fuzzy *if-then* rules can model the qualitative aspects of human reasoning processes without using accurate quantitative analysis [7]. Fuzzy inference is a process of obtaining new knowledge through existing knowledge using fuzzy logic. This process of formulating the mapping from a given input to an output produces a basis on which decisions can be made or from which patterns can be discerned. In this approach, the solution to a problem derives from the human interpretation of data, expertise, etc.

In a fuzzy inference model (approximate reasoning) the reasoning process is based on a series of *if-then* rules as a kind of expert knowledge [8, 9]. The conditional statement (or proposition) contains a *premise*, the *if-part*, and a *conclusion*, the *then-part* [8, 10]. The knowledge incorporated in a fuzzy control system is made up of a collection of several parallel rules in the form ‘*if X is A then Y is B*’, or more generally ‘*if X₁ is A₁ and...and X_n is A_n then Y is B*’, where A, A_n, B are fuzzy sets [11]. The *knowledge base*, which contains the general knowledge concerning a problem domain, and which connects antecedents with consequences, premises with conclusions, or conditions with actions [12] (see Fig. 1). An FIS is composed of three blocks. The first one, *fuzzification*, converts the crisp value input to a linguistic variable using the membership functions stored in the fuzzy knowledge base. To the second block, the *inference engine*, is assigned the task of evaluating the input’s degree of membership to the fuzzy output sets using the fuzzy rules [13]. Finally, the defuzzifier block transforms the fuzzy output into a crisp value. The inference stage utilizes the fuzzy input values to activate the inference rules and generate the fuzzy output value. There are two main approaches to fuzzy inference, which are usually denoted as the Mamdani type and the Takagi-Sugeno-Kang type (or simply the Sugeno type) FIS [12]. Although many methods for the composition of fuzzy relations (e.g., min-max, max-max, min-min, max-min, etc.) are available

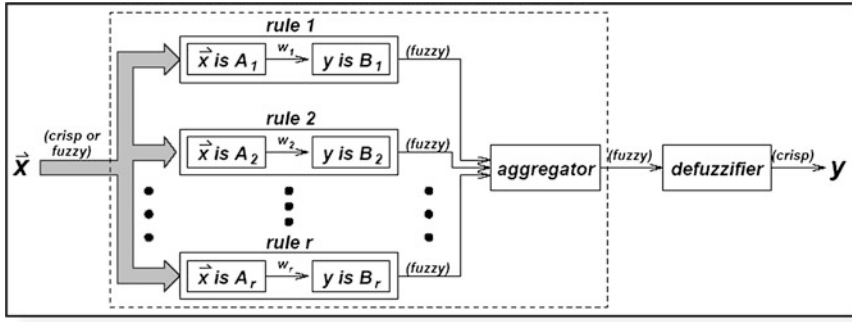


Fig. 1 Fuzzy inference engine. *Source* [14]

in the literature, the max-min is the most frequently used technique. For example, a two-rule max-min composition Mamdani FIS model is the following [14]:

$$\mu_{Ck}(Z) = \max[\min[\mu_{Ak}(\text{input}(x)), \mu_{Bk}(\text{input}(y))]] \quad (1)$$

$K = 1, 2, \dots, r$ where μ_{Ck} , μ_{Ak} and μ_{Bk} are the membership functions of output Z for rule k input A and input B . Even so, other minor fuzzy inference methods have been proposed. The most popular and precise operator is the *centre of gravity* developed by Sugeno in 1985. It is given by the following equation [12]:

$$b = \frac{\int \mu_B b \cdot db}{\int \mu_B \cdot db} b \in \tilde{B} \quad (2)$$

where \tilde{B} is a fuzzy set with the membership function μ_B .

3 A FIS Model to Assess the Environmental Pressure of Electricity Production

In order to address future investments in containing the environmental damage caused by electricity production it is necessary to acquire knowledge about the environmental impact of energy technologies and the projected energy scenarios [2]. Therefore we propose a fuzzy inference model to measure the environmental sustainability of some power plants. To design the framework of fuzzy model some experts have defined the parameters and ranges of the membership functions. Five input parameters were selected and an overall environmental pressure index, represented by a score on a scale of zero to 100, was obtained. The first input parameter used in the model is the life-cycle CO_2 emissions per kWh of electricity produced (CO_2/kWh) by electric power sources. The literature is really very

detailed on this topic; in particular we can cite the last IPCC report [15] in which the emission intensity of the electricity production used in this study was reported. The second indicator employed is “land use” (LU). This is very important because it represents the area destined for power generation and removed to other human activities and flora and fauna [16]. The third indicator is “water consumption” (WC). This refers to the portion of extracted water not returned to the immediate water environment. As reported by Evans et al., water consumption is the indicator more appropriate to represent the impact of water use across the full life cycle [2]. The four indicators correspond to the “pressure on ecosystems” (PC), and because ecosystems are closely connected to their environment, every environmental change has ecological consequences [17]. The increase in air and water pollution caused by energy technologies can cause alterations to crop production, migration, or the disappearance of wildlife species by destroying their habitat [17]. Finally, the last indicator defines the “external cost” to the environment (EC). Cost can be defined as external when it is produced by the activity of one subject but is incurred by another subject. The use of energy causes damage to the environment which is not reflected in the market price of energy. The European Union commissioned an important research project on the monetary valuation of the impact on the environment and society of electricity production processes (for a synthesis of the input parameter data, see Table 1). Finally we obtain the value, after defuzzification, on a scale of zero to 100 of the “Environmental Pressure Index” (EPI). This measures the impact of energy technologies on the environment.

Membership function is the core of the inference model. In order to classify both the input and output parameters, three membership functions are used such as *optimal*, *acceptable*, *not-acceptable*. An example of the pattern (land use) is depicted in Fig. 2. The output membership functions of the EPI in the form of linguistic ratings are described as *very low*, *low*, *middle*, *middle high*, *high*, and *very high* (see the pattern in Fig. 3). Once the fuzzy variables and membership functions have been described, 243 *if-then* fuzzy rules base have been specified. To test the FIS model an open source software was used [20]. The literature data, used for the computation of the EPI of the main energy technologies, are reported in Table 1. For information about CO₂ and water consumption, we noticed remarkable differences between several of the consulted sources. In other cases, for example water consumption, the data were only available in a wide range (min-max). In this case

Table 1 Input parameters

Input variables	Linguistic values	Base variable	Range
Carbon dioxide ^a	(Optimal, acceptable, not-acceptable)	gCO _{2eq} /kWh	[0–1000]
Land use ^b	“	Km ² /TWh	[0–15]
Water cons. ^c	•	Kg/kWh	[0–250]
Pressure on Ecosystem ^d	“	Score	[0–10]
External cost ^e	•	€c/kWh	[0–10]

Data source ^a[15, 18], ^b[4, 18], ^c[2, 18], ^d[19], ^e[4]

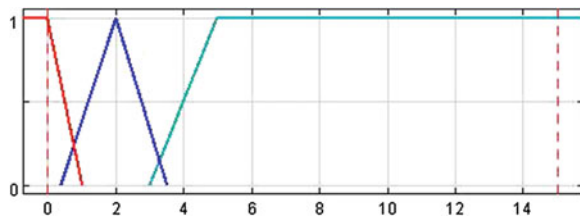


Fig. 2 Memberships function for “land use”

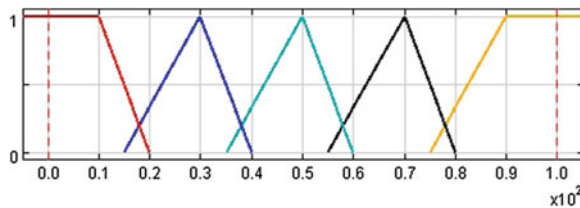


Fig. 3 Membership function for the EPI index

Table 2 Input data and the EPI for some selected technologies

Technologies	Input data					E_{nv}	Pressure	I_{index}
	CO_2	LU	WC	PE	EC			
<i>Wind</i>	12	1.57	1	0.3	0.083	27.88		
<i>PV</i>	50	0.33	10	0.2	0.16	27.64		
<i>CSP</i>	35	0.26	5	0.35	0.19	37.70		
<i>Hydro</i>	24	3.9	40	0.4	0.32	47.79		
<i>Biomass</i>	230	12.6	90	0.25	0.4	67.88		
<i>Geothermal</i>	38	0.74	60	0.45	0.5	47.88		
<i>Gas</i>	500	0.31	78	0.6	2.48	68.05		
<i>Coal</i>	820	0.39	78	0.9	4.96	98.71		

we used the median value from the collected data. It is very important to highlight that the parameter data used for this application must not be understood in an absolute sense. For some technologies the range of data is very wide. This difference depends on the power plant configuration. In Table 2 the testing results are reported for the selected energy technologies. Based on these input values the lowest EPIs are obtained for wind (27.88), PV (27.64), and CSP (37.70); after that in the middle position we have geothermal (47.88), hydro (47.79) and biomass (67.88), and finally gas (68.05) and coal (98.71).

4 Conclusion

In this paper a model based on fuzzy inference systems (FIS) was proposed to assess the pressure on the environment from electricity production technologies. The results of testing and using the Mamdani fuzzy inference approach appear to be very promising for effectively dealing with environmental issues. A fuzzy index (EPI) has been developed to measure the pressure from energy technologies on the environment. After testing the model we obtained the following results for the EPI: wind (27.88), PV (27.64), CSP (37.70), geothermal (47.88), hydro (47.79), biomass (67.88) and finally gas (68.05) and coal (98.71). Future research will deal with the improvement of the model using others parameters and more accurate data.

References

1. E. Santoyo-Castelazo, A. Azapagic, Sustainability assessment of energy systems: integrating environmental, economic and social aspects. *J. Clean. Prod.* **80**(1), 119–138 (2014)
2. A. Evans, V. Strezov, T.J. Evans, Assessment of sustainability indicators for renewable energy technologies. *Renew. Sustain. Energy Rev.* **13**(5), 1082–1088 (2009)
3. V.R. Prakash, I.B. Bhat, Energy, economics and environmental impacts of renewable energy systems. *Renew. Sustain. Energy Rev.* **13**(9), 2716–2721 (2009)
4. A. Maxim, Sustainability assessment of electricity generation technologies using weighted multi-criteria decision analysis. *Energy Policy* **65**, 284–297 (2014)
5. F. Cavallaro, L. Ciraolo, Sustainability assessment of solar technologies based on linguistic information, in *Assessment and Simulation Tools for Sustainable Energy Systems: Theory and Applications*, ed. by F. Cavallaro (Springer, 2013)
6. F. Cavallaro, Fuzzy TOPSIS approach for assessing thermal-energy storage in concentrated solar power (CSP) systems. *Appl. Energy* **87**(2), 496–503 (2010)
7. Y. Chai, L. Jia, Z. Zhang, Mamdani model based adaptive neural fuzzy inference system and its application. *Int. J. Inf. Math. Sci.* **5**(1), 22–29 (2009)
8. A.M.G. Cornelissen, J. Van den Berg, W.J. Koops et al., Assessment of the contribution of sustainability indicators to sustainable development: a novel approach using fuzzy set theory. *Agric. Ecosyst. Environ.* **86**(2), 173–185 (2001)
9. B. Öztayisi, H. Behret, Ö. Kabak, et al., Fuzzy inference systems for disaster response, in *Decision Aid Models for Disaster Management and Emergencies*, ed. by B. Vitoriano, L. Montero, D. Ruan (Atlantis-Springer, 2013)
10. J.C. Bezdek, Fuzzy models—what are they, and why? *IEEE Trans. Fuzzy Syst.* **1**(1), 1–6 (1993)
11. D. Dubois, F. Esteva, L. Godo, et al., in *Fuzzy-set Based Logics—An History-oriented Presentation of Their Main Developments*, ed. by D.M. Gabbay, J. Woods. *Handbook of the History of Logic*, vol. 8 (Elsevier BV, 2007)
12. G.J. Klir, B. Yuan, *Fuzzy sets and fuzzy logic—theory and applications* (Prentice Hall, New Jersey, 1995)
13. A. Reveiz, C. León, Operational Risk Management Using a Fuzzy Logic Inference System. *Borradores de Economía*, Banco de la República Colombia, n.574 (2009)
14. A. Saberi Nasr, M. Rezaei, M. Dashti Barmaki, Analysis of groundwater quality using mamdani fuzzy inference system (MFIS) in Yazd Province, Iran. *Int. J. Comput. Appl.* **59**(7), 45–53 (2012)

15. IPCC Working Group III—Mitigation of Climate Change, Special Report on Renewable Energy Sources and Climate Change Mitigation, Annex III Technology—specific cost and performance parameters (2011)
16. V. Fthenakis, H. Chul Kim, Land use and electricity generation: A life-cycle analysis. *Renew. Sustain. Energy Rev.* **13**(6–7), 1465–1474 (2009)
17. E.E. Michaelides, Environmental and ecological effects of energy production and consumption, in *Alternative Energy Sources*, ed. by E.E. Michaelides (Springer, Berlin Heidelberg, 2012)
18. S.J.W. Klein, E.S. Rubin, Life cycle assessment of greenhouse gas emissions, water and land use for concentrated solar power plants with different energy backup systems. *Energy Policy* **63**, 935–950 (2013)
19. M.Z. Jacobson, Review of solutions to global warming, air pollution, and energy security. *Energy Environ. Sci.* **2**, 148–173 (2009)
20. S. Guillaume, B. Charnomordic, Learning interpretable fuzzy inference systems with FisPro. *Inf. Sci.* **181**(20), 4409–4427 (2011)

Part X
Carbon Capture and Storage

Molasses Based Activated Carbons as CO₂ Sorbents

J. Młodzik, K. Główka, U. Narkiewicz, A.W. Morawski, R.J. Wróbel
and B. Michalkiewicz

Abstract Research treats about creating new sorbents, which would be able to adsorb CO₂, and then to perform photocatalytic reaction of obtaining organic compounds. Activated Carbons (ACs) were produced in KOH presence as activation agent, and with TiO₂ addition, from sugarcane molasses—low priced by-product of sugar industry. Properties were tested by liquid N₂ adsorption method, using BET equation, DFT method, and volumetric CO₂ adsorption method. Results suggested that using TiO₂ decreases the surface area of ACs but of small amounts can make it effective photocatalysts.

1 Introduction

High priority of reducing emission of CO₂ is the result of a common opinion, that it is one of the most harmful greenhouse gasses. Those compounds are claimed as causes of greenhouse effect, which is widely considered as the main reason of global warming. Vast emission of CO₂ by industry, and other human acts, increases the content of it in atmosphere, and it requires complicated geological processes, which take ages, to reduce it. It is highly needed to reduce the emission, but it would be even better to convert harmful gasses into energy source. One of possibilities can be photocatalytic reaction of turning CO₂ into organic compounds [1–6].

TiO₂ is widely used material nowadays. Certain properties make it, combined with activated carbon, very promising photocatalyst. Some of them are high surface area, high photostability, and ability to work efficiently at high ambient temperature.

J. Młodzik (✉) · K. Główka · U. Narkiewicz · A.W. Morawski · R.J. Wróbel ·
B. Michalkiewicz

West Pomeranian University of Technology, Institute of Chemical and Environment
Engineering, Ul. Pułaskiego 10, 70-322 Szczecin, Poland
e-mail: jacek.mlodzik@zut.edu.pl

The most important though is the fact, the simplicity of separation, regeneration and work-up [5–9].

Quality of ACs, as well as the composition, structure, and all the characteristics are determinate by preparation procedure, activating agent, and crucially by physical and chemical properties of starting materials [9]. Considering this feature, in recent years plenty of raw materials were tested as such source e.g. residual wastes and agricultural products: straw, corn straw, corn cob and hulls, eucalyptus maculate, wheat birch wood, almond shells, nut shells, sunflower shells, peanut hulls, rice hulks, husks and straw, peach pits, cherry pits, apricot pits, olive pits and residues, pine cones and needles, rapeseed, miscanthus, sugarcane bagasse. There are also materials, which have not been tested at all. One of barely noticed is molasses, which was considered only once [5, 7, 9, 10].

Producing activated carbons requires appropriate activating agent. Chemical activation usually needs to be performed in relatively lower temperatures than physical activation, which also provides lower surface area of final product. It was proven that it is plausible to produce high surface area materials using KOH, although studies needs to be continued, to systemize knowledge about influence of activation conditions on final AC's properties such as porosity and surface area [7, 10–15].

The aim of this study was to evaluate CO_2 adsorbing abilities of molasses based ACs, and verify effect of TiO_2 addition on the surface area, porosity, and uptake of CO_2 .

2 Materials and Methods

Dense liquid—molasses, has been mixed with grounded potassium hydroxide, to obtain homogenic mixture. To obtain optimized material mass of dry molasses has been calculated, so as mass of TiO_2 , or dry KOH, which has been used as activating agent. The ratios of dry masses have been 1:1. Mass ratios of starting materials are presented in Table 1.

The mixture has been left for 3 h. Drying has been performed in temperature of 473 K for 19 h. Materials have been grounded afterwards. Obtained powder has been placed in quartz boat, which has been placed in vertical tube furnace. Pyrolysis has been performed simultaneously with chemical activation. The temperature of

Table 1 Obtained activated carbons

Name of the sample	Mb: TiO_2	Mb:KOH
AC1		1
ACT1	0.08	
ACT4	0.16	
ACT5	0.08	1
ACT6	0.32	

process has been settled at 1023 K, obtained with a heating rate of 10 deg/min, and it has been performed in constant nitrogen flow 18 dm³/min, for 1 h. After pyrolysis materials have been grounded. Powder has been washed with water to neutral pH, to remove as much potassium from it, as possible. Then all materials have been soaked with HCl in concentration of 0.1 mol/dm³ for 19 h, and washed with water again to neutral pH.

Adsorbing abilities have been tested by volumetric adsorption of CO₂ method at 313 K by HIDEN ISOHEMA device. Adsorption of CO₂ has been measured in high pressure conditions, although it has been uptake at 1 bar pressure, which has been considered as the most important because of conditions, in which, according to the project assumptions, our sorbents will be used. Specified surface area (S_{BET}) of produced materials has been calculated with BET method, according to isotherms of adsorption and desorption of liquid nitrogen in 77 K. The total pore volume was estimated from N₂ adsorption data as volume of liquid N₂ at p/p₀ equal to 0.99. Micropore volume has been calculated by DFT method, for pores smaller than 2 nm in diameter.

3 Results and Discussion

On the basis of values are presented in Table 2. It was found that increasing mass ratio between molasses and TiO₂ in ACT1, ACT4, decreases the specific surface area, and disturbs porous structure of tested materials. Using activation agent increases vastly these parameters, what is noticeable in AC1, ACT5 and ACT6. Producing process of ACT6 also required using KOH. Addition of TiO₂ was 4 times bigger, than in ACT5, considering the weight. This is possibly reason of decreasing surface area of ACT6.

Main task of obtained materials is to adsorb CO₂, so the great meaning had adsorption abilities. Figure 1 presents high pressure adsorption isotherms of all the materials. ACT5 uptake maintained at the similar level, comparing to AC1 material. Adding this amount of TiO₂ decreases the CO₂ uptake insignificantly. The rest of ACT materials were able to adsorb much smaller amount of CO₂. In lower pressure, up to 1.4 bar, presented in Fig. 2, it is noticeable that ACT1 and ACT5, had very

Table 2 Properties of AC surface

Name of the sample	S _{BET} (m ² /g)	Total pore volume (cm ³ /g)	Micropore volume (cm ³ /g)
AC1	1985	0.9424	0.7138
ACT1	523	0.2454	0.1859
ACT4	298	0.1561	0.1089
ACT5	1728	1.762	0.5999
ACT6	385	0.4501	0.1006

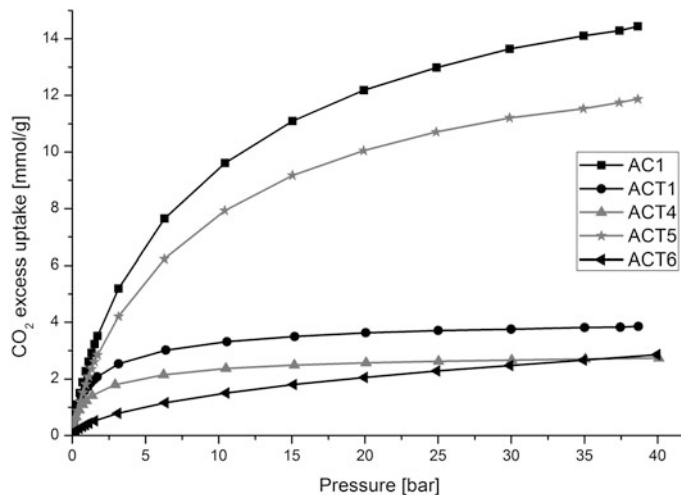


Fig. 1 High pressure CO₂ adsorption diagram

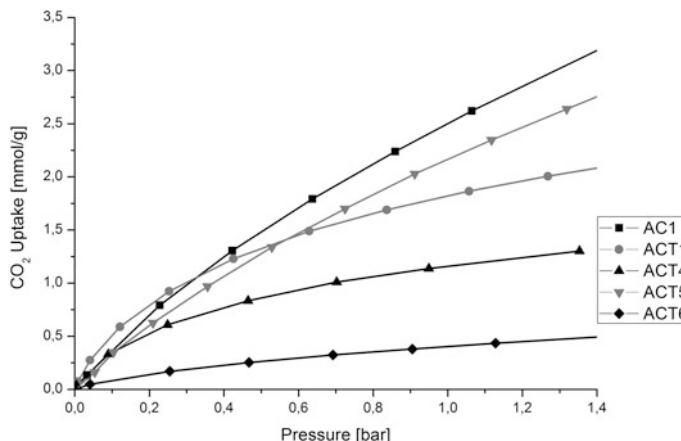


Fig. 2 CO₂ adsorption at pressure around 1 bar

promising isotherm. Until the pressure crosses 0.30 bar the adsorption of ACT1 was higher, than in case of AC1. The bigger the pressure though, the uptake abilities of ACT1 got worst. At 1 bar pressure the best adsorbing turned out to be AC1.

DFT method has been used, and the pore distribution curves have been drawn. Figure 3 has been created for AC1 and ACT5 materials, which curves are quite similar, and most of the pores had measured size in range between 0 and 2 nm diameters. It is also noticeable, that ACT5 allowed obtaining much more mesoporous structures, as its curve stays raised over abscissa periodically, when the AC1 curve stays flat very near the axis. Figure 4 presents pore size distribution in ACT1,

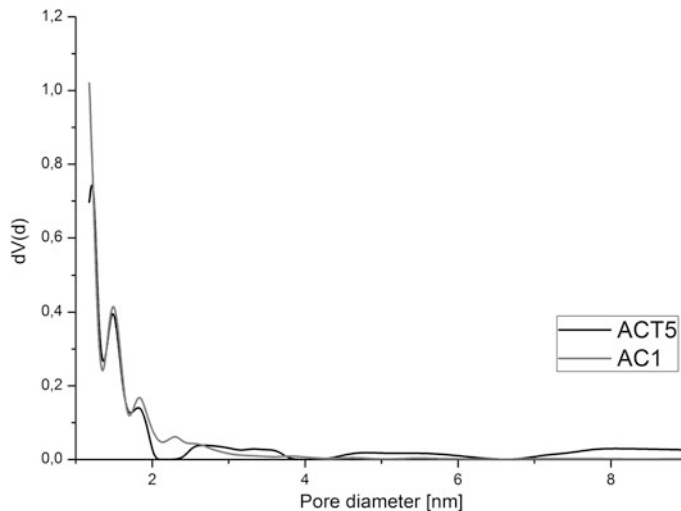


Fig. 3 Pore size distribution curves of AC1—gray and ACT5—black

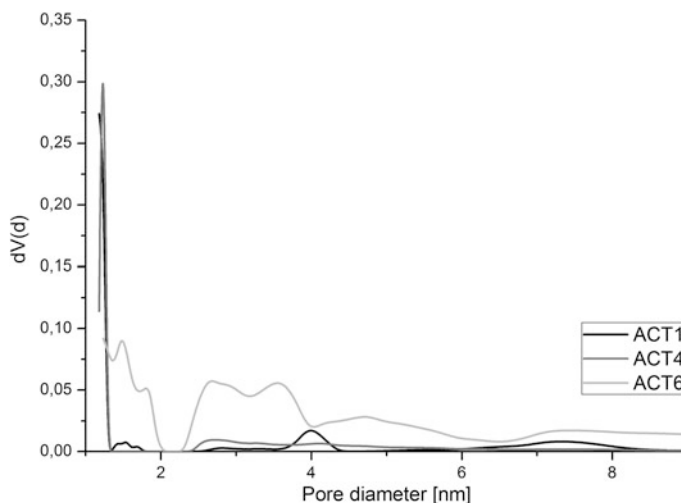


Fig. 4 Pore size distribution for ACT1—black, ACT4—grey and ACT6—light grey

ACT4 and ACT6. Among these materials the higher total pore volume is a property of ACT6, which finds confirmation in this diagram. In range up to 2 nm, some micropore arrays are noticeable. Figure 4 also confirms porous ACT6 advantage regarding to ACT1 and ACT4. The curve shows that ACT6 has mesoporous structure as well. Also here it is noticeable, that material containing KOH and TiO₂, allows obtaining more mesoporous structure, which is indicated by curve periodically raised over abscissa.

4 Conclusions

Series of tests, that was provided confirmed, that molasses is very efficient carbon source. Sorbents based on molasses are very effective, and it is plausible to obtain micropore structure, using simple producing process. It has been also proved, that using KOH, as activation agent, improves specified surface area, and develops highly advanced porous structures. Adding TiO_2 to carbons activated with KOH slightly decreases its adsorbing abilities, and blocks micropore forming, but on the other hand makes them useful as photocatalyst.

Further tests still needs to be done to prove relations between surface area, micropore volume, and the adsorption abilities of produced sorbents. Nevertheless research that was made determinates direction of future research, and properties, which improving will be the objective for the future.

Acknowledgments Project funded by the Norwegian funds, under the Polish-Norwegian Cooperation Research carried out by the National Centre for Research and Development 2009-2014. nr Pol-Nor/237761/98/2014.

References

1. S. Ahmad, Ch. Li, G. Dai, M. Zhan, J. Wang, S. Pan, C. Cao, *Soil Tillage Res.* **106**, 54–61 (2009)
2. M. Asiltürk, Ş. Şener, TiO_2 -activated carbon photocatalysts: preparation, characterization and photocatalytic activities. *Chem. Eng. J.* **180**, 354–363 (2012)
3. Q. Yang, Y. Liao, L. Mao, Kinetics of photocatalytic degradation of gaseous organic compounds on modified TiO_2/AC composite photocatalyst. *Chin. J. Chem. Eng.* **20**, 572–576 (2012)
4. G. Li, A. Puma, D. Bono, J.G. Krishnaiah, Collin, Preparation of titanium dioxide photocatalyst loaded onto activated carbon support using chemical vapor deposition: a review paper. *J. Hazard. Mater.* **157**, 209–219 (2008)
5. K. Ayyogari, P. Sidhya, M.K. Pandit, *Int. J. Agric. Environ. Biotechnol.* **7**(1), 145–155 (2014)
6. O. Ioannidou, A. Zabaniotou, *Renew. Sustain. Energy Rev.* **11**, 1966–2005 (2007)
7. J. Sreńcek-Nazzal, W. Kamińska, B. Michalkiewicz, Z.C. Koren, *Ind. Crops Prod.* **47**, 153–159 (2013)
8. K.Y. Foo, B.H. Hameed, Porous structure and adsorptive properties of pineapple peel based activated carbons prepared via microwave assisted KOH and K_2CO_3 activation. *Microporous Mesoporous Mater.* **148**, 191–195 (2012)
9. K.Y. Foo, B.H. Hameed, Utilization of rice husks as a feedstock for preparation of activated carbon by microwave induced KOH and K_2CO_3 activation. *Bioresour. Technol.* **102**, 9814–9817 (2011)
10. W. Zhang, Z. Huang, Z. Guo, C. Li, F. Kang, *Mater. Lett.* **1868–1870**, 64 (2010)
11. Y. Xia, B. Gates, Y. Yin, Y. Lu, *Adv. Meter* **693–713**, 12 (2000)
12. K.T. Lee, J.C. Lytle, N.S. Ergang, S.M. Oh, A. Stein, *Adv. Funct. Meter* **547–556**, 15 (2005)
13. D. Cao, P. Feng, J. Wu, *Nano Lett.* **1489–1492**, 4 (2004)
14. S.V. Mayani, V.J. Mayani, K.P. Sueng, S.W. Kim, *Mater Lett.* **82**, 120–123 (2012)
15. S.V. Mayani, V.J. Mayani, S.H. Ko, S.K. Lee, *Adsorption* **19**, 251–257 (2013)

Part XI
Bio-Assessment and Toxicology

Influence of the *Staphylococcus Aureus* Bacteria Cells on the Zeta Potential of Graphene Oxide Modified with Alumina Nanoparticles in Electrolyte and Drinking Water Environment

A. Jastrzebska, E. Karwowska and A. Olszyna

Abstract The aim of this study was to describe the different aspects of the modification of surface charge of graphene oxide by deposition of Al_2O_3 nanoparticles on its surface. The novel reduced graphene oxide/ Al_2O_3 nanocomposites were evaluated as an adsorbent for *Staphylococcus aureus* bacteria cells in electrolyte and drinking water environment. The zeta potential of GO flakes, Al_2O_3 nanoparticles and RGO/ Al_2O_3 nanocomposite was investigated alone and in the presence of bacteria cells with a special emphasis on the analysis of the zeta potential curves. Our obtained results indicate that the chemical composition of water environment have a significant influence on the electrostatic interactions between sorbent and bacteria. In most cases, the adsorption of bacteria onto adsorbent surface changed its surface charge to similar to adsorbed cells. However, by taking into consideration the sensitiveness and variability of living system such as bacteria cell, we observed that the phenomenon of adsorption (i.e. the physical interactions with sorbent surface) also changed the surface charge of bacteria cells themselves.

A. Jastrzebska (✉) · A. Olszyna

Faculty of Material Science and Engineering, Warsaw University of Technology,

Woloska 141, 02-507 Warsaw, Poland

e-mail: agnieszka.jastrzebska@inmat.pw.edu.pl

A. Olszyna

e-mail: agnieszka.jastrzebska@inmat.pw.edu.pl

E. Karwowska

Faculty of Environmental Engineering, Warsaw University of Technology,

Nowowiejska 20, 00-653 Warsaw, Poland

e-mail: karwowska@is.pw.edu.pl

1 Introduction

Microbial adsorption to solid surfaces plays a fundamental role in bioengineering, environmental protection as well as water filtration [1]. So far, graphene and graphene oxide attracted great scientific attention as a potential effective sorbents for removal of heavy metal [2], chlorophenols [3], polycyclic aromatic hydrocarbons [4], trace peptide toxins [5], acrylonitrile, p-toluenesulfonic acid, 1-naphthalenesulfonic acid and methyl blue [6]. It is generally accepted that solid surfaces in natural environments often carry their own electrostatic charge [7, 8]. Theory of the charged surface sights developed for the metal oxide particles can also be adjusted to explain the zeta potential of graphene oxide surface. It is known that the zeta potential of graphene and graphene oxide dispersions is pH dependent [9] as well as zeta potential of bacteria cells [10]. It is also expected that filtration materials possessing the greatest difference in zeta potential sign from the bacteria would have the best bacterial adsorption [11] and it was found that adsorption of bacteria to inorganic porous media decreases as their negative zeta potential increases [12]. Other reported studies were only devoted to materials such as natural clay. These experiments have shown that the presence of clay particles in the filtration media influences the adhesion of bacteria [13]. High adhesion to clay was explained by electrostatic adhesion between positively charged groups, on the edges of the crystal lattice of the clay particles, and the negatively charged bacteria [14, 15].

According to our best knowledge novel reduced graphene oxide/Al₂O₃ (RGO/Al₂O₃) nanocomposites haven't been evaluated yet as adsorption media for bacteria cells (*Staphylococcus aureus*) removal from drinking water. Also, the aim of this study was to describe the differences in modification of the surface charge of the graphene oxide (GO) by Al₂O₃. In our study, we have chosen Al₂O₃ nanoparticles due to the lack of biocidal properties [16–19].

2 Results and Discussion

The dry sol-gel synthesis method of RGO(5.7 %)/Al₂O₃(19 ± 5 nm) nanocomposite characterized by 242.4 m²/g BET specific surface area utilized metal organic aluminium compound (triethylaluminium) as Al₂O₃ precursor and was described elsewhere [20].

Due to allow observing electrical charge change phenomenon on the surface of the analyzed nanopowders and bacterial cells, the zeta potential measurements were performed separately for three independent (separate) experimental systems such as: (i) suspensions of GO, Al₂O₃ and RGO/Al₂O₃ in electrolyte solution (0.85 % NaCl) or drinking water, (ii) suspensions of *Staphylococcus aureus* cells in electrolyte solution or drinking water, (iii) suspensions of GO, Al₂O₃ and RGO/Al₂O₃ in presence of bacteria cells in electrolyte solution or drinking water. The Zetasizer Nano ZS particle characterization system (Malvern) equipped with an MPT-2

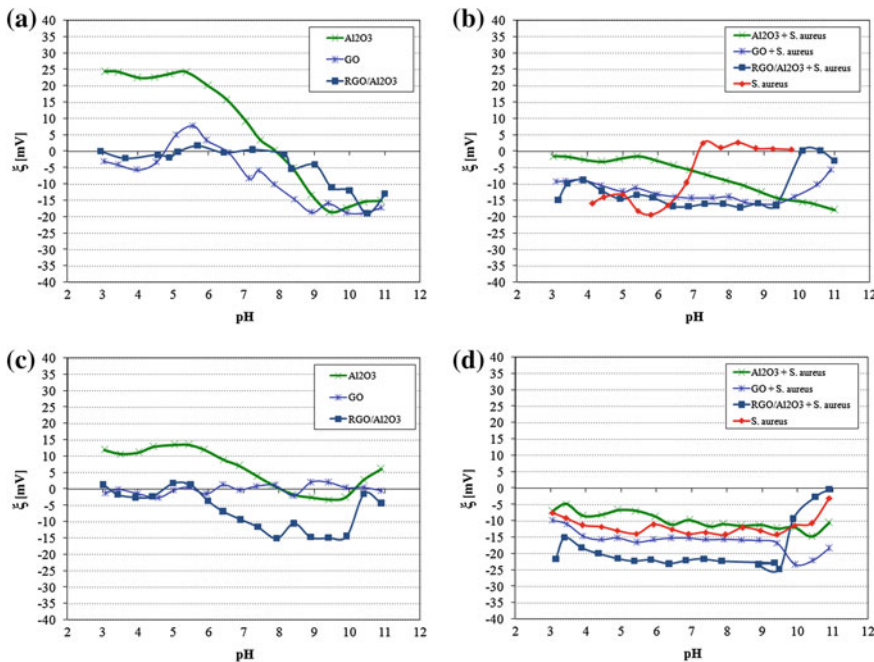


Fig. 1 Zeta potential curves obtained for GO flakes, Al_2O_3 nanoparticles and RGO/ Al_2O_3 composite suspended in electrolyte solution (a) and drinking water environment (c) as well as suspended in the presence of *S. aureus* cells suspended in electrolyte solution (b) and drinking water environment (d)

automatic titrator and titration media degasser, was used to measure the zeta potential (ζ) as a function of pH (from 3 to 11). The 0.1 M solutions of sodium hydroxide (NaOH) and hydrochloric acid (HCl) were used as a titration media to automatically adjust the pH values.

The zeta potential investigations results obtained for analyzed suspensions are presented in Fig. 1. They indicate that the zeta potential of the analysed nanomaterials was pH-dependent, except that of pure GO flakes suspended in drinking water environment which was characterized by ζ close to 0 value. However, modification of its surface by Al_2O_3 nanoparticles (NPs) changed the surface charge of resulted RGO/ Al_2O_3 nanocomposite to mainly negative, which benefits for adsorbing cations (Fig. 1c). In electrolyte solution, in acidic environment, GO possess ζ close to 0 value. Then, it changed to more negative in neutral and basic environment. Modification of its surface by Al_2O_3 NPs shifted the surface charge of RGO/ Al_2O_3 nanocomposite to less negative in neutral environment (Fig. 1a). The investigated *S. aureus* cells in electrolyte solution, in acidic environment, possess negative surface charge which changes to slightly positive in basic environment (Fig. 1b). On the other hand, in drinking water environment, the ζ of *S. aureus* cells is negative in the whole investigated pH range.

It is generally expected that the adsorption of bacteria onto adsorbent surface should change its surface charge to similar to adsorbed cells by simple covering of adsorbent surface. However, when taking into consideration the sensitiveness and variability of living system such as bacteria cell, it should be considered that the phenomenon of adsorption (i.e. the physical interactions with sorbent surface) may also change the surface charge of the cell itself. Our investigations results confirmed these assumptions.

The adsorption of *S. aureus* cells onto the surface of investigated nanomaterials is most visible for drinking water environment as dispersion medium (Fig. 1d). The observed changes in ζ of Al_2O_3 and $\text{RGO}/\text{Al}_2\text{O}_3$ were the result of covering of their surface by *S. aureus* cells which subsequently resulted in adjusting of their ζ to that of *S. aureus*. Moreover, the general lowering of ζ (much below ζ of *S. aureus* pure suspension) was observed for $\text{RGO}/\text{Al}_2\text{O}_3$ nanocomposite. This suggests some of the changes in surface charge characteristics of *S. aureus* cells as a result of adsorption process. These mentioned changes are also clearly observed for the absorption of *S. aureus* in electrolyte solution (Fig. 1b). The surface charge of *S. aureus* cells in the neutral and slightly basic environment changed dramatically during adsorption on the surface of $\text{RGO}/\text{Al}_2\text{O}_3$ nanocomposite from slightly positive to highly negative. On the other hand, it can be seen that the adsorption of *S. aureus* cells to Al_2O_3 NPs didn't changed the overall shape of pH curve of Al_2O_3 NPs. However, the lowering of ζ of Al_2O_3 NPs was observed.

3 Conclusion

Zeta potential of GO flakes, Al_2O_3 nanoparticles and $\text{RGO}/\text{Al}_2\text{O}_3$ nanocomposite were investigated alone and in the presence of *S. aureus* cells with a special emphasis on the analysis of the zeta potential curves as a function of pH. Our obtained results indicate that the chemical composition of water environment have a significant influence on the electrostatic interactions between sorbent and bacteria. In most cases, the adsorption of bacteria onto adsorbent surface changed its surface charge to similar to adsorbed cells. However, by taking into consideration the sensitiveness and variability of living system such as bacteria cell, we observed that the phenomenon of adsorption (i.e. the physical interactions with sorbent surface) also changed the surface charge of bacteria cells themselves.

The adsorption of *S. aureus* cells onto the surfaces of investigated nanomaterials depended not only by their surface electrical properties but also bacterial cells surface charge. The surface charge is formed separately on the sorbent surface and bacteria cell surface, and changes significantly in the real time during sorption process progress. In our opinion, such an approach is of high importance in the development of modern sorbent systems.

Acknowledgments The study was accomplished thanks to the funds allotted by the National Science Centre within the framework of the research projects No: UMO-2013/09/D/ST8/04001

and 504P/1090/0856/001. This work has also been supported by the European Union in the framework of European Social Fund through the Warsaw University of Technology Development Programme, realized by Center for Advanced Studies.

References

1. E. Kłodzińska, M. Szumski, E. Dziubakiewicz, K. Hrynkiewicz, E. Skwarek, W. Janusz, B. Buszewski, Effect of zeta potential value on bacterial behavior during electrophoretic separation. *Electrophoresis* **31**(9), 1590–1596 (2010)
2. X. Deng, L. Lu, H. Li, F. Luo, The adsorption properties of Pb(II) and Cd(II) on functionalized graphene prepared by electrolysis method. *J. Hazard. Mat.* **183**, 923–930 (2010)
3. Q. Liu, J. Shi, L. Zeng, T. Wang, Y. Cai, G. Jiang, Evaluation of graphene as an advantageous adsorbent for solid-phase extraction with chlorophenols as model analytes. *J. Chromatogr. A* **1218**, 197–204 (2011)
4. H. Zhang, W.P. Low, H.K. Lee, Evaluation of sulfonated graphene sheets as sorbent for micro-solid-phase extraction combined with gas chromatography–mass spectrometry. *J. Chromatogr. A* **1233**, 16–21 (2012)
5. X. Hu, L. Mu, J. Wen, Q. Zhou, Immobilized smart RNA on graphene oxide nanosheets to specifically recognize and adsorb trace peptide toxins in drinking water. *J. Hazard. Mater.* **213–214**, 387–392 (2012)
6. T. Wu, X. Cai, S. Tan, H. Li, J. Liu, W. Yang, Adsorption characteristics of acrylonitrile, p-toluenesulfonic acid, 1-naphthalenesulfonic acid and methyl blue on graphene in aqueous solutions. *Chem. Eng. J.* **173**, 144–149 (2011)
7. J.T. Gannon, Y. Tan, P. Baveye, M. Alexander, Effect of Sodium chloride on transport of bacteria in a saturated aquifer material. *Appl. Environ. Microbiol.* **57**, 2497–2501 (1991)
8. D.C. Ellwood, C.W. Keevil, P.D. Marsh, C.M. Brown, J.N. Wardell, Surface-associated growth. *Philos. Trans. R. Soc. Lond. B Biol. Sci.* **297**, 517–532 (1982)
9. D. Li, M.B. Muller, S. Gilje, R.B. Kaner, G.C. Wallace, Processable aqueous dispersions of graphene nanosheets. *Nat. Nanotechnol.* **3**, 101–105 (2008)
10. A.T. Poortinga, R. Bos, W. Norde, H.J. Busscher, Electric double layer interactions in bacterial adhesion to surfaces. *Surf. Sci. Rep.* **47**, 1–32 (2002)
11. M.A. Scholl, A.L. Mills, J.S. Herman, G.M. Hornberger, The influence of mineralogy and solution chemistry on the attachment of bacteria to representative aquifer materials. *J. Contam. Hydrol.* **6**, 321–336 (1990)
12. C. Krekeler, H. Ziehr, J. Klein, Influence of physicochemical bacterial surface properties on adsorption to inorganic porous supports. *Appl. Microbiol. Biotechnol.* **35**, 484–490 (1991)
13. F. Huysman, W. Verstraete, Water-facilitated transport of bacteria in unsaturated soil columns: influence of cell surface hydrophobicity and soil properties. *Soil Biol. Biochem.* **25**, 83–90 (1993)
14. F. Huysman, W. Verstraete, Effect of cell surface characteristic on the adhesion of bacteria of to soil particles. *Biol. Fertil. Soil.* **16**, 21–26 (1993)
15. M. Fletcher, G.I. Loeb, Influence of substratum characteristics on the attachment of a marine pseudomonas to soil surfaces. *Appl. Environ. Microbiol.* **37**, 67–72 (1979)
16. A. Jastrzębska, E. Karwowska, A. Tabernacka, P. Mosdorf, P. Polis, P. Kurtycz, A. Olszyna, A.R. Kunicki, New non phyto- and eco-toxic alumina-stabilized silver and praseodymium nanoparticles. *Int. J. Appl. Ceram. Technol.* 1–9 (2012). doi:10.1111/j.1744-7402.2012.02834.x
17. A. Jastrzębska, E. Radziun, M. Rosłon, A. Kunicki, A. Olszyna, J. Dudkiewicz-Wilczyńska, E. Anuszecka, E. Karwowska, In vitro assessment of antibacterial properties and cytotoxicity of Al_2O_3 -Ag nanopowders. *Adv. Appl. Ceram.* **110**, 353–359 (2011)

18. A.M. Jastrzębska, A.R. Kunicki, A.R. Olszyna, E. Karwowska, Al_2O_3 –Ag nanopowders—new method of synthesis, characterization and biocidal activity. *Adv. Appl. Ceram.* **110**, 108–113 (2011)
19. E. Radziun, J.D. Wilczynska, I. Ksiazek, K. Nowak, E.L. Anuszewska, A. Kunicki, A. Olszyna, T. Zabkowski, Assessment of the cytotoxicity of aluminium oxide nanoparticles on selected mammalian cells. *Tox. In Vitro* **25**(8), 1694–1700 (2011)
20. A.M. Jastrzębska, J. Jureczko, A.R. Kunicki, A.R. Olszyna, New reduced graphene oxide/alumina ($\text{RGO}/\text{Al}_2\text{O}_3$) nanocomposite: innovative method of synthesis and characterization. *Int. J. Appl. Ceram. Technol.* 1–7 (2013)

Part XII
Air Pollution from Mobile
and Stationary Sources

The State of Art Technique of Pre-ozonation Processes for Intensification of Emission Control from Stationary Sources

Kinga Skalska

Abstract This work demonstrates state of art technique in the field of environmental engineering research, i.e. utilization of ozone for waste gases treatment in power and chemical plants as well as refineries. The special focus is put on the mercury removal due to recently signed Minamata Convention.

1 Introduction

Air pollution has been an issue of public concern even before the beginning of industrial era in nineteenth century. However, the first steps to protect atmosphere from contamination were taken in twentieth century after the series of catastrophic air contamination episodes, like London Great Smog of 1952. This is when the well known emission control technologies were starting to emerge. In general energy industry is responsible for the main part of global air contamination together with mobile sources which contribution still grows. Among many contaminants emitted into the atmosphere from both sources the most important are nitrogen oxides (NO and NO₂ jointly called NO_x) and sulfur dioxide. They are connected with several environmental problems, i.e. acid rains (NO_x and SO₂), photochemical smog, tropospheric ozone etc. Air contamination can also cause severe health problems in human population. Therefore, various emission abatement technologies have already been developed and studies around the world are under way to find new and better solutions. One of such state of the art solutions is pre-ozonation process for the intensification of emission control technologies. Current work will shortly present the progress that has been done in this field in last century (Fig. 1).

K. Skalska (✉)

Faculty of Process and Environmental Engineering, Lodz University of Technology,
Wolczanska 213, 90-924 Lodz, Poland
e-mail: kinga.skalska@p.lodz.pl

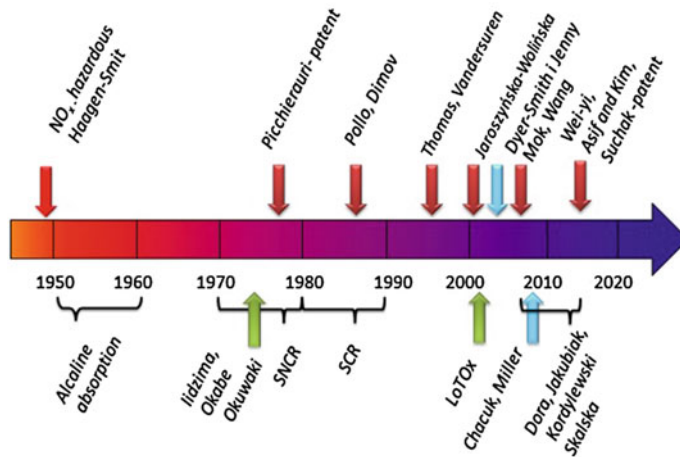
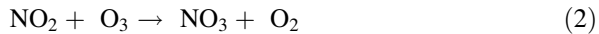
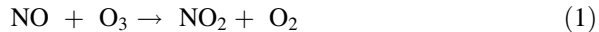


Fig. 1 Timeline of NO_x abatement technologies development

2 NO_x Ozonation

The idea of using ozone to oxidize NO into NO₂ in order to intensify the NO_x removal through absorption process was first patented in 1976 by Picchieraui. At that time the production yield of ozone generators was smaller than nowadays and not sufficient enough for industrial application as a result the idea was not immediately applied to control NO_x emission. The interest in the application of ozone for flue gas treatment did not stop at that point. Since then more patents were issued [1–7] and many research papers were published [8–19]. Dimov in 1986 studied the influence of ozone addition on the alkaline absorption in packed and tray columns. In 2001 the process called Low-Temperature NO_x absorption (LoTOx) won the Kirkpatrick Award. LoTOx enables to obtain 90 % efficiency of NO_x emission reduction [8]. This technology has been already installed in several facilities in the USA, i.e. Medical of College of Ohio; J&L Specialty Steel Midland, PA; Lion Oil Company in Eldorado, AR; Marathon-Ashland Oil in Texas City, TX [20]. The main concept of ozone utilization in flue gases treatment is to increase the ratio NO₂/NO_x in treated gases, because for flue gases from incineration processes this ratio is around 0.05 whereas for flue gases from chemical industry it might be 0.5 or even close to 1. Ozone was used by various authors, including author of this work [16–19] for oxidation of nitrogen oxides NO_x into nitrogen species, i.e. N₂O₅ that has better solubility in water (NO: 0.063 g/L; NO₂: 1.26 g/L; N₂O₅: 500 g/L). It was proven that for the pure NO gas stream the minimal O₃/NO molar ratio needed to convert NO_x into N₂O₅ and HNO₃ is 1.5. However, industrial applications prove that for real off-gases the required molar ratio will be higher (based on off-gas parameters). Presence of ozonation products in flue gases significantly increases NO_x removal rate in the absorption process. Simplified mechanism of the process is as follows:



It involves the main reactions that occur in the complicated NO_x , O_3 , H_2O system. Depending on the process temperature different reactions can become important [21]. This is crucial since off-gases from various stationary sources differ in temperatures. It is noteworthy since O_3 and N_2O_5 decompose at temperature higher than 180 °C.

Flue gases after the pre-ozonation can be treated with different existing and well established emission control technologies, i.e. absorption in water, alkaline or acidic solutions, selective catalytic reduction (SCR), and wet flue gas desulfurization (WFGD) etc. The combination of ozonation processes with SCR, WFGD or absorption were studied by various authors [8–19, 24, 25]. Furthermore, as it has been proved ozone can also be used to oxidize nitrogen oxides and nitrous acid to nitric acid in the liquid phase [22]. This could take place in absorption columns and even in the production process itself [23].

3 Simultaneous Removal of Various Contaminants

Different kinds of air pollutants are emitted from incineration processes used in various industries. Among them SO_2 and NO_x are the most abundant air contaminants in flue gas. But other contaminants are also dangerous. Recently signed (by 122 countries) Minamata Convention puts great interest at the mercury removal from environment. The emission of this heavy metal from coal fired electric power plants has been already regulated in the USA since 2006 (under Clear Air Mercury Rule). The emission limits has been set in several countries already: Germany, Netherlands and USA oscillate around 2–5 $\mu\text{g}/\text{Nm}^3$. Traditionally mercury is removed through: good dedusting, addition of CaBr_2 , addition of active carbon and many others.

Individual treatment strategies result in high investment and operational costs. Efforts are made worldwide to develop emission control technologies capable of removing several pollutants at the same time. As literature and patent survey prove ozone can also be used for elimination of multiple contaminants like: NO_x , SO_2 , Hg , HCl [21, 24, 25]. Oxidized NO_x (NO_2 , NO_3 and N_2O_5) can be easily removed in the WFGD process. In general the results presented in scientific literature and pilot test reports that can be found on the internet [26] suggest that generally ozonation does not influence the SO_2 removal rate, at best enhances it by additional 5 %. In 2011 different solution was described in the work of Wei-yi et al. [25].

They have used pyrolusite solution as a sorbent (a mineral mainly composed of MnO_2). In this process the removal rates reach 82 % for NO and 100 % for SO_2 . Byproducts formed in this process were $Mn(NO_3)_2$ and $MnSO_4$. Wang et al. 24 described removal of such contaminants as NO_x , SO_2 , Hg due to the injection of ozone before the absorption process in 1 % solution of $CaOH$ [24]. In this method the 360 ppm of O_3 were introduced into simulated off-gas stream containing 215 ppm NO, 220 and 50 $\mu g/m^3$ Hg. The removal rates were as follows 97 % NO_x , 100 % SO_2 and 89 % Hg. Recent years have also brought new patents concerning the use of ozone for the intensification of absorption process [1, 4, 6]. One of them describes the method for the simultaneous removal of NO_x and SO_2 from flue gases emitted from incineration processes and chemical processed. NO_x and SO_2 are oxidized by means of ozone and removed in the absorption column [1]. Acids that are formed in this process are neutralized and transferred to a municipal wastewater treatments plant. Whereas Suchak describes a process for simultaneous removal of NO_x , SO_2 , Hg and HCl for industrial flue gases [4].

4 Summary

The concept of ozone application emerged in the late 1970s as a way to intensify NO_x absorption in water and acidic and alkaline solutions. Up to now it evolved into the state of the art technology capable to simultaneously remove various contaminants. Already quite reach literature, patent and application news have surely provided evidence that this solutions should be taken under consideration especially when dealing with numerous contaminants at ones. As it was shortly presented above many variations of the pre-ozonation based emission control technologies exist already.

Due to still quite high costs of ozone generators and high demand for ozone in large scale industrial and chemical plants this method might not be the best solution. However, the opposite situation occurs in the case of small power plants (successful tests were performed at 25 MW boiler), refineries and chemical plants.

Acknowledgments This work was supported by the grant IP2011 049871 founded by Polish Ministry of Science and Higher Education.

References

1. Skelley et al., US 5 316 737 A—process for removing NO_x and SO_2 from exhaust gas. 31.05.1994
2. Suchak et al., EP 2 719 440 A1—method for removing contaminants from exhaust gases by adding ozone. 16.04.2014
3. Tseng et al., US 6 231 824 B1—removal of nitric acid from gas streams. 15.05.2001

4. N. Suchak et al., EP 1 524 023 A1—improved process for the removal of contaminants from gas streams. 20.04.2005
5. S.-C. Hwang et al., EP 1106238A1—process for the removal of nitrogen oxides from gas streams. 13.03.2001
6. N. Suchak et al., EP 1852172A1—removal of contaminants with ozone. 07.11.2007
7. J. Hsieh et al., US7534400B2—wet scrubbing apparatus for controlling NO_x emission. 19.05.2009
8. Anon., Low-temperature NO_x absorption wins top prize. *Chem. Eng. (N.Y.)* **108**(11), 92–93 (2001)
9. M. Asif, W.-S. Kim, Numerical study of NO_x abatement using ozone injection integrated with wet absorption. *Ozone Sci. Eng.* **36**, 472–484 (2014)
10. J. Dora, M.A. Gostomczyk, M. Jakubiak, W. Kordylewski, W. Mista, M. Tkaczuk, Parametric studies of the effectiveness of oxidation of NO by ozone. *Chem. Process Eng.* **30**, 621–634 (2009)
11. M. Jakubiak, W. Kordylewski, The effect of ozone feeding mode on the effectiveness of NO oxidation. *Chem. Process Eng.* **32**(3), 229–239 (2011)
12. J. Jaroszyńska-Wolińska, Ozone application to a two-stage NO removal from waste gases. *Pol. J. Chem. Technol.* **4**, 5–7 (2002)
13. Y.S. Mok, I.S. Nam, Reduction of nitrogen oxides by ozonation-catalysis hybrid process. *Korean J. Chem. Eng.* **21**(5), 976–982 (2004)
14. Y.S. Mok, E.Y. Yoon, Effect of ozone injection on catalytic reduction of nitrogen oxide. *Ozone-Sci. Eng.* **28**, 105–110 (2006)
15. Y.S. Mok, Absorption-reduction technique assisted by ozone injection and sodium sulfide for NO_x removal from exhaust gas. *Chem. Eng. J.* **118**, 63–67 (2006)
16. K. Skalska, J.S. Miller, S. Ledakowicz, Effectiveness of nitric oxide ozonation. *Chem. Pap.* **65** (2), 193–197 (2011)
17. K. Skalska, J.S. Miller, S. Ledakowicz, Kinetic model of NO_x ozonation and its experimental verification. *Chem. Eng. Sci.* **66**(14), 3386–3391 (2011)
18. K. Skalska, J.S. Miller, S. Ledakowicz, a. Intensification of NO_x absorption process by means of ozone injection into exhaust gas stream. *Chem. Eng. Process.* **61**, 69–74 (2012)
19. K. Skalska, J.S. Miller, M. Wilk, S. Ledakowicz, Nitrogen oxides ozonation as a method for NO_x emission abatement. *Ozone Sci. Eng.* **34**, 252–258 (2012)
20. CATC, Using non-thermal plasma to control air pollutants. The Clean Air Technology Centre (2005). EPA-456/r-05-001. <http://www.epa.gov/tnn/catc/dir1/fnonthrm.pdf>
21. Ch. Sun, N. Zhao, Z. Zhuang, H. Wang, Y. Liu, X. Weng, Z. Wu, Mechanism and reaction pathway for simultaneous oxidation of NO_x and SO₂ by ozone determination by in situ IR measurements. *J. Hazard. Mater.* **274**, 376–383 (2014)
22. A. Chacuk, J.S. Miller, M. Wilk, S. Ledakowicz, Intensification of nitrous acid oxidation. *Chem. Eng. Sci.* **62**, 7446–7453 (2007)
23. P. Dyer-Smith, P. Jenny, Application of ozone to avoid the production of nitrous gases (NO_x) during industrial nitrification and oxidation with nitric acid. IAO 17th World Ozone Congress-Strasbourg, 2005, VII.3.11
24. Z. Wang, J. Zhou, Y. Zhu, Z. Wen, J. Liu, K. Cen, Simultaneous removal of NO_x, SO₂ and Hg in nitrogen flow in a narrow reactor by ozone injection: experimental results. *Fuel Process. Technol.* **88**, 817–823 (2007)
25. S. Wei-yi, D. Sang-lan, Z. Shan-shan, S. Shi-jun, J. Wen-ju, Simultaneous absorption of NO_x and SO₂ from flue gas with pyrolusite slurry combined with gas-phase oxidation of NO using ozone. *J. Hazard. Mater.* **192**, 1 (2011)
26. Process Optimization Guidance for Reducing Mercury Emissions from Coal Combustion in Power Plants, Geneva, Switzerland, November 2010. http://www.chem.unep.ch/mercury/Sector-Specific-Information/Coal_combustion.htm

Part XIII
Transport of Air Pollutants

The Energy Performance Model of Mechanical and Natural Ventilation

Richard Nagy, Danica Košičanová and Jan Lojkovics

Abstract The paper deals with the energy efficiency of the ventilation systems (ventilation units) in different design alternatives (with heat recovery, without recovery, effective fans, etc....). The alternatives of operation of the mechanical and natural ventilation system at intervals during the day are presented. The calculation of the airflow was executed in accordance with laws and standards valid in the EU and Slovakia (EN 15251, EN 13779, STN 730540, etc.). A large potential for energy savings in the Slovak building generally, due to the fact that majority of the buildings were constructed before 1989, before first important requirements for energy performance and savings of building.

1 Introduction

This paper highlights the importance of environmental protection regarding the reduction of energy consumption while keeping the living standard. The aim of article is to examine the effect of mechanical and natural ventilation to energy consumption and building operation. The next task is to specify buildings intended for an unavoidable installation of ventilation unit equipped also with a recuperation system. In the past but also in present time, there is a great interest of quality housing, economical operation of buildings and especially the performance and health of the occupants of buildings in the world. Using high-quality healthy (e.g. natural) materials, mechanical ventilation with heat recovery and air distribution

R. Nagy (✉) · D. Košičanová · J. Lojkovics

Department of Indoor Technologies and Building Services, Civil Engineering Faculty,
Institute of Architectural Engineering, Technical University of Košice, Košice, Slovakia
e-mail: richard.nagy@tuke.sk

D. Košičanová

e-mail: danica.kosicanova@tuke.sk

J. Lojkovics

e-mail: jan.lojkovics@tuke.sk

system (ventilation system) which is suitably selected and also suitably chosen of fresh air volume, ventilation and ultimately the right choice and distribution element can fulfil these requirements. Research on these aspects in the world dedicated to various studies [1].

2 Research Conditions

To produce the heat-load corresponding to fully occupied classroom. Heat source-simulators were placed in the room. Also carbon dioxide concentrations were simulated by 21 CO₂ person-simulators which were placed in the room in breathing zone of sitting person (1.05 m above the floor). All measurements were carried for 2 types of ventilation (natural ventilation and mechanical ventilation) and conditions and results are shown in Table 1.

3 Heat Recovery Conditions

Indoor air quality in the facility significantly improves that humidity is maintained at a low value and the interior is fed heated (or cooled in summer) fresh filtered air. Continuous ventilation reduces the relative humidity, and thus relieves the ideal conditions for the proliferation of mites and mold spores. It is ideal for asthma, allergies, and problems of radon. In cases of non-use complex ventilation system can be fitted to any room separate recuperation units. Such a system provides ventilation without energy loss and prevents the formation of mold and dust mites [2]. The principle of heat recovery is presented in Fig. 1.

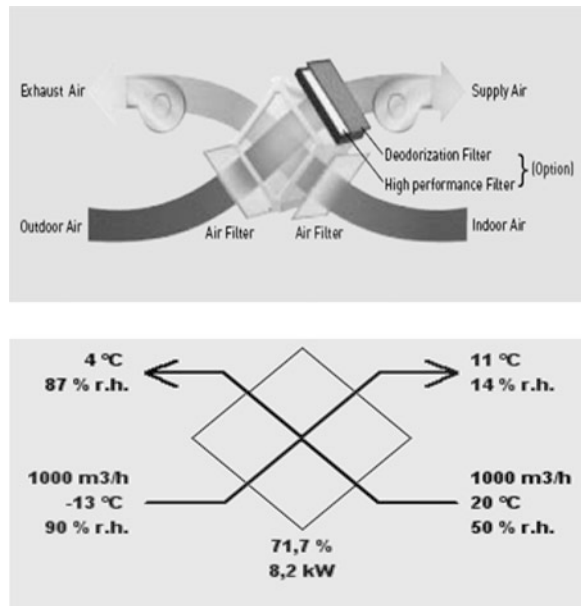
4 Energy Calculation Conditions

Wind, humidity and temperature conditions for calculations for heating period (Standards STN 73 0540-2012, STN EN 12 831, STN EN 15251): wind region 1, wind country coefficient B = 9 Pa^{0.67}, temperature region 2, outdoor design

Table 1 Conditions of research for 2 types of ventilation

Ventilation system	Ventilation rate q _{TOT} (l/s)	Average supply air temperature (°C)	Average supply air humidity (%)	Average CO ₂ concentration (ppm)
Natural ventilation	70	18–22	65	1600
Mechanical ventilation	278	20	60	800

Fig. 1 Total ventilation heat recovery unit scheme—principle and main values of humidity and temperature (before humidification of supply air)



temperature $\Theta_{ae} = -13 \text{ }^{\circ}\text{C}$ (Kosice city), outdoor design temperature $\Theta_e = -13 \text{ }^{\circ}\text{C}$, outdoor air relative humidity $\varphi_{ae} = 85\text{--}90 \text{ \%}$, average indoor space temperature for heating $\Theta_{ai} = 20 \text{ }^{\circ}\text{C}$, heating damped indoor air temperature drop to 10 K, relative humidity of the indoor air φ_{ai} in the space 60 % (after humidification) [3–5].

4.1 System Without Heat Recovery Ventilation—Calculation

The total heat loss for the designed space is divided to the loss of transmission and ventilation. Heat loss by transmission $\Phi_p = 1950 \text{ W}$ in full the convection heating (heating tackled a project), therefore not included in the calculation. Ventilation heat losses by ventilation $\Phi_{va} = 11 220 \text{ W}$ (total ventilation air flow $1000 \text{ m}^3/\text{h}$, design temperature before the heater $-13 \text{ }^{\circ}\text{C}$ and after heater $20 \text{ }^{\circ}\text{C}$). The total quantity of energy per year represents a value in (1a, b):

$$E_{uk,a} = \Phi_{uk} \cdot 24 \cdot d \cdot \varepsilon \cdot [(\Theta_{is} - \Theta_{es}) / (\Theta_i - \Theta_e)] = 97 \text{ GJ/heating period} \quad (1a)$$

$$\begin{aligned} E_{uk,a} &= \Phi_{uk} \cdot 24 \cdot d \cdot \varepsilon \cdot [(\Theta_{us} - \Theta_{es}) / (\Theta_i - \Theta_e)] \cdot 3.6 \times 10^{-3} \\ &= 27 131 \text{ kWh/heating period} \end{aligned} \quad (1b)$$

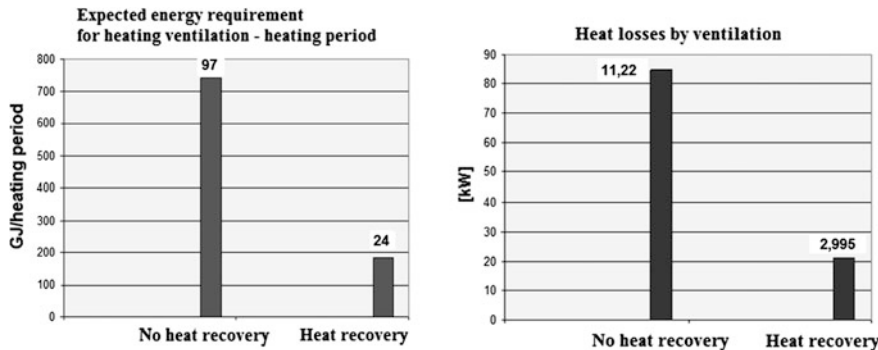


Fig. 2 Graphical comparison of the estimated energy requirement and heat loss results before and after the proposed heat recovery (distinction present of heat recovery performance)

4.2 System with Heat Recovery Ventilation—Calculation

Total heat loss to the room designed for single transmission losses and ventilation losses. Heat loss by transmission $\Phi_p = 1950$ W in full the convection heating (heating project solution) is not included in the calculation. Heat losses by ventilation heat losses $\Phi_{vb} = 2995$ W (total ventilation air flow 1000 m³/h, design temperature before the heater 11 °C and after heater 20 °C, the average efficiency of heat recovery 70–75 %). The total quantity of energy per year represents a value in (2a, b):

$$E_{uk,b} = \Phi_{uk} \cdot 24 \cdot d \cdot \varepsilon \cdot ((\Theta_{is} - \Theta_{es}) / (\Theta_i - \Theta_e)) \cdot 3.6 \times 10^{-3} = 24 \text{ GJ/heating period} \quad (2a)$$

$$E_{uk,b} = \Phi_{uk} \cdot 24 \cdot d \cdot \varepsilon \cdot ((\Theta_{is} - \Theta_{es}) / (\Theta_i - \Theta_e)) \cdot 3.6 \times 10^{-3} \\ = 6705 \text{ kWh/heating period} \quad (2b)$$

These calculations are also possible to simulate in software (Ansys) for more accurately results or for more results in time (per day, per week, etc.) [6]. Graphical comparison of the estimated energy requirement and heat loss results before and after the proposed heat recovery are presented in Fig. 2. The total energy consumption of ventilation without heat recovery equipment is 4 times larger value than with heat recovery equipment. The necessary values are observed in heat losses by ventilation. Also it is given by mathematical dependence in formulas.

5 General Preliminary Conclusions

Standard operation of indoor spaces is characterised by fluctuations and balance of indoor environmental loading, which has been taken into account and energy performance (energy savings, energy losses). From this reason it is necessary to apply sensors of the temperature, humidity and CO₂ concentration in rooms with staying of persons in order to ensure sufficiently the acceptable indoor air quality. There is a real assumption that application of the proper measuring and control technology can reduce a minimum value of air exchange because the ventilation technology will be able to ensure the required air quality also by means of the reduced air exchange.

Acknowledgments This work was funded by project VEGA 1/0748/11 Theoretical and experimental analysis of Building services and HVAC systems from the point of view of microbiological risk and regarding to effective use of renewable sources.

References

1. P. Kapalo, A. Pauliková, C. Muntea, F. Domnița, Evaluation of ventilated rooms. In: *Știința modernă și energia: Producerea, transportul și utilizarea energiei*
2. T. Karimipanah, M. Sandberg, H.B. Awbi, A comparative study of different air distribution systems in a classroom. In: Proceeding of International Conference on Indoor Air Quality and Climate. Roomvent, pp. 1013–1018
3. STN 73 0540–2013. Thermal protection of buildings. Thermal performance of buildings and components
4. STN EN 15251-2007. Indoor environmental input parameters for design and assessment of building energy performance regarding to indoor air quality, thermal environment, lighting and acoustics
5. STN EN 12 831. Method for design and calculation of thermal power
6. T. Brestovič, N. Jasminská, Software support development for numerical solution of Ansys CFX. *Acta mechanica et automatica*. 7(4), 215–221 (2013). ISSN 1898-4088

Part XIV

Environment-Friendly Construction

and Development

How to Refurbish ‘80s *Brutalist Architecture*, Turning It into NZEB: The Case Study of the High School “Enrico Fermi” in Muro Lucano (Potenza, Italy)

Francesco Paolo R. Marino and Filiberto Lembo

Abstract The brutalist *architecture* of the ‘70s and ‘80s has the responsibility to have promoted the creation of buildings that, to better adhere to the poetics of exposed concrete, have often overlooked any principle of environment-Friendly quality. Many buildings, as this case study, a school built after the 1980s earthquake in Basilicata, as USAID gift, in Paul Rudolph’s style, have the exterior walls made in exposed concrete, without any type of insulation and lacking of flashings, but of downpipe too, so as to resemble, now, a picturesque ruin; have roofing systems wrongly designed; windows partly insufficiently sized to ensure natural lighting, but partly without any protection against dazzling; internal walls not performing acoustic performances fixed by Standards, and all grater spaces (atrium and corridors, auditorium, sports hall) with reverberation time many times the standard value. The building envelope disperses 50 kWh/m³ year, so to be placed in the worst performance classes of actual Italian thermal rules. Becoming the conditions of use and management increasingly heavy and almost unbearable, this study detected the strategies and solutions by means of which to resolve the design faults, transforming the building in a NZEB eco-Friend, which produces from renewable sources the energy required for its necessities, recovering its original appearance and formal configuration.

F.P.R. Marino (✉) · F. Lembo

School of Engineering, University of Basilicata, Viale dell’Ateneo Lucano n.10,
85100 Potenza, Italy

e-mail: francesco.marino@unibas.it

F. Lembo

e-mail: filiberto.lembo@unibas.it

1 Introduction

On the evening of November 23, 1980, an earthquake of magnitude 6.9 on the Richter scale struck the Campania and Basilicata regions, causing more than 2,900 deaths, 8,850 injuries and more than 280,000 homeless. Among the Government Agencies that moved more decisively to bring aid to people affected by the earthquake, it was the *United States Agency for International Development* (USAID): the United States Congress appropriated a total of more than \$70 million, of which \$51.4 million were used in the design and construction or re-construction of 28 school buildings in 12 municipalities in the Campania and Basilicata regions, to be reconstructed in a maximum of 45 months. In Basilicata, the school buildings were identified in 3 municipalities: Picerno (Higher Technical Institute "Albert Einstein") [1]; Muro Lucano (Scientific High School "Enrico Fermi", examined in this report); Rionero in Vulture (Institute Of Higher Education "Giustino Fortunato") [2]. The three buildings designed at the same time and by the same *équipe* (Interplan Design Studio of Naples, professor's architects Alberto Izzo and Camillo Gubitosi, in cooperation with the firm Blurock Partnership, Newport Beach, California) and realized, after public contract, by the same enterprise, have the same characteristics and the same defects and suffer from the same pathologies.

2 Research Subject

The school of Muro Lucano is located in a large plot of 17,350 m², 2.5 km from the city center, in an area with average gradient of 30 % to the South, and then very sunny, with an altimetry variable between 580 and 610 m above sea level. From the typological point of view, the building follows a "plate" and "functional units" scheme. The building, which has a total net area of 3,383 m², has two floors in the South (normal classrooms and library) (see Photo 1) and one in the North (Gym and special classrooms for labs) (see Photos 2 and 3) (under which, there is a basement, dug but



Photo 1 View of South elevation

Photo 2 Northern view of the Gym



Photo 3 Exterior view of the laboratories



not used). In the center, a double-height atrium-corridor creates a Le Corbusier's *promenade architéctonique*, involving the library in the din of the hall (see Photos 4, 5 and 6).

The volumetric approach is unequivocally inspired by the '60s architecture of Paul Rudolph, in heavy overhangs projections and sculpted openings, with windows backward from the line of façades.

These are the years in which the *brutalism* goes so out of fashion, by pushing designers to propose exposed concrete surfaces both inside and outside, thereby not complying with the rules, while existing at the time, about the risk of condensation related to thermal bridges and energy consumption (U from 2.74 to 3.06 and up to 3.43 W/m² K, leakage through the envelope 50 kWh/m³); the reverberation time (more than 8 s in the Gym, 2 s in the hallway of classrooms, 1.5 s in the Great Hall and in the teachers' lounge) (see Fig. 1); the natural lighting of the rooms (average daylight factor $\eta = 3\%$ required by the standard; 0.89 in the multimedia lab, in the physics

Photo 4 Exterior view of the atrium-library



Photo 5 Internal view of the atrium-library



Photo 6 Internal view of the *upper* atrium



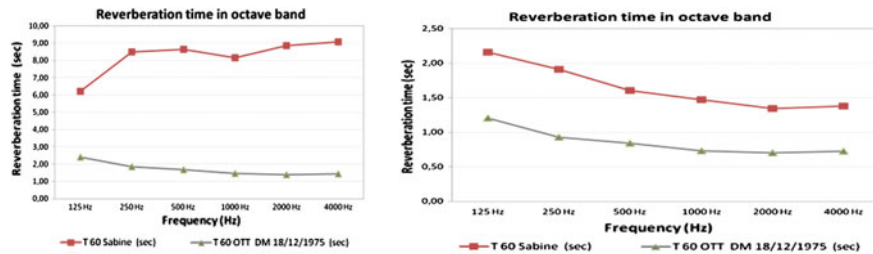


Fig. 1 Reverberation time in the Gym (left) and teachers' lounge (right)

Photo 7 The dripping of water from the rainspouts



laboratory and in the classrooms IB, IIA and IIB; 1.07 in drawing laboratory; 1.48 in the computer lab and science-Great Hall, but, conversely, $\eta = 7.63$ in the atrium, 6.56 in the hallway, 5.27 in the living room of the guardian, 3.47 in the deposits of the gym and 4.03 in the classrooms on the first floor). In each device, such as covers, downspouts, window sills, the correct "rules of art" have been neglected. So, for example, it depends on not following correct "rules of art" the fact of forgetting to put a vapor barrier under slabs of the slopes in coverage ($U = 0.74 \text{ W/m}^2 \text{ K}$), so that those that appear as stains moisture from rain water in some places are also stains moisture from condensation; ensuring that, to the North, the building is black, becoming covered in mold corresponding to the areas where the water is concentrated and drip free from the rainspouts placed several meters in height (see Photo 7); making sure that the flat coverings become "lagoons" for the failure of the slopes or occlusion of the rainspouts

Photo 8 Water-logging on the caretaker's apartment



Photo 9 Slab propped up with steel beams



(see Photo 8); ensuring that the insufficient reinforcement concrete cover of the not-visible structures (bottom intrados of the floor, to the basement not used) compromises their stability so as to make it necessary for them to shoring (see Photo 9).

And yet, the school room have the same endowment of windows facing South, with an unobstructed view of the sky, and those facing North, with tall trees nearby and the slope of the hill looming, which limits the visible portion of the sky (reprehensible, to have set special classrooms and laboratory spaces facing North, precisely because they require greater illumination than the normal classrooms). The lack of any device for the elimination of glare, forces on the south side, students and teachers, to stick on the windows newspapers or sheets of black plastic and, on the north side, condemns them to remain in a state of gloom.

Similar negative evaluations are those that relate to the natural and artificial ventilation of the rooms of the school. Natural ventilation (for permeability of the fixtures and their openness) is low, due to the widespread use of sliding and/or fixed doors. The mechanical ventilation works only in the Gym, while in the classrooms

has been irreparably damaged by vandalism. All this, in a building less than 30 years ago, and despite the clear indications in the legislation for school construction (Ministerial Decree of 18 December 1975 n.18): effect of design errors obviously and easily avoidable, as proof of what often cited in the literature about the impact of the errors on the total design of the causes of pathologies [3].

3 Aim and Content of the Research

A specific method of refurbishment and technological (in particular thermal) upgrade has been identified and such as to be used in all cases of “brutalist” architecture, that in the city of Potenza and its province counts several schools, a psychiatric hospital, and the Court: these buildings, to a greater or lesser extent, have the same problems under examination. The constraint was to obtain a formal result that would preserve the values of the textural image of the building, innovating it only in order to consider the different cultural climate of today, more sensible to the typological importance of the colour and to its content of communication.

The study started with a careful consideration of site environmental data and the orientation of the building. Muro Lucano is located at latitude $40^{\circ}45'12''60$ N, longitude $15^{\circ}29'11''76$ E, 600 m osl, 2,000 degree-days, Climatic Zone D, “Csa” according to the classification of W. Koppen (“*sub-continental temperate*” “*wet summer with very hot (T > 22 °C) dry*”), even according to the ENEA “3F₁”, which brings comfortable 3 months, and more than 6 months cold or very cold. The two hottest months are July and August, with average monthly temperature of 23.4 °C. The coldest months are January (5.1 °C) and February (5.8 °C), followed by December (6.7 °C) and March (8.3 °C). The monthly average outdoor relative humidity is very high: 75.6 % in January, 73.8 % in February, 67.5 % in March, up to a minimum of 59.9 % in August, before rising to 68.5 % in September, gradually increasing up to 78.7 % in December. And it is the average relative humidity: in fact, in the winter months it is not uncommon to encounter, for several consecutive days, an outdoor relative humidity greater than 90 %. This means that if a natural air exchange is carried out, the “clean” air introduced is more humid than air expelled, and the risk of surface and interstitial condensation proportionally increase. The prevailing wind direction is from 240° West-South/West, and the annual average speed of 3.80 m/s. The average annual rainfall is between 600 and 750 mm; analysis of solar irradiation was performed with *Autodesk Ecotect Analysis*, and were built shading masks for all the major surfaces of the façades and roof of building (also expecting to use for the installation of photovoltaic panels), through which, among other things, it has been found that the outdoor theatre on the North side is in the shade for most of the year, except from 10.30 to 16.00 approximately, from March to October. This is the obvious reason that made it unused and abandoned.

After verifying that the *seismic vulnerability* of the building meets the current Italian regulations, the first intervention involved the review of all the surfaces of

exposed concrete deteriorated for carbonation, through the application of a comprehensive care cycle *Sto Cretec* type. The use of parts of the ground excavated, but not used, on the front of the North, was then expected: the places were lit and, for the purposes of fire safety, made accessible through the implementation of an overdraft basement corridor, 2.60 m wide and with two emergency staircases. The destination of these spaces is of Chemistry and Physics laboratories, with its stores, changing rooms and toilets. Their natural lighting, and that of many other parts of the building, including the Great Hall, has been optimized through the provision of *solar tubes*, starting from the coverage of the floor above (see Figs. 2 and 3). The Gym and drawing and computer laboratories located above those already mentioned, were instead provided with sheds, and arranged with openings windows facing north and with the roof surface covered with photovoltaic panels (see Fig. 4).

The building envelope was brought to performance similar to those of a “passive house”, applying 12 cm of EPS with expanded graphite, with a synthetic plaster coats, sandpapered and washed with bark effect, lead-gray, very similar to a concrete-face view, water-repellent, self-cleaning. The volume of the Gym, which is separate from the main building, is colored differently with a particular tone green grass. The windows were doubled with others, also in aluminum and with sliding, but in thermal cutting and high performance, and in the space between the two windows was placed a blind, creating a *Double Skin Façade* [4], and thereby all the problems of glare and overheating resolving, if any. The U transmittance of the external walls becomes $0.192 \text{ W/m}^2 \text{ K}$, the phase shift becomes 12.42 h and the thermal bridges are all eliminated. Similarly it is obtained for roofs, on which is

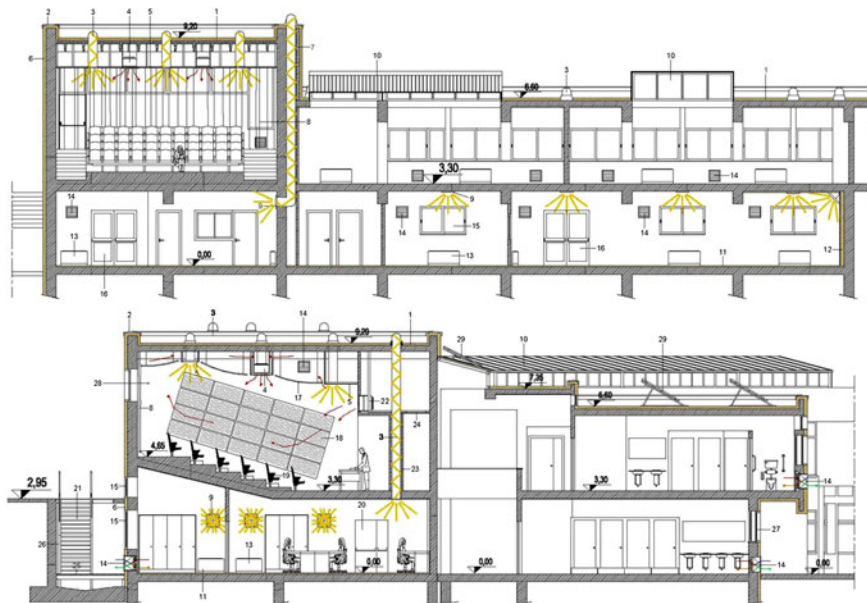


Fig. 2 Natural lighting with solar tubes and acoustical devices of Great Hall

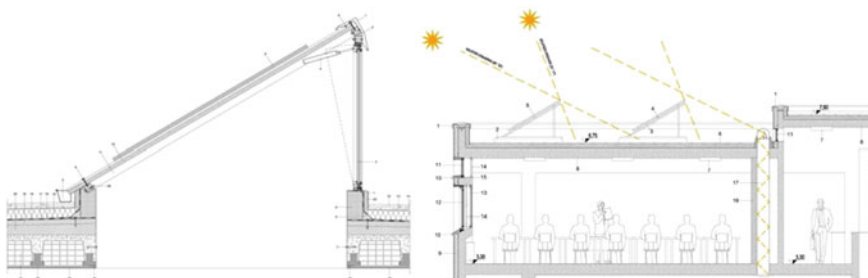


Fig. 3 Natural lighting (shed with PV panels on the roof) optimized through the provision of solar tubes



Fig. 4 Overall external view South-East side shows the different color finishes of the main building envelope and Gym, and the placement of photovoltaic panels on the roof of the sheds

applied an “inverted roof ventilated” XPS 10 cm, with semi-rigid PVC circular spacers and above FRC white tiles, with $U = 0.167 \text{ W/m}^2 \text{ K}$ and phase shift of 17.72 h. The problems of lack of sound insulation between classrooms and corridors, due to the wrong choice of design components, are treated with the application of additional sheets of drywall, with different surface mass, and soundproofing mats in the cavities. The problems of higher value of reverberation time in the Gym are solved with the application on the walls (most exposed to footballs), up to 3.10 m height, of RMIG panels 42 mm thick, coated with 5/10 mm perforated aluminium and internal mineral wool, with excellent sound absorbing power, especially at medium and high frequencies. The solution provided for the ceilings is to coat them with sound-absorbing panels of mineral wool, 40 mm thick, glued directly beneath the beams to TT slabs, with the result of bringing the reverberation time T_{60} well below the standard value, between 1.50 and 1 s, depending on the octave band considered.

The problem of noise and excessive reverberation time in the hall/library/hallway is solved through the division of the space of the library from the atrium and the corridor through a structural glass, screen-printed with photos of Enrico Fermi, which enables to maintain the visual unity of space, intervening only on the propagation of noise. This solution is here laid on the ceiling and on the walls: on the first, placing a new false ceiling in mineral wool panels 1.5 cm thick; on the latter, through counter-walls containing mineral wool panels 27 mm thick,

consisting of granulated recycled glass panels with surface coating of aluminium. In some places, the attachment of additional sound-absorbing panels is provided with screen prints of works by Keith Haring (see Fig. 5). A careful study of the colours makes the surfaces lively and interesting and better defines the geometry (see Fig. 6).

Similar solution has been designed for the Great Hall (in Fig. 2), which is currently used as Natural Science Laboratory. The intervention involves the use of: (1) sound-absorbing panels on the ceiling of mineral wool thickness of 3.2 cm, suspended with adjustable tie-rods; (2) granulated recycled glass panels, and (3) wooden perforated acoustic panels on the walls.

The reverberation time T_{60} becomes equal to 0.5 s at all frequencies, well below what is required by the Standard. The substitution of devices for mechanical controlled ventilation, with heat recovery, where damaged, is scheduled, and their installation in the new laboratories. The replacement of a part of the fan-coils, now out of service, has been foreseen, as well as the replacement of the generator to condensation with two new heat pumps of the type "water-water", allowing the complex building-plant to reach energy efficiency Class A+. On covers, rehabilitated and isolated, the placement of solar panels until the exhaustion of the free surfaces sunny, is planned for a power of 61.5 kW.

Fig. 5 Overall internal view of the atrium with acoustic panels steel coated



Fig. 6 Overall internal view of the atrium: it is evident the careful study of color which makes the surfaces lively and interesting and better defines the geometry



4 Conclusions

In summary, the following results were obtained:

- the building, as restored, is in energy Class A+, with an Epi equal to 5.2 kWh/m³ year [5]. As demonstrated in other studies [6], the savings generated by the intervention allow us to have a payback period of about 15 years;
- the useful life of the building changes from 90 to 120 years;
- the market value of the building increases;
- the intervention is advantageous, and above all, perfectly compatible with the conservation of the formal characteristics of the building, expression of the relevant international architectural culture of the '80s.

Contributions The contribution of the authors in the research and in editing and writing the text of the paper, was equal.

References

1. F. Lembo, Pathologies of the contemporary constructions. The case study of a school building realized in mixed-traditional technique. in *Building a Better World CIB 2010 World Congress*, ed. by P. Barrett, D. Amaralunga, R. Haigh, K. Keraminiyage, C. Pathirage (Salford Quays, United Kingdom, 2010). ISBN 9781905732913
2. F. Lembo, F.P.R. Marino, The High School "Giustino Fortunato" in Rionero in Vulture (Potenza, Italy): how to refurbish an higher education institute made in brutalist architecture of '80, leading it to be a NZEB and preserving its formal features. in *XIII DBMC - International Conference on Durability of Building Materials and Components* (Escola Politecnica, University of São Paulo, São Paulo State Housing Syndicate (Brasil), 2014), Publication CIB – RILEM, pp. 745-752
3. F.P.R. Marino, Relations among pathologies, building technologies and building typologies. in AA.VV. "A State-of-the-Art Report on Building Pathology"- *CIB W086 Building Pathology*, ed. by V.P. De Freitas, CIB Publication 393 (Rotterdam, NL, 2013), pp. 153–159. ISBN 9789063630829
4. F. Lembo, F.P.R. Marino, G. Lacava, Double skin Façades: definition of an ideal depth for cavities. in *4th International Research Symposium (SCRI)*, ed. by C. Abbott, G. Aquad, M. Kagioglu, L. Ruddock (Salford, UK, 2007), pp. 147–160. ISBN 9781905732210
5. F.P.R. Marino, M. Grieco, *La certificazione energetica degli edifici. D.Lgs. 192/2005 e 311/2006 –IV edizione aggiornata alle UNI TS 11300—Algoritmi di calcolo ed esperienze internazionali. Edifici ad alta efficienza* (EPC Libri, Roma, 2009), p. 720. ISBN 9788863101133
6. F. Lembo, Transforming a brutalist monument into an energy efficient building without destroying the formal appealing: the example of the Mediterranean Bank in Potenza (Italy). in *International Congress on Energy Efficiency and Energy Related Materials (ENEFM2013)*, ed. by A.Y. Oral et al., Springer Proceedings in Physics, vol. 155 (Springer International Publication, Switzerland, 2014), pp. 83–90. ISBN 9783319055206, doi: [10.1007/978-3-319-05521-3_11](https://doi.org/10.1007/978-3-319-05521-3_11)

The Environment-Friendly Architecture Come Through Wooden Architecture

Filiberto Lembo and Francesco Paolo R. Marino

Abstract If you have a building well designed, with bioclimatic approach, NZEB, and you want to change step-by-step building design in way to achieve higher scores in an environmental appraisal system, qualitative type as BREEM or Italian ITACA, or quantitative type, as those based on LCA Method and with use of software GaBi or SimaPro, you invent that you can't go further 4.3 on 5 or so on, also if the building is comfortable, good enlighten by the sun and built with reused and recyclable materials; and primary energy balance is ever negative. And that, also if the functional phase is about 87 % of GWP, 94 % of ODP and 71 % of EP. The only way to achieve a full score, 5 on 5, that is a positive primary energy balance at least of some of analysis factors, is to build with materials from renewable sources, which is in wood. In Basilicata, local woods are hardwoods: there are some 4 million cubic meters of *Quercus Cerris* timber tree, and they grow at the rate of 2,40,000 cubic meters per year. With appropriate hygro-thermal conditioning, according to a protocol drawn by Authors in the La.Te.C. Laboratory of Engineering School of Basilicata University at Potenza, this hardwood allows to realize glued laminated timber beams which can work with bending tension of 40.9 N/mm^2 , much more than normal elements in resinous glued laminated timber. This new material can be combined with new structural earthquake-resistant moment resistant timber frame with post tensioning and energy dissipating system, developed by Prof. F.C. Ponzo and other Researchers in SisLab Laboratory of Engineering School of Basilicata University and by Department of Civil and Natural Resources Engineering of University of Cambridge, Christchurch, New Zealand, and in this way is possible to realize high rise framed buildings, which can resist to more violent earthquakes, with a positive ecologic balance.

The contribution of the authors in the research and in editing and writing the text of the paper, was equal.

F. Lembo (✉) · F.P.R. Marino
School of Engineering, Basilicata University, Viale dell'Ateneo Lucano n.10,
85100 Potenza, Italy
e-mail: filiberto.lembo@unibas.it

F.P.R. Marino
e-mail: francesco.marino@unibas.it

1 Introduction

The design of a sustainable building requires new reference design models, other than the above. It is no longer enough that the building is properly designed to take advantage of the free solar gains, heats and cools itself naturally through, for example, the partial burial [1], the radiative cooling by contact with the ground [2], the use of slope winds, the super-insulation of the opaque parts and the fenestrated, the external protection from unwanted solar radiation through shading and ventilated walls [3], *passive house* windows and double-skin façades [4]. It is not enough that the building alone produces the energy it needs from renewable sources and locally, through geothermal devices, solar thermal panels, photovoltaic panels, wind turbines [5]. Its ecological balance is always negative; so that at the end of its useful life, the resources consumed are greater than those produced. To check step-by-step what happens when we modify the characteristics of a project in terms of its sustainability, and in this way to build a *pattern system* that will guide the environmental meta-design of the buildings, a multi-year research project at the Engineering School at the Basilicata University has been built, which has availed itself in particular of the contribution of two young architect-engineers, in their Master Thesis: Paolo Franco Biancamano and Tiziana Pace.

2 The Case Study—Current Status—Qualitative and Quantitative Environmental Sustainability Ratings

Object of the analysis was a building consisting of 66 apartment houses in six floors on a basement garage at Potenza (Italy), Poggio Tre Galli, completed in 2009. The building complex (see Photo 1), built by the ATER of Potenza, was from the same ATER classified as “*experimental building*”, “*with particular reference to saving resources and improving environmental quality.*” Instead, after a rigorous analysis it turns out that its walls in multilayer thermal brick and mineralized wood Eraclit in the cavity, do not comply with the applicable current legislation on energy consumption ($U = 0.51 \text{ W/m}^2 \text{ K}$), as well as the lower floors ($U = 0.85 \text{ W/m}^2 \text{ K}$) and the upper ($U = 1.03 \text{ W/m}^2 \text{ K}$); the exterior windows are equipped with non-insulated roller shutter casing and the envelope is full up of thermal bridges; greenhouses are leaning for the most part poorly oriented (to the West) and have no night insulation systems nor the control of the summer radiation, so as to produce supercooling in the winter and overheating in the summer. The result is a global energy needs for each apartment, variable, depending on location, from 168 to 98 kW/m^2 per year, placing the housing below the regulatory limit of Class C (max 96.9 kW/m^2 year), in the Class D (max 119.6 kW/m^2 year), E (max 162.1 kW/m^2 year) and F (max 227.3 kW/m^2 year). The global energy classification turns out to be E. The total CO_2 emissions amounted to 129,900 kg/year.



Photo 1 Building complex object of study

Performing an analysis of environmental sustainability, was primarily made use of the Italian system of qualitative assessment score, *ITACA Basilicata Protocol 2009*, adopted by Resolution of the Regional Council n. 695 of 14/04/2010: “*A system for the evaluation of energy and environmental sustainability of buildings*”. According to it, all six buildings that form the complex have reached the same score of 1.16 on a scale where -1 indicates a “*Performance below the standard and the current building practice*”; 0 indicates a “*Minimum acceptable performance defined by laws or regulations. Represents the current building practice*”; 1 means “*Slight improvement in performance compared to existing regulations and the current building practice*”; and so on up to the highest level, 5, “*Advanced performance considerably better than the current building practice. Experimental*”. From the analysis performed, it appears that, in particular, the factors that had a negative impact on the level of energy and environmental sustainability achieved by the building are primarily due to the architectural and construction relative to the building envelope, and the non-use of energy produced from renewable sources.

The assessment of the environmental impact was then repeated, by examining the life cycle of the “building product”, in an end of life scenario with selective demolition, using the GaBi software (Ganzheitlichen Bilanzierung) of PE INTERNATIONAL and SimaPro of PRé Consultants. We have assumed a useful life of the building equal to 100 years, and the significance of potential environmental impacts was assessed by two different methods: *ILC recommendations*, the method recommended by the European Commission; *CML 2001 (Nov. 10)*, a method developed by the Centre of Environmental Sciences (CML) at the University of Leiden in the Netherlands [6]. The results, reported below, show that the *functional phase* is the one that presents the greater environmental impact, on average around 80 %. Thus, it is confirmed that in order to increase the sustainability of buildings is necessary, first of all, to isolate (see Table 1, ILCD method).

Similar results we have obtained employing the software SimaPro, using the method *EPD 2007*: clearly states that the phase of the life cycle that has greatest impact on potential environmental impacts is the *functional phase*, for all impact categories, with the exception of *eutrophication*. On average, the percentage of incidence of the functional phase of the environmental impacts on the total stands at around 75 % (see Table 1, EPD 2007 method).

Table 1 Building “as built”: LCA building product interpretation using *ILCD method* and *EPD 2007 method*

LCA “Building Product” interpretation					
ILCD recommendations	Production phase	Functional phase	End-of-life phase	Total	Functional phase (%)
GWP (kg CO ₂ Equiv)	7.28E006	5.06E007	3.32E+06	6.12E+07	82.68
ODP, steady state (kg CFC-11 Equiv)	7.41E-4	0.0137	1.92E-01	2.06E-01	6.63
Human tox (cancer) (CTUh)	7.88E-3	0.0116	-1.28E-03	1.82E-02	63.74
Human tox (non cancer) (CTUh)	1.24	1.26	-4.99E-01	2.00E+00	62.97
Particular matter (kg PM2.5 Equiv)	1.49E003	7.17E003	-3.70E+02	8.29E+03	86.49
Ionising radiation (kg U235 eq)	9.17E008	1.7E0010	-6.72E+08	1.72E+10	98.58
POCP (kg NMVOC Equiv)	1.37E004	6.75E004	3.90E+04	1.20E+05	56.15
AP (Moles of N or S Equiv)	5.54E003	3.57E004	9.96E+03	5.12E+04	69.73
EP (Moles of N or S Equiv)	5.73E004	4.16E005	4.10E+04	5.14E+05	80.89
EP water (kg P Equiv)	20.5	49.6	-1.45E+01	5.56E+01	89.21
Eco tox (CTU Eco)	6.08E005	9.09E005	-5.04E+05	1.01E+06	89.73
Water (kg)	2.29E006	1.63E008	1.10E+07	1.76E+08	92.46
ADP elements + fossil (kg Sb-Equiv)	73.2	2.35E003	-7.80E+01	2.35E+03	100.20

LCA “Building Product” interpretation					
EPD 2007	Production phase	Functional phase	End-of-life phase	Total	Functional phase (%)
Global warming (GWP100) (kg CO ₂ eq)	9.15E+0 6	3.07E+07	4.49E+05	4.03E+07	76.18
Ozone layer depletion (ODP) (kg CFC-11 eq)	5.46E-01	3.36	11.18E-02	3.92E+00	85.76
Photochemical oxidation (kg C ₂ H ₄)	4.35E+03	8.49E+03	5.29E+01	1.29E+04	65.85
Acidification (kg SO ₂ eq)	2.75E+04	7.66E+04	9.10E+01	1.04E+05	73.52
Eutrophication (kg PO ₄ eq)	3.98E+0 3	5.55E+0 3	1.81E+0 3	1.13E+04	48.94
Non renewable, fossil (MJ eq)	1.13E+08	5.08E+0 8	-3.65E+05	6.21E+08	81.85

3 Energy Upgrade—Forecast of a PV Plant

It was therefore sought, in a second step, to eliminate the problems highlighted in the building as realized, by designing an intervention of energy upgrades to improve the performance of the envelope and to equip the building of systems of autonomous production of energy from renewable sources. It has been suggested the use of a ventilated wall StoVentec R, plastered recycled glass plates and aluminum and stainless steel structure (which allows to keep the current image of the building, and improves the behavior in the summer and the watertightness to rain),

affixing an additional 8 inches of insulation from the outside (cork), which improves the transmittance (U walls $0.26 \text{ W/m}^2 \text{ K}$) and resolves fully the thermal bridges, eliminating them for the most part. So for the floors on outer spaces by the upper or lower side, with similar transmittances. It was speculated to have second double-glazed windows with $U_w = 1.8 \text{ W/m}^2 \text{ K}$, aligned with the outer insulation, which makes the double windows $U_w = 1.4 \text{ W/m}^2 \text{ K}$; and to achieve a Double Skin Façade that rising progressively tilts to the outside, with blinds shielding and ventilation openings from floor to floor, placed in correspondence of the huddled green-houses. This device, verified with the software ECOTECT of Autodesk, has a total U_w of $1.15 \text{ W/m}^2 \text{ K}$ and resolve both the summer and the winter problems, improving the performance of buffer space and passive solar collectors.

It was also hypothesized to place on the cover a photovoltaic system, with industrial modules located on a support structure purpose-made “on scales of a snake”, to allow their optimal solar orientation, despite the different alignment of the various parts of the building. There are 1,333 panels covering 333.25 m^2 , producing 41.70 kW/h . The result is the passage of all parts of the building in energy class B, the halving of energy consumption, and therefore emissions, which are now equal to kgCO_2 66,607/year. Applying the *ITACA Basilicata Protocol 2009*, the overall sustainability score has more than doubled: 2.63, intermediate between 2: “*Moderate improvement in performance compared to existing regulations and building practice*” and 3 “*Significant improvement in performance compared to regulations and common practice. Best current practice*”. A quantitative approach, the software GaBi, applied to this first hypothesis of the energy upgrade and supply of energy from renewable sources, shows the results in terms of impact categories, listed in the following table. The potential environmental impacts have been reduced significantly, except for the ODP and Eco Tox categories, related to the realization of photovoltaic panels. Similar results are obtained by applying the software SimaPro of PRÉ Consultants, in particular assessing the potential environmental impacts of the operational phase, as it is the one part of the life cycle that has changed as a result of the planned interventions of the energy retrofit. It is clear that potential impacts have decreased by about 50 % for all impact categories. But they are still far from to be limited, as it is required of a project that has sustainability as a key issue.

4 Further Improvements to the Project—Wind Power Plant—Solar Heating System

From the analysis of the energy calculations, it was possible to verify that there are still parts of the project that continue to adversely affect, as the accumulation wall in the solar greenhouse. The proposed intervention is to equip it with “insulating shutters,” purpose-made, wood wool 10 cm thick and $2 \times 6 \text{ mm}$ plywood, which gives the wall a U of $0.287 \text{ W/m}^2 \text{ K}$, improves the phase shift (which becomes 12 h)

and the attenuation factor (0.16), corresponding to the second level of performance quality; so for the walls towards the stairs, for which 10 cm of wood wool are now provided, protected by an hydraulic thick plaster with double glass fibre mesh, with similar performance.

We have also worked to improve the illumination of the different rooms, which is not up to the standards of the Italian regulations, providing some internal light shelf where necessary. As the initially planned PV system covers only 35 % of the building's electricity needs, and the site is particularly windy throughout the year, it was assumed to install on the pitched roof seven vertical axis wind turbines from 5 kW, each capable to produce about 8,500 kW/year of energy; furthermore, it is designed to have, along the ridge line of the roof, n. 26 horizontal axis generators, said "Venturbine", that exploit the Venturi effect, each able to annually produce 1,200 kW of electricity. With such devices, you could cover an additional 35 % of the energy demand of housings.

To reduce the consume associated with the production of domestic hot water, the solution that we have assumed is to have on the façades, ahead the parapets of the windows of the South-West and tilted at 30° to the horizontal, two solar thermal vacuum panels for each apartment, with a surface area each of 1.16 m². Their efficiency check was made with the Autodesk Ecotect Analysis software. The planned budget satisfies entirely the needs of hot water required.

Following the intervention hypothesized, all the accommodations would fall in Class A+ and CO₂ emissions in the *operational phase* would be close to zero. By subjecting the project to the qualitative analysis of the *ITACA Basilicata Protocol 2009*, we can observe that the various parts of the building have scores between 3.97 and 4.04. We are therefore in the presence of a "*Moderate increase in the best building practice*". Conducting a quantitative analysis through the application of LCIA methodology using the GaBi software, it is found that in the *functional phase* we obtained a reduction of all impact categories, averaging around 50 %, except for the ODP, the potential Ozone depletion, and for ADP, the potential depletion of elements and abiotic fossil fuels, both related to the use of PV for the production of electricity (see Table 2). It is possible to achieve similar results also through the software SimaPro, which displays the results that are obtained gradually in relation to the different indicators.

5 Use of Recycled Materials

At this point, the only hypothesis that can be done, without changing completely the construction type of the building, it is to assume that the building has been made with recycled and local materials, both as regards the reinforced concrete structures, for which there are no regulatory impediments, except the necessary controls; both for the infill walls, which may well be realized in concrete blocks made with recycled aggregate; and also with regard to the insulating and whatnot. Flooring can

Table 2 LCIA functional phase comparison, using *ILCD recommendations* method

LCIA functional phase comparison				
ILCD recommendations	As built (A)	Project N°1 (B)	(A) – (B)	(A) – (B)/(A) (%)
GWP (kg CO ₂ Equiv)	5.06E007	1.81E007	–3.25E+07	–64.23
ODP (kg CFC-11 Equiv)	0.0137	0.0298	0.0161	117.52
Human tox (cancer) (CTUh)	0.0116	6.84E-3	–4.76E-03	–41.034
Human tox (non cancer) (CTUh)	1.26	0.858	–4.02E-01	–31.90
Particular matter (kg PM2,5 Equiv)	7.17E003	4.79E003	–2.38E+03	–33.19
Ionising radiation (kg U235 eq)	1.7E0010	9.59E009	–7.41E+09	–43.58
POCP (kg NMVOC Equiv)	6.75E004	2.91E004	–3.84E+04	–56.88
AP (Moles of N or S Equiv)	3.57E004	1.68E004	–1.89E+04	–52.94
EP (Moles of N or S Equiv)	4.16E005	2E005	–2.16E+05	–51.92
EP water (kg P Equiv)	49.6	44.4	–5.20E+00	–10.48
Eco tox (CTU Eco)	9.09E005	8.24E005	–8.50E+04	–9.35
Water (kg)	1.63E008	1.47E008	–1.60E+07	–9.81
ADP elements + fossil (kg Sb-Equiv)	2.35E003	1.68E004	1.45E+04	614.89

be laid with linoleum instead of ceramics; the roof tiles can be made with recycled plastic instead of baked clay, and so on.

But, subjecting again the project to the qualitative analysis of the *ITACA Basilicata Protocol 2009*, scores between 4.09 and 4.17 are obtained, that are slightly different from those of previous hypothesis. The building it is therefore always in the same qualitative condition, in the presence of a “*Moderate increase of the best current building practice*”. Carrying out, once again, a quantitative analysis through the application of LCIA methodology using the software SimaPro—EPD 2007, limited improvements are found in environmental impacts. Essentially, the use of recycled materials is useful, but not decisive (see Table 3).

6 Use of Materials from Renewable Sources

At this point it is clear that the only way to achieve a full score with qualitative evaluation methods, or to obtain a positive energy balance with analytical ones, is to make use of materials from renewable sources: par excellence, the wood.

The convenience of the use of wood as a renewable material also depends on the change of the end of life scenario, if it provides for the re-use or production of energy, which can make positive the overall budget; provided, however, that in the packaging of laminated timber, structural or otherwise, have not been in use

Table 3 Quantitative analysis results

Quantitative evaluation			
LCIA functional phase (SimaPro)			
EPD 2007	E.R.P. intervention (As built)	E.R.P. intervention (Energetic upgrade and PV on roof hypothesis)	E.R.P. intervention (Project N°1-2)
Global warming (GWP100) (kg CO ₂ eq)	3.07E7	1.49E7	6.73E6
Ozone layer depletion (ODP) (kg CFC-11 eq)	3.36	1.54	0.575
Photochemical oxidation (kg C ₂ H ₄)	8.49E3	4.49E3	2.34E3
Acidification (kg SO ₂ eq)	7.66E4	4.72E4	3.2E4
Eutrophication (kg PO ₄ eq)	5.55E3	3.35E3	2.17E3

substances hazardous to health, such as glues or protections from the fire, that make it, on the contrary, a special waste.

In Basilicata region, local woods are hardwoods: there are some 4 million cubic meters of *Quercus Cerris* timber tree, and they grow at the rate of 2,40,000 cubic meters per year. With appropriate hygro-thermal conditioning, according to a protocol drawn by the Authors in the La.Te.C. Laboratory of Engineering School of Basilicata University at Potenza, this hardwood allows to realize glued laminated timber beams which can work with bending tension of 40.9 N/mm², much more than normal elements in resinous glued laminated timber [7]. This new material can be combined with new structural earthquake-resistant, moment resistant, timber frame with post tensioning and energy dissipating system, developed by Prof. F.C. Ponzo and other Researchers in SisLab Laboratory of Engineering School of Basilicata University and by Department of Civil and Natural Resources Engineering of University of Cambridge, Christchurch, New Zealand, and in this way is possible to realize *high rise framed buildings*, which can resist to more violent earthquakes, *with a positive ecologic balance*.

References

1. F. Lembo, F.P.R. Marino, in *Semi-underground buildings: design models for the contemporary cities*, ed. by Y. Zhou, J. Cai, R. Sterling. Advances in Underground Space Development, Proceedings of ACUUS 2012 Congress (Research Publishing, Singapore, 2012). pp. 139–149, ISBN 978-981-07-3757-3, doi:[10.3850/978-981-07-3757-3_RP-111-P154](https://doi.org/10.3850/978-981-07-3757-3_RP-111-P154)
2. F. Lembo, F.P.R. Marino, Raffrescare naturalmente un edificio con le tecniche costruttive storiche dell' architettura pugliese. PROTECTA, Speciale: “Greencity & Eco-Building”, vol. 4 (2012), pp. 70–73, ISSN 1121–3124
3. F. Lembo, in *Transforming a brutalist monument into an energy efficient building without destroying the formal appealing: the example of the Mediterranean Bank in Potenza (Italy)*, ed. by A.Y. Oral et al. International Congress on Energy Efficiency and Energy Related Materials

(ENEFM 2013), Springer Proceedings in Physics, vol. 155 (Springer International Publisher, Switzerland, 2014), pp. 83–90, ISBN 9783319055206, doi:[10.1007/987-3-319-05521-3_11](https://doi.org/10.1007/987-3-319-05521-3_11)

4. F. Lembo, F.P.R. Marino, G. Lacava G, in *Double skin Façades: definition of an ideal depth for cavities*, ed. by C. Abbott, G. Aquad, M. Kagioglu, L. Ruddock. 4th International Research Symposium (SCRI) (University of Salford (UK), Salford (Greater Manchester), 2007), pp. 147–160, ISBN 9781905732210

5. F.P.R. Marino, *The re-invention of the tower house for the construction of green buildings NZEB, integrated with the vertical axis small wind system*, ed. by A.Y. Oral et al. International Congress on Energy Efficiency and Energy Related Materials (ENEFM 2013), Springer Proceedings in Physics, vol. 155 (Springer International Publisher, Switzerland, 2014), pp. 91–97, ISBN 9783319055206, doi:[10.1007/987-3-319-05521-3_12](https://doi.org/10.1007/987-3-319-05521-3_12)

6. R.J. Cole, Building environmental assessment methods: redefining intentions and roles. *Build. Res. Inf.* **33**(5), 455–467 (2005). doi:[10.1080/09613210500219063](https://doi.org/10.1080/09613210500219063)

7. F. Lembo, F.P.R. Marino, in *Floors realized in Quercus Cerris (Turkish Oak) laminated timber in buildings with structure in masonry, performing anti-seismic functions*, ed. by B.P. Sinha, L. Tanaçan. ISSM08—8th International Seminar on Structural Masonry (Istanbul Technical University, 2008), pp. 441–448, ISBN 978-975-561-342-0

Energy Efficiency Engineering—Towards an Integrated Method Framework for Energy-Oriented Product and Production Development

Pascal Stoffels, Dirk Bähre, Georg Frey and Michael Vielhaber

Abstract Energy efficiency in all areas of the product lifecycle gets more and more important. Besides the use phase that is often addressed through technological solutions, the production phase is also in focus as it determines the environmental impacts of a company to a high degree. Established operational methods that consider energy efficiency reactively are often already exploited. This contribution therefore focuses on methods that are applied in early phases of the product and production development process. On the basis of a correlation matrix that correlates the interrelationships between the three dimensions product, material and production, promising areas in the product creation process are analysed. This framework provides a general basis for the development and application of integrated analysis and improvement methods.

1 Introduction

Energy efficiency is further rising in importance across all areas of the product lifecycle. One focus is put on the products' use phase, generally addressed through technological solutions. Another focus area with strongly rising significance is the production phase, which influences both the product's lifecycle assessment and the organization's environmental footprint. Regarding this area, the method of choice has so far generally been to improve the operation through, e.g., energy value stream optimizations.

P. Stoffels
ZeMA gGmbH, 66121 Saarbruecken, Germany

D. Bähre · G. Frey · M. Vielhaber (✉)
Saarland University, 66123 Saarbruecken, Germany
e-mail: vielhaber@lkt.uni-saarland.de

With efficiency demands further rising, such operational or end-of-pipe approaches reach their limits. The challenge is then to define approaches targeting already the earlier product and production development phases, which promise higher improvement potentials [1], but may be more complex to implement. Such approaches are just at their beginning in industrial contexts, as they require longer term improvement focuses as well as the interdisciplinary involvement of product development, production development and operation experts.

This paper focuses on methods which can be applied in the early phases of product and production development and which target energy efficiency optimizations in the production phase. It builds on a general integration framework developed by the authors as a basis for multiple product and production engineering integration aspects.

2 Energy Efficiency Methods

Energy efficiency is in focus all along the product lifecycle, and it can be addressed through methods all along the product lifecycle as well. Higher impacts can however be expected through methods applied in the early product and production development phases. As a drawback, such methods tend to be more complex or more restricted through boundary conditions. The energy efficiency method matrix in Fig. 1 visualizes these circumstances by categorizing energy efficiency-related methods by their application area, on the one hand, and the life cycle phase whose energy efficiency they are impacting, on the other.

The research of the authors targets the highlighted high impact area. It strives for integrated methodical approaches for the product and production engineering phases. In a first step, it is therefore inevitable to find a consolidated view on this application field.

application area \ impact area	Materials	Production	Use/end-of-life
Material definition			
Product development		High impact, high complexity	
Production development			<i>out of scope</i>
Production	Low impact, low complexity		
Use/end-of-life			

Fig. 1 Energy efficiency method matrix

3 Product and Production Engineering

“Product and Production Engineering” describes the phases in the product lifecycle in which all aspects of an envisioned product are conceptualized, laid out and detailed together with the respective production equipment. In parallel and closely interrelated, the product’s material is determined and defined.

Thus, product, production and material definition build the three dimensions of product and production engineering, see Fig. 2.

3.1 Dimensions of Product and Production Engineering

Holistic approaches and methods in this area have therefore to consider these three dimensions and their interrelationships in an integrated way. Engineering processes in all three dimensions follow similar maturation phases from a concept via a layout to a detail level, see Fig. 3.

Product and production engineering processes are impacted by various constraints and impacts as shown in the left column of Fig. 4. They significantly determine the outputs of products as well as of production systems across all the dimensions shown in the right column of Fig. 4.

The three dimensions together with their respective maturation steps as well as the inputs and outputs of product and production engineering build the basis for the integration framework introduced in the following chapter.

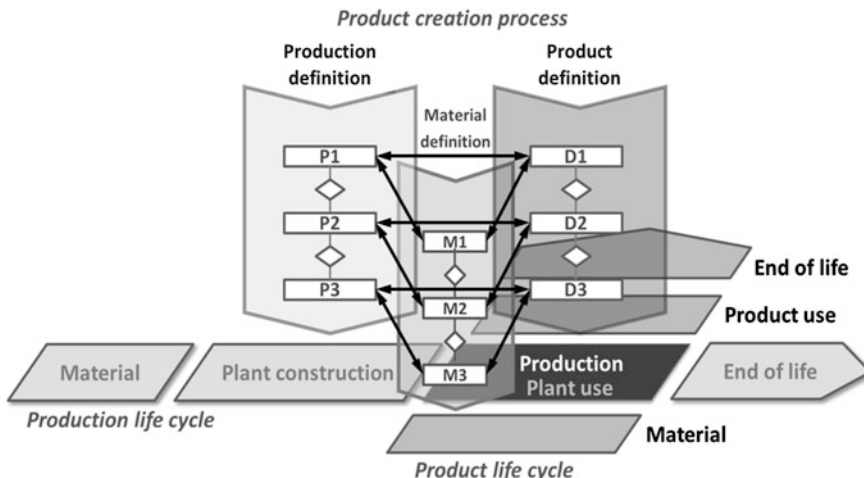


Fig. 2 Dimensions of product and production engineering (based on [2])

	Concept level	Layout level	Detailed level
Product Definition	D1: Functional design	D2: Principle design	D3 Detailed design
Material Definition	M1: Property definition	M2: Class selection	M3:Material specification
Production Definition	P1: Technology definition	P2: Process design	P3: Process specification

Fig. 3 Maturation phases in product and production engineering

Inputs (Impacts)	Outputs (Requirements)
I1: Raw materials	O1: Time
I2: Equipment	O2: Costs
I3: Human resources	O3: Quality
I4: Organization	O4: Environment
I5: Culture	O5: Social effects

Fig. 4 Impacts and requirements of product and production engineering

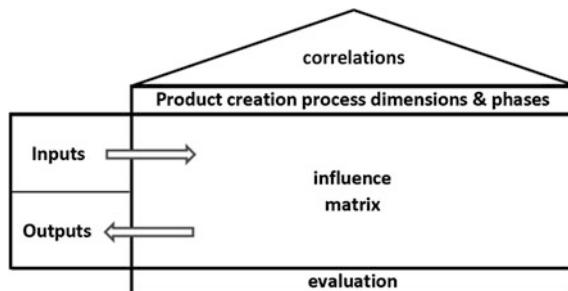
3.2 Product and Production Engineering Integration Framework

The integration framework presented here intends to provide a generic basis for the development of analysis and synthesis methods for a wide range of integrated product and production development aspects.

For the visualization, it makes use of known matrices such as the house of quality from the Quality Function Deployment (QFD) method, see Fig. 5.

On the horizontal axis of the main matrix, it features the dimensions and phases of product and production engineering as part of the product creation process according to Fig. 3. On the vertical axis, this matrix shows both boundary conditions (inputs) and results (outputs) for and of the determinations. The matrix area, then, correlates the inputs and outputs with the dimensions and phases of the product creation process, and—depending on the method application—offers the possibility to evaluate and weight the influences. The upper matrix adds a roof to the horizontal axis showing correlations between the phases, and vice versa.

Fig. 5 House of quality adaptation to product and production engineering



		correlations between phases (directed from vertical to horizontal)									
		Process specification	P3	0	0	2	1	2	1	0	1
Product definition	Process design	P2	0	2	2	1	1	1	0	2	
	Technology definition	P1	1	2	2	1	2	1	1	3	1
	Material specification	M3	0	0	2	2	0	2	1	2	2
	Class selection	M2	2	3	3	2	2	3	3	3	1
	Property definition	M1	1	1	1	1	3	3	1	1	1
	Detailed design	D3	0	1	1	3	3	2	2	2	3
Production definition	Principle design	D2	1	1	3	3	3	2	3	3	1
	Functional design	D1	1	3	1	2	2	1	1	0	0
	Product definition			Material definition			Production definition				
	D1	D2	D3	M1	M2	M3	P1	P2	P3		
	Raw materials	I1	0	2	2	2	3	3	2	1	1
	Equipment	I2	0	1	2	1	2	2	3	3	3
Inputs	Human resources	I3	1	3	2	1	2	2	2	3	2
	Organization	I4	1	2	1	1	2	1	2	2	1
	Culture	I5	1	2	1	1	2	1	2	2	1
	Time	O1	1	3	3	1	2	1	3	3	2
	Costs	O2	2	3	3	2	3	2	3	2	2
	Quality	O3	2	3	3	2	2	3	2	2	3
Outputs	Environment	O4	2	3	3	1	3	1	2	2	1
	Social effects	O5	1	2	0	2	3	1	2	2	0

0
no ...

1
weak ...

2
medium ...

3
strong ... correlation/influence

Fig. 6 Product and production engineering integration framework

Figure 6 shows a detailed version of the framework, with the matrices filled based on an interview study with research and industry experts.

4 Use Case Energy Efficiency

Applying the framework from chapter “[Entering the Bio Based Economy—Verification of Demand on Education in the Field of Green Economy](#)” to the use case of energy efficiency can help in defining best-suitable methods for the respective applications.

For this use case, the output area focuses on (especially energy-related) environmental aspects. Impacts and requirements are detailed and weighted, accordingly. Then, depending on the boundary conditions on the input side, the process influences can be adapted, the process dimensions and phases can be evaluated regarding the potential they offer, and the best area to be addressed by energy-related methods can be identified. Figure 7 gives a principle visualization of this approach.

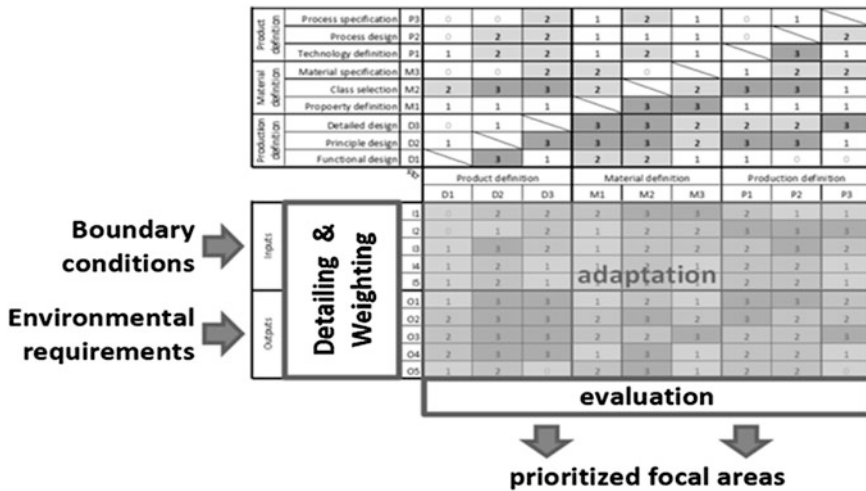


Fig. 7 Framework applied to the use case of energy efficiency

5 Discussion and Conclusion

The presented framework for product and production engineering offers a formalized view on the product, material and production dimensions of engineering together with their interrelationships. It thereby supports a holistic, domain-spanning understanding which can help to manage the high complexity in this field. Thereby, it provides a basis for the development and application of integrated analysis and improvement methods.

With the example of energy efficiency it was shown how such a formalized framework can substantiate the prioritization of energy-related engineering concepts and methods based on environment-oriented input and output factors. It thereby goes beyond known approaches to environment-oriented adaptions of QFD matrices (e.g. [3–5]), as it elaborates especially on the interdependencies between the process dimensions and phases of both product and production engineering in an integrated way, and can thereby lead to holistic, process-spanning energy efficiency optimizations.

In future work, the presented framework will be further developed by the authors to be further detailed on the energy efficiency use case, on the one hand, and applied also on other use cases in the area of integrated product and production engineering, on the other hand.

References

1. D. Pape, F. Mantwill, Ein Konzept zur Integration der Energieanforderung für eine frühzeitige energetische Produktbeeinflussung am Beispiel des automobilen Karosseriebaus (2013), <http://edoc.sub.uni-hamburg.de/hsu/volltexte/2014/3059/>
2. M. Vielhaber, P. Stoffels, Product development versus production development. Proceedings of 24th CIRP Design Conference 2014, 14.04.-16.04.2014, Milano, Paper ID PROCIR-D-13-00192
3. J. Grossmann, S. Hansen, L. Melzer, J. Günther, EuP-implementierung, in *EcoDesign—Von der Theorie in die Praxis*, ed. by E. Abele, R. Anderl, H. Birkhofer, B. Ruettinger (Springer, Berlin, 2008), pp. 13–46
4. T. Sakao, A QFD-centred design methodology for environmentally conscious product design. *Int. J. Prod. Res.* **45**(18–19), 4143–4162 (2007)
5. Y. Zhang, Green QFD-II: a life cycle approach for environmentally conscious manufacturing by integration LCA and LCC into QFD matrices. *Int. J. Product. Res.* **37**(5), 1075–1091 (1999)

Modeling the Air Channel Ventilation in Ansys CFX of a Romanesque Church

Anna Sedlakova and Ladislav Tazky

Abstract Moisture is a major source of damage in historic solid masonry. Rising damp is a well-known phenomenon around the world and occurs when groundwater flows into the base of a construction and is allowed to rise through the pore structure. From practical experience it is known that many factors may play a role regarding permeability problems in masonry. The amount of possible causes of moisture problems in historic masonry underlines the complexity of this phenomenon. Evaporation is an important factor in rising damp. The surface of an affected wall contains moisture that has risen from the ground and this moisture is then subject to evaporation. The factors controlling evaporation include: temperature, humidity, air movement and surface.

1 History of the Church

The church in Gemersky Jablonec is the oldest in the micro region Medves, which is a valuable monument of the Romanesque architecture. In the construction of the church architect used different materials. The foundation is made of bricks and above stone blocks is used. The walls were probably plastered. In the 18th century the church was modified. The original Romanesque windows on the south side of the church were walled up and new and larger ones were created instead. The new windows are a feature of Baroque architecture. In the 18th century the sacristy was added to the north side. In 1933 the church was renovated. In 1969 an archaeological survey was conducted where archaeologists discovered the remains of the fortification walls protecting the building (Fig. 1).

A. Sedlakova · L. Tazky (✉)
Civil Engineering Faculty, Institute of Architectural Engineering,
Technical University of Kosice, Kosice, Slovakia
e-mail: Ladislav.tazky@tuke.sk

A. Sedlakova
e-mail: anna.sedlakova@tuke.sk

Fig. 1 The church Gemersky Jablonec nowadays



2 Geometry of the Ventilated Air Channel

The drain pipes will be replaced with outdoor air channels. The channel must be masoned of ceramic burned bricks with lime-cement mortar to ensure the natural evaporation of moisture from the soil through the brick masonry. The bottom of the air channel will be filled with gravel; the drain pipe will be placed in this layer to ensure the drainage of water. The next step will be the coverage of the channel with precast concrete panels.

2.1 Simulated Variant of Air Channel

We designed the cross-section dimensions of ventilated air channel in 10 variants. The size and values of air pressures and air velocities are shown in the Table 1. The air pressure and air velocity values are from the second simulation. In the second simulation we used the values of air pressure what we obtained from the first simulation. We designed the church and terrain in the first simulation to get the properties of the wind on the surf (Fig. 2).

2.2 Boundary Conditions of Numerical Model

The Fig. 3 shows the church grid generation and design parameters of the domain meshing. The general numerical domain consist two sub-domains: the first constructed by deducting the church amount from a parallelepiped and the second by deducting of this parallelepiped from the external domain. Part of the windward

Table 1 Air velocity and air pressure in the air channel for each variants

Versions	Size (mm)	Velocity (m/s)	Pressure (Pa)
Variant 1	450 × 400	0.16268	0.01275
Variant 2	450 × 450	0.15365	0.01340
Variant 3	450 × 500	0.14253	0.01219
Variant 4	450 × 550	0.13280	0.01115
Variant 5	450 × 600	0.12529	0.01041
Variant 6	500 × 400	0.16319	0.01351
Variant 7	500 × 450	0.14922	0.01215
Variant 8	500 × 500	0.13762	0.01103
Variant 9	500 × 550	0.12830	0.01020
Variant 10	500 × 600	0.12141	0.00945

Fig. 2 Visualization of the air channel



numerical model was $L_1 = 5$ W, $Y = 6$ H, and the leeward domain L_2 was 20S. The 3D mesh comprised of 254,481 nodes. All results for the church were calculated with the standard $k-\varepsilon$ model.

The first model was realized with an air flow of 3 m.s-1, during the summer 25 ° C (Fig. 4). In the second model we used obtained values of pressure in monitored points, what represented the location of the inlets on the wall in the first model (Fig. 5).

2.3 Results of Simulation

In the Fig. 6 is displayed dependence of the air velocity on the depth of the air channel. If the depth of the air channel is higher air velocities are lower. Therefore in the final numerical simulation we used lower depth of the air channel with the

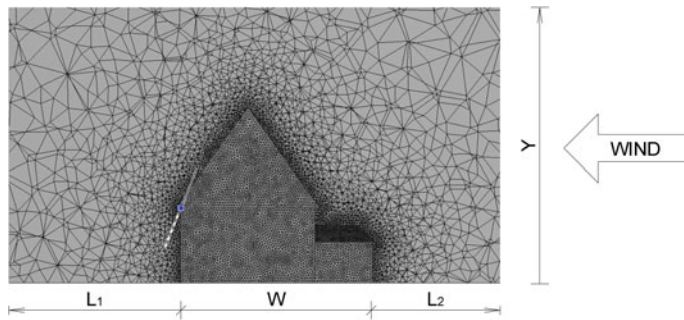
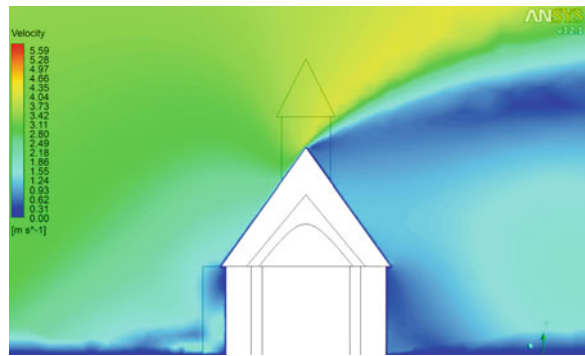


Fig. 3 Dependence of the velocity and depth of air channel

Fig. 4 Air velocity around the church



enlarged width. Final cross-section dimension of the air channel are 500×400 mm (Variant 6).

The air velocity on the depth of the air channel we can calculate with the logarithmic (1):

$$v = -0.101 \ln(h) + 0.7715 \quad (1)$$

where: h —height of the channel.

The Fig. 5 displayed contours air in the air channel around the apse of church. The streamlines air is coloured according to air velocity. In this part of the church is the worst situation, because the water content in the masonry is around 9 %. The tested samples have been collected from the bottom part of the masonry wall. Results obtained from the numerical simulation in the software ANSYS CFX are satisfactory in the complicated parts of the church as well as at the apse.

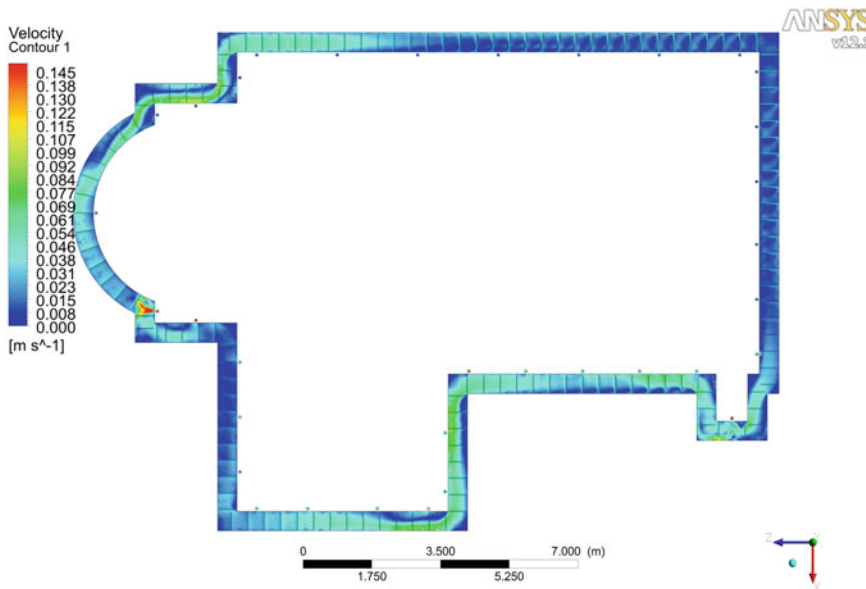


Fig. 5 Contours coloured by air velocities in the variant 6 around the church

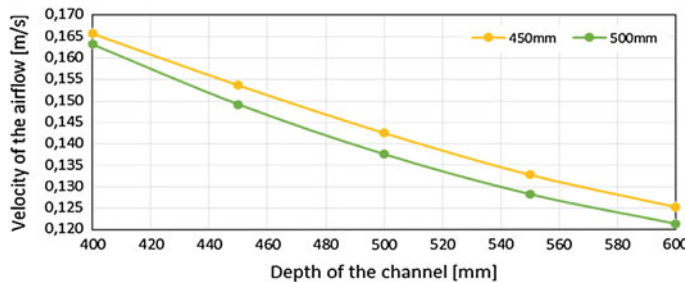


Fig. 6 Dependence of the velocity and depth of air channel

3 Conclusion

The air channel around the church Gemersky Jablonec is simulated in many different variants, see Table 1. Results obtained from the numerical simulation in the software ANSYS CFX showed cross-section 500 × 400 mm (Variant 6) as the best for this church. In this case is air velocity in the air channel highest as well as maximal drying effect of the masonry. Final results showed average air velocity in the air channel on the value 0.032 m/s, more.

Acknowledgments This article was written as a project solution “The use of the virtual laboratory for designing energy-efficient buildings” Project code: 052TUKE-4/2013.

References

1. B. Michael et al., *Dehumidification of buildings* (Grada, Praha, 2008)
2. B. Michael, Drying of the masonry. Grada, praha 2009
3. F. Pavel, Examples of remediation basements against moisture, *Construction Yearbook*, 2007th edn. (Jaga, Bratislava, 2007), pp. 103–108
4. R. Jozef, Survey of drainage tunnels in the monastery Milevsko. <http://old.speleo.cz/soubory/speleo/sp16/milevsko.htm>. Accessed: 12 March 1993
5. B. Eva, M. Robert Proposal for remediation of damp masonry church Giles in Mliesk. In: ASB newspaper. Bratislava. Available via DIALOG. <http://old.speleo.cz/soubory/speleo/sp16/milevsko.htm>. Accessed 18 June 2008
6. H. Miroslav, H Procedure for remediation of damp masonry locks on the upper Vimperk In: ASB newspaper. Bratislava. Available via DIALOG. <http://www.asb.sk/stavebnictvo/rekonstrukcia/postup-sanacie-vlhkeho-muriva-horneho-zamku-vo-vimperku>. Accessed 24 May 2012
7. R. Tomas, S. Anna, Assessment of underfloor ventilation of historic buildings using Ansys cfx. Paper presented at the Budownictwo o zoptimalizowanym potencjale energetycznym, Krakow, Poland, 2013
8. B. Tomas, J. Natalia, K. Michal Development of software support for ANSYS CFX. Paper presented at the 32. Stretnutie katedier mechaniky tekutín a termomechaniky, Žilina, Slovakia, 25–28 June 2013

Part XV
Energy Management Systems

Many Kinds of Energy Source in Our Surroundings at Home

Takashi Yoshikawa

Abstract We are studying the Energy Harvesting in our surroundings at home. Our aim was to supply the energy to the sensor terminal that communicates to other terminals wirelessly (sensor network nodes). The average energy consumption for each terminal is estimated to be around 2.6 mW supposing to be used as Rich HEMS (Home Energy Management System) terminal. In order to get such energy from our surroundings, we have tried to use vibration energy caused by the human step on the floor, the hydroelectric power generation from the water pipe, the ventilation wind at kitchen. As the result we have succeeded in getting much power of 30 mW from the water pipe experiment. Moreover we have tried to use magnetic flux leakage energy from the light bulb driven with inverter. In this measurement we could get the average power of 4 mW. In this paper we will discuss the results for each power generation method.

1 Introduction

HEMS (Home Energy Management System) is widely recognized as the useful technology for saving energy. On the other hand HEMS is never influenced around common people. The reason is supposed like the following three points. 1. High initial cost, 2. Location dependence (The present HEMS is mounted into the wall), 3. Personal unconcern for energy saving. Then I introduce the novel concept for HEMS apparatus. The idea is introducing sensor network technology taking the place of the conventional wired system.

In addition to that, by introducing energy harvesting technology into the power source of the sensor network nodes, each node can continue to work without battery or AC power supply cable. To examine the validity of its concept, we have studied step by step. At first we have defined the HEMS category according to the energy

T. Yoshikawa (✉)
Kindai University Technical College, Nabari-shi, Japan
e-mail: yoshikawa@ktc.ac.jp

consumption amount by sensor network nodes, i.e. various functional HEMS needs much energy as shown in Table 1.

As the next step, we have made the prototype model of the sensor network nodes for HEMS. The node is equipped with amorphous silicon solar cell because the energy source is room illumination. The average energy consumption of the sensor network node aiming at Model5 HEMS is estimated to be around 100 μ W involving power conditioning energy. For compensating for the energy, we have prepared the 45 mm \times 56 m solar cell. Then we have performed the practical experiment of modeled 7 days life style and shown the energy balance between product and consumption are good agreement. Moreover we have examined the ability of other kinds of power generation, vibration, thermal gradient, and wireless power transmission. According to the above results, we have been able to conclude that our novel concept of sensor network HEMS with energy harvesting is valid [1]. But in above previous study, the data renewal period was more than 10 min as shown in Table 1. Such type HEMS can provide the energy saving management system but can not provide other rich services such as health, comfortable, security management. In order to attain those services, the period of data acquisition needs less than 10 s. That causes frequent data traffic and consumption power of sensor node is higher. We call such HEMS “Rich HEMS” because the HEMS demands rich

Table 1 Power consumption of the sensor network node for each HEMS Model

Model	Power (mW)	T (ms)	1	2	3	4	5	6	
Sleep	4.50E-03	–							
Comm.	42	3							
RF	22.5	30							
Temp. sens.	22.5	1	O	O	O	O	O	O	O
Moist. sens.	0.073	8000		O	O	O	O	O	
Illumi. sens.	22.5	1	O	O	O	O	O	O	O
Motion sens.	0.002	–	O	O		O	O	O	Location
Door sens.	22.5	1	O	O		O	O	O	
Acc. sens.	21.6	1000					O		O
Vital sens.	10.1	1000			O		O		O
Used pow mon	43.5	10		O		O	O	O	
Control	200	24			O	O		O	
Comm times			1	1	1	2	2	3	2
Moni./ctrl			Moni.	Moni.	Moni.	Ctrl.	Ctrl.	Moni.	Ctrl
Fix/mov.			Fix	Fix	Mov.	Fix	Fix	Mov.	Mov.
Update (min)			30	10	30	10	10	30	3
Ave. used pow (μ W)			6.98	9.65	10.91	18.98	18.98	23.47	48.10
									35.49

Moni. Monitoring HEMS, *Ctrl.* Control HEMS, *Fix.* Fixed use, *Mov.* Movable use

Table 2 Power consumption of the sensor network node for rich HEMS model

Model	Power(mW)	T(ms)	1	2	3	RICH HEMS
Sleep	4.50E-03	—				
Comm.	42	3				
RF	22.5	30				
Temp. Sens.	22.5	1	○	○	○	○ ○
Moist. Sens.	0.073	8000	○	○		○
Illumi. Sens.	22.5	1	○	○	○	○ ○
Motion Sens.	0.002	—	○	○		○
Door Sens.	22.5	1	○	○		○
Acc. Sens.	21.6	1000				○
Vital Sens.	10.1	1000		○		○
Used Pow Moni.	43.5	10	○			○
Control	200	24				○
Comm times			1	1	1	2 2
Moni./Ctrl			Moni.	Moni.	Moni.	Ctrl Moni.
Fix/Mov.			Fix	Fix	Mov.	Fix Mov.
Update(min)			30	10	30	0.05 0.05
Ave. used Pow (μ W)			6.98	9.65	10.91	2500 11120

Moni. Monitoring HEMS, *Ctrl.* Control HEMS, *Fix.* Fixed use, *Mov.* Movable use

energy and provides rich services. The revised estimation for Rich HEMS is shown as Table 2. The object of this paper is to seek for the richer energy harvesting method in our surroundings at home so as to generate more than 2.6 mW (containing power conditioning energy). Hereafter we will go advanced to next generation HEMS.

2 Energy Harvesting Scene at Home

We have shown the potential for the illumination power generation by room the light equipment and the thermal gradient power generation between human body and room temperature at home. Each harvester can generate power over wide area in the house for long but the generated average power is less than 100 μ W [1]. Then now we seek for other places and other power generation methods as following.

- (i) Wind power generation by an ventilation fan at kitchen
- (ii) Human step power generation on the floor at kitchen
- (iii) Micro hydroelectric power generation at kitchen or bath tab
- (iv) Magnetic flux leakage energy from the light bulb

These situations are hopeful for higher power generation but the place to be set are restricted. The conceptual view is described in Fig. 1.

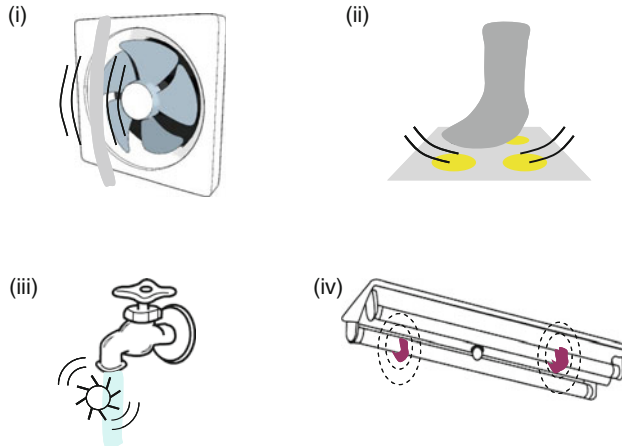


Fig. 1 Energy harvesting Scenes at home. (i) Wind power generation. (ii) Human step power generation. (iii) Hydroelectric power generation. (iv) Magnetic flux leakage power generation

3 Experimental Results for Energy Harvesting

The experiments for each scene in Sect. 2 using various energy harvesting methods are performed and the results are as following (refer Fig. 2).

- (i) We adopt the fan belt type electric power generator because such type of generator can work under gradually weak wind less than 0.3 m/s. The resonant frequency is depended on the tensilon. In this experiment the tension is set at 10 kgf and resonant frequency is 40 Hz, maximum power is 200 μ W under ventilation wind. Considering life condition, the average power is estimated as 33 μ W. In this experiment, generated power was very low.
- (ii) Twenty Piezoelectric elements are arrayed in the rectangle elastic board with twenty holes. If foot step presses the upper board, the bush presses piezoelectric element and the voltage occurs. Five line elements are connected in parallel and connected group is rectified. Four rectified line are connected in parallel. In this circuit generated maximum power is 270 μ W. Considering life style, the average power is estimated as 45 μ W. The result was greatly less than 1 mW, too.
- (iii) The water wheel has eight blades and the axis of rotation is connected to coils surrounded with permanent magnet. The generated alternative voltage is rectified. In general the flow speed of water from the valve at kitchen is 4.2×10^{-3} /min. In such condition, the generated power is 200 mW, and the average power is estimated as 30 mW. This is very hopeful way of energy harvesting.
- (iv) The magnetic flux leakage power generation is based on Ampere's law and Faraday's law of induction. Then this method is largely depends on frequency.

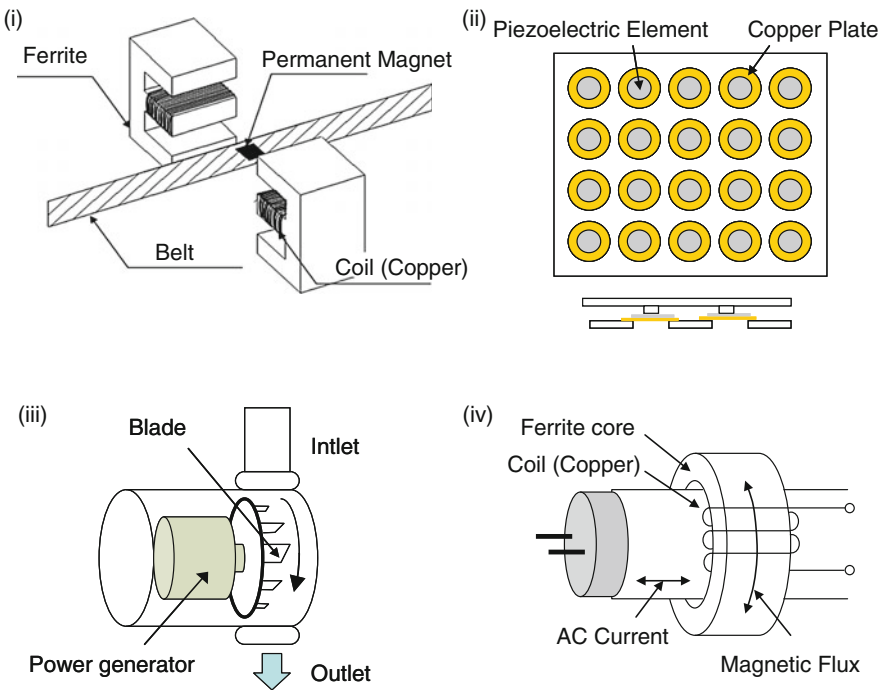


Fig. 2 The schematics of method of energy harvesting. (i) Wind power generation. (ii) Human step power generation. (iii) Hydroelectric power generation. (iv) Magnetic flux leakage power generation

The generated power is proportional to the square of frequency. For such reason, this method is effective for inverter lighting. We use the 18 W, 50 [kHz] inverter fluorescent light. The fluorescent light is surrounded by the toroidal inductor. The output maximum power is 13 mW, the average power during a day is 4 mW.

4 Discussion for Rich Hems and Conclusion

Four types of energy harvesting were described in Sects. 2 and 3. And we have already clarified the potential of room illumination and human temperature gradient power generation [1]. The characteristics of six types of energy harvesting mentioned above are shown in Fig. 3 referring to fundamental two axis, “number of setting points” and “average power generation” under standard life condition. As the result, useful two energy harvesting methods for Rich HEMS are clarified. One is the hydroelectric power generation that can generate over 10 mW, although used in the very few places. And the other is magnetic flux leakage power generation that

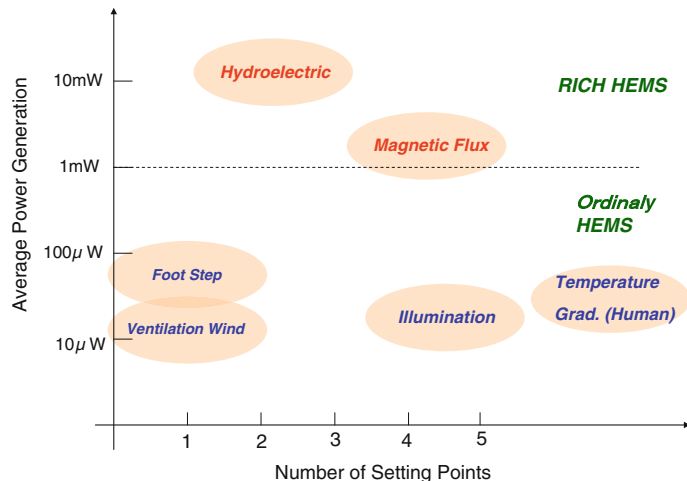


Fig. 3 The characteristics of six types of energy harvesting

can be used at almost all of the rooms, although its generated power is inferior to hydroelectric one. By obtaining those results and understanding useful method of energy harvesting, we can go to next stage for Rich HEMS.

Reference

1. Takashi Yoshikawa, “Novel Concept for HEMS Apparatus”, Elsevier Science Direct 2012. Energy Procedia **14**, 1273–1279 (2012)

Optimizing Residential Energy Consumption in Romania

Ion Smeureanu, Francesco Moresino, Marian Dardala, Adriana Reveiu and Felix Furtuna

Abstract This paper proposes a modelling approach based on TIMES/VEDA systems, designed to optimize energy system model and connected aspects, like economic development and consumer behaviour, in order to decrease energy consumption in households. The economic and technological factors have been used to set-up the energy model. A case study of Romania's residential energy consumption model is included.

1 Introduction

The essence of European energy policy is the idea that the whole advantage of the energy prices liberalization has to be turned to the end consumers, starting from the premise that effective competition in supply will lead to lower prices, increased quality of services, innovations in the supply energy and consumption.

In the Romanian socio-economic context, the analysis of energetic area assumes detailed insights revealing the consumer behaviour and typologies, based on their attitude towards consumption. Based on deep correlations between the energy market supply and demand, the investors try to maximize their profits, while the final consumers try to identify savings possibilities.

A set of factors are influencing the consumer's behaviour such as price, quality, the affinity for a specific type of energy [1], the education degree regarding the new energetic sources and the swarm effect, based on the presumption that a large group of consumers are acting together to achieve efficiency.

I. Smeureanu · M. Dardala · A. Reveiu (✉) · F. Furtuna
Bucharest University of Economic Studies, Bucharest, Romania
e-mail: reveiu@ase.ro; adriana_rev@yahoo.com

F. Moresino
Haute Ecole de Gestion de Genève, Geneva, Switzerland

2 Times/Veda Typical Model

TIMES (The Integrated MARKAL EFOM System) is developed by the Energy Technology Systems Analysis Programme, under the International Energy Agency. It is widely used for modelling a specific energy system at the national, regional, provincial, or community level. The model is driven by least-cost approach, and it is used in order to identify cost-effective responses to emission reduction targets.

The set of relations that are established between the magnitudes of variables that appear in the model, regarding the extraction, transportation, storage, energy conversion processes from one form to another, towards the final consumer, form the Reference Energy System.

From the spatial point of view, the model can be local, national or multiregional. In terms of time, the model has a reference year, a period of calibration and refinement and a horizon time for the forecast.

The model takes into account the processes of the conversion technologies, describing equationally the efficiency of transforming the primary resources into energy, taking into account the technical transformation coefficients, costs, installed capacities coefficients, operating and maintenance time and costs [2].

The constraints of the model describe all energy flows: production of electricity and centralized heat, industrial processes, consumption by end-use technologies and lastly energy services.

The model restrictions are related to the legislation or market, being driven by the cost of obtaining a unit of energy and hence, the selling price; however, to a large extent, the market restrictions are in turn influenced by the relationships between suppliers and consumers, the consumer behaviour having an crucial role.

From a mathematical perspective, the model fits in linear programming with a dynamic solution; the objective function aims to minimize the total cost throughout the time horizon, using an update of the annual costs based on a discount rate.

The mathematical description using TIMES is based on the concept of a Reference Energy System, as a network of three basic entities: technologies and commodities connected by commodity flows.

- **Technologies** are representations of physical processes and equipment that transform commodities into other commodities. Processes can involve a primary resource (e.g. oil extraction, mining processes etc.), or transformation activities (such as power generators, refineries) or end-use demand specific devices, such as cars, heating systems, etc.

Process technologies produce storable energy carrier (like technologies used for hydrogen generator, refineries, pipelines, boilers, and emission reduction devices), while conversion technologies produce non-storable energy carrier, such as heat or electricity.

- **Commodities** are materials, fuels, energy carriers, energy services, monetary flows and emissions; a commodity is either produced or consumed by one or several technologies.

- **Commodity flows** are the connections between processes and commodities. A flow has the same nature as a commodity, but is attached to a particular process, and represents one input (such as coal for electricity power plants) or one output of that process (for example, electricity generation from wind).

These three entities are used to describe the energy system that characterizes the country or region in question. All TIMES models have a reference energy system, which is a basic model of the energy system before it is refined in accordance with a particular region or for a particular scenario.

Decision variables represent the “choices of technology” suggested by the model in order to minimize loss in welfare, e.g. wind power instead of bioenergy, led bulbs instead of incandescent ones.

3 Results: Model Implementation for Romania

TIMES are frequently used to analyse the entire energy domain, but may also be used to study in detail just related aspects to a single segment (e.g. household energy consumption, as our model does).

The proposed model is a partial equilibrium model of the Romanian energy market [3] to perform technological, economic, environmental and social analysis.

Main objectives of the model are:

- Evaluation of the final energy demand;
- Achievement of EU targets by 2020 concerning energy savings and new technologies;
- Projection of residential energy efficiency scenarios, for Romania.

The description of demand side, for Romania, is detailed for the following areas:

1. Household energy consumption, based on different energy carriers or services:
 - Lighting (Kerosene, Incandescent, Fluorescent, LED),
 - Space Cooling (Electricity),
 - Space Heating (Natural Gas, Biomass/Wood, Oil Products, Coal, Solar),
 - Hot Water (Natural Gas, Biomass/Wood, Oil Products, Coal, Solar),
 - Combined Space Heating—Hot Water SH-HW,
 - Refrigeration (Electricity),
 - Washing machine (Electricity),
 - Dish Washing (Electricity),
 - Cloth Dryers (Electricity),
 - Others (Electricity).
2. Individual (private) transport: small/medium/large size car (Gasoline, Diesel, LPG)
3. Public Passenger Transport (Urban, Long Distances)
4. Demand Transport Freights.

Figure 1 includes the Reference Energy System TIMES model used for Romania's household sector.

The TIMES model use for transport sector is presented in Fig. 2.

Because data about domestic lighting energy consumption is not available, we conducted a sociological survey to estimate the available bulbs, their types and consumption, for Romanian's households.

The generation of the model was made by using TIMES software tool. Model implementation is based on the GAMS (General Algebraic Modelling System), a

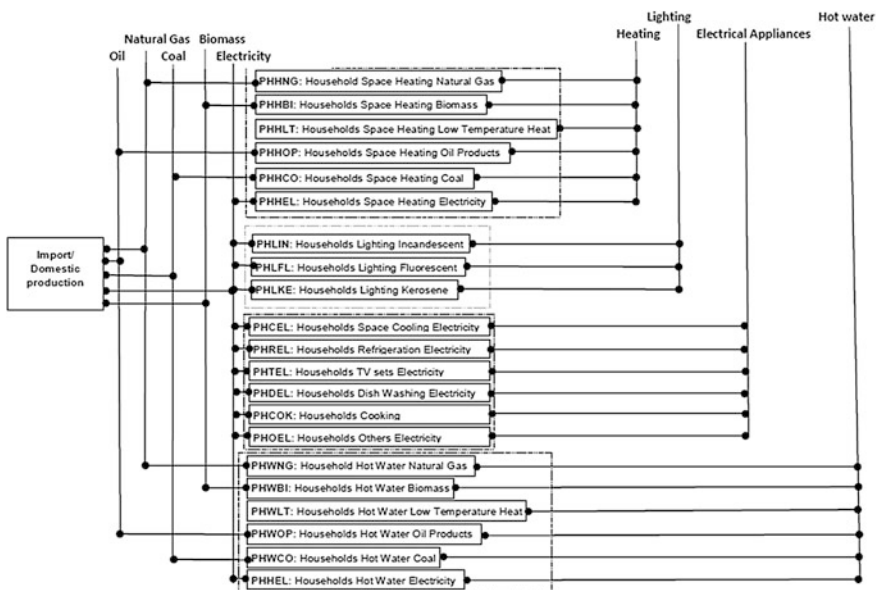


Fig. 1 Reference energy system for romania times households sector

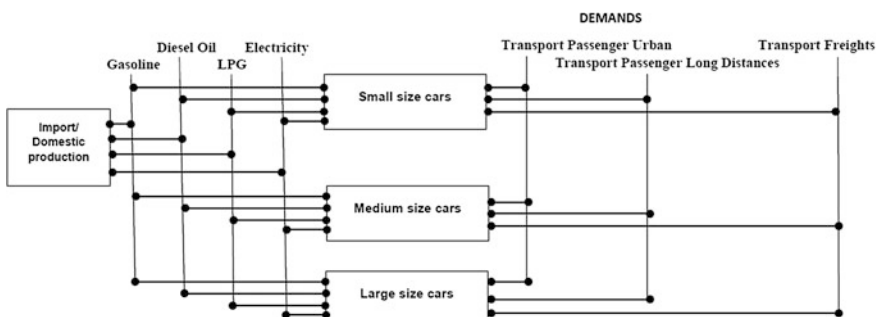


Fig. 2 Proposed reference energy system for transport sector

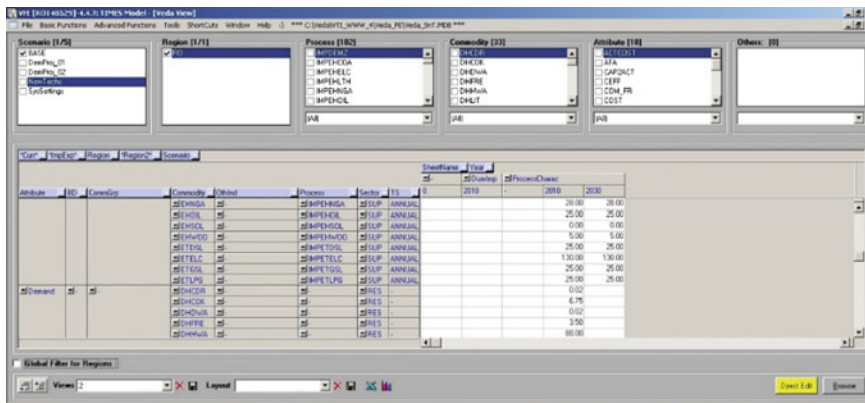


Fig. 3 VEDA front end browser. Romania's model

computer language specifically created to facilitate the development of algebraic models (Fig. 3).

Construction, handling, and maintenance of large scale models are difficult without a performing user-friendly interface. VEDA (acronym for VErsatile Data Analyst), offers a user customized interface for handling files, databases and results from large—scale mathematical and economic models. The proposed implementation makes use of both VEDA components:

- VEDA-FrontEnd which supports MARKAL and TIMES models, for input data handling, being used in several multi-region applications in USA and Europe;
- VEDA-BackEnd which is a very versatile and powerful interface to look at a variety of data, including exposure of results from the model.

The model operates with an initial period (2010 in our case), a model calibration period (2011, 2012, 2013) for testing and refining and a forecast period (2014–2030), detailing yearly the period from 2010 to 2020 and from three to three years the remaining period.

Once completed, the mathematical description of the model is provided as an input for solver module; the solver is a software package built in GAMS which resolves the mathematical programming problem produced by the model generator.

Some results of achieved from TIMES energy model for Romania are

- Electric energy for lighting (DHLIT) got the peak in 2013, and it will stay almost constant due to the ban of incandescent lamps and rising price of electric energy; another factor driving to consumption reduction is the LED technology penetration (~5 % of marketed bulbs are LED).
- The energy demand for cooking energy (DHCOK), freezer and refrigerator (DHFRE & DHREF) in households have slight increases (energy price increasing is balanced by the consumption specific to new technologies).

- Energy demand for TV-set (DHTVS) and washing machine (DHWMA) is just slowly increasing due to the efficiency of consumption.
- Demand for biomass/wood (EHWOO), oil for heating (EHOIL), coal (EHC0A), low temperature heating (EHLTH), and household heating, by using natural gas (EHNGA) will decrease until 2026, in favour of electrical energy consumption in households (EHESH). The changes follow the rapport between energy prices.

4 Conclusions

We consider very useful for Romania, and not only, the scientific results achieved, presented inside the papers because of some specificity of Romania's economy: a deep restructuring industry, an agriculture requiring major investments and energy consumption per household of more than 3 times higher than in some EU countries.

Liquidation energy subsidies, liberalization of the energy market and last but not least, structural remodelling of energy consumption in the context of developing new production technologies (wind, solar), and end-use technologies (convection, light) must determine significant changes, both in national energy policies and the behaviour of individual consumers.

Acknowledgments This work was supported by the Swiss Enlargement Contribution in the framework of the Romanian-Swiss Research Programme (Grant IZERZ0_142217, Design of a sustainable energy model by inclusion of behavioural and social parameters, 2012–2015).

References

1. R. Kanala, E. Fragnière, F. Moresino, M. Dârdală , First insights on socio-Markal approach applied on Times-Romania country model, in *Proceedings of the IE 2013 International Conference on Economic Informatics*, Bucharest, 2013, pp. 585–588
2. E. Fragnière, R. Kanala, N. Turin, An energy optimization framework for sustainability analysis: inclusion of behavioral parameters as a virtual technology in energy optimization models, in: Zongwei Luo (ed.), *Mechanism Design for Sustainability*, Springer 2013, pp. 107–120
3. T. Furtună, A. Reveiu, M. Dârdală, R. Kanala, Analyzing the spatial concentration of economic activities: a case study of energy industry in Romania, *Journal of Economic Computation and Economic Cybernetics Studies and Research*, no. 4/2013, vol 47, pp. 35–52, ISSN 0424-267X

Part XVI
Materials for Sustainable Energy

Determination of Assessment Scale for Selected Indicators in Slovak Building Environmental Assessment System BEAS

Silvia Vilčeková, Eva Krídlová Burdová and Monika Čuláková

Abstract By assessed different material compositions of building envelope which comply U-value of energy standard and nearly zero energy residential buildings it is possible to compare the impact of increasing insulation materials in structure compositions on embodied energy. The selection of building materials for building structures which has a significant share of total environmental performance of building and the potential of improvement is analyzed in this paper. By evaluating of large quantity of different material compositions of conventional and alternative environmental suitable structures of building envelope were determined criteria for environmental indicators such as embodied energy, $\text{CO}_{2\text{eq}}$ emissions and $\text{SO}_{2\text{eq}}$ emissions. The criteria for the evaluation of mentioned environmental indicators are determined on the base of alternative material compositions of structures which are assessed in order to identifying the most optimal solutions in terms of environmental sustainability by LCA within system boundary “cradle to gate”. The aim of this paper is to introduce the Slovak building environmental assessment system (BEAS) and to determine the criteria for environmental indicators such as embodied energy, $\text{CO}_{2\text{eq}}$ emissions and $\text{SO}_{2\text{eq}}$ emissions for the purpose of their implementation to BEAS. Worldwide used building environmental assessment systems and tools were the base of new system development for Slovak conditions. The fields and indicators were proposed on the bases of available information analysis from particular fields of building environmental assessment and also on the base of our experimental experiences.

1 Introduction

The sustainable building is a further development from a simple building labeling—the energy performance based certificate—to more complete consideration of buildings and their impact on the environment according to Seinre [1]. The new

S. Vilčeková · E. Krídlová Burdová (✉) · M. Čuláková
Faculty of Civil Engineering, Institute of Environmental Engineering,
Technical University of Košice, Košice, Slovakia
e-mail: eva.kridlova.burdova@tuke.sk

approach of sustainability assessment of buildings requires the quantification of impacts and aspects for the environmental, social and economic performance of buildings using quantitative and qualitative indicators. These indicators are included in building environmental assessment systems and tools used in different countries for evaluating the integrated building performance. The Building Research Establishment Assessment Method (BREEAM) was the first real attempt and various schemes such as Sustainable Building Tool (SBTool) [2]. After that, other methodologies, such as the Comprehensive Assessment System for Building Environmental Efficiency (CASBEE) from Japan [3], the Building and Environmental Performance Assessment Criteria (BEPAC) from Canada [4], the Building Environmental Assessment Method (BEAM) from Hong Kong [5], the Green Building Rating System (SABA) from Jordan [6], the LiderA from Portugal [7], the National Australian Building Environmental Rating System (NABERS) from Australia [8], the Green Globes from Canada [9], the Sustainable Building Assessment Tool (SBAT) from South Africa [10], the Estidama from United Arab Emirates [11] and the Leadership in Energy and Environmental Design (LEED) from the United States were developed and are currently widely applied [12]. These systems used method of life-cycle assessment (LCA) for evaluation of their fields and indicators by respecting the life cycle of buildings. LCA is a process whereby the material and energy flows of a system are quantified and evaluated. Typically, upstream (extraction, production, transportation and construction), use, and downstream (deconstruction and disposal) flows of a product or service system are inventoried first. Subsequently, global and/or regional impacts (e.g. global warming, ozone depletion, eutrophication and acidification) are calculated; based on energy consumption, waste generation, etc. LCA allows for an evaluation of impacts of different processes and life cycle stages on the environment [13]. LCA is a tool for systematically analyzing environmental performance of products or processes over their entire life cycle, including raw material extraction, manufacturing, use, and end-of-life (EOL) disposal and recycling. Hence, LCA is often considered a “cradle to grave” approach to the evaluation of environmental impacts [14–16]. According to Ferreira [17] the design phase of a building is the one where the major decisions about its performance are made and therefore this decision-making phase is the most important to implement criteria of sustainable construction. As stated in the Alshamranis study [18] that many researchers worked with LCA based tools, Analytical hierarchy process (AHP), and other criteria scoring systems such as LEED, CASBEE, BREEAM and SBTool. Moreover, depending on the type of building, location and assessment objectives, development of novel models and techniques have also been reported. However, effective incorporation of LCA into the aforementioned criteria scoring systems is at the exploratory stage [19]. The aim of this paper is to introduce BEAS and to determine the criteria for environmental indicators such as embodied energy, $\text{CO}_{2\text{eq}}$ emissions and $\text{SO}_{2\text{eq}}$ emissions for the purpose of their implementation to BEAS.

2 Methods

Assessment of different material compositions of building envelope which comply U-value of energy standard and nearly zero energy residential buildings allows the comparison of embodied energy impacts on increasing insulation materials in structure compositions. The material compositions are divided into three groups A, B and C. The group A involves 100 designed conventional material solutions for Slovak energy standard according to STN 730540, the group B involves 80 conventional material compositions for Slovak nearly zero energy residential buildings and the group C involves analyzed material compositions of 164 alternative solutions for design of nearly zero energy residential buildings. The resultant values of embodied energy and U-values of each evaluated building envelope indicate that alternatives of group C can achieve lower embodied energy than conventional energy standard solutions which consist of lower amount of building materials (mainly insulations). The most of alternatives from group C with higher embodied energy than 900 MJ/m² consist of cross laminated wood panel with wood fibre-board insulation. The suitable material selection, especially using nature materials, is possible for design of nearly zero energy residential buildings with minimal environmental impacts.

2.1 Embodied Energy and Emissions of Building Envelope

The values of embodied energy and emissions determined for building envelope are presented in Table 1.

Table 2 illustrates the results of embodied energy and emissions for structures designed for buildings accomplished thermal requirement to year of 2012 (group A), low energy buildings (group B) and nearly-zero energy buildings (group C) in Slovakia. High value of embodied energy was achieved in group B of building envelope and least value was achieved in group C as well as in ECO₂ emissions and

Table 1 The value of embodied energy and emissions of floor, external wall and roof structures

	EE (MJ/m ²)	ECO ₂ (kg CO _{2eq} /m ²)	ESO ₂ (kg SO _{2eq} /m ²)
Floor—group A	1368.831	78.964	0.438
Floor—group B	2010.541	98.256	0.572
Floor—group C	978.972	-115.193	0.463
External wall—group A	838.789	41.971	0.235
External wall—group B	1157.869	83.563	0.333
External wall—group C	675.864	-100.302	0.294
Roof—group A	1313.689	34.877	0.446
Roof—group B	1787.6	50.614	0.627
Roof—group C	984.72	-99.862	0.415

Table 2 The value of embodied energy and emissions for building envelopes

	EE (MJ/m ²)	ECO ₂ (kg CO _{2eq} /m ²)	ESO ₂ (kg SO _{2eq} /m ²)
Building envelope—group A	1173. 77	51.94	0.373
Building envelope—group B	1652.00	77.48	0.51
Building envelope—group C	882.18	-104.62	0.392

ESO₂ emissions. These results are implemented to evaluation of indicators proposed in the Slovak building environmental assessment system BEAS.

2.2 Building Environmental Assessment

Lately the evaluation of building performance in terms of environmental, social and economic aspects has become a topic of discussion in the Slovak Republic. A new Building Environmental Assessment System (BEAS) has been developed at the Institute of Environmental Engineering, Technical University of Košice. Systems and tools used in many other countries were the foundation of this new system development for application in Slovak conditions. BEAS as a multi-criteria system includes environmental, social and cultural aspects. The proposed fields and indicators respect and adhere to Slovak standards, rules, studies and experiments. The presented system was developed for design stage of residential buildings. This system has six main fields: A—Site Selection and Project Planning, B—Building Construction, C—Indoor Environment, D—Energy Performance, E—Water Management and F—Waste Management. The total number of indicators in system BEAS is 52. Each main field has several indicators which have the intent of assessment and the scale of assessment. This scale is from negative (-1 point), acceptable practice (0 point), good practice (3 point) and best practice (5 point). Result of each indicator is obtained so that the point from scale is multiplying with weight of indicator. Main field “Building construction” marked as B has two sub-field of assessment: Materials (B1) and LCA (B2). The criteria of indicators evaluation are determined according to study presented above. The weights of significance of indicators, sub-fields and fields are determined by Saaty method. Building materials in BEAS has a percentage weight of 20.59 %. First sub-field of assessment Materials has a percentage weight of 75 % and has 5 indicators (B1.1 Product environmental labelling, B1.2 Use of materials that are locally produced, B1.3 Use of recycled materials, B1.4 Use of substitutes in concrete and B1.5 Radioactivity of building materials). Second sub-field of assessment LCA has a percentage weight of 25 % and has 3 indicators of assessment (B2.1 Embodied energy, B2.2 Global warming potential and B2.3 Acidification potential). In the Table 3 is shown way of assessment of sub-field of LCA.

Table 3 Assessment of field Building construction and sub-field of LCA

B2	LCA	25 %	
B2.1	Embodied energy	40.00 %	
Purpose	To ensure using of building materials with a lower value of embodied energy	Point	Weight
Indicator	The percentage of built-in building materials with lower value of embodied energy		
Negative practice	The predicted embodied energy of built-in building materials is	>1500 MJ/m ²	-1
Acceptable practice		1001–1500 MJ/m ²	0
Good practice		600–1000 MJ/m ²	3
Best practice		<600 MJ/m ²	5
B2.2	Global warming potential	40.00 %	
Purpose	To minimize the production of atmospheric emissions of CO ₂ from mining, manufacturing, transport and construction of building that may result in global warming potential	Point	Weight
Indicator	CO ₂ equivalent in kg per unit net area		
Negative practice	The predicted emission from non-renewable sources of CO ₂ equivalent in kg per unit area net	>100 kg/m ²	-1
Acceptable practice		51–100 kg/m ²	0
Good practice		10–50 kg/m ²	3
Best practice		<10 kg/m ²	5
B2.3	Acidification potential	20.00 %	
Purpose	To minimize the production of atmospheric emissions of SO ₂ from mining, manufacturing, transport and construction of building that may result in acidification	Point	Weight
Indicator	SO ₂ equivalent in kg per unit net area		
Negative practice	The predicted emission from non-renewable sources of SO ₂ equivalent in kg per unit area net	>0.45 kg/m ²	-1
Acceptable practice		0.35–0.40 kg/m ²	0
Good practice		0.25–0.34 kg/m ²	3
Best practice		<0.25 kg/m ²	5

3 Conclusions

The selection of building materials for structures which has significant share of total environmental performance of building and the potential of improvement is analyzed in this paper. By evaluating of large quantity of different material compositions of conventional and alternative environmental suitable structures of building envelope were determined the criteria for environmental indicators such as embodied energy, CO_{2eq} emissions and SO_{2eq} emissions. The criteria for the evaluation of mentioned environmental indicators are determined on the base of alternative material compositions of structures which are assessed in order to identifying the most optimal solutions in terms of environmental sustainability by LCA within system boundary “cradle to gate”. The proposed fields and indicators in

system BEAS respect Slovak standards, rules, studies and experiments. Building construction field has two subfields. First is assessment of Materials with weight of 75 % and second subfield is assessment of LCA with weight of 25 %.

Acknowledgments This study was financially supported by the Grant Agency of Slovak Republic (project VEGA No. 1/0405/13).

References

1. E. Seinre, J. Kurnitski, H. Voll, Building sustainability objective assessment in Estonian context and a comparative evaluation with LEED and BREEAM. *Build. Environ.* **82**, 110–120 (2014)
2. S.H. Alzami, Y. Reygui, Sustainable building assessment tool development approach. *Sustain Cities Soc.* **5**, 52–62 (2012)
3. CASBEE. CASBEE® for New Construction (2010 Edition). CASBEE-NCe_2010v1.0
4. R.J. Cole, D. Rousseau, G.T. Theaker, *Building Environmental Performance Assessment Criteria (BEPAC)* (BEPAC Foundation, Vancouver, 1993)
5. BEAM Plus., BEAM society. Building environmental assessment method. NB—New Buildings (2009), p. 219
6. D.F. Ciambrone, *Environmental life cycle analysis* (Lewis, Boca Raton, 1997)
7. S. Joshi, Product environmental life-cycle assessment using input–output techniques. *J. Ind. Ecol.* **2–3**, 95–120 (1999)
8. L.F. Cabeza et al., Life cycle assessment (LCA) and life cycle energy analysis (LCEA) of buildings and the building sector: a review. *Renew. Sustain. Energ. Rev.* **29**, 394–416 (2014)
9. H.A. Hakmat, F. Sab, Developing a green building assessment tool for developing countries—case of Jordan. *Build. Environ.* **44**, 1053–1064 (2009)
10. LiderA, Voluntary system for assessment of sustainable construction
11. NABERS, NABERS Office Building Trial (2008)
12. Green Globes, *Assessment and Rating System. Program Summary and Users Guide* (Green Building Initiative, Oregon, 2008)
13. B. Whitehead et al., Assessing the environmental impact of data centres part 2: building environmental assessment methods and life cycle assessment. *Buildn Environ.* 1–11 (2014)
14. Estimada (2014), <http://www.estidama.org/estidama-and-pearl-rating-system.aspx?lang=en-US>. Accessed 11 Oct 2014
15. LEED 2009 for new construction and major renovations. For public use and display. USGBC Member Approved November 2008, p. 117
16. T. Ramesh, R. Prakash, K.K. Shukla, Life cycle energy analysis of buildings: an overview. *Energ. Buildings* **42**, 1592–1600 (2010)
17. J. Ferreira, M.D. Pinheiro, P. Brito, Portuguese sustainable construction assessment tools benchmarked with BREEAM and LEED: an energy analysis. *Energ. Buildings* **69**, 451–463 (2014)
18. O.S. Alshamrani, K. Galal, S. Alkass, Integrated LCA-LEED sustainability assessment model for structure and envelope systems of school buildings. *Build. Environ.* **80**, 61–70 (2014)
19. M.M. Mer'eb, GREENOMETER-7: a tool to assess the sustainability of a building's life cycle at the conceptual design phase. Dissertation, Cleveland State University (2008)

Effect of Ni Seed Layer for Electroplating ^{63}Ni in Beta Voltaic Battery

Y.R. Uhm, B.G. Choi, K.J. Son and D.H. Jeong

Abstract Ni seed layers with a thickness of 200, 500, and 1000 Å were deposited by e-beam irradiation on a single trench P-N absorber in a beta voltaic battery. The optimum thickness of ^{63}Ni on the seed layer was determined to be about 2 μm regarding the minimum self-shielding effect of a beta-ray (β -ray). The electroplating was carried out using two-step processes such as preparation of ionic solution including ^{63}Ni , and coating processes on the seed layer. The electroplating of Ni on the seed layer was carried out at current density of 20 mA/cm². Both the conductivity and uniformity of the seed layer are enhanced, as the thickness of deposit layer is increased. However, self-shielding of β -ray from measuring photo-voltaic (I-V curves) is significantly increase, as the thickness of the seed layer become thick. To fabricate the effective β -voltaic battery, the thickness of seed layer about 500 Å has been determined in view of both preventing self-shielding β -ray and increasing conductivity on the surface.

1 Introduction

Radioisotope batteries derive their energy from the spontaneous decay of radioisotopes, as distinguished from nuclear fission energy created in reactor power systems. To apply power source, devices with small volume convert radioactive decay into electricity to provide high energy densities for several decades, where

Y.R. Uhm (✉) · K.J. Son

Radioisotope Research Division, Korea Atomic Energy Research Institute (KAERI),
Daejeon 305-353, Korea
e-mail: uyrang@kaeri.re.kr

B.G. Choi

Human Interface SoC Research Section, Electronics and Telecommunications Research
Institute (ETRI), Daejeon, Korea

D.H. Jeong

Dongnam Institute of Radiological and Medical Science, Busan, Korea

harvestable energy is unavailable [1]. As a result, a variety of nuclear-based small-scale power sources have been developed with varying degrees of success and maturity. A nuclear battery with a diode junction is a device that converts nuclear radiation directly into electric power [2]. The mechanism of a nuclear battery is same as the P-N junction diode for solar cell application. The photovoltaic is operated by photons converted into electrical energy in the junction. In betavoltaic battery, beta particles are collected and converted to electrical energy through a similar principle as photovoltaic. A very low current, on the order of nano or micro amperes, is generated in devices [2, 3]. If a radioisotope (RI) with a long half-life (over 50 years) is used, a lifetime of a power source is extended as long as half-life time of RI [4]. Some special applications require long-lived compact power sources. These include space equipment, sensors in remote locations (space, underground, etc.), and implantable medical devices. Conventionally, these sources rely on converting chemical energy to electricity. This means they require a large storage of chemical “fuel” since the amount of energy released per reaction is small [5, 6]. A nuclear battery is a novel solution to solve the power needs of these applications. For the ^{63}Ni beta-source we used, the half-life is 100.2 years. Hence, the power sources we describe can extend a system’s operating life by several decades or even a century, during which time the system can gain learned behavior without worrying about the power turning off. Radioactive thin-film-based power sources also have energy density orders of magnitude higher than chemical-reaction-based energy sources. This enables submillimeter-scale power sources, which is significant given the crucial role that metrics of power and energy density play in determining pervasive computing systems’ usefulness in applications limited by size [7]. In this study, a beta voltaic battery using ^{63}Ni coated on single trenched PN absorber was fabricated and measured short circuit current from I-V curves. For electrodeposition of ^{63}Ni , the seed layer should be coated on the P-N junction. The thickness dependent self-shielding effect of the seed layer was studied by using both simulation using MCNP code and measurement of I-V curve [8].

2 Experimental

2.1 P-N Junction Formation

To fabricate the P-N absorber, new type of 3D single trenched P-N absorber was developed for easy trenching and doping process. The 3D structure of P-N absorber with single trench was applied. In order to turn the P-N junction wafer into a substrate on which ^{63}Ni can be deposited and power output can be measured, metallic contacts have to be on the wafer that served as seed layer for ^{63}Ni electroplating. Ni seed layers with thickness of 200, 500, and 1000 Å were deposited by an e-beam irradiation on the single trench P-N absorber in beta voltaic battery.

2.2 ^{63}Ni Electroplating

Nickel (Ni) coatings were deposited by DC electroplating at current densities of 20 mA/cm^2 . The deposit condition for the ^{63}Ni is explained at [9]. The basic composition of the bath was 0.2 M Ni and boric acid (H_3BO_3). Ni metal powders were dissolved in a mixture of HCl and distilled water. Boric acid is used in nickel-plating solutions for buffering purposes. The pH of the bath was adjusted to 4.0 ± 0.2 by addition of KOH. The dimension of deposit layer on P-N junction is $4 \times 4 \text{ mm}^2$ as an anode.

3 Results and Discussion

For the performance characteristic of the P-N junction without seed layer, e-beam illumination test was carried out using e-beam energy of 17 keV as shown in Fig. 1. The P-N spacing was changed as 50, 110, and 190 μm . The electron beam induced current technique has been employed to experimentally simulate the beta emission of ^{63}Ni and to estimate the total device current. The open circuit voltages were found to be 0.29, 0.27 and 0.41 V for P-N spacing of 50, 110, and 190 μm , respectively. The short circuit currents were 3.3, 1.97, and 3.7 μA for P-N spacing of 50, 110, and 190 μm , respectively. The power outputs were found to be 66.5, 36.9, and 105.3 $\mu\text{W/cm}^2$. From the e-beam illumination test, we confirm the good operation of PN absorber.

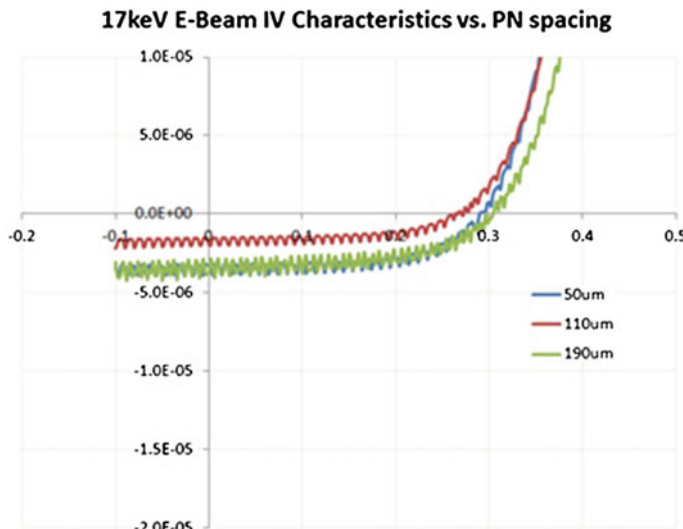


Fig. 1 I-V characteristics for P-N junction with spacing 50, 110, and 190 μm by using e-beam illumination method (e-beam energy: 17 keV)

Ni seed layers with thickness of 200, 500, and 1000 Å were observed by scanning electron microscopy (SEM). The nonhomogeneous surface of the seed layer with thickness, 200 Å was measured. The Ti-Ni seed layer was coated with poor dispersion on the P-N junction. Otherwise, the seed layer with thickness of seed layer thicker than 500 Å was well coated with fully covered by Ti-Ni as shown in Fig. 2. So, the seed layers with thickness of 500 and 1000 Å were applied to beta voltaic battery.

A Ni-plating solution is prepared by dissolving metal particles, and the deposition conditions have been optimized by studying the influence of the current density at previous study. Also, the proposed prototype condition was applied to radioactive ^{63}Ni electroplating. The electroplating was carried out by two-step processes such as preparation of ionic solution including ^{63}Ni , and coating processes on the substrate. The prototype of electroplating ^{63}Ni was carried out at the glove box in a hot cell (Bank-2, HANARO Reactor in KAERI). The specific radioactivity for the starting material (Ni powder) was about 10 mCi. The specific radioactivity of the electroplated Ni including ^{63}Ni was estimated to be about 0.1 mCi. The specific activity was measured by portable activity meter (PAM 1704). Also, we prepared electroplated ^{63}Ni with specific activity of 2.5 mCi for characteristic of nuclear battery. The morphologies of the coating layer were measured by using natural Ni prepared in same bath and plating conditions as radioactive sample. Figure 3 presents SEM images for Ni coating layer at the same current densities but different seed layer conditions following the thickness of 500, and 1000 Å.

Both the conductivity and the uniformity of the seed layer are improved, as the thickness of deposit layer is increased. So, the smoothness of the coated layer was gradually progress, as the thickness of seed layer is increased. However, the penetration depth of the beta particles is related to the junction depth and depletion region width. The penetration depth of the particles in the silicon device was reported at Katz-Penfold range equation [10]. This equation considers only the

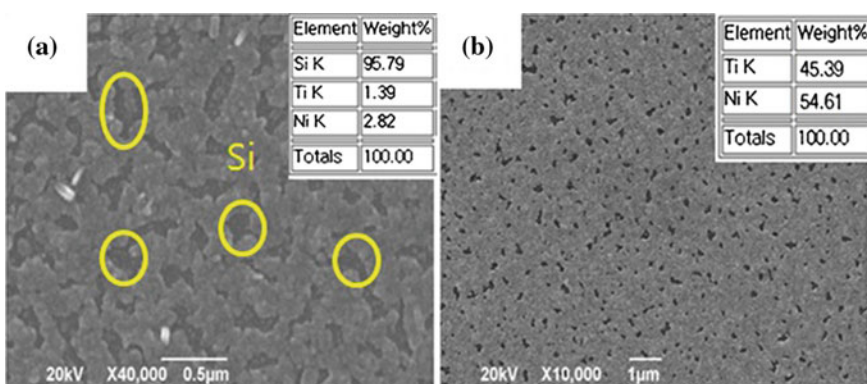


Fig. 2 SEM images for seed layer with thickness of **a** 200 Å and **b** 500 Å

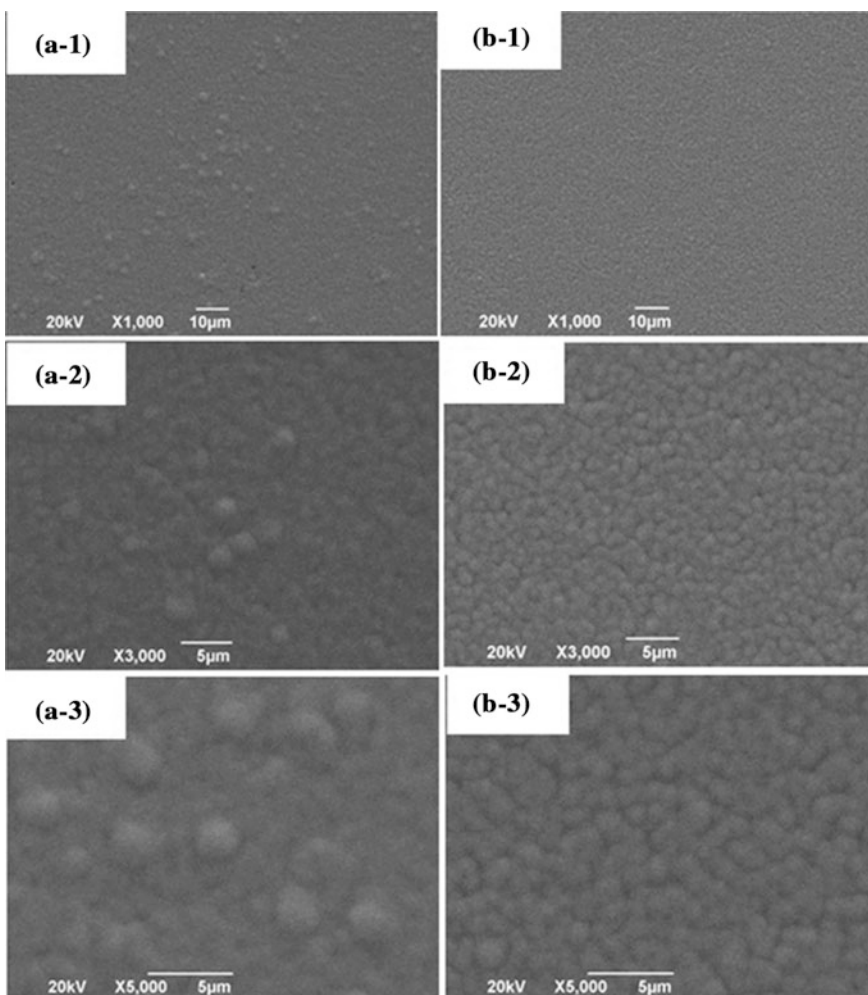


Fig. 3 SEM images for electroplated Ni on seed layer with thickness of **a-1, a-2, a-3** 500 Å, and **b-1, b-2, b-3** 1000 Å

density of the materials and energy of the particles. From the equation, the maximum range of the average beta particles energy from ^{63}Ni into silicon is 2.2 μm .

We modeled the energy deposition as a function of depth in silicon using the Geant4 Monte Carlo code. The seed layer thickness strongly attenuates the low energy beta particles. Figure 4 shows ^{63}Ni self-shielding effect and locus of beta particles in Si. The essentially zero response for a total thickness of 2 μm of ^{63}Ni and seed layer indicates that the self-shielding effect. According to the self-shielding and covering of the surface, the thickness of the seed layer was determined at 500 Å. The performance characteristic of the nuclear battery with P-N spacing of 5 μm using 2.5 mCi of ^{63}Ni was tested using an I-V meter.

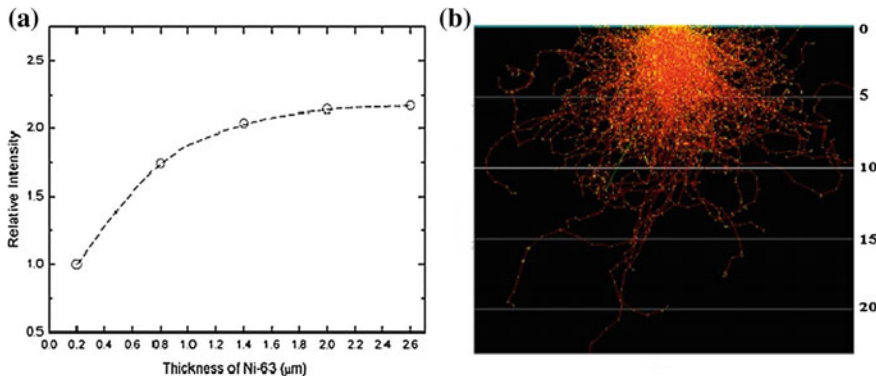


Fig. 4 **a** Energy absorption in silicon as a function of Ni-63 thickness, and **b** beta ray trajectories in the silicon from Ni-63 radioisotope (The unit of vertical axis is μm .)

I-V curves of both pre-deposition and post deposition are shown at almost same values. The difference between the pre-deposition and post deposition could be obtained by magnification [10]. The difference of the short circuit current between the pre-deposition and post deposition of ^{63}Ni on seed layer with thickness of 500 \AA was found to be 5 nA. However, the strong noisy unsuitable to publish exist in magnified graph. If the specific radioactivity is increased, magnified I-V curves will be clear. The short circuit current of the post deposition of ^{63}Ni on seed layer with thickness of 1000 \AA was found to be same values of P-N junction without radioactive layer.

4 Conclusion

Ni seed layers were deposited by an e-beam on the single trench P-N absorber with spacing 5, 110 and 190 μm . The optimum total thickness of ^{63}Ni and seed layer was determined to be about 2 μm regarding the minimum self-shielding effect of beta-ray (β -ray). The electroplating of Ni on the seed layer was carried out at current density of 20 mA/cm². Both the conductivity and the uniformity of the seed layer are enhanced, as the thickness of deposit layer is increased. However, self-shielding of β -ray is significantly increased, as the thickness of the seed layer become thick. To fabricate effective β -voltaic battery, the thickness of a seed layer about 500 \AA was determined.

Acknowledgments This work was performed with financial support from the Industrial Source Technology Development Program (10043868) of the Ministry of Trade, Industry & Energy, Korea.

References

1. T. Christen, M.W. Carlen, J. Power Source **91**, 210 (2000)
2. L.C. Olsen, (1973) 13:117
3. M.V.S. Chandrashekhar, C.I. Thomas, H. Li, M.G. Spensor, A. Lal, Adv. Mater **17**, 1230 (2006)
4. G. Miley, *Direct conversion of nuclear radiation energy* (American Nuclear Society, La Grange, 1970)
5. H. Li, A. Lal, J. Appl. Phys. **92**, 1122 (2002)
6. H. Guo, A. Lal, Digest of of technical paper, tranducers (2003)
7. L. Katz, A.S. Penford, Rev. Mod. Phys. **24**, 28 (1952)
8. Y.R. Uhm, K.Y. Park, S.J. Choi, Res. Chem. Intermed. (2014). doi:[10.1007/s11164-013-1518-0](https://doi.org/10.1007/s11164-013-1518-0)
9. J. Braun, A. Fermvik, A. Stenback, J. Phys. E **6**, 727 (2002)
10. B. Ulmen, P.D. Desai, S. Moghaddam, G.H. Miley, R.I. Massel, J. Radioanal Nucl. Chem. **282**, 601 (2009)

Structural Properties of Polystyrene (PS)/Ferroelectric Barium Stannate Titanate Ba $(\text{Ti}_{0.9}\text{Sn}_{0.1})\text{O}_3$ Ceramic (BST) Composite

M-Ali Al-Akhras, Subhi Saq'an and Zeinab Ghadieh

Abstract Barium Stannate Titanate (BST) ceramics was studied early as a prototype of ferroelectrics with diffused phase transition. Nowadays, many studies on the phase transition, electrical and dielectric properties take place. BST is a binary solid solution system composed of ferroelectric barium titanate and non-ferroelectric barium stannate. A composite of polystyrene PS/Ferroelectric Barium Stannate Titanate BST with different BST concentration was prepared. Structural measurement of XRD, TGA, and SEM showed that they formed a good composite for all concentrations with the exception of the 10 % BST concentration; this behavior was explained by a non-additive law and critical mass of BST.

1 Introduction

Barium Stannate Titanate (BST) is a binary solid solution system composed of ferroelectric barium titanate and non-ferroelectric barium stannate. The effect of adding a ferroelectric ceramic to the polystyrene was prepared for many applications and various purposes. This material system has many applications with various purposes because of the Curie temperature or dielectric maximum which can be widely shifted by changing the tin content. Previous study by Wei and Yao, showed that samples with different tin content are of single phase perovskite structure and they optimized the processing route of BST to prepare a full composition range of solid solution samples and proposed a linear empirical relation between crystal lattice and tin content [1]. Except for barium titanate, the non-cubic peak splitting is observed for compositions with tin content $\geq 10\%$, even in high angle refraction. Narin et al. found poor adhesion between the ceramic and polymer phases, with interface gaps up to 1.0 μm . Perpetrating the ceramic with a

M.-A. Al-Akhras (✉) · S. Saq'an · Z. Ghadieh
Bio-Medical Physics Laboratory, Department of Physics,
Jordan University of Science & Technology (JUST), P.O. Box 3030, Irbid 22110, Jordan
e-mail: alakmoh@just.edu.jo

compatibilizing agent improves adhesion at the interface with polymer but decreases overall conductivity in the case of compatibilizer [2]. Singh et al. reported the role of the dispersal of ferroelectric ceramic materials enhanced the ionic conductivity of a conducting polymer electrolyte (PEO: NH₄I). They found that the addition of 3 wt% of Ba_{1-x}Sr_xTiO₃ (x = 0.30 and 0.12) results in increased conductivity by one to two orders of magnitude [3]. Zihlf et al., studied some physical properties of Rockwool fiber/PS as a function of filler concentration. They reported that the glass transition temperature and mechanical properties are influenced by the fiber concentration [4]. In this study, the major objectives are to investigate structural properties of Polystyrene/Ferroelectric BST Ceramic as a function of concentration using XRD, TGA and SEM.

2 Materials and Methods

Barium Stannate Titanate Ceramic Ba (Ti_{0.9} Sn_{0.1} O₃) was prepared from regent grade TiO₂ (99.995 %), BaCO₃ (99.999 %) and SnO₂ (99.99 %) predetermined amount was weighted out to yield about 10 gm mixture of the composition desired in terms of oxides. Polystyrene granules was dissolved in dichloromethane solvent and stirred at 30 °C by a magnetic stirrer for 2–4 h until highly viscous polymer solution is formed. The fine powder of BST (0, 1 %, 5 %, 10 %, and 15 %wt) were added and stirred again until the solution composition became highly viscous and homogeneous, more detailed can be found in our previous work [5].

3 Results and Discussion

XRD pattern is shown in Fig. 1 for pure polystyrene, powder BST and PS/BST composites from 1 to 15 wt%. The peaks of polystyrene and BST were found in the composites for 1, 5, and 15 wt%, while the composite of 10 wt% concentration had a different behavior. The characteristic broad peaks of polystyrene that appear at (2θ = 50°) that reflect the dimension of polystyrene cross section, the second peak appears at position (2θ = 23.72°) indicated the average polystyrene chain length. The third peak appearing at (2θ = 13.93°) characterizes the chain-chain separation. The chain-chain separation and the average length of the polymer were estimated from the angle positions of peaks and for composites that had a common behavior (1, 5, and 15 wt% samples) as shown in Table 1. The table shows that the chain-chain separation, *d*, increases with increasing the BST concentration. This result confirms that the BST entered into polystyrene and a good composite without any reaction is obtained. The increment of chain-chain separation wasn't uniform, so it is accepted that the addition of BST to Polystyrene in these composites follows the non-additive law in Chemistry. The non-uniform behavior of sample PS/BST 10 wt% may occurred when it reaches a critical mass for BST, and may a chemical

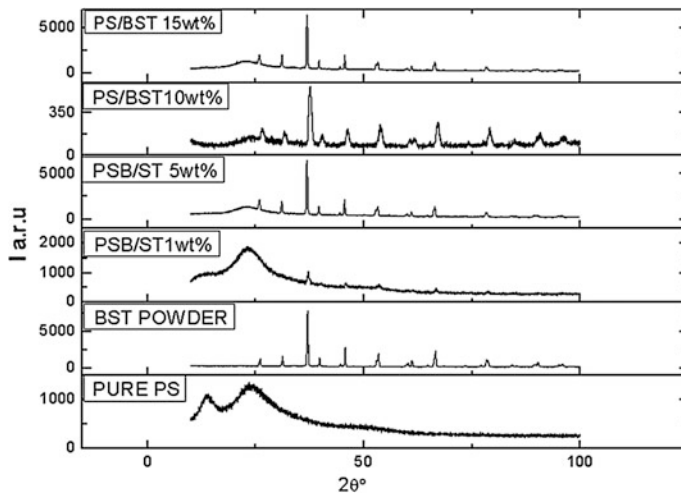


Fig. 1 XRD pattern for all samples

Table 1 Peak angle, chain-chain separation, intensity, temperature and weight loss/gain BST concentration

Sample	$2\theta^\circ$	$d(\text{\AA})$	Intensity	Temp. range (°C)	Weight loss/gain (mg)	(%)
PURE PS	23.72	4.352	1295	144–250	−0.08	0.79
	13.98	7.350	1128			
PS/BST	23.32	4.426	1885	130–250	−0.05	0.71
1 wt%	12.64	8.126	969			
PS/BST	22.84	4.518	1402	134–250	−0.09	0.62
5 wt%	12.52	8.203	666			
PS/BST	—	—	—	142–250	−0.08	1.60
10 wt% PS/BST	22.78	4.529	1352	144–250	−0.04	1.13
15 wt%	11.28	9.102	609			
BST powder	—	—	—	132–250	−0.01	0.90

reaction take place at this point which leads to change in composite structure at this concentration.

The TGA measurements were carried out for all samples. A weight loss of 0.62–1.13 % was observed for temperatures above 100 °C. In Table 1, it is seen that weight loss affected neither the electrical nor the optical measured quantities and this weight loss may be due to moisture.

SEM micrograph was taken in order to study the annealing effect on the composites structure. One sample (PS/BST 15 wt%) was examined before and after annealing as shown in Fig. 2. BST grains are randomly distributed within polystyrene matrix with no surface contact between them, the BST grains appears in white dots.

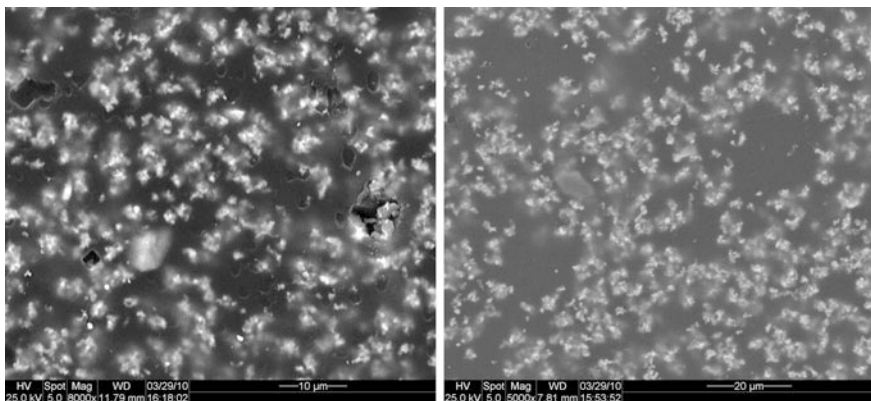


Fig. 2 SEM of PS/BST 15 wt% before annealing (*left*) and after annealing (*right*)

This is another proof that they are inserted in polystyrene and made a good composite. Also it may have surface charges with noticeable holes disappearing after annealing.

4 Conclusion

This research covers some of XRD, TGA, and SEM of Polystyrene PS/Ferroelectric Barium Stannate Titanate Ba $(\text{Ti}_{0.9}\text{Sn}_{0.1})\text{O}_3$ Ceramic (BST) composite with a concentrations between 1 and 15 %wt as a function of concentration. The results showed that they form a good composite for all samples except at BST concentration 10 %; this was explained by a non-additive law and critical mass of BST. Exposing the samples to the vapor of solvent increases their conductivities, possibly by assisting ions to move between the polymer and the ceramic.

Acknowledgments This work was supported by a grant from the Deanship of Scientific Research at Jordan University of Science and Technology (JUST) No. 112/2009.

References

1. X. Wei, X. Yao. Preparation, structure and dielectric property of barium stannate titanate ceramics, *Mater. Sci. Eng.* **137**, 184–188 (2007)
2. K. Narin, A. Best, P. Newman, D. Mac Farance, M. Farsyth, Ceramic Polymer interface in composite electrolytes of lithium aluminium titanium phosphate and polytherurethane polymer electrolyte. *Solid State Ionic* **12** 115–119 (1999)
3. P. Singh, A. Chandra, Role of the Dielectric Constant of Ferroelectric Ceramic in Enhancing The Ionic Conductivity of Polymer Electrolyte Composite, *J.Phys. D:Appl. Phys.* **36**, 93–96 (2003)

4. A. Zihlif, G. Rogosta, A Study on the Physical Properties of Rockwool Fiber—Polystyrene Composites, *J. Thermoplastic Composites Mater.* **16**, 273–283 (2008)
5. M-Ali H. Al-Akhras, S. Al saqan, Z. Ghadieh, Optical Properties s of Polystyrene (PS)/ Ferroelectric Barium Stannate Titanate $\text{Ba}(\text{Ti}_{0.9}\text{Sn}_{0.1})\text{O}_3$ Ceramic (BST) Composite.in *AIP Conference Proceedings* 1569, 23 (2103) doi: [10.1063/1.4849221](https://doi.org/10.1063/1.4849221)

Part XVII

**Materials for Renewable Energy Storage
and Conversion**

Waynergy Vehicles—An Innovative Pavement Energy Harvest System

Francisco Duarte, Adelino Ferreira and João Champalimaud

Abstract This paper describes an innovative pavement energy harvest system, called Waynergy Vehicles, developed in Portugal by Waydip in partnership with the Pavement Mechanics Laboratory of the University of Coimbra. The Waynergy Vehicles was installed in a road pavement in the campus of the University of Beira Interior, which allowed us to test a prototype. During a peak hour, between 1 and 2 p.m., the Waynergy Vehicles system was able to generate 37,800 J or 10.5 W.h. The electrical energy generated by several modules of the Waynergy Vehicles located, for example, in speed humps and speed bumps, can be used not only to charge batteries for electric vehicles, but also for general consumption through injection into the electricity grid or direct use by electrical equipment, such as public lighting traffic lights, and outdoor advertising.

1 Introduction

At the present time there is a need to change the paradigm in electrical energy generation due to the increasing cost of fossil fuels and their adverse effects on the environment. It has become increasingly evident that fossil fuels used to generate energy are not unlimited and that their use is harmful to the environment due to the greenhouse effects. Electrical energy must be increasingly generated using renew-

F. Duarte (✉) · A. Ferreira

Pavement Mechanics Laboratory, Department of Civil Engineering, University of Coimbra,
Rua Luís Reis Santos, 3030-788 Coimbra, Portugal
e-mail: uc2013127588@student.uc.pt

A. Ferreira

e-mail: adelino@dec.uc.pt

J. Champalimaud

Waydip, Parkurbis, Parque de Ciência e Tecnologia da Covilhã, 6200-865 Covilhã, Portugal
e-mail: joao.champalimaud@waydip.com

able energy sources, preferably where it will be consumed, in order to reduce the costs of transport and distribution [1].

Energy is mainly consumed in cities, although it is almost always produced outside cities. Consequently, to reduce transport and distribution costs, we must take advantage of all the energy that can be produced inside the city, near the point of consumption. It is here that pavements have an important role to play. In cities vehicles move around almost everywhere on pavements, and every time they move they release kinetic energy to the pavement. This energy is not usually captured or used for anything, but it could be converted into electrical energy. Additionally, there are plenty of pavement surfaces in cities which could be used to install systems capable of capturing kinetic energy and converting it into other types of energy.

This paper describes an innovative pavement energy harvest system, called Waynergy Vehicles, developed in Portugal by Waydip in partnership with the Pavement Mechanics Laboratory of the University of Coimbra, to convert energy released by vehicles into electricity.

2 Prototype Application Tests

The Waydip Company, a Portuguese startup, has been working on pavement energy harvest systems since 2009. Recently, it developed the Waynergy Vehicles system in partnership with the Pavement Mechanics Laboratory of the University of Coimbra [2–4]. This system consists of blocks with different shapes that can be applied on road and street pavements, containing an electric power generation mechanism that registers a small displacement on the vertical axis each time a vehicle moves over the blocks, which is enough to run the electromagnetic system that generates electric energy. Waynergy blocks for vehicles are large-element paving units, between $0.7 \times 0.8 \times 0.2$ and $3.0 \times 0.8 \times 0.2$ m³. These Waynergy blocks can be used by municipalities in urban areas to generate electric energy for public illumination, outdoor advertising, traffic lights, or electrical supply. They could also be used by private companies in areas with a high motorized traffic volume. Suitable places for applying these blocks are speed control humps, speed control bumps, toll plazas, etc.

The Waynergy Vehicles prototype was designed to harvest maximum energy taking into account the weight of vehicles, which is much greater than the weight of people. To maximize the harvested energy per wheel, the surface area was increased to 0.7×0.8 m². It was concluded that with a two-generator configuration, it is possible to convert more kinetic energy into electrical energy, and the prototype was developed using this main principle.

The prototype was installed in the pavement of the car parking access road of the Engineering Faculty of the University of Beira Interior, which allowed us to test the electric energy generation at this location (Fig. 1). The prototype consists of a module with $0.70 \times 0.8 \times 0.2$ m³, in which a displacement of the surface of 10 mm

Fig. 1 Waynergy vehicles prototype installed in an access road pavement



was induced each time the system was activated. A convex surface was built to simulate a speed bump.

Prototype application tests were conducted by considering vehicles weighing 900 kg (V_1), 1,350 kg (V_2), and 2,000 kg (V_3), varying the vehicle speed when in contact with the prototype surface, which affects the force induced on it. Five different vehicle speeds were tested for each vehicle weight: 10; 20; 30; 40; and 50 km/h. The top speed considered was 50 km/h because it is the speed limit in Portuguese cities. Furthermore, at higher vehicle speeds, deterioration of the Waynergy system would increase due to wheel contact and pressure. The electric power in watts and, consequently, the electric energy in joules of the prototype application, which was connected to a resistance load, were measured.

3 Results and Discussion

Table 1 presents the results of the experimental tests with the Waynergy Vehicles prototype. The speed at which each vehicle passes over it has a great influence on the force induced on it and, consequently, in the electric energy generation.

Table 1 Waynergy vehicles prototype results

Vehicle type	Vehicle weight (kg)	Vehicle speed (km/h)	Peak power (W)	Electric energy (J)
V ₁	900	10	122	18.5
		20	134	24.0
		30	148	27.0
		40	140	31.0
		50	150	31.5
V ₂	1350	10	150	29.5
		20	155	34.5
		30	160	41.1
		40	162	42.0
		50	165	43.0
V ₃	2000	10	160	55.0
		20	170	69.5
		30	180	80.0
		40	185	88.0
		50	190	92.0

Analyzing all the results, the following conclusions can be drawn:

- For the same weight, the generated electric energy increases with vehicle speed, but the increase is less for the higher speeds. The increase of the generated electric energy generated by a vehicle moving at 50 km/h instead of 10 km/h is justified by the faster contact between the vehicle wheels and the surface of the prototype.
- The best performance of the prototype was for vehicles moving at 50 km/h, which is the speed limit in Portuguese cities.
- For the same vehicle speed, the generated electric energy increases with vehicle weight. For example, at 50 km/h vehicle speed, the increase in the generated electric energy by a vehicle weighing 1,350 kg instead of 900 kg is 37 %. For a vehicle weighing 2,000 kg instead of 1,350 kg, the increase in the generated electric energy is 114 %.
- The peak power generated by the prototype doesn't increase greatly between each vehicle speed. For example, for a vehicle weighing 950 kg, the increase in peak power at 50 km/h instead of 10 km/h is 23 %. For a vehicle weighing 1,350 kg, the increase in peak power is only 10 %, while it is 19 % for a vehicle weighing 2,000 kg.

The installation of the prototype in the pavement of the car parking access road of the Engineering Faculty of the University of Beira Interior allowed us to monitor the electric energy generated by vehicles in motion at this location. During a peak hour, between 1 and 2 p.m., 715 vehicle passages were measured at this location. Figure 2 shows the electric energy generated during this peak hour. The graph shows that the electric energy generated by the prototype was 37,800 J or 10.5 W.h.

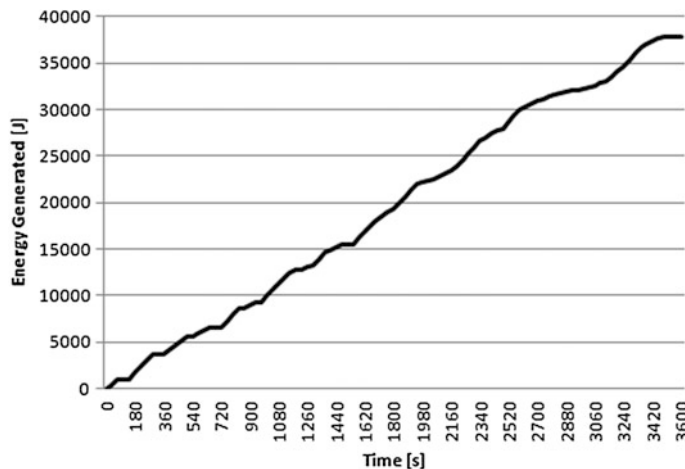


Fig. 2 Electric energy generated during one peak hour

4 Conclusions and Future Research

Pavement energy harvest systems have become progressively more interesting over the last few years. Piezoelectric and electromagnetic systems are adequate solutions for capturing the kinetic energy that is typically lost, and for converting it into usable electrical energy.

In this paper was presented an electromagnetic system, called Waynergy Vehicles, to convert energy released by vehicles into electric energy. A prototype was tested using three different vehicles, with three different weights, moving at five different vehicle speeds. The prototype tests allowed us to conclude that the generated electric energy increases with vehicle speed and with vehicle weight. Comparing the results of the Waynergy Vehicles prototype tests with the results of the Waynergy People prototype tests [5–7], we may conclude that the amount of energy generated by vehicles is much greater. For the Waynergy People prototype, values of 1.0 J were measured per activation by a pedestrian weighing 75 kg, while for the Waynergy Vehicle prototype values of 92.0 J were measured per activation of only two wheels of a vehicle weighing 2,000 kg. In 1 h, the electric energy generated by the Waynergy Vehicles prototype was 37,800 J or 10.5 W.h, while it was only 525 J or 0.15 W.h for the Waynergy People prototype.

In the near future, our research into pavement energy harvesting will follow three main directions. First, efforts will be made to optimize all the components of the Waynergy system, including the development of technology to store the generated electric energy, for example, using rechargeable batteries. Second, the Waynergy People system will be installed in a pedestrian crossing on an urban road to generate electrical energy, which will be used to illuminate warning panels to

promote road safety for both people and vehicles. Third, the Waynergy Vehicles system will be installed in a speed control hump of an urban road to generate electrical energy from the movement of vehicles, which can be used not only to charge batteries for electric vehicles, but also for general consumption via injection into the electricity grid or direct use by electrical equipment, such as public lighting, traffic lights, outdoor advertising, etc.

The enormously high level of traffic on municipal and urban roads will enable us to produce a considerable amount of electric energy, reduce the consumption of fossil fuels and thus improve the quality of the environment. Given the growing need to minimize the carbon footprint, the Waynergy People system and the Waynergy Vehicles system are feasible solutions for institutions to engage with sustainability and low carbon initiatives.

Acknowledgments The authors are grateful to the University of Beira Interior and other Institutions for the awards (WinUBI 2010, EDP Richard Branson 2010, ISCTE-IUL MIT Portugal Venture Competition 2010, and EEP Awards 2011) that provided some of the financial support for the development of the Waynergy research project. The present research work has been carried out in the framework of project WAYNERGY VEHICLES—Electrical Energy Generation System by the Movement of Vehicles (CENTRO-07-0202-FEDER-024580) and project EMSURE—Energy and Mobility for Sustainable Regions (CENTRO-07-0224-FEDER-002004). Francisco Duarte is also grateful to the Portuguese Foundation of Science and Technology for the financial support provided to this study through Grant SFRH/BD/95018/2013.

References

1. A. Ferreira, Briefing: Recent developments in pavement energy harvest systems. *Proc. Inst. Civ. Eng. Municipal Eng.* **165**(4), 189–192 (2012)
2. INPI, *Electromechanical System to Generate Electric Energy from a Surface Motion* (Instituto Nacional de Propriedade Industrial, National Patent Application, Lisboa, Portugal, 2012), pp. 1–31 (in Portuguese)
3. Waydip, Waynergy. (Waydip—Energia e Ambiente, Lda, Covilhã, Portugal, 2014), <http://www.waydip.com/>. Accessed 06 Sept 2014
4. WIPO, Electromechanical system for electric energy generation and storage using a surface motion. International Patent Application No. PCT/IB2013/050616. (World Intellectual Property Organization, Geneva, Switzerland, 2013), <http://patentscope.wipo.int/search/en/WO2013114253>. Accessed 06 Sept 2014
5. F. Duarte, F. Casimiro, D. Correia, R. Mendes, A. Ferreira, Waynergy people: A new pavement energy harvest system, municipal engineer. *Proc. Inst. Civ. Eng. Municipal Eng.* **166**(4), 250–256 (2013)
6. INPI, *Sustainable Pavement for Generation of Electric Energy from the Movement of People and Vehicles* (Instituto Nacional de Propriedade Industrial, National Patent Application, Lisboa, Portugal, 2011), pp. 1–18 (in Portuguese)
7. WIPO, Pavement module for generating electric energy from the movement of people and vehicles. International Patent Application No. PCT/IB2011/052164. (World Intellectual Property Organization, Geneva, Switzerland, 2011), <http://www.wipo.int/patentscope/search/en/WO2011145057>. Accessed 06 Sept 2014

Nanostructured TiO_2 Film Deposition by Supersonic Plasma Jet Source for Energetic Application

E.C. Dell'Orto, S. Caldirola, H.E. Roman and C. Riccardi

Abstract Titanium dioxide (TiO_2) materials are widely used in a variety of applications in the environmental and energy fields, such as self-cleaning surfaces, sensors, hydrogen generation by water photo-electrolysis, and photo-electrochemical conversion (e.g. DSSC and thin film solar cells) Paulose et al. (Nanotechnology 17:398, 2006) and Burschka et al. (Nature 499:316–319, 2013). In this work we use Plasma Assisted Supersonic Jet Deposition (PA-SJD) to realize TiO_2 thin film deposition Biganzoli et al. (J Mod Phys 3:1626, 2012). Vaporizable and stable monomer could be employed as the source of the oxides, the semiconductors or even the metals. In this work Titanium isopropoxide ($\text{Ti}\{\text{OCH}(\text{CH}_3)_2\}_4$), commonly referred as TTIP, is used as organometallic precursor. We have studied TiO_2 thin film roughness and morphology, and we have compared it to results obtained from numerical simulation of deposition process. So it is possible to relate surface morphology to film structure properties.

1 Introduction

Titanium dioxide (TiO_2) materials are used in a variety of applications which are related to TiO_2 photo-induced processes, which occur upon the absorption of ultraviolet (UV) light corresponding to the energy band gap (about 3 eV) and the formation of photo-generated charge carriers [1, 2].

The nano-structure of a TiO_2 material influences many of its properties, such as its photo-catalytic performance, and also its surface area, adsorption, reflectance, adhesion, and carrier transportation properties [3]. For this reason in the last years the study of TiO_2 morphology and structure has been very attractive [4]. In particular columnar structures (e.g. nano-rods and nano-wire) have showed interesting

E.C. Dell'Orto (✉) · S. Caldirola · H.E. Roman · C. Riccardi
Dipartimento di Fisica, Università degli Studi di Milano-Bicocca,
Piazza della Scienza 3, Milano, Italy
e-mail: elisa.dellorto@unimib.it

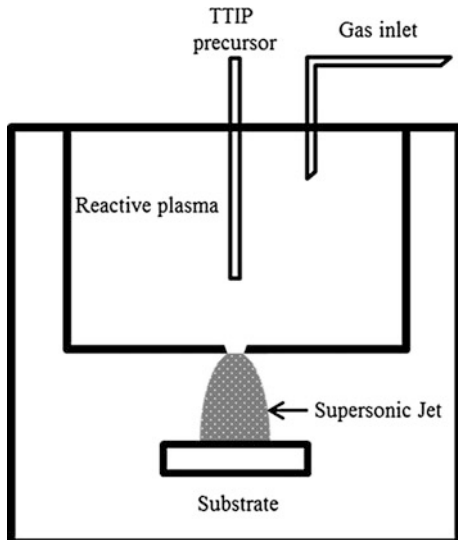
features. These configurations are reported to have some advantages in charge carriers transfer rate and in hole-electron recombination behavior. These effects are favorable for photo-catalytic reactions and solar cells efficiency.

2 Experimental

Nanostructured thin film growth by PA-SJD is based on the separation of the deposition process into two steps: the precursor dissociation in a reactive plasma environment and the nanoparticles nucleation and aggregation by means of a sonic jet (Fig. 1). The extraction of a supersonic plasma jet allows to focus the precursor flow on the substrate and to control atoms kinetic energy and clusters size. By changing deposition parameters it is possible to change film porosity and the hierarchical nano-structure. In the first chamber non-thermal inductively coupled plasma is generated by means of a three-loop copper antenna in a planar configuration powered by a RF generator through an L-type matching box. The plasma discharge is ignited using an oxygen–argon feedstock gas mixture with controlled partial pressures. TTIP is mixed in the gas mixture and then injected into the plasma chamber as a precursor. The plasma jet from the nozzle hits a substrate (FTO or Silicon) located at a fixed distance from the nozzle (from 7 to 14 mm).

After the deposition, the films are annealed at 500 °C for 20 min. The TiO₂ films are characterized by a mechanical profilometer, to analyze the thickness, AFM (used in semi-contact mode), to analyze surface morphology, and by TEM to study the nano-structure. Optical Emission Spectra (OES) were measured inside the plasma chamber to analyses precursor dissociation and chemical reactions inside

Fig. 1 PA-SJD system

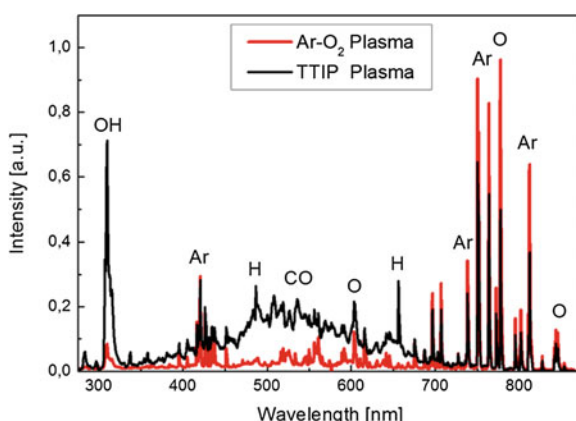


the plasma [5]. From quartz windows facing the plasma chamber optical emission spectra (OES) were acquired using a low resolution spectrometer (AvaSpec-2048 by Avantes) and an optical fiber. Looking at the intensity ratio of nearby emission lines from the main reactive radicals and inert argon we can estimate radical concentrations by actinometry analysis and gain an insight on the TTIP dissociation and combustion reactions [6].

3 Results

Optical emission spectroscopy results are shown in Fig. 2. Different emission lines of excited atoms and molecules were identified and their intensity was measured during each plasma deposition. Optical spectra measured before the TTIP precursor injection is dominated by emission lines of neutral atoms of argon and oxygen. When the titanium precursor is vaporized and injected inside the plasma reactor, many new lines appear in the spectra from hydrogen, carbon monoxide and hydroxyl radical. Varying the temperature used to vaporize the TTIP we can control the precursor flow inside the plasma chamber. In Fig. 3 the intensity of the 796 nm wavelength line of argon was used to obtain the radical concentration of carbon monoxide and oxygen at different precursor temperatures. As the temperature increases more precursor molecules are injected into the reactor, this can be controlled observing the increase of CO and other dissociation products while the radical oxygen concentration greatly decreases during the combustion process. In this way we can monitor the abundance of the precursor inside the plasma chamber and control the deposition rate from few nanometers for minute up to 200. AFM investigations allow analyzing the effect of the substrate on films. Results are showed in Fig. 4. The film grown on silicon (a) has a roughness (rms) about 2 nm, and on the surface spheres with a diameter about 10–20 nm are present. The film grown on FTO (b) shows a larger rms, more than 10 nm, and it is possible to

Fig. 2 Two successively optical emission spectra measured in a simple argon-oxygen plasma discharge (red line) and injecting the TTIP precursor (black line)



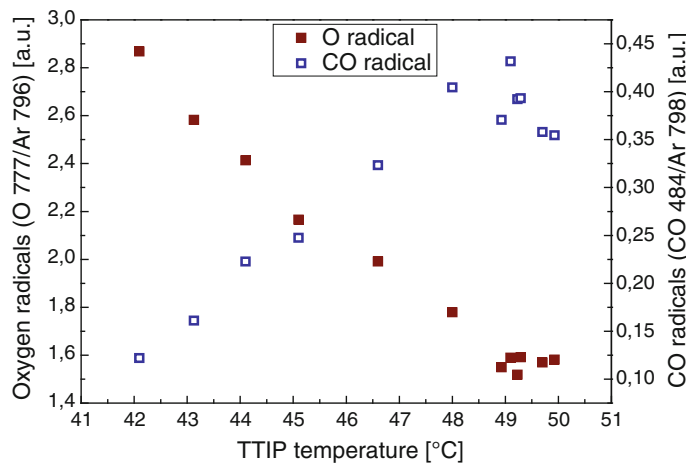


Fig. 3 Radical concentrations obtained from the emission line of atomic oxygen at 777 nm and of carbon monoxide at 484 nm as a function of the TTIP precursor temperature in the vaporizer

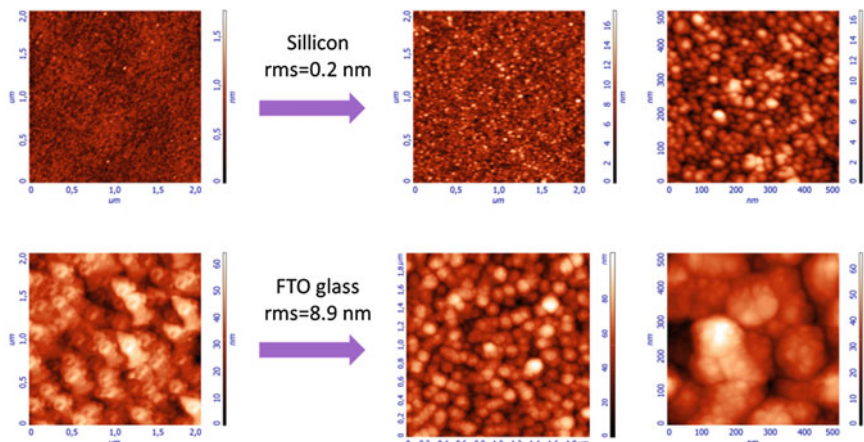


Fig. 4 Dependence of surface roughness by the substrate surface morphology. $\text{rms}_{a,1} = 2.1 \text{ nm}$, $\text{rms}_{a,2} = 2.4 \text{ nm}$, $\text{rms}_{b,1} = 10.1 \text{ nm}$, $\text{rms}_{b,2} = 14.9 \text{ nm}$

observe clusters about tens of nm on the surface. These results will be compared with numerical simulations in the next sections.

The influences of deposition parameters on deposition rate and surface morphologies have been studied. Results are summarized in Fig. 5. Three different samples, growth on silicon, were analyzed: sample a (see Fig. 4), sample b ($T_{\text{TTIP}} = 49 \text{ }^{\circ}\text{C}$, distance substrate-nozzle = 14 mm), and sample c ($T_{\text{TTIP}} = 49 \text{ }^{\circ}\text{C}$, distance substrate-nozzle = 9 mm). Increasing TTIP temperature, the deposition rate

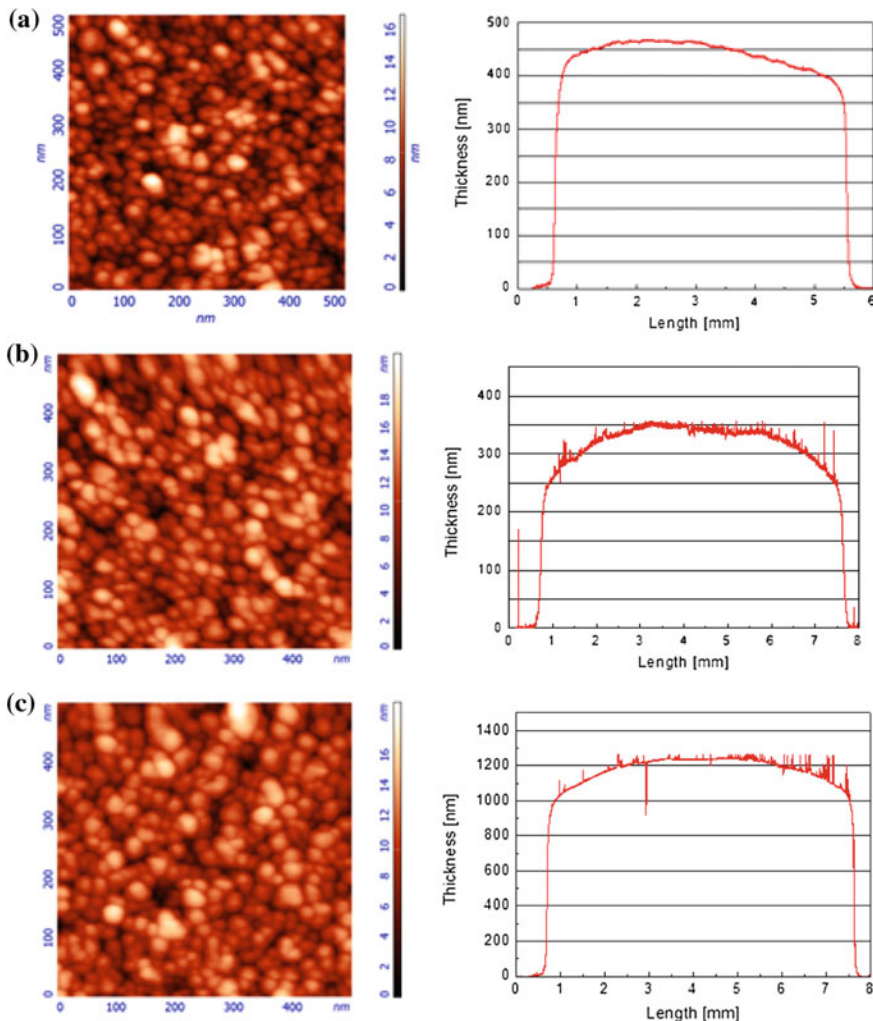


Fig. 5 Effect of deposition parameters on TiO₂ films deposition. Sample **a** $T_{\text{TTIP}} = 41\text{ }^{\circ}\text{C}$, distance substrate-nozzle = 14 mm, sample **b** $T_{\text{TTIP}} = 49\text{ }^{\circ}\text{C}$, distance substrate-nozzle = 14 mm, sample **c** $T_{\text{TTIP}} = 49\text{ }^{\circ}\text{C}$, distance substrate-nozzle = 9 mm

rises. This data is in agreement with the graph of Fig. 2, which shows as precursor molecules presence increases in plasma chamber as temperature growths. Also the substrate position has a key role to determine the growth rate: less the distance between the nozzle and the substrate is, more high the deposition rate is. AFM images indicate that surface morphology is not affected by deposition parameters. Profilometer scans show how the films have a uniform growth rate on all the deposition area. This is a very important characteristic for technological applications.

3.1 Numerical Simulations

We simulated the growth of thin films deposited by PA-SJD using an approach based on Slippery Ballistic Deposition (SBD) [7]. The deposition is performed on an (x, y)-substrate of size 166×166 sites, assuming a lattice constant equal to 3 nm. We model TiO_2 nanoparticles creating solid spherical objects with a fixed diameter (from TEM and AFM measurements we chose 18 nm) made up of several lattice elements. These nanoparticles fall vertically from the top of the system independently of each other. Each particle can execute a transversal motion according to their lateral speeds. A nanoparticle falls until it either touches the substrate, or gets stuck on another previously deposited particle. Different parameters, describing the sticking probabilities and the probability for lateral motion, are varied in order to reproduce the deposited film morphologies observed in the experiments. In this work we used a lateral and vertical sticking probability of respectively 0.1 and 1. In Fig. 6 a section of two different simulations is shown where the influence of the substrate roughness can be understood. The film deposited on silicon exhibits a

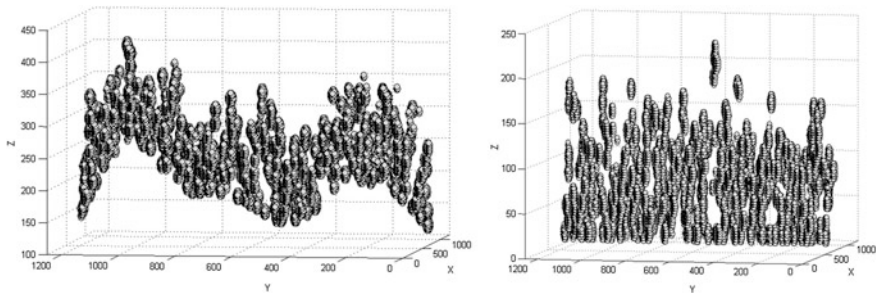
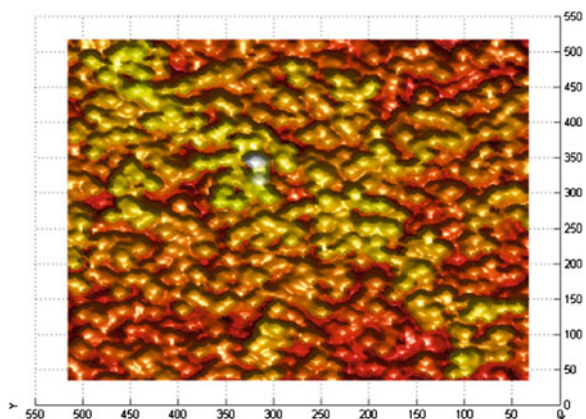


Fig. 6 A section of results obtained from numerical simulation of TiO_2 deposition on FTO (left) and silicon (right)

Fig. 7 Simulation of TiO_2 deposition on silicon



more compact and columnar structure, while the film deposited onto rough surface appears more irregular as the growth is influenced by shadowing effects. Film of about few microns can be simulated depositing about 106 nanoparticles, an example is shown in Fig. 7. The roughness of a simulated film can be calculated and compared with the experimental results obtained by AFM.

4 Conclusion

PA-SJD reveals to be an efficient technique to realize thin film depositions. It is possible to control the morphology and the growth rate. Some TiO₂ films have been used to realize solid state solar cells, sensitized by perovskite crystals, with efficiency over 7 %.

References

1. M. Paulose, O.K. Varghese, G.K. Mor, C.A. Grimes, K.G. Ong, *Nanotechnology* **17**(2), 398 (2006)
2. J. Burschka, N. Pellet, S.J. Moon, R. Humphry-Baker, P. Gao, M.K. Nazeeruddin, M. Grätzel, *Nature* **499**(7458), 316–319 (2013)
3. I. Biganzoli, F. Fumagalli, F. Di Fonzo, R. Barni, C. Riccardi, *J. Mod. Phys.* **3**(10), 1626 (2012)
4. X. Chen, S.S. Mao, J. Nanosci. *Nanotechnol.* **6**(4), 906–925 (2006)
5. R. Barni, S. Zanini, C. Riccardi, *Vacuum* **82**(2), 217–219 (2007)
6. R.A. Gottscho, V.M. Donnelly, *J. Appl. Phys.* **56**(2), 245–250 (1984)
7. A. Robledo, C.N. Grabill, S.M. Kuebler, A. Dutta, H. Heinrich, A. Bhattacharya, *Phys. Rev. E* **83**(5), 051604 (2011)

A Method for Building a Simple and Applicable Power Inverter

Mohamed Abdelati and Georg Frey

Abstract In the last few years, people in the Gaza Strip started to rely on power inverters as part of a backup power system due to frequent failure of the mains utility. The simplest backup system consists of a battery, a battery charger, and an inverter. At least one house out of four in the Gaza Strip is equipped with such a system. The inverters' market is shared by few local and plenty foreign manufacturers. Although imported inverters are either cheaper than or functionally superior to locally made ones, the majority of people prefer to utilize the local inverters. This is due to not only encouragement reasons, but also the ease of maintenance. Foreign inverters use to be manufactured with high-tech and state-of-the-art components which do not fit with available resources and expertise. Moreover, due to current political situations, most import and export transactions are neither insured nor time predictable. In this work, design of a viable single phase inverter is addressed. It is low-cost and has an integrated battery charger making it a challenging competitor to present choices. The device functions are controlled by PIC16F877 microcontroller and the proposed design is experimentally demonstrated and evaluated for various loads.

1 Introduction

The primitive inverter produces a square wave output and the sophisticated one produces a sinusoidal waveform. The modified sine wave inverter is a compromise; it reduces the harmonics significantly lending itself to drive most loads while being simple and efficient. The modified sine waveform is a square wave with gaps in

M. Abdelati (✉)
Electrical Engineering Department, IUG, Gaza, Palestine
e-mail: muhammet@iugaza.edu

G. Frey
Chair of Automation, Saarland University, Saarbrücken, Germany
e-mail: georg.frey@aut.uni-saarland.de

between. The sine wave period is replaced by two square pulses whose amplitude equals the peak value of the sine wave ($220 * \sqrt{2} = 311$ V). The duration of each pulse is 5 ms which is one fourth the sine wave period. Therefore, the root mean square value (V_{rms}) of this waveform is identical to the sine wave. Drop in the battery voltage as well as increasing the load at the inverter usually lead to a drop in the pulse amplitude. Hence, the duration of the pulse is usually increased through an automatic feedback to maintain the rated V_{rms} . In [1] it has been shown that the minimum total harmonic distortion (THD) occurs when the pulse duration is about 35 % of the pulse period. In this work, designing a 1 kVA modified sine wave inverter running on 12 V battery is considered. The design is simply modified for 2, 3, and 4 kVA when running on 24, 36, and 48 V battery banks respectively. The device works as battery charger when mains is available and is equipped with an automatic changeover relay to facilitate the operation of inverter mode and mains mode. Current and Voltage signals are monitored by PIC16F877A microcontroller and software is implemented to protect and control the operation of the device. The methodology presented here is a compromise between the sophisticated approach presented in [2–4] and the amateur way presented in [5]. The rest of this paper is organized as follows: The inverter blocks are detailed in Sect. 2 while the device control is addressed in Sect. 3. The experimental results are presented in Sect. 4 and finally in Sect. 5, concluding remarks and an outlook of future work are given.

2 Inverter Blocks

The inverting circuitry is composed of four sections; the push-pull signals generator, the MOSFET power drivers, the power transformer and the regulation feedback section. The first section is built around the LM3524D integrated circuit as shown in Fig. 1a.

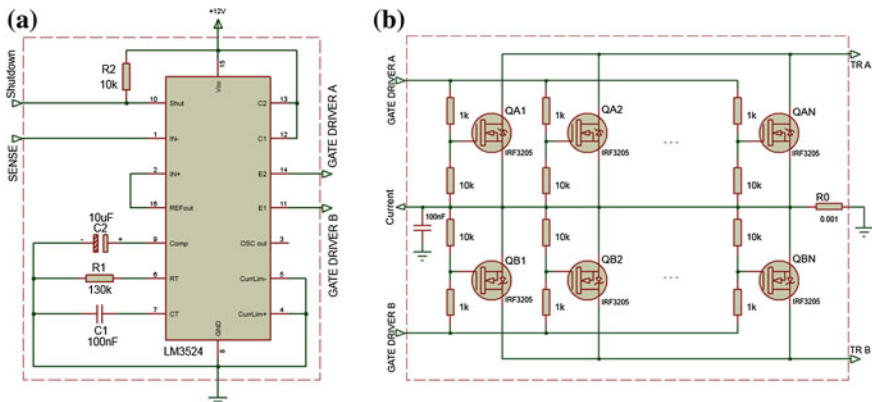


Fig. 1 Push-pull signals generator and MOSFET drivers

The LM3524D is an improved version of the industry standard 3524 pulse width modulator. It has improved specifications and additional features such as reducing the need for additional external circuitry often required in the original version [6]. The complementary outputs at E1 and E2 will drive the push-pull MOSFET banks. The frequency of the push-pull signals is set by R_1 and C_1 according to the formula:

$$f \cong \frac{0.65}{R_1 C_1} \quad (1)$$

A 100 nF capacitor and a 130 k Ω will yield the required 50 Hz signals. However, R_1 will be implemented as two serial resistors; one has a value 120 k Ω and the other is variable 20 k Ω . This will facilitate fine adjustment of the output frequency. There are two control inputs of this push-pull signal generator block; the disabling signal (Shutdown) and the regulating feedback signal (SENSE). A 10 k Ω resistor (R_2) is used to pull up the Shutdown signal so that the module is normally off. The 10 μ F capacitor (C_2) is required for compensating the error amplifier and enhancing noise immunity of the circuit. The regulating feedback signal is compared to the reference value (5 V) at pin 2 and the error signal adjusts the duty cycle of the outputs so that 220 V is produced at the secondary of the output transformer. The output push-pull signals at E1 and E2 will feed the MOSFET driver unit illustrated in Fig. 1b. The two MOSFET banks will switch the transformer winding taps (TR A and TR B) to the supply voltage alternatively. A small high-power resistor (R_0) is added to facilitate measuring the drawn DC current. Each bank comprises a number of parallel IRF3205 transistors. Gates of these transistors has 10 k Ω pull down transistors to protect them from accidental switch ON. Equation (2) calculates the average DC current (I_{DC}) drawn from a battery to supply a load whose power is (P) and power factor is (λ).

$$I_{DC} = \frac{P}{\eta V \lambda} \quad (2)$$

where η is the power efficiency of the inverter and V is the present battery voltage. Since two push-pull transistor banks share switching this current, the average current conducted by each bank I_a will be $I_{DC}/2$. For a square wave output the maximum current (I_m) conducted by each transistor bank will be identical to I_a . However, for modified sine wave, MOSFETs will conduct a fraction ($\mu \cong 25\%$) of full period. Therefore, during their conduction period they should be able to carry the maximum current:

$$I_m = \frac{I_a}{\mu} = \frac{P}{2\mu\eta V \lambda} \quad (3)$$

One can show that for a regulated V_{rms} , the conduction fraction should satisfy $\mu = 0.25(V_n^2/V^2)$ resulting in

$$I_m = \frac{2\beta P}{\eta \lambda V_n} \quad (4)$$

where β is the ratio of the battery voltage to its nominal value V_n . For a 1 kVA inverter having a typical efficiency of 85 % and running on a fully charged 12 V battery ($\beta = 12.65/12$), I_m will be 206.7 A and I_a will be 46.5 A. When the battery is almost discharged (its voltage reach 11.0 V under heavy load), I_m will be 180 A and I_a will be 53 A. Selection of transistor type and deciding the sufficient number of transistors in each bank not only depend on these average and maximum currents, but also MOSFETs should withstand at least double the battery voltage and their losses should be as low as possible in order to maximize the inverter efficiency. Moreover, transistors should be common, low-cost, and viable. It is also preferable not to use additional gate drivers. Under these constrains and after experimenting the available MOSFET series and reading their datasheets, the IRF3205 MOSFET is recommended [7, 8]. It has a $V_{DSS} = 55$ V and withstands a continuous drain current of 80 A. Three parallel transistors in each bank seem enough to conduct the maximum current. However, thermal losses will be too high resulting in poor efficiency and severe ventilation requirements. Each transistor has 0.008Ω drain-to-source on-resistance ($R_{DS(ON)}$). This value increases to 0.017Ω at maximum junction temperature 175°C . With N parallel transistors in each bank, the voltage drop is

$$V_{DS\max} = \frac{I_m \times R_{DS(ON)\max}}{N} = \frac{3.5}{N} \quad (5)$$

Experiments showed that a bank of 9 transistors easily fits in a practical size board and can also be safely driven by the LM3524. The resultant voltage drop is about 0.39 V which is about 3 % of the 12 V battery.

The power transformer is custom made $12 \times 2/311$ V/1 kVA. It has a 220 V tap that will be connected to the mains during battery charging mode. The voltage feedback signal which should be about 5 V DC during nominal operation may be prepared by utilizing a step down transformer, rectifier, a smoothing capacitor, and a voltage divider. Alternatively, it is easier to take the feedback from the primary windings. This is due to the fact that the dominant factor of voltage variation is the variation of the battery voltage. The resultant inverter circuitry is illustrated in Fig. 2. Only one transistor is shown in each bank for simplicity. RL1 is the changeover relay, and the RC element on the common contact dampens voltage spikes. The battery enters the charging process if RL2 is switched on. This relay connects the mains supply to the 220 V windings. The 12 V windings of the transformer become the secondary windings and the induced voltage is rectified by means of the body diodes of the MOSFETs. The dotted square shows the border of the Printed Circuit Board (PCB) which also includes a microcontroller circuitry that manages changeover, overload, battery charging, and over-discharge protection.

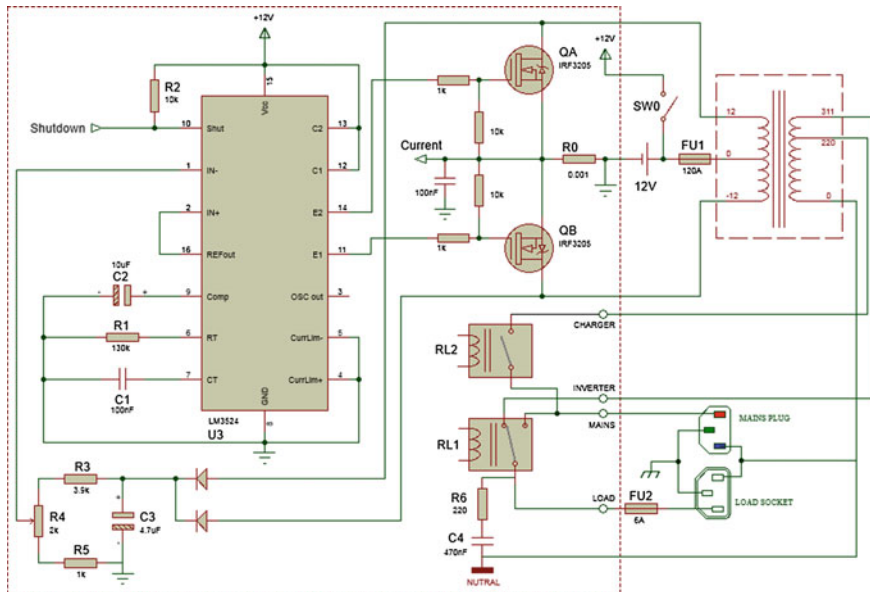


Fig. 2 Resulting inverting circuitry

3 Device Control

PIC16F877 microcontroller has been chosen to realize the control operations of the device. Its circuitry is illustrated in Fig. 3. This circuit together with the circuit presented in Fig. 2 completes the device hardware.

The input AC voltage sensing will enable switching to mains mode when AC mains fall in the designated voltage level. Sensing is achieved by stepping down the mains voltage through a 2 VA transformer followed by a rectifier and a voltage divider. The transformer is necessary to insure galvanic isolation. When the mains mode is sensed, firstly the inverter is disabled (if it was set online) by activating the Shutdown signal.

Then, the load is switched to the mains supply through RL1. The toggle switch connected to RD4 is helps setting the device either online or offline. On the other hand, battery voltage sensing will facilitate battery charging process during the mains mode as well as over discharge protection while being in the inverter mode. A simple voltage divider is sufficient to interface the battery voltage to the microcontroller.

The program flowchart is illustrated in Fig. 4. The variables Battery and Charger are Boolean. They are defined to reflect the status of the battery and provide a histories zone during discharging and charging respectively. The variable Overload

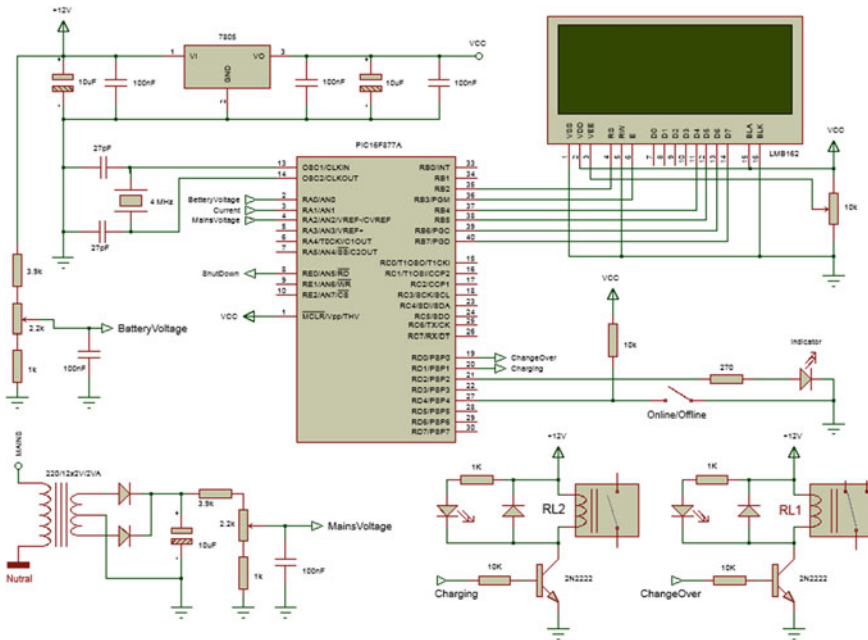


Fig. 3 Microcontroller circuit

is a float variable which is defined to calculate the moving window average of the battery current during inverter mode. This value is estimated as a weighted sum of the instantaneous current value and the previous average value.

4 Experimental Results

The evaluation version of the device is shown in Fig. 5. With resistive load, the power efficiency of the inverter is found to be in the range of 88 %. The shape of output waveforms significantly depends on the load type and value. In order to give some insight of the inverter operation the RC damper has been disconnected and the gates, drains and output wave forms are recorded and depicted in Fig. 6. Afterwards, the loaded output signals are examined under various loads.

The first point to highlight is that Fig. 6c, d represent the voltage on the primary windings relative to the ground not to the center tap which is shifted by the DC battery voltage. Now it is easy to correlate the applied voltage on one half of the primary winding and the induced voltages on the other half as well as the secondary windings. The second point is that with an ideal transformer, one will not face the voltage surge phenomena that happens immediately after switching off any of the primary windings; that is at time instants 10, 20 ms, and so on. It happens here due to the leakage inductance of the windings which generates a voltage component

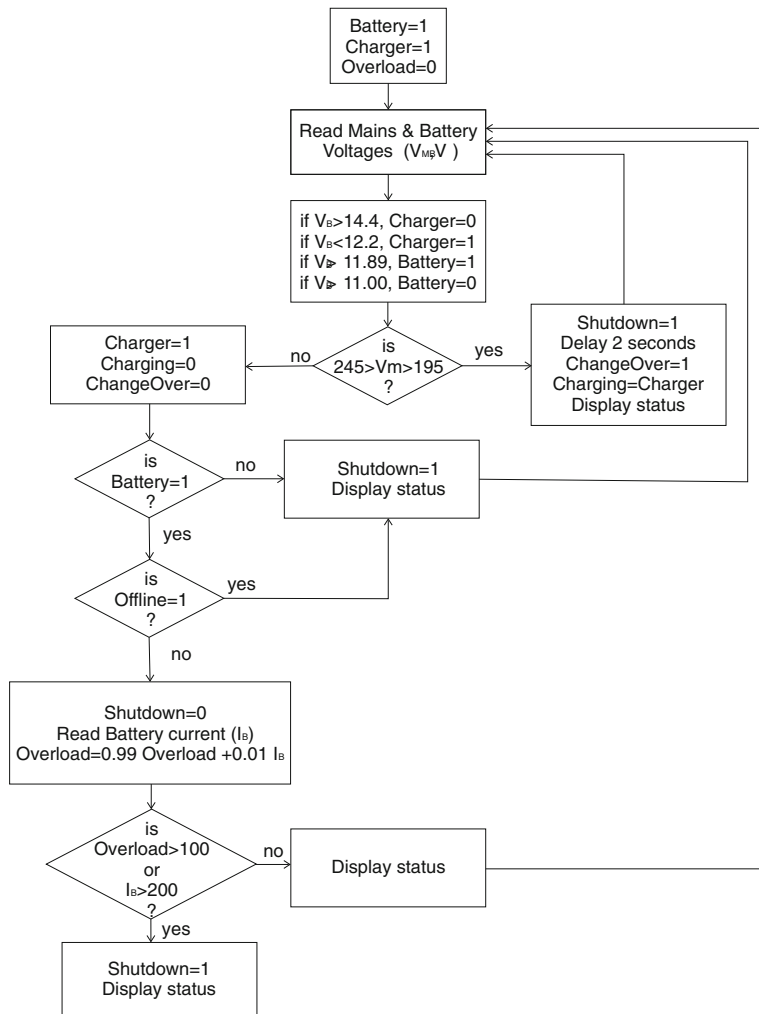


Fig. 4 The program flowchart

Fig. 5 Evaluation version of the inverter



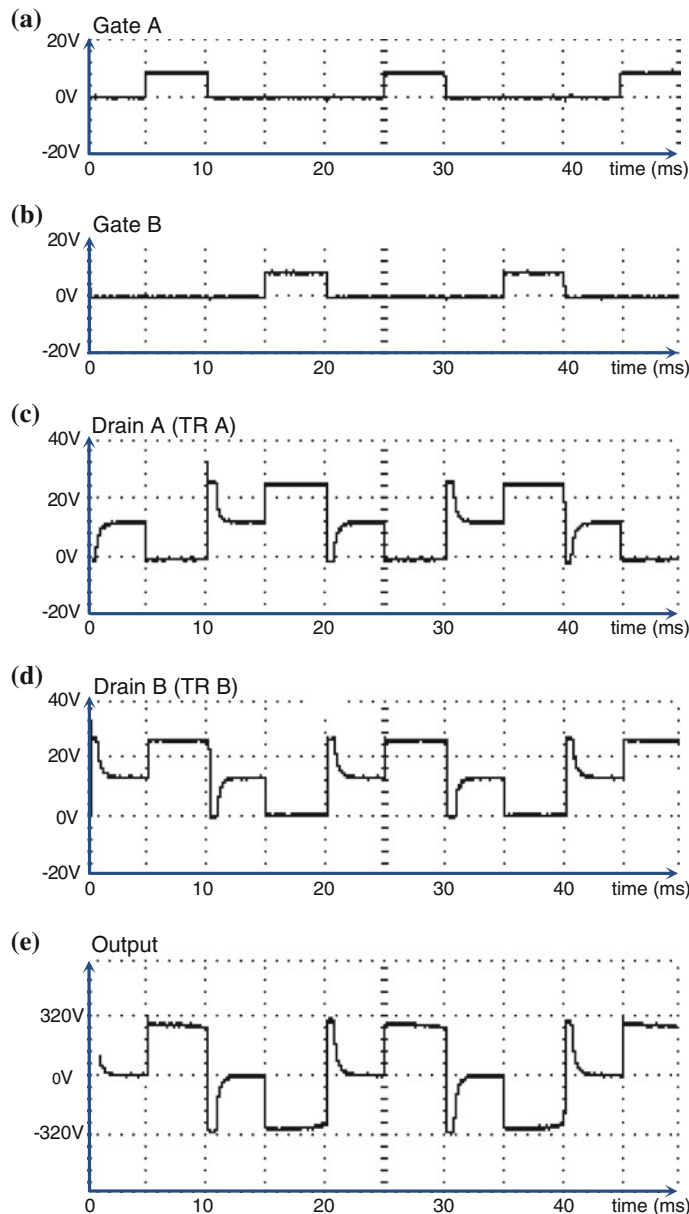


Fig. 6 Idle signals

proportional to the rate of change of the switched current. This surge component is soft and disappears when loading the inverter with resistive loads as shown in Fig. 7.

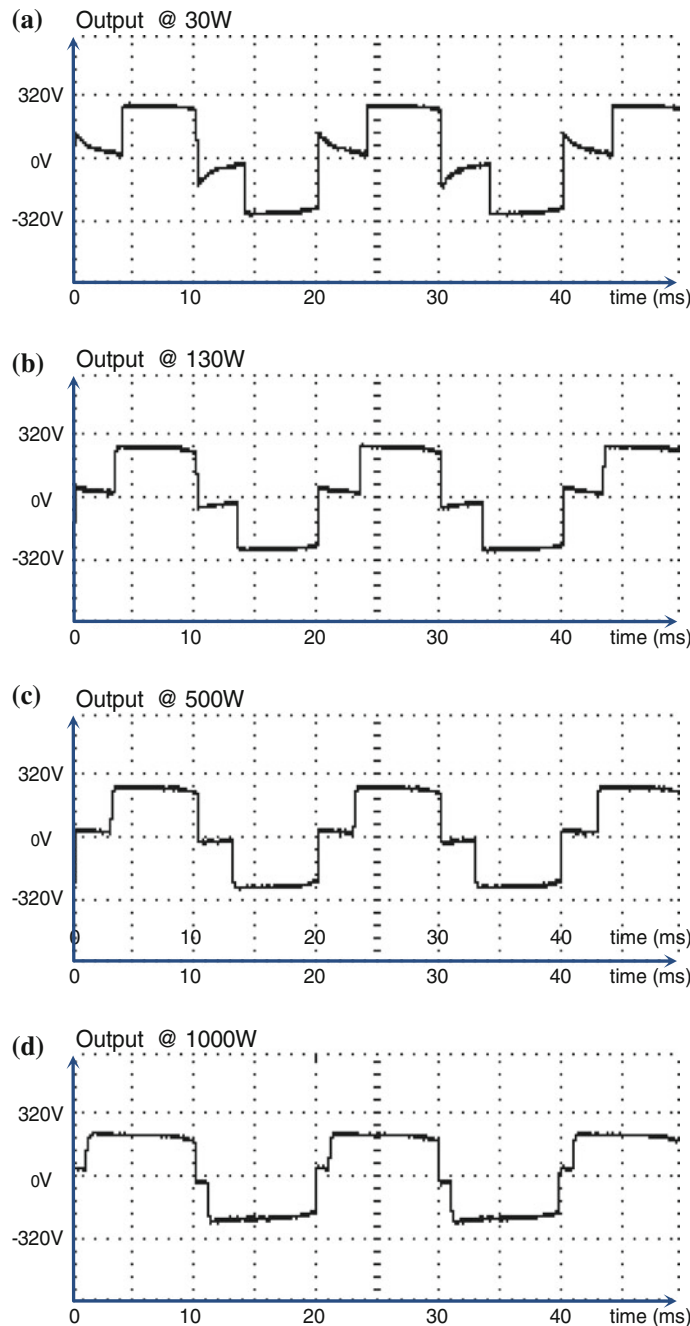


Fig. 7 Output waveforms at different loads

In order to improve the waveforms by farther smoothing sharp edges, the damper circuit is included. High values of the capacitor may improve the shape of output waveform and help improving the power factor when connecting inductive loads. However, it is a burden on the inverter and decreases the inverter efficiency especially under light loads. Therefore, an RC damper whose component values $220\ \Omega$ and 470 nF is found good enough. Figure 8 shows the output waveform at no load while the damper is connected. The damper's capacitance is so small to help in running heavy inductive loads. It is strongly advised to compensate the power factor of inductive loads for safe and efficient use of this type of inverters. Figure 9a

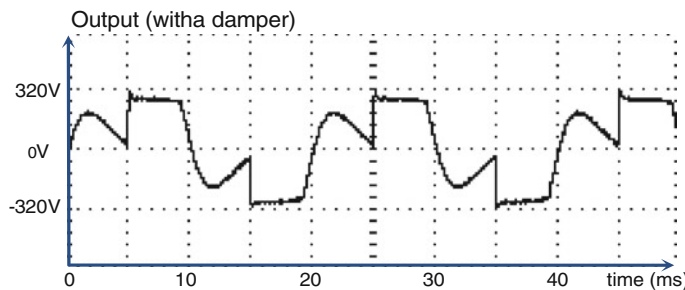


Fig. 8 Inverter output with a damper

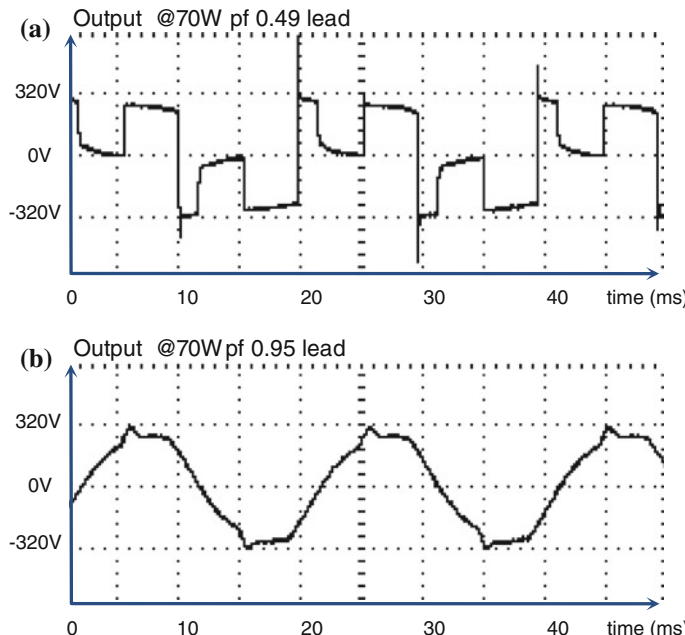


Fig. 9 Effect of power factor correction of fluorescent light

illustrates the output waveforms under an uncompensated classical 70 W fluorescent light while Fig. 9b depicts the waveform after adding a parallel 8 μ F capacitor which improved the power factor from 0.49 to 0.95.

5 Comments and Outlook

This work presents design and implementation of a 1 kVA modified sine wave inverter. The used components and employed technology respect special conditions found in Gaza but also many other developing areas. The design methodology and practical results described in this manuscript may serve also as a valuable tutorial for electrical engineering students as it utilizes knowledge of many subjects. Although the paper focuses on a 1 kVA design, upgrading to inverters up to 5 kVA is quite straight forward. It is mainly done through scaling the power transformer and utilizing appropriate transistors. In a future work it is planned to elaborate on the microcontroller circuitry in order to implement a multi stage battery charging algorithm.

References

1. J.H. Hahn, Modified sine-wave inverter enhanced. Power Electronics Technology, pp. 20–22 (2006)
2. B.J. Pierquet, D.J. Perreault, A single-phase photovoltaic inverter topology with a series-connected energy buffer. IEEE Trans. Power Electron **28**(10), 4603–4611 (2013)
3. ST Microelectronics, 1 kW dual stage DC-AC converter based on the STP160N75F3. Application note AN2794, Doc ID 14827 Rev 2, January 2012
4. S. Dixit, A. Tripathi, V. Chola, 800 VA pure sine wave inverter's reference design. Texas Instruments Incorporated, Application Report SLAA602 (2013)
5. Z. Nick, 250 to 5000 watts PWM DC/AC 220V Power Inverter, <http://www.instructables.com/id/250-to-5000-watts-PWM-DCAC-220V-Power-Inverter/>
6. Datasheet SNVS766E, LM2524D/LM3524D Regulating Pulse Width Modulator. Texas Instruments Incorporated, June 2009–Revised May 2013
7. Futurlec, MOSFET Transistors—IRF Series, <http://www.futurlec.com/TransMosIRF.shtml>
8. IRF3205 datasheet, HEXFET® Power MOSFET. International Rectifier, <http://www.irf.com/product-info/datasheets/data/irf3205.pdf>

Part XVIII

Fuel Cells

Evaluation of Electrocatalytic Activity of Pt-Co/Ti Towards Methanol Oxidation

E. Norkus, Ž. Činčienė, A. Balčiūnaitė, A. Zabielaite, I. Stankevičienė, J. Vaičiūnienė, A. Selskis and L. Tamašauskaitė-Tamašiūnaitė

Abstract The Pt-Co catalysts were deposited onto the titanium surface using simple and cost-effective chemical methods: electroless Co deposition followed by a spontaneous Pt displacement from the Pt(IV)-containing solution. The morphology, structure and composition of the prepared catalysts were examined by means of FESEM, EDX and ICP-OES. Electrocatalytic activity of Pt(Co)/Ti towards the oxidation of methanol was investigated by means of cyclic voltammetry and chronoamperometry. It has been determined that the Pt(Co)/Ti catalysts with low Pt loadings in the range from 19 up to $98 \mu\text{g}_{\text{Pt}} \text{cm}^{-2}$ exhibited an enhanced electrocatalytic activity towards methanol oxidation as compared to that of pure Pt and Co/Ti.

1 Introduction

One type of alkaline fuel cells—direct methanol fuel cells (DMFCs) is being developed especially for portable power supply. Since methanol is used as fuel a great deal of effort has been put into the exploration of cost-effective, active, and stable catalysts able to substitute Pt or allow reducing the amount of it in low temperature fuel cell anodes. Search of alternative catalyst compositions with high activity towards the oxidation of methanol is still in progress.

Preparation of the Pt-Co catalysts, deposited onto the titanium surface (denoted as Pt(Co)/Ti), using simple and cost-effective chemical methods: electroless Co deposition followed by a spontaneous Pt displacement from the Pt(IV)-containing solution, is presented in this study. The morphology, structure and composition of the prepared catalysts were examined by means of Field Emission Scanning Electron Microscopy (FESEM), Energy Dispersive X-ray Spectroscopy (EDX) and Inductively Coupled

E. Norkus (✉) · Ž. Činčienė · A. Balčiūnaitė · A. Zabielaite · I. Stankevičienė ·

J. Vaičiūnienė · A. Selskis · L. Tamašauskaitė-Tamašiūnaitė

Center for Physical Sciences and Technology, A. Goštauto 9, 01108 Vilnius, Lithuania
e-mail: norkus@ktl.mii.lt

Plasma Optical Emission Spectroscopy (ICP-OES). Electrocatalytic activity of Pt(Co)/Ti towards the oxidation of methanol was investigated by means of cyclic voltammetry and chronoamperometry.

2 Experimental Details

The Pt(Co)/Ti catalysts were prepared via electroless metal deposition followed by galvanic displacement of Co by Pt. Briefly, prior to electroless cobalt deposition, the titanium sheets (99.7 % purity, from Aldrich, 1 × 1 cm of 0.127 mm thickness) were degreased with ethanol, rinsed with deionized water and dried in an Ar stream. Then the Pt-Co catalysts were deposited onto the titanium surface according to the following procedures: (a) immersion of the Ti surface in a 8.3 g l⁻¹ SnCl₂ solution for 60 s, (b) subsequent rinsing of the activated surface with deionized water; (c) followed by immersion in a 0.5 g/l PdCl₂ acidic solution for 60 s; (d) subsequent rinsing of the activated surface with deionized water; (e) followed by immersion of the activated sample into an electroless cobalt bath containing 0.1 M cobalt sulfate, 0.6 M glycine, 0.3 M sodium hypophosphite and 0.3 M succinic acid for 15 min. The bath operated at a temperature of 80 ± 1 °C. The solution pH was maintained at 9.0.

Then the prepared Co/Ti electrodes were immersed in the solution containing 1 mM H₂PtCl₆ + 0.1 M HCl at a temperature of 25 °C for 5, 15 and 30 min. The surface-to-volume ratio was 1.3 dm² l⁻¹. After plating, the samples were taken out, thoroughly rinsed with deionized water and air dried at room temperature. Then, the prepared catalysts were used for measurements of methanol electro-oxidation without any further treatment.

The morphology and composition of the fabricated catalysts were characterized using a SEM/FIB workstation Helios Nanolab 650 with an energy dispersive X-ray (EDX) spectrometer INCA Energy 350 X-Max 20. The Pt metal loading was estimated from inductively coupled plasma (ICP) optical emission spectrometry measurements.

A conventional three-electrode electrochemical cell was used for the cyclic voltammetry and chrono-techniques. The Pt, Pt(Co)/Ti and Co/Ti electrodes with a geometric area of 2 cm² were employed as working electrodes, an Ag/AgCl/KCl_{sat} electrode was used as a reference electrode and a Pt sheet was used as a counter electrode. The presented current densities are normalized with respect to the geometric area of catalysts.

All electrochemical measurements were made with a Metrohm Autolab potentiostat (PGSTAT100) using Electrochemical Software (Nova 1.6.013). Steady state linear sweep voltammograms were recorded in a 0.5 M NaOH solution containing 1 M CH₃OH at a linear potential sweep rate of 50 mV s⁻¹ from the stationary E_s value in the anodic direction up to 0.3 V versus Ag/AgCl/KCl_{sat} at a temperature of 25 °C. The electrochemically active areas (ESAs) of Pt surface in the catalysts were determined from the cyclic voltammograms of pure Pt and Pt(Co)/Ti catalysts

recorded in a deaerated 0.5 M H₂SO₄ solution at a scan rate of 50 mV s⁻¹ by calculating the charge associated to hydrogen adsorption (220 μ C cm⁻²) [1].

The chronoamperometric curves for the Pt(Co)/Ti catalysts were recorded in a 1 M CH₃OH + 0.5 M NaOH at a constant potential of -0.25 V for 2 min.

3 Results and Discussion

Herein the simple and low-cost approach for preparation of the Pt-Co catalysts deposited onto the Ti surface is presented. The Pt-Co catalysts with low Pt loadings were deposited onto Ti by chemical methods: electroless Co deposition followed by a spontaneous Pt displacement from the Pt(IV)-containing solution. Figure 1 presents FESEM images of Co/Ti (a) and Pt(Co)/Ti (b-d) catalysts.

As evident from Fig. 1a, electroless Co deposited onto the titanium surface produced a layer of polycrystalline Co with the average size of crystallites ca. 1.4 μ m. The thickness of the electroless Co layer was ca. 2 μ m. Immersion of Co/Ti in the Pt(IV)-containing solution for 5 min results in the formation on the Co surface of nonspherical platinum crystallites ca. 15–50 nm in size. The Pt crystallites appear as light oblong nanorods and are quite uniform in size and well

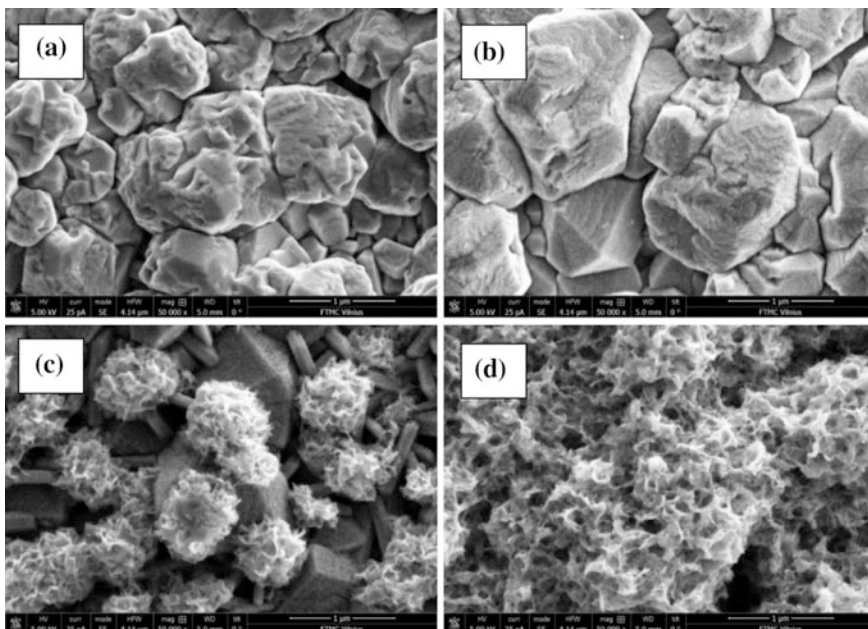


Fig. 1 FESEM images of Co/Ti (a) and Pt(Co)/Ti (b-d). The PtCo/Ti catalysts were prepared by immersion of Ti in electroless Co plating bath at 80 °C for 15 min, followed by immersion in 1 mM H₂PtCl₆ + 0.1 M HCl at 25 °C for 5 (b), 15 (c) or 30 (d) min

separated. After immersion of the Co/Ti electrodes into the Pt(IV)-containing solution for a longer time periods of 15 and 30 min, the size of Pt crystallites increase and flowerlike character of the structures is evident. The Pt nanoflowers are not spherical and consist of a large number of spearlike nanorods of size ca. 450–850 nm which are bonded to each other to form bigger secondary 3D flowerlike architectures.

The Pt loadings of the as-prepared catalysts were analyzed by means of ICP-OES. It has been determined that the Pt loadings were 19, 40 and 98 $\mu\text{g cm}^{-2}$ in the as-prepared catalysts after immersion of the Co/Ti surfaces in the 1 mM $\text{H}_2\text{PtCl}_6 + 0.1 \text{ M HCl}$ solution for 5, 15 and 30 min, respectively.

The ESAs of Pt surface in the catalysts were determined from the cyclic voltammograms of the pure Pt and Pt(Co)/Ti catalysts recorded in a deaerated 0.5 M H_2SO_4 solution between -0.2 and 1.3 V at a sweep rate of 50 mV s^{-1} (Fig. 2).

The calculated ESA value for pure Pt is 6 cm^2 . The ESAs values for the Pt(Co)/Ti catalysts, obtained after immersion of Co/Ti in a 1 mM $\text{H}_2\text{PtCl}_6 + 0.1 \text{ M HCl}$ solution for 5, 15 and 30 min, are 11, 35 and 57 cm^2 , respectively. These results show that the ESAs values of the catalysts prepared by galvanic displacement of Co layer by Pt nanoparticles are ca. 1.8, 5.8 and 9.5 times higher than that of pure Pt.

Figure 3a presents the positive-potential going voltammograms (10th cycles) of the oxidation of methanol recorded on pure Pt (dotted line), Co/Ti (solid line) and different Pt(Co)/Ti catalysts at a potential scan rate of 50 mV s^{-1} . As seen from the obtained data in Fig. 3a, the oxidation of methanol on the Co/Ti electrodes with the Pt loadings of 19, 40 and $98 \mu\text{g Pt cm}^{-2}$ proceeds in the same manner as that on pure Pt (dotted line), furthermore, the oxidation peaks are significantly higher than those on pure Pt. Methanol oxidation current densities are ca 3.8, 5.1 and 4.1 times

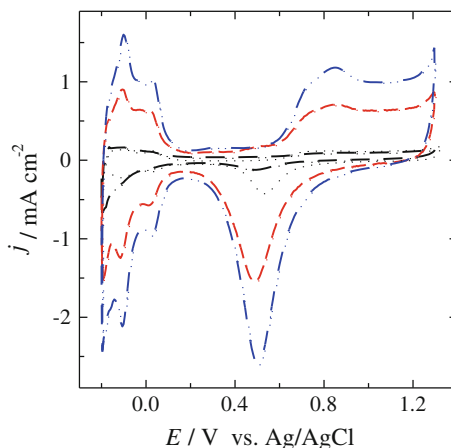


Fig. 2 CVs of pure Pt (dotted line) and Pt(Co)/Ti catalysts recorded in 0.5 M H_2SO_4 at 50 mV s^{-1} . The Pt(Co)/Ti catalysts were prepared by immersion of Ti in electroless Co plating bath at 80°C for 15 min, followed by immersion in 1 mM $\text{H}_2\text{PtCl}_6 + 0.1 \text{ M HCl}$ at 25°C for 5 (dash-dotted line), 15 (dashed line) or 30 (dash-dot-dotted line) min

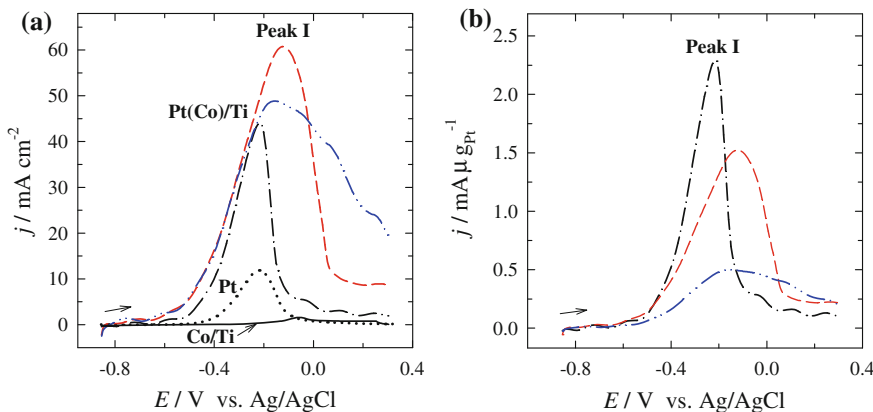


Fig. 3 **a** Positive-potential going CVs for Pt (dotted line), Co/Ti (solid line) and Pt(Co)/Ti catalysts with the Pt loadings of 19 (dash-dotted line), 40 (dashed line) and 98 (dash-dot-dotted line) $\mu\text{g}_{\text{Pt}} \text{ cm}^{-2}$ recorded in 1 M $\text{CH}_3\text{OH} + 0.5 \text{ M NaOH}$ at 50 mV s^{-1} . **b** The same data are normalized by the Pt loadings to represent Pt mass activity of methanol oxidation for these catalysts

higher at Pt(Co)/Ti with the Pt loadings of 19, 40 and 98 $\mu\text{g cm}^{-2}$, respectively, than those at pure Pt.

An enhanced activity of the Pt(Co)/Ti catalysts towards methanol oxidation may be related to the PtM alloy formation and the Pt electronic structure change due to the presence of M, Pt–Pt distance, and d-electron density in Pt [2–10]. Figure 3b presents Pt-mass normalized peak current densities of 10th cycles. It is clear that the Pt mass peak current of the Pt(Co)/Ti catalyst with the Pt loading of $19 \mu\text{g Pt cm}^{-2}$ is 1.5–4.5 times greater than those on the Pt(Co)/Ti catalysts with the Pt loadings of 40 and $98 \mu\text{g Pt cm}^{-2}$, respectively (Fig. 3b).

The performance of the as-prepared Pt(Co)/Ti catalysts as compared to pure Pt for the oxidation of methanol can be further observed from chronoamperometric measurements (Fig. 4). The Pt(Co)/Ti with the Pt loadings in the range from 19 to $98 \mu\text{g}_{\text{Pt}} \text{ cm}^{-2}$ and pure Pt catalysts show a current drop-off for methanol oxidation reaction. At the end of the experimental period ($t = 130 \text{ s}$), the current densities of the Pt(Co)/Ti catalysts are higher than those on Pt (Fig. 4a). The latter catalysts have a higher catalytic activity and a better stability for the oxidation of methanol than pure Pt. These data are in agreement with the results of cyclic voltammetry curves. The methanol oxidation current values normalized to the Pt loadings show that the highest Pt mass activity was obtained on the Pt(Co)/Ti catalyst with the higher Pt loadings of 48 or $98 \mu\text{g}_{\text{Pt}} \text{ cm}^{-2}$.

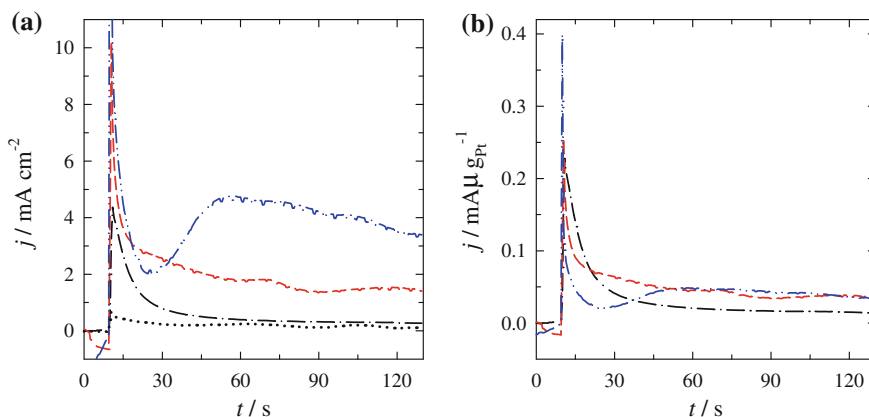


Fig. 4 **a** Chronoamperometric data for Pt (dotted line) and Pt(Co)/Ti catalysts with the Pt loadings of 19 (dash-dotted line), 40 (dashed line) and 98 (dash-dot-dotted line) $\mu\text{g}_{\text{Pt}} \text{cm}^{-2}$ recorded in 1 M $\text{CH}_3\text{OH} + 0.5$ M NaOH at -0.25 V for 2 min. **b** The same data are normalized by the Pt loadings for each catalyst

4 Conclusions

In this study a simple and cost-effective chemical methods: electroless Co deposition followed by a spontaneous Pt displacement from the Pt(IV)-containing solution were used to prepare PtCo catalysts deposited onto Ti surface. It has been determined that the average size of Pt crystallites deposited by galvanic displacement of Co adlayer varies from 15 up to 850 nm depending on the immersion time of Co/Ti electrode into the Pt(IV)-containing solution.

It has been determined that the Pt(Co)/Ti catalysts with low Pt loadings in the range from 19 up to 98 $\mu\text{g}_{\text{Pt}} \text{cm}^{-2}$ exhibited an enhanced electrocatalytic activity towards methanol oxidation as compared to that of pure Pt and Co/Ti and seem to be promising anode material for DMFCs.

Acknowledgments This research was funded by a Grant (No. ATE-08/2012) from the Research Council of Lithuania.

References

1. H. Angerstein-Kozlowska, B.E. Conway, W.B.A. Sharp, *J. Electroanal. Chem.* **43**, 9–36 (1973)
2. E. Antolini, J.R.C. Salgado, E.R. Gonzalez, *Appl. Catal. B: Environm.* **63**, 137–149 (2006)
3. G.J. Wang, Y.Z. Gao, Z.B. Wang, C.Y. Du, J.J. Wang, G.P. Yin, *J. Power Sources* **195**, 185–189 (2010)

4. V. Stamenkovic, T.J. Schmidt, P.N. Ross, N.M. Markovic, *J. Phys. Chem. B* **106**(2002), 11970–11971 (1979)
5. L. Xiong, A. Manthiram, *J. Mater. Chem.* **14**, 1454–1460 (2004)
6. H.A. Gasteiger, S.S. Kocha, B. Sompalli, F.T. Wagner, *Appl. Catal. B: Environ.* **56**, 9–35 (2005)
7. M.M. Jaksic, *Int. J. Hydrogen Energy* **26**, 559–578 (2001)
8. J.R. Kitchin, J.K. Nørskov, M.A. Bartaeu, J.G. Chen, *J. Chem. Phys.* **120**, 10240–10246 (2004)
9. J. Greeley, M. Mavrikakis, *Catal. Today* **111**, 52–58 (2006)
10. S. Papadimitriou, A. Tegou, E. Pavlidou, S. Armyanov, E. Valova, G. Kokkinidis, S. Sotiropoulos, *Electrochim. Acta* **53**, 6559–6567 (2008)

The Origin of Electrocatalytic Activity of Gold Nanoparticles Modified Pt-Based Surfaces Towards Formic Acid Oxidation

Gumaa A. El-Nagar, Ahmad M. Mohammad, Mohamed S. El-Deab and Bahgat E. El-Anadouli

Abstract Recently, direct formic acid fuel cells (DFAFCs) have received much attention in both industry and academia, due to their unique properties. Despite of their broad benefits, DFAFCs have two major drawbacks that limit its lifetime and efficiency; the poor electrocatalytic activity (due to CO and Halides poisoning) and stability of the Pt-based electrodes. Herein, the electrocatalytic activity, stability and tolerance against poisoning species (CO and Halides) of Pt-based electrode (Pt/GC) towards formic acid (FA) oxidation; essential anodic reaction of DFAFCs, are shown to increase via interrupting the Pt surface with gold nanoparticles (AuNPs). Electrochemical measurements show that gold nanopartciles (AuNPs) modified Pt/GC (Au/Pt/GC) electrode supports a significant enhancement on the direct FA oxidation to CO_2 (the dehydrogenation pathway). On the other hand, the oxidative treatment of GC (GC_{ox}) in acidic medium results in 2 times increases on the catalytic activity of unmodified and AuNPs modified Pt electrodes towards direct FA oxidation to CO_2 compared to un-oxidized GC electrode. This significantly enhanced activity of AuNPs modified Pt/GC catalysts can be attributed to noncontiguous arrangement of Pt sites in the presence of the neighbored AuNPs, which promotes direct oxidation of FA to CO_2 and retards the adsorption of CO at Pt surface. Moreover, AuNPs modified Pt/GC catalyst has satisfactory stability and show high tolerance against halides poisoning.

G.A. El-Nagar (✉) · A.M. Mohammad · M.S. El-Deab · B.E. El-Anadouli (✉)
Chemistry Department, Faculty of Science, Cairo University, Cairo 12613, Egypt
e-mail: Gumaa@sci.cu.edu.eg

B.E. El-Anadouli
e-mail: bahgat30@yahoo.com

A.M. Mohammad
e-mail: ahmad.mohammad@bue.edu.eg

M.S. El-Deab
e-mail: msaada68@yahoo.com

1 Introduction

Fuel cells (FCs) have received growing attention as they have been proved efficient, eco-friendly, reliable, quiet, long-lasting, easily installed and moved, economic and perfect for residential, and transportation uses and portable electronic applications. Of these, the DFAFCs are attractive candidate to replace methanol and hydrogen fuel cells as a promising candidate for portable and mobile applications, due to the unique advantages of FA as a fuel [1, 2]. Nevertheless, DFAFCs experience a severe problem where the catalytic activity of the Pt anodes, on which the FA electro-oxidation (FAO) proceeds, ceases with time, due to the accumulation of the poisoning CO intermediate resulting from the “*non-faradaic*” dissociation of FA (i.e., dehydration pathway) [3–5]. Therefore, the development of efficient and stable anodes overcoming the CO poisoning for FAO is a central issue. Another grave concern challenging the commercialization of FCs is the electrolyte’s contamination with hydrocarbons (released from piping, blowers, pumps and heat exchangers) and species of a high adsorption tendency such as halides (where most of the high-surface area FCs catalysts are often synthesized from halide-containing educts) [6–9]. Herein, we report on the superior electrocatalytic activity, stability and the tolerance of a bimetallic modified GC electrode with gold nanoparticles (AuNPs) and platinum nanoparticles (PtNPs) toward the electrooxidation of FA.

2 Experimental

Glassy carbon (GC, d = 3.0 mm) electrode served as the working electrodes. An Ag/AgCl/KCl (sat) and a spiral Pt wire were used as reference and counter electrodes, respectively. PtNPs and AuNPs were electrodeposited on polished (assigned as GC) or electrochemically treated GC (assigned as GC_{ox}) surfaces as described elsewhere [2–6]. The electrochemical treatment of polished GC electrode was performed by anodic polarization in 0.5 M H₂SO₄ at 2.25 V for various times [10]. The real surface area of platinum deposit (A_{Pt}) was estimated using the charge of Hydrogen adsorption/desorption in cyclic voltammograms (from –0.2 to 0.15 V) of Pt/GC and Pt/GC_{ox} electrodes, see Table 1 [2–6]. The electrocatalytic activities of the prepared electrodes

Table 1 Parameters of Pt/GC electrodes with different oxidation times prior to Pt deposition

Electrode, oxidation time (s)	Pt loading W_{Pt} ($\mu\text{g}/\text{cm}^2$)	Pt surface area A_{Pt} (cm^2)	Specific catalyst area S_{Pt} (m^2/g)	$Q_{\text{direct}}/\text{mC}$	$Q_{\text{indirect}}/\text{mC}$
Pt/GC, 0.0 s	65.50	0.633	13.8	0.4	2.3
Pt/GC _{ox} , 5.0 s	66.11	0.789	17.0	0.7	1.3
Pt/GC _{ox} , 10 s	65.92	0.982	21.3	1.0	1.0
Pt/GC _{ox} , 20 s	64.89	1.325	29.2	1.2	0.8
Pt/GC _{ox} , 30 s	67.12	1.553	33.1	1.5	0.5
Pt/GC _{ox} , 40 s	65.87	1.632	35.4	2.0	0.3

toward FAO are examined in an aqueous solution of 0.3 M FA. All measurements were performed using an EG&G potentiostat (model 273A) operated with Echem 270 software. A field emission scanning electron microscope, FE-SEM, (QUANTA FEG 250) coupled with an energy dispersive X-ray spectrometer (EDAX) unit was employed to evaluate the electrode's morphology and surface composition.

3 Results and Discussion

3.1 Material and Electrochemical Characterizations

Figure 1A, B depicts that oxidation of GC leads to a formation and growth of oxide layer, causing higher roughness and more defects on the surface as indicated from the EDAX analysis (see inset of each image). on the other hand, Figure 1C, D shows that PtNPs were electrodeposited at the GC (Fig. 1C) and GC_{ox} (Fig. 1D) surface in spherical crystallite aggregates with an average particle size of ca. 70 and 45 nm, respectively.

Furthermore, AuNPs have a flower-shaped geometry with an average particle size of ca. 100 nm for Au/GC electrode (Fig. 1E) and have a nano-wires like structures with average particle size 80 nm for Au/GC_{ox} electrode (Fig. 1F). Interestingly, the deposition of AuNPs on Pt/GC and Pt/GC_{ox} surfaces resulted in a decorated nanowire and a core-shell structures that homogeneously covered the entire surface of the GC electrode for Au/Pt/GC (Fig. 1G) and Au/Pt/GC_{ox} (Fig. 1H) electrodes, respectively. EDAX analysis showed the oxygen amount increased after the electrochemical treatment of the GC in acidic medium

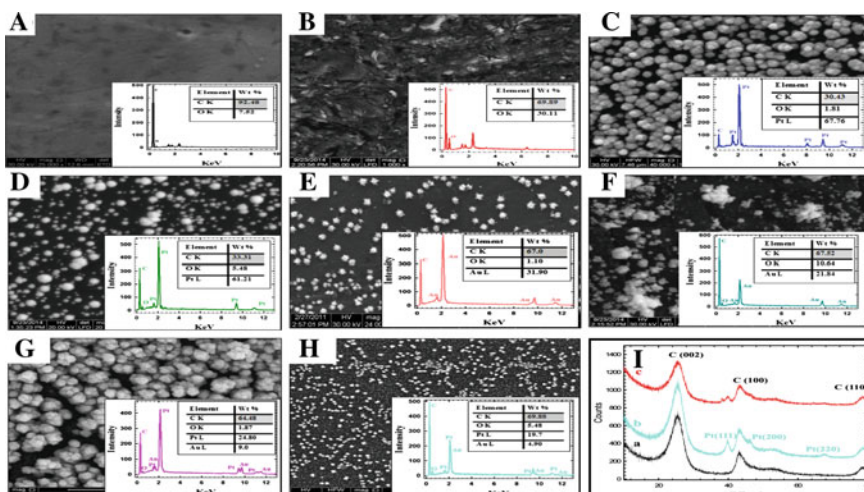


Fig. 1 FE-SEM images of **A** GC, **B** GC_{ox}, **C** Pt/GC, **D** Pt/GC_{ox}, **E** Au/GC, **F** Au/GC_{ox}, **G** Au/Pt/GC and **H** Au/Pt/GC_{ox} (inset shows the EDAX analysis of each electrode). **I** XRD pattern of GC (*a*), Pt/GC (*b*) and Au/Pt/GC (*c*) electrodes

(insets of Fig. 1). Furthermore, the crystal structures of prepared GC, Pt/GC and Au/Pt/GC electrodes were studied using XRD as shown in Fig. 1I. All electrodes showed a broad peak at about $2\theta = 25^\circ$ which is associated with carbon support (002). From the other hand, Pt/GC (curve b) and Au/Pt/GC (curve c) electrodes show the typical characteristic peaks for Pt (110), (200), (220), and (311), which demonstrates that the catalyst has a face-centered cubic (fcc) structure [2–6]. Bare Pt (Fig. 2A (curve a)) and Pt/GC (Fig. 2A (curve b)) electrodes show a typical CV of clean poly-crystalline Pt electrode [2–6]. Polished GC (Fig. 2A(g)) has no features under the experimental conditions, while oxidized GC (GC_{ox}) show redox peak at 0.4 V, related to the redox reaction quinon/hydroquinon in acidic solution (Fig. 2B (g')) [10]. Pt/ GC_{ox} (Fig. 2B (curve b')) electrode reveal that characteristic peaks for Pt and oxidized GC are present at the same potentials as corresponding peaks at GC_{ox} and at Pt. Same behaviors obtained for Au/GC (Fig. 2A(c)) and Au/ GC_{ox} (Fig. 2B(c')). Interestingly, upon electrodeposition of AuNPs on Pt/GC (assigned as Au/Pt/GC, Fig. 2A(e)) or Pt/ GC_{ox} (assigned as Au/Pt/ GC_{ox} , Fig. 2B(e')) electrodes, PtO reduction peak around ca. 0.48 V decrease but still can be

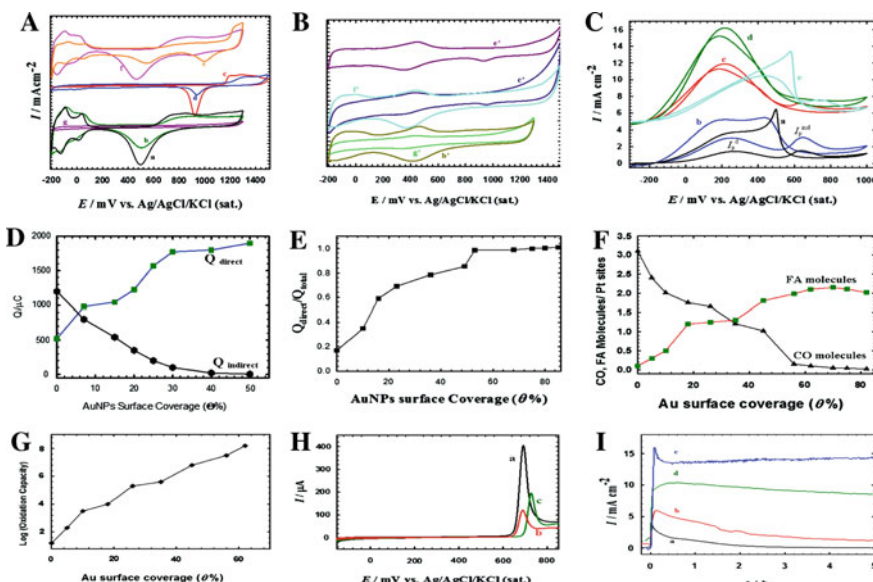


Fig. 2 A and B CVs in 0.5 M H_2SO_4 for (a) bare Pt, (b) Pt/GC ((b') Pt/ GC_{ox}), (c) bare Au, (d) Au/GC ((d') Au/ GC_{ox}), (e) Au/Pt/GC ((e') Au/Pt/GC), (f) Pt/Au/GC ((f') Pt/Au/ GC_{ox}) and (g) GC bare ((g') GC_{ox}) electrodes at 100 $mV s^{-1}$. C FAO at (a) Pt/GC, (b) Pt/ GC_{ox} , (c) Au/Pt/GC, (d) Au/Pt/ GC_{ox} and (e) Pt/Au/GC electrodes in 0.3 M FA in 0.5 M H_2SO_4 . D Variation of Q_{direct} and $Q_{indirect}$, E Variation of Q_{direct}/Q_{total} with AuNPs surface coverage, F number of CO and FA molecules per active PtNPs sites and G Log oxidation capacity (OC) of direct FAO with AuNPs surface coverage. H CO stripping at (a) Pt/GC, (b) Au/Pt/GC and c Pt/Au/GC in 0.5 M H_2SO_4 at 50 $mV s^{-1}$. I $i-t$ obtained during FAO at (a) Pt bare, (b) Pt/GC, (c) Au/Pt/GC and (d) Pt/Au/GC at +0.3 V

observed and the other oxide reduction peak appeared at ca. 0.9 V which corresponding to Au oxide reduction. A closer look at the evolution of the Au oxide reduction peak at ca. 0.9 V for Pt/Au/GC (Fig. 2A(f)) and Pt/Au/GC_{ox} (Fig. 2B(f')) electrodes reveals that the complete disappearance of the Au oxide reduction peak when PtNPs were electrodeposited on modified Au/GC or Au/GC_{ox}, while the PtO reduction peak still exist, when PtNPs were electrodeposited on modified Au/GC electrode suggests that the AuNPs are completely coated by the PtNPs and so a core-shell structure is formed but, on the other hand, the existing of the two peaks of Au and Pt oxide reduction peaks for Au/Pt/GC and Au/Pt/GC_{ox} means that the Au and Pt nanoparticles are exposed at the surface and so a decorated structure is obtained.

Electrocatalytic activity towards formic acid oxidation (FAO) A typical CV of FAO at was obtained at Pt/GC (curve a) and Pt/GC_{ox} (curve b) electrodes, where two oxidation peaks were observed in the forward direction, at ca. 0.23 (direct pathway I_p^d) and at 0.63 V (indirect or dehydration pathway, I_p^{ind}) [2–6, 11–13]. Figure 2C (curves a and b) reveals that Pt/GC_{ox} electrode has a higher electrocatalytic activity towards FAO than Pt/GC electrode with the same PtNPs loading, and the degree of enhancement increases with time of GC oxidation in acidic medium at 2.25 V (see Table 2.1). Thus, it is reasonable to assume that the main reason for enhanced activity of Pt/GC_{ox} regarding to Pt/GC is increased amount of reactive oxygen containing species (OH species) which leads to the lower coverage by CO_{ads} and permit the dehydrogenation path to increase in rate. Interestingly, upon electrodeposition of AuNPs on Pt/GC (Fig. 2C (curve c)) or Pt/GC_{ox} (Fig. 2C (curve d)) surfaces results in almost disappear of the I_p^{ind} (CO poisoning peak) with concurrent increases in the I_p^d (desirable peak) which means that FAO occurs exclusively via the dehydrogenation pathway instead of dehydration, and the Au/Pt/GC_{ox} has activity 2.0 times higher than that of Au/Pt/GC electrode with the same amount of AuNPs and PtNPs. Moreover, the degree of enhancement increase with AuNPs loading as indicated from the increase in direct FAO peak charge (Q_{direct}) and decrease charge of indirect FAO peak ($Q_{indirect}$) with AuNPs loading (see Fig. 2D). We believe that AuNPs interrupting the contiguity of Pt sites necessary for CO adsorption which leads to resist the formation of CO by which called ensemble effect [4, 5]. Moreover, the ratio between the direct FAO charge (Q_{direct}) and total FAO charge (direct and indirect); Q_{direct}/Q_{total} , increase with AuNPs surface coverage till $\theta \leq 57\%$ and after that value this ratio remain constant at 1.0, which means that after that value FAO exclusively via dehydrogenation pathway (Fig. 2E). One fundamental issue, in the preparation of an efficient catalyst towards a target reaction, is the proper design of the catalyst with efficient use of its constituents specially the precious metal. In this context, it is essential to investigate the influence of the deposition sequence of PtNPs and AuNPs on the electrocatalytic performance toward FAO. Figure 2D(c&e) compares the CVs for FAO obtained at Au/Pt/GC (curve c) and Pt/Au/GC (curve e) electrodes. Obviously and as evident from these two curves, the deposition sequence of the two species influences the electrocatalytic activity towards FAO. That is, the activity obtained at Au/Pt/GC electrode was better than that obtained at its “*mirror image*” Pt/Au/GC electrode.

This can be explained in view of the necessity of a certain adsorption sites for FA and CO on Pt surface. The deposition of AuNPs as a topmost surface layer could interrupt this contiguity and eventually inspire a better electrocatalytic activity. In order to reveal the adsorption mode of FA onto the Pt surface at different θ , the number of adsorbed FA and CO molecules was estimated from the amount of charge consumed in the direct and in direct peaks, respectively, of FAO assuming 2-electron transfer processes (data are plotted in Fig. 2F) [6, 7]. Interestingly, Fig. 2F reveals the existence of two adsorption modes for FA onto the Pt surface. At low θ ($\leq 40\%$), every molecule of FA is bound to a single Pt site (the FA/Pt ratio is ~ 1) because of the availability of plenty active Pt sites for FAO. On the other hand, at high θ ($\geq 40\%$), the shortage in the available free Pt sites may stimulate another adsorption mode, in which two molecules of FA are likely adsorbed onto a single Pt site. A similar phenomenon has recently been observed for the adsorption of acrylonitrile onto nano-Pt/GC surfaces [6]. Note also the continuous reduction of the CO/Pt ratio (from 3 down to less than 0.5) with θ , which highlights the remarkable improvement in the catalytic tolerance of the Pt/GC electrode against the CO poisoning. We have recently developed another important index, “oxidation capacity (OC)”, to probe the catalytic activity, which normalizes the charge consumed in the direct oxidation peak (Q_{direct}) to the number of available Pt active sites, as this ratio increase means that the electrode has more CO tolerance [6, 7]. Figure 2G shows that the oxidation capacity of the Au/Pt/GC electrode increases with surface coverage reach to about 8 order of magnitude, however the deposition of AuNPs decrease the area of the Pt/GC electrode. The presence of AuNPs on the surface of PtNPs increase the number of active Pt sites available for direct FAO and decrease the number of active Pt sites for CO adsorption via third-body effect which leads to increase in oxidation capacity towards formic acid oxidation.

To test this, CO was adsorbed on bare Pt/GC, Pt/Au/GC and Au/Pt/GC electrodes and then oxidized in the CO-free electrolyte 0.5 M H₂SO₄ data are presented in Fig. 2H. As clearly seen in this figure, the Au/Pt/GC (curve b) and Pt/Au/GC (curve c) electrodes have less amount of CO than Pt/GC (curve a) as calculated from the charge used for CO stripping peaks at the three electrodes. The oxidation of CO_{ads} on Pt/Au/GC (curve c) is delayed for ~ 0.15 V with respect to Pt/GC (curve a) with less amount of CO formed which give an evident for presence of electronic interaction between AuNPs and PtNPs. This figure clearly shown that, the presence of Au does not facilitate CO oxidation at low potential, but due to resist the CO formation via interrupt the PtNPs contiguity surface (third-body effect). Figure 2I depict that Au/Pt/GC and Pt/Au/GC electrodes supports higher oxidation about 9.0 and 15 times current than that obtained at Pt/GC, respectively. This level of enhancement could still be observed after 5 h of continuous measurement. This again demonstrates the preference of the direct oxidation path of FA at the AuNPs modified Pt/GC electrodes and its high CO tolerance.

3.2 Temperature Effect and Halides Tolerance

Effort was further dedicated to evaluate the influence of halides ions (e.g., Cl^- , Br^- and I^-) presence in the electrolyte of the anodic compartment of DFAFCs, which may act similarly as the poisonous CO, and the degree of tolerance of each electrode against it. Figure 3 shows the effect of existence halides ions on the effective surface area of Pt (ECSA) for the Pt/GC (Fig. 3a) and Au/Pt/GC (Fig. 3b) electrodes. These two figures depict that, (i) the presence of halides ions on the electrolyte of anodic compartment of DFAFCs resulted in a significant decrease on the ECSA of PtNPs, (ii) ECSA of PtNPs decrease with lower rate for Au/Pt/GC compared to Pt/GC electrode, for instance presence of 60 ppm of Cl, Br or I ions resulted in a completely poisoning the PtNPs surface (Fig. 3a), while same concentrations lead to only 38, 42 and 80 % decrease on the ECSA of PtNPs of Au/Pt/GC electrodes (Fig. 3b). We believe the different adsorption tendency of halide ions on Au and Pt is a key to understand this behavior, and soon we will continue the investigation to evaluate the essence of this issue, and (iii) the effect of halides on ECSA has the following order $\text{Cl}^- < \text{Br}^- < \text{I}^-$ and this expected behavior as the

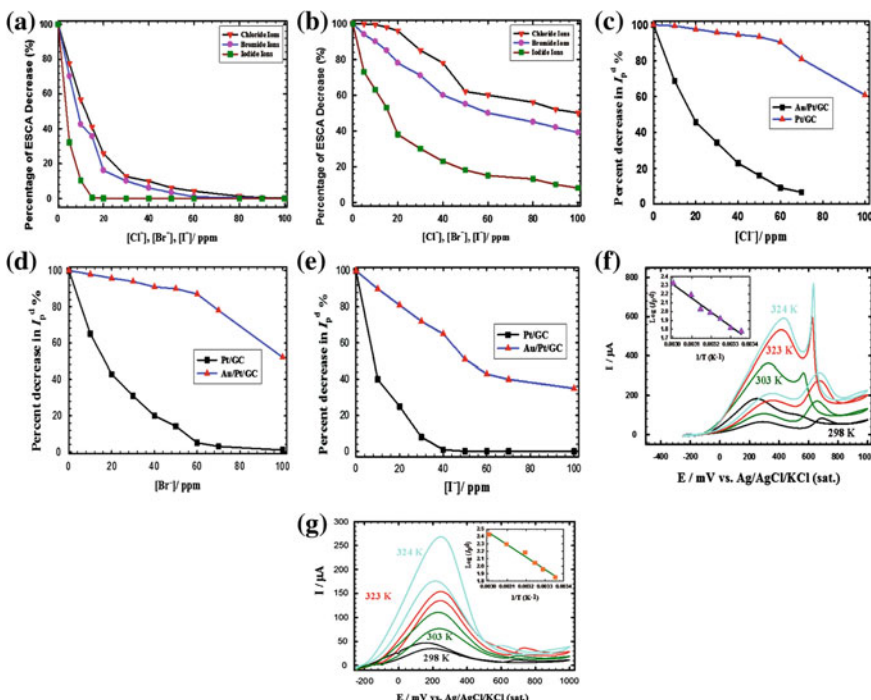


Fig. 3 Variation of ECSA of Pt in Pt/GC (a) and Au/Pt/GC (b) with halides concentrations. Percent decrease in the direct FAO peak (I_p^d %) with **c** chloride, **d** Bromide and **e** Iodide ions concentrations. Effect of temperature on FAO at **f** Pt/GC and **g** Au/Pt/GC electrodes (inset shows the Arrhenius plot)

difference in electronegativity, ionic radii and solvation ability between chloride and bromide ion. Figure 3 (C-E) compares the percent decrease in I_p^d as a function of the (C) Cl^- , (D) Br^- and (E) I^- ions concentration at both of the Pt/GC (black-squared lines) and Au/Pt/GC (red-triangle lines) electrodes. As obviously seen, the degrees of tolerance of the Au/Pt/GC electrodes against poisoning with halides (Cl^- , Br^- , I^-) are much better than that at the Pt/GC electrode at all concentrations of halides (Cl^- , Br^- , I^-) ions in the range investigated. For instance, the catalytic activity of the Au/Pt/GC electrode was reduced only to ca. 97, 95 and 50 % in 60 pm Cl^- , Br^- and I^- ions, respectively. While the same concentrations decreased the catalytic activity of Pt/GC electrode to about 2 % (see Fig. 3c-e). The solution temperature is another vital parameter in determining the catalytic performance of the proposed AuNPs modified Pt electrode. Figure 3g, f shows an increase of forward and backward current of FAO at Pt/GC (Fig. 3g) and Au/Pt/GC (Fig. 3g) electrodes with temperature up to 60 °C. An increase forward and backward current of FAO with temperature reflects a more favorable kinetics of the FAO at both potential scan directions. The value of an apparent activation energy (E_a) is calculated by plotting the current (I) at a specific potential as a function of temperature (T in K) according to Arrhenius equation (insets of Fig. 3 f, g). insets of Fig. 3f, g shows a representative Arrhenius plot for the oxidation of FA in which $\log I$ is plotted against T^{-1} at a potential of 0.2 V and the linear plot gives 20 and 16.2 kJ mol^{-1} as E_a for Pt/GC and Au/Pt/GC, respectively, and that result can be explained why Au/Pt/GC electrode has a higher electrocatalytic activity towards FAO compared to Pt/GC electrodes.

4 Conclusion

The current investigation addresses the development of a binary PtNPs and AuNPs catalyst for the efficient FAO. A mechanistic interpretation for the catalytic activity assumed the necessity of Pt surface sites for the adsorption of FA. The deposition of AuNPs on the Pt/GC electrode interrupted the contiguity of the Pt sites, which is necessary for the CO adsorption. The Au/Pt/GC electrode showed an excellent stability and tolerance against the poisoning effect of halides ions than Pt/GC electrode. The electrochemical treatment of GC before PtNPs deposition resulted in 2 times higher on the catalytic activity of Pt/GC electrode towards FAO.

References

1. X. Yu, P.G. Pickup, Recent advances in direct formic acid fuel cells (DFAFC). *J. Power Sources* **182**(1), 124–132 (2008)
2. G.A. El-Nagar, A.M. Mohammad, M.S. El-Deab, B.E. El-Anadouli, Facilitated electro-oxidation of formic acid at nickel oxide nanoparticles modified electrodes. *J. Electrochem. Soc.* **159**(7), F249–F254 (2012)

3. G.A. El-Nagar, A.M. Mohammad, M.S. El-Deab, B.E. El-Anadouli, Electrocatalysis by design: Enhanced electrooxidation of formic acid at platinum nanoparticles–nickel oxide nanoparticles binary catalysts. *Electrochim. Acta* **94**(1), 62–71 (2013)
4. G.A. El-Nagar, A.M. Mohammad, Enhanced electrocatalytic activity and stability of platinum, gold, and nickel oxide nanoparticles-based ternary catalyst for formic acid electro-oxidation. *Int. J. Hydrogen Energy* **39**(23), 11955–11962 (2014)
5. G.A. El-Nagar, A.M. Mohammad, M.S. Mohamed, B.E. El-Anadouli, Electro-oxidation of formic acid at binary platinum and gold nanoparticle-modified electrodes: effect of chloride ions. *Int. J. Electrochem. Sci.* **9**, 4523–4534 (2014)
6. G.A. El-Nagar, A.M. Mohammad, M.S. El-Deab, T. Ohsaka, B.E. El-Anadouli, Acrylonitrile-contamination induced enhancement of formic acid electro-oxidation at platinum nanoparticles modified glassy carbon electrodes. *J. Power Sources* **265**(1), 57–61 (2014)
7. M.S. El-Deab, A.M. Mohammad, G.A. El-Nagar, B.E. El-Anadouli, Impurities contributing to catalysis: enhanced electro-oxidation of formic acid at Pt/GC electrodes in the presence of vinyl acetate. *J. Phys. Chem. C* **118**(39), 22457–22464 (2014)
8. M.S. El-Deab, F. Kitamura, T. Ohsaka, Impact of acrylonitrile poisoning on oxygen reduction reaction at Pt/C catalysts. *J. Power Sources* **229**(1), 65–71 (2013)
9. M.S. El-Deab, F. Kitamura, T. Ohsaka, Poisoning effect of selected hydrocarbon impurities on the catalytic performance of Pt/C catalysts towards the oxygen reduction reaction. *J. Electrochem. Soc.* **160**(6), F651–F658 (2013)
10. V.M. Jovanović, D. Tripković, A. Tripković, A. Kowal, J. Stoch, Oxidation of formic acid on platinum electrodeposited on polished and oxidized glassy carbon. *Electrochim. Commun.* **7**(10), 1039–1044 (2005)
11. J. Joo, T. Uchida, A. Cuesta, M.T.M. Koper, M. Osawa, Importance of acid-base equilibrium in electrocatalytic oxidation of formic acid on platinum. *J. Am. Chem. Soceity* **135**(1), 9991–9994 (2013)
12. J. Joo, T. Uchida, A. Cuesta, M.T.M. Koper, M. Osawa, The effect of pH on the electrocatalytic oxidation of formic acid/formate on platinum: a mechanistic study by surface-enhanced infrared spectroscopy coupled with cyclic voltammetry. *Electrochim. Acta* **129**, 127–136 (2014)
13. G. Samjeské, A. Miki, S. Ye, M. Osawa, Mechanistic study of electrocatalytic oxidation of formic acid at platinum in acidic solution by time-resolved surface-enhanced infrared absorption spectroscopy. *J. Phys. Chem. B* **110**, 16559–16566 (2006)

The Effect of Humidification Strategies on Efficiency and Durability of Hydrogen Fuel Cells in Automotive Application

F. Migliardini, A. Unich and P. Corbo

Abstract In this paper the effect of different humidification strategies on performance of fuel cell systems (FCS) based on proton exchange membrane (PEM) fuel cells was analyzed taking into account the specific requirements of an automotive application. The experiments were conducted on PEM fuel cell systems of different power, ranging from 2.4 to 14 kW. The results showed that the optimal humidification strategy was function of stack operation mode and energy management inside the overall system, and evidenced the benefits and limitations of the self-humidification strategy for an automotive application.

1 Introduction

In the last years considerable funds and research resources have been invested in development of PEM fuel cells as a source of electrical energy to power vehicles [1, 2]. The necessity of adequate membrane hydration involves the risk of flooding, while evaporation can cause drying out, then the stack operative conditions have to be carefully tuned to avoid both the above phenomena [3–7].

The different humidification approaches can be classified as internal or external methods. Internal humidification means that humidification procedure concerns exclusively the inner spaces of fuel cell stack, while external humidification involves modifications in feeding stream humidity ratio outside of the stack [8–11]. Most common humidifier devices are mainly used for air hydration, more rarely also for hydrogen stream, and are based on bubblers, water evaporators, enthalpy wheels, pumps for liquid water injection, or membranes. Membrane humidifiers

F. Migliardini · P. Corbo (✉)

Istituto Motori, National Research Council of Italy, Via Marconi, 8, Naples, Italy
e-mail: p.corbo@im.cnr.it

A. Unich

Dipartimento di Ingegneria Industriale e dell'informazione, Second University of Naples,
Via Roma, 29, Aversa CE, Italy

represent an interesting passive solution, i.e. differently from other devices they do not need additional equipment, thus reducing both complexity and parasitic energy consumption of the FCS [12].

The aim of the present work was to investigate the effect of different humidification strategies on FCS performance, considering the automotive field as a possible application. The following approaches were investigated: saturation of reactant streams at different temperatures, humidification by selective membranes, water injection into the cathode manifold and self-humidification without the use of external devices.

2 Experimental

The experiments relative to the study of different humidification strategies were carried out on three fuel cell systems based on PEM stacks of different maximum power and cell number fuel cells: 14 kW/80 cells, 2.4 kW/34 cells and 6.2 kW/96 cells. They operated at low reactant pressure, in dead end anode configuration and were cooled by deionized water recirculation devices. A purge electric valve was placed at the hydrogen line outlet to drain the excess of water diffusing from the cathode to the anode side through the polymeric membrane. Purge strategy was optimized for all systems in order to avoid possible flooding phenomena.

The experiments were conducted in steady state conditions, which were reached starting from room temperature and using a power increase rate of 20, 5 and 10 W/s for the systems of 14, 2.4 and 6.2 kW, respectively. Three humidification devices were tested (bubbler, membrane humidifier and water injector) on 14 and 2.4 kW systems. The system of 6.2 kW was tested without any humidification equipment.

3 Results and Discussion

The experimental results relative to tests conducted with different humidification approaches are discussed in this paragraph utilizing the difference (ΔT) between T_{stack} and the cathode air inlet temperature ($T_{saturated\ air\ inlet}$) as main operative variable for evaluating the effects on stack performance. The durability was analyzed using the deactivation rate (ΔR) as evaluation criterion, calculated as ratio between voltage decrease (ΔV) due to the reversible performance loss and the duration (Δt) of the steady state test, normalized with respect to initial voltage (V_{in}), according to the following formula: $DR = \Delta V / (\Delta t V_{in})$.

All steady state tests were carried out at low reactant relative pressure (below 80 kPa) and varying the air stoichiometric ratio (R) from 6 at very low loads to about 2 for the entire power range investigated.

The 14 kW system was firstly characterized by using the heated bubbler. Figure 1 reports the results of this system with bubbler in terms of ΔT and DR

versus stack power. ΔT values reported below 4 kW refer to experiments realized at T_{stack} lower than 320 K, in particular two groups of tests were conducted at a bubbler outlet air temperature (T_b) of 287 and 305 K, then ΔT values were changed in the range 5–25 K. The low T_b values adopted implied that the water concentration into the air stream exiting from the bubbler was approximately close to that of ambient air. DR resulted practically negligible, indicating that the stack external humidification in these experimental conditions was not necessary to obtain a reliable operation, with an efficiency decrease caused exclusively by the load increase. However during the experiment conducted at the lowest power (0.4 kW), realized at 313 K as stack temperature with a ΔT of about 8 K, an appreciable DR was detected (0.1 h^{-1}), due to the poor water production by the electrochemical reaction, together with the not negligible evaporation at 313 K.

For the experiments above 4 kW the role of ΔT became relevant, in fact increasing the power from 4 to 10 kW (with T_{stack} ranging from 323 to 338 K) it was necessary to hold ΔT below 20 K in order to control DR increase under 0.2 h^{-1} . The major difference in DR values was observed during the experiments realized at highest loads (12.8 and 13.8 kW) and stack temperatures (348 and 342 K, respectively). At 12.8 kW a ΔT lower than 10 K was not sufficient to contain the DR increase, which resulted about 0.4 h^{-1} . This value would imply an efficiency loss not compatible with a reliable stack operation just after few minutes of working. For the last experiment at 13.8 kW T_{stack} was slightly decreased (from 348 to 342 K) while ΔT was reduced of 50 %, this was sufficient to DR abatement, avoiding also any efficiency loss.

The results of Fig. 1 indicate that a ΔT lower than 5 K is required for an efficient and reliable stack working (zero deactivation rate) in the range of high power and stack temperature, which would permit the maximum exploiting of stack performance. On the other hand, at lower power and temperature, the control of ΔT values was less crucial, as it could reach also values higher than 20 K without negative impact on deactivation rate.

The possibility to approximate the above operative conditions by a membrane humidifier was verified characterizing the 14 kW system equipped with a

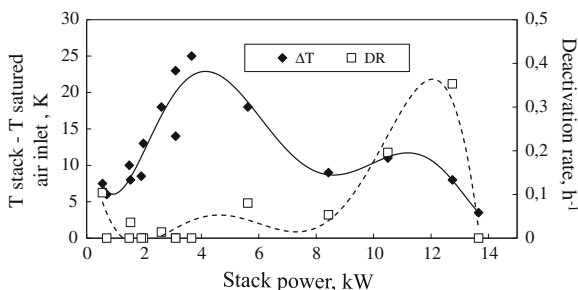


Fig. 1 ΔT and DR versus stack power for 14 kW fuel cell system equipped with bubbler humidifier

membrane device. Since the device utilized did not permit the realization of ΔT lower than 5 K, the experiments were carried out maintaining the stack temperature lower than 330 K in the range of higher power (8–14 kW). In this power range the stack temperature was controlled at about 325 K, and the profiles of ΔT shown in Fig. 2 evidence that the humidification device realized a ΔT of about 12 K. In these conditions the deactivation rate resulted not completely acceptable, being comprised between 0 and 0.1 h^{-1} . Instead in the low power range the device assured conditions and performance comparable to those already shown in Fig. 1 for the bubbler experiments, with ΔT variable between 8 and 11 K.

The experiments on the 2.4 kW system were firstly conducted without water injection at stack temperature lower than 330 K and power lower than 1.2 kW (Fig. 3). The maximum ΔT value (25 K) was realized at 0.2 kW, where T_{stack} was 315 K. In this condition the deactivation rate resulted about 0.3 h^{-1} , due to not only to the absence of external humidification but also to the low stack power, with consequent scarce water production from the electrochemical reaction. In fact, in the absence of humidification the power increase up to 1.2 kW was sufficient to abate the deactivation rate, despite ΔT values higher than 15 K.

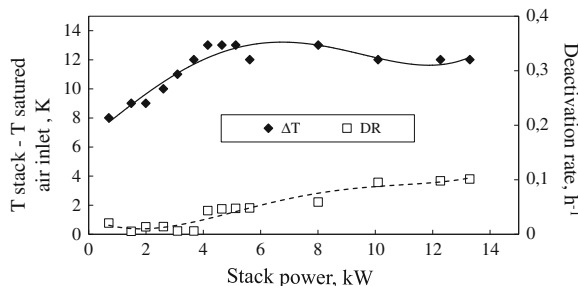


Fig. 2 ΔT and DR versus stack power for 14 kW fuel cell system equipped with membrane humidifier

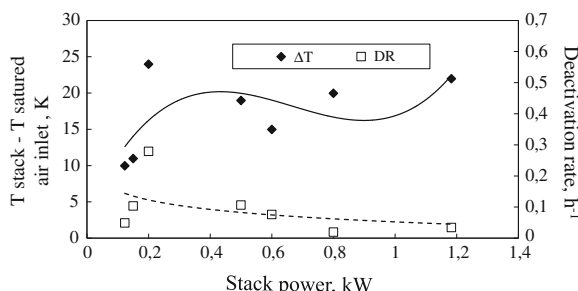


Fig. 3 ΔT and DR versus stack power for 2.4 kW fuel cell system without humidification at low power and temperature

The water injection on the 2.4 kW system started at 333 K and the experiments were carried out for the whole stack power range (0–2 kW), with a stack temperature ranging from 331 to 336 K (Fig. 4). The positive effect of water production was confirmed for power higher than 1.4 kW, in fact in these conditions the deactivation rate was practically zeroed also in the absence of external humidification (T_{stack} between 331 and 333 K), with ΔT of about 30 K. Under 1.4 kW the stack temperature was set at 333–336 K and a significant deactivation rate (higher than 0.5 h^{-1}) was observed in all experiments, in spite of the intervention of external injection. In this case the water production and the external injection did not compensate the water evaporation because of the higher T_{stack} values.

The 6.2 kW system was characterized without any external humidification device, but the self-humidification approach was adopted as a method suitable for automotive applications, which require the maximum simplicity of the system layout. A lower limit was set on the stack power (about 20 % of the maximum power) and the stack temperature profile was controlled in the range 303–328 K between 20 and 90 % of maximum power.

Figure 5 shows that the deactivation rate was always zero except for two experiments carried out at 1.5 kW. In this condition DR reached values of 0.2 and 0.3 h^{-1} , respectively for ΔT equal to 11 and 16 K (T_{stack} of 316 and 321 K). Except

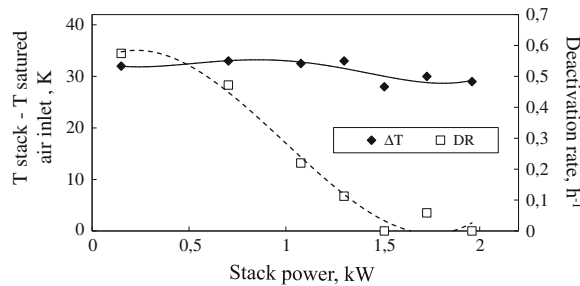
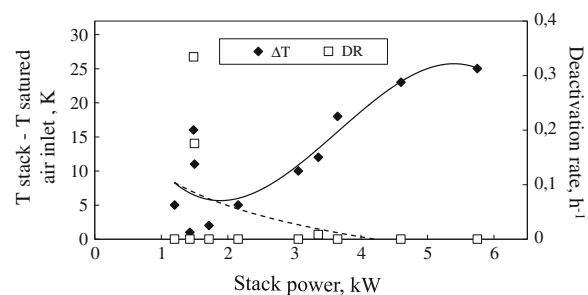


Fig. 4 ΔT and DR versus stack power for 2.4 kW fuel cell system in the entire power range and high temperature with water injection

Fig. 5 ΔT and DR versus stack power for 6.2 kW fuel cell system without humidification



these specific points the stack temperatures adopted assured a reliable stack operation in the entire power range. The negative implication of this approach was an efficiency worsening at maximum loads due to the lower stack temperatures.

4 Conclusions

The results evidenced how the key parameters for optimization of membrane hydration, i.e. stack temperature and power, and water content of the cathodic stream, should be tuned to assure an efficient and reliable stack working.

At low power (below 30 % of the maximum power) the stack temperature was to be maintained under about 310 K, in order to avoid membrane dehydration. In these conditions the role of the external water supply did not result relevant. At higher power and at maximum operative temperature, necessary to reach the optimal efficiency, the correct membrane humidification required a saturation temperature of the cathodic stream very close to stack temperature (difference below about 5 K).

Among the different devices utilized, the bubbler permitted to explore in detail the effect of different saturation temperatures of the cathodic stream, even if it was not suitable for an automotive application. The membrane humidifier was selected as a passive device suitable for the application on vehicles and permitted to control the difference between stack and saturated air inlet stream temperature below 12 K, with results not fully satisfactory in the high power range. The liquid water injector into the cathode manifold was also considered as a simple device for installation on vehicles, but did not result effective after the beginning of dehydration phenomena.

The results obtained by the above devices were utilized to define the experimental conditions suitable for utilization of the self-humidification approach. In particular, by controlling the stack temperature profile in the range 303–328 K between 20 and 90 % of maximum power, it was possible to avoid any external device but at the expense of a not optimized stack efficiency.

References

1. A. Veziroglu, R. Macario, *Int. J. Hydrogen Energy* **36**, 1001–1007 (2011)
2. B.G. Pollet, I. Staffell, J.L. Shang, *Electrochim. Acta* **84**, 235–249 (2012)
3. J. Larminie, A. Dicks, *Fuel Cell Systems Explained* (Wiley, Chichester, 2000)
4. M. Ciureanu, *J. Appl. Electrochem.* **34**, 705–714 (2004)
5. Y.H. Park, J.A. Caton, *J. Power Sources* **179**, 584–591 (2008)
6. C. Chen, T.F. Fuller, *Polym Degrad Stabil* **94**, 1436–1447 (2009)
7. G. Karimi, F. Jafarpour, X. Li, *J. Power Sources* **187**, 156–164 (2009)
8. F.N. Buchi, S. Srinivasan, *J. Electrochem. Soc.* **144**(8), 2767–2772 (1997)
9. M.V. Williams, H.R. Kunz, J.M. Fenton, *J. Power Sources* **135**, 122–134 (2004)

10. S.H. Jung, S.L. Kim, M.S. Kim, Y.S. Park, T.W. Lim, *J. Power Sources* **170**(2), 324–333 (2007)
11. H. Sun, G. Zhang, L.J. Guo, S. Dehua, H. Liu, *J. Power Sources* **168**, 400–407 (2007)
12. S.K. Park, E.A. Cho, I.H. Oh, *Korean J. Chem. Eng.* **22**, 877–881 (2005)

Electrocatalytic Activity of NiO_x Nanostructured Modified Electrodes Towards Oxidation of Small Organic Molecules

Sayed M. El-Refaei, Guma A. El-Nagar, Ahmed M. Mohammad,
Mohamed S. El-Deab and B.E. El-Anadouli

Abstract Nickel oxide nanostructured modified platinum nanoparticles (PtNPs) supported in glassy carbon electrode (NiO_x/Pt/GC) was used as an effective anode for formic acid (FA), methanol (ME) and ethanol (ET) electrooxidation in 0.3 M NaOH solution. GC surface was fabricated with NiO_x nanostructured and Pt nanoparticles electrochemically. The modified electrodes were characterized using cyclic voltammetry (CV) and scanning electron microscopy (SEM). The catalytic improvement observed at NiO_x/Pt/GC electrode for FAO, MEO, and ETO was not only confined in the large increase of the oxidation current but also in a negative shift in the onset potential of the oxidation reactions. The influence of temperature on the oxidation current was investigated and the apparent activation energy, E_a , for each fuel was calculated at a specific potential. Furthermore, NiO_x/Pt/GC electrode showed a satisfactory stability for FAO, MEO, and ETO in 0.3 M NaOH solution.

S.M. El-Refaei · G.A. El-Nagar (✉) · A.M. Mohammad · M.S. El-Deab ·

B.E. El-Anadouli (✉)

Chemistry Department, Faculty of Science, Cairo University, Cairo 12613, Egypt

e-mail: gumaa@sci.cu.edu.eg

B.E. El-Anadouli

e-mail: bahgat30@yahoo.com

S.M. El-Refaei

e-mail: selrefaei@sci.cu.edu.eg

A.M. Mohammad

e-mail: ammohammad@cu.edu.eg

M.S. El-Deab

e-mail: msaada68@yahoo.com

A.M. Mohammad · M.S. El-Deab

Department of Chemical Engineering, Faculty of Engineering,

The British University in Egypt, Cairo 11837, Egypt

1 Introduction

Fuel cells (FCs) have received increasing attention in many applications due to their unique advantages such as high efficiency, renewable, clean and low emissions energy resources. The use of H_2-O_2 as a fuel in FCs presents some significant drawbacks related to their transportation and storage [1–4]. In this context, small organic molecules which rich with hydrogen start to replace H_2 fuel. Of these, formic acid (essential anodic reaction of direct formic acid fuel cell; DFAFC) [2] methanol (vital anodic reaction of direct methanol fuel cell; DMFC) [3] and ethanol (the main anodic reaction of direct ethanol fuel cell; DEFC) [4] appeared promising in terms of the ease handling, transporting and storage in addition to their interesting oxidation efficiency.

The mainly used anodes in fuel cells are Pt and Pt-based materials. These catalysts have been one of most expensive materials in the fabrication of components for FCs. The generation of several poisoning intermediates at the anode during the fuel electrooxidation induces a considerable reduction in the electrocatalytic activity of the anode. The modification of Pt with metal oxide (e.g., MoO_x, MnO_x, SnO_x, TaO_x, NiO_x or NbO_x) is a possible way to modify the electrocatalytic properties of Pt in order to overcome poisoning and to reduce the cost of the catalyst considerably [2–4].

Herein, the possibility of the fabrication of Pt and NiO_x binary catalysts on the GC electrode by electrodeposition as a highly active catalyst for FA, ME and ET oxidation in alkaline medium was investigated. Scanning electron microscopy (SEM), cyclic voltammetry (CV) and chronoamperometry techniques are used to characterize and measure catalytic activity of the prepared electrodes towards FA, ME and ET electrooxidation.

2 Experimental

GC (d = 3.0 mm and its area is 0.07 cm²) served as a working electrode. A spiral Pt wire and an Ag/AgCl/KCl (sat.) are used as counter and reference electrodes, respectively. Conventional method used to cleaning the working electrode and its modification with Platinum nanoparticles (PtNPs) and NiO_x were described elsewhere [2]. Electrochemical measurements were performed in a conventional two-compartment three-electrode glass cell at various temperature using an EG&G potentiostat (model 273A) operated with Echem 270 software. A field emission scanning electron microscope (FE-SEM, QUANTA FEG 250) is employed to evaluate the electrode's morphology. The electrocatalytic activity of the modified GC electrodes with Pt and NiO_x nanoparticles toward FA, ME and ET oxidation was examined in a solution of 0.3 M NaOH containing 0.3 M FA, ME and ET, respectively. All chemicals (analytical grades) are used without further purification. Current densities calculated on the basis of the real surface area of Pt. The surface

coverage (θ) of NiOx on Pt/GC electrode was estimated from the decrease of the peak current intensity at ca. -0.32 V corresponding to the reduction of the Pt surface oxide formed during the anodic scan (surface coverage of NiOx $\approx 25\%$) (Fig. 1d) [2].

3 Results and Discussions

3.1 Materials and Electrochemical Characterization

Figure 1 shows FE-SEM images of Pt/GC (a), NiOx/Pt/GC (b). CVs of Pt/GC (c) and NiOx/Pt/GC (d) electrodes in 0.3 M NaOH solution at scan rate 200 mVs $^{-1}$, respectively. Figure 1a depicts that, round-shape Pt nanoparticles with uniform size of ca. 100 nm are observed. At the NiOx/Pt/GC electrode (Fig. 1b), a flower-like Pt and Ni nanostructures are obtained with a significantly larger average particle size

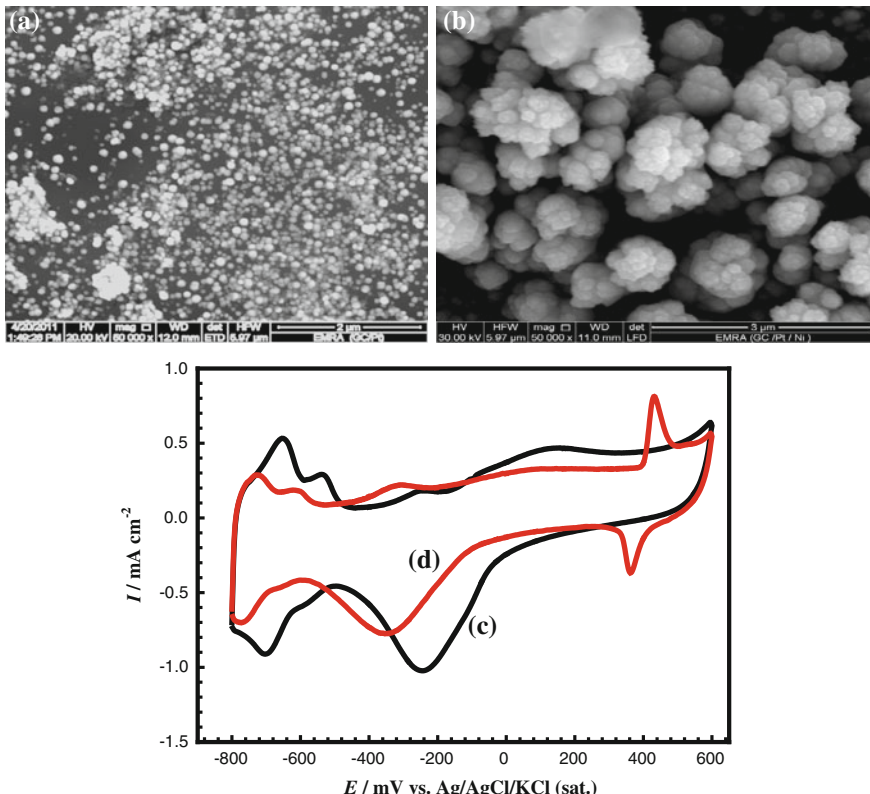


Fig. 1 FE-SEM micrographs obtained for Pt/GC (a), NiOx/Pt/GC (b). CVs of Pt/GC (c) and NiOx/Pt/GC (d) electrodes in 0.5 M NaOH at scan rate 200 mV s $^{-1}$, respectively

compared with Fig. 1a. Pt/GC electrode gives a characteristic CV response of the polycrystalline bulk Pt surface (Fig. 1c) [2]. On the other hand, the modification of the Pt/GC electrode with NiOx (Fig. 2d) resulted in a new noticeable changes in the characteristic CV including decrease in the intensity of the Pt oxide reduction peak (at ca. -0.34 V) along with a decrease in the current intensity of the $\text{H}_{\text{ads/des}}$ peaks (in the potential region from -0.6 to -0.8 V). In addition, a redox pair is appeared at ca. 0.45 V corresponding to the Ni(II)/Ni(III) reversible transformation [2].

3.2 Electrocatalytic Activity Toward FAO, MEO and ETO

Figure 2 shows CVs obtained at Pt/GC (a, c and e) and NiOx/Pt/GC (b, d and f) electrodes for FAO, MEO and ETO, respectively in 0.3 M NaOH solution. Figure 2a shows the typical CVs of FAO at Pt/GC electrode (where two oxidation peaks are observed in the forward direction which are corresponding to the direct oxidation of FA to CO_2 (at ca., 0.23 V, desired one) and CO oxidation (ca., 0.65 V) which resulted from non-faradic dissociation of FA (indirect FA oxidation, undesired pathway) [2]. Interestingly, on the modification of Pt/GC electrode with NiOx (Fig. 2b) a significant enhancement of direct oxidation pathway current (I_p^d) with a concurrent suppression of indirect oxidation pathway current (I_p^{ind}) is observed, indicating that the direct pathway is enhanced and CO tolerance increase [2].

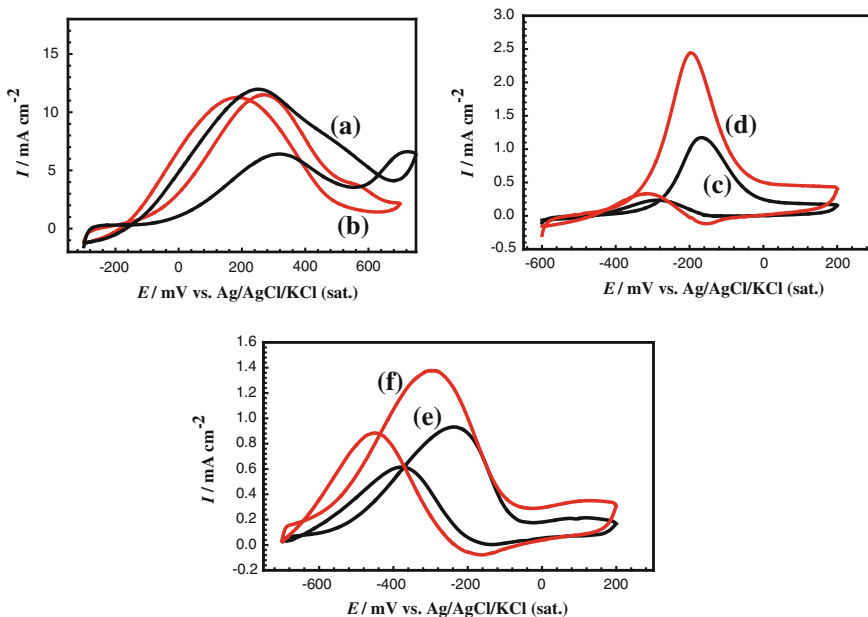


Fig. 2 CVs for Pt/GC (a, c and e) and NiOx/Pt/GC (b, d and f) electrodes in 0.3 M NaOH containing 0.3 M FA (a, b), ME (c, d) and ET (e, f) oxidation measured at 200 mV s^{-1} , respectively

Figure 2c–f shows CV for MEO and ETO at Pt/GC and NiOx/Pt/GC electrodes, respectively. Inspection of Fig. 2c, e discloses the presence of anodic peaks (I_f) at ca. -190 and -235 mV at the Pt/GC electrode for ME and ET, respectively. Another backward anodic peak (I_b) appears, which was assigned to the oxidation of the incompletely oxidized species formed in the forward scan (e.g., CO) at the freshly reduced PtO surface. This figure shows also that, the modification of Pt with NiOx causes a negative shift in the onset potential of alcohol oxidation in comparison with Pt/GC electrode concurrently with a significant increase in the oxidation peak current (I_f). The enhanced activity of NiOx/Pt/GC for alcohol oxidation in alkaline media can be attributed to the synergistic role of Pt and nickel oxides/hydroxides in the catalytic enhancement. The poisoned Pt nanoparticles surface with CO_{ad} can be regenerated via the mediated oxidation of CO_{ad} with nickel oxides/hydroxides on the catalyst surface [3, 4].

3.3 Stability of the Binary Catalyst

The steady state behavior for the oxidation of the FA, ME and ET are studied using chronoamperometric measurements at different potentials according the oxidized fuel. Figure 3a–f shows the I - t plots measured at Pt/GC (a, c and e) and NiOx/Pt/GC

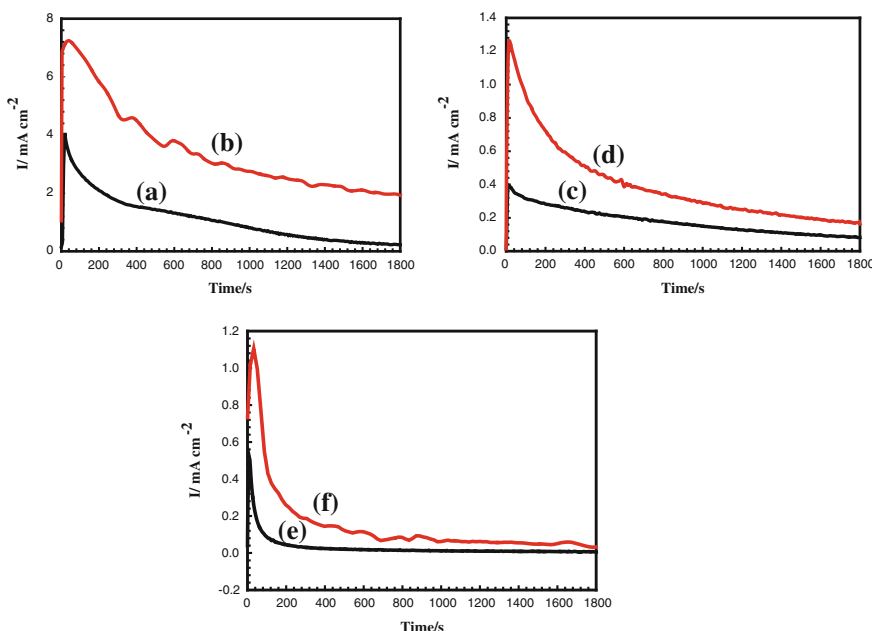


Fig. 3 I - t transient measured for Pt/GC (a, c and e) and NiOx/Pt/GC (b, d and f) electrodes in 0.3 M NaOH containing 0.3 M FA (a, b), ME (c, d) and ET (e, f), respectively

(b, d and f) electrodes in 0.3 M NaOH containing 0.3 M FA, ME and ET at 0.3, -0.2 and -0.35 V respectively. For FAO (Fig. 3a, b) NiOx/Pt/GC electrode supports a higher current density than Pt/GC electrode over the employed electrolysis time, the decay in current might be due to accumulation of CO at the electrode surface with the time [2]. Similarly, the same behavior is observed for ME (Fig. 3c, d) and ET (Fig. 4e, f) at Pt/GC and NiOx/Pt/GC electrodes [3, 4].

3.4 Effect of Temperature

Temperature is one of the most important factors affecting the catalytic activity of catalysts according to Arrhenius equation. In this regard we aim to study the effect of solution temperature on the oxidation of FA, ME and ET at Pt/GC and NiOx/Pt/GC electrodes. Figure 4 shows LSVs response for FA, ME and ET oxidation at NiOx/Pt/GC in 0.3 NaOH containing 0.3 M of each fuel at different temperatures (insets shows a representative Arrhenius plot for the oxidation of 0.3 M of each fuel in 0.3 M NaOH at Pt/GC (dashed) and NiOx/Pt/GC (solid) line). Inspection of this figure reveals that, an increase of the oxidation current with temperature up to 60 °C occurs, reflecting a more favorable kinetics for the oxidation of the three fuels at the

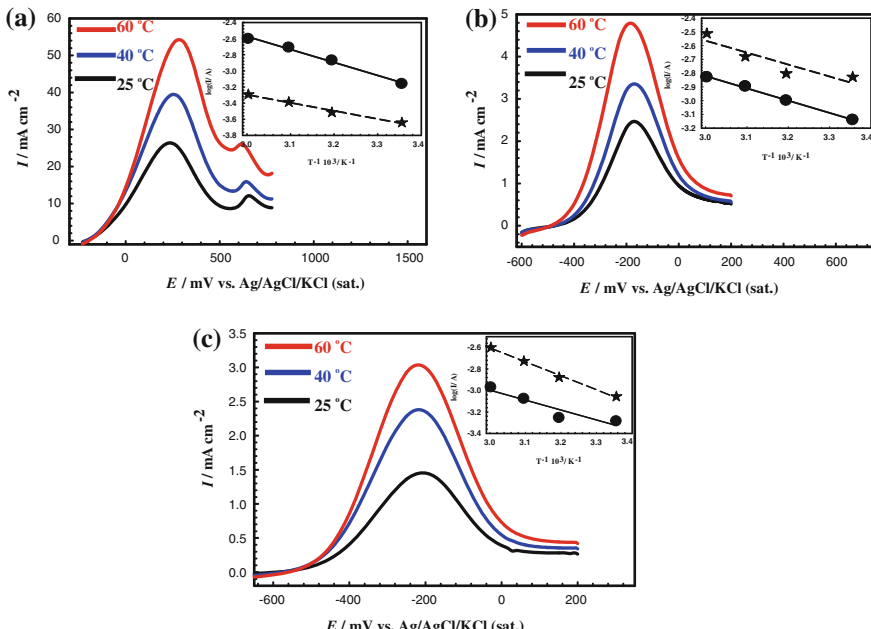


Fig. 4 LSVs for FA (a), ME (b) and ET (c) oxidation at NiOx/Pt/GC in 0.3 NaOH at different temperatures at scan rate 200 mV s⁻¹. Insets show a representative Arrhenius plot for the oxidation of each fuel at Pt/GC (dashed) and NiOx/Pt/GC (solid) line

proposed electrode. The values of the apparent activation energy (E_a) are calculated by plotting the current (I) at a specific potential as a function of T. From the analysis of Fig. 4 insets E_a is calculated to be 19.136, 16.665 and 24.867 kJ/mole at Pt/GC electrode and 30.725, 17.151 and 17.664 kJ/mole at NiOx/Pt/GC electrode for FA, ME and ET, respectively. And these values are comparable to that reported in literature for FA, ME and ET oxidation [4–6].

4 Conclusions

In summary, nickel oxide (NiOx) and platinum nanoparticles (Pt) are supported on GC electrode electrochemically and characterized using CV and FE-SEM. NiOx/Pt/GC in comparison with Pt/GC electrode shows high catalytic activity for the oxidation of (FA, ME and ET). In fact, NiOx could acts as a catalytic mediator which facilitates the charge transfer during the oxidation process and/or providing the oxygen species necessary for promoting the oxidative removal of the poisoning species produced during the reaction. The influence of temperature on the catalytic activity of the proposed electrodes towards FA, ME and ET is also tested. Furthermore, the NiOx/Pt/GC electrode shows a acceptable stability for FAO, MEO, and ETO when used in constant potential applying (chronoamperometry) which makes it more attractive for fuel cell applications.

References

1. O.Z. Sharaf, M.F. Orhan, An overview of fuel cell technology: fundamentals and applications. *Renew. Sustain. Energy Rev.* **32**, 810–853 (2014)
2. G.A. El-Nagar, A.M. Mohammad, M.S. El-Deab, B.E. El-Anadouli, Electrocatalysis by design: Enhanced electrooxidation of formic acid at platinum nanoparticles–nickel oxide nanoparticles binary catalysts. *Electrochim. Acta* **94**, 62–71 (2013)
3. L. Xiong, X. Yang, M. Xu, Y. Xu, D. Wu, Pt–Ni alloy nanoparticles supported on multiwalled carbon nanotubes for methanol oxidation in alkaline media. *J. Solid State Electrochem.* **17**, 805–810 (2013)
4. L. Jiang, A. Hsu, D. Chu, R. Chen, Ethanol electro-oxidation on Pt/C and PtSn/C catalysts in alkaline and acid solutions. *Int. J. Hydrogen Energy* **35**, 365–372 (2010)
5. T. Okada, Molecular catalysts for fuel cell anodes, in *Molecular Catalysts for Energy Conversion*, ed. by T. Okada, M. Kaneko (Springer, Berlin, 2009), pp. 103–137
6. J.L. Cohen, D.J. Volpe, H.D. Abruna, Electrochemical determination of activation energies for methanol oxidation on polycrystalline platinum in acidic and alkaline electrolytes. *Phys. Chem. Chem. Phys.* **9**, 49–77 (2007)

Part XIX
Hydrogen Storage

Computational Design of Dual Cation Ammine Metal Borohydrides: $\text{LiTi}(\text{BH}_4)_5(\text{NH}_3)_x$

Yusuf Kışlak and Adem Tekin

Abstract Global energy need is mostly fulfilled via fossil fuels. Usage of these sources causes harmful consequences to both environment and human beings. Besides, they have limited reserves and therefore alternative fuels must be discovered. Hydrogen is one of these alternatives due to its high energy content and environmentally friendly nature. However, there are many challenging problems waiting to be addressed for its widespread use. One of them is hydrogen storage which is especially very important for on-board applications. Even hydrogen can be stored as in the form of gas or liquid, these mediums are not practical in everyday use. As an alternative, hydrogen can also be stored in the solid form. For this purpose, both metal borohydrides and ammines are proposed due to their high gravimetric and volumetric densities. Metal borohydrides have some severe drawbacks e.g., requirement of a very high temperature for the hydrogen decomposition. Therefore, they can be mixed with ammines to produce new materials with a better thermodynamics. Dual-cation ammine metal borohydrides (AMBs) just suit well for this purpose. In this study, we computationally designed new AMBs in the form of $\text{LiTi}(\text{BH}_4)_5(\text{NH}_3)_x$ $x = 2, 3, 4$ using a strategy which combines crystal structure prediction with density functional theory computations.

1 Introduction

Energy consumption of the world mostly relies on fossil fuels such as coal, natural gas and liquid fuel. These sources have many handicaps, they are harmful to environment besides their reserves are very limited. Therefore, alternative ways need to be found to satisfy the world's energy need. Hydrogen is a strong candidate

Y. Kışlak (✉) · A. Tekin

Informatics Institute, Istanbul Technical University, 34469 Maslak Istanbul, Turkey
e-mail: yusufkislak@gmail.com

A. Tekin
e-mail: adem.tekin@be.itu.edu.tr

for future renewable energy solution. Hydrogen storage is a technically challenging barrier that prevents widespread use of hydrogen as a form of energy. Even though hydrogen can be stored in the conventional forms like a gas or liquid, arising handicaps e.g., high pressure and cryogenic temperature block its widespread usage. As an alternative, hydrogen may be stored in the solid state with a very high density. For this purpose, many distinct families of materials have been investigated such as carbon nanotubes, metal organic frameworks, metal hydrides, metal borohydrides and metal ammines (it is an indirect storage medium, since ammonia is stored instead of hydrogen). Among them, metal borohydrides and ammines took special interest due to their high gravimetric and volumetric hydrogen storage capabilities. However, metal borohydrides are very stable complexes and hence they require very high temperatures for their decomposition. This might be prevented by the inclusion of ammonia forming Ammine Metal Borohydrides (AMBs). In spite of their peculiar properties, AMBs might lead to the undesirable release of ammonia during the dehydrogenation. This can be prohibited with the addition of a second metal atom into AMBs leading to dual cation AMBs with a general formula of $M_1M_2(BH_4)_y(NH_3)_x$. Since there is only a very limited experimental investigations carried out for dual-cation AMBs so far, little is known about their crystal structures. With this study, we aim to explore the crystal structures of these materials ($LiTi(BH_4)_5(NH_3)_x$ $x = 2, 3, 4$) using a hybrid methodology combining crystal structure prediction with density functional calculations. For the crystal structure predictions, we employed our in-house developed code CASPESA which was successfully applied to both metal ammines [1, 2] and borohydrides [3-6].

2 Computational Details

2.1 Crystal Structure Prediction

One of the most important information about a material is its crystal structure because this structure determines almost all properties of a material. If the structure is known, even the material is not synthesized, most of properties of a material can be computed. Computational approaches play a crucial role for the crystal structure prediction and therefore several algorithms have been developed such as USPEX [7], CALYPSO [8], XtalOpt [9] and GULP [10]. In this study, we used CASPESA approach due to its fast and robust nature.

CASPESA requires a unit cell and predefined bond constraints to start the crystal prediction. In the following details of the model used to run CASPESA has been exemplified for $LiTi(NH_3)_2(BH_4)_5$: (1) as a unit cell, two formula units of $LiTi(NH_3)_2(BH_4)_4$ has been employed, (2) a fixed coordinate system is used for Ti

$(\text{NH}_3)_2(\text{BH}_4)_4$ (NH_3 and BH_4 groups are coordinated to Ti as a octahedral fashion), (3) a Li atom is placed to the origin and the spherical coordinates of the others are parameterized, (4) three Euler angle parameters (Θ , Φ , Ψ) are used to rotate the $\text{Ti}(\text{NH}_3)_2(\text{BH}_4)_4$ complex and the free BH_4 group, (5) the lattice vectors are used as parameters, (6) the resulting 30 (36 for $\text{LiTi}(\text{BH}_4)_5(\text{NH}_3)_3$ and 42 for $\text{LiTi}(\text{BH}_4)_5(\text{NH}_3)_4$) parameters are globally optimized to maximize the number of interactions between hydrogens of BH_4 molecules and Li atoms. To avoid any unphysical structure, we employed the following bond constraints: Mg–Mg, Li–Mg and Li–Li distances must be longer than 6.00, 4.80 and 4.10 Å, respectively. As an objective function, the number of Li–B distance, which is between 2.85 and 3.31 Å, has been maximized. The resulting most distinct structures have been chosen for the subsequent periodic DFT calculations.

2.2 DFT Calculations

We used Quantum Espresso software package for DFT calculations. The GGA exchange-correlation approximation of Perdew, Burke, Ernzerhof (PBE) [11] has been used for norm conserving pseudo potentials of all atoms. The kinetic energy and density cutoffs are set to 80 and 320 Ry, respectively. The electronic Brioullin zones were sampled with $(2 \times 2 \times 2)$ k-points. The energy and force thresholds were set to 10^{-5} and 10^{-4} a.u, respectively.

3 Results

$\text{LiTi}(\text{BH}_4)_5(\text{NH}_3)_x$ ($x = 2, 3, 4$) is not yet synthesized so its crystal structure is unknown. Therefore, employment of a crystal structure prediction algorithm is necessary and the only way to get information about these systems.

In Fig. 1, six different crystal structures of $\text{LiTi}(\text{BH}_4)_5(\text{NH}_3)_2$ found by CASPESA are shown. The Fig. 1a is the lowest energy structure and the energies of other structures are given relative to it. The lowest energy structure has a triclinic unit cell with lattice parameters $a = 7.65535$, $b = 8.61676$, $c = 12.513$, $\alpha = 73.56^\circ$, $\beta = 81.44^\circ$, $\gamma = 85.74^\circ$. In this structure, two NH_3 and four BH_4 molecules coordinated with Ti in an octahedral fashion, three BH_4 molecules coordinated with Li and two Li atoms share one BH_4 group.

Five different crystal structures have been found for $\text{LiTi}(\text{BH}_4)_5(\text{NH}_3)_3$ and they are shown in Fig. 2. Among them, the Fig. 2a is the lowest energy structure and it has a monoclinic cell with lattice parameters $a = 9.27$, $b = 18.44$, $c = 8.69$, $\beta = 94^\circ$ and belongs to Cc symmetry space group. In this structure, Ti has an octahedral

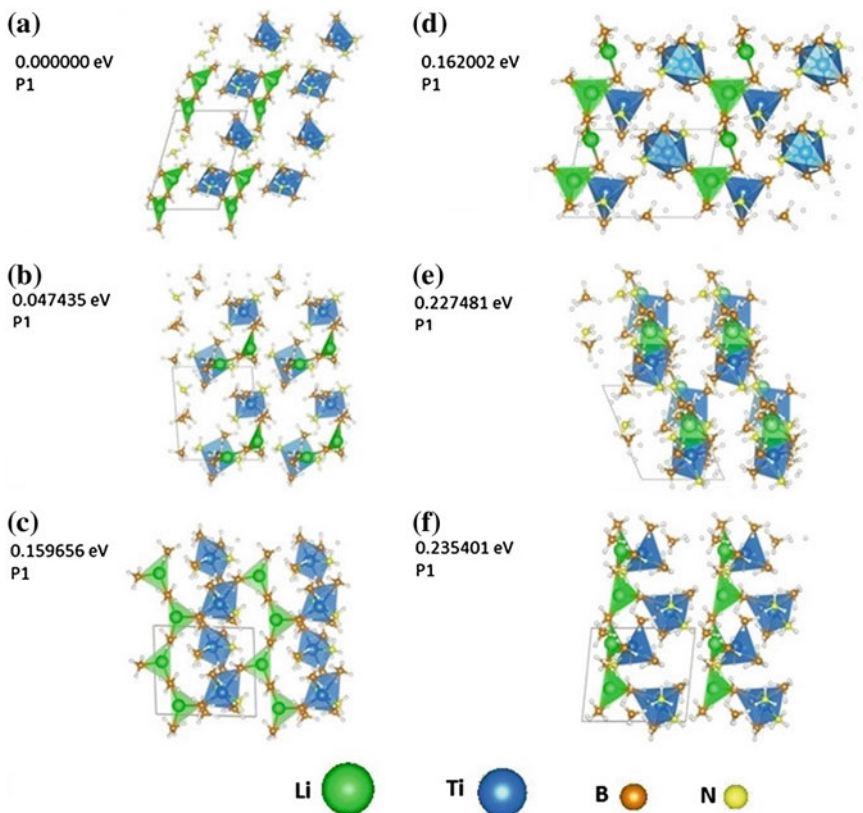


Fig. 1 Crystal structures of $\text{LiTi}(\text{BH}_4)_5(\text{NH}_3)_2$ predicted by CASPESA

coordination with three NH_3 and BH_4 molecules. Similar to $\text{LiTi}(\text{BH}_4)_5(\text{NH}_3)_2$, three BH_4 molecules around Li atoms constitute a triangle and Li atoms are joined together by sharing one BH_4 group.

Figure 3 shows four different crystal structures which have been predicted for $\text{LiTi}(\text{BH}_4)_5(\text{NH}_3)_4$. The structure in Fig. 3a was obtained to be the lowest energy structure which has a triclinic cell with lattice parameters $a = 8.78$, $b = 9.32$, $c = 12.52$, $\alpha = 101^\circ$, $\beta = 98^\circ$, $\gamma = 90^\circ$ and it belongs to P1 symmetry space group. In this structure, five BH_4 molecules around Ti form a trigonal bipyramidal and four NH_3 molecules are coordinated with Li tetrahedrally. In the rest of the structures Ti is an octahedral coordination with BH_4 and NH_3 groups.

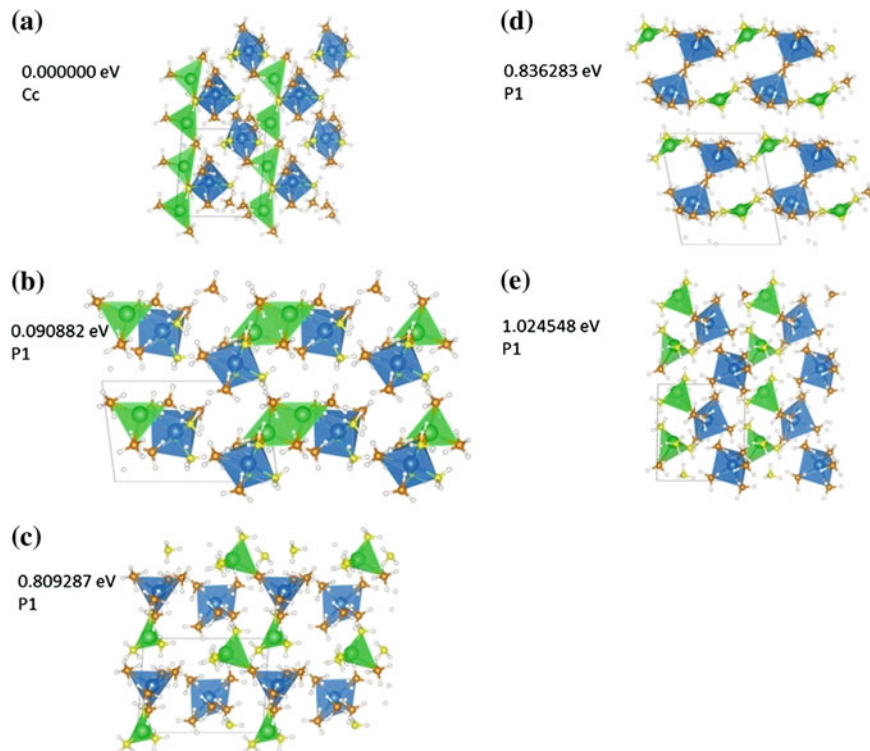


Fig. 2 Crystal structures of $\text{LiTi}(\text{BH}_4)_5(\text{NH}_3)_3$ predicted by CASPESA

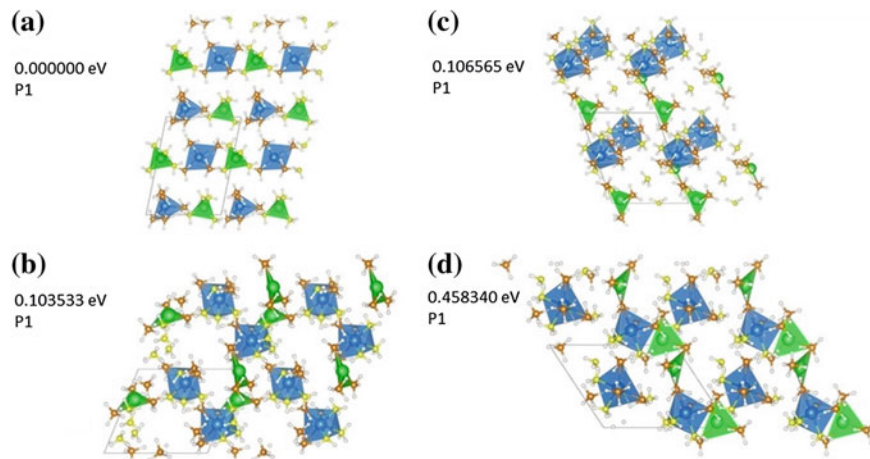


Fig. 3 Crystal structures of $\text{LiTi}(\text{BH}_4)_5(\text{NH}_3)_4$ predicted by CASPESA

4 Conclusions

A recent interest has been devoted to the dual cation AMBs due to their very promising hydrogen storage capabilities. Since this class of materials is new, there is no enough experimental study to determine their crystal structures. In this study, complex crystal structures of $\text{LiTi}(\text{BH}_4)_5(\text{NH}_3)_x$ ($x = 2, 3, 4$) were predicted using CASPESA algorithm. These crystal structures will contribute to understand physical properties of $\text{LiTi}(\text{BH}_4)_5(\text{NH}_3)_x$ which is not yet synthesized. All these structures can be further exploited by subsequent calculations to investigate the other interesting phenomenon e.g., hydrogen or ammonia dynamics.

Acknowledgments This work financially supported by the TUBITAK (112T988). Computing resources used in this work were provided by the National Center for High Performance Computing of Turkey (UYBHM) under grant number 20662009 and Informatics Institute of Istanbul Technical University.

References

1. A. Tekin et al., *Energy Environ. Sci.* **3**, 448 (2010)
2. A.J. Churchard et al., *Phys. Chem. Chem. Phys.* **13**, 16955 (2011)
3. R. Caputo, A. Tekin, W. Sikora, A. Züttel, *Chem. Phys. Lett.* **480**, 203–209 (2009)
4. A. Tekin, R. Caputo, A. Züttel, *Phys. Rev. Lett.* **104**, 215501 (2010)
5. R. Caputo, A. Tekin, *J. Solid State Chem.* **184**, 1622 (2011)
6. R. Caputo, A. Tekin, *Inorg. Chem.* **51**, 9757 (2012)
7. A.O. Lyakhov, A.R. Oganov, H.T. Stokes, Q. Zhu, *Comp. Phys. Comm.* **184**, 1172 (2013)
8. Y. Wang, J. Lv, L. Zhu, Y. Ma, *Comput. Phys. Commun.* **183**, 2063 (2012)
9. D.C. Lonie, E. Zurek, *Comput. Phys. Commun.* **182**, 372 (2011)
10. J.D. Gale, *JCS Faraday Trans.* **93**, 629 (1997)
11. J.P. Perdew, K. Burke, M. Ernzerhof, *Phys. Rev. Lett.* **77**, 3865 (1996)

Discovery of New Dual Cation Metal Ammine Borohydrides: A Computational Study

Samet Demir and Adem Tekin

Abstract World's growing energy need is mostly reliant upon fossil fuels. Fossil fuels are considered to be non-renewable energy sources because it needs million years to form and reserves are being depleted much more faster than new reserves are being made. Usage of fossil fuels comes with harmful consequences. It is responsible for 20 % of global warming pollution. To avoid these harmful effects, new energy sources must be discovered. As an alternative to fossil fuels, hydrogen can be used for energy needs and it has a lot of benefits over fossil fuels such as being environmentally friendly, carrying high energy content and being renewable. To use hydrogen as an energy source instead of fossil fuels, some challenging problems must be solved. One of them is hydrogen storage. Hydrogen can be stored as gas or liquid but these types of storage are not so efficient for widespread use. A more convenient way is to store hydrogen in the form of solid. For this purpose, metal borohydrides and amines can be used due to their high gravimetric and volumetric densities. To decompose hydrogen, metal borohydrides requires very high temperatures and this situation can be moderated by mixing them with amines. To achieve this goal, in this study we designed dual-cation ammine metal borohydrides (AMBs) in the form of $\text{LiSc}(\text{BH}_4)_4(\text{NH}_3)_x$ ($x = 2, 3$) using an approach which combines crystal structure prediction with density functional theory computations.

1 Introduction

With the emergence of the mechanical age, energy need of the world increased rapidly and this need has been mainly fulfilled by fossil fuels. As a consequence of this huge need, fossil fuel sources are running out day by day and they are not

S. Demir (✉) · A. Tekin

Informatics Institute, Istanbul Technical University, 34469 Maslak Istanbul, Turkey
e-mail: sametdemir@gmail.com

A. Tekin

e-mail: adem.tekin@be.itu.edu.tr

renewable. Fossil fuels have limited sources and last observations show that as of 2042, the fossil fuels, except coal, will be depleted [1]. Fossil fuels also have many harmful effects to the environment. Hydrogen could be a great replacement for fossil fuels with its high energy content, renewability and environment friendly features. However, there is a major problem that must be solved to use hydrogen in everyday life: an efficient storage of hydrogen. Hydrogen can be stored in the form of solid, liquid and gas but storing hydrogen as gas or liquid has big drawbacks. Wide range of materials can be used for storing hydrogen in the solid form, such as carbon nanotubes, metal hydrides, metal organic frameworks, metal borohydrides and metal ammines. With their high volumetric and gravimetric hydrogen storage capabilities, metal borohydrides and ammines have big advantages over the other materials but also they have drawbacks too i.e., need of high temperatures for decomposing hydrogen from metal borohydrides [2]. This weakness can be eliminated by adding ammonia to metal borohydrides and forming Ammine Metal Borohydrides (AMBs) but also adding ammonia can cause undesirable release of ammonia during the process of dehydrogenation. To prevent the undesired ammonia release, a second metal atom can be added into AMBs. With this addition the general formula of the AMBs becomes $M_1M_2(BH_4)_x(NH_3)_y$. Sun et al. [3] has already synthesized $LiMg(BH_4)_3(NH_3)_2$ and they pointed out that the synthesized complex does not emit ammonia during the dehydrogenation. However, there are only a very limited number of experimental studies concerning AMBs. Therefore, computational studies should strongly be helpful for the discovery of new AMBs. By keeping in mind this goal, in this study, $LiSc(BH_4)_4(NH_3)_x$ with $x = 2, 3$ have been investigated. Since nothing is known about their crystal structures, the first task is to predict some possible crystal structures. For the crystal structure prediction, there are many available codes. In this study, we employed the recent algorithm, CrystAl Structure Prediction via Simulated Annealing (CASPESA) [4], due to its fast and robust nature. The crystal structures obtained from CASPESA were further relaxed at the Density Functional Theory (DFT) for the assessment of the energy order.

2 Computational Methods

2.1 Crystal Structure Prediction

To calculate the physical properties of a material, it is a requisite to know its crystal structure. The crystal structure information can be experimentally determined. However, there might be some cases where experiments might not be conducted. In such cases, computational crystal structure prediction (CCSP) becomes the only source that one can apply to get information about the considered systems. For the CCSP, various algorithms were developed such as USPEX [5], CALYPSO [6], XtalOpt [7] and GULP [8]. These algorithms mostly based upon genetic algorithms and swarm optimization. There is also another recently developed approach [4]

called as CrystAl Structure Prediction via Simulated Annealing (CASPESA) and it has been successfully applied to both metal borohydrides and ammines. Due to its remarkable efficiency CASPESA has been employed for CCS of AMBs considered in this study. CASPESA algorithm basically tries to increase stability of the structure by increasing the number of predefined structural motifs which tend to lower energy of the crystal structure. To run the CASPESA, atoms or atom groups inside the unit cell must be parameterized and their motion are controlled by some predefined bond length constraints. The experimental crystal structures of AMBs show that alkaline metals in AMBs tend to make bonds with BH_4 groups while earth alkaline and transition metals tend to make bonds with both BH_4 and NH_3 groups [9]. With knowing this, while doing the parameterization of the unit cell with CASPESA, $\text{Sc}(\text{BH}_4)_x(\text{NH}_3)_y$ has been taken as a fixed complex and depending on the model free BH_4 molecules were added to the system. Two formula units in a unitcell were used in each model. One of the Li atom was fixed to the origin while $\text{Sc}(\text{BH}_4)_x(\text{NH}_3)_y$ group and other Li atom (also free BH_4 if exist) was able to change their position via spherical coordinates. Except atomic species, the rest of the groups are able to rotate around their centers. In order to better search the space, CASPESA has been individually started for each different lattice type (cubic, hexagonal, monoclinic, rhombohedral, orthorhombic, tetragonal and triclinic). In the parameterization, the required bond length constraints were determined with the help of experimental structure. When CASPESA is finished, the resulting structures were further relaxed at the DFT level.

2.2 DFT Calculations

We used Quantum Espresso software package for DFT calculations. The GGA exchange-correlation approximation of Perdew, Burke, Ernzerhof (PBE) has been used for norm conserving pseudo potentials of all atoms. The kinetic energy and density cutoffs are set to 80 and 320 Ry, respectively. The electronic Brioullin zones were sampled with $(2 \times 2 \times 2)$ k-points. The energy and force thresholds were set to 10 $^{-5}$ and 10 $^{-4}$ a.u, respectively.

3 Results

$\text{LiSc}(\text{BH}_4)_4(\text{NH}_3)_x$ ($x = 2, 3$) is not a synthesized material, therefore its crystal structure is not yet known. We predicted the crystal structure of this material using the CASPESA algorithm. Figure 1 shows ten different predicted crystal structures of $\text{LiSc}(\text{BH}_4)_4(\text{NH}_3)_2$. Figure 1a is the lowest energy structure. Energies of the other structures are given relative to Figure 1a. The lowest energy structure has a triclinic unit cell with lattice parameters are $a = 7.92886$, $b = 9.13552$, $c = 10.21695$, $\alpha = 92.06302$, $\beta = 92.37535$, $\gamma = 115.35266$. In this structure, two

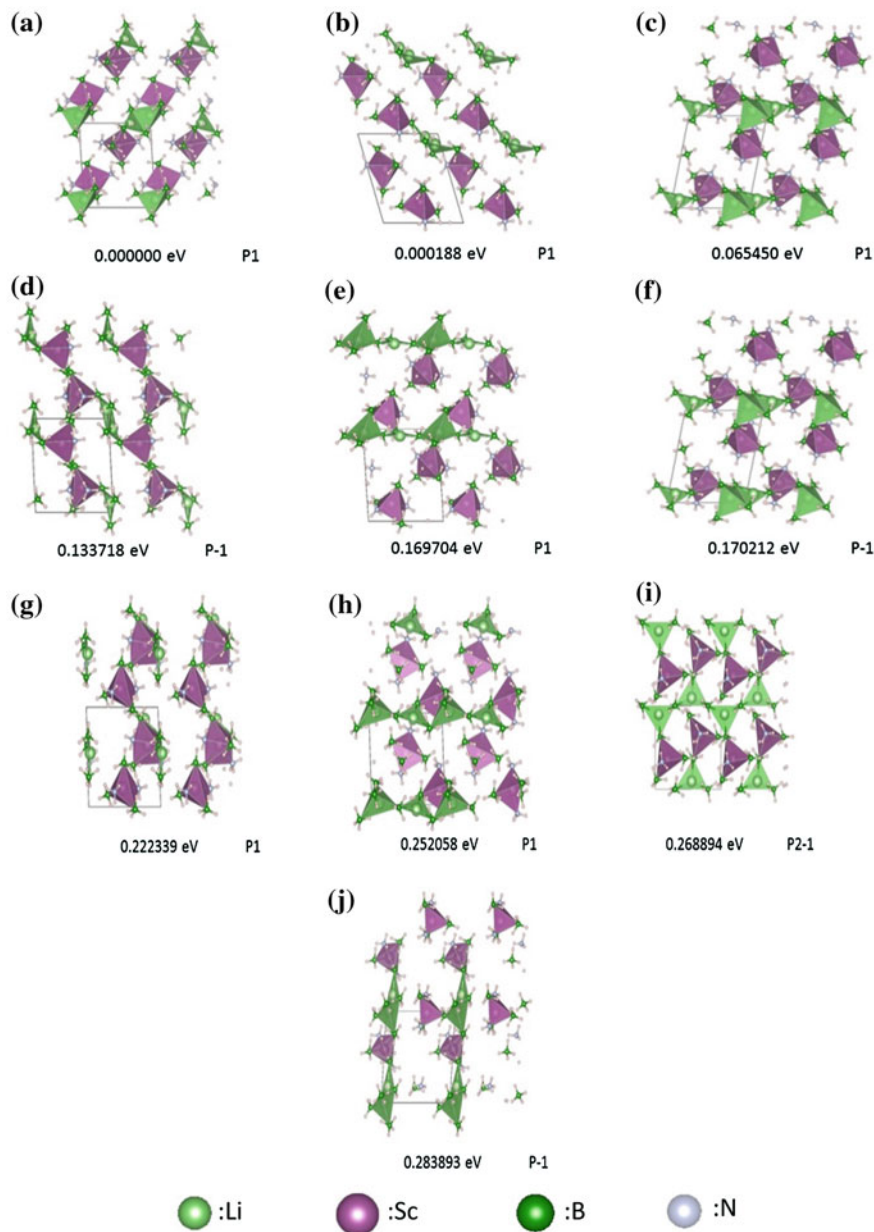


Fig. 1 Predicted crystal structures for $\text{LiSc}(\text{BH}_4)_4(\text{NH}_3)_2$

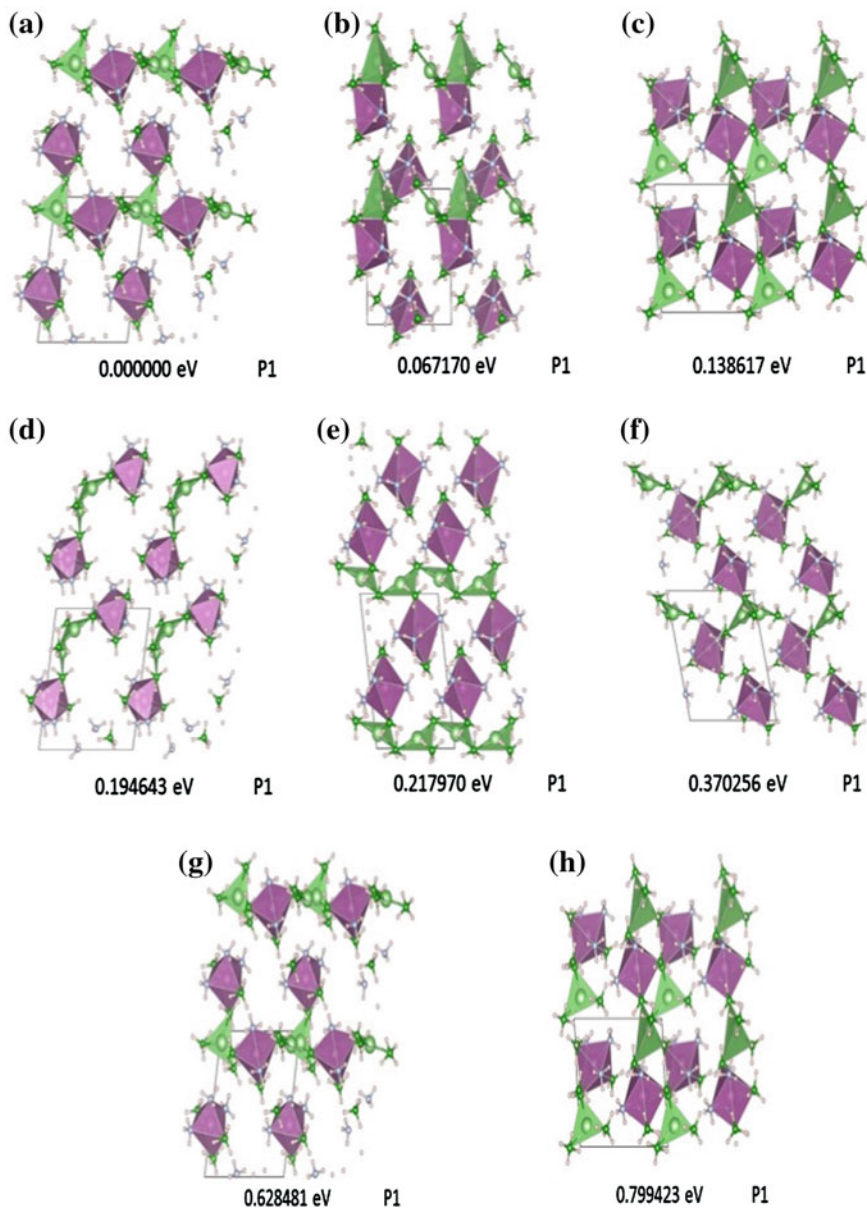


Fig. 2 Predicted crystal structures for $\text{LiSc}(\text{BH}_4)_4(\text{NH}_3)_3$

BH_4 and NH_3 molecules coordinated with Sc in a tetrahedral fashion. Li atoms prefer a triangle and tetrahedral coordinations with BH_4 groups. Li atoms are connected to each other by sharing two of their BH_4 molecules. In addition, tetrahedrally coordinated Li atom is attached to Sc by sharing a BH_4 group.

Predicted crystal structures for $\text{LiSc}(\text{BH}_4)_4(\text{NH}_3)_3$ are shown in Fig. 2. The lowest energy structure is Fig. 2a and it also has a triclinic cell with lattice parameters $a = 8.26468$, $b = 8.65674$, $c = 10.51631$, $\alpha = 78.49739$, $\beta = 77.13621$, $\gamma = 81.23732$. In this structure, Sc forms an octahedron with three BH_4 and NH_3 molecules. All Li atoms have triangular arrangements of BH_4 groups and they share one of their BH_4 groups. In the meantime, Li atoms share their two BH_4 molecules with Sc.

4 Conclusions

AMBs have a great potential to be used for hydrogen storage but there are not enough experimental studies for the determination of their crystal structures. In this study, crystal structures of $\text{LiSc}(\text{BH}_4)_4(\text{NH}_3)_2$ and $\text{LiSc}(\text{BH}_4)_4(\text{NH}_3)_3$ were predicted with CASPESA. The method used for this predictions may easily applied to other compounds. Predicted crystal structures allows us to understand the physical properties, e.g., ammonia or borohydride dynamics of not yet synthesized materials.

Acknowledgments This work financially supported by the TUBITAK (112T988). Computing resources used in this work were provided by the National Center for High Performance Computing of Turkey (UYBHM) under grant number 20662009 and Informatics Institute of Istanbul Technical University.

References

1. S. Shafiee, E. Topal, When will fossil fuel reserves be diminished? *Energy Policy* **37**(1), 181–189 (2009). doi:[10.1016/j.enpol.2008.08.016](https://doi.org/10.1016/j.enpol.2008.08.016)
2. L. Schlapbach, A. Zuttel, Hydrogen-storage materials for mobile applications. *Nature* **414** (6861), 353–358 (2001)
3. W. Sun, X. Chen, Q. Gu, K.S. Wallwork, Y. Tan, Z. Tang, X. Yu, A new ammine dual-cation (Li , Mg) borohydride: synthesis, structure, and dehydrogenation enhancement. *Chem. A Eur. J.* **18**(22), 6825–6834 (2012). doi:[10.1002/chem.201102651](https://doi.org/10.1002/chem.201102651)
4. A. Tekin, R. Caputo, A. Züttel, First-principles determination of the ground-state structure of LiBH_4 . *Phys. Rev. Lett.* **104**(21), 215501 (2010)
5. A.O. Lyakhov, A.R. Oganov, H.T. Stokes, Q. Zhu, New developments in evolutionary structure prediction algorithm USPEX. *Comput. Phys. Commun.* **184**(4), 1172–1182 (2013). doi:[10.1016/j.cpc.2012.12.009](https://doi.org/10.1016/j.cpc.2012.12.009)
6. Y. Wang, J. Lv, L. Zhu, Y. Ma, CALYPSO: A method for crystal structure prediction. *Comput. Phys. Commun.* **183**(10), 2063–2070 (2012). doi:[10.1016/j.cpc.2012.05.008](https://doi.org/10.1016/j.cpc.2012.05.008)

7. D.C. Lonie, E. Zurek, XtalOpt: An open-source evolutionary algorithm for crystal structure prediction. *Comput. Phys. Commun.* **182**(2), 372–387 (2011). doi:[10.1016/j.cpc.2010.07.048](https://doi.org/10.1016/j.cpc.2010.07.048)
8. J.D. Gale, GULP: A computer program for the symmetry-adapted simulation of solids. *J. Chem. Soc. Faraday Trans.* **93**(4), 629–637 (1997). doi:[10.1039/A606455H](https://doi.org/10.1039/A606455H)
9. G. Xia, Q. Gu, Y. Guo, X. Yu, Ammine bimetallic (Na, Zn) borohydride for advanced chemical hydrogen storage. *J. Mater. Chem.* **22**(15), 7300–7307 (2012). doi:[10.1039/C2JM16370E](https://doi.org/10.1039/C2JM16370E)

Part XX
Photovoltaics and Solar Cells

Properties of CdS Deposited by the SILAR Method Using Cd(II) Organic Salt as Precursor

L. Tamašauskaitė-Tamašiūnaitė, B. Šimkūnaitė-Stany�ienė,
G. Grincienė, A. Žielienė, L. Naruškevičius, A. Selskis,
V. Jasulaitienė and E. Norkus

Abstract In this study the thin CdS films were deposited onto the glass sheets by means of the successive ionic layer adsorption and reaction method using cadmium 2,4-pentanedionate and sodium sulfide precursors. The morphology and composition of the as-prepared CdS thin films were characterized using Field-Emission Scanning Electron Microscopy, Energy Dispersive X-ray Spectroscopy and X-ray Photoelectron Spectroscopy. The optical properties of the CdS thin films deposited onto glass sheets were investigated by means of UV/VIS spectrophotometric measurements. It was found that the thin CdS films deposited onto the glass sheets have a crystalline structure with CdS particles of ca. 20–80 nm in size. The thickness of obtained films is ca. 20–80 nm. The determined band gap energy decreases slightly from 2.35 to 2.2 eV with increase in number of deposition cycles from 40 to 100.

1 Introduction

Thin films of metal sulfides show promise for application as photovoltaic converters, optoelectronic and thermoelectric devices, and photodiode arrays. Cadmium sulfide is one of the most important II-VI semiconductors with a direct-band transition and with a band gap (E_g) of 2.42 eV. A variety of methods have been developed to prepare CdS such as vacuum evaporation, electrochemical synthesis, spray deposition, chemical vapor deposition, electrodeposition, chemical bath deposition (CBD) and etc. Nowadays the successive ionic layer adsorption and reaction (SILAR) method has advantageous due to it allows to control the film thickness at atomic level, which is difficult by the conventional chemical bath deposition (CBD) and electrodeposition methods.

L. Tamašauskaitė-Tamašiūnaitė (✉) · B. Šimkūnaitė-Stany�ienė · G. Grincienė · A. Žielienė · L. Naruškevičius · A. Selskis · V. Jasulaitienė · E. Norkus
Center for Physical Sciences and Technology, A. Goštauto 9, 01108 Vilnius, Lithuania
e-mail: lortam@ktl.mii.lt

This work is focused on the deposition of the thin CdS films by the SILAR method using cadmium 2,4-pentanedionate and sodium sulfide precursors. The morphology and composition of the as-prepared CdS thin films were characterized using Field-Emission Scanning Electron Microscopy, Energy Dispersive X-ray Spectroscopy and X-ray Photoelectron Spectroscopy. The optical properties of the CdS thin films deposited onto glass sheets were investigated by means of UV/VIS spectrophotometric measurements.

2 Experimental

The CdS films were deposited onto the glass sheet by means of the SILAR method. At first, the glass sheet was dipped at ambient temperature for 30 s in a solution containing cadmium 2,4-pentanedionate. Then, after rinsing of the treated surface with deionized water, the electrode was immersed for 30 s into a solution containing 0.1 M Na_2S and rinsed with deionized water. This constitutes one deposition cycle (N) of the CdS film. The whole cycle described was carried out repeatedly for the required number of deposition cycles. The CdS films were formed by 40, 70 and 100 cycles.

The morphology and composition of the CdS films were characterized using a SEM/FIB workstation Helios Nanolab 650 with an energy dispersive X-ray (EDX) spectrometer INCA Energy 350 X-Max 20.

The elemental analysis of deposits was performed by XPS. The X-ray photoelectron spectroscopy analysis was performed by using an “ESCALAB MK II” spectrometer (VG Scientific, UK) equipped with an $\text{Mg K}\alpha$ X-ray radiation source (1253.6 eV) operated at 300 W, at a fixed pass energy of 20 eV. The pressure of 1.33×10^{-6} Pa was kept in the UHV analysis chamber. To obtain depth profiles, the samples were etched in the preparation chamber with ionized argon under vacuum of 5×10^{-4} Pa. The accelerating voltage of ca. 1 kV and the beam current of $\sim 20 \mu\text{A cm}^{-2}$ were used which corresponded to the etching rate of ca. 4 nm min^{-1} . The XPS spectra were recorded for Cd3d, S2p and O1s. The sensitivity factors of these elements were taken from [1]. The spectra obtained were compared with the standard ones [2–4].

Optical absorption studies of the films deposited on glass substrates were carried out in the wavelength range of 300–800 nm using UV/VIS spectrophotometer (Perkin Elmer Lambda 35 UV/VIS).

3 Results and Discussion

The thin CdS films were deposited onto the glass sheets by the SILAR method using cadmium 2,4-pentanedionate and sodium sulfide precursors. Figure 1 presents the FESEM views of CdS deposited onto the glass sheets. As evident from Fig. 1,

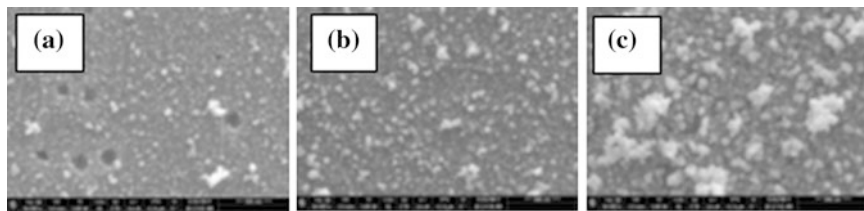


Fig. 1 FESEM images of CdS deposited onto the glass sheet by the SILAR method. $N = 40$ (a), 70 (b) and 100 (c)

Table 1 Surface atomic composition of the CdS films deposited onto the glass sheets by EDAX analysis

Number of deposition cycles of CdS (N)	Elements, at %		Ratio of Cd/S	Thickness of CdS films, nm
	Cd	S		
40	48.1	51.9	0.93	18
70	49.0	51.0	0.96	44
100	48.0	52.0	0.92	78

The catalysts are the same as in Fig. 1

Table 2 XPS analysis of the elemental composition of as-deposited CdS film onto the glass sheet ($N = 70$) and corresponding composition after Ar^+ sputtering (rate 4 nm min^{-1})

Ar^+ sputter time (s)	Cd3d		S2p		O1s		C1s		Cd/S
	E_b , eV	at %							
0	404.86	25.39	161.39	19.99	536.62	12.62	284.76	41.99	1.3
30	405.02	34.26	161.51	25.27	532.66	40.47	–	–	1.4

the thin CdS films having a crystalline structure with CdS particles of ca. 20–80 nm in size were deposited onto the glass sheet by the SILAR method.

Surface atomic composition by the energy dispersive X-ray spectroscopy analysis of the CdS films deposited onto the glass sheets by 40, 70 and 100 SILAR cycles is presented in Table 1. In all cases, the elemental composition is close to CdS. The thickness of as-deposited CdS films is ca. 20–80 nm.

The as-deposited CdS layers were analyzed by X-ray photoelectron spectroscopy and are presented in Table 2. As evident from the data in Table 2, Cd, S and O were detected both on the surface and at a film depth of 2 nm. The binding energies of Cd3d at 405.02 eV and that of S2p at 161.51 eV correspond to formation of CdS [2–4]. The presence of carbon and oxygen was observed as impurities in the as-deposited films.

The optical absorption spectra for all the CdS samples were recorded in the wavelength range of 300–800 nm at room temperature. Figure 2 shows the absorbance and transmittance spectra of the investigated CdS samples.

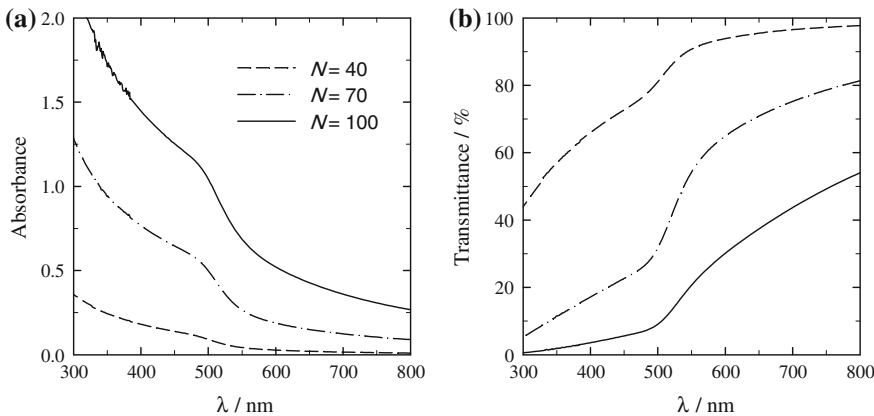


Fig. 2 Absorbance (a) and transmittance (b) spectra of CdS/glass. SILAR deposition cycles (N): 40 (a), 70 (b) and 100 (c)

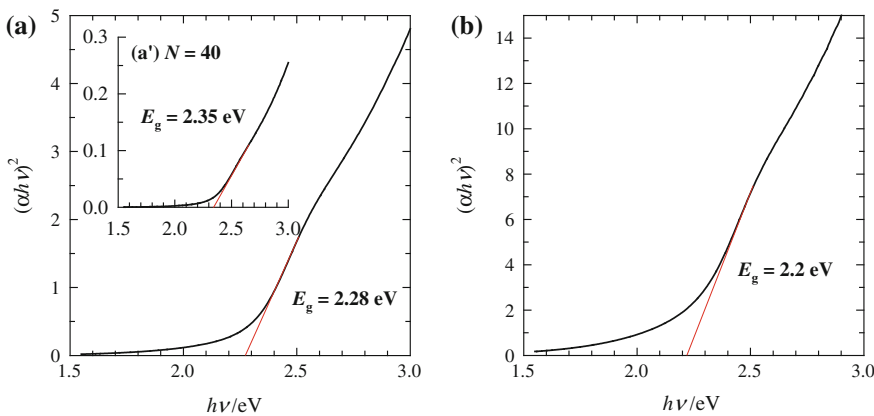


Fig. 3 Plot of $(ahv)^2$ versus $h\nu$ for the CdS films deposited on glass sheets. SILAR deposition cycles (N): 40 (the inset, a'), 70 (a) and 100 (b)

In order to confirm the nature of optical transition in all samples, the optical data were analyzed using classical absorption equation:

$$\alpha = \frac{\alpha_0 (h\nu - E_g)^n}{h\nu} \quad (1)$$

where α_0 is a constant, $h\nu$ is the incident photon energy, E_g is the separation between bottom of conduction band and top of the valence band and n is the constant. For allowed direct transition, $n = 1/2$, and for allowed indirect transition

$n = 2$. The plots of $(ahv)^2$ versus $h\nu$ for all the CdS samples for various cycles are shown in Fig. 3.

The nature of plots suggests direct interband transition. Extrapolation of the linear portion of the curve to the x-axis, leads to the estimation of band gap energy of material. From Fig. 3, it is clear that band gap energy decreases slightly from 2.35 to 2.2 eV with increase in number of immersion cycles from 40 to 100.

4 Conclusions

The thin CdS films were deposited onto the glass sheets by means of the successive ionic layer adsorption and reaction method using cadmium 2,4-pentanedionate and sodium sulfide precursors. The CdS films were formed by 40, 70 and 100 cycles and the thickness of obtained films is ca. 20–80 nm.

It was found that the thin CdS films deposited onto the glass sheets have a crystalline structure with CdS particles of ca. 20–80 nm in size. The determined band gap energy decreases slightly from 2.35 to 2.2 eV with increase in number of deposition cycles from 40 to 100.

Acknowledgments The work was carried out within the project VP1-3.1-ŠMM-08-K-01-009 that is partly supported by the National Programme “An improvement of the skills of researchers” launched by the Lithuanian Ministry of Education and Science.

References

1. D. Briggs, M.P. Seach (eds.), *Surface analysis by Auger and X-ray photoelectron spectroscopy* (Mir, Moscow, 1987)
2. C.D. Wagner, W.M. Riggs, L.E. Davis, J.F. Moulder, G.E. Muilenberg, *Handbook of X-ray photoelectron spectroscopy* (Perkin-Elmer Corporation, Minnesota, 1978)
3. N.S. McIntyre, M.G. Cook, *Anal. Chem.* **47**, 2208–2213 (1975)
4. <http://srdata.nist.gov/xps/>

Analysis of the Performance a PV System Based on Empirical Data in a Real World Context

Seyed Amin Tabatabaei and Jan Treur

Abstract The performance of solar energy production systems consisting of photovoltaic solar panels strongly depends on the location and orientation of the solar panels. Previously a computational model has been developed to predict this performance depending on location and orientation; this model allows for prior analysis of a PV system before it is actually built. In the current paper the performance of solar panels according to their location and orientation is analyzed based on empirical real world performance data, and compared to the data generated by the previously developed computational model. These empirical data have been collected from a number of solar panels at different locations and orientations day-by-day and panel-by-panel for a whole year. The data is analyzed and used to deepen the prior analysis, and to evaluate the computational model thereby generating suggestions for improvement of this model. These suggestions are a basis for an improved computational model in order to enhance the quality of prior analysis of a PV system before it is actually built. Such a pre-analysis is useful as a support for decision making by estimating how much loss different options for locations will have, before actually placing the solar panels.

1 Introduction

In recent years, the production of solar energy by photovoltaic panels has increased substantially, which goes hand in hand with strongly decreasing costs of solar panels over the years; e.g., [1–3]. To consider a site for a solar energy plants the

S.A. Tabatabaei (✉) · J. Treur

Agent Systems Research Group, Department of Computer Science, VU University Amsterdam, De Boelelaan 1081, 1081HV Amsterdam, The Netherlands
e-mail: s.tabatabaei@vu.nl

J. Treur
e-mail: j.treur@vu.nl
URL: <http://www.cs.vu.nl/~treur>

circumstances of the site play an important role. For example, how much shadow occurs over the year, is a perfect southward position possible, and is optimal vertical angle of the panels possible? And if not, how much loss is implied by the imperfections of the site? These are not trivial issues to address. For example, if shadow occurs, the extent of the entailed loss in production depends on the specific day in the year and hour of the day. All these have to be aggregated to obtain how much loss this entails over a year. In [4] this has been addressed by an (agent-based) computational model, allowing performing simulations over a whole year. Such a model is very useful for a prior analysis of a site and the different locations within the site, as a basis for decisions on which locations within the site to use. However, the validity of such a computational model has to be assessed based on empirical data. This was not yet done in [4], but is the focus of the current paper.

In the current paper, the performance of solar panels according to their location and orientation is analyzed based on empirical real world performance data. Moreover, the empirical results are compared to the data generated by the computational model described in [4]. The empirical data have been collected at the same site addressed in [4] from a number of solar panels at different locations and orientations day-by-day and panel-by-panel for a whole year. The data is analyzed and used on the one hand to deepen the prior analysis, and on the other hand to evaluate the computational model. This will also provide suggestions for improvement of the computational model. These suggestions are useful as a basis for an improved computational model in order to enhance the quality of prior analysis of a PV system before it is actually built.

In the paper, in Sect. 2 a brief description of the computational model is given; for a more extensive description, see [4]. Section 3 discusses the empirical data, and in Sect. 4 these data are compared to data predicted by the computational model. In Sect. 5 suggestions are discussed for improvements of the computational model.

2 The Computational Model

The computational model introduced in [4] describes how at any point in time, the efficiency of the production of a panel depends on situational circumstances. In general, the energy production can be described at each point in time as a function of:

- the available irradiation irr
- the efficiency factor ρ_a due to angle and orientation of the panel
- the efficiency factor ρ_s due to shadow
- the efficiency factor ρ_{panel} of the panel
- the efficiency factor ρ_{inv} of the micro-inverter

Here it is assumed that the inverter has a peak power that is high enough to process all power provided by the panel. The following relations are assumed:

$$P_{panel} = \rho_a \rho_s \rho_{panel} irr$$

$$P_{out} = \rho_{inv} P_{panel} = \rho_{inv} \rho_a \rho_s \rho_{panel} irr$$

where P_{panel} is the power provided by panel and P_{out} by the inverter. Note that ρ_{panel} and ρ_{inv} are given characteristics of the panel and inverter, and ρ_s , ρ_a , and irr are situational variables that can be manipulated or depend on time of the day and year. In an ideal situation, it holds $\rho_s = \rho_a = 1$ (no shadow and most optimal angles). For input on irradiation for different times in a year, realistic empirical data were acquired (from the Dutch Meteorological Institute KNMI). Note that such information for Europe can also be obtained at [5].

Moreover, note that to compare the situational aspects for two different options for locations (1) and (2) at the same site (when it is assumed that $\rho_{inv}(2) = \rho_{inv}(1)$, $\rho_{panel}(2) = \rho_{panel}(1)$ and $irr(2) = irr(1)$), by dividing some of the factors can be left out:

$$\frac{P_{panel}(2)}{P_{panel}(1)} = \frac{\rho_{inv}(2)\rho_a(2)\rho_s(2)\rho_{panel}(2) irr(2)}{\rho_{inv}(1)\rho_a(1)\rho_s(1)\rho_{panel}(1) irr(1)} = \frac{\rho_a(2)\rho_s(2)}{\rho_a(1)\rho_s(1)}$$

In particular, when situation (1) is an ideal situation it holds $\rho_a(1)\rho_s(1) = 1$, then $\rho_a(2)\rho_s(2)$ indicates how situation (2) performs in comparison to most optimal. Given this, the loss percentage of a situation in comparison to an ideal situation can be obtained as $100 * (1 - \rho_a \rho_s)$ or as an approximation $100 * (1 - \rho_s) + 100 * (1 - \rho_a)$. For a real world site there may not be such an ideal situation. Then a relative loss percentage can be used, with respect to the most optimal situation within the site.

2.1 Modeling Shadow Effects: The Variable ρ_s

How shadow affects the energy production (the variable ρ_s) directly relates to obstacles on the one hand, and positions of the sun on the other hand. The position of the sun (seen from the earth) is characterized by two angles (see also [6]): the vertical angle above the horizon, and the horizontal angle with the direction of North. These are modeled as a function of time and based on this by geometry for each relevant obstacle the shadow length over time is determined, from which it is found at which time points a given location has shadow.

2.2 Modeling the Effects of Panel Orientation and Angle: The Variable ρ_a

The orientation and angle under which the panel is positioned is another important factor (the variable ρ_a). For example, at [7] a schematic overview is shown of how

efficiency relates to the vertical and horizontal angle of a panel, taken over a year. This is modeled for the South South West orientation of the site as an approximation (with α the panel angle with the horizontal plane)

$$\rho_a = 0.58 \sin(\alpha + 55) + 0.39$$

3 The Real World Situation and the Empirical Data

In this section the considered real world situation and the empirical data that have been collected will be described.

3.1 The Locations and the Data Collection

The considered real world situation fulfills the requirement that it consists of locations that are not ideal. Overall, the real world situation concerns a three storey family house (a net-zero house using a heat pump for heating) in an environment with many high trees, near Alkmaar, the Netherlands (about 52.6 latitude, 4.7 longitude). More specifically, all of the considered locations suffer from periods with shadow, and most of the locations do not allow for panel positions with an ideal vertical angle. Furthermore, the orientation of the whole site is not South but South West. All these dimensions of imperfection, inherent to real life and real world sites, provide good possibilities to investigate in a comparative manner how they affect the production over a year. Four possible locations for solar panels have been used, as briefly described below (Table 1). Note that location 2 has been left out of consideration here because no adequate data for a full year were available for it (due to a change of positions within the year).

Table 1 Possible locations for solar panels

<p><i>Location 1 (6 panels)</i> Shelter in the garden with an almost flat roof oriented South South West with shadow from the house with height 5.00 m at a distance of 6.00–10.00 m South East and from various trees. Vertical panel angle is 15°</p>	
<p><i>Location 3 (8 panels)</i> Flat roof at top of a dormer oriented South South West with shadow from a row of trees East South East at a distance of 8.50–15.50 m and height 5.50 m above the</p>	

(continued)

Table 1 (continued)

roof and from the rooftop South South West at a distance of 0.85–3.00 m with height 0.50 m. Vertical panel angles are 1° and 10°	
<i>Location 4 (7 panels)</i> Sloped roof oriented South South West with shadow from a row of trees East South East at a distance of 8.50–15.50 m and height 5.50 m above the roof. Vertical panel angle is 30°	

The panels used are Renesola [8] 265 Wp monocrystalline panels. Moreover, Power One [9] 300 W micro-inverters are used, allowing to monitor each panel separately through the Aurora CDD central monitoring device which communicates radio graphically with all micro-inverters and through Wi-Fi with a computer.

For these locations every day data were collected for the day production for every panel. This has been done from the beginning of June 2013 and is still continuing during fall 2014. In the current paper the data are used for exactly 1 year: from the beginning of June 2013 to the end of May 2014.

3.2 Initial Analysis of the Empirical Data

In this section the available data are briefly reviewed. In Sect. 4 the analysis goes further and focuses on comparison with the predicted data. First, in Fig. 1 the year production is shown for each panel. Indeed the different locations show different yields, with location 4 as the best. Also within the locations differences are shown. For example, a clear trend is visible that the panels more close to the row of trees have lower production. In the graph, two lines have been added that indicate the levels predicted by a rule of thumb often used in the Netherlands. This rule of thumb (in principle meant for ideal locations) says that a PV system of p Wp will provide a year production of $0.85 p$ kWh, i.e., $\text{kWh/Wp} = 0.85$ (conservative variant, red line), or $0.9 p$ kWh, i.e. $\text{kWh/Wp} = 0.9$ (more optimistic variant, green line). As can be seen location 4 provides more than this, but most other locations less.

It turns out that the first panel of location 4 has the maximum output. Therefore, this panel is used as a norm, and loss percentages have been determined in comparison to this panel. This is shown in Fig. 2 below: loss percentages compared to loc4-1.

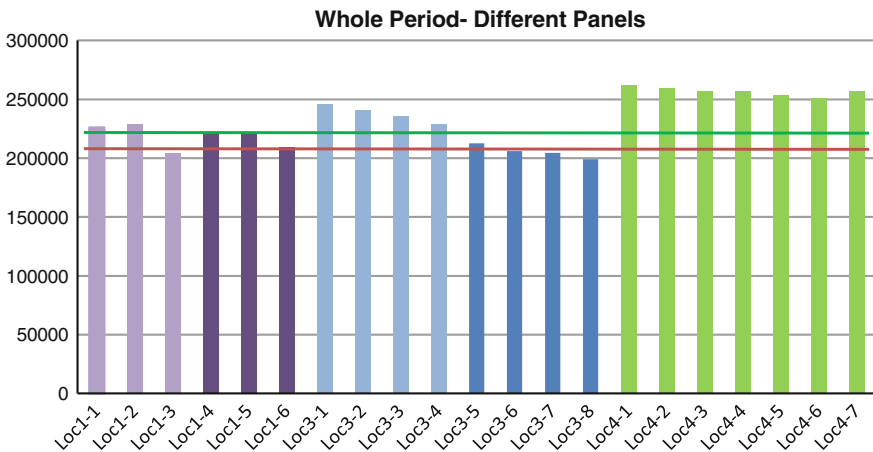


Fig. 1 Empirical data: production of each panel in the 12 months period June 2013–May 2014

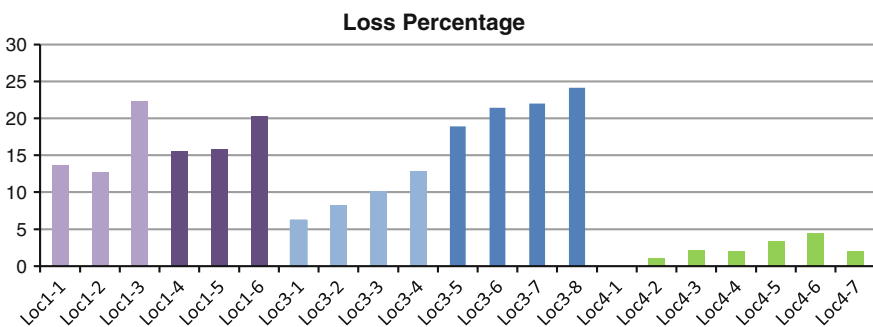


Fig. 2 Loss percentage of each panel in the period of 12 months (June 2013–May 2014)

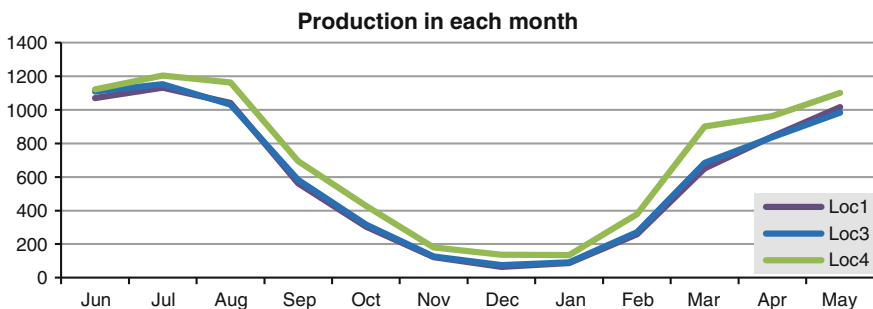


Fig. 3 Empirical data: average production of panels of each group in different months

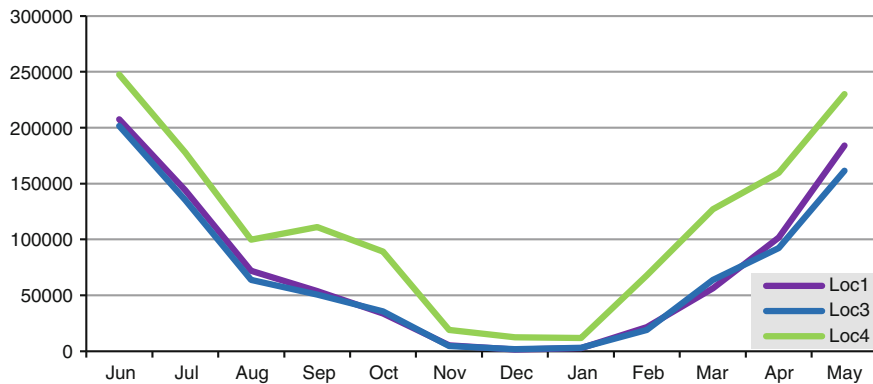


Fig. 4 Empirical data: variance of average of daily production

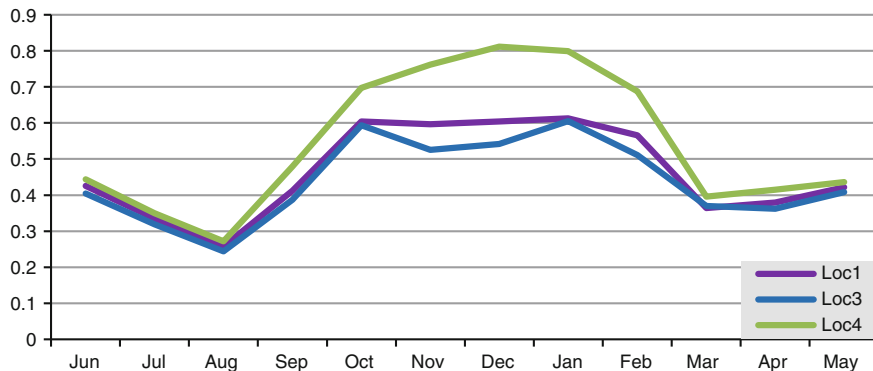


Fig. 5 Empirical data: coefficient of variance of average of daily production in each month

It is shown that within location 4 there is also some loss compared to the norm panel up to 4 %. The other locations show a higher loss percentage. For location 1 the loss goes from 6 to 25 %. Location 3 shows losses from 18 to 24 %.

In Fig. 3 the production of the three locations over the months is shown. It turns out that location 1 and 3 have practically equal production every month and location 4 has a substantially higher production every month.

The production per day shows much variation, especially when the average production per day is high, for example in the months April to August. This is shown in Fig. 4 below. If this is considered relative by dividing the variance by the average, this relative variation (coefficient of variance) is higher in the months October to February (see Fig. 5).

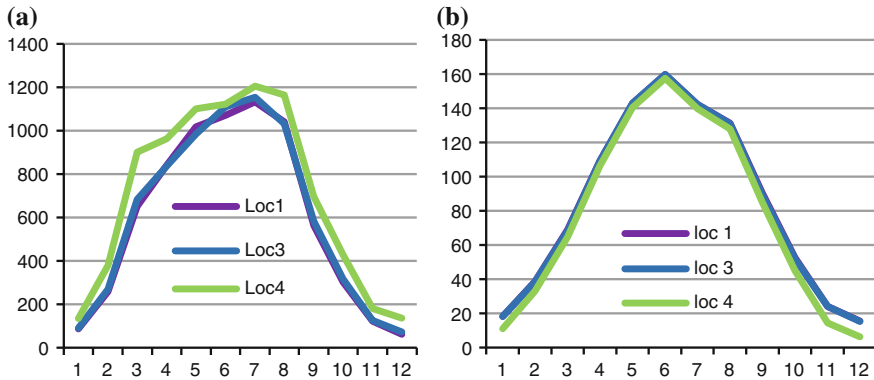


Fig. 6 **a** Monthly production: empirical data. **b** shadow effects predicted in previous paper

$$C_v = \frac{\text{standard deviation}(\sigma)}{\text{mean}(\mu)}$$

4 Comparative Analysis

In this section some of empirical data are compared to the predicted data obtained by the computational model. In Fig. 6a, the same data are depicted as in Fig. 3, but re-ordered from January to December. In this form they can be easily compared to a similar graph for the corresponding predicted data for ideal angles shown in Fig. 6b. In both figures it is clear that the production of location 1 and location 3 is equal for every month, so in that sense the empirical data confirm the predicted data. However, for location 4 in the empirical data a difference is shown with the other two locations, whereas there is almost no such difference in the predicted data in Fig. 6b. This can be easily explained, as for the predictions ideal angles were assumed, whereas in the real world case for location 4 the ideal angle of 30° occurs, but for locations 1 and 3 the angle is less ideal (more in the range of 5°–15°). Therefore in Fig. 6b the differences in irradiation due to shadow are shown and not differences due to angle, whereas in Fig. 6a the differences both due to shadow and angle are shown. It turns out that differences in production due to shadow concentrate in the months September to March, whereas differences in production due to angle differences occur through the whole year.

Note that only the month June seems to be a slight exception, as then location 3 and location 4 shows the same value. This may be an indication that in June relatively often a cloudy weather type has occurred (compared to the average weather in June over the years). For cloudy weather the diffusion radiation plays a most important role, and panels with higher angles have a disadvantage then, as they get radiation from a smaller part of the sky.

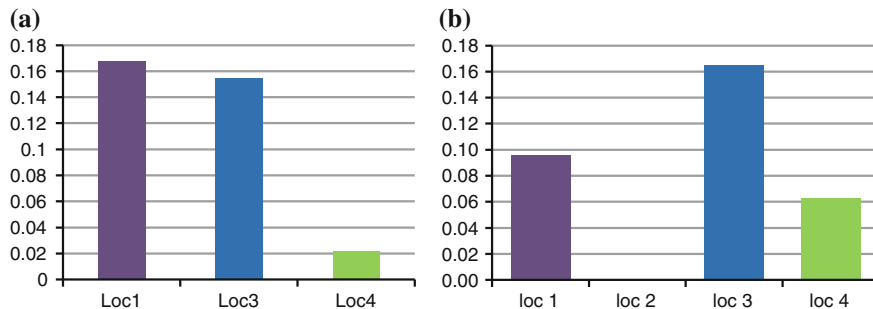


Fig. 7 Yearly loss percentages **a** empirical data, **b** predictions from previous paper

Moreover, the top in the empirical data is in July whereas the top in the predicted data is in June. This can be explained by the fact that the predicted data is based on average irradiation over the years, whereas in the real world data for only one particular year. Apparently in 2013 the month July provided relatively more irradiation than average, in comparison to June. This is in line with the suggestion above that June may have had more cloudy weather than average.

A check in the meteorological archives from the Dutch Meteorological Institute KNMI for the Netherlands at [10] confirms the explanations suggested above: in June 2013 there were 184 sun hours' versus 201 normally, which indicates 8 % lower than normal. In contrast, for July 2013 it was noted at [11] that there were 255 sun hours' versus normally 212, which is 20 % higher than normal. This indeed confirms the explanations suggested above.

Only when empirical data are collected over 10–20 years averages can be made that can be more similar to the predicted average data. Unfortunately, such empirical data are not available for the considered site.

In Fig. 7a, the loss percentages are shown per location; this is a form of abstraction of the data for loss percentages per panel depicted in Fig. 2. These loss percentages can be compared to the predicted loss percentages (assuming the realistic angles) from [4] shown in Fig. 8b. Note that the graphs are not fully comparable, as in Fig. 8b it shows the losses with respect to an ideal panel, whereas in Fig. 7a losses with respect to a real panel (which by itself is not ideal) are shown. If x would be the loss percentage of this real panel, then approximately this x should be added to the values in Fig. 7a. It is not known whether x is just 1 or 2 % or maybe more, for example 5 %. Suppose this x is 3 %. Then for location 4 the numbers are almost the same (5 % vs. 6 %), and for location 3 also (18 % vs. 17 %). For these two locations the empirical data seem to confirm the predicted ones. However, for location 1 there is a huge difference (20 % vs. 10 %). In the real world the loss percentage for this location is twice the predicted loss percentage. But there is an explanation for this. In the computational model, to determine the loss due to shadow, the relevant obstacles have to be identified and incorporated. For location 1, only the house as an obstacle was taken into account, as it was the closest

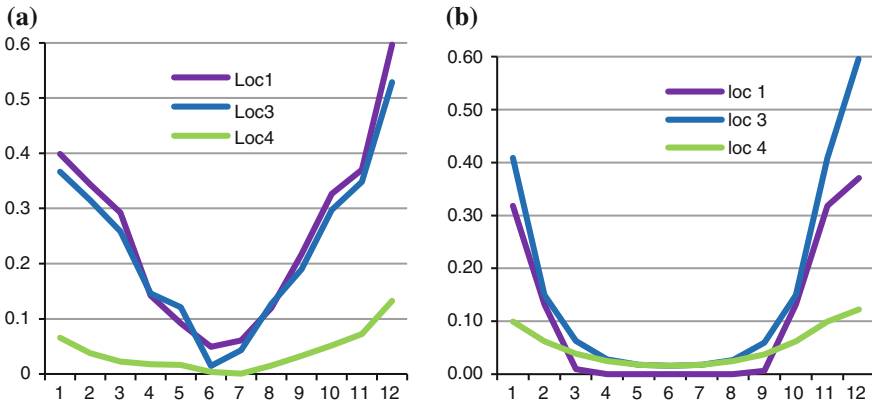


Fig. 8 Loss percentage in different months **a** empirical data, **b** predictions previous paper

obstacle. However, due to its low position various trees also provide shadow at location 1, both from the row of trees from the front side and from trees in the gardens at the backside. For the sake simplicity, these trees were left out of the calculations, and therefore their effect was just neglected. Now, with the empirical data at hand it may be concluded that this was not a justified modeling decision.

In Fig. 8a the loss percentages are shown for the different locations based on the empirical data. In Fig. 8b the predicted loss percentages are shown for these locations, assuming ideal angles. Again, it becomes clear that the effect of different angles entails differences in loss percentages in Fig. 8a for the months March to September that are not there in Fig. 8b, where the angles are assumed all ideal.

5 Discussion and Conclusion

The performance of photovoltaic solar energy production plants (e.g., [1, 2]) can be analyzed prior to their installation based on a computational model, instead of analyzing during their operation based on empirical data (e.g., [12, 13]). Some examples of approaches that can be used for prior analysis based on a simulation model and/or sensitivity analysis are [4, 7, 14].

A plant at a certain site usually is distributed over a number of locations within the site. Often such locations in a site are not always ideal, and may entail loss of efficiency, due to effects of shadow and/or to non-optimal orientations and angles for the panels. The effects of such situational circumstances vary with time of the day and day of the year. Evaluation of performance of an operational plant may be most accurate after at least 1 year, but still the weather circumstances in that year may not be representative for other years. Therefore a prior analysis based on a

computational model is a relevant approach. However, such an approach can benefit much if at least some validation is possible by comparing its results to empirical data.

In this paper the performance of solar panels according to their location and orientation was analyzed based on empirical real world performance data and compared to the data generated by the computational model introduced in [4]. These empirical data have been collected day-by-day and panel-by-panel for 1 year. The data enabled to substantiate the prior analysis. Moreover, they were used to evaluate the computational model, and based on that suggestions for improvement of this model will be discussed here.

The first suggestion for improvement of the computational model concerns the way in which the effects of shadow were modeled. The approach is based on the identification of obstacles one by one and for each of them calculation of the position and length of its shadow at all points in time. It has turned out in Sect. 4 that this is feasible for one or two obstacles. For example, this was the case for location 3 at the considered site, where two obstacles play a role, and the results of the model were not much different from the empirical data. However, when a larger number of obstacles play role, this computational approach easily leads to neglecting some of the obstacles, as each of them requires a lot of work. This was what happened for location 1 of the considered site, and as a result for this location the outcomes from the computational model were about 50 % different from the empirical data. Given this experience, the following suggestion for improvement can be considered. If only one or two obstacles are present, then the current method can be used. But in cases with more obstacles, an alternative method may work with contours of the horizon from a point in the location and compare that to the sun's orbit, such as is advocated, for example, by the Solar Pathfinder [15], or by the method described at [16]. Also this method may require quite a bit of work. Especially as it is point-based, to get accurate results it may have to be applied to different points of a location. But it still may be more feasible than considering a large number of obstacles one by one.

A second suggestion for improvement concerns the role of indirect sunlight due to diffusion. In particular on days with grey or cloudy weather this type of irradiation plays an important role. As discussed in Sect. 4, this may affect production results. For example, panels with an angle of 0° or close to it have an advantage in such circumstances as they are open for receiving irradiation of the whole sky, whereas panels with an angle of, for example, 35° are open for irradiation of only a part of the sky. In the current computational model, such circumstances were not addressed separately. It may be a suggestion to refine the model by handling such type of radiation separately.

The suggestions discussed above can be used as a basis for an improved computational model in order to enhance the quality of prior analysis of a PV system before it is actually built.

References

1. M.A. Eltawil, Z. Zhao, Grid-connected photovoltaic power systems: technical and potential problems—a review. *Renew. Sustain. Energy Rev.* **14**, 112–129 (2010)
2. B. Parida, S. Iniyani, R. Goic, A review of solar photovoltaic technologies. *Renew. Sustain. Energy Rev.* **15**, 1625–1636 (2011)
3. V.V. Tyagi, N.A. Rahim, J.A. Selvaraj, Progress in solar PV technology: research and achievement. *Renew. Sustain. Energy Rev.* **20**, 443–461 (2013)
4. J. Treur, in *Analysis of configurations for photovoltaic solar energy production using agent-based simulation*, eds. by M. Klusch, M. Thimm, M. Paprzycki. Proceedings of the Second International Workshop on Smart Energy Networks and Multi-Agent Systems, SEN-MAS'13. Lecture Notes in Artificial Intelligence, vol. 8076 (Springer, Verlag, 2013), pp. 372–385
5. URL Irradiation data, <http://re.jrc.ec.europa.eu/pvgis/apps4/pvest.php>
6. C.B. Christensen, G.M. Barker, in *Effects of Tilt and Azimuth on annual incident solar radiation for United States Locations*. Proceedings of Solar Forum 2001—Solar Energy: The Power to Choose. Washington, DC. (2001)
7. H. Ziar, H.K. Karegar, Sensitivity analysis of solar photovoltaic modules to environmental factors through new definitions and formulas. *J. Renew. Sustain. Energy* **5.5** (2013)
8. URL Renesola, <http://www.renesola.com>
9. URL Power One Aurora, <http://www.power-one.com/renewable-energy/products/solar/string-inverters/panel-products/aurora-micro/series-0>
10. URL meteorological archives for the Netherlands in June 2013, http://www.knmi.nl/klimatologie/maand_en_seizoenoverzichten/maand/jun13.html
11. URL meteorological archives for the Netherlands in July 2013, http://www.knmi.nl/klimatologie/maand_en_seizoenoverzichten/maand/jul13.html
12. V. Sharma, S.S. Chandel, Performance analysis of a 190 kWp grid interactive solar photovoltaic power plant in India. *Energy* **1–10** (2013). doi:[10.1016/j.energy.2013.03.075](https://doi.org/10.1016/j.energy.2013.03.075)
13. L.S. Pantić, T.M. Pavlović, D.D. Milosavljević, A practical field study of performances of solar modules at various positions in Serbia. *Thermal Science* **00** (2014)
14. T. Ma, H. Yang, L. Lu, Solar photovoltaic system modeling and performance prediction. *Renew. Sustain. Energy Rev.* **36**, 304–315 (2014)
15. URL Solar Pathfinder, <http://www.solarpathfinder.com>
16. URL Sun path chart program, <http://solardat.uoregon.edu/SunChartProgram.html>

Efficient Models of Partially Shaded PV Modules for Energy System Design

Lukas Exel, Felix Felgner and Georg Frey

Abstract To simulate the power output of a photovoltaic module (PM) under partial shading conditions each cell has to be simulated individually. The following contribution will present a method how the simulation effort can be reduced with little or even no loss in simulation accuracy under typical shading conditions. This reduction is required if the PM is part of a heterogeneous distributed energy system which shall be efficiently analyzed on system level. The core idea is a *grouping model* approach which maps each strand of a PM on only three, two or one *grouping cell(s)* whose respective parameters are scaled by a factor. These parameters, as well as the irradiation values given to the individual grouping cells (s), are determined dynamically by a pure algebraic clustering algorithm during simulation runtime. The proposed method is implemented and demonstrated in Modelica/Dymola.

1 Introduction

The power output of a photovoltaic module PM plant depends on the characteristics of the individual solar cells, their total surface area, the solar irradiance, and the maximum peak point (MPP) tracking algorithm. If the individual cells of a PM are subject to non-uniform irradiation due to partial shading effects, the electric panel layout strongly affects the power output. As a consequence, to determine the correct output power of a PM, each cell has to be simulated individually, based on appropriate models like the single-diode model. These models describe the

L. Exel (✉) · F. Felgner · G. Frey
Saarland University, 66123 Saarbrücken, Germany
e-mail: lukas.exel@aut.uni-saarland.de

F. Felgner
e-mail: felix.felgner@aut.uni-saarland.de

G. Frey
e-mail: georg.frey@aut.uni-saarland.de

non-linear voltage-current characteristic in an implicit form. Therefore, the model of a typical PM with 60 cells ends up in a system with 60 non-linear equations. Although there exist proper solvers, the computation is expensive and too time-consuming to use such models for long-term simulations. The contribution investigates how the simulation effort can be reduced with little loss in simulation accuracy. Based on the behavior of one PV cell, Sect. 2 derives the mathematical model of an entire PM. Then, we introduce the algorithm used in the presented grouping model. Section 3 presents simulation results and investigates the accuracy, and the speed-up of the proposed model. A conclusion is drawn in Sect. 4.

2 Efficient Complexity Reduction by Clustering Algorithm

At first, we consider a series connection of K cells. The behavior of the k -th cell can be described by a set of equations, which are known as single-diode model [3, 4]:

$$i_k = I_k^{Ph} - I_k^D \left(e^{\frac{u_k + i_k R_S}{nU_k^T}} + e^{\frac{-u_k + U_{Br}}{nBU_k^T}} - 1 \right) - \frac{u_k + i_k R_S}{R_{Sh}}, \quad (1)$$

$$I_k^{Ph} = f_{I,Ph}(G_k, T_k), \quad I_k^D = f_{I,D}(G_k, T_k), \quad U_k^T = f_{U,T}(T_k), \quad k = 1, \dots, K \quad (2)$$

For the voltage across the series connection and the current, it holds:

$$u_{sc} = \sum_{k=1}^K u_k, \quad i_{sc} = i_1 = i_2 = i_3 = \dots = i_K. \quad (3)$$

with

- i output current of solar cell
- u voltage across solar cell
- R_{Sh} shunt resistance
- n ideality factor
- B scaling factor
- T temperature
- i_{sc} current of series connection
- I^{Ph} photogenerated current
- R_s series resistance of cell model
- U^T thermal voltage
- U_{Br} breakdown voltage
- G Irradiation
- u_{sc} voltage across series connection

Now, we assume that those K cells have the same temperature and are subject to identical irradiation values, i.e. $G_k = : G$ ($k = 1, \dots, K$), it holds $u_{sc} = K u_k$. Inserted in (1), the characteristic curve of a series connection with K cells can be described by:

$$i_{sc} = I^{Ph} - I^D \left(e^{\frac{u_{sc} + K \cdot i_{sc} R_S}{K \cdot n \cdot U_j^T}} + e^{\frac{-u_{sc} + K \cdot U_{Br}}{K \cdot n \cdot B \cdot U_j^T}} - 1 \right) - \frac{u_{sc} + K \cdot i_{sc} R_S}{K \cdot R_{Sh}}, \quad (4)$$

Based on the voltage-current characteristic curve of one cell, the scaling factor K stretches the curve along the voltage axis. Equation (4) is often used to model entire PV modules with less simulation effort. However, under many operating conditions of PV modules, this model is not appropriate. Under typical shading condition as shown in Fig. 1, there exist two or more groups of cells in the same strand whose cells are irradiated with different values than the cells of the other group(s). For this reason, we finally consider a strand of S series-connected cells which belong to M differently irradiated groups. In order to describe the behavior of the j -th group, containing K_j identical cells with irradiation G_j , we just have to include the group index j (with $j = 1, \dots, M$) in (4):

$$i_{sc,j} = I_j^{Ph} - I_j^D \left(e^{\frac{u_{sc,j} + K_j \cdot i_{sc,j} R_S}{K_j \cdot n \cdot U_j^T}} + e^{\frac{-u_{sc,j} + K_j \cdot U_{Br}}{K_j \cdot n \cdot B \cdot U_j^T}} - 1 \right) - \frac{u_{sc,j} + K_j \cdot i_{sc,j} R_S}{K_j \cdot R_{Sh}}. \quad (5)$$

Then, the voltage u_m and the current i_m of the entire strand are given as:

$$u_m = \sum_{j=1}^M u_{sc,j}, \quad i_m = i_{sc,1} = \dots = i_{sc,M}, \quad S = K_1 + \dots + K_M. \quad (6)$$

In the following, we elaborate the “*N-Cell Model*”; it is a grouping model where $N < M$ groups approximate a strand which actually contains M differently irradiated groups (e.g., “Shading Condition III” given in Fig. 1 is modeled by a 2-Cell Model). As a consequence, we need a “clustering algorithm” that shall map K irradiation and temperature values onto N values and define a scaling factor K_x for each group:



Fig. 1 Typical partial shading conditions for solar module. The numbers indicate the irradiation value of each cell

$$\mathbf{G} = (G_1, \dots, G_S) \xrightarrow{\text{cluster algo.}} \mathbf{G}^* = (G_1^*, \dots, G_N^*) \quad (7)$$

$$\mathbf{T} = (T_1, \dots, T_S) ; \xrightarrow{\text{cluster algo.}} \mathbf{T}^* = (T_1^*, \dots, T_N^*) \quad (8)$$

$$(\mathbf{G}, \mathbf{T}) ; \xrightarrow{\text{cluster algo.}} \mathbf{K} = (K_1, \dots, K_N) \quad (9)$$

The cluster algorithm is motivated by the fact that the characteristic curve of series-connected PV-cells is dominated by the characteristic curve of the lowest irradiated cell. Consequently, these cells should be modeled exactly, whereas the cells with the highest, but differing, values can be grouped and modeled less accurately. The following MATLAB-like pseudo-code is valid if $0 < N \leq M \leq S$. For better readability, we focus on the clustering of the irradiation:

```

Input: G, N, Output: G*,K
G_sort           = sort(G);
G_sort_unique   = unique(G_sort);
K_sum           = 0;
for (n=1:N-1) {
    G_star(n)=G_sort_unique(n);
    K(n)=count(G==G_star(n));
    K_sum=K_sum+K(n);
}
G_star(N) = mean(G_sort((K_sum+1):end));
K(N)= count(G)-K_sum;
//sort irradiation values
//build unique set
//determine K four group n
//calculate G for last group

```

In the later used implementation, the frequently occurring case $N < M$ is treated by splitting the groups into multiple groups with identical irradiation values.

3 Implementation and Simulation Results

The PV grouping model is implemented in the open modeling language Modelica [1]. The used modeling language allows straight-forward modeling by means of the equations given in Sect. 2. The clustering algorithm is implemented in C/C++ and is included into the model. An overview to the simulation model is given in Fig. 2. Following the component oriented and acausal modeling concept of Modelica, the mathematical description as well as the clustering algorithm is encapsulated in a component whose interface represents the electrical connection. This interface (electrical pin) is inherited from the Modelica standard library [2] and is defined by a flow variable (current) and a potential variable (voltage). Consequently, the model can be connected to any other model that uses this interface—for example the current sensor and voltage source, which are shown in Fig. 2. The base model (Model of K-Cell) of all PV-models is also indicated in Fig. 2 by its graphical

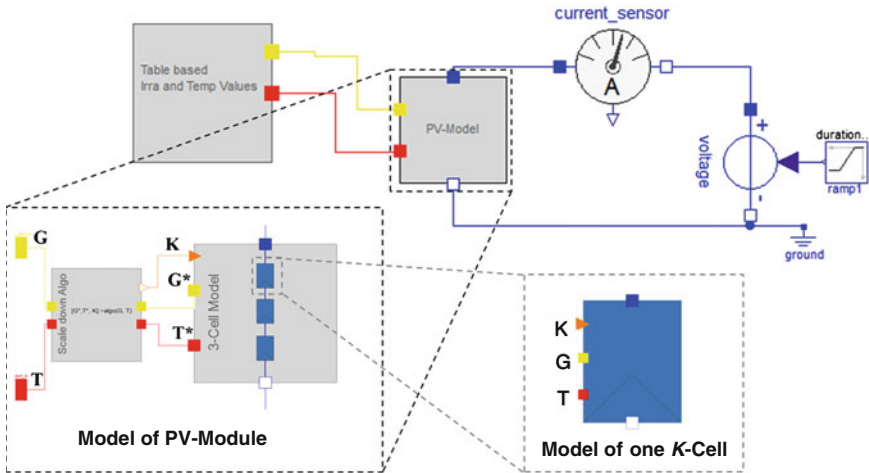


Fig. 2 Top-level diagram of the simulation model in Dymola. The mathematical model as well as the clustering algorithm is encapsulated in the component “PV-Model”. Following the acausal modeling concept of Modelica, the model can be connected to any other electrical components via the electrical pins

Irradiation G in W/m^2 on each individual cell

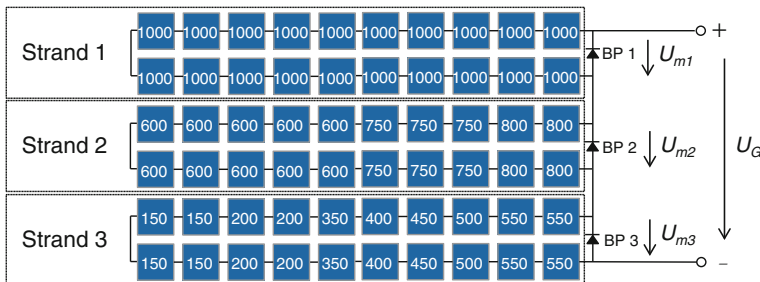


Fig. 3 Electrical design of the PV module used in the test case. The number inside each cell indicates the used irradiation in W/m^2

representation. It implements (4) and the functions indicated in (2) to calculate I^{P_h} , I^P and U^T from the given temperature and irradiation values and several cell parameters that are extracted from the PM data sheet and are deposited in the model [3]. The scaling factor K is an additional input.

To assess the accuracy of the proposed model and the expected speed-up of the simulation, we set up the following test case: The voltage-current characteristic of a whole PV module (all parameters are extracted from [5]) under the irradiation conditions given in Fig. 3 is simulated by an exact model (wherein each cell is modeled individually) and subsequently compared with the proposed 3-, 2- and

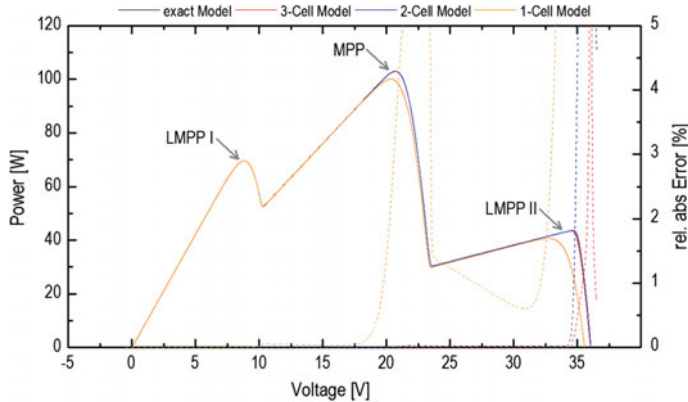


Fig. 4 Simulated voltage-power curve for the conditions shown in Fig. 3. The rel. abs. error $e = (|P_{exactModel}(u) - P_{NCellModel}(u)|)/P_{exactModel}(u)$ is shown on the right scale (dotted curves). The curve of the exact model (black) is widely hidden under the curve of the 3-Cell Model

Table 1 Simulation error at local maximum peak points (LMPP) and global maximum peak point (MPP) for the different models $e_{MPP} = (MPP_{NCellModel} - MPP_{exactModel})/MPP_{exactModel}$

	Exact model	3-Cell Model		2-Cell Model		1-Cell Model	
	(W)	(W)	Error (%)	(W)	Error (%)	(W)	Error (%)
LMPP I	69.59	69.59	0.00	69.59	0.00	69.59	0.00
MPP	102.96	102.96	0.00	102.97	0.01	100.08	-2.80
LMPP II	43.52	43.53	0.03	43.66	0.32	40.63	-6.64

1-Cell Model. It has to be considered, that the electrical design of the PV module includes three bypass-diode bridges, each of them connected in parallel to one strand to improve the efficiency of the modules under partial shading conditions. Thereupon, we apply the proposed grouping model to each strand individually.

The simulation result of the test case is given in Fig. 4. It shows that all models correctly represent the basic form of the voltage-current characteristic. It is conspicuous that the range up to ~ 10 V (LMPP I) is simulated exactly by all models, whereas the range up to ~ 22 V (MPP) is only simulated correctly by the 3-Cell Model. In the range ~ 22 V (LMPP II), there is a small difference between the exact model and 3-Cell Model (cf. dotted curves Fig. 4). Table 1 shows the simulation errors at the local and global peak points. In contrast to the dotted curves in (Fig. 4), Table 1 shows the more relevant errors between the global and local maximum peak points. The finding, that the models are correct in a specific range and incorrect in other ranges can be explained by the electric design of the PV module: For negative voltage values u_m , the characteristic voltage current curve of each strand is dominated by the diode bridge. This is the case for strand 2 and 3 at the given irradiation

Table 2 Overview to the speed-up of the simulation. The number of steps relates to the number of (power, voltage) value pairs determined by the simulation. All test runs were done on a standard PC (i5-3320 m, 8 GB Ram, Dymola 2015)

Simulation model	Number of equations	50,000 steps		5,000 steps		500 steps	
		CPU-time (s)	Reduction (%)	CPU-time (s)	Reduction (%)	CPU-time (s)	Reduction (%)
Exact	60	49.23	—	3.90	—	0.844	—
3-Cell Model	9	2.22	95.48	0.27	93.00	0.047	94.47
2-Cell Model	6	1.61	96.73	0.19	95.25	0.025	97.08
1-Cell Model	3	1.01	97.95	0.12	96.81	0.015	98.22

conditions in the range up to ~ 10 V. Consequently, the inexact modeling of the cells of these two strands does not affect the correctness of the overall characteristic of the module in this range, where it is dominated by the behavior of strand 1 that can be exactly captured by a 1-Cell Model due to equal irradiation values.

The speed-up of the simulation is shown in Table 2. All together, the computation time can be reduced by more than ~ 93 % (3-Cell Model) or even ~ 95 % (2-Cell Model) without much loss in accuracy.

4 Conclusion

The presented *grouping model* can reduce the simulation time by ca. 95 % compared with an exact model. In a realistic example, the accuracy loss w.r.t. the LMPP/MPP in the voltage-power characteristics could be kept below 0.4 % (2- and 3-Cell Model), which we consider accurate enough for model-based energy system design.

References

1. Website of the Modelica Association, <http://www.modelica.org>
2. Modelica standard library, <http://modelica.github.io/Modelica/>
3. T. Esram, Modeling and control of an alternating-current photovoltaic module. Ph.D. Thesis. <https://www.ideals.illinois.edu/handle/2142/15501>. Accessed 10 Oct 2014
4. V. Quaschning, *Simulation der Abschattungsverluste bei solarelektrischen Systemen* (Verlag Dr. Köster, Berlin, 1996)
5. Datasheet of Sunmodule SW 240 poly. http://www.solarworld.de/fileadmin/downloads_new/produkt/sunmodule/datenblaetter/de/poly/poly_240-250_de.pdf. Accessed 10 Oct 2014

Part XXI

**Hydrogen Production and Fuel
Generation from Renewables (Catalysis)**

Modelling and the Analysis of the Power Supply System for the Generator of Hydrogen

Krzysztof Górecki, Janusz Zarębski, Paweł Górecki
and Sławomir Halbryt

Abstract In the paper the manner of characterising properties of the generator of hydrogen and the form of the computer model of this generator are presented. The model was formulated in the form of a subcircuit for SPICE software. The structure of this model is described and the values of parameters of the model are presented. With the use of the proposed model some dc and frequency characteristics of the considered generator are calculated and compared to the measured characteristics. Some results of analyses of the considered generator operating in different supply conditions are presented and discussed.

1 Introduction

Hydrogen belongs to more and more commonly used ecological sources of energy, and its great advantage is the fact that the product of combustion is only aqueous vapour [1]. A popular method of producing hydrogen is hydrolysis, which demands the appropriate amount of electrical energy [2]. In the classical case, one uses, accordingly, dc power supplies. However, a disadvantage of this solution is an increase, sometimes considerable, in the device temperature as a result of exothermic character of the process of water electrolysis [2]. The dissipation of this heat lowers the watt-hour efficiency of the process. This efficiency can be increased by optimizing parameters of the output signal of the power supply.

As it results from the classical theory of electrolysis, the mass of hydrogen produced during the electrolysis is proportional to the charge Q transfluent through the electrolyte [3]. As it is stated in the paper [2], impedance Z of the generator of hydrogen shows resonance. Therefore, one can expect that at a certain frequency

K. Górecki (✉) · J. Zarębski · P. Górecki

Department of Marine Electronics, Gdynia Maritime University, Gdynia, Poland
e-mail: k.gorecki@we.am.gdynia.pl

S. Halbryt
SESCOM S.A, Gdańsk, Poland

the greatest watt-hour efficiency of the process of the production of hydrogen η appears. This efficiency is equal to the quotient of masses of the produced hydrogen m and the energy received from the power source. In order to find the optimum conditions of the power supply of the hydrogen generator the computer model of this device is indispensable.

In the paper the manner of characterising properties of the generator of hydrogen and the form of the computer model of this generator are presented. The model was formulated in the form of a subcircuit for SPICE software.

Using the worked out model, computer simulations illustrating the influence of parameters values of the control signal of this generator on the efficiency of hydrogen production at different values of volume and concentration of the electrolyte are performed.

2 Structure of the Model of the Hydrogen Generator

The network structure of the model of the hydrogen generator is shown in Fig. 1. It was worked out using the method proposed in [4, 5], on the basis of the measured dc current-voltage and frequency characteristics of the considered generator of hydrogen.

The considered model contains of two diodes D1 and D2, which together with resistors R1, RL11, R2, RL21 shape dc characteristics of the modeled device. Remaining reactance elements decide about the course of frequency characteristics. Values of the model parameters depend on concentrations of liquor situated in the hydrogen generator. It is proper to underline that parameters values of elements situated in both branches of the model are identical. The difference between these branches is directions of the diodes D1 and D2. The values of parameters of the model are estimated with the use of the original measuring-set and the authors' estimation procedure.

Parameters values of the model of the hydrogen generator containing the aqueous liquor KOH of high concentration and of low concentration are estimated. The parameters values of the model corresponding to low concentration of liquid

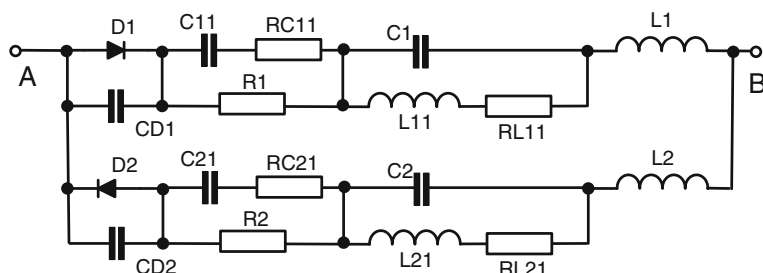


Fig. 1 Network representation of the hydrogen generator

Table 1 Parameters values of the model at low concentration of liquid

Parameter	ISR (mA)	NR	IS (μ A)	N	CD1 (mF)	C11 (mF)
Value	2.5	16	1.5	8	150	15
Parameter	RC11 (m Ω)	R1 (m Ω)	C1 (mF)	L11 (μ H)	RL11 (m Ω)	L1 (μ H)
Value	170	170	50	50	170	7

Table 2 Parameters values of the model at high concentration of liquid

Parameter	ISR (mA)	NR	IS (μ A)	N	CD1 (F)	C11 (μ F)
Value	2	13	1	6.5	2	30
Parameter	RC11 (m Ω)	R1 (m Ω)	C1 (mF)	L11 (mH)	RL11 (m Ω)	L1 (μ H)
Value	50	75	250	1	50	8

are collected in Table 1, whereas the values of these parameters for high concentration of liquid are collected in Table 2.

As one can notice, the change of the value of concentration of liquid causes essential changes in the parameters values of the considered model.

3 Verification of the Model

In order to verify the correctness of the presented model of the generator, measurements and calculations of its dc and frequency characteristics were performed. In all the figures in this section points mark the results of measurements, and lines —the results of calculations.

In Fig. 2 dc characteristics of the examined hydrogen generator obtained for different concentrations and volumes of the electrolyte are shown. As it is visible, the good agreement between the calculated and measured dc characteristics is observed. The obtained characteristics show symmetry in relation to the coordinate origin. It is worth noticing that a decrease in concentration of the electrolyte causes an increase in the series resistance of the liquid, appearing with the voltage rise on the liquid at the fixed value of the current of the power supply. It is also visible that the change of the volume of liquid does not cause visible changes in the course of dc characteristics of the examined generator (curves obtained for different volumes of liquid are covered).

Figures 3 and 4 present the calculated and measured dependences of the module and the phase of impedance of the considered hydrogen generator containing KOH liquid of both the considered concentrations, obtained at the offset voltage $U_{DC} = 1.45$ V. In the presented characteristics one can notice that series resonance is observed at the frequency in the range from 100 Hz to 1 kHz. The value of the resonance frequency weakly depends on the offset voltage of the signal supplying

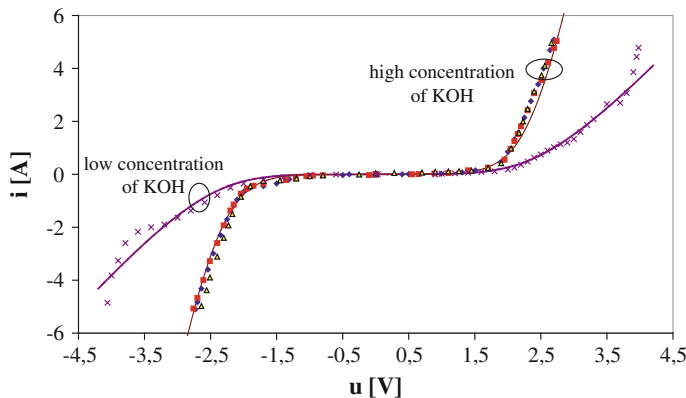


Fig. 2 Calculated and measured dc characteristics of the hydrogen generator

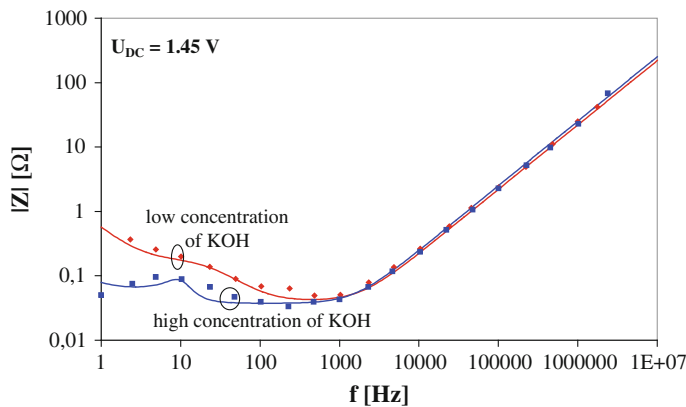


Fig. 3 Calculated and measured dependences of the impedance module of the hydrogen generator on frequency

this generator. The dependence of the impedance module on the frequency within the range of low frequencies is almost flat. The minimum-value of this module amounts to about 40 mΩ.

4 Results of Analyses

Using the worked out and experimentally verified model of the hydrogen generator the transient analyses of the considered generator at the excitation by the trapezoidal voltage of fixed voltage levels equal to 0 and 5 V, respectively, with rise and fall times equal to 0.5 μ s and the duty factor equal to 0.5, are performed. The value of frequency was changed within the range from 10 Hz to 100 kHz.

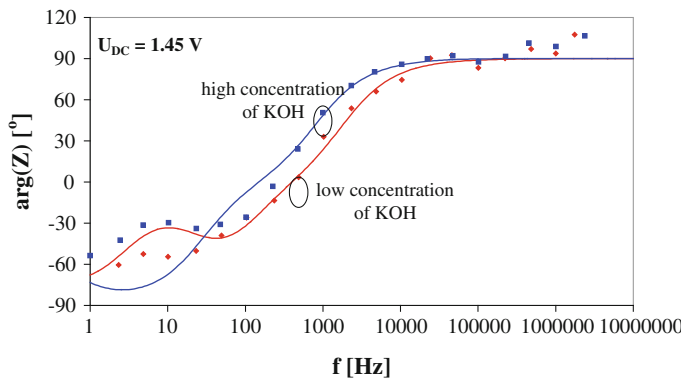


Fig. 4 Calculated and measured dependences of the impedance phase of the hydrogen generator on frequency

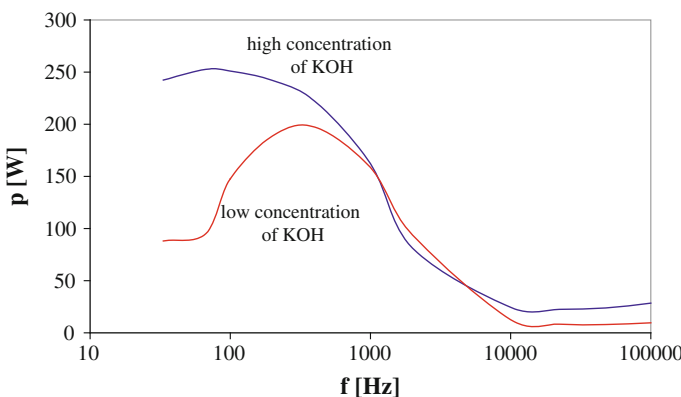


Fig. 5 Calculated dependence of the average value of the power supplying the hydrogen generator on frequency

Due to the shape of the exciting signal and mainly the inductive character of the generator impedance, the waveforms of the current, which have positive and negative actual values, were obtained. Such a shape of the current waveform causes that on both the electrodes alternately oxygen and hydrogen is emitted. If these gases are burnt just after their producing, it is not dangerous for the user.

In order to delimit the mass of the produced hydrogen (on both the electrodes of the generator) the value of the charge introduced to the liquid of KOH is indispensable. This value is equal to the integral of the module of the current flowing through the generator. Therefore, the average increase of the hydrogen mass in the time unit is proportional to the mean value of the current module.

Figures 5 and 6 show the properly calculated dependences of the mean value of the power given by the power supply and the quotient of the mean value of the

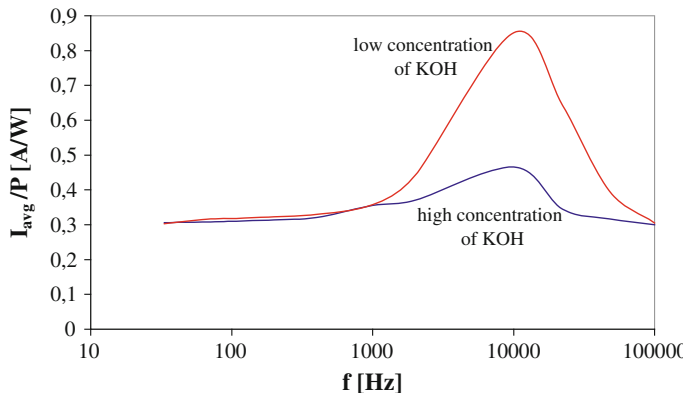


Fig. 6 Calculated dependence of the quotient of the average value of the current of the hydrogen generator and the power supplying this generator on frequency

current flowing through the liquid and the power from the power supply (at which the quotient is proportional to the efficiency of the hydrogen generation) on frequency of the feeding signal.

As one can notice, the dependence $P(f)$ at both the considered concentrations of KOH has the maximum at the frequency in the range from 100 to 1000 Hz. Higher average values of the current module and the power can be observed at higher concentrations of KOH. The similar shape can be found in the dependence $I_{avg}(f)$, however the watt-hour efficiency of the process of hydrogen production is the highest at frequency equal to about 10 kHz. Of course, due to the big value of the impedance module of the liquid at this frequency, obtaining the desirable efficiency of the process of hydrogen generation demands using the high value of the amplitude of the supplying voltage.

5 Conclusions

In the paper the form of the model of the hydrogen generator for SPICE software is proposed and the sets of the parameters values of this model for two values of concentrations of KOH liquid included in this generator are given. Thanks to the comparison of the calculated and measured dc and frequency characteristics of the examined generator, high reliability of the worked out model is shown.

Results of the transient analysis of the considered generator supplied from the voltage source with the rectangular pulses train showed that the supply current accepts positive and negative actual values, and the highest watt-hour efficiency of the process of the hydrogen production is reached at frequency of the supply voltage equal to about 10 kHz.

Acknowledgments This project is financed from the funds of SESCOM S.A.

References

1. M.H. Rashid, *Power Electronic Handbook* (Academic Press, Elsevier, 2007)
2. K. Mazloomi, N. Sulaiman, S.A. Ahmad, N.A. Yunus, Analysis of the frequency response of a water electrolysis cell. *Int. J. Electrochem. Sci.* **8**, 3731–3739 (2013)
3. K. Mazloomi, N. Sulaiman, H. Moayedi, An Investigation into the electrical impedance of water electrolysis cells—with a view to saving energy. *Int. J. Electrochem. Sci.* **7**, 3466–3481 (2012)
4. K. Górecki, The electrothermal macromodel of switching voltage regulators from L4970 family. *Int. J. Numer. Model. Electron. Networks Dev. Fields* **21**(6), 455–473 (2008)
5. K. Górecki, J. Zarebski, SPICE-aided modeling of monolithic PWM switched voltage regulators including the bipolar output stage with selfheating taken into account. *Przegląd Elektrotechniczny* **85**(10), 83–90 (2009)

Conductometric Titration to Analyze Nafion® 117 Conductivity

María José Lavorante and Juan Isidro Franco

Abstract Nafion® membrane presents good chemical, thermal and mechanical stability and excellent protonic conductivity when the material is previously well-hydrated. This type of perfluorosulphonic acid membrane is widely used in a great variety of devices, being mainly applied in the field of renewable energy, for fuel cell and electrolyzers of polymeric electrolytes. Focusing on electrolyzers, it is well known that nowadays, they represent the most promising method for the production of hydrogen, being a well-established, robust and easy to use technology. Using Nafion® membrane in alkaline water electrolyzers as a separator, the aim of this study is to analyze its behaviour under alkaline conditions. Samples of Nafion® 117 membranes in their original state and samples submitted to a previous cleaning treatment and specific hydration treatment were used. This hydration treatment assured an amount of molecules of water per sulphonic acid group ($\lambda = 17-20$). The ionic exchange rate between the hydrogen ion of the sulphonic group of Nafion® membrane and the sodium and potassium cations present in the alkaline solution were studied. The chemical kinetics of the reaction was determined with the purpose of establishing the time to carry out conductometric titration of the membrane using sodium and potassium hydroxide as titrants. Results show that the exchange rate of the alkaline ions, in the solution, present a first order kinetics reaction, at the concentration of hydroxide ions in that solution.

Keywords Nafion® 117 · Conductivity of aqueous solutions · Conductometric titration

M.J. Lavorante (✉) · J.I. Franco

Departamento de Investigación y Desarrollo de Energías Renovables (CITEDEF-EST),
San Juan Bautista de La Salle 4397, B1603ALO Provincia de Buenos Aires, Argentina
e-mail: mjlavorante@gmail.com

1 Introduction

Hydrogen supply is one of the issues that will make hydrogen economy possible. Among all known industrial methods of hydrogen production, water electrolysis is the least used, representing only 4 % of the annual production [1]. Nevertheless, this method can be widely spread to satisfy hydrogen and oxygen demand from different types of users through individual units, forming part of energy systems, at fuelling stations or in industrial applications [2]. So it can be said that there are a lot of commercial electrolyzers that can provide a wide range of hydrogen production that goes from a few $\text{N cm}^3 \text{ min}^{-1}$ to thousand of $\text{N m}^3 \text{ h}^{-1}$ [3]. Nowadays, electrolysis is the most expensive method known because of its high consumption of electricity (near 4.5–5 kWh/m 3 H₂) [4, 5]. But in the near future the cost of fossil fuels will go up and the capital cost of the electrolyzers will go down due to the increasing demand and manufacture.

The main problem in electrolysis is the high amount of energy that the devices require to start the process and besides the type of energy sources to make that possible. The objective is to make the equipment work with the excess of energy provided by wind turbines, solar cells or the electrical grid when energy demand is relatively low (during night time) [6]. If a renewable energy source is used, the electrolysis process can be more attractive for hydrogen production. The technological challenge is to make electrolyzers work intermittently as renewable sources of energy are available [7].

During the latest years, alkaline water electrolyzers have become more attractive as energy transformers because, apart from being a well known, simple and robust technology, they are less expensive than the polymeric electrolyte membrane (PEM) or solid oxide electrolyzers [8]. In the particular case of PEM electrolyzers, their cost is influenced by the use of electrocatalyzers based on noble metals such as platinum (Pt), iridium (Ir) and ruthenium (Ru), the current collectors, the use of specific materials for their manufacture such as titanium (Ti), the membranes and the high requirement of water purity [9]. The first three are necessary for the medium acidity, which is equivalent to a 10 wt% sulphuric acid (H₂SO₄) solution pH [10].

Having in mind a more efficient alkaline water electrolysis method, we focused on working on diaphragms and in particular on Nafion® membranes. Nafion® is a copolymer of tetrafluoroethylene and monomers such as perfluoro-3,6-dioxa-4-methyl-7-octene sulphonic acid, prepared by du Pont. Due to its exceptional properties (thermal stability, oxidative and hydrolytic resistance), it is ideal to be used in water electrolyzers. In alkaline solutions the sulphonic acid groups of the membrane are neutralized. This has an effect on its physical properties such as: glass transition temperature, thermal stability and tensile strength. The glass transition temperature increases from 110 to 220 °C, and the increase in the other two properties is highly marked. This allows to work with the membrane in conditions where the temperature can be over 250 °C [10].

The system under study consists of a piece of Nafion® 117 membrane (solid) immersed in distilled water and an aqueous solution. The contact with each other (membrane-aqueous solution) allows the ion exchange until equilibrium is reached. In the particular case of a system formed by an acid Nafion® membrane to which an alkaline solution is added (MOH where M could be sodium (Na^+) and potassium (K^+) cations, the counter ions in the sulphonic groups will be exchanged by the cations of the alkaline solution. This is followed by the medium neutralization. Therefore, the electric mobility (349.8 and 198.6 $\text{cm}^2/\Omega \text{ mol}$ at 25 °C, respectively), will generate a change in the solution conductivity, which, in turn, will be detected measuring its conductivity. The electric mobility of those ions stand out if they are compared with alkali metals ions like sodium and potassium (50.1 and 73.5 $\text{cm}^2/\Omega \text{ mol}$, at 25 °C, respectively).

The reaction under study is: $\text{RSO}_3\text{H} + \text{MOH} \rightarrow \text{RSO}_3\text{M} + \text{H}_2\text{O}$, where R is the copolymer matrix and M the same as above.

At its initial state, conductivity is high because of the electric mobility of the hydroxide ions. As the neutralization reaction occurs, conductivity gradually decreases until it disappears (when the reaction is complete). For that reason the conductometric titration is chosen as an appropriate method to study the behaviour of Nafion® 117 membrane in alkaline solutions to be used in alkaline water electrolyzers at high temperature.

In this research the conductivity of a system consisting of Nafion® 117 in distilled water with the addition of an amount of sodium and potassium hydroxide is studied by conductometric titration.

2 Experimental

In this research work, two types of samples were used: pieces of Nafion® 117 membrane in their original state and pieces of Nafion® 117 to which previous treatment of cleaning and conditioning were applied. The size selected for the pieces was $15 \times 40 \times 15 \times 40$ mm approximately. The cleaning treatment consists of taking advantages of the oxidant power of hydrogen peroxide (H_2O_2) in order to eliminate any kind of pollutant that may be blocking the specific points where ionic exchange occurs. For this purpose, each piece was dipped into an H_2O_2 3 % solution, just below boiling point during 45 min or until the membrane loses its brownish colour or becomes completely colourless and transparent. Then, the sample is rinsed in distilled water with the purpose of eliminating the excess of hydrogen peroxide and the oxydated pollutant. The conditioning treatment is composed of three steps. The first implies dipping the piece in a solution of H_2SO_4 0.25 M just below boiling point during 3 h in order to transform all the available points to their protonic form. As a second step, once this time has elapsed, the piece is taken out and rinsed in distilled water to eliminate the excess of acid. Finally, the piece is dipped in distilled water just below boiling point for 3 h, after which the piece is stored in distilled water until needed for the experiment [11].

The device used to perform the conductometric titrations consists of a Pyrex beaker where the sample is placed, the stirrer and 70 mL of distilled water. The beaker is dipped into a big water container, thermically insulated, which works as a thermostat regulating temperature in ± 0.1 °C. This equipment was installed on top of a magnetic stirrer (Decalab S.R.L.; 2000 rpm; 280 °C) with the purpose of gently stirring the system under study (membrane and aqueous solution). The bench conductivity meter was Eutech Instrument Pte. Ltd/Oakton Instrument CON 510. The meter was packaged with a two ring stainless steel Ultem-Body Conductivity/TDS electrode (cell constant $K = 1.0$) with built in temperature sensor for automatic temperature compensation (ATC) and an integral electrode holder. The solutions of sodium and potassium hydroxide used in the experience were dispensed into a Pirex beaker through a burette (IVA, certificate number A-03819, serial number 005-02-08, tolerance ± 0.05 mL, uncertainty ± 0.03 mL, $K = 2$).

The first experiences carried out were aimed at determining reaction rate to exchange all the counter ions of the membrane. In order to accomplish this objective, it was necessary to find the amount of alkaline solution needed to neutralize the acid membrane. The equation used is $DWC = (T^*M)/W$, where DWC is the dry weight capacity, T is the amount of titre, M is the concentration of the alkaline solution and W is the weight dry resin. Dry weight capacity, which is the total number of equivalents of exchangeable ions in a stated form, per dry kilogram of the resin, representing an intrinsic characteristic of the resin as it is manufactured. Clearing T from the previous equation the volume of alkaline solution is obtained.

3 Discussion and Results

To perform conductometric titration of the systems, it is necessary to know the rate of neutralization reaction. For that purpose the conductivity of the solution where Nafion®117 membrane is immersed is measured by the minute during 120 min. The systems under study are 4: two of them with samples of Nafion® in its original state (Mos) and the other two with a cleaning and conditioning treatment (Mt). The measurements are made after adding a specific amount of a NaOH and KOH solution. The membranes which received a cleaning and conditioning treatment have a content of approximately 18 molecules of water per sulphonic group ($\lambda \approx 18$). Figure 1 shows the results obtained in those experiences.

Figure 1 shows that the rate of reaction is faster in the systems with the addition of KOH than in the ones with NaOH. Those preliminary results show that the conductivity of the solution of the systems with addition of KOH are higher. Referring to the experimental results obtained, the conductivity of the systems with the membrane in its original state have higher conductivity than the systems with the membrane with cleaning and conditioning treatment, but to confirm the results the experiences have to be made at the same temperature, to verify the results. It is important to remember that the mobility of the majority of the ions increases in approximately 2 % for each higher degree of temperature.

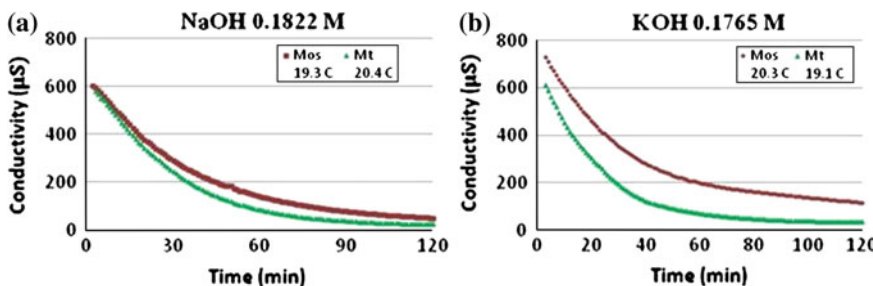
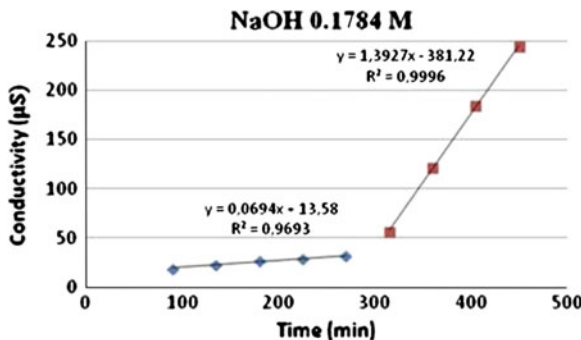


Fig. 1 Graphic representation of the conductivity of the solution of the system as a function of time: **a** Mos and Mt with the addition of NaOH solution and; **b** Mos and Mt with the addition of KOH solution

Fig. 2 Conductometric titration with the addition of equal volumes of NaOH every 45 min



The first conductometric titration is done with a sample of Nafion® 117 which has the cleaning and conditioning treatment ($\lambda = 19$) adding 0.2 mL of 0.1784 M NaOH solution every 45 min. The purpose of doing that is that the results are not influenced by the rate of neutralization reaction. Figure 2 shows the results obtained in the conductometric titration (time has a direct relation with the amount of mL added, for example 45 min equals 0.2 mL).

The first straight line represents the exchange of protons for the sodium cations. The conductivity is maintained low during that period of time, because the neutralization reaction is developing and the formation of water is taking place. Once the equivalent point is reached (when the neutralization reaction is complete) the conductivity increases fast by the further addition of alkaline solution (second straight line) because of the great mobility that the hydroxide ions have.

The graphic representation of the natural logarithm of the conductivity values obtained for the previously 4 analyzed systems shows that the neutralization reaction of Nafion® membranes presents a first-order (Fig. 3).

Linear equations allow to calculate the value of the slope which is the constant rate or the specific reaction rate of the systems under study.

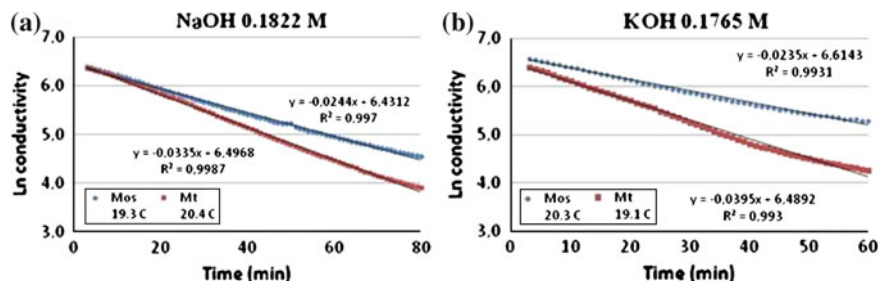


Fig. 3 Graphic representation of the linear plot for the 4 systems under study: **a** with the addition of NaOH solution and **b** with the addition of KOH solution

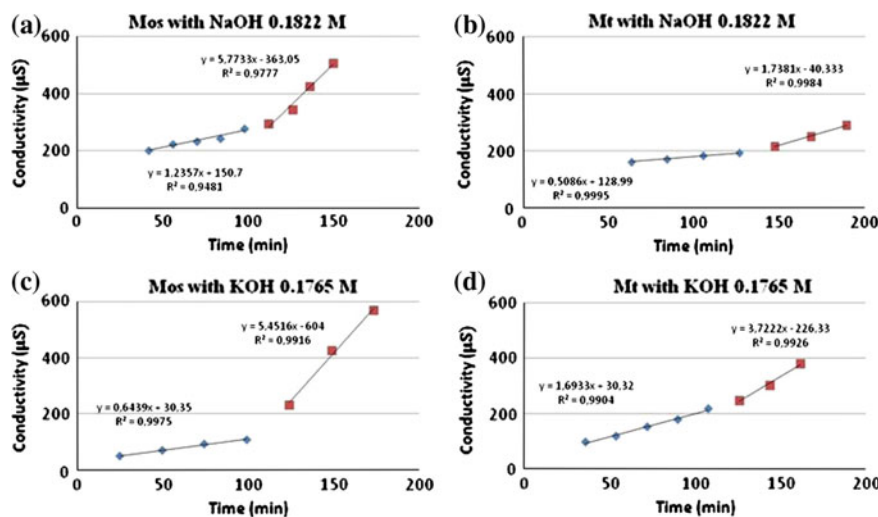


Fig. 4 Conductometric titration of: **a** Mos with the addition of 0.2 mL NaOH solution every 14 min, **b** Mt with the addition of 0.2 mL NaOH solution every 21 min, **c** Mos with the addition of 0.3 mL of KOH solution every 30 min and **d** Mt with the addition of 0.2 mL of KOH every 18 min

Table 1 Half-life period and the DWC of the analyzed systems

	NaOH 0.1822 M		KOH 0.1765 M	
	Mos	Mt	Mos	Mt
τ (min)	28.40	20.69	29.49	17.54
Time (min)	113.18	137.71	131.94	126.50
DWC (meq/dry g)	1351.92	1141.75	1067.68	1223.54

The values of the constant rate permit to obtain a parameter known as the half-life period of the reaction. The half-life period is defined as the time necessary for half the specific reactant to be used up. But it is not the half time required to

complete the reaction. The simple relation between the half-life period and the constant rate is given by the equation: $\tau = \ln 2/k$ where τ is the half-time period and k the constant rate. Conductometric titration of 4 different systems was carried out. The first one is consisted of Mos with the addition of 0.2 mL of NaOH 0.1822 M solution every 14 min, the second one is a Mt with the addition of 0.2 mL of NaOH 0.1822 M solution every 21 min. The third system is a Mos with the addition of 0.3 mL of KOH 0.1765 M solution every 30 min and the fourth, and the last system is a Mt with the addition of 0.2 mL of KOH 0.1765 M solution every 18 min (Fig. 4). Table 1 shows the results obtained for the half-time periods of the different systems.

Three of the four experiences are carried out with approximately half-life period calculated (systems b, c and d). The crossing point of the two straight lines is where the neutralization reaction of the Nafion® membrane occurs and dry weight capacity can be calculated. In Table 1 obtained values are represented.

4 Conclusions

In this research work the reaction rate to exchange all the counter ions of the membrane is calculated. It is observed that the systems with KOH present higher conductivity and faster reaction rate than the ones with NaOH. Nafion® 117 membranes with alkaline solutions present a first-order neutralization reaction. Parameters such as constant rate and half-life period were calculated for all the systems under study. The conductometric titration method allow to know the approximated time when the neutralization reaction is finishing and the amount of alkaline solution needed to exchange all the counter ions. The 24 h neutralization reaction time proposed can be reduced for periods of 30 min approximately (depending of the membrane mass and the alkaline solution used) using the conductometric titration method.

Further investigation work has to be done to understand the mechanism of the reaction in more detail.

Acknowledgments Authors want to thank the Defence Ministry for the PIDDEF 21/11 and 22/11. Authors are grateful to Dr. Héctor José Fasoli for the equipment provided to make the experiences.

References

1. J. Mbah, E. Weaver, S. Srinivasan, B. Krakow, J. Wolan, Y. Goswami, E. Stefanakos, Low voltage H₂O electrolysis for enhanced hydrogen production. *Energy* **35**, 5008–5012 (2010)
2. H. Gorgun, Dynamic modelling of a proton exchange membrane (PEM) electrolyzer. *Int. J. Hydrogen Energy* **31**, 29–38 (2006)

3. A. Ursúa, L. Marroyo, E. Gubía, L.M. Gandía, P.M. Diéguez, P. Sanchis, Influence of the power supply on the energy efficiency of an alkaline water electrolyzer. *Int. J. Hydrogen Energy* **34**, 3221–3233 (2009)
4. V.M. Nikolic, G.S. Tasic, A.D. Maksic, D.P. Saponjic, S.M. Miulovic, M.P.M. Kaninski, Raising efficiency of hydrogen generation from alkaline water electrolysis—energy saving. *Int. J. Hydrogen Energy* **35**, 12369–12373 (2010)
5. K. Zeng, D. Zhang, Recent progress in alkaline water electrolysis for hydrogen production and applications. *Prog. Energy Combust. Sci.* **36**, 307–326 (2010)
6. T. Oi, Y. Sakaki, Optimum hydrogen generation capacity and current density of the PEM-type electrolyzer operated only during the off-peak period of electricity demand. *J. Power Sources* **129**, 229–237 (2004)
7. M.J. Lavorante, J.I. Franco, P. Bonelli, G.M. Imbrioscia, H.J. Fasoli, *Zirfon® as separator material for water electrolysis under specific conditions*, eds. by A.Y. Oral, Z.B. Bahsi, M. M. Ozer. International Congress on Energy and Energy Related Materials (ENEFM2013), Springer Proceedings, pp. 225–231 (2014)
8. T.G. Douglas, A. Cruden, D. Infield, Development of an ambient temperature alkaline electrolyser for dynamic operation with renewable energy sources. *Int. J. Hydrogen Energy* **38**, 723–739 (2013)
9. S.A. Grigoriev, V.I. Porembsky, V.N. Fateev, Pure hydrogen production by PEM electrolysis for hydrogen energy. *Int. J. Hydrogen Energy* **31**, 171–175 (2006)
10. P.W.T. Lu, S. Srinivasan, Advances in water electrolysis technology with emphasis on use of the solid polymer electrolyte. *J. Appl. Electrochem.* **9**, 269–283 (1979)
11. M.J. Lavorante, B. Scalise, C. Lopez, A. Sanguinetti, J. Franco, H. Fasoli, Estudio sobre la hidratación de la membrana de Nafion® 117 a diferentes concentraciones de ácido sulfúrico. Proceeding of Iberoamerican Congress HYFUSEN **2009**, 06–129 (2009)

High Thermal Conductivity Structured Bimetallic Catalysts for Low Temperature Ethanol Steam Reforming

Vincenzo Palma, Concetta Ruocco, Filomena Castaldo
and Antonio Ricca

Abstract This study focuses on the development of bimetallic structured catalysts, supported on CeO_2 and $\text{CeO}_2\text{--ZrO}_2$, active in Ethanol Steam Reforming (ESR) reaction at low-temperature (300–600 °C) and characterized by improved heat transfer properties. ESR reaction was carried out on ceramic foams and on powders catalysts. In particular, catalytic test were performed on two reactor configurations (annular and tubular), evidencing that the better thermal management of the foams, tested in the tubular reactor, results in very higher conversions mainly due to the overcoming heat transfer limitations. Moreover, the effect of catalytic support on system performances was investigated.

1 Introduction

One of the best ways to reduce oil and gasoline depletion and green gas emissions is by encouraging clean energy production. Unlike fuel fossils, H_2 appears as a suitable fuel to meet future energy supply [1]. Although the most common technologies for producing hydrogen involve thermo-catalytic processes of natural gas or heavy oils [2], sustainable generation is possible only by using environmentally friendly methods. In particular, bioethanol production from biomass and its conversion to hydrogen via steam reforming seems to be a very promising alternative strategy [3–5]. Moreover, the route of feeding bioethanol to a steam reformer is very attractive, mostly due to the deeper knowledge of reforming technologies with respect to other alternative methods to produce hydrogen. Ethanol steam reforming can theoretically provide 6 mol of H_2 per mole of reacted $\text{C}_2\text{H}_5\text{OH}$:



V. Palma · C. Ruocco (✉) · F. Castaldo · A. Ricca
University of Salerno, D.I.In, Via Giovanni Paolo II 132, 84084 Fisciano, SA, Italy
e-mail: cruocco@unisa.it

However, the reaction system is very complex, resulting as the subsequence of several reactions that could occur reducing H_2 yield and selectivity [6, 7], and resulting in catalyst deactivation. In particular, in order to minimize CO content in the produced stream a crucial role is covered to operating conditions, since low operating temperature may improve WGS reaction. In addition, increasing temperatures affect significantly on hydrogen production costs, both in term of operating and plant charges. Therefore, the chance of performing ethanol steam reforming in the low temperature range appears particularly interesting. However, low reaction temperature may negatively affect on reaction kinetics, resulting in a too slow reaction system. A proper choice of catalytic formulations may results in a selective reaction rate increasing that in turn drive the system to a better by-products selectivity and hydrogen yield. Ni based catalysts exhibited a relevant ability in promoting C–C bonds breaking and hydrogenation/dehydrogenation reactions [8]. However, Ni dispersed on Al_2O_3 , may promote dehydration reactions, followed by polymeric carbonate species formation [9], while decreasing carbon formation rates were observed if supported on rare earths oxides [10]. In particular, Ni/ CeO_2 catalysts were shown to be very active towards ESR, even in stoichiometric operating conditions. The ESR promotion related to CeO_2 supports can be improved by adding proper dopants, such as CeO_2 – ZrO_2 in optimized ratios, enhances ceria reducibility properties and in turn catalytic activity [11]. Moreover, the formulation enrichment with noble metals, such as Pt, and in particular if available at gas-solid interface [12] assures high ethanol conversions in a wider temperature range (Fig. 1).

In the process intensification direction, structured catalysts, such as highly thermal conductive monolithic foams, may overcome the typical powders drawbacks by enhancing mass and heat transfer, so flattening axial thermal profile [13].

In this work, catalytic performances of Pt–Ni/ CeO_2 and Pt–Ni/ CeO_2 – ZrO_2 based catalysts for low-temperature steam reforming were investigated both in powder and foam shapes.

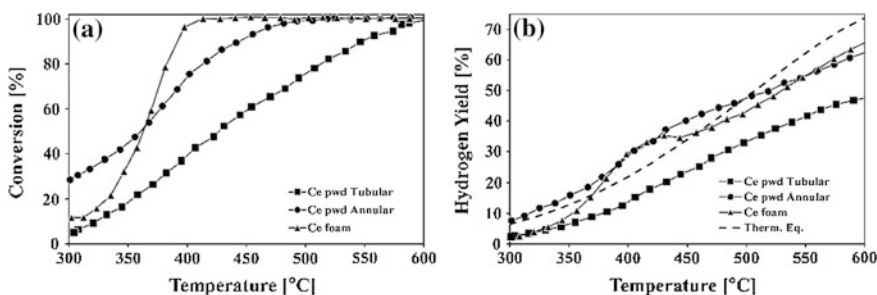


Fig. 1 C_2H_5OH conversion (a) and H_2 yield (b) for CeO_2 based catalysts as a function of temperature

2 Experimental

Nickel-Platinum based catalysts were prepared on CeO_2 and $\text{CeO}_2\text{-ZrO}_2$, both in powder and deposited on ceramic foams. Powder catalysts were prepared by wet impregnation method: platinum chloride and nickel acetate supplied by Sigma-Aldrich) were selected as precursors, while CeO_2 and $\text{CeO}_2\text{-ZrO}_2$ were supplied by Rhodia. Ni deposition was carried out earlier than Pt one. Structured catalysts were obtained starting from ceria and ceria-zirconia silicon carbide foams (30 ppi, void fraction 85 % provided by IKTS) in a cylindrical shape sized $D14.2 \times 21.1$ mm. Ni and Pt deposition was realized by dip impregnation method. All the prepared catalysts (both powders and foams) consisted of 3 wt% Pt and 10 wt% Ni on supports.

The samples were characterized by several techniques to investigate the catalyst deposition effect. The specific surface area was evaluated by B.E.T. method using a Costech International 1040 Kelvin Sorptometer. The nickel crystallite sizes were evaluated by starting from XRD analysis carried out by a D8 Brucker micro-diffractometer. The H_2 -TPR measurement was carried out from room temperature to 600 °C with a heating rate of 20 °C/min by using a reducing stream composed by 5 % H_2 in N_2 . The TPR analysis was carried out in the reaction system.

Powder and foam catalysts were tested in a tubular reactor ($D_{in} = 19$ mm), while further tests on powder catalysts were performed in an annular reactor ($D_{in} = 15$ to 19 mm), to reduce heat transfer limitations and then thermal radial-gradient. System heating was assured by an electrical furnace; process temperature was monitored by a thermocouple placed at the middle of the catalytic outer section. Catalytic foams were held in place through a ceramic pad while catalytic powders (180–355 μm) were sandwiched between quartz flakes. Catalytic tests were carried out by feeding an ethanol and steam mixture ($\text{H}_2\text{O/EtOH} = 3$), moreover nitrogen was used as diluent ($\text{N}_2/\text{EtOH} = 16$). The product composition analysis was performed by an on-line Nicolet Antaris IGS FT-IR multi-gas analyzer, coupled to a thermal conductivity ABB-CALDOS 27 analyzer for hydrogen content measurement.

Catalytic tests were performed at atmospheric pressure in the temperature range 300–600 °C (from 600 to 300 °C @ 3 °C/min), with a GHSV of $114,350 \text{ h}^{-1}$. For the powder samples tests, a mass of catalyst equal to the amount loaded on the respective foams was used (0.789 g for the CeO_2 , 0.548 g for the $\text{CeO}_2\text{-ZrO}_2$), diluted with quartz (1:1 vol, 500–710 μm) to reduce pressure drops.

3 Results and Discussion

The samples characterization was summarized in the Table 1:

As reported in Table 1, CeO_2 sample showed highest S.S.A. value as bare support. Active species deposition caused a specific area reduction in both cases, even if weaker for the CeZr sample. The highest specific surface of the Ce-based

Table 1 Powder catalyst characterization results

Sample	S.S. A (m ² /g)	Platinum			Nickel			
		Red. peak T (° C)	Exper. H ₂ uptake (μmol/g)	Theor. H ₂ consum. (μmol/g)	Support crystallite size (Å)	Red. peak T (° C)	Exper. H ₂ uptake (μmol/g)	Theor. H ₂ consum. (μmol/g)
CeO ₂	127							
3%Pt/10% Ni/Ce	72	214	624	308	105	332	1710	1704
CeO ₂ –ZrO ₂	64							
3%Pt/10% Ni/CeZr	49	202	2336	308	166	257	1898	1704

catalyst is probably responsible for the lowest average size of the nickel oxide crystallites. Lower reduction temperatures were observed in the CeO₂–ZrO₂ supported catalyst for both PtO₂ and NiO. The phenomenon can be ascribed to the ZrO₂ incorporation in ceria lattice that makes Ce⁴⁺ ions more active than the ceria alone toward redox reactions [14]. For both samples, in the TPR measurement H₂ consumption very higher than the expected was observed in the PtO₂ reduction: this phenomenon can be linked to the H₂ spillover ascribed to the Ce-based catalyst, more evident for the CeZr sample.

Ceria supported samples were preliminarily tested in order to investigate the influence of reactor configuration on activity (Fig. 1).

By comparing powder catalyst tests, results confirmed that the annular configuration minimized temperature gradients in radial direction, ensuring a higher thermal control, resulting in a higher ethanol conversion and an appreciable approach to thermodynamic equilibrium values, in terms of H₂ yield, in the whole temperature range. Foam sample reached total EtOH conversion in a wider temperature range, moreover H₂ yields were comparable with what observed in the annular configuration. The optimal thermal conductivity of silicon carbide, in fact, decreased the typical heat transfer limitation of the tubular reactor, assuring a more uniform radial temperature [15]. In addition, the foams geometry was able to impose a chaotic flux to reactant mixture, enhancing heat and mass transfer rates [16, 17].

The influence of catalytic supports (ceria and ceria-zirconia) on ESR activity was also studied and results are summarized in Fig. 2.

Despite the good performances of all the samples, foam catalysts were shown to be more active even at quite lower temperature. More interesting results were observed for the CeO₂–ZrO₂ catalysts, for both powder and foam. The worst performances recorded for CeO₂ based samples may be ascribed to a catalyst deactivation during the activity screening. In fact, ceria-zirconia solid solutions, when optimized, as in the present study, in terms of Ce/Zr molar ratios [18], are characterized by oxygen storage and release properties higher than ceria alone, thus enhancing coke gasification reactions and limiting deactivation in a wider temperature range.

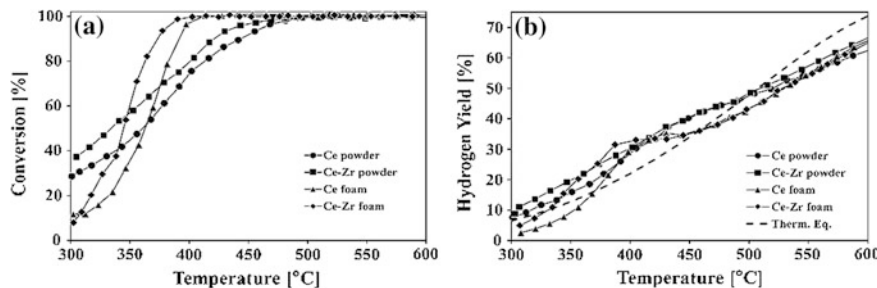


Fig. 2 $\text{C}_2\text{H}_5\text{OH}$ conversion (a) and H_2 yield (b) for CeO_2 and $\text{CeO}_2\text{--ZrO}_2$ based catalysts as a function of temperature

The performances of foam catalysts, in terms of H_2 yields, were very similar at $T > 420$ °C. However, at lower temperatures, H_2 production is higher in the presence of ceria-zirconia due to the enhanced WGS activity, linked to the better oxygen storage capacity. The very pronounced H_2 yield hump, recorded over both the foam catalysts between 350 and 450 °C, can be ascribed to the higher activity of these samples towards CH_4 steam reforming. Also for powder catalysts very similar H_2 yields values were recorded, especially in the middle temperature range (T ranging from 400 to 500 °C). The better results recorded at $T < 500$ °C over $\text{Pt-Ni}/\text{CeO}_2\text{--ZrO}_2$ powder highlighted the ability of the support in promoting ethanol reforming reaction.

4 Conclusions

Preliminary studies on structured bimetallic catalysts based on $\text{Pt-Ni}/\text{CeO}_2$ and $\text{Pt-Ni}/\text{CeO}_2\text{--ZrO}_2$, employed for low temperature ESR, were reported. Results confirmed the interesting behavior of the catalytic formulations, since very appreciable ethanol conversions and hydrogen yields were observed even in highly severe operating conditions ($T < 500$ °C; $\text{GHSV} > 100,000 \text{ h}^{-1}$), suggesting good resistance of catalytic formulations to deactivation phenomena. The high GHSV values resulted in a heat transfer limited process, since the powder catalyst showed good performances only in an optimized annular reactor able to lower radial thermal gradient. On the other hand, structured catalyst prepared on open-cells SiC foams exploits SiC foam heat transfer properties, showing high performances in very easy tubular reactor geometry. The comparison of bimetallic ceria and ceria-zirconia supported catalysts displayed the more promising results of the latter catalytic formulation, mainly due to its enhanced oxygen storage and release properties, resulting in earlier catalyst reducibility, that in turn improve the reforming reactions rate.

References

1. A. Haryanto et al., *Energy Fuel* **19**, 2098–2106 (2005)
2. S. Venkata Mohan et al., *Int. J. Hydrogen Energy* **32**, 2286–2295 (2007)
3. J. Llorca et al., *Appl. Catal. B-Environ.* **43**, 355–369 (2003)
4. F. Aupretre et al., *J. Catal.* **233**, 464–477 (2005)
5. A. da Lima Silva, CdF Malfatti, I.L. Müller, *Int. J. Hydrogen Energy* **34**, 4321–4330 (2009)
6. M. Benito et al., *J. Power Sources* **151**, 11–17 (2005)
7. W. Wang, Y. Wang, *Int. J. Energy Resour.* **33**, 5035–5044 (2008)
8. H. Muroyama et al., *Int. J. Hydrogen Energy* **35**, 1575–1581 (2010)
9. A.N. Fatsikostas, X.E. Verykios, *J. Catal.* **225**, 439–452 (2004)
10. L. Wang et al., *Int. J. Hydrogen Energy* **112**, 654–661 (2013)
11. S.Y. Lin, D. Kim, S. Ha, *Catal. Lett.* **122**, 295–301 (2008)
12. V. Palma et al., *Int. J. Hydrogen Energy* **38**, 6633–6645 (2013)
13. V. Palma, A. Ricca, P. Ciambelli, *Int. J. Hydrogen Energy* **38**, 406–416 (2013)
14. N.A. Saidina Amin, C.M. Chong, *Chem. Eng. J.* **113**, 13–25 (2005)
15. V. Palma, A. Ricca, P. Ciambelli, *Chem. Eng. J.* **207–208**, 577–586 (2012)
16. M. Lacroix et al., *Chem. Eng. Sci.* **62**, 3259–3267 (2007)
17. M. Maestri et al., *Catal. Today* **105**, 709–717 (2005)
18. E. Aneggi et al., *J. Alloy. Compd.* **408–412**, 1096–1102 (2006)

Experimental Investigations on Structured Catalysts in CH₄ Steam Reforming Intensification

**V. Palma, A. Ricca, E. Meloni, M. Martino, M. Miccio
and P. Ciambelli**

Abstract Highly thermal conductive honeycomb structures were proposed as catalyst supports to enhance the heat and material transfer properties of catalysts. This work focuses on the experimental testing of the methane steam reforming reaction performed on a Ni-loaded SiC monolith packaged into an externally heated tube. In particular, the two flow configurations of Flow Through and Wall Flow were investigated and compared, the impact of a washcoat deposition was evaluated. The experimental tests indicate that the Wall Flow configuration may overcome the fixed-bed reactor problems, yielding a more uniform temperature distribution and more effective mass transport.

1 Introduction

The continuous growth of the world population, the technological advancement, the natural tendency of countries (especially emerging markets) to achieve higher standards of living are the main reasons of the increase in energy demand and the consequent development of greenhouse gases. The hydrogen, from the energy point of view, is an ultraclean fuel and generates energy without producing harmful waste for the environment. Despite the growing interest in renewable resources, due to the wide diffusion of fossil fuels and their low relatively costs, hydrocarbons fuel processing still remains the best solution for a period of transfer toward a hydrogen-based economy. The purpose of a fuel processor is to convert a hydrocarbon fuel (natural gas, gasoline, diesel) into a H₂-rich stream to feed a fuel cell system. A typical fuel processor consists of 3 main steps: a reforming unit, in which syngas is produced from hydrocarbons, a water gas shift unit and a preferential oxidation unit, aimed to removing CO from syngas. There are three primary techniques used to produce hydrogen from hydrocarbon fuels: steam reforming (SR), partial oxi-

V. Palma · A. Ricca (✉) · E. Meloni · M. Martino · M. Miccio · P. Ciambelli
University of Salerno, D.I.in., Via Giovanni Paolo II 132, 84084 Fisciano (SA), Italy
e-mail: aricca@unisa.it

dation (POX) and auto-thermal reforming (ATR). Currently, the widely diffused technology to produce hydrogen from hydrocarbon fuels is steam reforming since it assures the highest hydrogen yield with respect to the other two approaches. Steam reforming is a catalytic endothermic process in which a hydrocarbon (e.g., methane) reacts with steam to produce mainly hydrogen and carbon monoxide:



The process endothermicity implies that very high reaction temperatures and heat fluxes towards the reaction system are required to achieve high methane conversion. Great attention must be also devoted to the catalyst structure (e.g. powder, pellets, honeycomb, foams, etc.). In the process intensification direction, previous studies [1] have demonstrated that high thermal conductivity supports may allow for a flatter axial thermal profile along the catalytic bed, thus resulting in a higher average temperature at the outlet section of the reactor, and consequently in larger hydrocarbon conversion [2]. In addition, the highly conductive supports ensure a more uniform radial temperature profile, thus resulting in a better heat transfer and reduction of hot-spot phenomena [3].

The present study compares the reaction performances of catalyzed SiC wall-flow (WF) and flow-through (FT) monoliths in the methane SR process. Moreover, the effect of ceria (CeO_2) based washcoat deposition was investigated.

2 Materials and Methods

Silicon Carbide (SiC) monoliths (Pirelli Ecotechnology, 150 cpsi), were selected as a support for the preparation of the structured catalysts. The choice of a SiC based support was determined by the thermal conductivity values (about $350 \text{ Wm}^{-1} \text{ K}^{-1}$ at 25°C) that are significantly higher than those typically reported for widely applied supports materials like alumina (about $30 \text{ Wm}^{-1} \text{ K}^{-1}$ at 25°C) or cordierite (about $3 \text{ Wm}^{-1} \text{ K}^{-1}$ at 25°C). The SiC monoliths were activated by nickel deposition, with and without a previous deposition of a washcoat.

The monolith washcoating was obtained by the dip impregnation in a lab-made slurry followed by drying and calcination steps. Slurry was realized by CeO_2 (Rhodia) dispersed in a solution of methyl cellulose (Sigma Aldrich) and pseudo-bohemite (2:1 weight-base) (CONDEA PURAL SB01). The dipping was repeated several times in order to reach a loading of 20 %wt of CeO_2 on the support. The nickel deposition on the washcoated and non-washcoated samples was by wet repeated wet impregnations steps in 1 M nickel acetate solution ($\text{C}_4\text{H}_6\text{O}_4\text{Ni} \cdot 4\text{H}_2\text{O}$) followed by drying (120°C , 30 min) and calcination ($20^\circ\text{C min}^{-1}$ up to 600°C , 2 h). 4 samples were so obtained, 3 on the non-washcoated support (10%Ni/SiC, 20%Ni/SiC, 31.8%Ni/SiC) and 1 on washcoated support (20%Ni/20%Wc/SiC).

The samples were characterized by several techniques in order to investigate the catalyst deposition effect. The specific surface area was evaluated by B.E.T. method

using a Costech International 1040 K Sorptometer. The nickel crystallite sizes were evaluated by starting from XRD analysis carried out by a D8 Bruker micro-diffractometer. The porosimetric characteristics of the samples have been measured by the Hg penetration technique using the "PASCAL 140" and "PASCAL 240" Thermo Finnigan instruments. The H₂-TPR measurement was carried out from room temperature to 900 °C with a heating rate of 3 °C/min by using a reducing stream of 1000 Ncc/min composed by 5 % H₂ in He. The TPR analysis was carried out in the reaction system.

The experimental tests were carried out in a lab-scale tubular reactor (D_{in} = 18 mm) in isothermal conditions. The monolithic catalysts were placed in the reactor enveloped by a thermal-expanding mat (INTERAM-3M), in order to avoid the gas stream bypass. The temperature control of the reaction was assured by an annular electrical oven (nominal power 4 kW) provided with 3 different heating zones, each driven by a TLK38 regulator linked to a thermocouple in contact with the reactor wall. Reaction temperatures monitoring were assured by two thermocouples placed in the middle of the inner and outer section on catalytic system.

The activity tests were performed on the catalytic monoliths in the FT and WF configurations, decreasing temperature from 800 to 600 °C by using a cooling rate of 2 °C min⁻¹, with a H₂O/CH₄ feed ratio of 3:1 and with GHSV (Total flow rate/Total catalytic volume) variable in the range 750–25,000 h⁻¹.

3 Results and Discussion

The samples characterization was summarized in the Table 1.

As reported in Table 1, surface area increased by increasing nickel deposition values, probably due to the increasing surface roughness due to the calcination steps. The washcoat deposition resulted in a clear s.s.a. increasing, up to 2 orders of magnitude higher than the bare support. The lower specific surface area values seem to promote the nickel dispersion, and in turn the low nickel crystallite size. The

Table 1 Samples characterization results

Sample	S.S. A (m ² /g)	Crystallite size (Å)	Mean pores size (μm)	H ₂ -TPR		
				Red. peak T (°C)	Exper. H ₂ uptake (μmol/g)	Theor. H ₂ consumption (μmol/g)
SiC	0.25		17.40			
10%Ni/SiC	0.56	247.6				
20%Ni/SiC	0.81	199.0				
31.8Ni/SiC	1.10	165.2		412	0.033	0.029
20%W/SiC	29.79		11.13			
20%Ni/ 20%W/SiC	21.91	145.0	4.40	370	0.026	0.572

mean monolith pores diameter decreased after slurry coating and nickel deposition, so evidencing that both washcoat and active phase were well deposited inside porosity of the monolith. Finally, the TPR analysis assessed that washcoat deposition improved sample reducibility (by anticipating the reduction temperature), while the very higher H₂ uptake than the theoretical one was devoted to the spillover phenomena due to the Ni/CeO₂ interactions [4].

Activity tests were carried out in the WF and FT configuration catalysts by feeding 25 %_{vol} CH₄ and 75 %_{vol} H₂O; the activity test were performed with washcoated and non-washcoated monoliths. Main results were summarized in Fig. 2.

The nickel load effect on the catalytic activity was firstly investigated (Fig. 1a) on non-washcoated flow-through monoliths. The reported results remarked that the methane conversion strictly depends on the Ni loading; in particular in the investigated range a linear dependence between the methane conversion and Ni load seemed to occur. Moreover lower GHSV increased methane conversion.

The temperature effect on the reaction was investigated for the 31.8%Ni/SiC FT sample by fixing the GHSV to 5000 h⁻¹. As reported in Fig. 1b, a clear dependence between operating temperatures and catalyst performances was shown. The products concentrations approached the equilibrium values only at temperatures close to 800 °C. From this analysis, it emerges that a temperature of 800 °C is required by the Ni/SiC catalyst to achieve high CH₄ conversion and high H₂ yields.

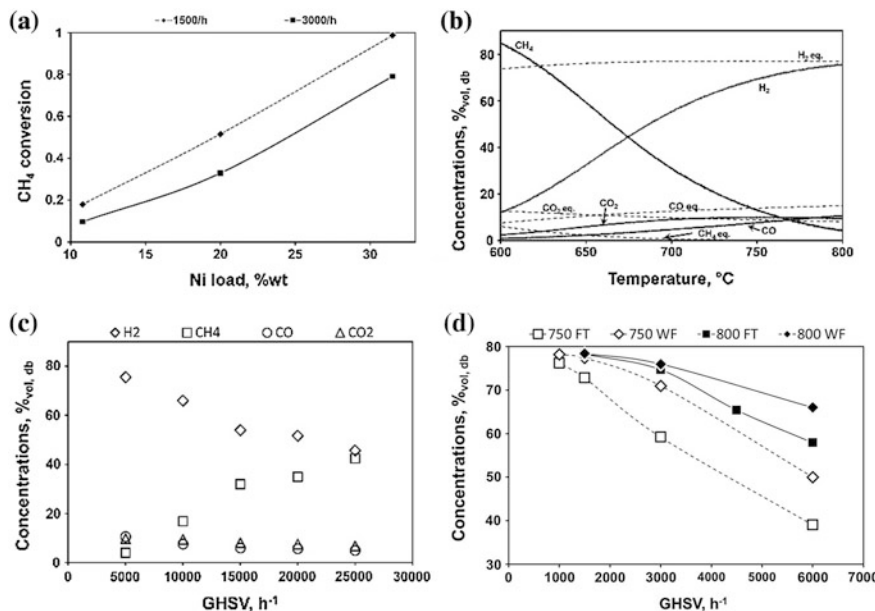


Fig. 1 Catalytic performances of Ni/SiC samples vs **a** Nickel loading; **b** Operating temperature; **c** Gas hourly space velocity; **d** Flux geometry

Once the temperature was fixed, the GHSV effect on the product composition was studied (Fig. 1c). A clear worsening in catalytic performances was observed as the GHSV increases, due to the reduction of the contact time between the gas stream and the catalytic surface.

Finally, the geometric effect of the catalytic system was investigated, by comparing catalyst performances in the flow-through and wall-flow configurations. The activity tests results, summarized in Fig. 1d, highlighted the better performances of the WF configuration than the FT, in terms of hydrogen production at the same temperature and GHSV. The WF configuration enhancement was more evident in the more extreme conditions, i.e., at the lowest operating temperatures and at highest reactant flow rates where the heat and mass transfers are limited. Obtained results highlight the real benefit of the wall flow configuration that in one hand optimizes solid-gas contact in the wall porosity of the catalyst so maximizing mass transfer rate between the phases, on the other contributes to the flattening of the radial thermal profiles, so optimizing thermal management in the catalytic volume.

As a final step, activity tests were performed on the wash-coated monoliths; the results for the monoliths in FT and WF configurations are reported in Fig. 2.

The reported results evidenced the better performances of WF configuration than the FT. The wall-flow catalysts played a crucial role especially for the more severe operating conditions (high GHSV, low temperature) in which heat and mass transfer rates become a key parameter. At the lower GHSV value, the WF catalyst resulted in a product composition very close to the thermodynamic equilibrium in the main part of the investigated temperature range.

The role of the washcoat on catalytic performances was highlighted in Fig. 3. Reported results assessed that washcoated samples were able to dramatically reduce the gap with the thermodynamic equilibrium, resulting in a more than twice methane conversion up to 700 °C (in conditions far to the thermodynamic equilibrium). The oxygen-storage capacity, proper to the cerium oxide, accelerates the migration of oxygen from steam to the carbon [5], so resulting in a clear increasing in catalytic system performances.

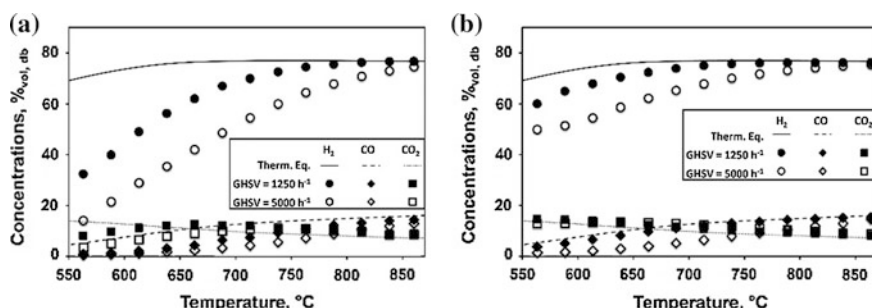
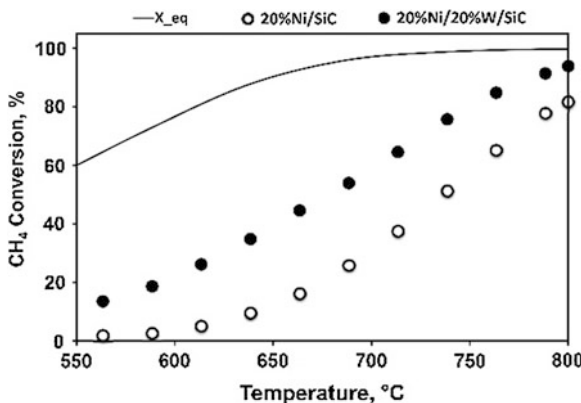


Fig. 2 Catalytic activity of 20%Ni/20%W/SiC samples in FT (a) and WF (b) configuration

Fig. 3 Comparison of CH_4 conversion in non-washcoated and washcoated activated wall-flow monoliths ($\text{GHSV} = 5000 \text{ h}^{-1}$)



4 Conclusions

An advanced experimental reaction system was set-up in order to verify the influence of flow configuration in monolithic catalysts on methane SR. The activity tests showed the better performances of the monolithic reactor in the WF configuration with respect to the FT, in terms of hydrogen yields at the same temperature and GHSV: in particular the results highlighted that the preliminary deposition of a washcoat on the support increases the specific surface area, so allowing a better dispersion of the active species and a consequent better catalytic activity, particularly at lower temperatures. Finally, the experimental results demonstrated that high thermal conductivity monolithic catalyst in wall flow configuration allowed to overcome the energy and mass limitations, which are the main bottlenecks of the commercial steam reforming catalysts.

References

1. V. Palma, E. Palo, P. Ciambelli, *Catal. Today* **147**, S107–S112 (2009)
2. M.H. Halabi et al., *Chem. Eng. J.* **168**, 872–882 (2011)
3. V. Palma, A. Ricca, P. Ciambelli, *Chem. Eng. J.* **207–208**, 577–586 (2012)
4. V. Sharma et al., *Catal. Today* **180**, 2–8 (2012)
5. K. Polychronopoulou, C.M. Kalamaras, A.M. Efthathiou, *Recent Patents on Materials Science* **4**, 122–145 (2011)

Catalysts for the Intensification of the Water Gas Shift Process

V. Palma, D. Pisano, M. Martino, A. Ricca and P. Ciambelli

Abstract Nowadays the Water Gas Shift process (WGS) is performed in two stages, a first step at high temperature (HTS), carried out at 623–873 K, and a low temperature step (LTS) at 423–573 K, to reach a favorable thermodynamic equilibrium condition. This kind of configuration is expensive and requires complex operative conditions, so to make preferable process intensification. This could be achieved through the development of new structured catalytic formulations, characterized by enhanced thermal transfer properties, able to improve the heat distribution along the catalytic bed. For this purpose the most promising catalytic systems are precious metal based supported on open cells metallic foam carriers. In this paper we report a preliminary study on the preparation and the evaluation of differently-supported Pt-based catalysts, as promising precursors in the preparation of structured catalysts for the process intensification of WGS reaction.

1 Introduction

The water gas shift reaction involves the conversion of carbon monoxide in carbon dioxide and hydrogen; it is used to improve the H₂ yield and/or modulate the H₂/CO mixtures ratio in the syngas coming from reforming processes. Moreover the growing interest towards the employment of hydrogen for Fuel Cells [1], which occurred in the last decades, highlights the relevance of the CO cleaning processes in a H₂ rich stream, especially in the processes intensification direction.

The water gas shift is an exothermic reaction; it is thermodynamically favored at low temperature and kinetically favored at high temperature, making it convenient to use a two-stage process. The high temperature stage (HTS) is conventionally carried out in the temperature range 623–873 K, on Fe/Cr-based catalyst, with fast kinetics and high CO conversion; the low temperature stage (LTS) is carried out in the temperature range of 453–633 K on a Cu/Zn-based catalyst, in this stage, kinetically

V. Palma · D. Pisano (✉) · M. Martino · A. Ricca · P. Ciambelli
University of Salerno, D.I.in, Via Giovanni Paolo II 132, 84084 Fisciano, SA, Italy
e-mail: dpisano@unisa.it

slow, the thermodynamic conditions allow to obtain the almost complete CO conversion (CO is in the order of few p.p.m). This kind of configuration is very effective but it shows several disadvantages, the global system kinetics is very slow, requiring a high catalyst mass, that in turn results in long activation time, the presence of the intercooling increases the overall process energy requirements and the plant cost. Furthermore, the LTS catalyst shows pyrophoricity, resulting not able to sustain frequent start up and shut down stages and then it is not suitable for mobile fuel cell applications. For these reasons process intensification is needed and, in this context, the development of new non-pyrophoric catalytic formulation, highly efficient in a wider range of temperature could help to achieve an effective process intensification. To this purpose, the most promising catalytic systems are precious metals based structured catalysts [2]; ceramic or metallic monolith and open cells foam structures could represent the best choice to enhance the heat transfer of the catalytic bed in order to try to realize heat redistribution along the reactor [3]. In this paper we report a preliminary study on the choice of a highly active powder catalyst, which will be subsequently used in the preparation of a structured catalyst.

The most promising catalysts in view of process intensification are for sure the noble metal based catalysts, showing high yields in a wide temperature range even at lower metal loads; moreover, they are perfectly compatible with a fuel processor system. Many examples on the use of Gold [4], Platinum [5], Rhodium [6], Palladium [7] and Ruthenium [7] are known, however the best performances are reported for Platinum and Gold. The gold catalysts show an excellent activity for LTS, but, at the same time, the tendency to deactivate rapidly because of sintering phenomena [4] whereby, to anchor the active phase to the support, complex strategies are necessary [8]. The Platinum based catalysts seem to be highly active and stable and, at the same time, the best choice for the preparation of a highly productive catalyst. Many studies on platinum based catalysts supported on reducible oxides were reported [9]. On the basis of this information we compared the performances of some platinum based catalysts supported on differently modified ceria based supports; in particular we compared the performances of 1%Pt/CeO₂, 1%Pt/CeO₂/ZrO₂ and 1%Pt14%CeO₂/γ-Al₂O₃.

2 Experimental

Supports: the 14%CeO₂/γ-Al₂O₃ (14CeAl) was prepared in our laboratory by impregnation of γ-Al₂O₃ (Sasol) with 4 equimolar aliquots of a water solution of Ce(NO₃)₃·6H₂O (Aldrich). In each impregnation the mixture was warmed and stirred, then dried at 393 K for 3 h and calcined at 673 K for 9 h.

Precursors: The Pt(NO₃)₄ solution was prepared by Vasilchenko method [10].

Catalysts: The 1%Pt/CeO₂ (PtCe) and 1%Pt/CeO₂/ZrO₂ (PtCeZr) catalysts, were prepared by impregnation of the proper support (both by Rhodia) with an aqueous solution of PtCl₄ (Aldrich), the mixture was warmed and stirred, then dried at 393 K for 3 h and calcined at 873 K for 3 h.

The 1%Pt/14CeAl (Pt14CeAl) was prepared by impregnation of 14CeAl with the proper amount of the platinum nitrate solution; the mixture was warmed and stirred, then dried at 393 K for 3 h and calcined at 673 K for 6 h.

Energy Dispersive X-ray fluorescence (EDXRF) spectroscopy (Thermo-Scientific Quant'X) was used to determine the effective metal loading of the catalysts; the powder XRD (Cu $\text{K}\alpha$ radiation) were recorded by a D8-Advance Bruker WAXRD spectrometer; the specific surface area (SSA) was determined by B.E.T. method, by using a Costech Sorptometer 1,040. The temperature programmed reduction (TPR) was carried out on 3 cm^3 of samples in powder form, and performed in an annular stainless steel tube. A 5 % H_2/N_2 gas mixture (flow rate: 1,000 Ncm^3/min) was fed to the reactor, and temperature was raised up to 673 or 873 K (depending on the analyzed sample) with a heating rate of 10 K/min. A FT-IR Antaris IGS on-line analyzer was utilized for recording the hydrogen uptake.

The Water Gas Shift tests were performed at atmospheric pressure, in a temperature range of 423–673 K. The activity of the catalysts was tested in a fixed bed tubular stainless steel reactor having an internal diameter of 18 mm. All the samples were crushed into powder and sieved (180–355 μm) to reach 6 cm^3 of catalyst, diluted 1:1 vol with quartz (500–700 μm), in order to minimize the pressure drops and the thermal effect of the exothermic reaction. The reacting mixture (500 Ncm^3/min) consisted of 5 % CO, 25 % H_2O and Helium balance. The gas hourly space velocity (GHSV) was 5,000 h^{-1} . Products were continuously analyzed by a Hiden Analytical quadrupole Mass Spectrometer. All the catalysts were reduced by TPR before reaction.

The best catalyst in terms of activity and selectivity was further investigated; a preliminary stability test was made up at a temperature of 473 K on a reactants mixture containing 8 % CO, 30 % H_2O and N_2 balance, with a GHSV = 15,000 h^{-1} .

3 Results and Discussion

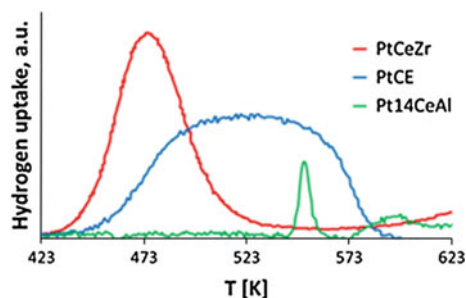
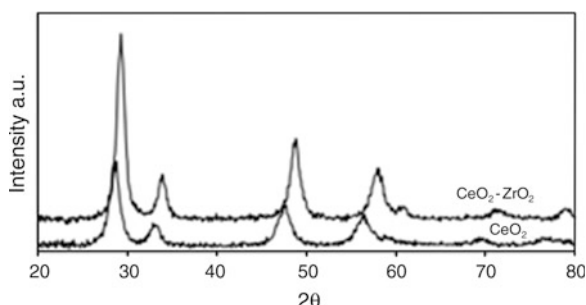
The specific surface areas values (Table 1) showed that the platinum loading generated only a slight reduction of the s.s.a. for all catalysts except for PtCeZr.

The crystallites size of the supports, determined using the Scherrer equation (Table 1), showed that all the samples had a support average size less than 10 nm. Actually, the addition of the active species caused an increase in the crystallite size of the support for Ce and 14CeAl samples, while no increase was observed for the ceria-zirconia one.

The hydrogen uptake showed a marked difference between Pt14CeAl and the other two catalysts; the most reducible catalyst was PtCeZr, followed closely by PtCe, with Pt14CeAl that resulted much less reducible than the other samples. This phenomenon is of course related to the type of support, with alumina that is widely known as a non-reducible oxide. Moreover, looking at Fig. 1, which shows the first reduction peak of the three samples (related to the presence of Pt [11]), it can be seen that the pattern seems to follow a trend of platinum's temperature reduction probably correlated to the uptake; the PtCeZr catalyst was reduced at lower temperature, PtCe

Table 1 Characterization of the samples: main results

Sample	Pt load. %w/w	S.S.A. (m^2/g)	Crist. size (nm) (plane)	H_2 uptake ($\mu\text{mol/g}$)
$\gamma\text{-Al}_2\text{O}_3$	–	158.4	5.35 (440)	–
14CeAl	–	137.46	6.09 (CeO_2 (111))	–
Pt14CeAl	1.08	132.3	6.78 (CeO_2 (111))	134
CeO_2	–	127.2	5.66 (111)	–
PtCe	0.76	125.7	6.60 (CeO_2 (111))	983
$\text{CeO}_2\text{-ZrO}_2$	–	64.45	7.21 (111)	–
PtCeZr	0.75	65.35	7.22 ($\text{CeO}_2\text{-ZrO}_2$ (111))	1205

Fig. 1 First reduction peak of the investigated samples**Fig. 2** XRD comparison between CeO_2 and $\text{CeO}_2\text{-ZrO}_2$ 

was located at higher temperature but nearby PtCeZr while, at much higher temperature, Pt14CeAl. This behavior once again suggests the importance of the supports (PtCeZr showed a more intimate interaction between active species and support) resulting in a better reducibility of the whole catalyst [12].

The XRD pattern of the ceria support showed the characteristic cubic fluorite type phase, the main peaks were located (JCPDS 34-0394) at 28.6, 33.4, 47.8 and 56.7°, corresponding to the reflections in the (111), (200), (220) and (311) crystalline planes. Likewise the diffraction pattern of the ceria/zirconia (Fig. 2) showed the same peaks but shifted towards higher 2θ values, to indicate the formation of a solid solution between ceria and zirconia [13]. No peak corresponding to platinum species was detected for all samples, probably due to the too low Platinum loading.

In Fig. 3 the catalytic activity and selectivity results are summarized. What immediately stands out in the eyes is that platinum ceria-zirconia was more active in the low temperature range than platinum ceria, and so platinum ceria alumina. Indeed, in particular PtCeZr reached the equilibrium composition at 453 K. On the other hand, PtCe showed a very good conversion also at 473 K (90 %), but the conversion decayed to 60 % at 453 K, and moreover Pt14CeAl showed an equilibrium conversion value in the range 513–673 K, while the CO conversion was only 5 % at 473 K. Another thing that has to be pointed out is that PtCeZr is an active catalyst for the WGS reaction also at very low temperatures; in fact, it showed a 30 % conversion at 423 K, a very low temperature for the WGS.

These catalytic results are of course correlated to the reduction behavior of the catalysts. In fact, looking at Fig. 1, which shows the platinum reduction peaks of all catalysts, it can be seen that the reduction sequence suggests the activity of the catalysts, both in quantitative terms (PtCeZr was the more reducible catalyst, followed by PtCe and then Pt14CeAl) that in terms of reduction temperature. Turning back to Fig. 3, regarding the selectivity to the different products it can be noticed that all catalysts showed a very good hydrogen and CO_2 selectivity, in all the temperature range. Only PtCeZr showed a little amount of methane selectivity, but it was only of few ppm, and only at the higher temperatures.

So, it can be assumed without any sort of doubt that PtCeZr was the best catalyst in terms of activity and selectivity. We decided to make also a preliminary stability test on this promising catalyst.

Stability test results are summarized in Fig. 4. It is observed that, under the selected operative conditions, typically very stressful for the WGS catalyst, the CO

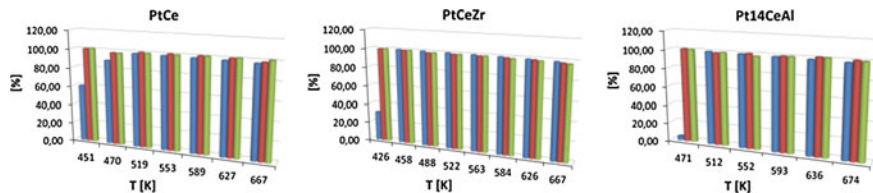
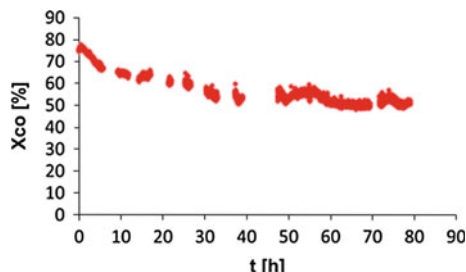


Fig. 3 CO conversion (in blue), H_2 (in red) and CO_2 (in green) selectivity of the three catalysts (GHSV = 5000 h^{-1} , $\text{CO}_{\text{vol.}\%} = 5\%$)

Fig. 4 PtCeZr, stability test
(T = 473 K;
GHSV = 15,000 h^{-1})



conversion started from a value of about 80 %, in the first 40 h decayed to a value of about 50 %, then it remained almost constant. Regarding the reasons for the partial deactivation followed by stabilization, it can be assumed that probably sintering phenomena may occur [14], but it has to be confirmed by further experiments. Moreover, the stabilization of the conversion suggests that the initial deactivation is not a dramatic phenomenon (also it's to be remembered that the operating conditions chosen for the stability test were very stressful for the catalyst).

4 Conclusions

In this work different platinum based catalysts supported on ceria were prepared, trying to modify the support composition to show the importance of the interaction between active species and the support itself. In fact, the modification of the ceria bulk by the introduction of Zr atoms brought to the formation of a solid solution, as detected by XRD, which enhances the oxygen mobility, the reducibility, and so the activity of the catalyst. Moreover, it is well known that ceria, when used in a WGS catalyst, undergoes the carbonation phenomenon, this limiting the catalyst overall activity. So, the presence of zirconium could have also limited this effect, enhancing the activity also at lower temperatures. The catalytic tests showed that the PtCeZr powder sample was able to attain an equilibrium conversion even at 453 K, and also a 30 % CO conversion at 423 K, which is a very low temperature.

So, the PtCeZr catalyst could be a very promising catalyst for the intensification of WGS process via deposition over a structured carrier to enhance the heat transport properties inside the catalytic bed of the WGS reactor.

References

1. D.B. Levin et al., *Int. J. Hydrogen Energ.* **29**, 173–185 (2004)
2. P. Panagiotopoulou et al., *Catal. Today* **112**, 49–52 (2006)
3. V. Palma et al., *Catal. Today* **147S**, S107–S112 (2009)
4. Y. Mi. et al., *J. Am. Chem. Soc.* **135**, 3768–3771 (2013)
5. Q. Fu et al., *Science* 935–938 (2003)
6. C.A. Cornaglia et al., *Appl. Cat. A-Gen.* **435–436**, 99–106 (2012)
7. P. Mierczynski et al., *Cent. Eur. J. Chem.* **11**, 912–919 (2013)
8. N. Ta et al., *J. Am. Chem. Soc.* **134**, 20585–20588 (2012)
9. C.A. Franchini et al., *Appl. Catal. B-Environ.* **117–118**, 302–309 (2012)
10. D. Vasilchenko et al., *Inorg. Chem.* **52**, 10532–10541 (2013)
11. Ricote et al., *Appl. Catal. A-Gen.* **303**, 35–47 (2006)
12. W. Lin et al., *J. Phys. Chem. C* **112**, 5942–5951 (2008)
13. N.D. Petkovich et al., *J. Phys. Chem. C* **115**, 21022–21023 (2011)
14. Azzam et al., *Appl. Catal. A, Gener.* **338**, 66–71 (2008)

Hydrogen Production by Steam Conversion of a Model Biogas Over the Co-based Supported Catalysts

S.S. Itkulova, G.D. Zakumbaeva, Y.Y. Nurmakanov, A.M. Abdullin and A. Ospanova

Abstract In this work, the new multicomponent Co-based catalysts promoted by additives of the VIII Group metal and rare earth element and supported on alumina have been synthesized and tested in dry and steam conversion of a model biogas. The processes were carried out under conditions: atmospheric pressure, GHSV— 1000 h^{-1} , and varying temperature within $300\text{--}800\text{ }^{\circ}\text{C}$. The catalysts were characterised by using electron microscopy, BET, and X-Ray analysis. Adding steam in amount up to 40 vol% leads to increasing both the methane conversion and the hydrogen yield at lower temperatures. Almost complete methane conversion is occurred at $T < 700\text{ }^{\circ}\text{C}$ at steam reforming of biogas. Syngas is enriched with hydrogen, ratio of $\text{H}_2/\text{CO} > 1.5$. The catalysts are high effective ones. The $5\%\text{Co-M}_1\text{-M}_5/\text{Al}_2\text{O}_3$ catalyst has showed the stable activity during 80 h of its continuous test in the steam conversion of a model biogas.

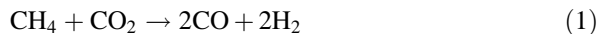
1 Introduction

Clean energy and alternative energy have become major areas of research worldwide for sustainable energy development. The utilization of greenhouse gases, such as carbon dioxide (CO_2) and methane (CH_4), is among the most important challenges in the area of energy research. To solve these challenges the new alternative cheap and renewable sources for power generation, petrochemistry and the ways for environment protection, in particular mitigation of greenhouse gases effect should be found. Due to the limited and inevitable depletion of oil reserves, the efforts are aimed to using the widespread, underused wastes and/or environmentally harmful products, including greenhouse gases as a raw material.

S.S. Itkulova (✉) · G.D. Zakumbaeva · Y.Y. Nurmakanov · A.M. Abdullin · A. Ospanova
D.V. Sokolsky Institute of Organic Catalysis and Electrochemistry, 142, Kunaev Str.,
Almaty, Kazakhstan
e-mail: s.itkulova@ioce.kz

Biogas is a renewable and one of the most common universal sources of energy in the world. Biogas is a mixture of gases formed in a result of the anaerobic digestion process of the residual biomass from various sources (animal waste, sewage treatment plants or industrial wastewater, landfills, etc.). Biogas is composed mainly of methane (CH_4 up to 70 %) and carbon dioxide (CO_2 up to 45 %), and also may include traces of other gases depending of its origin [1]. Thus, biogas is a promising energy source for its renewable nature, on the one hand, and its major source, on the other.

The use of biogas is quite versatile [2]. One of the attractive ways of biogas use is its conversion into high valuable products such as hydrogen and syngas [1–7]. Actually, biogas containing carbon dioxide and methane is ready feedstock to produce syngas by the reaction so-called carbon dioxide methane conversion or dry reforming of methane (DRM) (1). DRM has attracted the considerable scientific interest in recent years, because using both of CO_2 and CH_4 as reactants is a potential method to utilize the greenhouse gases. Syngas formed by DRM has a ratio of H_2/CO close to unity (1), which is suitable for Fischer-Tropsch synthesis (FTS), production of methanol, and oxo-synthesis [8, 9].



Hydrogen is used in petroleum refineries to produce clean transportation fuels, and its consumption is expected to increase dramatically in the near future as refiners need to process increasingly heavier and sour crudes. Furthermore, hydrogen recently regarded as promising alternative and clean energy carrier [10, 11]. It is considered ideal eco-fuel, which produces water as a result of its use. H_2 has high energy capacity, with the largest amount of energy per mass unit than any other known substance. The production of H_2 from renewable sources, such as biogas, leads to reducing greenhouse gas emissions.

In practice, biogas enriched in methane could not be completely converted into H_2 and CO alone via DRM because the CH_4/CO_2 ratio is higher than the stoichiometric ratio (1). The combination of carbon dioxide and steam reforming (CSDRM) seems to be more preferable. It also allows producing the hydrogen-enriched mixture.

The processes for producing syngas and hydrogen from biogas are catalytic ones. The main issue that needs to be addressed for the DRM reaction is coke deposition, which causes deactivation and prevents the industrial use of the process [12–16]. The primary issue with the reforming catalysts is their lifetime. For these reasons, the main efforts are directed to development of the high effective catalysts resistant to coke formation or not producing coke.

In this work the new catalysts based on Co with adding noble and rare earth metals supported on alumina were synthesized and tested. The catalytic performance of the catalysts has been investigated in the dry and steam reforming of model biogas with a ratio of $\text{CH}_4:\text{CO}_2 = 1:1$.

2 Experimental

The Co-containing catalysts were prepared by impregnating alumina with an aqueous solution of Co, a noble metal (M_1), and a rare earth element compounds followed by thermal treatment. The amount of rare earth metal (M_5) was varied from 2 to 10 wt%. The content of Co and noble metals in the catalysts was constant and equal to 5 wt%.

The physicochemical properties of the catalysts were studied using TEM, BET, and X-ray analysis.

The catalytic testing was carried out in a laboratory flow quartz reactor supplied with programmed heating and a controlled feeding velocity. The gas hourly space velocity (GHSV) was 1000 h^{-1} and process was operated under the atmospheric pressure. The temperature was varied from 300 to $800\text{ }^\circ\text{C}$. The model biogas had a ratio of $\text{CH}_4:\text{CO}_2 = 1:1$. For steam conversion of biogas 10–40 vol% of steam was added. The initial and final reaction products were online analyzed using the GC's.

The conversion degrees of carbon dioxide (X_{CO_2}) and the methane (X_{CH_4}) were calculated in order to compare the catalyst activity.

3 Results and Discussions

The effect of temperature on steam and for comparison on dry conversion of biogas over the 5%(Co- M_1)-5% $M_5/\text{Al}_2\text{O}_3$ catalyst is presented in Fig. 1a, b respectively. It is shown that the processes are significantly activated at temperatures $>500\text{ }^\circ\text{C}$. Complete methane conversion ($X_{\text{CH}_4} = 100\text{ %}$) occurs at 700 and $730\text{ }^\circ\text{C}$, while conversions of carbon dioxide are 98.8 and 96.2 % in steam and dry reforming respectively. Synthesis gas is the only product of biogas conversion over the catalyst.

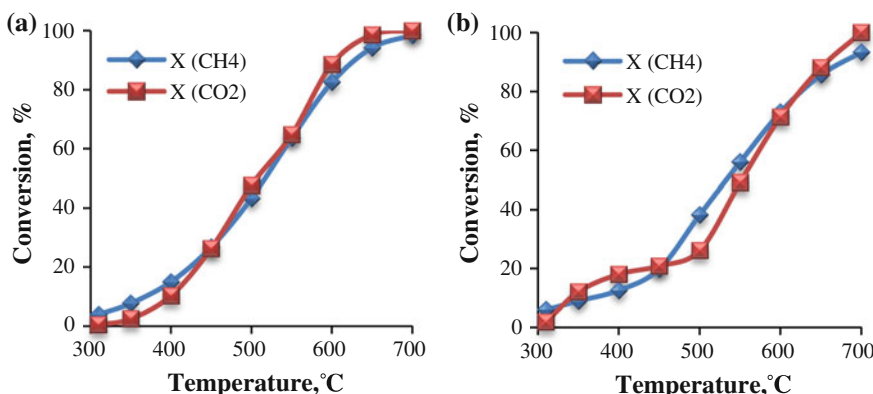


Fig. 1 Effect of the temperature on the steam (a) and dry (b) biogas conversion over the 5%(Co- M_1)-5% $M_5/\text{Al}_2\text{O}_3$ ($\text{GHSV} = 1000\text{ h}^{-1}$, $P = 0.1\text{ MPa}$)

Also, the effect of the amount of the rare metal has been examined. In terms of complete methane conversion, the catalyst with 5 wt% of M₅ is more active. 100 % of CH₄ conversion is occurred over this catalyst at 700 °C (Table 1). Whereas the complete carbon dioxide conversion in steam reforming of biogas is reached at the same temperature over the catalyst with a higher content of rare metal—10 wt%. In comparison with the Co-containing catalysts studied by authors [17], the specific of the catalysts promoted with additives of rare metal M₅ is close to CH₄ or higher carbon dioxide conversion. Syngas enriched with hydrogen is produced in steam biogas reforming. The H₂/CO ratio gets in maximum 1.5–1.6 over the catalysts (Table 1).

With an aim to determine the stability, the catalyst with 5 wt% of rare metal, which is the optimal one from point of view of higher product conversion and hydrogen yield, has been long studied. The results of the steam and dry biogas conversion are presented in Fig. 2a, b respectively. During testing the same catalyst sample in steam and then in dry biogas conversion no loss of its activity was observed.

X-ray analysis did not show the difference between the fresh and used samples of the multicomponent catalysts. There is no diffraction from the metal phase due to their high dispersion state. By TEM the high dispersive phase, which does not give microdiffraction has been observed for the fresh samples. BET analysis did not show the any significant changes in surface area of the fresh and exploited samples.

Table 1 Effect of content of rare earth metal on behavior of the 5 % (Co-M₁)-M₅/Al₂O₃ catalysts in the biogas conversion at GHSV = 1000 h⁻¹, P = 0.1 MPa

Amount of rare metal (wt%)	Process	T (°C)	Conversion (%)		Ratio H ₂ /CO in syngas formed
			CH ₄	CO ₂	
2	Dry reforming	600	59.3	69.2	0.9
		700	87.9	95.2	0.85
		730	93.0	98.4	0.8
	Steam reforming	600	63.2	63.6	1.1
		700	89.9	85.2	1.1
		730	97.4	89.3	1.1
5	Dry reforming	600	79.8	57.2	1.2
		700	99.3	89.9	1.2
		730	100	96.2	1.2
	Steam reforming	600	82.5	73.0	1.6
		700	100	98.8	1.5
		730	100	100	1.4
10	Dry reforming	600	71.4	71.4	1.0
		700	92.8	97.3	1.0
		730	95.2	98.9	1.0
	Steam reforming	600	78.5	81.5	1.4
		700	97.2	100	1.3
		730	98.8	100	1.3

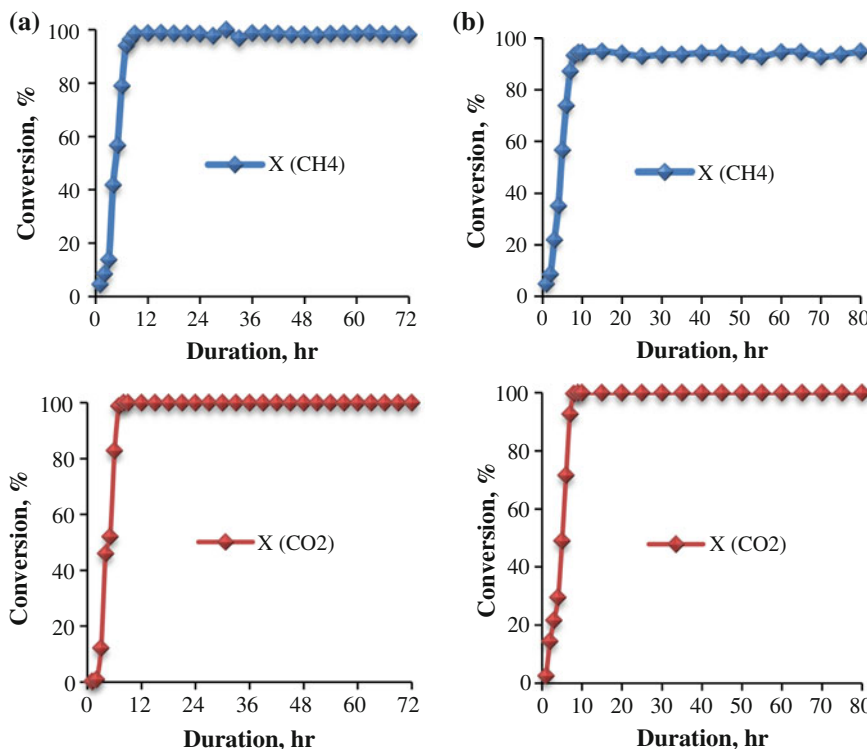


Fig. 2 Effect of process duration on steam (a) and dry (b) biogas conversion over the Co-M₁-5 % M₅/Al₂O₃ (T = 700 °C from τ = 9 h, GHSV = 1000 h⁻¹, P = 0.1 MPa)

4 Conclusions

The results obtained show that the new multicomponent catalysts based on Co with additives of noble and rare earth metals and supported on alumina have the high activity and stability in the steam and dry conversion of biogas. Temperature has the most effect on the conversion degree of both of methane and carbon dioxide. The biogas is completely converted at comparatively low temperature—730 °C over 5%(Co-M₁)-5%M₅/Al₂O₃ catalyst. Addition of steam into biogas causes enriching syngas with hydrogen. The catalysts may be considered as the promising ones for the effective production of hydrogen enriched gas from biogas.

Acknowledgments The authors wish to thank the Ministry of Education and Science of the Republic of Kazakhstan for sponsoring this research (Grant No. 0112RK00660).

References

1. P. Kolbitsch, C. Pfeifer, H. Hofbauer, Catalytic steam reforming of model biogas. *Fuel* **87**, 701–706 (2008)
2. H.J. Alves, C. Bley, R.R. Niklevicz, E.P. Frigo, M.S. Frigo, C.H. Coimbra-Arau, Overview of hydrogen production technologies from biogas and the applications in fuel cells. *Int. J. Hydrol. Energy* **38**, 5215–5225 (2013)
3. O.A. Bereketidou, M.A. Goula, Biogas reforming for syngas production over nickel supported on ceria-alumina catalysts. *Catal. Today* **195**, 93–100 (2012)
4. M.R. Hamed, A. Tsolakis, C.S. Lau, Biogas upgrading for on-board hydrogen production: reforming process CFD modelling. *Int. J. Hydrol. Energy* **39**, 12532–12540 (2014)
5. M. Balat, Potential importance of hydrogen as a future solution to environmental and transportation problems. *Int. J. Hydrol. Energy* **33**, 4013–4029 (2008)
6. K.-H. Lin, H.-F. Chang, A.C.C. Chang, Biogas reforming for hydrogen production over mesoporous $\text{Ni}_{2x}\text{Ce}_{1-x}\text{O}_2$ catalysts. *Int. J. Hydrol. Energy* **37**, 15696–15703 (2012)
7. L. Pino, A. Vita, M. Lagana, V. Recupero, Hydrogen from biogas: catalytic tri-reforming process with Ni/LaCeO mixed oxides. *Appl. Catal. B: Environ.* **148–149**, 91–105 (2014)
8. D.J. Wilhelm, D.R. Simbeck, A.D. Karp, R.L. Dickenson, Syngas production for gas-to-liquids applications: technologies, issues and outlook. *Fuel Proc. Technol.* **71**, 139–148 (2001)
9. J.R. Rostrup-Nielsen, New aspects of syngas production and use. *Catal. Today* **63**, 159–164 (2000)
10. C.-J. Winter, Hydrogen energy—Abundant, efficient, clean: a debate over the energy-system-of-change. *Int. J. Hydrol. Energy* **34**, S1–S52 (2009)
11. M. Ball, M. Wietschel, The future of hydrogen—opportunities and challenges. *Int. J. Hydrol. Energy* **34**, 615–627 (2009)
12. A.T. Ashcroft, A.K. Cheetham, M.L.H. Green, P.D.F. Vernon, Partial oxidation of methane to syngas using carbon dioxide. *Nature* **352**, 225–226 (1991). London
13. Y.H. Hu, E. Ruckenstein, Catalytic conversion of methane to syngas by partial oxidation and CO_2 reforming. *Adv. Catal.* **48**, 297–345 (2004)
14. M.F. Mark, W.F. Maier, CO_2 -reforming of methane on supported Rh and Ir catalysts. *J. Catal.* **164**, 122–130 (1996)
15. M.C.J. Bradford, M.A. Vannice, CO_2 Reforming of CH_4 . *Catal. Rev. -Sci. Eng.* **41**, 1–42 (1999)
16. X.E. Verykios, Catalytic dry reforming of natural gas for the production of chemicals and hydrogen. *Int. J. Hydrol. Energy* **28**, 1045–1063 (2003)
17. S.S. Itkulova, A.K. Yermaganbetova, G.D. Zakumbaeva, Y.Y. Nurmakanov, A.A. Mukazhanova, Syngas production by bireforming of methane over the Co-based alumina supported catalysts. *Catal. Today* **228**, 194–198 (2014)

Nanostructured Co-B Catalysts for Hydrogen Generation

David Richardson and Fernando M.F. Rhen

Abstract We have prepared nanostructured Co-B catalysts via electroless deposition on a porous polycarbonate membrane for use as a hydrogen evolution catalyst from a sodium borohydride solution. Amorphous Co-B alloy is deposited to form nanotubes, connected together by a thin film at both ends. We have varied the deposition time to form a range of Co-B nanostructures to maximise hydrogen release. We have found that Co-B nanostructures with low deposition times of 20 s have the largest hydrogen generation rate per unit mass of $11,000 \text{ ml min}^{-1} \text{ g}^{-1}$. However, deposition times of 80 s have the largest rate per unit area of $18,000 \text{ ml min}^{-1} \text{ m}^{-2}$. For larger deposition times the nanotube pore diameter decreases which results in a reduction in the hydrogen generation rate, due to a decrease in the catalytic surface area. The activation energy of the Co-B nanostructures is found to be between $40\text{--}50 \text{ kJ mol}^{-1}$, indicating that they are suitable catalysts for hydrogen production.

1 Introduction

The viability of hydrogen technology as a future alternative to non-renewable energy sources requires low cost fuel cells, safe and cheap storage media and efficient methods of hydrogen generation. The stored chemical energy of hydrogen is 3 times larger than that of hydrocarbons, 142 MJ Kg^{-1} compared to 47 MJ Kg^{-1} [1] and the by-product of hydrogen combustion is water making it an environmentally friendly energy source.

D. Richardson (✉) · F.M.F. Rhen
Department of Physics and Energy, Materials and Surface Science Institute,
University of Limerick, Limerick, Ireland
e-mail: david.richardson@ul.ie

F.M.F. Rhen
e-mail: fernando.rhen@ul.ie

Hydrogen storage for portable applications is currently an important area of research. Metal hydrides, such as sodium borohydride (NaBH_4), are a possible storage mechanism due to the relatively large amount of stored hydrogen and their stability in a basic solution [2]. In the presence of a catalyst pure hydrogen is released from NaBH_4 according to the reaction shown in (1).



A variety of noble metal catalysts [3–5] have been shown to produce hydrogen at a large rate. However due to the cost involved they are not suitable for large scale catalysis in future technologies. Therefore alternative cheap non-noble transition metal catalysts are the focus of research in the area. Investigated catalysts include Co-B [2, 6–9], which is the most promising due to its large activity, Ni-B [9], Co-P [10], Co-Ni-B [11] and Co-Fe-B [12].

The largest activities of Co-B catalysts to date have been $11,000 \text{ ml min}^{-1} \text{ g}^{-1}$ [8] and $24,400 \text{ ml min}^{-1} \text{ g}^{-1}$ [6]. These were both deposited via electroless deposition onto a Ni foam substrate. These are comparable to the activities recorded for noble metals due to the large surface area of the deposit with a nanosheet like morphology. In this work we present a novel Co-B nanotube structure deposited via electroless deposition for use as a catalyst in hydrogen production. Due to the nanostructured nature of the catalysts there is a large surface area and large catalytic activity.

2 Experimental

Catalyst Preparation: Co-B nanostructures were prepared via electroless deposition on a porous polycarbonate membrane. The pores of the membrane have a diameter of 400 nm and are 20 μm in length. Prior to Co-B deposition the membranes were sensitized in a solution of 0.013 M SnCl_2 in 0.24 M HCl at 40 °C for 10 min. Catalytic palladium nuclei were then deposited throughout the membrane by placing it in an activating solution of 1.4×10^{-3} M PdCl_2 solution at 65 °C for 10 min. The activated membranes were then placed in a deposition solution comprising of 0.143 M lactic acid, 0.3 M CoSO_4 , 0.052 M diammonium citrate and 0.07 M dimethylamine borane (DMAB). The deposition solution was held constant at a pH of 9 which was controlled using concentrate NaOH.

Hydrogen Generation: A NaBH_4 solution with a pH of 12 was used as the hydrogen source for our experiments. We investigated the hydrogen generation for a variety of catalyst deposition times and bath temperatures. The solution was placed in small round bottomed flask and the nanostructured Co-B catalyst was added. The hydrogen volume was recorded using a water displacement method. The flask was placed in a sonicator bath to ensure complete release of hydrogen bubbles from the catalyst surface and to control the temperature.

3 Results and Discussion

DMAB is used as a reducing agent for the deposition of cobalt on the polycarbonate membrane. This results in the co-deposition of cobalt and boron to form a Co-B alloy. Amorphous Co-B deposits are obtained forming nanotubes, which are connected together by a thin film at both ends as shown in Fig. 1. The nanotubes have a length of 20 μm and an outer diameter of 400 nm. The composition of the deposit was determined to be $\text{Co}_{70}\text{B}_{30}$ via XPS.

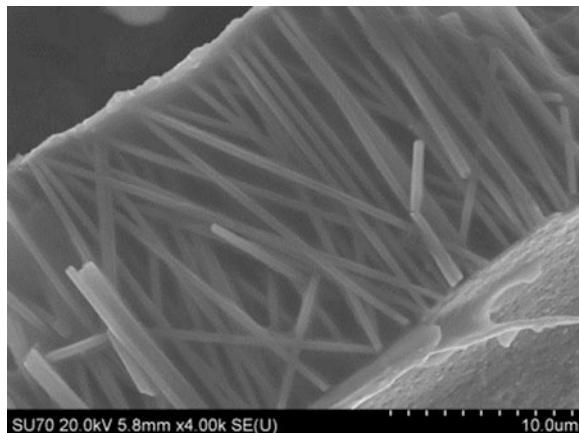
Initial Co-B deposition occurs at a fast rate due to nucleation at Pd catalytic sites throughout the membrane. Once a Co-B layer is deposited the reaction then becomes self-catalysing forming Co-B islands from around each nucleation point. As deposition continues the Co-B islands coalesce together to form a continuous film. We have found that this process occurs at a faster rate on the membrane surface than within the membrane pores as reaction is limited by the diffusion rate of the electrolyte within the pores. Due to the large deposition rate on the membrane surface the nanotube pores diameter decreases as deposition occurs as shown in Fig. 2.

At low deposition times Co-B islands are deposited throughout the polycarbonate membrane and on the membrane surface. A complete Co-B film is formed on the membrane surface after approx. 30 s of deposition. However, due to the lower deposition rate within the nanotube pores the formation of continuous nanotubes doesn't occur until 90 s of deposition.

The hydrogen generation rates for varying Co-B deposition times are shown in Fig. 3a. Large hydrogen production rates per unit mass of Co-B were recorded at low deposition times and decreased as deposition time increased. The maximum recorded rate was $10,800 \text{ ml min}^{-1} \text{ g}^{-1}$ at a deposition time of 20 s. At large deposition times the hydrogen generation rate is low due to the formation of a thick film on the membrane surface.

However, the hydrogen generation rate per unit area has a maximum value of $17,900 \text{ ml min}^{-1} \text{ m}^{-2}$ at a deposition time of 90 s as shown in Fig. 3b. At low

Fig. 1 SEM image of electroless deposited Co-B nanotube array connected at both ends by a Co-B film



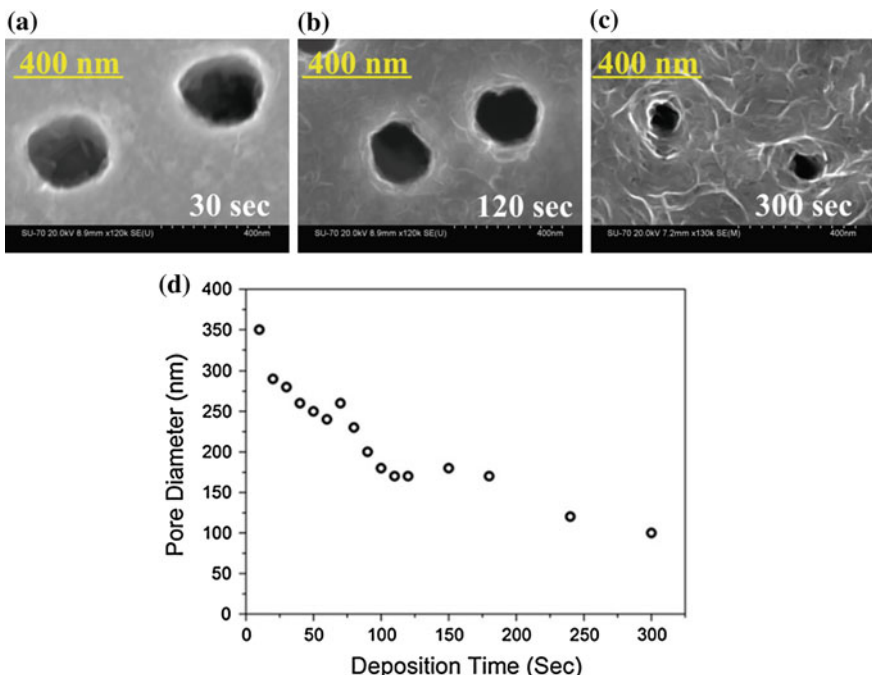


Fig. 2 SEM images of pore diameter at deposition times of **a** 30 s, **b** 120 s, **c** 300 s and **d** pore diameter versus deposition time

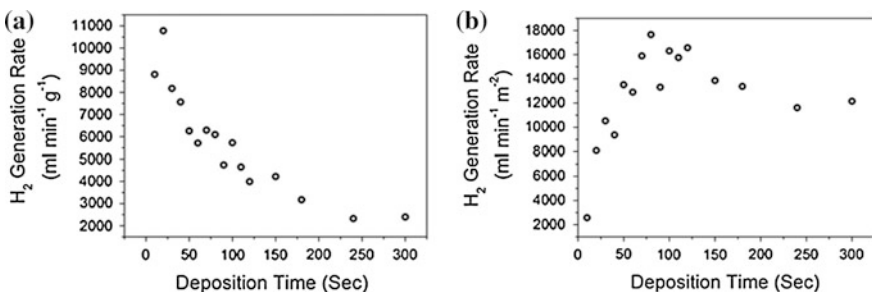


Fig. 3 Hydrogen generation rate **a** per unit mass and **b** per unit area for a variety of Co-B deposition times

deposition times the total hydrogen production rate is minimised due to incomplete nanostructures deposited throughout the membrane. A deposition time of approx. 90 s has the largest overall rate as the Co-B nanostructure is fully formed and the catalytic surface area is maximised. The decrease in hydrogen generation for deposition times greater than 90 s is attributed to a closing pore diameter decreasing the catalytic surface area and restricting diffusion of NaBH_4 within the nanotube pores.

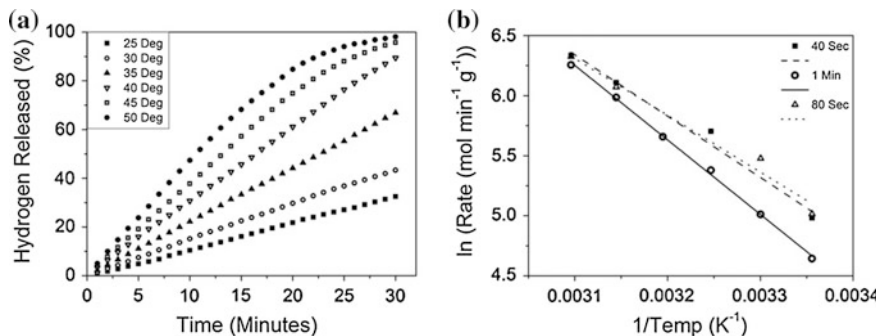


Fig. 4 **a** Percentage released of hydrogen from NaBH_4 as a function of time at different temperatures and **b** Arrhenius plot of hydrogen generation rate of the Co-B nanostructures

The activation energy of the Co-B nanostructures were determined by investigating the hydrogen generation rates with respect to temperature. The effect of temperature on the Co-B nanostructure is shown in Fig. 4a. All nanostructures displayed similar temperature dependence with an increase in the hydrogen generation rate irrespective of deposition time. The maximum hydrogen production that we recorded at high temperature was for a deposition time of 20 s at 50 °C with a value of $12,600 \text{ ml min}^{-1} \text{ g}^{-1}$. Initial hydrogen generation follows a zeroth order reaction as the rate remains at a constant value until 85 % of the available hydrogen has been released. After 85 % of the available hydrogen has been released the generation rate follows a first order reaction.

An Arrhenius plot of this data is shown in Fig. 4b. The activation energies recorded for deposition times of 40, 60 and 80 s were 43, 50 and 41 kJ Mol^{-1} . These values are comparable to the activation energies found previously for Co-B deposited on Ni foam of 44 kJ Mol^{-1} [7] and 33 kJ Mol^{-1} [8].

4 Conclusion

We have prepared Co-B nanostructures via electroless deposition for use as catalysts in the production of hydrogen using a NaBH_4 solution. We have found that low deposition times of only 20 s give the largest hydrogen generation rate per unit mass of $11,000 \text{ ml min}^{-1} \text{ g}^{-1}$ due to the sparsely deposited Co-B across a large surface area. However, the largest hydrogen production rate per unit area of catalyst is recorded at a deposition time of 80 s of $18,000 \text{ ml min}^{-1} \text{ m}^{-2}$. This is due to the formation of a complete nanostructure with a large catalytic surface area and large pore diameter. We have found the activation energy of the Co-B nanostructure is between 40 and 50 kJ mol^{-1} , demonstrating that the Co-B nanostructures have good catalytic properties.

Acknowledgments This research is supported by the Irish Research Council (RS/2011/270), Science Foundation Ireland (12/IP/1692) and the Irish Research Council New Foundations grant.

References

1. L. Schlapbach, A. Züttel, Hydrogen-storage materials for mobile applications. *Nature* **414**, 353–358 (2001)
2. S.S. Muir, X. Yao, Progress in sodium borohydride as a hydrogen storage material: development of hydrolysis catalysts and reaction systems. *Int. J. Hydrogen Energy* **36**, 5983–5997 (2011)
3. H.C. Brown, C.A. Brown, A Simple Preparation of Highly Active Platinum Metal Catalysts for Catalytic Hydrogenation. *J. Am. Chem. Soc.* **84**, 1494–1495 (1962)
4. S.C. Amendola, S.L. Sharp-Goldman, M.S. Janjua, M.T. Kelly, P.J. Petillo, M. Binder, An ultrasafe hydrogen generator: aqueous, alkaline borohydride solutions and Ru catalyst. *J. Power Sources* **85**, 186–189 (2000)
5. V.I. Simagina, P.A. Storozhenko, O.V. Netskina, O.V. Komova, G.V. Odegova, T.Y. Samoilenco et al., Effect of the nature of the active component and support on the activity of catalysts for the hydrolysis of sodium borohydride. *Kinet. Catal.* **48**, 168–175 (2007)
6. S.S. Muir, Z. Chen, B.J. Wood, L. Wang, G.Q. Lu, X. Yao, New electroless plating method for preparation of highly active Co–B catalysts for NaBH₄ hydrolysis. *Int. J. Hydrogen Energy* **39**, 414–425 (2014)
7. P. Krishnan, S.G. Advani, A.K. Prasad, Thin-film CoB catalyst templates for the hydrolysis of NaBH₄ solution for hydrogen generation. *Appl. Catal. B* **86**, 137–144 (2009)
8. H.-B. Dai, Y. Liang, P. Wang, H.-M. Cheng, Amorphous cobalt–boron/nickel foam as an effective catalyst for hydrogen generation from alkaline sodium borohydride solution. *J. Power Sources* **177**, 17–23 (2008)
9. A.A. Vernekar, S.T. Bugde, S. Tilve, Sustainable hydrogen production by catalytic hydrolysis of alkaline sodium borohydride solution using recyclable Co–Co₂B and Ni–Ni₃B nanocomposites. *Int. J. Hydrogen Energy* **37**, 327–334 (2012)
10. K. Eom, K. Cho, H. Kwon, Effects of electroless deposition conditions on microstructures of cobalt–phosphorous catalysts and their hydrogen generation properties in alkaline sodium borohydride solution. *J. Power Sources* **180**, 484–490 (2008)
11. J.C. Ingersoll, N. Mani, J.C. Thenmozhiyal, A. Muthaiah, Catalytic hydrolysis of sodium borohydride by a novel nickel–cobalt–boride catalyst. *J. Power Sources* **173**, 450–457 (2007)
12. Y. Liang, P. Wang, H.-B. Dai, Hydrogen bubbles dynamic template preparation of a porous Fe–Co–B/Ni foam catalyst for hydrogen generation from hydrolysis of alkaline sodium borohydride solution. *J. Alloy. Compd.* **491**, 359–365 (2010)

Part XXII
Carbon Dioxide Sequestration
and Conversion

Carbon Dioxide Conversion of Biogas with Producing Syngas Over the Polymetallic Supported Catalysts

**Y.Y. Nurmakanov, V.S. Yemelyanova, S.S. Itkulova,
G.D. Zakumbaeva and N.N. Nurgaliyev**

Abstract The polymetallic Co-based alumina supported catalysts with additives of VIII group metal and rare earth element were synthesized and tested in biogas conversion. As a feed a model mix corresponding to the biogas produced by anaerobic fermentation of horse manure and containing carbon monoxide and hydrogen as well as water vapour has been used. Some amount of carbon dioxide has been added to adjust the composition of biogas to a ratio of a $\text{CH}_4:\text{CO}_2 = 1:1$. The biogas conversion was carried out in a flow laboratory reactor operated at atmospheric pressure. Gas hourly space velocity (GHSV) was 1000 h^{-1} . The effects of the amount of rare earth metal and presence of carbon monoxide, hydrogen, and steam in a feed on biogas conversion over the $\text{Co}-\text{M}_1-\text{M}_5/\text{Al}_2\text{O}_3$ catalysts were studied at varied temperature. The catalysts perform the high activity in biogas conversion. At 740°C , the CO_2 completely converted, while the CH_4 conversion is higher than 96 %. Syngas is a main reaction product. Under these conditions, the H_2/CO ratio is 1.1–1.2. The catalysts are the high stable in the biogas conversion.

1 Introduction

Biogas is considered as a clean and environmental friendly fuel that is produced from anaerobic digestion of biomass, manure etc. Biogas contains mainly of CH_4 and CO_2 , and may be associated with traces of other gases such as hydrogen sulphide, ammonia, hydrogen, carbon oxide, nitrogen, oxygen, and vapour water. Content of associated gases depends on a source from which biogas is originated.

Y.Y. Nurmakanov (✉) · S.S. Itkulova · G.D. Zakumbaeva · N.N. Nurgaliyev
D.V. Sokolsky Institute of Organic Catalysis and Electrochemistry, 142,
Kunaev Str., Almaty, Kazakhstan
e-mail: y.nurmakanov@ioce.kz

V.S. Yemelyanova
Research Institute of New Chemical Technologies and Materials, Almaty, Kazakhstan

Hydrogen sulphide is certainly an undesirable component in biogas, since it is a corrosive gas and poisons for the catalysts and should be removed from biogas before its use. Effect of other admixes seems to be depended on the catalyst nature.

The technologies for biogas reforming reaction are the same that is used for the natural gas reforming: Steam Reforming of Methane (SRM), Dry Reforming (DRM), Partial Oxidation (POX) and Autothermal Reforming. Carbon dioxide reforming of biogas is an attractive way of utilization of both greenhouse gases (1). Also, its exploitation would be advantageous from financial point of view [1, 2]. Other advantages to consider are the high reaction enthalpy, which is appropriate for energy storage and transport [3], and the production of syngas with a H₂/CO ratio close to unity, useful for Fisher-Tropsch synthesis of long-chain hydrocarbons and oxygenates [4–6].



However, there is still no large-scale application of CO₂ reforming of CH₄ because of absence of the efficient and stable catalysts. Carbon dioxide reforming of biogas is endothermic reaction that requires a high reaction temperature. The major drawback of this process, which occurs at temperatures above 640 °C, is catalysts deactivation [5]. Therefore more efforts are being expended in the development of new catalysts that will represent activity, resistance to coking, as well as, long-term stability. Ni and Co-based catalysts are preferable over noble metals because of the availability and low cost [7, 8]. But using these catalysts deal with deactivation of the catalysts due to coke formation [9]. Thus, investigation into supports [10, 11] and the addition of promoters has been conducted [12, 13] with the aim of improving the coke resistance [14].

In this work, the new Co-containing catalysts with adding noble and rare earth metals and supported on alumina were synthesized and tested. The catalytic performance of the catalysts has been investigated in reforming of a model biogas corresponding to the biogas produced by anaerobic bacteria fermentation of horse manure and containing carbon monoxide and hydrogen.

2 Experimental

The polymetallic Co-containing catalysts were prepared by impregnating alumina with an aqueous solution of Co, a noble metal (M₁), and a rare earth element compounds followed by thermal treatment. The amount rare earth metal (M₅) was varied from 5 to 10 wt%. The content of Co and noble metals in the catalysts was constant and equal to 5 wt%.

The physicochemical properties of the catalysts were studied using TEM, BET, and X-ray analysis.

The process was carried out in a laboratory flow quarts reactor supplied with programmed heating and a controlled feeding velocity. The gas hourly space

velocity (GHSV) was 1000 h^{-1} and process was operated under the atmospheric pressure. The temperature was varied from 300 to $800\text{ }^{\circ}\text{C}$. The reforming of biogas was studied over the abovementioned catalysts. The model biogas corresponding to biogas produced by anaerobic bacteria fermentation of horse manure at the Research Institute of New Chemical Technologies and Materials has been used. Content of carbon monoxide and hydrogen was 1 vol % each. Steam was added in amount of 0–10 vol %. The ratio of $\text{CH}_4:\text{CO}_2 = 1:1$.

The initial and final reaction products were analyzed on-line using the GC's.

The conversion degrees of carbon dioxide (X_{CO_2}) and the methane (X_{CH_4}) were calculated according to formulas (2, 3) respectively. Thus, the activity of catalysts was compared.

$$X_{\text{CO}_2} = \left([\text{CO}_2]_{\text{init}} - [\text{CO}_2]_{\text{fin}} \right) \times 100\% / [\text{CO}_2]_{\text{init}} \quad (2)$$

$$X_{\text{CH}_4} = \left([\text{CH}_4]_{\text{init}} - [\text{CH}_4]_{\text{fin}} \right) \times 100\% / [\text{CH}_4]_{\text{init}} \quad (3)$$

Where $[\text{CO}_2]$ is the concentration of CO_2 , $[\text{CH}_4]$ is the concentration of CH_4 , and the subscripts *init* and *fin* refer to initial and final quantities, respectively.

The conversion of water was not calculated because of the complexity resulting from differentiating between unreacted water and water formed due to the secondary reactions.

3 Results and Discussions

The effect of temperature on biogas conversion over the new polymetallic supported catalysts was studied. The catalysts activity was tested in the dry reforming of biogas. The effect of water on biogas conversion was studied or by other words steam reforming of biogas was carried out. In addition, the effect of CO and H_2 presence in the biogas was investigated. Also, the influence of the amount of the rare earth metal was examined.

The dependence of conversion on the temperature over the 5%(Co-M₁)-7%M₅/Al₂O₃ catalyst in the dry and steam reforming of biogas containing CO and H₂ is presented in Fig. 1a. The rise in temperature leads to increasing conversion over this catalyst in these processes. In the temperature range of 300–500 °C in both dry and steam reforming reactions proceed slowly. A further increase in temperature leads to a rapid increase in the conversion both of carbon dioxide and methane. In the dry reforming the conversion of methane and carbon dioxide is 98.2 and 100 % respectively at $T = 795\text{ }^{\circ}\text{C}$. In the steam reforming, conversion of CO_2 and CH_4 are 100 and 98.9 % respectively at 780 °C.

To study the influence of the amount of the rare earth metal the catalyst with higher amount of M₅ = 10 wt% was synthesized and examined. The effect of temperature on the dry reforming of biogas containing CO and H₂ over the 5%

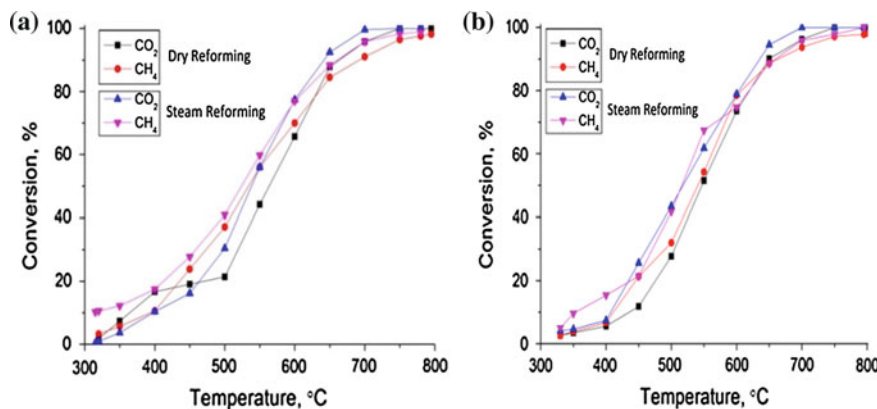


Fig. 1 Effect of the temperature on the dry and steam reforming of biogas over the 5%(Co-M₁)-7%M₅/Al₂O₃ **a** and 5%(Co-M₁)-10%M₅/Al₂O₃ **b** catalysts at CH₄:CO₂:CO:H₂ = 1:1:0.01:0.01, GHSV = 1000 h⁻¹, P = 0.1 MPa

(Co-M₁)-10%M₅/Al₂O₃ catalyst is shown in Fig. 1b. The process proceeds slowly between 300–400 °C and is drastically activated at temperatures above 400 °C. At 650–800 °C, the increase in the conversion of CH₄ and CO₂ slows. Conversion of CH₄ is less than CO₂. X_{CH4} = 98.2 % at 800 °C, while complete CO₂ conversion is observed at 740 °C.

The same effect of temperature on steam reforming of biogas over 5%(Co-M₁)-10%M₅/Al₂O₃ catalyst is shown in Fig. 1b. Comparison of the dry and steam reforming of biogas over the catalyst demonstrates that almost complete methane conversion is achieved at the same temperatures. At 795 °C the conversion of CH₄ and CO₂ is 100 %. It should be noted that complete conversion of CO₂ in the steam reforming of biogas was reached at 700, whereas in the dry reforming at 750 °C.

Syngas is the only product of CO₂ and steam reforming of biogas over the catalysts. The increase in conversion of CH₄ and CO₂ leads to growing H₂ and CO producing. In the dry reforming over the 5%(Co-M₁)-7%M₅/Al₂O₃ catalyst, the H₂/CO ratio near to 1.0 was obtained. The ratio of H₂/CO is 0.9 in the dry reforming of biogas over the catalyst with high content of rare metal—10 wt%. The syngas formed in the steam reforming of biogas over these catalysts is enriched in hydrogen and has a ratio of H₂/CO = 1.2 in both cases.

In Table 1, the comparative data on biogas conversion over the 5%(Co-M₁)-M₅/Al₂O₃ catalysts are presented.

As it is shown in Table 1, the addition of steam into a biogas leads to improving the process characteristics: conversion of both methane and carbon dioxide is increased, while syngas is enriched with hydrogen, H₂/CO = 1.2.

The presence both of carbon monoxide and hydrogen promotes the methane and carbon dioxide decomposition that causes the slight increase in degree of conversion of methane from 95.0–95.9 to 96.4–96.9 %.

Table 1 Comparative characteristics of the 5%(Co-M₁)M₅/Al₂O₃ catalysts in the biogas reforming at GHSV = 1000 h⁻¹, P = 0.1 MPa

Amount of rare metal (wt%)	Amount of admixes in biogas (vol %)			T (°C)	Conversion (%)		Ratio H ₂ /CO in syngas formed
	CO	H ₂	H ₂ O		CH ₄	CO ₂	
5 %	0	0	0	740	95.0	96.4	1.2
	1	0	0	740	96.0	99.1	1.1
	1	1	0	740	96.9	99.4	1.1
	1	0	10	740	96.5	100	1.1
	1	1	10	740	98.4	100	1.2
7 %	1	1	0	740	96.5	100	1.1
	1	1	0	795	98.2	100	1.1
	1	1	10	740	97.8	100	1.2
	1	1	10	780	98.9	100	1.2
10 %	0	0	0	740	95.9	100	1.1
	1	1	0	740	96.4	100	1.1
	1	1	0	800	98.2	100	0.9
	1	1	10	740	97.4	100	1.2
	1	1	10	795	100	100	1.2

The increase in the rare metal content in the catalyst leads to growing the carbon dioxide conversion and negligible decrease in methane conversion. There is no effect on the H₂/CO ratio in syngas formed.

The data obtained indicate that all the synthesised 5%(Co-M₁)-M₅/Al₂O₃ catalysts exhibit activity in the dry and steam reforming of biogas.

The X-Ray analysis of the catalysts does not give a diffraction pattern that is an evidence of high dispersed state of the catalysts. By TEM, the particles with a size of 5–10 nm were observed.

4 Conclusions

The results obtained show that the new multicomponent catalysts based on Co with additives of noble and rare earth metals and supported on alumina have the high activity and stability in the dry and steam reforming of biogas. The presence of 1 vol % of hydrogen and carbon oxide in biogas slightly increases in methane conversion. Addition of steam in biogas causes enriching the syngas with hydrogen.

Acknowledgments The authors wish to thank the Ministry of Education and Science of the Republic of Kazakhstan for sponsoring this research (Grant No. 0112RK00660) and the Laboratory of Physicochemical studies of Catalysts of the IOCE.

References

1. O.A. Bereketidou, M.A. Goula, Biogas reforming for syngas production over nickel supported on ceria-alumina catalysts. *Catal. Today* **195**, 93–100 (2012)
2. J. Xu, W. Zhou, Z. Li, J. Wang, J. Ma, Biogas reforming for hydrogen production over nickel and cobalt bimetallic catalysts. *Int. J. Hydrol. Energy* **34**, 6646–6654 (2009)
3. N. Gokon, Y. Osawa, D. Nakazawa, T. Kodama, Kinetics of CO_2 reforming of methane by catalytically activated metallic foam absorber for solar receiver-reactions. *Int. J. Hydrol. Energy* **34**, 1787–1800 (2009)
4. D. San, M.J. Jose-Alonso, M.C. Illan-Gomes, Roman-Martines, Low metal content Co and Ni alumina supported catalysts for the CO_2 reforming of methane. *Int. J. Hydrol. Energy* **38**, 2230–2239 (2013)
5. A. Serrano-Lotina, L. Daza, Influence of the operating parameters over dry reforming of methane to syngas. *Int. J. Hydrol. Energy* **39**, 4089–4094 (2014)
6. S. Ozkara-Aydinoglu, E. Ozensoy, A.E. Aksaylu, The effect of impregnation strategy on methane dry reforming activity of Ce promoted Pt/ZrO_2 . *Int. J. Hydrol. Energy* **34**, 9711–9722 (2009)
7. L. Jin, Y. Li, P. Li, H. Hu, CO_2 reforming of methane on $\text{Ni}/\gamma\text{-Al}_2\text{O}_3$ catalyst prepared by dielectric barrier discharge hydrogen plasma. *Int. J. Hydrol. Energy* **39**, 5756–5763 (2014)
8. I. Luisetto, S. Tuti, E.D. Bartolomeo, Co and Ni supported on CeO_2 as selective bimetallic catalyst for dry reforming of methane. *Int. J. Hydrol. Energy* **37**, 15992–15999 (2012)
9. A.R. Gonzales, Y.J.O. Asencios, E.M. Assaf, J.M. Assaf, Dry reforming of methane on Ni-Mg-Al nano-spheroid oxide catalysts prepared by the sol-gel method from hydrotalcite-like precursors. *Appl. Surf. Sci.* **280**, 876–887 (2013)
10. K.Y. Koo, H.S. Roh, Y.T. Seo, D.J. Seo, W.L. Yoon, S.B. Park, A highly effective and stable nano-sized $\text{Ni/MgO-Al}_2\text{O}_3$ catalyst for gas to liquids (GTL) process. *Int. J. Hydrol. Energy* **33**, 2036–2043 (2008)
11. T.V. Reshetenko, L.B. Avdeeva, Z.R. Ismagilov, A.L. Chuvilin, V.A. Ushakov, Carbon capacious $\text{Ni-Cu-Al}_2\text{O}_3$ for high temperature methane decomposition. *Appl. Catal. A* **247**, 51–63 (2003)
12. A.E. Castro, M.E. Luna, Iriarte, Carbon dioxide reforming of methane over a metal modified $\text{Ni-Al}_2\text{O}_3$ catalyst. *Appl. Catal. A* **343**, 10–15 (2008)
13. Y.H. Taufiq-Yap, U. Sudarno, Z. Rashid, Zainal, $\text{CeO}_2\text{-SiO}_2$ supported nickel catalysts for dry reforming of methane toward syngas production. *Appl. Catal. A* **468**, 359–369 (2013)
14. M.S. Fan, A.Z. Abdullah, S. Bhatia, Catalytic technology for carbon dioxide reforming of methane to synthesis gas. *ChemCatChem* **1**, 192–208 (2009)

Part XXIII
Materials for Energy Saving

Effects of Cobalt on the Crystalline Structures of the Ni-Mn-In Giant Magnetocaloric Heusler Alloys

Amila Madiligama, P. Ari-Gur, V. Shavrov, V. Koledov, Y. Ren, S. Calder and A. Kayani

Abstract The giant inverse magnetocaloric effect driven by a merged magneto-structural transformations in Ni-Mn-In-Co Heusler alloys, makes them highly promising as solid state refrigerants near room temperature. Knowledge of the crystallographic behavior of these alloys at a broad temperature range is critical to the understanding of the giant magnetocaloric effect. In this study, three Ni-Mn-In-Co alloys were investigated by neutron and synchrotron diffraction techniques. The chemical compositions of the alloys, determined by the Rutherford Backscattering Spectrometry (RBS) technique, were $\text{Ni}_{41}\text{Mn}_{39}\text{In}_{12}\text{Co}_8$, $\text{Ni}_{48}\text{Mn}_{34}\text{In}_{12}\text{Co}_6$ and $\text{Ni}_{52}\text{Mn}_{25}\text{In}_{16}\text{Co}_7$. The austenitic (A) phase of all three alloys was cubic $\text{L}2_1$ ($\text{Fm}\bar{3}\text{m}$). Martensitic (M) phase of the $\text{Ni}_{41}\text{Mn}_{39}\text{In}_{12}\text{Co}_8$ alloy was a mix of 8M and 6M modulated monoclinic structures, while the other two alloys had a M composed of a mix of 7M and 5M modulated monoclinic structures. All modulated structures belong to the $\text{P} 1\ 2/m\ 1$ space group. Site occupancy refinements of the A phases of all three alloys, revealed that almost all the Co atoms ($\sim 97\%$) occupy the regular Ni (8c) sites. In the studied temperature range (50–250 K) of the M phase of the $\text{Ni}_{41}\text{Mn}_{39}\text{In}_{12}\text{Co}_8$ alloy has very low magnetization. Also, no antiferromagnetic ordering was observed in the neutron diffraction refinement of the M phase. Therefore by eliminating the possibilities of ferromagnetism and antiferromagnetism, it is concluded that the M phase of the $\text{Ni}_{41}\text{Mn}_{39}\text{In}_{12}\text{Co}_8$ alloy is spin glass.

A. Madiligama (✉) · P. Ari-Gur · A. Kayani
Western Michigan University, Kalamazoo, MI 49008, USA
e-mail: amila.bandara@wmich.edu

V. Shavrov · V. Koledov
Kotelnikov Institute of Radio-Engineering and Electronics of RSA, Moscow, Russia

Y. Ren
Advanced Photon Source, Argonne National Laboratory, 60439 Argonne, IL, USA

S. Calder
Quantum Condensed Matter Division, Oak Ridge National Lab, Oak Ridge, TN, USA

1 Introduction

Magnetic cooling technology based on the Magnetocaloric Effect (MCE), has been known for more than a century. Even so, a proof of concept of a feasible magnetic cooling system, working near room temperature, was first introduced in 1997 [1]. The growth this technology depends on suitable magnetocaloric materials; those are readily available, durable, economically feasible, and work under moderate magnetic fields. A large magnetocaloric effect is usually exhibited by magnetic materials that undergo first-order magneto-structural phase transformations [2].

Among other competitors, which exhibit first-order magnetic phase transitions, Ni-Mn-X (X = In, Sb, Sn) Heusler alloys gain considerable attention because of their first-order, metamagnetic phase transformations, which occurs near room temperature [3]. For instance, large MCE was reported in a number of Ni-Mn-X alloys such as, Ni-Mn-In [4], Ni-Mn-Sn [5], and Ni-Mn-Sb [6]. At a certain temperature range, under sufficient magnetic field, Ni-Mn-X alloys transform from the low symmetry, martensitic (M) phase to higher symmetry austenitic (A) phase. The large cooling effect observed here is mostly due to the structural transition from M to A phase. Nevertheless, the contribution from spin alignment is also important as the driving force of the magnetostructural transformations [3]. For a wide range of compositions, the A phase of these alloys is cubic L₁ [3, 7–9]. However, depending on the compositions, the M structure could be a single phase or a mix of two phases. Non-modulated L₁ [9], 5M modulated orthorhombic [8, 10], 5M [3, 8], 6M [9] and 7M modulated monoclinic [8], and a mix of 5M and 7M modulated martensite [7] are some of the structures reported for the M phase. The substitution of a small percentage of Co for Ni in Ni-Mn-X alloys significantly increases the MCE [3]. Additionally, Co makes it possible to tune the M transformation temperature [11]. To develop these Ni-Mn-In-Co alloys as better magnetocaloric materials, a thorough understanding of the effects of Co substitution on crystalline structure and magnetic ordering is essential. Thus, the primary objectives of the present study were to determine the structures, chemical order, and magnetic ordering of the M phase as a result of Co substitution.

2 Experimental Techniques and Sample Preparation

Polycrystalline samples were prepared by the arc-melting method. Sample 03 (Ni₄₁Mn₃₉In₁₂Co₈) was used in the as-cast state. The others were heat treated by annealing for 50 h at 1020 K. The chemical compositions of the alloys were determined by the RBS technique using 15 MeV O⁺⁴ ion beam. The RBS experiment was carried out at the 6 MeV tandems Van de Graaff accelerator at Western Michigan University. The RBS data were analyzed by SIMNRA [12]. Neutron diffraction measurements of the Ni₄₁Mn₃₉In₁₂Co₈ alloy were carried out in the high-resolution constant wavelength (0.15374 nm) neutron powder diffractometer

HB2A at Oak Ridge National Laboratory [13]. Data were collected at different temperatures in the range, 50–600 K. In situ synchrotron diffraction measurements of the $\text{Ni}_{48}\text{Mn}_{34}\text{In}_{12}\text{Co}_6$ and $\text{Ni}_{52}\text{Mn}_{25}\text{In}_{16}\text{Co}_7$ alloys were carried out at beamline 11-ID-C of the Advanced Photon Source at Argonne National Laboratory [14], using a wavelength of 0.0108040 nm. Diffraction data were collected at different temperatures and under different magnetic fields. Rietveld refinements of both the neutron and synchrotron diffraction data were carried out using GSAS [15] and GSAS EXPGUI [16].

3 Results and Discussion

In the RBS experiment, the projectile ion type, energy of the ion beam and scattering angle were selected to maximize the energy resolution between scattered ions from the Ni and Co atoms, which have similar atomic masses. The chemical compositions of the alloys determined by the RBS technique are summarized in Table 1.

A critical aspect of this experiment was the accurate determination of site occupancies of the Co atoms. Even small changes in the magnetic interactions of Co with other atoms with different magnetic moments (Ni and Mn) greatly affects the magnetic behavior. Three different crystallographic sites, 4a, 4b, and 8c, (regular sites of Mn, In and Ni respectively), can potentially be occupied by the Co atoms. To determine the chemical order, site occupancy refinements of the neutron diffraction data of the $\text{Ni}_{41}\text{Mn}_{39}\text{In}_{12}\text{Co}_8$ alloy, collected at 3 different temperatures (600, 450 and 400 K) in the A phase, were carried out. The site occupancy refinements of the A phase of the other two alloys were carried out using their synchrotron diffraction data collected at 300 K. In the refinements, all the possible ways of occupying a crystallographic site by each atom were considered; the results are summarized in Table 2. The site occupancy results revealed that ~97% of the substituted Co atoms occupy the regular Ni sites and the rest in the Mn sites. This observation is in good agreement with the formation energy calculations of the A phase carried out by J. Bai et al., that studied the site preference of Co in Ni-Mn-Ga alloy [17]. In all 3 alloys, the regular In sites are occupied by both Mn and In atoms, with approximately 50% of each Mn and In. Mn atoms occupy all 3 sites. However,

Table 1 Summary of the RBS analysis of the 3 alloys, calculated elemental compositions

Alloy	Incident/scattering angle (°)	Ni	Mn	In	Co
$\text{Ni}_{52}\text{Mn}_{25}\text{In}_{16}\text{Co}_7$	0/150	52.19 ± 0.40	24.89 ± 0.62	16.02 ± 0.23	6.96 ± 0.98
$\text{Ni}_{41}\text{Mn}_{39}\text{In}_{12}\text{Co}_8$	0/150	40.68 ± 0.30	39.22 ± 0.23	11.60 ± 0.12	8.50 ± 0.65
$\text{Ni}_{48}\text{Mn}_{34}\text{In}_{12}\text{Co}_6$	0/150	47.98 ± 0.33	33.74 ± 0.30	12.38 ± 0.27	5.96 ± 0.90

Table 2 Summary of the site occupancy refinements of the alloys (Ni₅₂Mn₂₅In₁₆Co₇-01, Ni₄₈Mn₃₄In₁₂Co₆-02, and Ni₄₁Mn₃₉In₁₂Co-03) in the A phase at different temperatures

Alloy	T (K)	Cyst. Site	Occupation of each site (%)				Elemental composition (%)			
			Ni	Co	Mn	In	Ni	Co	Mn	In
01	300	4a	37.68	0	62.32	0	52.40	7.42	24.10	15.51
		4b	0	0	33.95	62.05				
		8c	85.96	14.80	0	0				
02	300	4a	15.40	0	84.60	0	48.05	5.81	34.19	11.95
		4b	0	0	52.17	47.83				
		8c	88.40	11.6	0	0				
03	400	4a	3.31	1.32	95.6	0	39.90	8.71	39.20	11.70
		4b	0.81	0	53.3	46.8				
		8c	79.3	16.8	4.03	0				
	450	4a	5.11	0	94.9	0	40.80	8.06	39.60	12.00
		4b	0	0	51.3	48				
		8c	79	16.1	6.04	0				
		4a	2.58	0	97.4	0				
	600	4b	0	0	52.1	47.2	40.30	8.39	39.50	11.80
		8c	79.2	16.8	4.16	0				

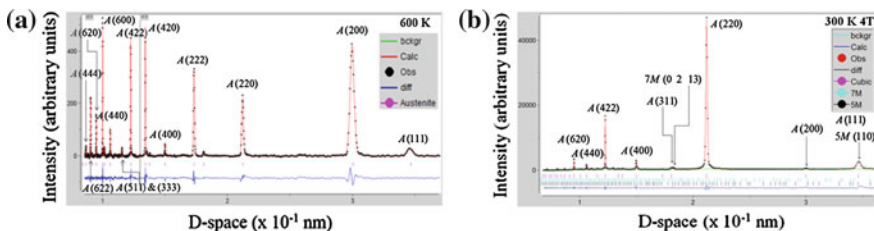


Fig. 1 Refinements of the A phase of two alloys. **a** Neutron diffraction of the Ni₄₁Mn₃₉In₂Co₈ alloy collected at 600 K and **b** synchrotron diffraction of Ni₅₂Mn₂₅In₁₆Co₇ alloy collected at 300 K under 4 T applied magnetic field

most of the Mn atoms are concentrated in the regular Mn sites. Compositions calculated by site occupancy refinements show a good agreement with the values obtained by RBS analysis. The final compositions of the alloys were determined to be Ni₄₁Mn₃₉In₂Co₈, Ni₄₈Mn₃₄In₁₂Co₆ and Ni₅₂Mn₂₅In₁₆Co₇ (Fig. 1).

The crystalline structures of Ni₄₁Mn₃₉In₁₂Co₈ alloy at various temperatures in the range from 50 to 600 K was found by refinements of the neutron diffraction data; while the structures of the other two alloys were found by refinements of their synchrotron diffraction data. Above the M transformation temperature, the structure of all 3 alloys was found to be cubic L₂₁ (Fm³m) with similar lattice parameters. In the refinements of modulated M structures, the following steps were taken to reduce the number of refinement parameters [18–20]: (1) the lattice modulation occurs

Table 3 Agreement factors [16] of the refinements and lattice parameters of different phases

Alloy	T (K)	Structure	a (nm)	b (nm)	c (nm)	β (°)	R_{wp}	R_p	χ^2
01	300	A	0.599	0.599	0.599	90	6.7	4.2	3.3
	205	5 M/7 M	0.451/ 0.427	0.580/ 0.548	2.254/ 2.863	89.12/ 91.05	2.9	1.8	1.1
02	300	A	0.599	0.599	0.599	90	5.7	4.2	4.6
	230	5 M/7 M	0.450/ 0.427	0.577/ 0.551	2.252/ 2.859	89.26/ 91.28	3.0	1.9	1.2
03	600	A	0.601	0.6007	0.601	90	4.9	3.6	3.1
	250	6 M/8 M	0.440/ 0.443	0.554/ 0.557	2.582/ 2.3.288	93.65/ 91.05	1.9	1.4	1.2

along the [001] direction of the monoclinic unit cell (the [110] direction of the A phase), (2) both x and y coordinates of all atoms in the M phase were allowed to refine, while the z coordinate was kept constant, (3) because the modulation involves the periodic transversal displacements of (001) atomic layers, the amplitude of modulation of every atom in that plane was taken to be the same value. Crystalline structures of the M phase of $\text{Ni}_{48}\text{Mn}_{34}\text{In}_{12}\text{Co}_6$ and $\text{Ni}_{53}\text{Mn}_{25}\text{In}_{15}\text{Co}_7$ alloys were found to be a mixture of two monoclinic structures with 5M and 7M modulations (P 1 2/m 1). Even though they have significantly different compositions, their crystalline structures and lattice parameters are very similar. The M crystalline structure of the $\text{Ni}_{41}\text{Mn}_{39}\text{In}_{12}\text{Co}_8$ alloy was different from the rest. It was a mix of 6M and 8M modulated monoclinic structures (P 1 2/m 1). All modulated martensite have similar **a** and **b** lattice parameters. However, the **c-axis** and the modulation vary. Lattice parameters of all the structures in both phases and the agreement factors [16] of the respective refinement cycle are summarized in Table 3.

Below 250 K, $\text{Ni}_{41}\text{Mn}_{39}\text{In}_{12}\text{Co}_8$ alloy is a mixture of M phases. According to the thermomagnetic measurements, the magnetization of the M phase is very low compared to the A phase [21]. Therefore, the possible magnetic structures for the M phase of this alloy are either antiferromagnetic or disordered spin glass. Three of the constituent atoms of this alloy, (Ni, Mn, and Co), have net magnetic moments that interact with the neutrons. If there is any antiferromagnetic ordering present in the M phase, there should be extra diffraction peaks that belong to the antiferromagnetic ordering because the magnetic structure is enlarged compared to the M crystalline structure. Refinement of the neutron diffraction data (Fig. 2a) collected below the M transformation temperature (250 K), shows a very good agreement with the experimental diffraction pattern even at the small d spacing values (Fig. 2b). No additional diffraction peaks which could belong to the antiferromagnetic ordering were observed. Therefore, by elimination of other possibilities, it can be concluded that the M phase of the $\text{Ni}_{41}\text{Mn}_{39}\text{In}_{12}\text{Co}_8$ alloy is spin glass. In order to confirm the spin glass nature of the M phase of this alloy, diffuse neutron diffraction studies are planned. In other circumstances, AC-SQUID would have been another option; it is impossible, however, to carry these measurements due to

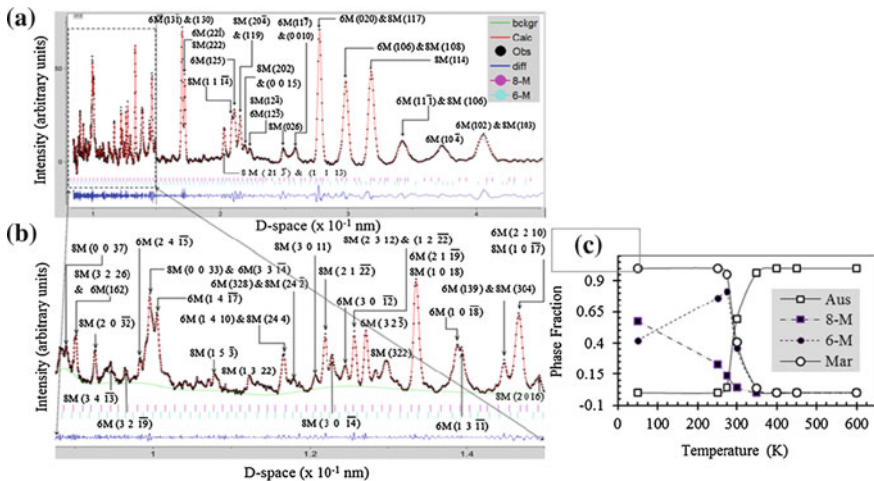


Fig. 2 **a** Rietveld refinements of neutron diffraction data of the Ni₄₁Mn₃₉In₁₂Co₈ alloy collected at 250 K (alloy is a mix of two martensitic phases: 6M & 8M martensite. **b** An enlarged portion of the diffraction pattern up to d spacing is 0.15 nm. **c** Variation of the phase fractions of the A and M phases from 50 to 600 K

the high transformation temperature. All the Co atoms reside in the regular Ni sites. Mn atoms are present in all 3 crystallographic sites. Ni atoms occupy both regular Ni and regular Mn sites. Therefore, the atoms which contribute to the magnetization, occupy randomly all crystallographic sites in the A phase. During the diffusionless M transformation, the magnetic disorder increases with the modulation of the M structures. This highly disordered distribution of magnetic moments in the M phase could lead to spin glass disorder.

Phase Fractions of the $\text{Ni}_{41}\text{Mn}_{39}\text{In}_{12}\text{Co}_8$ alloy at each temperature in the range from 50 to 600 K were calculated by the refinement. The studied temperature range can be classified into 3 regions (Fig. 2c). In the first region (600–350 K) the alloy is a single-phase austenite. In the second region (350–270 K), all 3 phases, austenite, 6M and 8M martensite co-exist. Nevertheless, the weight fraction of the 8M modulated phase is less than 5%. In the final region (275–50 K) two M phases, 6M and 8M modulations coexist. In this region, the weight fraction of the 6M martesite, the dominant phase below transformation temperature, decreases with decreasing temperature, which is compensated by the increase in the fraction of the 8M martensite and it dominates at 50 K. This behaviour of M phases results from the entropy of the structures; the highly ordered 8M modulated phase has lower entropy than the 6M modulated phase. Therefore, 8M modulated structures are energetically favorable at lower temperatures.

4 Conclusions

The compositions of the alloys determined by the RBS technique were found to be $\text{Ni}_{41}\text{Mn}_{39}\text{In}_{12}\text{Co}_8$, $\text{Ni}_{48}\text{Mn}_{34}\text{In}_{12}\text{Co}_6$ and $\text{Ni}_{52}\text{Mn}_{25}\text{In}_{16}\text{Co}_7$. These values show a good agreement with the compositions calculated by the site occupancy refinements. For all 3 alloys, the A structure was cubic $\text{L}2_1$ ($\text{Fm}\bar{3}\text{m}$). However, the M phase of the $\text{Ni}_{41}\text{Mn}_{39}\text{In}_{12}\text{Co}_8$ alloy was a mix of 6M and 8M modulated structures, while that of the other two alloys was a mix of 5M and 7M modulated monoclinic structures. No antiferromagnetic ordering was observed in the M phase of the $\text{Ni}_{41}\text{Mn}_{39}\text{In}_{12}\text{Co}_8$ alloy. According to the thermomagnetic measurements, magnetization of the M phase is very low compared to the A phase. Therefore, it could be concluded that the spin glass magnetic disorder in the M phase of the $\text{Ni}_{41}\text{Mn}_{39}\text{In}_{12}\text{Co}_8$ alloy. The modulations of the M structures and highly disordered distribution of the magnetic moments in the M phase could lead to spin glass. In order to confirm the magnetic ordering in the M phase, diffuse scattering studies of the $\text{Ni}_{41}\text{Mn}_{39}\text{In}_{12}\text{Co}_8$ alloy are planned.

Acknowledgments This work was supported by Award No. RUP1-7028-MO-11 of the US Civilian Research & Development Foundation (CRDF Global) and by the National Science Foundation under Cooperative Agreement No. OISE-9531011. The authors also wish to acknowledge the US National Science Foundation award number NSF-0831951. Research at Oak Ridge National Laboratory was sponsored by the Scientific User Facilities Division, Office of Basic Energy Sciences and the US Department of Energy. APS use was supported by the US Department of Energy, Office of Science, under Contract No. DE-AC02-06CH11357. Last but not least, the authors wish to acknowledge Amila Dissanayake of the Department of Physics, Western Michigan University for his help in RBS experiments.

References

1. K.A. Gschneidner Jr., V.K. Pecharsky, A.O. Tsokol, *Rep. Prog. Phys.* **68**, 1479 (2005)
2. V.K. Pecharsky, J.K.A. Gschneidner Jr., *Phys. Rev. Lett.* **78**, 4494 (1997)
3. J. Liu, T. Gottschall, K.P. Skokov, J.D. Moore, O. Gutfleisch, *Nat. Mater.* **11**(7), 620 (2012)
4. Z.D. Han, D.H. Wang, C.L. Zhang, S.L. Tang, B.X. Gu, Y.W. Du, *Appl. Phys. Lett.* **89**, 182507 (2006)
5. T. Krenke, E. Duman, M. Acet, X. Moya, L. Mañosa, A. Planes, *J. Appl. Phys.* **102**, 033903 (2007)
6. M. Khan, N. Ali, S. Stadler, *J. Appl. Phys.* **101**, 053919 (2007)
7. W. Ito, Y. Imano, R. Kainuma, Y. Sutou, K. Oikawa, K. Ishida, *Metall. Mater. Trans. A* **38**-A, 760 (2007)
8. J. Liu, N. Scheerbaum, D. Hinz, O. Gutfleisch, *Appl. Phys. Lett.* **92**, 162509 (2008)
9. W. Ito, M. Nagasako, R.Y. Umetsu, R. Kainuma, T. Kanomata, K. Ishida, *Appl. Phys. Lett.* **93**, 232503 (2008)
10. A.K. Nayak, A.K. Nigum, K.G. Suresh, *J. Phys. D Appl. Phys.* **42**, 035009 (2009)
11. R. Kainuma, Y. Imano, W. Ito, H. Morito, Y. Sutou, K. Oikawa, A. Fujita, K. Ishida, S. Okamoto, O. Kitakami, *Appl. Phys. Lett.* **88-19**, 192513 (2006)
12. M. Mayer, *SIMNRA User's Guide, Report IPP 9/113* (Max-Planck-Institut Fur Plasmaphysik, Garching, Germany, 1997)

13. V. Garlea, B. Chakoumako, S. Moore, G. Taylor, T. Chae, R. Maples, R. Riedel, G. Lynn, D. L. Selby, *Appl. Phys. A* **99**, 531 (2010)
14. Advanced Photon Source: <http://www.aps.anl.gov/Beamlines/Directory/>. (2004)
15. A.C. Larson, R.B. Von Dreele, General structure analysis system (GSAS), Los Alamos National Laboratory Report LAUR 86 (2004)
16. B.H. Toby, *J. Appl. Cryst.* **34**, 210 (2001)
17. J. Bai, J.M. Raulot, Y. Zhang, C. Esling, X. Zhao, L. Zuo, *Appl. Phys. Lett.* **98**, 164103 (2011)
18. S. Kaufmann, U. Rößler, O. Heczko, M. Wuttig, J. Buschbeck, L. Schultz, S. Fähler, *Phys. Rev. Lett.* **104**, 145702 (2010)
19. L. Righi, F. Albertini, S. Fabbri, A. Paoluzi, *Mater. Sci. Forum* **684**, 105 (2011)
20. L. Righi, F. Albertini, E. Villa, A. Paoluzi, G. Calestani, V. Chernenko, S. Bessegini, C. Ritter, F. Passaretti, *Acta Mater.* **56**, 4529 (2008)
21. A. Kamantsev, V. Koledov, E. Dilmieva, A. Mashirov, V. Shavrov, J. Cwik, I. Tereshina, V. Khovaylo, M. Lyange, L. Gonzalez-Legarreta, B. Hernando, P. Ari-Gur, *EPJ Web of Conferences* **75**, 04008 (2014)

Analysis of the External Magnetic Field Influences on the Measurements Realized with a Single Strip Tester (SST) Using Finite Element Modeling

Veronica Manescu (Paltanea), Gheorghe Paltanea, Dorina Popovici and Gabriel Jiga

Abstract In this article it was studied the magnetic influence of an electromagnetic coil on the measurements, realized with a single strip tester. One major difficulty in modeling of the magnetic materials is the magnetic hysteresis. As a consequence, it was used the Frohlich-Kennelly model for defining the hysteresis of the soft magnetic material, from which is manufactured the magnetic core of the electro-technical devices. A numerical study, based on finite element analysis, is proposed in order to model a Single Strip Tester (SST). For this it was made a geometrical description based on technical data of a SST developed by Brockhaus Messtechnik, which measures magnetic properties of silicon iron strips with an area of $280 \times 30 \text{ mm}^2$.

1 Introduction

A single strip tester represents a measuring device, used in the magnetic characterization of different types of soft magnetic alloys. It consists of a primary coil, which generates the magnetic field, a secondary coil, used to measure the magnetic flux density that is produced by the sample and a magnetic yoke. In the national and international measurement standards have been adopted variously types of yokes. In literature have been investigated horizontal, single, double, and symmetrical yokes or vertical single and double C-yokes. The magnetic measurements are performed according to the standard regulations DIN 50462, which specifies a sinusoidal waveform for the magnetic polarization, measured with the secondary coil [1–3].

The yokes of the device must be made of strip-wound cut cores or stacked isolated sheets, in order to minimize the influence of the eddy currents. The specific energy losses of the magnetic core are much smaller than the losses of the

V. Manescu (Paltanea) · G. Paltanea · D. Popovici (✉) · G. Jiga
Politehnica University of Bucharest, 313 Splaiul Independentei, Bucharest, Romania
e-mail: karina_popovici@yahoo.com

specimen. Therefore, high-quality electrical steel or iron-nickel alloy is used. The main advantages, compared to the Epstein frame, are lower specimen mass, easier preparation and installation of the sample. The standardized SST yoke, according to IEC 60404-3 [4] regulations, is 500 mm long and wide. It is designed for samples with a minimum length of 500 mm. A square specimen allows measurement in and perpendicular to the rolling direction. Specimens with a reduced width can also be measured. For a sufficient measuring signal, they should cover at least 60 % of the yoke width. In practice down-scaled frames for smaller specimens sizes are also used [1, 2].

There are two main methods of measurement of magnetic field strength in sheet sample: magnetizing current and H-coil methods [5–7]. For the Brockhaus device the magnetic field H is determined according to Ampere's law, from the magnetizing current value I_1 :

$$H = \frac{N_1}{L_m} I_1 = \frac{N_1}{R_s L_m} U_1, \quad (1)$$

where N_1 is the number of turns of the excitation winding and L_m is the mean length of the magnetic flux path.

The number of windings and the magnetic length of the coil are determined by the geometry of the coil system. The necessary current is provided by a power amplifier and is measured by means of a precision resistor R_s (shunt), which is unaffected by temperature changes and electromagnetic interferences. The used voltage U_1 is digitalized with a data capture system and with automatic dynamic adjustments it enables exact measurement of the voltage with a digital resolution of 12 Bits [3].

The magnetic polarization J is determined by measuring the voltage U_2 induced in the secondary winding of the coil system:

$$\frac{dJ}{dt} = -\frac{U_2}{N_2 A_m} \Rightarrow J = -\frac{1}{N_2 A_m} \int_0^t U_2 dt, \quad (2)$$

where N_2 is the number of turns and A_m is the mean cross-section area of the measuring coil. Through a feedback loop it is ensured that the form factor of the magnetic polarization is kept at a value of 1.11, according to IEC 60404-3.

The Frohlich-Kennelly model provides a constitutive law for magnetic saturation, which depends on the variation of the magnetic field, and has been widely used for studying the nonlinear properties for a variety of magnetic applications. Under the Frohlich-Kennelly model, saturation begins to occupy the entire conducting domain even at low-moderate applied fields. Based on (3), one can calculate the variation of the magnetization \mathbf{M} in the laminated sample:

$$\mathbf{M} = \frac{M_s \mathbf{H}}{(C + |\mathbf{H}|)} \quad (3)$$

and also the magnetic permeability of soft magnetic materials:

$$\mu_r(\mathbf{H}) = 1 + \frac{I_s}{\mu_0(C + |\mathbf{H}|)} \quad (4)$$

where M_s is the saturation magnetization, I_s is the saturation polarization and C is a material constant determined by experiments. For the implementation of the SST a bi-dimensional geometry was created and studied in quasistatic state. To simulate the external magnetic field it was used a coil with perpendicular currents in the neighborhood of the single strip tester.

2 Modeling

It was carried out a numerical modeling using COMSOL Multiphysics to analyze the influence of external magnetic field on the measuring device. The software allows solving partial differential equations of electromagnetism on complex geometries taking into account the laws of material behavior. A two dimensional geometric structure, analyzed under the quasistatic state, was implemented. The 2D modeling assumes a dimension on $0z$ axis which is large compared with the other dimensions ($0x$ and $0y$). The electric currents are parallel to the $0z$ axis and magnetic field \mathbf{H} and magnetic flux density \mathbf{B} are perpendicular. Under these conditions the leakage flux is neglected along the $0z$ axis (Fig. 1).

The bi-dimensional problem with perpendicular currents has a geometric structure with the following principal domains (Fig. 2): CO1 and CO2 the yokes of the Single Strip Tester made from iron, R4 and R5 excitation (primary) coil made from copper, R2 and R3 measurement (secondary) coil for magnetic flux density made also from copper, R1 non-oriented silicon iron sheet and R7 and R8 external magnetic field coil.

It was introduced the magnetic permeability of the silicon iron sheet (R1) as a scalar expression according to the Frohlich-Kennelly model, by taking into account that the two parameters of the model C and I_s have the following values:

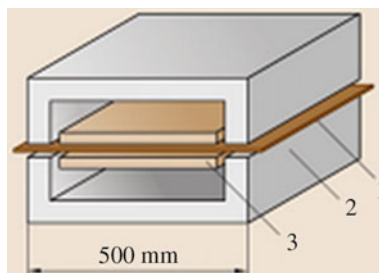


Fig. 1 Single sheet tester, 1 specimen, 2 yoke frame, 3 magnetizing and measuring coils [1]

Fig. 2 The 2D geometry of the problem

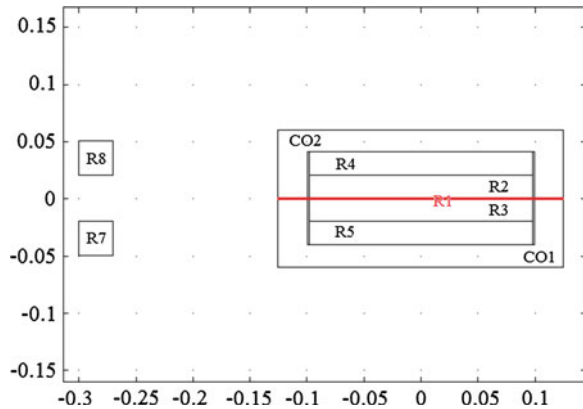
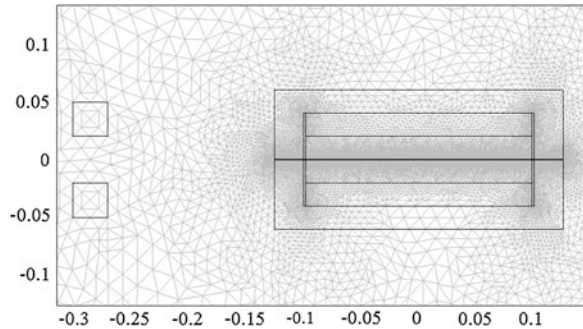


Fig. 3 The generated mesh consisting in 56,248 triangular elements



$C = 0.05 \times 10^4$, $I_s = 2.03$ T. On the boundary of the problem was set the magnetic insulation condition and the mesh of the problem consist of 56,248 elements (Fig. 3).

3 Results and Discussions

The experimental analysis was divided in three parts. In the first part it was considered that the single strip tester is placed in zero external field environment, after that the magnetic flux density is measured in the hysteretic material (R1), considering that the current density in the primary coil is $J = 9221.9$ kA/m² (Fig. 4). The obtained maximum value for the magnetic polarization is $I = 0.26$ T.

In the second case it is considered that the primary coil of the SST has zero current density value and only the external magnetic field coil is activated at a

Fig. 4 The variation of magnetic polarization in FeSi sheet (R1) in the absence of the external magnetic perturbation (first case)

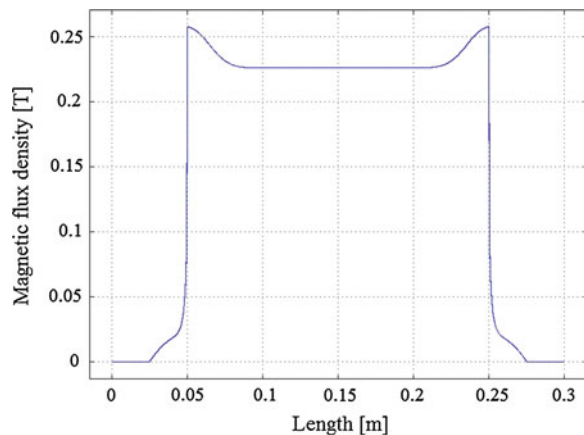
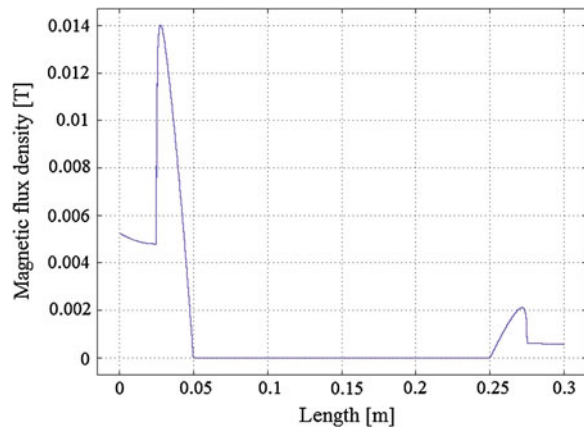


Fig. 5 The variation of magnetic polarization in FeSi sheet (R1) in the presence of the external magnetic perturbation (second case)



current density $J_{\text{ext}} = 19,444 \text{ kA/m}^2$. It can be observed that the magnetic polarization, measured in the sample, has zero value (Fig. 5).

In the third case (Fig. 6) the two energy sources (external coil and primary coil) are active and similar values of the magnetic polarization are found in the sample. It can be appreciated that the yokes of the single strip tester realize a good shielding from external magnetic fields.

In Fig. 7 are represented the contour lines of the magnetic potential A in the case of higher external field.

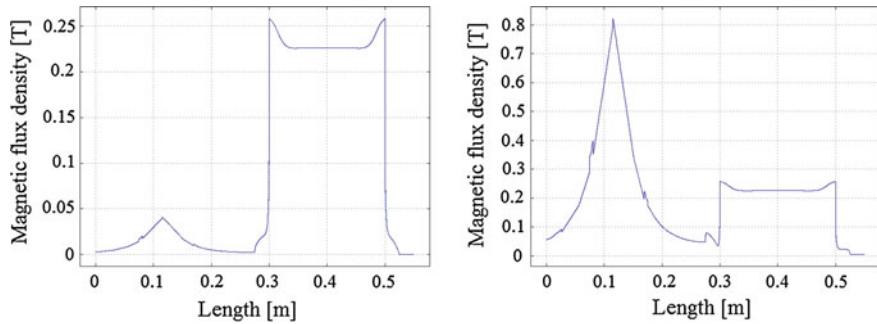


Fig. 6 The variation of magnetic polarization in electrical steel sheet (R1) (third case) in the presence of the two active energy sources, external coil (left figure $J_{\text{ext}} = 19,444 \text{ kA/m}^2$; right figure $J_{\text{ext}} = 388,880 \text{ kA/m}^2$) and primary coil ($J = 9221.9 \text{ kA/m}^2$). The maximum value of the magnetic polarization obtained in the sample is 0.26 T, the same as in the first analyzed case

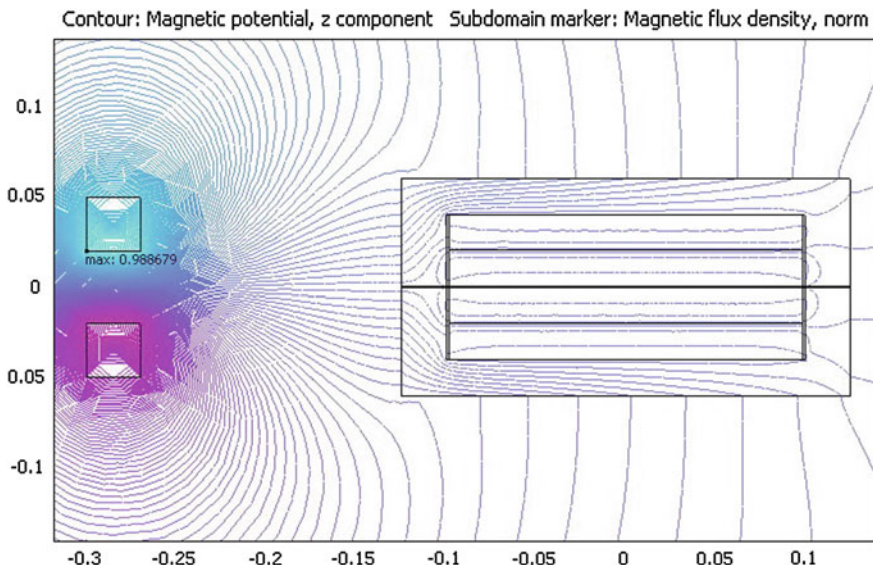


Fig. 7 The contour lines of the magnetic potential in the case of two energy sources: external coil ($J_{\text{ext}} = 388,880 \text{ kA/m}^2$) and primary coil ($J = 9221.9 \text{ kA/m}^2$)

4 Conclusions

The accuracy and reliability of the model can be done by comparing the Figs. 4, 5 and 6. One can appreciate that the yokes of the single sheet tester realize a good shielding from external magnetic fields, because the profile and the value of magnetic flux density is the same in all three figures.

Acknowledgments The work has been funded by the Sectoral Operational Programme Human Resources Development 2007-2013 of the Ministry of European Funds through the Financial Agreement POSDRU PERFORM/159/1.5/S/138963.

References

1. H. Czichos, T. Saito, L. Smith, *Springer Handbook of Materials Measurement Methods*, (Springer Science+Business Media, 2006)
2. H. Czichos, T. Saito, L. Smith, *Springer Handbook of Metrology and Testing* (Springer Verlag, Berlin, 2011)
3. F. Fiorillo, *Measurement and Characterization of Magnetic Materials*, (Elsevier Academic Press, 2004)
4. IEC 60404-3, Methods of measurement of the magnetic properties of electrical steel strip and sheet by means of a single sheet tester, 2009
5. Brockhaus, Single Strip Tester, User's manual
6. J. Sievert, M. Enokizono, Experimental studies on single sheet testers, *Anales de fisica*, 102–104 (1990)
7. T. Nakata, Y. Ishihara, M. Nakaji, T. Todaka, Comparison between the H-coil method and the magnetizing current method for the single sheet tester. *J. Magn. Mat.* **215–216**, 607–610 (2000)

Part XXIV
Thermoelectrics

Energy Harvesting from Open Fireplaces

Marco Nesarajah and Georg Frey

Abstract This contribution presents a green barbecue or fireplace, which recovers electrical energy from the heat of the fire by the use of thermoelectric generators (TEGs). TEGs use a temperature difference to generate electrical energy based on the Seebeck effect. To generate a sufficient temperature difference, the fireplace was designed to ensure a good heat transfer to the hot TEG sides. Furthermore, CPU cooling elements using heat pipes were mounted on the cold TEG sides. As a side effect, the recirculation of the preheated air from these coolers into the fire can improve the burning process. The gained energy is used to load a mobile device via an USB plug and to supply 12 V DC via a vehicle plug. Possible applications of the system are of course barbecues where the DC power may be used to support mobile devices or entertainment systems. A more serious application is found in rural areas without electrification where the electricity generated during cooking may replace expensive batteries or environmentally unfriendly diesel generators. Moreover, a simulation model for the green barbecue is created. The contribution will describe the construction of the green fireplace and the developed simulation model. Finally the simulation results are compared with real test readings and an outlook on further developments to a controlled fireplace is given.

1 Introduction

In this paper, a typical German barbecue fireplace is modified into an Energy Harvesting System (EHS) based on Thermoelectric Generators (TEG). The purpose is to use the heat of the fire to generate electrical energy, e.g. for loading mobile

M. Nesarajah (✉) · G. Frey
Chair of Automation and Energy Systems, Saarland University,
66123 Saarbrücken, Germany
e-mail: marco.nesarajah@aut.uni-saarland.de

G. Frey
e-mail: georg.frey@aut.uni-saarland.de

phones, supplying an amplifier to hear music or to supply an ice box. A further possibility is to store the generated energy in a rechargeable battery. This could be interesting for rural areas without electrification. With the gained energy during cooking, it is perhaps possible to replace environmentally unfriendly diesel generators or at least to reduce their usage.

TEGs are thermoelectric devices consisting of many thermocouples. One thermocouple consists of two thermolegs, mostly one p- and one n-doped leg, connected together with a metal bridge. The outer endings of a TEG are ceramic plates. Electrically the thermolegs are connected in series and thermally in parallel. For the temperature range of this fireplace, TEGs with the thermoelectric material Bi_2Te_3 are used [1]. In order that the TEGs produce electrical energy, a temperature gradient has to be applied over the TEGs. This means, one side has to be kept hot and the other cold. At this, the decisive physical effect is the Seebeck Effect, which says that with a temperature difference over the TEG an electrical voltage will occur (an electromotive force). The advantages of TEGs are their high reliability, their simple scalability and the low amount of maintenance required, due to the lack of mechanical or fluid components. Their disadvantage is their low efficiency of maximal 5 % and the relatively high cost.

In the following Sect. 2, the construction of the green fireplace is described, system challenges are highlighted and their solutions are delivered. In Sect. 3, the developed simulation model is depicted and simulation results are compared with test data. As simulation environment Dymola® is used, which is based on the open modeling-language Modelica®. Section 4 concludes with a summary as well as an outlook for further work on the green barbecue.

2 Construction of the Energy Harvesting System

2.1 Mechanical Setup

The presented EHS is based on TEGs and is attached on a common used fireplace for barbecue. To generate electricity, TEGs need a large temperature difference between their sides, meaning they have a hot and a cold side. Consequently, the most important thing for the mechanical setup is a very good thermal connection to the hot side as well as good heat dissipation on the cold side of the TEGs. Figure 1a shows the purchasable fireplace during measurements for finding out the optimal position at the outside walls to attach the TEGs. The measurements give good results and locate the optimal place for TEG mounting, however it was ascertained that the original material of the wall (steel) is unsuitable. The reason for this lies in the thickness of the steel wall. It is so thin, that it deforms under thermal stress and thus reduces the thermal connection to the TEGs extremely. Instead, a thicker copper plate is installed in the outside wall, cf. Figure 1b. Based on the thickness, there is no relevant deformation and thus, an optimal thermal connection to the

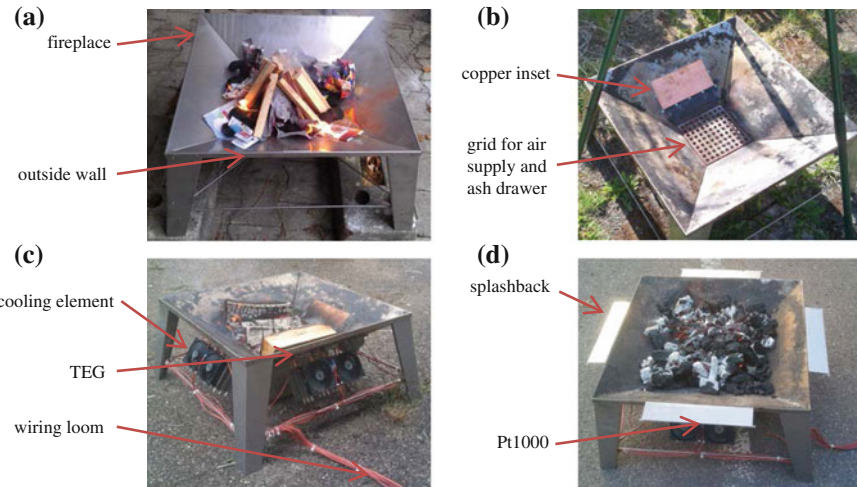


Fig. 1 The four figures show the development of a simple fireplace to a fireplace with a TEG-based EHS. **a** the original fireplace, **b** the modified fireplace with the first copper inset, obvious is the grid at the *bottom* of the fire bowl, **c** the almost finished EHS, now the TEGs and the cooling elements are installed and the cables go via a wiring loom to the switch box, **d** the current EHS containing splashbacks to protect the fans and Pt1000 temperature sensors, two (hot and cold) on each wall side

TEGs is ensured. Furthermore, the heat transfer through copper is substantial better than with steel and so the initially measured temperature only reduces slightly, although the material is now significantly thicker. Also visible in Fig. 1b is the grid on the bottom of the fire bowl. It serves for air supply to the fire and to catch the ash in the underlying ash drawer. After having the good heat transfer from the fire to the hot TEG side, a cooling method for the cold TEG side is necessary. As a liquid cooling system is excluded due to the complex structure for a portable device like the fireplace, air cooled elements are preferred. In general, there are two different types of air cooling methods, passive and active air cooling. To preserve a very high temperature difference, an active cooling method with a forced convection is selected. It is to note that the EHS has to raise minimum the energy, which will be consumed by the cooling elements, to run self-sufficient. As cooling element, a high-end CPU cooling element, known from computer applications is used, [2]. It has a heat spreader which is directly contacted with the TEG. From the heat spreader there are in total six heat pipes transferring the heat to a multitude of cooling fins, which are cooled down by a controllable fan. Figure 2 shows a close-up picture of the TEG and the cooling element in the laboratory and Fig. 1c shows the mounted cooling elements at the fireplace. TEGs, which are located between copper insets and cooling elements, are not visible. Totally, there are eight TEGs attached, two at each wall side. To protect the fans of fat splashes, splashbacks are

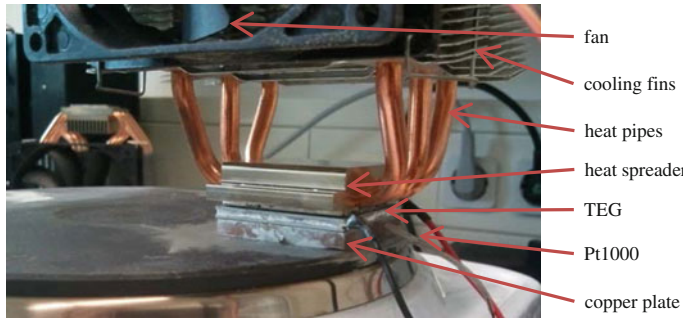


Fig. 2 Close-up picture of the TEG and the cooling element; also visible is a Pt1000 temperature sensor

mounted on each side as shown in Fig. 1d. Moreover, Pt1000 temperature sensors are installed to measure the hot and cold TEG side temperatures. They are needed later for controlling purposes. All cables (TEG, Pt1000, fans) are collected at one corner and go from there as one wiring loom to the switch box.

In the prospective EHS, the preheated air of the cooling elements should be recirculated into the fire through the grid (see Fig. 1b). This will improve the combustion process and even increase the hot side temperature. The description of the electrical setup follows in the next subsection.

2.2 Electrical Setup

The wiring loom (see Fig. 1c) goes from the fireplace to the switch box, whereas the current version of it is depicted in Fig. 3. There, the crucial elements of the electrical setup are marked. In this EHS, there are effective seven TEGs to supply the 12 V power line and one TEG to supply the 5 V power line. This one TEG is connected with an electrical circuit, which produces from the inconstant, fluctuating TEG input a constant 5 V power output. This 5 V power is directly connected with the USB plug and serves to supply mobile devices. The remaining TEGs supply the 12 V power line. They store their energy in a battery, which supplies the remaining electrical components (amplifier, 12 V vehicle plug, the fans of the cooling elements). Test runs have already shown that the system runs stable without a battery, meaning the TEGs output supplies directly the electrical components. At the moment, the battery is however needed to start the system.

For controlling purposes a microcontroller is already installed. To optimize the produced power a maximum power point tracking (MPPT) converter is under construction, based on the research of Montecucco and Knox [3].

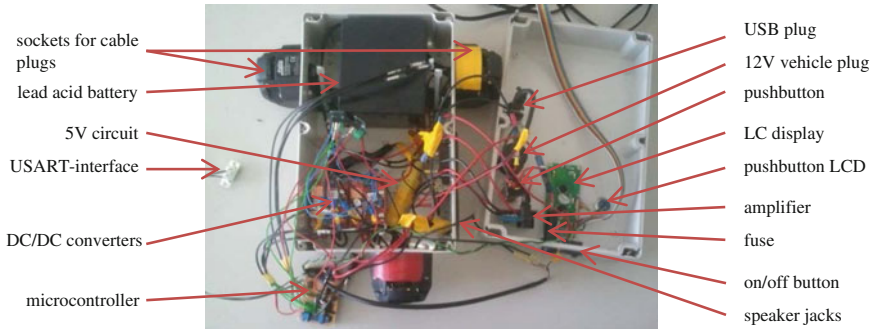


Fig. 3 Look into the inside of the switch box, all important elements are marked

3 Simulation Model

An object-oriented model of an EHS was already developed in Modelica[®]/Dymola[®] for an oil-fired household heating system in [4]. The modeling of the thermoelectric device itself is presented in [5] and was extended in [6]. Based on these, a simulation model for the green barbecue is now created. Real measurement data of the hot TEG side temperature (see Fig. 4) are feed into the simulation model. Figure 5 shows the structure of the simulation model, which is almost identical to the electrical structure in Sect. 2.2. In the simulation model, there are no consumers modeled. Instead of the DC/DC converters, the simulation model contains an ideal MPPT model, which means that the load resistance will be adapted in an optimal way to the internal resistances of the TEGs.

The maximum produced power of the 12 V power line during the measurement is at the 20th min and is 5.7 W. In the simulation model, with an ideal MPPT, the produced power at the 20th min reaches 23.49 W. This is a very interesting fact, showing that under the same conditions, but using an MPPT converter instead of simple DC/DC converters, the power output will significantly increase. By adding a variable load on the real structure and changing the load value by hand, this fact has been already confirmed. The development and integration of an MPPT is consequently very important for an increase in efficiency. A further increase in efficiency is possible with the control of the cooling fans. A control strategy is already developed, but is not yet implemented on the microcontroller.

4 Summary and Outlook

This paper presents an Energy Harvesting System attached to an open fireplace. It is shown that the system runs autarkic and additionally delivers extra energy, which can be stored in a battery or can be consumed by a variety of possibilities (e.g. to

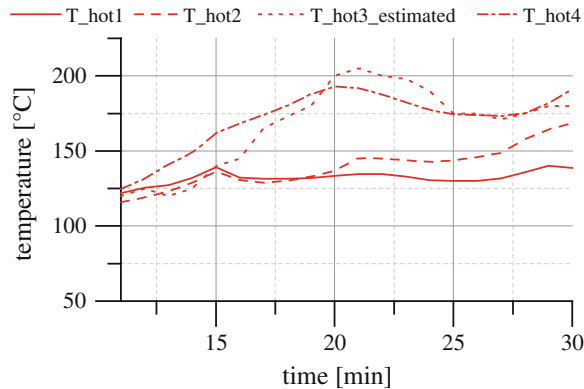


Fig. 4 Measured hot side temperatures at the green barbecue, except temperature of the third side (T_hot3 is estimated, due to a faulty sensor)

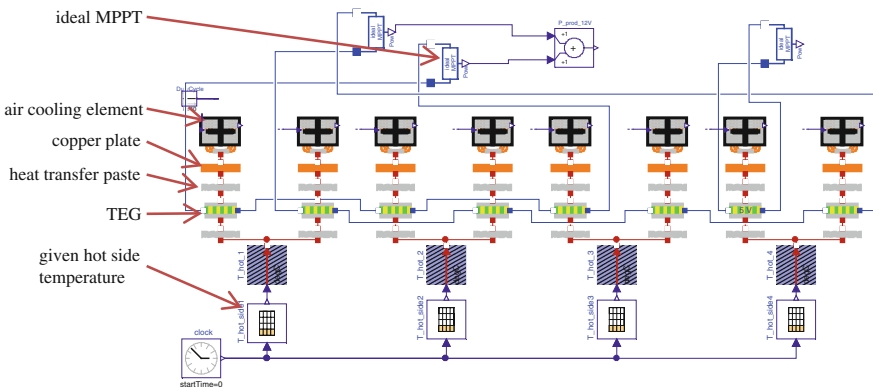


Fig. 5 Simulation model in Modelica®/Dymola®; the measured hot side temperatures are given to the model

load mobile devices, to use the entertainment system or to supply a 12 V DC via a vehicle plug). The prospective EHS will have an MPPT and a control for the cooling fans for a maximum power generation output. Moreover, the preheated air will be recirculated to the fire and thus will also increase the performance of the system. The green barbecue is a first prototype and shows that the application of TEG-based EHSs is a promising field of research.

References

1. Thermalforce, *Homepage thermalforce*. Available: <http://www.thermalforce.de/>
2. Scythe Co. LTD, *Scythe Katana 4: product page*. Available: <http://www.scythe-eu.com/unternehmen/firmenprofil.html>
3. A. Montecucco, A. Knox, Maximum power point tracking converter based on the open-circuit voltage method for thermoelectric generators, *IEEE Trans. Power Electron.*, 99 (2014) (DOI:10.1109/TPEL.2014.2313294)
4. M. Nesarajah, G. Frey, Object-oriented modeling of an energy harvesting system based on thermoelectric generators, in *Springer Proceedings in Physics, International Congress on Energy Efficiency and Energy Related Materials (ENEFM2013)*, ed. by A.Y. Oral, Z.B. Bahsi, M. Ozer (Springer International Publishing, Cham, 2014), pp. 211–216
5. F. Felgner, L. Exel, M. Nesarajah, G. Frey, Component-oriented modeling of thermoelectric devices for energy system design. *IEEE Trans. Ind. Electron.* **61**(3), 1301–1310 (2014)
6. M. Nesarajah, L. Exel, G. Frey, Modelica® library for dynamic simulation of thermoelectric generators, in *Proceedings of the 11th European Conference on Thermoelectrics*, ed. by A. Amaldi, F. Tang (Springer International Publishing, Cham, 2014), pp. 213–217

Part XXV
Energy Saving in Buildings

The Impact of Installing Variable Frequency Drives for Cooling Towers in Kuwait on Energy Consumption

Eitidal Al-Bassam

Abstract The application of Variable Frequency Drive (VFD) as a water and energy efficient control scheme for the operation of cooling towers (CTs) was experimentally verified using summer and winter season field data. A major concern during CT operation is the large flow of air required for cooler water temperatures that help in improving the performance of air-conditioning systems. However, this improved performance increases fan power and water consumption in dry and hot countries, such as Kuwait, due to the self-cooling property of air that results in additional water evaporation. The technical viability of VFDs for the CTs as a water and energy efficient device and to quantify the potential savings of water and electricity were experimentally verified using summer and winter season field data. The CT fans in the selected site, originally fitted with dual speed motor, were retrofitted with VFDs. The site was adequately instrumented to assess energy and water consumption of the cooling production system while operating the CTs' fans with constant air flow alternatively either at low or high speed through the building management system (BMS), and the VFD scheme keeping the CT leaving water temperature constant. The results were in favor of selecting CT with VFD as the best option to reduce electricity and water consumption.

1 Introduction

Cooling Towers (CTs) are the devices most commonly used to reject heat from water. It is used for water-cooled (WC) air-conditioning (AC) systems, and industrial process systems. CT performance is affected by wet-bulb temperature, dry-bulb and/or relative humidity, heat load, circulating water rate (GPM), range and approach [1] and interference such as wind and dust. While the power consumption in CT is affected by the CT fan, which is required for the circulation of

E. Al-Bassam (✉)

Energy and Building Research Center, Kuwait Institute for Scientific Research,
Kuwait City, Kuwait
e-mail: ebassam@kisr.edu.kw

air through the CT, in addition to the condenser water pump, which is required to pump the water to the stack heights of a CT and a pressure drop across the water nozzles. On other hand, the water consumption in CT is affected by many factors which are the evaporation process, blowdown, and drift process.

2 Description of the Selected Site and Its Cooling System

The Airport Commercial building at the Kuwait International Airport was selected for the study. The cooling production system in this building is comprised of four chillers, each having a rated capacity of 354 RT, and an additional chiller with a rated capacity of 490 RT. The five chillers have an equal number of primary chilled water pumps, condenser water pumps, and CTs; however, their chilled water and condenser water distribution systems are common. Originally, every CT fan was to be operated with two speed motors, which is connected to the chiller control panel through a dual speed starter. The chiller control panel has a built-in microprocessor-based controller that gives a signal to the BMS to switch between the fan speeds for automatically maintaining the leaving water temperature from CT. Subsequently, the CT fans were retrofitted with the VFD and controlled by BMS through a manual switch. The VFD capacity for the four CTs was 75 kW and the fifth large CT had a VFD capacity of 55 kW.

3 Scope of Work

The CT fans were retrofitted with VFDs and controlled by BMS through a manual switch, as shown in Fig. 1. Experimental data collection was carried out for the year-round operation. CTs were operated on alternate days with constant air flow, BMS, and with the VFDs. The performance parameters including heat rejection, makeup water consumption, power demand, and approach were analyzed. Water and power savings were estimated by operating CTs for alternative days with conventional and VFD schemes. The total power savings was based on the combined power of the chiller, the fan motor, and the energy cost of water production. Detailed system description and instruments installed are available in the article [2].

4 Results

By operating CTs alternatively with BMS mode with two speeds low and high with constant cooling tower leaving water temperature (CTLWT), and the VFD mode, the electricity and water consumption was obtained. The fan operating conditions are shown in Table 1. Results have been calculated on hourly basis for the peak summer and winter days for the electricity and water consumption along with the

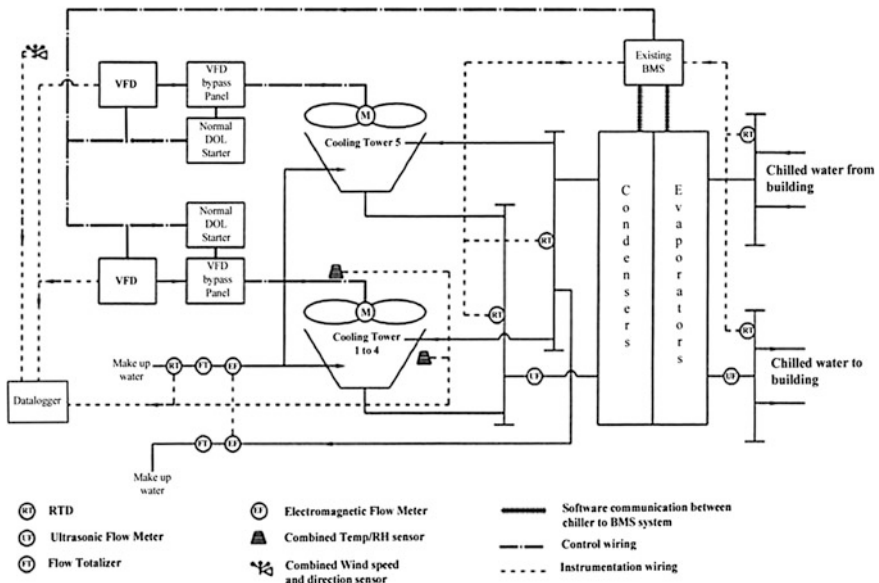


Fig. 1 Control and instrumentation diagram at the airport commercial building

Table 1 Fan operating conditions for the airport site

Operation mode	Design flow rate (%)	Controlling parameter	Fan power-actual (kW)	Fan power-theoretical (kW)
Normal high speed	100	None	98.5 ($16.6 \times 4 + 32.1$)	98.5
Normal low speed	50	None	32.6 ($5.6 \times 4 + 11.2$)	12.3
VFD controlled	Variable 40–100	Supply water temperature	7.6–98.5	6.3–98.5

environmental and operation factors. Furthermore, the results have been analyzed on a day-to-day basis as summary data or average values for different modes of operation. As an example, the daily energy consumption (E_d) of the cooling production system is estimated as summation of hourly cooling production system (P_s) where,

$$P_s = P_{\text{chiller}} + P_{\text{CTF}} + P_{\text{cwp}} + P_w$$

P_{CTF} , represent the cooling tower fan power, P_{cwp} , represents condenser water pump power, P_w , represents the equivalent power to generate desalinated water 22 kWh/m³ [3].

Hence, $E_d = \sum P_s$

The daily cooling production (Q_{cD}) and daily water consumption (W_{eD}) are estimated using summation of hourly chiller cooling capacity (Q_e) and W_e . Specific water consumption (ω), the water consumption per unit of cooling production

(l/RTh) and system power ratings (PRs), they have been considered as the two important parameters of optimization (Tables 2 and 3). Their daily average values can be estimated as follows:

$$\omega = W_{eD}/Q_{cD}$$

$$PRs = E_d / Q_{eD}$$

Table 2 Summary data for different operation modes at summer time

Operation mode	BMS	VFD
Operating hours (h)	367	713
Average DBT (°C)	39.69	39.3
Average WBT (°C)	21.98	21.61
Cooling production (RTh $\times 10^3$)	279.21	534.2
Chiller energy consumption (kWh $\times 10^3$)	220.01	407
Average chiller PR (kW/RT)	0.79	0.76
Average chiller loading (%)	73.2	75.38
Average CT return WT (°C)	33.12	33.24
Average CT supply WT (°C)	29.92	30.38
Average chilled water supply WT (°C)	7.19	7.66
Average fan power (kW)	39.90	17.76
Average CT approach (°C)	8.99	8.82
Average CT PR	0.05	0.0155
Specific water consumption (L/RTh)	10.77	9.35
Average system PR (kW/RT)	1.08	0.98

Table 3 Summary data for different operation modes at winter time

Operation mode	BMS	VFD
Operating hours (h)	168	96
Average DBT (°C)	18.31	14.55
Average WBT (°C)	11.64	9.68
Cooling production (RTh $\times 10^3$)	47.7	23.5
Chiller energy consumption (kWh $\times 10^3$)	35.5	16.9
Average chiller PR (kW/RT)	0.75	0.72
Average chiller loading (%)	82.9	69.2
Average CT return WT (°C)	34.41	32.29
Average CT supply WT (°C)	29.7	28.4
Average chilled water supply WT (°C)	7.93	6.92
Average fan power (kW)	4.63	0.84
Fan energy (kWh)	777.4	81
Average CT approach (°C)	18.06	18.72
Average CT PR	0.02	0.003
Total water consumption (L $\times 10^3$)	275.4	124
Specific water consumption (L//RTh)	5.84	5.27

5 Conclusion

VFD can satisfy the variable load requirements and, thereby, consume minimum energy of the CT fan motor, permitting it to perform at a predetermined level of demand for optimum efficiency of operation. The results were promising for water and electricity savings when using VFD control scheme in CT during summer and winter seasons. In summer, the savings for the specific water consumption (l/h/RT), average CT fan power and average cooling system power rating were 45.7, 92 and 21.8 % respectively. Whereas, the savings at winter time were 9.7 and 81.85 % for the specific water consumption and average CT fan power respectively.

Acknowledgments The author would like to thank the Kuwait Foundation for Advancement of Sciences and the Ministry of Electricity and Water for funding this study. Also, we would like to thank the project team members of this study for their cooperation.

References

1. ASHRAE, Fundamentals, american society of heating, refrigeration and air—conditioning engineers, Atlanta, Georgia, USA, 2004
2. E. Albassam, R. Asseri. Measurable energy savings of installing variable frequency drives for cooling towers' fans, compared to dual speed motors. *Energy and Buildings* **67**, (2013)
3. G.P. Maheshwari, M. Al-Ramadhan, M. Al-Abdulhadi, Energy requirement of water production in dual- purpose plants. *Desalination* **101**, 133–140 (1995)

Solutions of Ground Floor for Energy Efficient Buildings—Economic Evaluation

Anna Sedlakova, Pavol Majdlen and Ladislav Tazky

Abstract Do you think that passive houses are inventions of recent years? It is not exactly true. Even if they use more advanced technology, some of the basic principles goes back hundreds years. History of passive houses have their roots in the 19th century, where the first building was not a building, but research ship of polar explorer Fridtjof Nansen called From in 1883. Walls and sandwich construction deck had thickness of 400 mm, which fulfill the function of thermal insulation layer of felt and linoleum fulfill the function of a vapour barrier. Glass treated windows were triple and worked there controlled ventilation with electric ventilators.

1 Introduction

A very important consideration is the amount and type of thermal insulation. Also the combination and location of construction details are important factors. Compliance with these requirements is the deciding factor that contributes to the optimization of the final solution. An analysis of the actual construction detail involves the effect of the position, mutual combination of thermal insulation as well as the overall solution and correct proposal of the construction detail. In our case it is a detail of an external wall, basement and floor slab which are in contact with each other. In total six cases were modelled, but only four cases in this paper are

A. Sedlakova · P. Majdlen · L. Tazky (✉)
Technical University of Košice, Civil Engineering Faculty,
Institute of Architectural Engineering, Košice, Slovakia
e-mail: ladislav.tazky@tuke.sk

A. Sedlakova
e-mail: anna.sedlakova@tuke.sk

P. Majdlen
e-mail: pavol.majdlen@dek-sk.com

shown that characterize the possible location of a mutual combination of thermal insulation in the construction detail of the ground slab to satisfy all building standards and construction requirements [1–3]

2 Versions of the Lower Structure

Version A: Establishment with thermal insulation on foundation and external wall. This method is used in Slovakia for ordinary. Thermal insulation of the external wall continues up to the lower edge of the base strip. Thermal insulation in the floor is laid on the upper surface of the base plate. Thermal insulation of external walls and in the floor is separated with external construction (Fig. 1—left).

Version B, C: Establishment with special block, with plinth insulation. Thermal bridge, which forms the cladding in contact with the base plate can be interrupted by calcium-silicate blocks, (foam glass). These methods of foundations can still be combined with plinth insulation respectively without this insulation (Fig. 1—right and Fig. 2—left).

Version D: Establishment on a layer of foam glass is a relatively new solution. Foam glass is poured into the tub which is lined with extruded polystyrene boards. Backfill is compacted in a ratio of 1:1.25. Thereafter reinforced concrete is poured on the backfill of foam glass (Fig. 2—right).

Version E: Second and relatively new way of establishment on tub of extruded polystyrene boards. Firstly, to prepare a suitable substrate that can form e.g. compacted embankment of gravel. On the prepared surface are first mounted side boards of extruded polystyrene (XPS). Subsequently individual sheets of XPS are

$$\theta_{si} \geq \theta_{si,N} = \theta_{si,80} + \Delta\theta_{si} \quad (1)$$

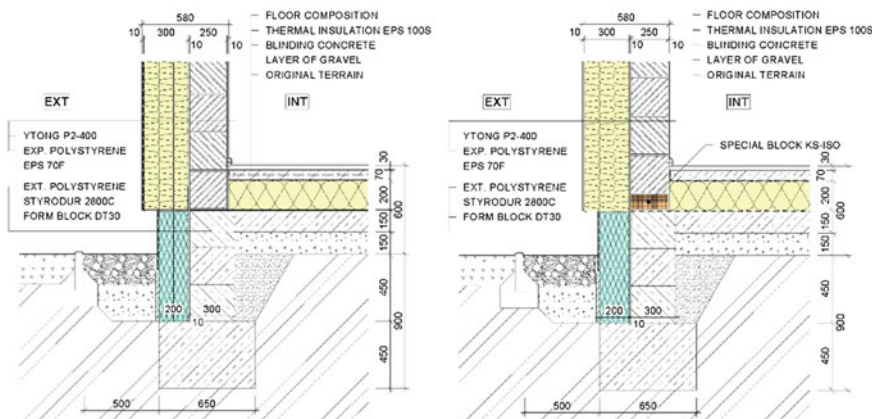


Fig. 1 Details of establishment version A (left) and version B (right)

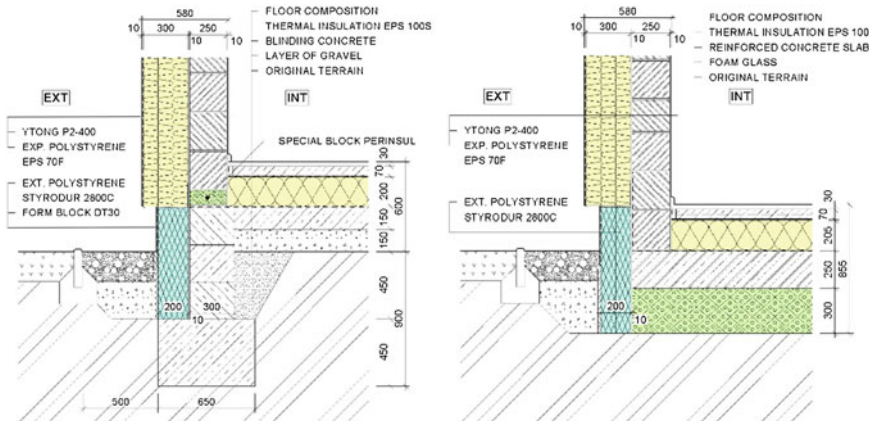


Fig. 2 Details of establishment version C (left) and version D (right)

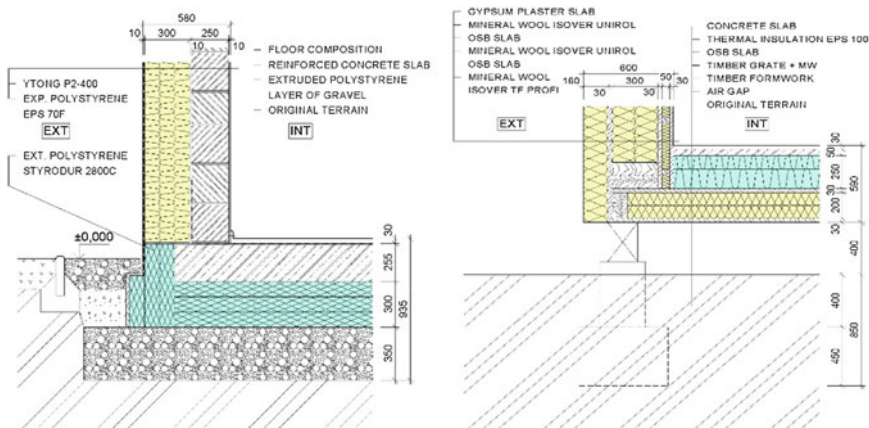


Fig. 3 Details of establishment version E (left) and version F (right)

stacked on the bottom of the tub. The rest of the tub is comprised of reinforced concrete that acts as the foundation slab (Fig. 3—left).

Version F: The last, but in this time relatively popular solution is the establishment on pilots. This type of foundation is used mainly for timber construction. A warm wooden floor is situated on the pilots which is contains an air gap. The entire wooden house is placed on the floor construction (Fig. 3—right).

Each designed versions of establishment was assessment to the critical temperature in critical corner. Each versions are satisfy the requirement in (1) from the building code STN 73 0540-2 (Figs. 4, 5 and 6).

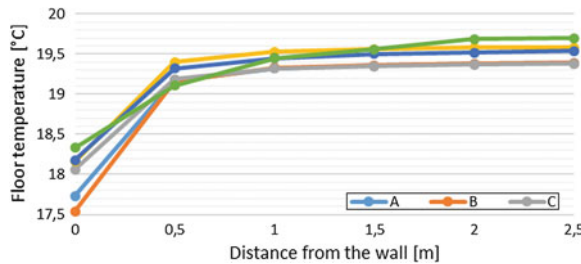


Fig. 4 Results of 2D modelling of details—temperature response of the floor

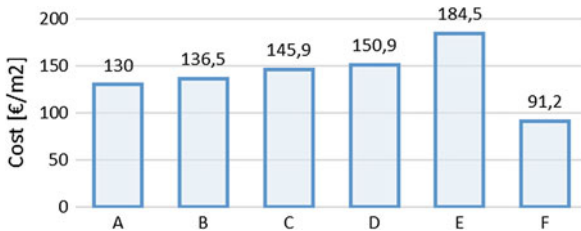


Fig. 5 Economic comparison of versions—cost €/m²

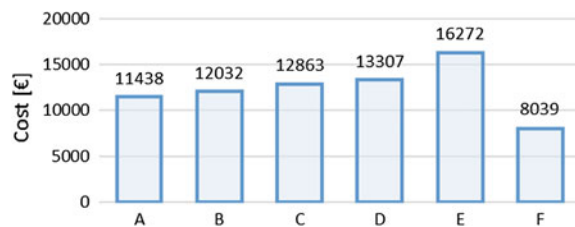


Fig. 6 Economic comparison of versions—total cost in €

3 Results of 2D Details Modeling in Psi-Therm

Boundary conditions Outside air temperature calculated in the winter to shall designate the location of the building, depending on the geographic location according to maps of temperature fields and, depending on altitude **Kosice 297 m above sea level** (2. temperature region), $\theta_e = -13$ °C. Calculated relative humidity of ambient air is determined by the ambient temperature as calculated: $\varphi_e = 84$ %. Calculation of the internal air temperature for the residential part of the building: $\theta_i = 20$ °C. Relative humidity of indoor air: $\varphi_i = 50$ %. Surcharge for heating temperatures dipped to decrease indoor air: **to 5** [4, 5].

Table 1 Results of economic comparison of each versions of establishment

Variants	Type of establishment	Costs (€)	Costs for 1 m ² (€)	%
Variant A	Establishment with thermal insulation of basis and external wall	11,438	130.00	100
Variant B	Establishment with special block KS-ISO KIMMSTEIN with plinth insulation	12,032	136.50	105
Variant C	Establishment with special block FOAMGLASS PERINSUL with plinth insulation	12,863	145.90	112
Variant D	Establishment on brash of foam glass	13,307	150.90	116
Variant E	Establishment on tub of extruded polystyrene boards	16,272	184.50	142
Variant F	Establishment on pilots	8,039	91.20	70

4 Economic Assessment

For each variant were developed itemized budgets, which are summarized in Table 1. Part of the budgetary costs were always earthworks, construction of horizontal (up to 1000 mm) and vertical load-bearing structures, thermal insulation, mortar, floor bearing plate. As part of the cost wasn't considered to labor costs for each operation.

It the starting variant is classic establishment, as seen from cost 100 %, can be in this case of alternative method of establishment achieved cost saving up to 30 %.

From the comparison it's clear that alternative means of establishing, by which the thermal bridge is eliminated by passing the vertical structure on the slab, may be compared with classical establishment, or for example added thermal insulation block in the first layer of masonry is significantly more favorable from the perspective of financial costs.

The choice of establishment variant of the house without basement depends on a number of parameters. As decisive are foundation conditions in location where we would like to build a house, selected structural system of the house. The aim of the article was to point for solutions of house establishment also in terms of heat loss and the amount of the costs to implement.

5 Conclusion

Thermal insulation is now a word that we heard all around particularly with respect to rising energy prices in line with long-term strategic goals of reducing emissions and improving energy efficiency in buildings. What is the subject of European Parliament and Council 2013/31/EU of 19th May 2010 on the energy performance of buildings. The European Union has committed to reduce by 2020 overall

greenhouse gas emissions by 20 % at least compared to year 1990. To the same date to reduce energy consumption in EU countries by 20 % and achieved in total energy consumption 20 % share of renewable energy sources. This can also contribute to solving the lower structure for a new generation of energy efficient buildings. The consumer model will be confronted with measurement in situ [2]. Based on the results of measurements and after fine-tuning simulations of the experimental building will be to obtain relevant results applicable in practice for the design of passive buildings, in compliance with basic hygienic requirements in terms of structures, internal environment and in terms of design and use of heating or ventilation systems.

Acknowledgments This article was written as a project solution entitled “The use of the virtual laboratory for designing energy-efficient buildings” Project code: 052TUKE-4/2013.

References

1. A. Antonova, Passive House for Latvia, Energy Efficiency and Technical-Economic Aspects, Thesis for the Degree of Master of Science. Latvia (2010)
2. H. Pifko, What is it Energy Efficient House. Paper presented at the 1st Conference of passive house, Bratislava, 14 Jun 2006
3. J. Smola, *Architecture of Passive Houses* (Bratislava, 2011)
4. J. Lstiburek, Building Science. Paper presented at the 7th North American Passive House Conference, Denver, California, 28 September 2012
5. A. Sedláková, M. Al Ali, Composite materials based on lightweight concrete, *Chemické listy*, vol. 105 (TUKE, Košice, 2011), pp. 445–447

Analysis of Air Velocity, Moisture and Thermal Regime in a Double-Shell Roof

Martin Kovac and Jaroslav Vojtus

Abstract This work was based on the need to gain a better understanding of the air velocity using CFD simulation as a form of verification of the functionality of ventilated air gaps in real constructions. The moisture regime of roofs with open air layers is theoretically assessed as satisfactory in terms of operational reliability by a sufficient margin. We used different simulation software in order to reveal local imperfections, in order to realize moisture diffusion from residential spaces through ceilings without a vapour barrier which would ensure the free flow of unwanted condensation on cold surfaces of the envelope leading to defects in the roof.

1 Introduction

Roof claddings of flat roofs are amongst the most important elements in building structures. They can be categorized as single or double skinned. Thermal analysis and evaluation in general is well known amongst professionals in the field of energy efficiency [1–3], but they become less erudite when the topic of double skinned roofs arises. The aim of this paper is to simulate the ventilation of air gaps and analyse the effects that ventilated roofs have on the thermal regime of roofs; for example, the roof cladding of a concrete panelled apartment building structural system P 01/14/15 commonly utilized in Slovakia. Roofs of the above mentioned building systems no longer meet thermal insulation requirements.

M. Kovac (✉) · J. Vojtus

Department of Architectural Engineering, Faculty of Civil Engineering, Technical University of Kosice, Vysokoskolska 4, 042 00 Kosice, Slovak Republic
e-mail: martin.kovac@tuke.sk

2 Structural Assembly of Prefabricated Buildings

The reason for this analysis is the recurrent failure of roof cladding for panel systems as a result of local defects, defects in the thermal insulation layer, ventilation and drainage and poor heat-moisture regime, hygiene discomfort in the form of water, moisture, and mould in apartments located directly under the roof. The aim is to clarify the implications of ventilation and thus verify whether defects are really due to the geometry of the double-skinned roof, which will aid in selecting the most efficient method of increasing the thermal insulation in the roof once renovation commences (Figs. 1, 2 and 3).

The roof is designed as a flat roof with a double skinned ventilated air gap. The roof is sloped slightly from the attics, with internal drainage to outlets located at the mid-span of each section. Thermal insulation in the form of perlite pillows is placed in the cavity of the roof. The air gap has a clearance height of 150 mm which is poorly ventilated (2 holes with a diameter of 60 mm for every panel). The upper skin consists of reinforced concrete panels on the roof which is covered with hydro-insulation in the form of bituminous sheeting. Thermo-technical parameters: Roof, $U = 0.52 \text{ W}/(\text{m}^2 \text{ K})$.



Fig. 1 Typical apartment block P 1.14/15 and details of ventilation openings



Fig. 2 Views above and below the air gap of the P 1.14/15 construction apartment block

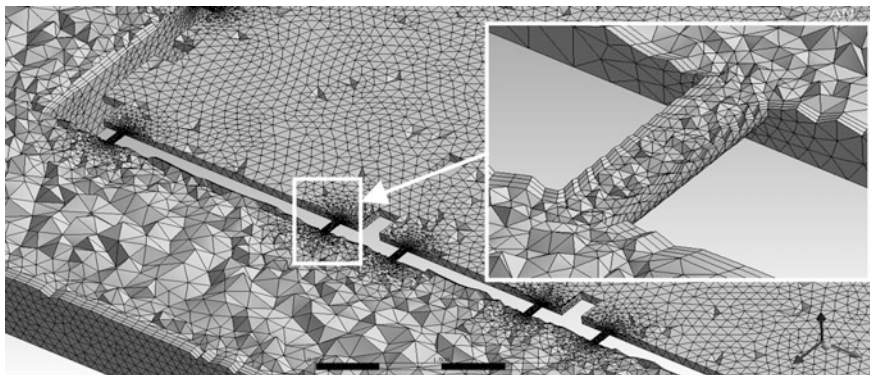


Fig. 3 Computational tetrahedral network incorporating a local network with finer openings for air intake and exhaust of the roof space

3 Details of 3D Modelling

Prerequisite: Based on the 2D thermal calculations it can be concluded that there is a situation—an external state (e.g. CALM), where condensation occurs on the lower surface of the upper skin of the roof resulting in condensed water that leaks into the living space! In addition it is possible that some of the water that pools in the air space of the roof originates from other sources!

For CFD (Computational Fluid Dynamics) [4] analysis, a geometric model with a corresponding geometry of the double-skinned flat roof was created. For the calculation an unstructured tetrahedral grid with local network densification was created at the openings for ventilation of the double skinned air gap. Since the object of CFD analysis was to obtain a graphical understanding of the air velocity in the air gap of the roof, a three-dimensional model was generated for an isothermal air stream. Boundary conditions for the air flow rate (wind induced) on the windward side varied between 1.0, 2.0 and 5.0 m/s. The standard wind speeds for Košice, ranges between 2.0 and 5.0 m/s [5]. The k-epsilon model is commonly used to describe the turbulent nature of the air flow. The results of CFD simulations were adopted after the residues were obtained with a min. power of 10–4, for the continuity equation, torque equation and the equation of turbulent kinetic energy and dissipation.

Initial and boundary conditions for the calculation:

• Initial temperature	20 °C
• Inlet velocity	1.0, 2.0, 5.0 m/s
• Heat transfer	Isothermal
• Turbulence model	k-epsilon
• Reference pressure	101,325 Pa
• Buoyancy	Non buoyant

4 Results of Modelling

The first step was to analyse the effects of a wind speed of 1.0 m/s on the roof. Figure 4 depicts the distribution of air velocity inside the double-skinned roof. Most of the roof space is unvented, with the exception of local spaces situated in close proximity to the air intakes, where air velocity reached a maximum of 0.17 m/s which is insufficient in relation to the roof area. At the same time the level of technical expertise incorporated at the time of construction should be taken into consideration. The air gap of the roof contains perlite insulation pillows that create air spaces, which may hold condensed water vapour. Inadequate roof ventilation, confirmed by the results of CFD simulations when considering wind speeds of 1.0 m/s, combined with poor thermal insulation properties of the roof cannot ensure the proper operation of the roof, without the risk of condensation and subsequent leaks into the residential space. If the very roof of the double skinned air gap simultaneously diffuses warm and humid air from the residential premises through any leaks between the prefabricated panels of the object, a risk of condensation in the roof arises, which is compounded by insufficient ventilation.

In the second step we used the next software called Mezera 2008 (Svoboda Stavební fyzika) in order to consider the risk of air condensation in the air gap of the double-shell roof. Initial results from Software Mezera 2008 say that there is not air condensation if the air velocity in the air gap is higher than 0.02 m/s. We used this value in order to display areas where the air velocity is lower than 0.02 m/s. You can see these areas in the next picture (Fig. 5). There is potential risk of air condensation. It is a state where the wind velocity is 1.0 m/s.

According to the retrieved data [5], the wind speeds for Košice varied between 2.0 and 5.0 m/s. Figure 6 reveals the effects of wind speeds of 5.0 m/s on the windward side of the roof. We see that the scope of the ventilated gap is wider than it was in the first case. Of course the question remains whether this is sufficient to

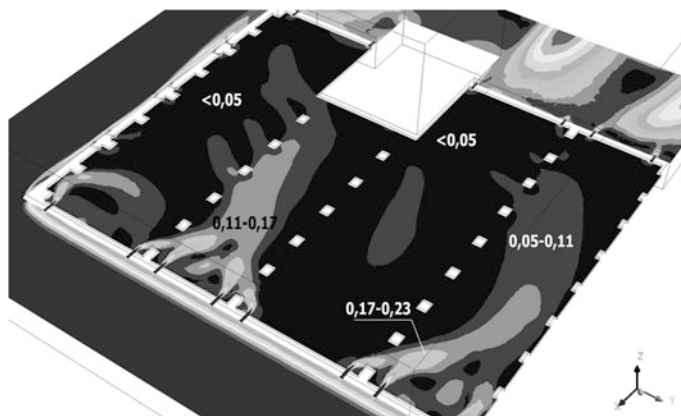


Fig. 4 Air velocity inside the double-skinned roof (wind speed 1.0 m/s)

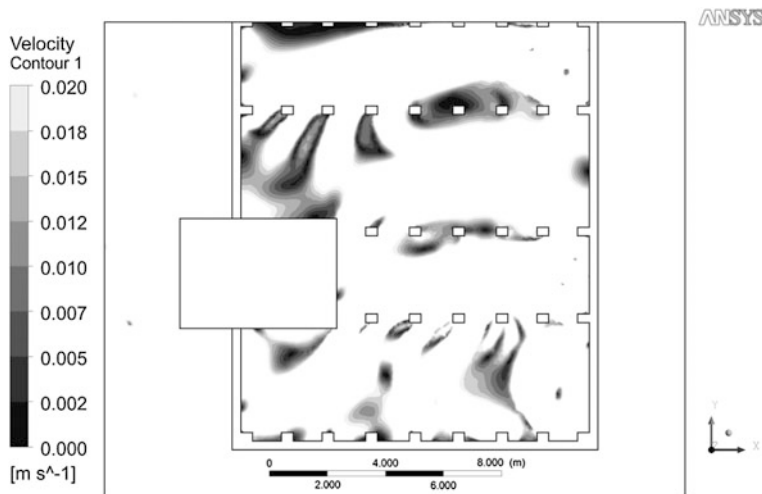


Fig. 5 Areas with air velocity lower than 0.02 m/s (wind speed 1.0 m/s)

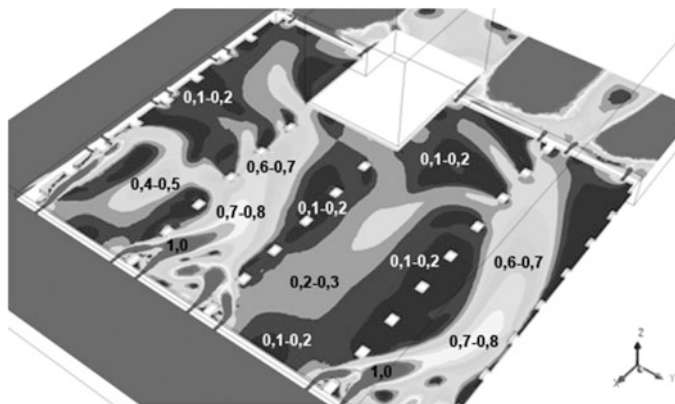


Fig. 6 Air velocity inside the double-skinned roof (wind speed 5.0 m/s)

dissipate the potential moisture occurring in the air gap of the double skinned roof. In the case where the wind velocity is 5.0 m/s we can see the ventilation of air gap which is more effective than in the case with the wind velocity at 1.0 m/s. Also in this case we use the results from the software Mezera 2008. There was calculated that the risk of condensation could be in the areas where the air velocity is lower than 0.02 m/s. If we look at the next picture (Fig. 7) we can see any areas where the air velocity is lower than 0.02 m/s.

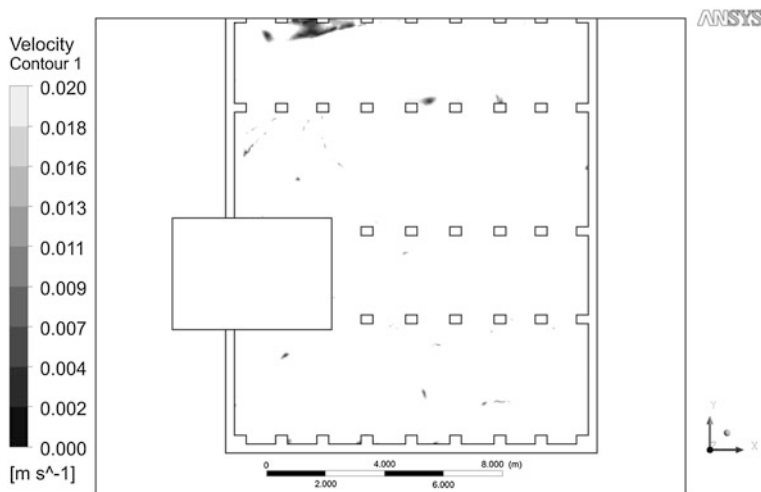


Fig. 7 Areas with air velocity lower than 0.02 m/s (wind speed 5.0 m/s)

5 Conclusion

We will continue in the analysis of thermal regime in the double-shell roof using CFD tool. In this article we only used CFD tool in order to gain results about air velocity in the air gap of double-shell roof. We would like to create a physical model of the roof with non-isothermal air flow where thermal properties of building construction are exactly defined. We could get some results about air temperature field in the air gap and also surface temperatures on the building constructions. On the base of these results we could analyse the function of double-shell roof more detailed.

Acknowledgments This article was written as a project solution entitled “The use of the virtual laboratory for designing energy-efficient buildings” Project code: 052TUKE-4/2013.

References

1. Ch. Diakaki et al., A multi-objective decision model for the improvement of energy efficiency in buildings. *Energy* **35**, 5483–5496 (2010)
2. Z. Chen et al., A multicriteria lifespan energy efficiency approach to intelligent building assessment. *Energy Build.* **38**, 393–409 (2006)
3. J. Morrissey, R.E. Horne, Life cycle cost implications of energy efficiency measures in new residential building. *Energy Build.* **43**, 915–924 (2011)
4. ANSYS CFX Introduction, Release 12.0, 2012, ANSYS Inc., Canonsburg, USA
5. STN 73 0540, 1–3: Thermal protection of buildings. Thermal performance of buildings and components. Part 1: Terminology, Part 2: Functional requirements, Part 3: Properties of environments and building products, SUTN 2012 (in Slovak)

Simulation of Energy Demand in a Shopping Centre—Case Study

Martin Kovac and Katarina Kovacova

Abstract The target of this contribution is the energy simulation of energy demand for the heating system in winter period and for the cooling system in summer period. The object of the energy simulation is the shopping centre situated in Kosice (Slovakia). It is solved the main passage of the centre that is basically the internal enclosed atrium connecting three stories. This space allows all customers to move in the centre and is also connected to the adjacent smaller shops. The passage has large glass surfaces on the exterior walls and on the roof. Mainly because of this state the interior is much overheated in summer period. There are proposed and analysed passive shading devices, there are solar window films. The energy simulation is elaborated in order to evaluate the yearlong operation of internal environment in term of energy demand.

1 Introduction

Energy savings are essential for the long term solution of the problem with use of energy. In buildings, to maintain a good indoor environment, energy is used for heating, cooling, lighting, ventilation. The important parts of buildings are windows that provide indoor daylight and a good view out. In the case of large glass surfaces they essential influence energy demand for cooling and heating [1]. The study results [2] have found that solar heat gains are important for saving energy for heating in buildings in temperate and cold climates. On the other side the large glass surfaces can also lead to an overheating of the building in summertime and result in poor thermal comfort. This problem can be solved by appropriate glazed area and shading devices. Equally, the study results [3] have found that energy demand for cooling is dominate in office buildings in cold climate like Oslo in Norway too.

M. Kovac (✉) · K. Kovacova

Department of Architectural Engineering, Faculty of Civil Engineering, Technical University of Kosice, Vysokoskolska 4, 042 00 Kosice, Slovak Republic
e-mail: martin.kovac@tuke.sk

2 Subject of a Case Study

The subject of this analysis is to know what is the influence of an exterior solar windows film on total energy demand of a passage in the shopping centre during the year. The space of a passage has large glass surfaces in the external walls and flat roof. This fact causes a large external load of a passage from direct sun beams during the summer months and consequently higher operation costs of cooling system too. Our target of this energy analysis is to know how much energy we can save for cooling system in the passage if we use exterior solar window films. Vice versa we want to know too how much energy we will need for heating system in the passage. Why? If we use exterior solar window film, we will reduce exterior solar gains during the summer. But we reduce exterior solar gains during the winter too. For our target of this article we used simulation software called DesignBuilder. This programme uses solution engine Energy Plus [4].

3 Geometrical Model

In the first step we created the geometrical model of a shopping centre in the simulation software DesignBuilder. The model of a shopping centre is shown in the next figure (Fig. 1). The space of a passage is an enclosed multi-stories space. The floor area of a ground floor is $3,267 \text{ m}^2$ and the total height of an atrium is about 17.0 m. The total inner volume of a passage is $64,322 \text{ m}^3$. The space of an atrium is displayed in the next figure like a gray block. And for this part were defined the boundary conditions of building constructions (Table 1). Dominating part of an external surfaces is glass.

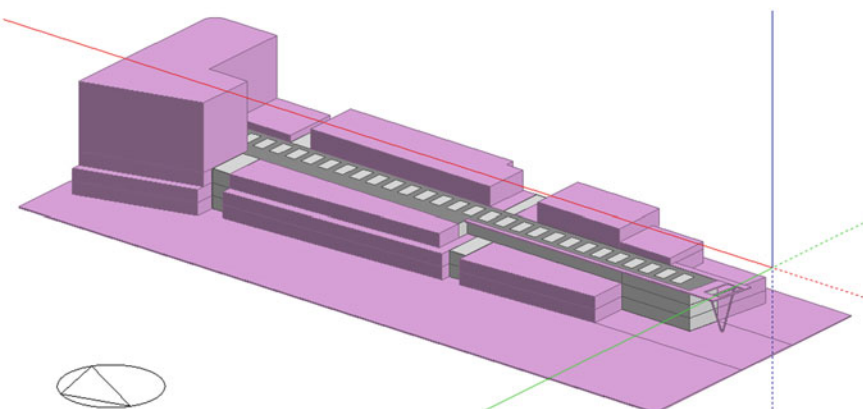


Fig. 1 Geometrical model of a shopping centre

Table 1 Coefficient of thermal transmittance of building constructions

Name of building construction	Coefficient of thermal transmittance U ($W/(m^2K)$)
Flat roof	$U = 0.2 \text{ W}/(\text{m}^2\text{K})$
Glass surfaces (nitrasklo climaplus 4S protect)	$U = 1.1 \text{ W}/(\text{m}^2\text{K})$

Table 2 Thermo optical properties of a glass surface

Nitrasklo climaplus 4S protect	Value
Solar heat gain coefficient (SHGC)	0.40
Shading coefficient	0.46

The most important factors in our energy analysis are the thermo optical properties of glass surfaces. The values were taken from the technical properties of windows and consequently were used in the programme (Table 2). In our proposed variant we use exterior solar window films on all glass surfaces in the external walls and flat roof in order to reduce external load from the sun during the summer period. The inner partitions which divide rooms with the same internal conditions were modelled as adiabatic constructions in DesignBuilder.

4 Parameters of an Internal Environment and HVAC

Parameters of an internal environment in the passage of a shopping centre are provided by using mechanical ventilation with the control of air temperature. Total volume flow rate of air is about $200,000 \text{ m}^3/\text{h}$ in the atrium of a shopping centre. The part of this volume flow rate of air is a fresh air at the value of 28 % or $56,000 \text{ m}^3/\text{h}$ ($30 \text{ m}^3/(\text{h}\cdot\text{person})$) (Fig. 2).

5 Analysis of an Energy Demand

Presented results in this part of an article are results from the simulation software DesignBuilder. These values describe how much energy (heat/cold) is needed to use in order to cover heat losses of a building in winter period or to cover heat load during the summer period if we apply exterior solar window films on glass surfaces. In this graph there was not calculated with any heat or cold source. We compared two states in term of energy demand in summer and winter. In the first step there was simulated the current state of an operation in the atrium. All thermal and optical properties of building constructions and parameters of internal environment are shown in the text above (Tables 1, 2, 4). In the second step there was simulated the proposed state of an atrium where the exterior solar window films were applied on all glass surfaces in the external walls and flat roof. Thermo optical properties of this

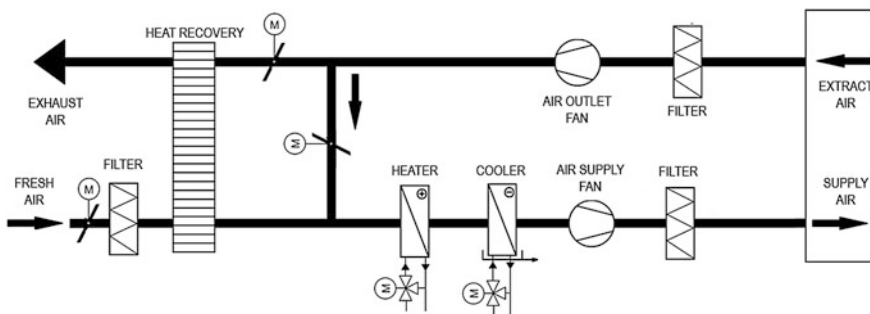


Fig. 2 Scheme of an air conditioning unit

Table 3 Thermo optical properties of solar window film [5]

Silver 20 exterior	Value
Transmission of solar	14 %
Reflection of solar	63 %
Absorption of solar	23 %
Shading coefficient	0.20

Table 4 Parameters of an internal environment in the atrium

Parameters	Value
Air temperature in summer (air conditioning unit is on)	22–26 °C
Air temperature in winter (air conditioning unit is on)	18–22 °C
Operation of mechanical ventilation	05:00 a.m. to 10:00 p.m.
Density people	4.0 m ² /person
Summer clothing	0.5 clo
Winter clothing	1.0 clo
Metabolic rate	140 W/person

film are shown in the table (Table 3) above. Regarding to the properties of solar window films we can reduce the energy demand for cooling at the value of 66 %. If we apply these exterior solar window films on all glass surfaces we will decrease external load from the direct solar radiation. But parallel we will decrease heat gains from the sun during the winter period too. So we decrease energy demand for cooling system in summer, but we increase the energy demand for heating in winter. And how much? The results from energy simulation of a building in DesignBuilder showed us that if we use solar window films we will increase the heat demand for heating about 18 %. You can see the total results in the next graph (Fig. 3).

The energy demand for cooling in summer period covers internal and external loads which are occupancy, solar radiation and external ventilation in cases, when

Fig. 3 Energy demand in winter and summer period

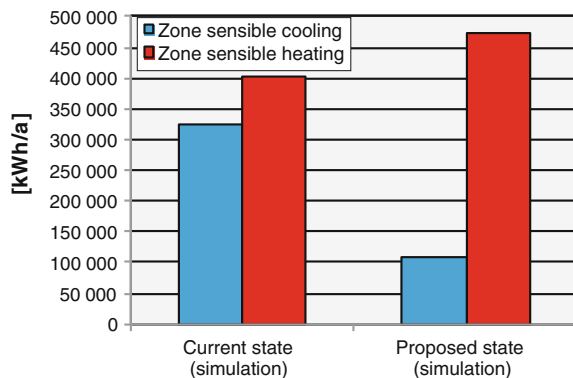


Table 5 Availability of a direct solar radiation in location Kosice, Slovakia [6]

Relative value of sunshine—Kosice, Slovakia												
Jan	Feb	Mar	Apr	May	June	July	Aug	Sep	Oct	Nov	Dec	
0.26	0.31	0.42	0.46	0.53	0.54	0.58	0.59	0.57	0.47	0.27	0.23	
Average period of sunshine in summer time												0.56
Average period of sunshine in winter time												0.35

the outside air temperature is higher than the air temperature in the atrium of a shopping centre. The energy demand for heating in winter covers heat transfer losses and ventilation heat losses.

6 Conclusion

The function of a solar window film is to reduce solar heat gains during the hot summer months. This solar protection belongs to the group of passive shading devices. We decrease heat load from the sun during the summer but we also decrease the heat gains from the sun in winter and this is the problem. This fact causes the higher energy demand for heating in winter. It would be better to use active solar shading devices for example an external moveable louvers. But the subject of this article was to analyse the impact of a solar window film on the energy demand during the year. If we use exterior solar window films on all glass surfaces we will decrease the energy demand for cooling at the value of 66 %. Vice versa we will increase the energy demand for heating at the value of 18 %. Availability of a direct solar radiation for our location Kosice is shown below in the next table (Table 5). The total result from energy simulation in DesignBuilder is that we could decrease the total energy demand at the value of 20 % during the year.

Acknowledgments This work was funded by the following project: KEGA 052 TUKE-4/2013 —“The implementation of a virtual laboratory for designing energy-efficient buildings”.

References

1. I.D.P. Santos, *Performance Evaluation of Solar Shading Systems* (Técnico Lisboa, 2007)
2. H. Many, P. Menti, Energy performance of glazings in European climates. *Renew. Energy* **37**, 226–232 (2012)
3. Grynnning et al., Windows in the buildings of tomorrow: energy losers or energy gainers? *Energy Build.* **61**, 185–192 (2013)
4. DesignBuilder Software, DesignBuilder Simulation+CFD Training Guide (2008), <http://www.designbuilder.co.uk/downloads/v1/doc/DesignBuilder-Simulation-Training-Manual.pdf>. Accessed 12 May 2014
5. A.F.F., s. r. o, <http://www.aff.sk/psolar.php>. Accessed 12 May 2014
6. T. Matuska, *Solarni tepelne soustavy (Solar heating system)* (Spolecnost pro techniku prostredi, Praha, 2009)

Build-in Transparent Collector Construction

Ján Lojkovics, Danica Košičanová, Richard Nagy, Marek Kušnír and Martin Štefanco

Abstract There are several ways to utilize renewable energy sources. Collectors are well known as one of the oldest build-in or post-mount construction at buildings. This paper presents idea of transparent sun collector based on insulation glass unit, with inner and outer liquid circulation. The heat absorbed from the sun in inner circuit liquid is transferred and transmitted by heat exchanger to the secondary circuit. Where energy can be stored or used in preheating devices in hot water delivery systems. This system can be applied in buildings with huge transparent or non-transparent glass based facades with suitable needs for hot water for example in administrative buildings, swimming pools, gyms etc. Research at current state deals with mechanical construction of window and prepares laboratory tests and build in measurements of construction itself.

1 Introduction

As was mentioned above construction of transparent collector is subject of interest due to joining advantages heat-accumulations and heat distributions systems. These functions are joined in one façade element—transparent liquid-filled collector. There is the presumption in money and room saving, due to partial simplifying of heat water supply or heating system as well [1].

The difference between classical (in this case flat plate collector, not evacuated tube collector) constructions and transparent collector is placement of insulation layer on back side of collector. This fact is resulting in high efficiency of collector. Non-absorbed heat is reflected back to the interspace of collector. Therefore

J. Lojkovics (✉) · D. Košičanová · R. Nagy · M. Kušnír · M. Štefanco
Department of Indoor Technologies and Building Services, Civil Engineering Faculty,
Institute of Architectural Engineering, Technical University of Košice, Košice, Slovakia
e-mail: jan.lojkovics@tuke.sk

D. Košičanová
e-mail: danica.kosicanova@tuke.sk

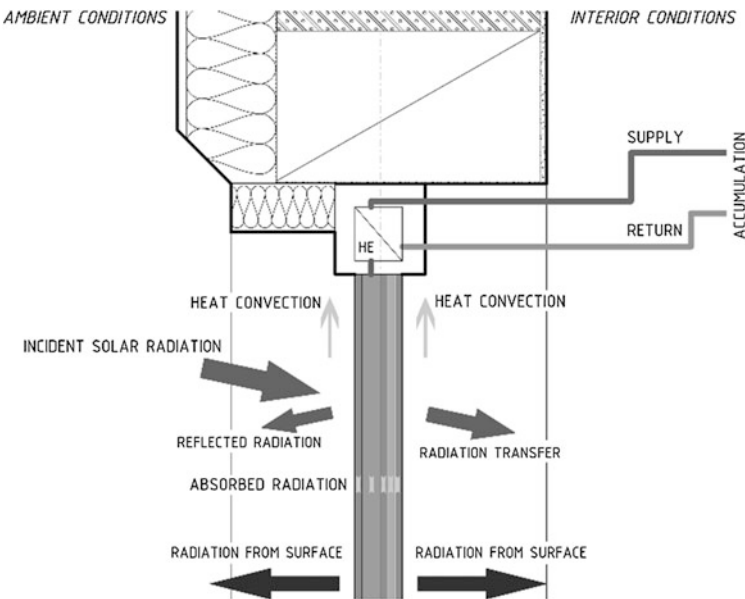


Fig. 1 Sun energy flow through the liquid window from exterior to interior

important part of collector is in front position antireflective glass pane. Another part of collector like frame or distribution system is principally identical.

In fact, window as transparent collector cannot be insulated as flat plate collector, therefore lower efficiency is expected. Photon as energy carrier can convert to energy only one time, so the thermal absorptivity of frontal, middle and back positional glass pane—from exterior can have significantly effect. This process is shown on Fig. 1.

2 Principal Schemes of Liquid-Filled Window

In fact, presence of liquid in cavity between two glass panes significantly affect the static properties of window in building scale. The weight of window depends from dimensions of panes. If it is considered dimensions 1170×1750 mm and thickness of liquid cavity 20 mm as shown Table 1—variant P1, water in this case, weight can be nearly 40 kg. Weight of basic IGU (insulation glass unit) window is thus doubled. For example the volume of hot water in basic heating element, in dimensions $600 \text{ mm} \times 2000 \text{ mm} \times 155 \text{ mm}$ is 17.4 l. The weight of element itself made of steel plates is 110.2 kg.

2.1 Full Scale Models

At this state of research we are ready to set up the system and prepare it for measuring in our test chamber. There are commonly used depth of windows from 60 mm up to 90 mm, and more in special cases. Our design is considering two types of window, basic plastic IGU, variant P1, and Fiberglass IGU, variant F1, without any reinforcement shown in Table 1.

Both systems P1 and F1 represents different ways in energy utilization. Main different lies in liquid volume between frontal—A, and middle—B glass pane. The energy absorbed on organic layer which is applied on glass surface 2 and 3, (Fig. 2) is transformed to the heat and subsequently transferred to the liquid layer. This process is described like heat transfer by heat convection, conduction and radiation in boundary layer of glass pane. The liquid flows in cavity with speed expected close to 0.001 m/s (natural flow) and all the types of heat transfers are different for every point in surface. These conditions are described as unsteady state.

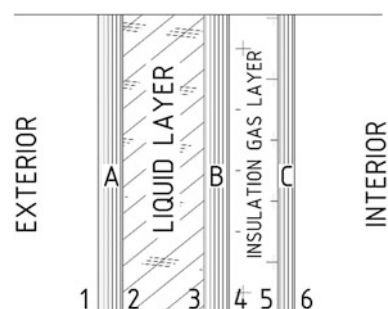
2.2 Glass Specification

There are several limits at design state of glass panes. As was mentioned above, photon as energy carrier can convert to energy only one time. This leads to dependence between energy gain and light constituent transferred to the interior space.

Table 1 Different alternatives of construction liquid-filled window

Type of window	Glass panes thickness from exterior (mm)	IG—insulation gas layer thickness (mm)	L—liquid layer thickness (mm)	Total thickness of system (mm)	Volume of liquid (m ³)
Variant P1	6-L-6-IG-4	16	20	52	0.0410
Variant F1	6-L-6-IG-4	10	10	36	0.0020

Fig. 2 Detail view of glass panes and cavities between panes



At design we are able to expect and manage the quantity of expected energy gain in liquid layer as well as the light constituent transferred through the construction.

Proposed construction of insulation glass unit is as follows (from exterior to interior): A—frontal glass pane, B—middle glass pane, C—rear glass pane, numbers 1–6 means surfaces of each glass pane, (increasing from exterior to interior). Between glass panes A and B lies liquid layer, behind that to interior lies insulation gas layer, between panes B and C.

As shown in Table 2. High energy performance is expected in contrast with direct solar radiation transmitted to the interior. Due to this high shading factor is expected. Energy indicator g represents the percentage of total solar radiant heat energy transmitted through glazing (the sum of energy transmitted directly and energy absorbed and re-emitted to the interior). Energy indicator TE represents the percentage of direct solar radiation transmitted through glazing, AE represents the percentage of absorbed energy in glazing.

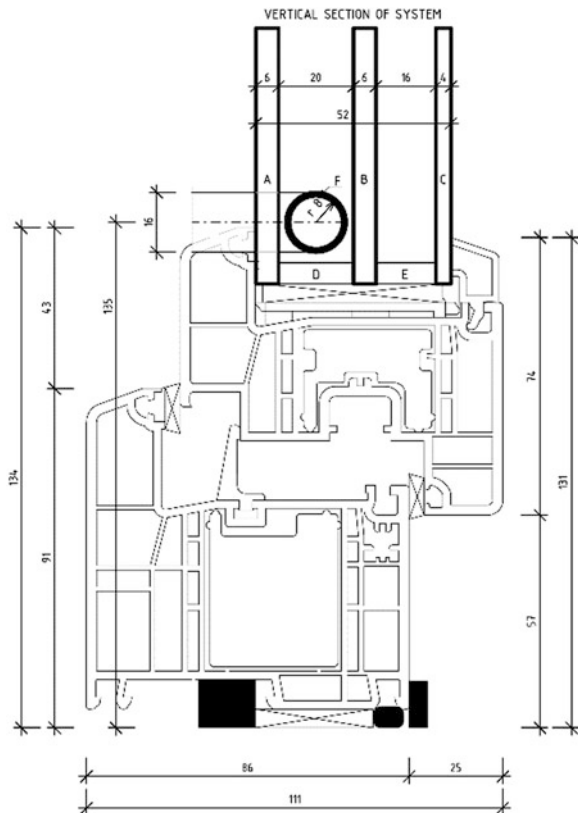
2.3 Distribution System

The whole system consist of two circuits, primary circuit, which is represented window collector itself and secondary circuit, which distribute accumulated energy to the hot water distributing system. It is necessary knowledge of material composition and fluid characteristics at design state of system. Properties of flooding media have direct affect on window and system durability. Due to anti-freeze and viscosity properties an alcohol mixtures are proposed as solution. Build-in pipes are made from copper diameter of 8 mm (Fig. 3), placed in window casement. For compensate pressure conditions in liquid-filled window are designed different lengths of pipes (supply pipe is 850 mm long, unlike return pipe, which is 50 mm long) (Fig. 3).

Table 2 Different properties of glass panes build-in liquid-filled window

Marking	Type of glass unit	Energy indicators			Position of surface
		TE (%)	AE (%)	g (-)	
A	Absorption	30	59	0.44	2
B	Absorption	50	25	0.58	3
C	Basic	83	10	0.85	—

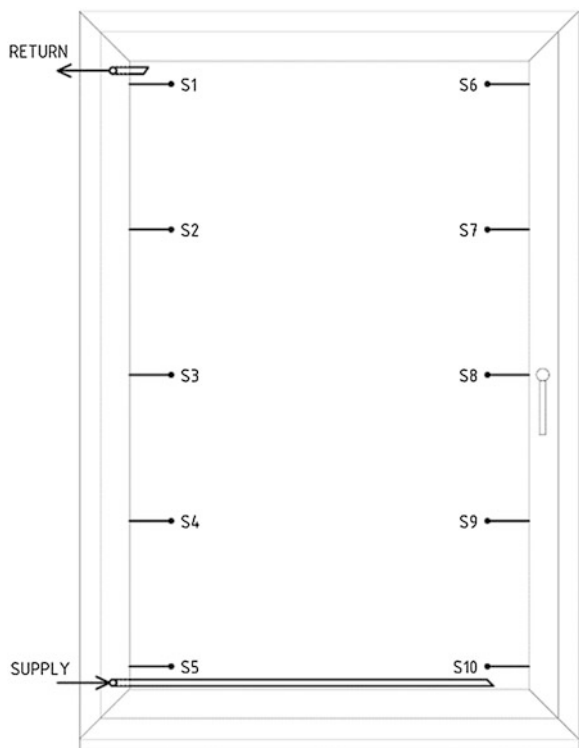
Fig. 3 Vertical section of system in window frame



2.4 Sensors Placements

Expected solar gains which can be transmitted due to flowing media will be measured sensors 1–10 as Fig. 4 shown. Sensors are metallic insulated wires places in space of liquid cavity. The space temperature will be measured and noted. In fact, temperature gradient will be observed. This data serve as comparative values during the creation of an analytical model of system.

Fig. 4 Sensors locations in space



3 Conclusions

Energy saving is one of the most important processes in common building. Research of liquid-filled window provides data's, which will be unnecessary during design state with huge transparent mostly south-faced surfaces, administrative buildings, gyms etc.

Acknowledgments This work was funded by project VEGA 1/0748/11 Theoretical and experimental analysis of Building services and HVAC systems from the point of view of microbiological risk and regarding to effective use of renewable sources.

Reference

1. T.T. Chow, C. Li, liquid-filled solar glazing design for buoyant water-flow. *Build. Environ.* **60**, 45–55 (2013)

Part XXVI

Modeling and Theoretical Aspects

in Energy Related Materials

Tensile and Torsional Loads Stress Distribution Along the Drill String for Deep Wells

Lallia Belkacem, Noureddine Abdelbaki, Mohamed Gaceb, Elahmoun Bouali, Hedjaj Ahmed and Mourad Bettayeb

Abstract Common knowledge and rule of thumb tell us that tensile failures will mostly occur in the pipe body, while torsion failures will occur in the tool joints. The total stresses on the drill string should be considered which are induced by combined bending, torsion and tensile stresses. The latter can usually be operating up until 80 % of the pipe body yield stress, a level which is considered as a safe working limit. Moreover, torque and drag are caused by the lateral forces and the friction between the borehole wall and the drill pipe. The lateral forces depend on the weight of the drill string. Torque and drag are sometimes overlooked when drilling simple wells. In deep well this is not acceptable. Proper decision made using correct torque and drag can make all the difference between TD drilling and suspended drilling. Therefore the over pull load plus the torque are the most important points to be considered in deep well drilling, since the resistance of the drill string body to the combined efforts will probably limit its tensional limit. By this I mean, exerting both a tension and torsion load on the drill string of this later will weaken its yield stress consequently applying a high tension effort combined with a significant torque lead to plastifying of the drill pipe body thus reducing its fatigue life. This problem is well observed in back-reaming operation. The results show that fatigue damage from rotation in dogleg during backreaming operation is a significant problem if the severity is greater than the critical value. So the position of drill pipe in the string will influence the amount of fatigue damage it sustains. Furthermore, back reaming can reduce the fatigue life of the drill pipe significantly because of the stress reversal of the drill string under tension in a dogleg.

An erratum to this chapter is available at DOI [10.1007/978-3-319-16901-9_74](https://doi.org/10.1007/978-3-319-16901-9_74)

L. Belkacem (✉) · M. Gaceb · E. Bouali · H. Ahmed · M. Bettayeb
University Akli Mohand Oulhadj, 10000 Bouira, Algeria
e-mail: lfep@umbb.dz

N. Abdelbaki
Laboratory of Petroleum Equipments Reliability and Materials, Faculty of Hydrocarbons and Chemistry Independence Street, University Mohamed Bougara, Boumerdes, 35000 Bougara, Algeria

1 Introduction

This paper outlines practically tensional and torsion loads which affect the drill pipe as a result of frequent back reaming operations. For this reason practical ways of eliminating this trouble or at least reducing this problem are explained in this paper. A better understanding of the stress distribution along the drill string will certainly lead to more optimized drill string designs.

Therefore, this article is based upon experiments on drill string failures which were done before in order to clarify this latter further. Firstly light will be shed on back reaming operation and then a synopsis on failure by torsion and tensile loading due to back reaming operation. This will be completed with few literature on torque and drag calculation via Lubinski model by using soft modeling (well plan software). Give An optimum solution to the problem will finally be given.

1.1 Backreaming Operation

Generally the backreaming is a term given to the backwards drilling to trip out of the hole when there is a problem with pipe pull-back operation freely without rotation and circulation in order to clean the hole to eliminate cuttings accumulation and hole caving [1].

The pipe tension during back reaming is lower than when pulling out of the hole with excessive drag, but torsional stress is introduced. The drill string is subjected to various loads such as: The loads due to contact of the drill string body with the wellbore, and which are known as side loading forces. These side forces are thought to be related to the weight of the string, the geometry of the wellbore, and the rotation of the string (axial, bending, and torsional forces = VON MISES stress) [1].

During backreaming, all drill string stresses are acting simultaneously; namely axial stress caused by tension, bending stress caused by the curvature of the string according to the wellbore tortuosity, and torsional stress caused by rotation.

1. The contact of the drill pipe and BHA components with the wellbore under this stressed condition will increase the friction caused by the tension and rotation, and thus will increase the side forces.
2. The excess side forces induced while backreaming along with incorrect practices can lead to accelerated casing and BHA wear and undesirable situations such as twist offs.
3. Backreaming can reduce the fatigue life of the drill pipe significantly because of the stress reversal of the drill string under tension in a dogleg [1].

1.2 BHA Restrictions

Bits and stabilizers are typically not designed to drill in reverse during backreaming, although some bits are now available that have cutters at the top of the gauge to facilitate the cutting action. It is important that all stabilizers are tapered at the top and the bottom to avoid problems while pulling and backreaming.

It is well known by measurement-while-drilling (MWD) personnel that backreaming out of hole with a bend in the BHA can lead to high shocks that can result in premature tool failures. Some of the reasons might be that the BHA is not in compression but in tension and is less constrained because there is no fixed end [1].

1.3 Drag and Friction Force

In addition to the drag force which create the friction between the drill string and the borehole wall when moving the BHA through wellbore. In a simple model, drag is the increased/decreased apparent hook-load when tripping plus the observed rotating hook-load at the equivalent depth [2, 3].

Friction force creates a combined motion decomposed into the two directions, axial motion and rotation. The effect of combined motion is well known, for example when rotating the drill string for running easier into the hole either for tripping in or out or back-reaming; a high rotational speed reduces axial drag considerably so we assume that during tripping operations an over pull may occur due to tight hole conditions. Further, research indicated that under the combined actions of axial load, centrifugal force and torque, the axis of the rotating drill string has a sinusoidal shape with changing wave length, and rotates as a rigid body, with the same speed and direction of the rotary table [2, 3].

1.4 Well Plan Torque and Drag Module

Normal Analysis involves calculating the torque, drag, normal force, axial force, buckling force, neutral point, stress and other parameters for a work string in a three-dimensional wellbore. With a Normal Analysis, all calculations are performed with the bit at one position in the wellbore, and with one set of operational parameters. One may choose to perform the analysis using either the soft or stiff string model. However, for now we will use the soft string model [2].

2 Engineering Overview of Back Reaming for 8½" Hole Section

Basic on the quick review conducted for the history of 8½" hole of two wells drilled in Algeria, it is imperative to point out that the severe wellbore instability, high torque peaks and stuck pipe problems encountered previously on this interval are still suspected to be one of the major challenges to encounter while drilling the 8½ hole section which is the longest one, approximately 2500 m. The possible root causes for the different hole problems encountered on the 8½ of well 1 and well 2 may be attributed to the following major factors: well 1 as an example.

1. Formation Nature and Characteristics (Dipping and Anisotropy)
2. Hole Geometry (Spiraling—Wellbore Tortuosity 8½")
3. Inharmonic in Drilling String and Parameters (WOB, RPM, BHA design, Bit selection) and Drilling Practice
4. Fluid characteristics (Fluid Density, Rheology, Salinity, Lubricity)
5. Frequent Reaming and Hard back Remaining while tripping (3200–5300 m)
6. Continuous Tight hole and high Over pull situation—specially when MW (<1.35 SG)
7. High torque peaks, while drilling and back reaming (12–18 Klb), specially from 4400 to 5100 m.
8. Sign of formation losses (seepage—partial) from 4450 to 4460 (Gedinnian)
9. Hole cleaning issues (Suspected specially at the start of section towards Trias Carbonate and Lias Argileux due to the low range of rheological properties maintained (YP 10)
10. Stuck Pipe (Twice) while drilling 8½ Hole in each well 1
11. Tectonic stress of the well bore [4].

2.1 Load Summary

From the load summary (Table 1), it is clearly seen that the drill-string is subjected to fatigue failure due to back reaming operation. This is confirmed within the well path curve, showed a variation in wall trajectory via tortuosity. This planned deviation with a dogleg of 5.88°/30 m has been created during side track operation of 8½ new hole, starting from 3171 to 4573 m where increased MW from 1.30 to 1.33 SG for improving hole stability. This dogleg regarded as an optimum angle to pass the drill string even the casing without any damage in drilling operation.

The problem will be intensified when the string is submitted to the more rigorous conditions present due to cyclic movement of the drill string due to tension and torsion load from back reaming operation which may lead to fatigue failure enhancement (As exposed in Figs. 1, 2 and 3).

Table 1 Load summary

Load condition	STF	B	Torque at the rotary table (ft/lbf)	Total windup with bit torque (revs)	Total windup without bit torque (revs)	Measured weight (tonne)	Total stretch (m)	Axial stress = 0	
								Distance from surface (m)	Distance from bit (m)
Backreaming	F	-	6722.2	4.0	3.8	205.72	12.43	4791.82	356.58

(-) No buckling, *S* sinusoidal, *H* helical, *L* lockup stress, *T* torque, *F* fatigue, *X* exceeds 90 % of yield, *Y* yield reached. Max over pull = 5.91 t over pull at bit = 11.00 t Torque at Bit = 200 ft-lbf

**Fig. 1** Well path

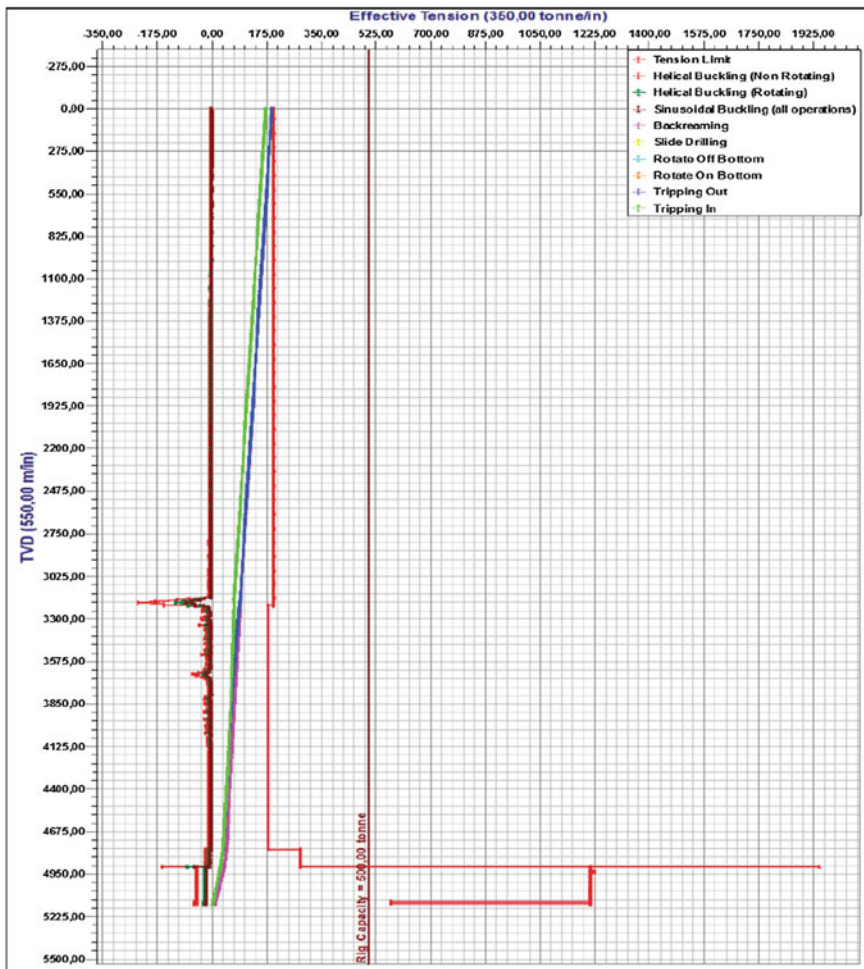


Fig. 2 Effective tension limits

Drill pipe fatigue damage occurs under cyclic loading conditions due to, for instance, rotation in a dogleg region. As a result, this dog leg makes the high stress concentration areas susceptible to fatigue damage in drill pipe which led to increase in fatigue ratio up to about 1.375 (minimum fatigue ratio is 1) as depicted in Fig. 4.

This minimum fatigue ratio about 1 is based on Lubinski torque and drag model which has defined curves where the permissible dogleg severity, below which no fatigue damage of drillpipes may occur, can be estimated from the tensile load and the drill pipes characteristics. These curves used to prevent static failure are the basis of the “API-RP-7G”.

To illustrate, these loads on drill string due to cyclic stress on drill pipe at depths between 3213.52 m and 3186.13 m are presented in back reaming load Table 2 showed in below.

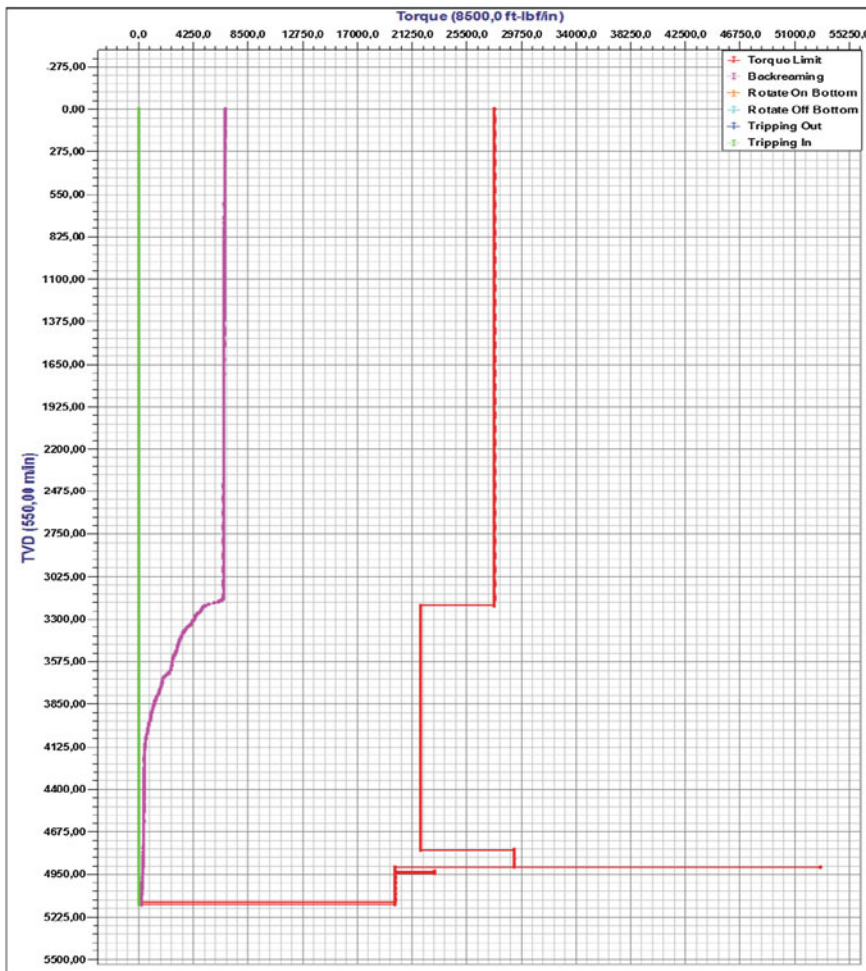


Fig. 3 Torque limits

Additionally, the measured torque data shows high fluctuations which can refer to drill string dynamics such as slip/stick vibration, restoring moment, torsional resistance as well as axial and lateral vibrations.

2.2 Analysis of Back Reaming Stresses

It is evidently seen from the Table 3 in below that the pipe section at the dogleg region may fail under the combined effects of axial tensile stress, radial stress, torsional stress and alternating repeated bending stress due to rotation. Failure at

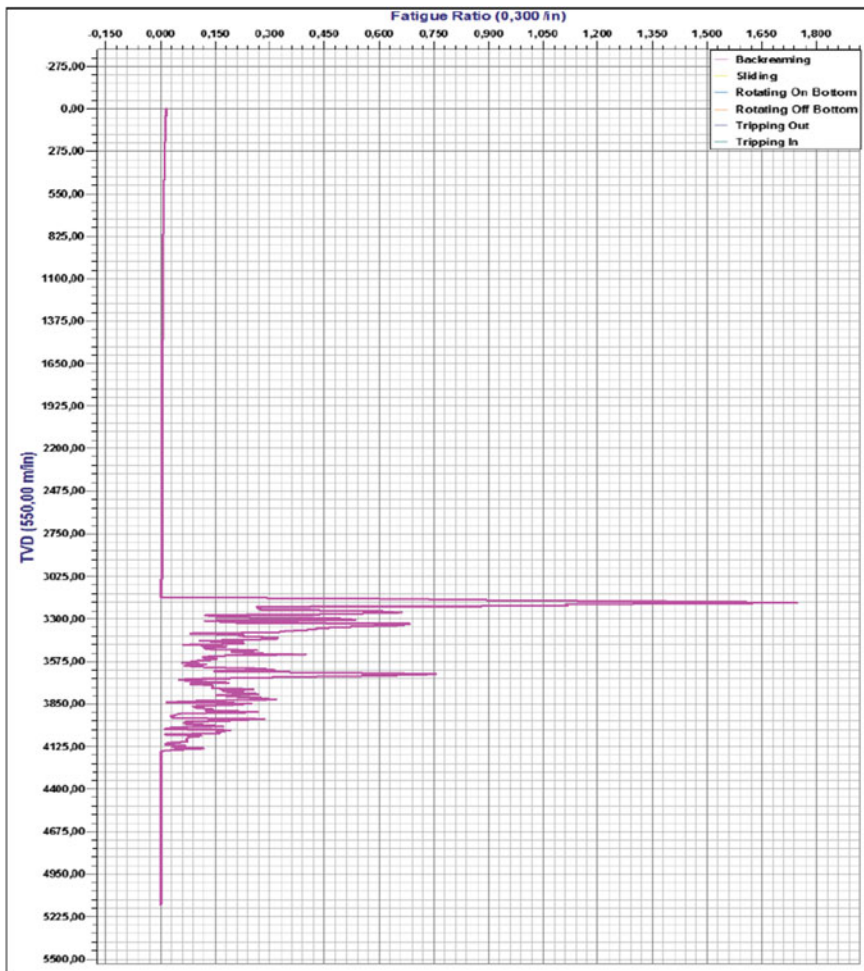


Fig. 4 Fatigue ratio

this section can be assessed by the VON MISES method of for equivalent yielding under combined loads [5].

Using 5.5" drill pipe with nominal weight of 21.9 lb/ft grade S135 in the cased hole and 5" grade G105 may reduce drill string failure due to cyclic tensile/torsional loads [6]. The Table 4 illustrates the decreasing of the number of pipes subjected to fatigue failure.

Table 2 Load data for backreaming

Measured Depth (m)	Component Type	Distance from Bit (m)	Internal Pressure (psi)	External pressure (psi)	Axial force Pressure Area (tonne)	Buoyancy (tonne)	Drag (tonne)	Torque (ft-lb)	Twist (revs)	Sinusoidal buckling (tonne)	Helical buckling (Rotating) (tonne)	B	STF	Contact force /9.45 (m) (lbf/length)
3.331.44	DP	1.816.96	6.158.36	6.158.36	69.52	86.32	0.00	4.102.2	0.4	-3.75	-5.31	~	~ ~ ~	1934
3.322.37	DP	1.826.03	6.141.78	6.141.78	69.82	86.57	0.00	4.146.9	0.4	-5.48	-7.75	~	~ ~ ~	611
3.313.30	DP	1.835.10	6.122.58	6.122.58	70.11	86.81	0.00	4.172.7	0.4	-6.05	-8.55	~	~ ~ ~	354
3.304.23	DP	1.844.17	6.105.06	6.105.06	70.41	87.06	0.00	4.282.8	0.4	-10.61	-15.00	~	~ ~ ~	1506
3.295.16	DP	1.853.24	6.088.05	6.088.05	70.70	87.31	0.00	4.378.2	0.4	-12.16	-17.20	~	~ ~ ~	1304
3.286.09	DP	1.862.31	6.075.23	6.075.23	71.00	87.57	0.00	4.407.5	0.4	-7.91	-11.19	~	~ ~ ~	401
3.277.02	DP	1.871.39	6.054.83	6.054.83	71.29	87.81	0.00	4.435.9	0.5	-5.26	-7.43	~	~ ~ ~	388
3.267.94	DP	1.880.46	6.038.13	6.038.13	71.59	88.06	0.00	4.536.4	0.5	-4.78	-6.76	~	~ ~ ~	1375
3.258.87	DP	1.889.53	6.022.22	6.022.22	71.88	88.31	0.00	4.672.9	0.5	-4.81	-6.80	~	~ ~ ~	1866
3.249.80	DP	1.898.60	6.006.20	6.006.20	72.18	88.56	0.00	4.798.0	0.5	-11.25	-15.90	~	~ ~ ~	1712
3.240.73	DP	1.907.67	5.991.19	5.991.19	72.47	88.81	0.00	4.854.5	0.5	-7.74	-10.90	~	~ ~ ~	772
3.231.66	DP	1.916.74	5.974.05	5.974.05	72.77	89.06	0.00	4.904.0	0.5	-10.57	-14.94	~	~ ~ ~	677
3.222.59	DP	1.925.81	5.956.30	5.956.30	73.06	89.31	0.00	4.953.0	0.5	-10.29	-14.95	~	~ ~ ~	670
3.213.52	DP	1.934.88	5.937.56	5.937.56	73.36	89.55	0.00	5.170.8	0.5	-27.34	-38.66	~	~ ~ F	2978
3.213.52	DP	1.934.88	5.937.56	5.937.56	71.16	89.55	0.00	5.170.8	0.5	-54.55	-77.14	~	~ ~ F	2978
3.204.39	DP	1.944.01	5.921.40	5.921.40	71.50	89.84	0.00	5.450.3	0.5	-54.40	-76.94	~	~ ~ F	3445
3.195.26	DP	1.953.14	5.903.86	5.903.86	71.85	90.14	0.00	5.892.0	0.5	-83.65	-118.29	~	~ ~ F	5443
3.196.13	DP	1.962.27	5.886.98	5.886.98	72.19	90.42	0.00	6.232.1	0.5	-63.67	-90.03	~	~ ~ F	4191
3.177.00	DP	1.971.40	5.870.10	5.870.10	72.53	90.71	0.00	6.446.3	0.6	-39.96	-56.51	~	~ ~ ~	2641
3.167.87	DP	1.980.53	5.854.31	5.854.31	72.87	91.00	0.00	6.595.8	0.6	-25.84	-36.54	~	~ ~ ~	1841
3.158.74	DP	1.989.66	5.836.33	5.836.33	73.21	91.29	0.00	6.595.8	0.6	-3.22	-4.56	~	~ ~ ~	1
3.149.61	DP	1.998.79	5.819.45	5.819.45	73.56	91.58	0.00	6.595.9	0.6	-3.22	-4.55	~	~ ~ ~	1

Table 3 Backreaming stresses

Measured depth (m)	Component type	Distance from Bit (m)	Hoop stress (psi)	Radial stress (psi)	Torsional stress (psi)	Shear stress (psi)	Axial stress (psi)	Buckling stress (psi)	Bending stress (psi)	BSMF	VonMises stress (psi)	VonMises ratio	Fatigue ratio
3.422.15	DP	1,726.25	-6,342.9	-6,342.9	4,222.4	425.3	35,331.5	0.0	3,702.7	3,868	45,950.7	0.438	0.321
3.413.08	DP	1,735.32	-6,306.9	-6,306.9	4,278.3	275.3	35,488.5	0.0	2,496.4	3,876	45,909.9	0.428	0.217
3,404.00	DP	1,744.40	-6,289.5	-6,289.5	4,339.5	301.1	35,645.5	0.0	2,615.2	3,885	45,182.8	0.430	0.228
3,394.93	DP	1,753.47	-6,274.9	-6,274.9	4,361.3	106.9	35,802.4	0.0	943.3	3,893	43,679.2	0.416	0.082
3,385.86	DP	1,762.54	-6,255.8	-6,255.8	4,447.1	422.3	35,959.4	0.0	3,669.3	3,902	46,532.3	0.443	0.321
3,386.79	DP	1,771.61	-6,239.4	-6,239.4	4,542.2	467.5	36,116.5	0.0	4,042.9	3,910	47,068.0	0.448	0.355
3,367.72	DP	1,780.68	-6,222.9	-6,222.9	4,655.4	557.0	36,273.2	0.0	4,825.6	3,918	48,013.4	0.457	0.424
3,358.65	DP	1,789.75	-6,206.4	-6,206.4	4,771.4	570.6	36,430.1	0.0	4,920.6	3,927	48,279.9	0.460	0.434
3,349.58	DP	1,798.82	-6,191.1	-6,191.1	4,915.8	709.9	36,586.9	0.0	6,126.2	3,935	49,655.0	0.473	0.541
3,340.51	DP	1,807.89	-6,174.5	-6,174.5	5,089.9	856.5	36,743.5	0.0	7,442.6	3,944	51,147.9	0.487	0.659
3,331.44	DP	1,816.96	-6,158.4	-6,158.4	5,271.6	893.9	36,900.2	0.0	7,703.1	3,952	51,599.5	0.491	0.683
3,322.37	DP	1,826.03	-6,141.8	-6,141.8	5,329.1	282.6	37,056.7	0.0	2,379.1	3,960	46,505.4	0.443	0.212
3,313.30	DP	1,835.10	-6,122.6	-6,122.6	5,362.3	163.4	37,213.2	0.0	1,391.5	3,969	45,682.3	0.435	0.124
3,304.23	DP	1,844.17	-6,105.1	-6,105.1	5,503.8	695.9	37,370.0	0.0	5,976.7	3,977	50,376.6	0.480	0.534
3,295.16	DP	1,853.24	-6,088.0	-6,088.0	5,626.3	602.6	37,526.5	0.0	5,278.4	3,985	49,865.6	0.475	0.472
3,286.09	DP	1,862.31	-6,075.2	-6,075.2	5,664.0	185.6	37,682.8	0.0	1,775.2	3,993	46,579.2	0.444	0.159
3,277.02	DP	1,871.39	-6,054.8	-6,054.8	5,700.5	179.2	37,839.4	0.0	1,392.0	4,002	46,351.1	0.441	0.125
3,267.94	DP	1,880.46	-6,038.1	-6,038.1	5,829.7	635.5	37,996.1	0.0	5,388.2	4,010	50,455.3	0.481	0.486
3,258.87	DP	1,889.53	-6,022.2	-6,022.2	6,005.0	862.3	38,152.4	0.0	7,338.5	4,018	52,573.9	0.501	0.663
3,249.80	DP	1,898.60	-6,006.2	-6,006.2	6,165.8	791.2	38,308.4	0.0	6,718.4	4,026	52,156.5	0.497	0.608
3,240.73	DP	1,907.67	-5,991.2	-5,991.2	6,238.4	357.0	38,464.6	0.0	3,050.7	4,034	48,723.7	0.464	0.277
3,231.66	DP	1,916.74	-5,974.1	-5,974.1	6,302.0	312.9	38,620.7	0.0	2,967.6	4,043	48,801.9	0.465	0.270
3,222.59	DP	1,925.81	-5,956.3	-5,956.3	6,365.0	309.8	38,777.0	0.0	2,916.9	4,051	48,911.8	0.466	0.266
3,213.52	DP	1,934.88	-5,937.6	-5,937.6	6,644.9	1,376.5	38,933.9	0.0	12,217.2	4,059	58,286.1	0.555	1.116

(continued)

Table 3 (continued)

Measured depth (m)	Component type	Distance from Bit (m)	Hoop stress (psi)	Radial stress (psi)	Torsional stress (psi)	Shear stress (psi)	Axial stress (psi)	Buckling stress (psi)	Bending stress (psi)	BSMF	VonMises stress (psi)	VonMises ratio	Fatigue ratio
3,213.52	DP	1,934.88	-5,937.6	-5,937.6	5,377.5	1,243.8	34,127.2	0.0	13,090.6	3,429	54,008.2	0.514	1.108
3,204.39	DP	1,944.01	-5,921.4	-5,921.4	5,668.2	1,447.9	34,291.0	0.0	13,121.6	3,437	54,288.0	0.517	1.113
3,195.26	DP	1,953.14	-5,903.9	-5,903.9	6,127.5	2,287.8	34,457.1	0.0	20,546.9	3,446	61,932.4	0.590	1.746
3,186.13	DP	1,962.27	-5,887.0	-5,887.0	6,481.2	1,761.8	34,618.4	0.0	15,803.6	3,454	57,498.1	0.548	1.346
3,177.00	DP	1,971.40	-5,870.1	-5,870.1	6,704.0	1,109.9	34,782.8	0.0	9,930.0	3,462	51,934.1	0.495	0.848

Table 4 Load data for backreaming with 5.5" drill pipe grade S135

Measured depth (m)	Component type	Distance from bit (m)	Internal pressure (psi)	External pressure (psi)	Axial force Pressure area (tonne)	Drag (tonne)	Torque (ft-lbf)	Twist (revs)	Sinusoidal buckling (tonne)	Helical buckling (Rotating) (tonne)	B	STF	Contact force /945 (m) (lbf.length)	
3.330.25	DP	1,818.15	6,155.46	6,155.46	69.56	86.35	0.00	3,388.9	0.4	-3.61	-5.10	~	~ ~ ~	1118
3.321.17	DP	1,827.23	6,138.65	6,138.65	69.86	86.60	0.00	3,421.6	0.4	-5.62	-7.95	~	~ ~ ~	429
3.312.09	DP	1,836.31	6,121.78	6,121.78	70.15	86.85	0.00	3,443.1	0.4	-6.06	-8.56	~	~ ~ ~	275
3.303.01	DP	1,845.39	6,103.90	6,103.90	70.45	87.10	0.00	3,523.1	0.4	-12.70	-17.96	~	~ ~ ~	1075
3.293.94	DP	1,854.46	6,086.72	6,086.72	70.74	87.35	0.00	3,629.5	0.4	-13.09	-18.52	~	~ ~ ~	1436
3.284.86	DP	1,863.54	6,072.97	6,072.97	71.04	87.60	0.00	3,642.4	0.4	-7.14	-10.10	~	~ ~ ~	158
3.275.78	DP	1,872.62	6,063.25	6,053.25	71.33	87.84	0.00	3,659.4	0.4	-5.26	-7.44	~	~ ~ ~	213
3.266.70	DP	1,881.70	6,036.49	6,036.49	71.63	88.09	0.00	3,763.2	0.4	-4.59	-6.49	~	~ ~ ~	1400
3.257.62	DP	1,890.78	6,020.08	6,020.08	71.92	88.34	0.00	3,905.6	0.5	-12.78	-18.07	~	~ ~ ~	1928
3.248.55	DP	1,899.85	6,003.63	6,003.63	72.22	88.59	0.00	3,980.9	0.5	-9.44	-13.35	~	~ ~ ~	1011
3.239.47	DP	1,908.93	5,987.64	5,987.64	72.51	88.84	0.00	3,982.3	0.5	-7.65	-10.82	~	~ ~ ~	0
3.230.39	DP	1,918.01	5,971.79	5,971.79	72.81	89.10	0.00	3,983.6	0.5	-10.50	-14.85	~	~ ~ ~	0
3.230.39	DP	1,918.01	5,971.79	5,971.79	67.01	89.10	0.00	3,983.6	0.5	-26.58	-37.59	~	~ ~ ~	0
3.221.26	DP	1,927.14	5,955.73	5,955.73	67.35	89.37	0.00	4,061.4	0.5	-26.46	-37.42	~	~ ~ ~	841
3.212.14	DP	1,936.26	5,935.73	5,935.73	67.68	89.63	0.00	4,246.5	0.5	-99.24	-140.34	~	~ ~ ~	2027
3.203.01	DP	1,945.39	5,919.99	5,919.99	68.01	89.91	0.00	4,556.8	0.5	-100.06	-141.49	~	~ ~ ~	3409
3.193.89	DP	1,954.51	5,902.02	5,902.02	68.35	90.18	0.00	5,022.1	0.5	-167.38	-236.69	~	~ ~ ~ F	5121
3.184.76	DP	1,963.64	5,885.13	5,885.13	68.68	90.45	0.00	5,426.5	0.5	-102.07	-144.35	~	~ ~ ~ F	4448
3.175.64	DP	1,972.76	5,868.24	5,868.24	69.02	90.72	0.00	5,648.8	0.5	-74.74	-105.70	~	~ ~ ~	2436
3.166.51	DP	1,981.89	5,852.06	5,852.06	69.35	90.99	0.00	5,749.9	0.5	-39.48	-55.83	~	~ ~ ~	1099

Table 5 Drill pipes 5.5 in grade S

2.3 Total BHA Stretch

From the comparison of two Tables (1 and 5) it is clearly seen that the drill pipe grade S135 is more suitable in mechanical characteristics than grade G105. This conclusion is confirmed from total stretch of the bottom hole assembly which was reduced by 0.8 m.

3 Conclusion

To sum up, the pipe section at the dogleg region may fail under the combined effects of axial tensile stress, radial pressure, torsional stress and alternating repeated bending stress due to rotation. For this the position and grade of drill pipe in the drill string will influence the amount of fatigue damage since continually rotated at severe dog-leg angle, such as a kick-off point will accumulate fatigue at a much higher amount for this; a permanent damage is appeared.

Furthermore, the over pull load plus the torque are the most important points to be considered in deep well drilling and back reaming, since the resistance of the drill string body to the combined efforts will limit probably its tensional limit by using mixed drill pipes G105 class premium in the 8.5" section, 5.5" in the cased hole and 5" in the open hole, has some limitation due to the axial loads for this drilling deep section requires stronger drill pipe to withstand the operational loads including appropriate design factors. Therefore using 5.5" drill pipe with nominal weight of 21.9 lb/ft grade S135 is necessary.

References

1. G. Yarim, G.M. Ritchie, R.B. May, A guide to successful backreaming: real-time case histories. *Soc. Pet. Eng.* **25**(1), 27–38 (2010)
2. B.S. Aadnoy, K. Andersen, Design of oil wells using analytical friction models. *J. Pet. Sci. Eng.* **32**, 53–71 (2001)
3. B.S. Aadnoy, M. Fazaelizadeh, G. Hareland, A 3-dimensional analytical model for wellbore friction. *J. Can. Pet. Technol.* (2009)
4. Daily drilling report of 8 ½" Hole Section of Well in Algeria Filed
5. Well Plan EDT_5000.1. Software System. Landmark Products. Torque Drag Analysis
6. G. Gabolde, in *Jean Paul Nguyen*, ed. by Drilling Data Handbook 8th edn. (IFP publications, 2006)

Computational Screening of Dual Cation Metal Ammine Borohydrides

Arash Emdadi, Yusuf Kişiak, Samet Demir and Adem Tekin

Abstract Hydrogen is one of the promising alternatives for the replacement of fossil-fuels. One of the major bottlenecks preventing its widespread commercialization for on-board applications is to find the most suitable storage medium. Metal borohydrides are one of the classes of solid materials studied intensively to store hydrogen due to their high theoretical hydrogen capacities. However, their high thermodynamic stability is one of the major problems limiting their usage. The requirement of high decomposition temperature can be lowered by the inclusion of ammonia. The resulting new complex containing both borohydrides and ammines is called as Ammine Metal Borohydrides (AMBs). However, some of the AMBs have insuppressible release of ammonia during the dehydrogenation. This can be solved by the inclusion of a second metal atom into AMBs leading to dual-cation AMBs with a general formula of $M_1M_2(BH_4)_y(NH_3)_x$. Experimental studies about one dual-cation AMBs ($LiMg(BH_4)_3(NH_3)_2$) indicate desired properties e.g., decomposition occurs below 200 °C and no release of ammonia. In this study, a computational screening using periodic density functional theory was performed to find promising dual-cation AMBs ($M_1M_2(BH_4)_y(NH_3)_x$ with $M_1 = Li, Na, K, M_2 = Mg, Ca, Sr, Zn, Mn, Ni$, $y = 3$, $x = 2, 3, 4, 5, 6$). The screening has been accomplished using template crystal structures generated by Crystal Structure Prediction via Simulated Annealing (CASPESA) method. Formation, alloying and simple decomposition reactions were employed for the evaluation of the complexes.

A. Emdadi (✉)

Energy Institute, Istanbul Technical University, Maslak, 34469 Istanbul, Turkey
e-mail: emdadi.arash@gmail.com; emdadia@itu.edu.tr

Y. Kişiak · S. Demir · A. Tekin

Informatics Institute, Istanbul Technical University, Maslak, 34469 Istanbul, Turkey
e-mail: yusufkislak@gmail.com

S. Demir

e-mail: sametdemir@gmail.com

A. Tekin

e-mail: adem.tekin@be.itu.edu.tr

1 Introduction

Hydrogen storage is one of the main challenges in developing fuel cell vehicles. Due to light weight and high capacity of hydrogen storage, Metallic Ammine Borohydrides (AMB) [1] are considered as one of the main carriers of hydrogen [2]. There are some advantages for dehydrogenation of AMB including lack of mass transport phenomena or interfacial reaction through different phases for amide-hydride connections which they lead to fast rate of dehydrogenation by local interaction of $N - H^{+\delta} \cdots H^{\delta-} - B$ between protic hydrogen atoms in NH_3 and hydride hydrogen atom in $[BH_4]^-$ [3]. High temperatures of hydrogen desorption and existence of ammonia is the main problem of dehydrogenation properties of mono metallic AMB. Studies [4–6] show the improvement in dehydrogenation properties of AMBs including different metal cations. The result is releasing pure hydrogen instead of ammonia at the temperature range to 75–300 °C [7]. In this study, crystal structure of bimetallic AMBs including $(M_1M_2(BH_4)_y(NH_3)_x)$ with $M_1 = Li, Na, K, M_2 = Mg, Zn, Ca, Mn, Sr, Ni, y = 3, x = 2, 3, 4, 5, 6$ using Crystal Structure Prediction via Simulated Annealing (CASPESA) method generated and these were further relaxed with the Density Functional Theory (DFT). After finding the crystal structure templates, a computational screening has been completed to find the most promising AMBs by considering the simple alloying and decomposition reactions at the DFT level.

2 Computational Methods

2.1 Prediction of Crystal Structures

One of the main unsolved problems in physical sciences is crystal structure prediction [8]. In this paper the crystal structures of AMBs have predicted by CASPESA approach which is based on simulated annealing [9–14], a popular local search meta-heuristic used to address discrete and, to a lesser extent, continuous optimization problems. All details about CASPESA can be found elsewhere [15].

2.2 Density Function Theory (DFT) Calculations

We employed Quantum Espresso software package for DFT calculations. The GGA exchange-correlation approximation of Perdew, Burke, Ernzerhof (PBE) has been used for norm conserving pseudo potentials of all atoms. The kinetic energy and density cutoffs are set to 80 and 320 Ry, respectively. The electronic Brioullin zones were sampled with $(2 \times 2 \times 2)$ k-points. The energy and force thresholds were set to 10^{-5} and 10^{-4} a.u, respectively.

2.3 Evaluation of Formation, Alloying and Decomposition Energies

After CASPESA calculations, formation, alloying and decomposition enthalpies of different AMBs evaluated to determine the most promising AMBs. Alloying, formation, and decomposition enthalpy of samples can be calculated through following equations:

$$\Delta E_{\text{alloy}} = E_{\text{M}_1\text{M}_2(\text{BH}_4)_{x+1}(\text{NH}_3)_y} - (E_{\text{M}_1\text{BH}_4} + E_{\text{M}_2(\text{BH}_4)_x} + yE_{(\text{NH}_3)})$$

$$\Delta E_{\text{alloy2}} = E_{\text{M}_1\text{M}_2(\text{BH}_4)_{x+1}(\text{NH}_3)_y} - (E_{\text{M}_1\text{BH}_4} + E_{\text{M}_2(\text{BH}_4)_x(\text{NH}_3)_y}) \quad \text{for } y = 2 \text{ and } 6$$

$$\Delta E_{\text{alloy2}} = E_{\text{M}_1\text{M}_2(\text{BH}_4)_{x+1}(\text{NH}_3)_y} - (E_{\text{M}_1\text{BH}_4} + E_{\text{M}_2(\text{BH}_4)_x(\text{NH}_3)_2} + (y-2)E_{\text{NH}_3})$$

for $y = 3, 4$ and 5

$$\Delta E_{\text{alloy3}} = (E_{\text{M}_1\text{M}_2(\text{BH}_4)_{x+1}(\text{NH}_3)_n} + (n-1)E_{\text{M}_1\text{BH}_4}) - (E_{\text{M}_2(\text{BH}_4)_x} + nE_{\text{M}_1\text{BH}_4\text{NH}_3})$$

In these equations, $E_{\text{M}_1\text{BH}_4}$, $E_{\text{M}_2(\text{BH}_4)_x}$, E_{NH_3} , $E_{\text{M}_1\text{M}_2(\text{BH}_4)_{x+1}(\text{NH}_3)_y}$, $E_{\text{M}_1\text{BH}_4\text{NH}_3}$ and $E_{\text{M}_2(\text{BH}_4)_x(\text{NH}_3)_2}$ are the total energies of M_1BH_4 , $\text{M}_2(\text{BH}_4)_x$, NH_3 , $\text{M}_1\text{M}_2(\text{BH}_4)_{x+1}(\text{NH}_3)_y$, $\text{M}_1\text{BH}_4\text{NH}_3$ and $\text{M}_2(\text{BH}_4)_x(\text{NH}_3)_2$, respectively. Among these systems, a crystal structure prediction must also be performed for $\text{M}_2(\text{BH}_4)_x(\text{NH}_3)_2$. For this purpose, CASPESA has been employed by setting $\text{M}_2 = \text{Mg}$. For the rest of the M_2 species, Mg was replaced with those metal atoms. In the meantime, theoretical and experimental crystal structures proposed for $\text{M}(\text{BH}_4)_2(\text{NH}_3)_2$ ($\text{M} = \text{Mg}$, Ca and Zn) by Chen et al. [16] was also considered. Similar to the structures found by CASPESA, M metal atom was changed in these structures and subsequently all the resulting structures were relaxed at the DFT level. Finally, the total energies of CASPESA and literature structures were compared and the lowest ones were used to calculate the alloying energy. For the calculation of ΔE_{alloy3} , the energy of $\text{M}_1\text{BH}_4\text{NH}_3$ is required. Very recently, Guo et al. [17] determined the crystal structure of LiBH_4NH_3 . In particular, they found that it has an orthorhombic cell ($a = 5.97$, $b = 4.64$ ve $c = 14.35$ Å) with space group of $Pnma$ (IT 62). Unfortunately, there is no reported structure for NaBH_4NH_3 and KBH_4NH_3 in the literature. In order to determine the energies of these systems, Li atom in LiBH_4NH_3 structure has been changed to Na and K and then the system was relaxed. For the decomposition and formation energies, the following equations were utilized:

$$\Delta E_{\text{decomp}} = E_{\text{M}_1\text{M}_2(\text{BH}_4)_x(\text{NH}_3)_y} - (E_{\text{M}_1\text{H}} + E_{\text{M}_2} + xE_{\text{B}} + (y/2)E_{\text{N}_2} + [(3y+4x-1)/2]E_{\text{H}_2})$$

$$\Delta E_{\text{form}} = E_{\text{M}_1\text{M}_2(\text{BH}_4)_x(\text{NH}_3)_y} - (E_{\text{M}_1} + E_{\text{M}_2} + xE_{\text{B}} + (y/2)E_{\text{N}_2} + [(3y+4x)/2]E_{\text{H}_2})$$

In the decomposition, it has been assumed that very stable alkali metal hydrides form. There are several unknown energies in these equations and they were calculated with the help of literature structures [11–13, 18–22].

3 Results

For selecting favorable models $-0.5 \leq \Delta E_{\text{Decomposition}} \leq 0.0 \text{ eV}/\text{H}_2$ and $\Delta E_{\text{alloy}} \leq 0.0 \text{ eV}/f.u$ can be utilized. However, very stable decomposition energies were obtained and therefore $\Delta E_{\text{alloy}} \geq -1.2 \text{ eV}/f.u$. constraint was employed. The computational screening results were shown in Fig. 1.

Since all the calculated ΔE_{decomp} and ΔE_{form} are quite negative, the alloying energy (ΔE_{alloy} , $\Delta E_{\text{alloy}2}$, $\Delta E_{\text{alloy}3}$) becomes more important when we select the best AMBs. In general, complexes including Mn have a very low ΔE_{decomp} and therefore they might require high energies for H_2 decomposition. Systems including either Zn

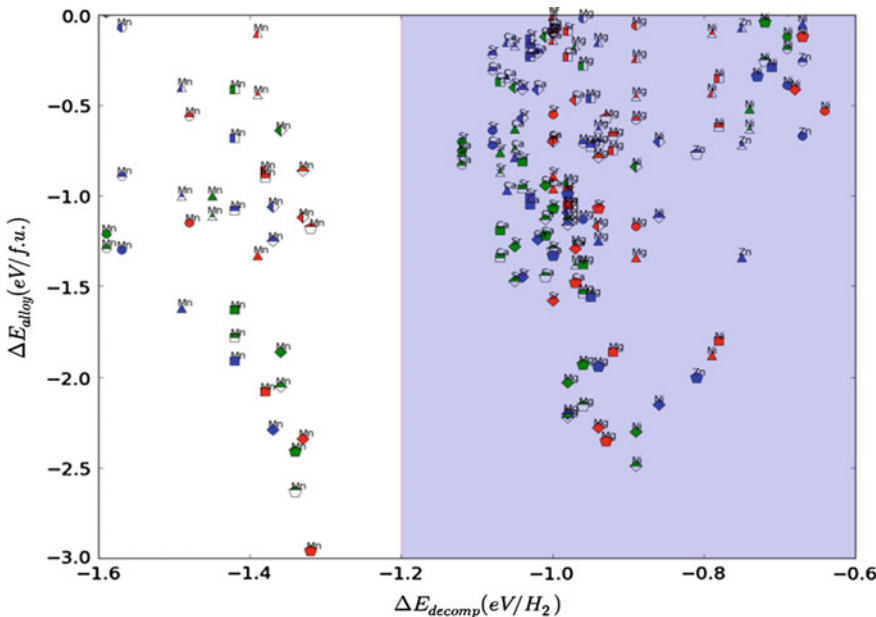


Fig. 1 The alloying energy, ΔE_{alloy} as a function of the decomposition energy, ΔE_{decomp} for all preferred alloy systems. Colors Li: (red), Na (blue) and K (green). Markers filled, left filled and top filled represent ΔE_{alloy} , $\Delta E_{\text{alloy}2}$ and $\Delta E_{\text{alloy}3}$ respectively. Circle, triangle, square, diamond and pentagram represent crystal structure of $\text{M}_1\text{M}_2(\text{BH}_4)_3(\text{NH}_3)_2$, $\text{M}_1\text{M}_2(\text{BH}_4)_3(\text{NH}_3)_3$, $\text{M}_1\text{M}(\text{BH}_4)_3(\text{NH}_3)_4$, $\text{M}_1\text{M}_{22}(\text{BH}_4)_3(\text{NH}_3)_5$ and $\text{M}_1\text{M}_2(\text{BH}_4)_3(\text{NH}_3)_6$ respectively. Blue region is favourable region for crystal structures

or Ni constitute promising AMBs with one of alkali metal species. For example, our screening suggests that $\text{NaZn}(\text{BH}_4)_3(\text{NH}_3)_2$ has desired properties and this system was already synthesized [23]. Up to now, complexes including NaMg , KMg , LiCa , NaCa , KCa , LiSr , NaSr , KSr have not been synthesized yet. Our screening also indicates that these systems are also quite promising.

4 Conclusions

In this study crystal structures of AMBs $(\text{M}_1\text{M}_2(\text{BH}_4)_y(\text{NH}_3)_x$ with $\text{M}_1 = \text{Li, Na, K}$, $\text{M}_2 = \text{Mg, Ca, Sr, Zn, Mn, Ni}$, $y = 3$, $x = 2, 3, 4, 5, 6$ were predicted by CASPESA and then they were further relaxed at the DFT level. In the computational screening, two selection criteria were employed to determine the stability of the considered alloy structures against phase separation and decomposition. In order to analyze phase separation three different alloying reactions were considered. Even AMBs follow very complex decomposition pathways; we considered a very simple reaction in which AMBs decompose into alkali hydrides, earth alkaline or transition metals, boron, N_2 and H_2 . Our screening indicates that except Mn, AMBs with other metals (Mg, Ca, Sr, Zn, Ni) are able to form stable complexes.

Acknowledgments This work financially supported by the TUBITAK (112T988). Computing resources used in this work were provided by the National Center for High Performance Computing of Turkey (UYBHM) under grant number 20662009 and Informatics Institute of Istanbul Technical University.

References

1. V.D. Aftandilian, H.C. Miller, E.L. Muetterties, Chemistry of boranes. I. Reactions of boron hydrides with metal and amine salts. *J. Am. Chem. Soc.* **83**(11), 2471–2474 (1961). doi:[10.1021/ja01472a012](https://doi.org/10.1021/ja01472a012)
2. W. Sun, X. Chen, Q. Gu, K.S. Wallwork, Y. Tan, Z. Tang, X. Yu, A new ammine dual-cation (Li, Mg) borohydride: synthesis, structure, and dehydrogenation enhancement. *Chem. A: Eur. J.* **18**(22), 6825–6834 (2012). doi:[10.1002/chem.201102651](https://doi.org/10.1002/chem.201102651)
3. G. Soloveichik, J.-H. Her, P.W. Stephens, Y. Gao, J. Rijssenbeek, M. Andrus, J.C. Zhao, Ammine magnesium borohydride complex as a new material for hydrogen storage: structure and properties of $\text{Mg}(\text{BH}_4)_2 \cdot 2\text{NH}_3$. *Inorg. Chem.* **47**(10), 4290–4298 (2008). doi:[10.1021/ic7023633](https://doi.org/10.1021/ic7023633)
4. D.Y. Kim, H.M. Lee, J. Seo, S.K. Shin, K.S. Kim, Rules and trends of metal cation driven hydride-transfer mechanisms in metal amidoboranes. *Phys. Chem. Chem. Phys.* **12**, 5446–5453 (2010)
5. T.A. Luedtke, T. Autrey, Hydrogen release studies of alkali metal amidoboranes. *Inorg. Chem.* **49**, 3905–3910 (2010)
6. X.D. Kang, J.H. Luo, P. Wang, Efficient and highly rapid hydrogen release from ball-milled $3\text{NH}_3\text{BH}_3/\text{MMgH}_3$ ($\text{M} = \text{Na, K, Rb}$) mixtures at low temperatures. *Int. J. Hydrogen Energy* **37**, 4259–4266 (2012)

7. F. Yuan, Q. Gu, X. Chen, Y. Tan, Y. Guo, X. Yu, Complex ammine titanium(III) borohydrides as advanced solid hydrogen-storage materials with favorable dehydrogenation properties. *Chem. Mater.* **24**(17), 3370–3379 (2012). doi:[10.1021/cm301387d](https://doi.org/10.1021/cm301387d)
8. J. Maddox, Crystals from first principles. *Nature* **335**(6187), 201–201 (1988)
9. A. Tekin, J.S. Hummelshoj, H.S. Jacobsen, D. Sveinbjörnsson, D. Blanchard, J.K. Norskov, T. Vegge, Ammonia dynamics in magnesium ammine from DFT and neutron scattering. *Energy Environ. Sci.* **3**(4), 448–456 (2010). doi:[10.1039/B921442A](https://doi.org/10.1039/B921442A)
10. A.J. Churchard, E. Banach, A. Borgschulte, R. Caputo, J.-C. Chen, D. Clary, K.J. Fijalkowski, H. Geerlings, R.V. Genova, W. Grochala, T. Jaron, J.C. Juanes-Marcos, B. Kasemo, G.-J. Kroes, I. Ljubic, N. Naujoks, J.K. Norskov, R.A. Olsen, F. Pendolino, A. Remhof, L. Romaszki, A. Tekin, T. Vegge, M. Zach, A. Züttel, A multifaceted approach to hydrogen storage. *Phys. Chem. Chem. Phys.* **13**(38), 16955–16972 (2011). doi:[10.1039/C1CP22312G](https://doi.org/10.1039/C1CP22312G)
11. R. Caputo, A. Tekin, W. Sikora, A. Züttel, First-principles determination of the ground-state structure of $Mg(BH_4)_2$. *Chem. Phys. Lett.* **480**(4–6), 203–209 (2009). doi:<http://dx.doi.org/10.1016/j.cplett.2009.09.019>
12. A. Tekin, R. Caputo, A. Züttel, First-principles determination of the ground-state structure of $LiBH_4$. *Phys. Rev. Lett.* **104**(21), 215501 (2010)
13. R. Caputo, A. Tekin, Ab-initio crystal structure prediction. A case study: $NaBH_4$. *J. Solid State Chem.* **184**(7), 1622–1630 (2011). doi: <http://dx.doi.org/10.1016/j.jssc.2011.05.006>
14. R. Caputo, A. Tekin, Lithium dihydorborate: first-principles structure prediction of $LiBH_2$. *Inorg. Chem.* **51**(18), 9757–9765 (2012). doi:[10.1021/ic301127q](https://doi.org/10.1021/ic301127q)
15. Y. Kışlak, A. Tekin, First-principles structure prediction of dual cation ammine borohydrides: $LiMg(BH_4)_3(NH_3)_x$, in *International Congress on Energy Efficiency and Energy Related Materials (ENEFM2013)*, ed. by A.Y. Oral, Z.B. Bahsi, M. Ozer. Springer Proceedings in Physics, vol. 155 (Springer International Publishing, 2014), pp. 457–462. doi:[10.1007/978-3-319-05521-3_58](https://doi.org/10.1007/978-3-319-05521-3_58)
16. X. Chen, X. Yu, Electronic structure and initial dehydrogenation mechanism of $M(BH_4)_2 \cdot 2NH_3$ ($M = Mg$, Ca , and Zn): a first-principles investigation. *J. Phys. Chem. C* **116**(22), 11900–11906 (2012). doi:[10.1021/jp301986k](https://doi.org/10.1021/jp301986k)
17. Y. Guo, Y. Jiang, G. Xia, X. Yu, Ammine aluminium borohydrides: an appealing system releasing over 12 wt% pure H_2 under moderate temperature. *Chem. Commun.* **48**(37), 4408–4410 (2012). doi:[10.1039/C2CC30751K](https://doi.org/10.1039/C2CC30751K)
18. Y. Nakamori, K. Miwa, A. Ninomiya, H. Li, N. Ohba, Towata S-i, A. Züttel, Orimo S-i, Correlation between thermodynamical stabilities of metal borohydrides and cation electronegativities: first-principles calculations and experiments. *Phys. Rev. B* **74**(4), 045126 (2006)
19. K. Miwa, M. Aoki, T. Noritake, N. Ohba, Y. Nakamori, Towata S-i, A. Züttel, Orimo S-i, Thermodynamical stability of calcium borohydride $Ca(BH_4)_2$. *Phys. Rev. B* **74**(15), 155122 (2006)
20. D.B. Ravnsbæk, E.A. Nickels, R. Černý, C.H. Olesen, W.I.F. David, P.P. Edwards, Y. Filinchuk, T.R. Jensen, Novel alkali earth borohydride $Sr(BH_4)_2$ and borohydride-chloride $Sr(BH_4)Cl$. *Inorg. Chem.* **52**(19), 10877–10885 (2013). doi:[10.1021/ic400862s](https://doi.org/10.1021/ic400862s)
21. T.D. Huan, M. Amsler, V.N. Tuoc, A. Willand, S. Goedecker, Low-energy structures of zinc borohydride $Zn(BH_4)_2$. *Phys. Rev. B* **86**(22), 224110 (2012)
22. S. Er, G.A. de Wijs, G. Brocks, Hydrogen storage by polylithiated molecules and nanostructures. *J. Phys. Chem. C* **113**(20), 8997–9002 (2009). doi:[10.1021/jp901305h](https://doi.org/10.1021/jp901305h)
23. G. Xia, Q. Gu, Y. Guo, X. Yu, Ammine bimetallic (Na , Zn) borohydride for advanced chemical hydrogen storage. *J. Mater. Chem.* **22**(15), 7300–7307 (2012). doi:[10.1039/C2JM16370E](https://doi.org/10.1039/C2JM16370E)

Analysis of Electricity Usage for Domestic Heating Based on an Air-to-Water Heat Pump in a Real World Context

Seyed Amin Tabatabaei and Jan Treur

Abstract In this paper a new computational model to estimate the performance of an air to water heat pump in relation to outdoor temperature is proposed and evaluated. This model is an extension and refinement of a model proposed in previous work. In the new model the following has been taken into account. Real empirical data for usage of a heat pump over a whole heating season have been used to obtain accurate parameter values. The energy which is used for heating sanitation water for the bathroom is taken into account in a separate submodel. According to some reports, around 15 % of domestic energy usage is for hot water. From the empirical data set, the fraction of energy which is consumed for this purpose is known, and it is used to model the usage for sanitation water heating as separate from the usage for heating. In this model the amount of energy which is used to keep the system working (active standby mode) is taken into account as well. The now available empirical data for the whole heating season have been used to estimate the parameter values for this model on the one hand and validation on the other hand.

1 Introduction

It is estimated that 43 % of the total energy usage in the European Union in 2006 was spent on heat related needs (cf. [1]). To reduce this part of energy usage, in addition to good isolation of the house, also domestic heating systems are considered, such as heat pumps that allow the use of renewable energy; e.g., [2]. They

S.A. Tabatabaei (✉) · J. Treur

Agent Systems Research Group, Department of Computer Science, VU University Amsterdam, De Boelelaan 1081, 1081HV Amsterdam, The Netherlands
e-mail: s.tabatabaei@vu.nl

J. Treur
e-mail: j.treur@vu.nl
URL: <http://www.cs.vu.nl/~treur>

take most of their energy (up to 80 %) from the heat available in the ambient air, water or soil. The remaining energy usage concerns electrical energy to run the heat pump, which also can be produced based on renewable energy sources such as solar or wind energy.

Domestic heat pump users are facing a challenge to estimate their own energy usage on heating mainly because the performance indicators given by heat pump manufacturers do often not cover the dynamic conditions of using it (e.g., indoor and outdoor temperatures). This paper focuses on how an empirically validated computational model can be used to get this estimation in case of an air to water heat pump (because of using the air as a source, it also called as air source heat pump or ASHP).

In designing new houses or renovating existing houses nowadays, often an aim is to come as close as possible to an *energy neutral* or *net zero* house; e.g., [3–9]. In a net zero house, the total amount of energy used by the building on an annual basis is roughly equal to the amount of renewable energy created on the site. In such houses often a PV system is used to produce the needed energy as solar energy. A computational model as described here can be useful to estimate the annual energy needs and base the decision on the dimensions of the PV system on that (like [10]).

The energy demand for heating of a house strongly depends on the ambient temperature. It is common to model the heating demand in a linear manner as a function of the outdoor and indoor temperatures, proportional to the number of degree days: the sum of the differences of indoor and outdoor temperatures over time. For traditional heating systems, in general their energy usage is modeled as proportional to the heating demand, where the proportion factor indicates the energy efficiency of the system. These linear relations between energy usage and indoor and outdoor temperatures make it easy to aggregate and average the usage over time. For example, the average energy usage over some time period can be determined directly on the basis of average indoor and outdoor temperatures over this period.

For an air to water heat pump the energy usage also depends in a linear manner on the energy demand and through that on the indoor and outdoor temperatures. But an important difference is that also its efficiency of heating (expressed as its Seasonal Performance Factor, SPF) depends on the outdoor temperature. Therefore in the overall relation between energy usage and temperatures, these temperatures have a double and nonlinear effect on the energy usage [10]. As a consequence, taking averages over longer time periods does not provide adequate estimations: for every occurrence of an ambient temperature the energy usage has to be calculated separately. Therefore, in this paper, the variation of outdoor temperature over the year is analyzed and it is determined by simulation over days how this variation affects the energy needed for heating.

In the paper, first in Sect. 2 some background theory on heating based on a heat pump and a computational model are presented. Next, in Sect. 3 it is shown how parameters representing characteristics of a given house and of the heat pump can be estimated based on empirical data. This provides a well-tuned model of the heat pump in the given house. Section 4 includes a discussion and future directions.

2 Background Knowledge and the Computational Model

In this section some background knowledge on domestic heating is discussed, and a computational model based on that. For domestic heating three important elements are:

- The characteristics of the heating system used; e.g., efficiency
- The characteristics of the house; e.g., how well isolated is the house
- The characteristics of the environment; e.g., the outdoor temperature.

To estimate the *efficiency* of a heat pump often the Seasonal Performance Factor, *SPF*, is used (usually for a particular period of time or a season) [11–13]:

$$SPF = \frac{\text{energy provided}}{\text{energy used}}$$

For air to water heat pumps in the marketplace, the Seasonal Performance Factor usually varies between 2 and 5 (e.g., for outdoor temperatures between -5 and 15 °C) [14]. Often it is between 3 and 4 (e.g., for ambient temperatures between 0 and 10 °C). In general, *SPF* is approximated by a mathematical function of the outdoor temperature T_{od} . Often a linear approximation is used; (e.g., [15, 16]), and the *SPF* for a given day is based on the average day temperature. For this paper the following new steps are made:

1. Not the average day temperature is used but the minimum and maximum day temperatures, T_{odmin} and T_{odmax}
2. As an approximation of *SPF*, a quadratic function in T_{odmin} and T_{odmax} is used
3. The parameters of this quadratic approximations are estimated based on a large real world empirical data set, available from the website <http://www.liveheatpumps.com>

Based on these steps the model for *SPF* gets the format

$$SPF = A + BT_{odmin} + CT_{odmax} + DT_{odmin}^2 + ET_{odmax}^2 + FT_{odmin}T_{odmax}$$

where the parameters A to F are tuned based on real world empirical data (see Sect. 3). Since $SPF = \frac{\text{energy provided}}{\text{energy used}}$ the energy usage can be easily determined from the energy demand:

$$\text{energy usage} = \frac{\text{energy demand}}{SPF}$$

The *energy demand for space heating* of the house also depends on the ambient temperature. To model this, the following linear function of the temperature differences has been used.

$$\text{energy demand for space heating} = B_1(T_{idavg} - T_{odmin}) + B_2(T_{idavg} - T_{odmax})$$

Here T_{idavg} is the average indoor temperature over 24 h, and B_1 and B_2 are parameters relating to the energy loss and to the role of lower and higher temperatures during the 24 h. This expression can easily be rewritten into:

$$\text{energy demand for space heating} = \varepsilon(T_{idavg} - (wT_{odmin} + (1-w)T_{odmax}))$$

$$\text{with } \varepsilon = B_1 + B_2 \text{ and } w = B_1/(B_1 + B_2)$$

Here ε is the energy loss per degree day, and w is a weight factor between 0 and 1. These are parameters of the house estimated in Sect. 3.

Together the above formulae provide the following model for *daily energy usage for space heating*:

$$\frac{B_1(T_{idavg} - T_{odmin}) + B_2(T_{idavg} - T_{odmax})}{A + BT_{odmin} + CT_{odmax} + DT_{odmin}^2 + ET_{odmax}^2 + FT_{odmin}T_{odmax}}$$

The energy demand for *heating of sanitation water* follows different patterns. Most of it depends on when and how much of this water is used. This is difficult to predict for each day separately, so it is considered to be an average value with fluctuations around it. However, there is also a slight dependence of the demand on outdoor temperature. Therefore this has been modeled as a linear function of the maximum and minimum outdoor temperature:

$$\text{energy demand for sanitation water} = A_1 + A_2T_{odmin} + A_3T_{odmax}$$

So the *daily energy usage for sanitation water* is modeled by

$$\frac{A_1 + A_2T_{odmin} + A_3T_{odmax}}{A + BT_{odmin} + CT_{odmax} + DT_{odmin}^2 + ET_{odmax}^2 + FT_{odmin}T_{odmax}}$$

Finally, the system has a default usage per day for its *active stand by function*, therefore a constant value S is added. Thus the overall model becomes:

$$\begin{aligned} \text{overall day energy usage} &= \text{active stand by usage} + \text{energy usage for space heating} \\ &\quad + \text{energy usage for sanitation water} \\ &= S + \frac{B_1(T_{idavg} - T_{odmin}) + B_2(T_{idavg} - T_{odmax}) + A_1 + A_2T_{odmin} + A_3T_{odmax}}{A + BT_{odmin} + CT_{odmax} + DT_{odmin}^2 + ET_{odmax}^2 + FT_{odmin}T_{odmax}} \end{aligned}$$

3 Tuning the Computational Model to a Real World Situation

In this section it will be discussed how the parameters of the introduced computational model have been estimated based on real world data for a specific type of heat pump, a specific house, and its specific environment.

To tune the parameters in such a way that results of our model match to the real world data, interior-reflective Newton method, described in [17, 18], have been used. Moreover, to get rid of the local optimum answers, for each set of parameters, the algorithm was run for 1000 times, and the best set of parameters (with minimal error) is reported in this paper.

The parameters can be partitioned into two groups:

- Parameters representing characteristics of the heat pump: the parameters in the model for SPF (A to F)
- Parameters representing characteristics of the house and its environment: the parameters used in the models for sanitation water heating and space heating demand (A_1, A_2, A_3, B_1, B_2).

3.1 Real World Datasets

In this work two different sets of real world data were used to tune the parameters of the proposed model. These datasets come from two houses which are equipped with the same type of heat pump considered (Fujitsu General Waterstage WOH14RIYF/WH16).

- **Dataset of house1:** This house is located in Lembeek, Belgium (about 50.4 latitude, 4.1 longitude). The empirical data for performance characteristics and outdoor temperatures of this house can be found at <http://www.liveheatpump.com>. From this Website empirical data on performance and daily maximum and minimum outdoor temperatures have been collected for this site for the period October 2013 to April 2014.
- **Dataset of house2:** This house concerns a reasonably well isolated three storey family house near Alkmaar, The Netherlands (about 52.6 latitude, 4.7 longitude). It is a netzero house using the aforementioned type of heat pump for space heating and heating of sanitation water. Daily data of minimum and maximum temperatures and energy usages of the heat pump for a whole year are available in this dataset. However, it is known that in the period from June to September, no space heating takes place, while in period of November to March, energy is used for both sanitation water and space heating. In the months April, May and October only occasionally space heating takes place.

3.2 Parameters Representing Characteristics of the Heat Pump

The data set of house 1 was used to estimate the parameters which represent the performance characteristics of the heat pump: the SPF. The outcome was:

$$A = 1.9869 \quad B = 0.1419 \quad C = 0.0053 \quad D = 0.1113 \quad E = -0.0024 \quad F = -0.0096$$

The following averages have been found:

Average of Absolute Error = 0.1566

Average of Relative Error = 0.0492

Average of Absolute Error/Average of SPF = 0.0487

In Fig. 1 it is shown how the obtained approximation follows the real values over the days.

3.3 Parameters Representing Characteristics of the House

As a next step, it is discussed how parameters involving characteristics of the house were estimated. First, the energy demand for heating of sanitation water is addressed. Empirical data of house 2 on daily usage were used for the period June to September, in which no space heating took place. So, all usage is for the active standby and for heating of sanitation water. From the days that no heating of

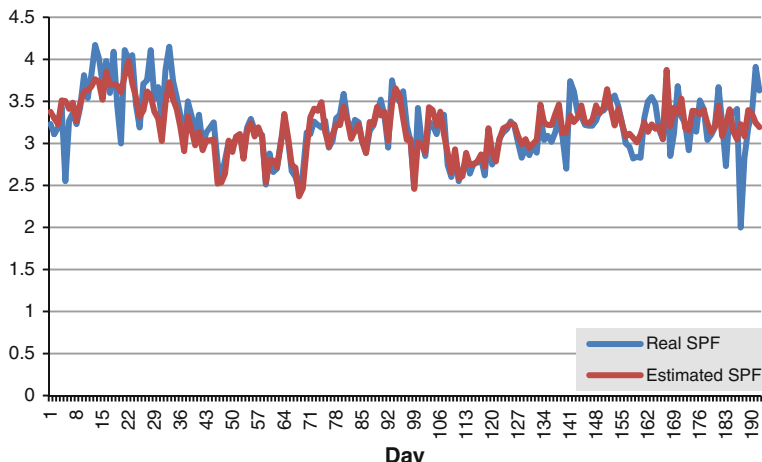


Fig. 1 Daily performance factors of the heat pump system for house 1: estimated versus real values

sanitation water took place it was found that the active standby takes 0.4 kWh per 24 h, so parameter $S = 0.4$. This value was subtracted from all values to remain the daily usages for sanitation water. These were used to estimate the value of parameters A_1 to A_3 for the water heating. The outcome was:

$$A_1 = 2.7275 \quad A_2 = -0.0210 \quad A_3 = -0.0481$$

Over the days of the considered time period the following averages have been found.

Average Real Sanitation Water Heating over Days = 0.8270

Average Predicted Sanitation Water Heating over Days = 0.8229

Deviation Predicted—Real Sanitation Water Heating Average = -0.0041
(= -0.5 %)

Average Absolute Error in Sanitation Water Heating over Days = 0.2542

Average Relative Error in Sanitation Water Heating over Days = 0.4059

Average Absolute Error over Days/Average Usage for Sanitation over Days = 0.3089

In Fig. 2, it is shown how this model approximates the real values of energy usage for water heating plus the 0.4 for active standby. Note that the deviations are mainly due to the unpredictable character (fluctuations) of the use of sanitation water.

After this, the average of the indoor temperature T_{idavg} , and the parameters B_1 and B_2 for the space heating model were estimated using the empirical data for the period November 2013 to May 2014. The values found are:

$$T_{idavg} = 17.3834 \quad B_1 = 0.8572 \quad B_2 = 1.9865$$

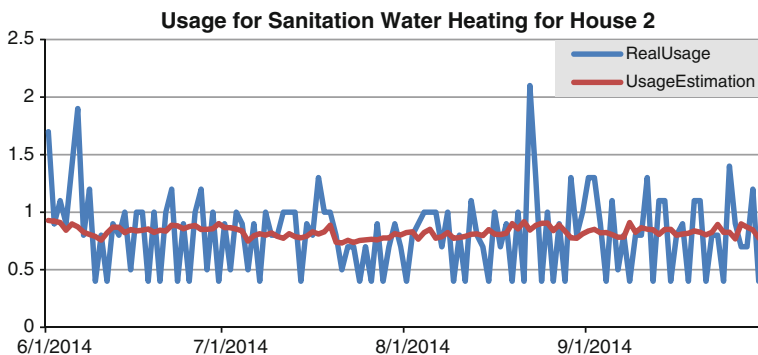


Fig. 2 Energy usage for sanitation water heating (and active standby), for house 2 from June to September 2014

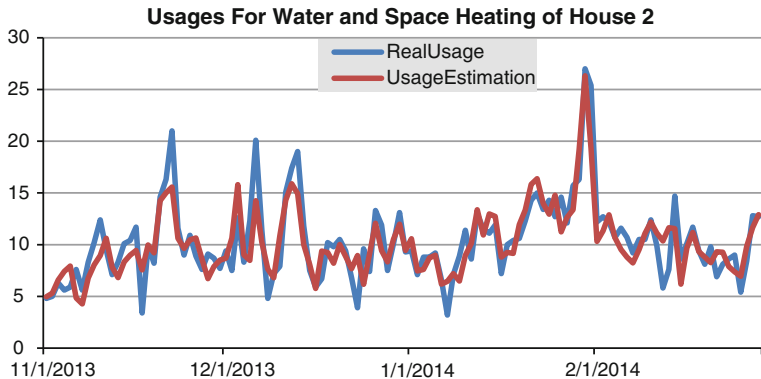


Fig. 3 Energy usage for both water and space heating (and active standby) for house 2, from November 2013 to March 2014

This entails

$$\varepsilon = 2.8437 \quad w = 0.3014$$

Over the days of the considered time period the following averages have been found for heating of sanitation water plus active standby:

Average Real Overall Usage over Days = 9.6396

Average Predicted Overall Usage over Days = 9.6617

Deviation Predicted - Real Overall Usage Average = 0.022 (= 0.2 %)

Average Error in Overall Usage over Days = 1.566

Average Relative Error in Overall Usage over Days = 0.1975

Average Error in Overall Usage over Days/Average Usage over Days = 0.1625

Figure 3 shows the results of the proposed model and the real value of overall daily usages for the period November 2013 to March 2014.

4 Discussion and Conclusion

In this paper, a new model is proposed to estimate the energy usage of an air to water heat pump system used for domestic heating purposes. The model can be used to perform simulations on energy usage of the heat pump day by day for arbitrary time periods (e.g., seasons or years). The model includes a number of parameters representing characteristics of the type of heat pump, the house and of the environment. It was shown how appropriate values for these parameters can be found to tune the model to the characteristics of a specific type of heat pump, and of a specific house and its environment. The data obtained by simulation of the model have been compared to real world data, and the error has been estimated.

The overall evaluation can be done through different evaluation measures. The average relative error in the model for the estimation of *SPF* based on minimum and maximum temperatures is 5 %. For the computational model for the heat pump usages, when evaluated for averages over a longer time period (for example, one year or one heating season), the computational model provides quite accurate predictions. For example, for the time periods considered in Sect. 3 the relative deviation between predicted and real average usage for sanitation water heating was 0.5 % and for overall usage of the heat pump the relative deviation was 0.2 %. However, predictions for specific days are less easy due to inherent day-by-day fluctuations. The average relative error in the prediction of usage for sanitation water heating over days is 40 %, while it is 20 % for overall usage (both water and space heating). One reason for a deviation in prediction of usage for a particular day is that in the considered house there is no fixed daily heating program. In fact, some days, nobody is in the house; therefore the space heating is off and thus does not keep the house on a higher space temperature. On other days, always somebody is in the house, and the temperature is kept high between 7 A.M. and 9 P.M. These fluctuations by themselves are an inherent source of error. By its design the model had no information about them and therefore was not able to take them into account. Given these sources of inherent error, an average error below 20 % could be considered not bad at all.

In future, this model will be validated with more empirical data. Moreover, an effort will be done to compare the accuracy of this model to that of a number of other existing models. Furthermore, it may be considered in how far the inherent fluctuations in demand both for sanitation water and space heating can be included in the model by adding log data on the behaviour of the persons in the house: e.g., when they are present, and when they use the bathroom.

Acknowledgment The authors are grateful to Jeroen Koole from Thercon representing Fujitsu in The Netherlands, who provided support to understand and analyse data available at <http://www.liveheatpump.com>.

References

1. B. Sanner, R. Kalf, A. Land, K. Mutka, P. Papillon, G. Stryi-Hipp, W. Weiss, *2020-2030-2050, Common Vision for the Renewable Heating and Cooling Sector in Europe* (Publications Office of the European Union, Luxembourg, 2011)
2. N. Aste, R.S. Adhikari, M. Manfren, Cost optimal analysis of heat pump technology adoption in residential reference buildings. *Renew. Energy* **60**, 615–624 (2013)
3. R. Charron, A.K. Athienitis, Design and optimization of net-zero energy solar homes. *ASHRAE Trans.* **112**(2), 285–295 (2006)
4. R. Charron, A. Athienitis, in *The use of genetic algorithms for a net-zero energy solar home design optimization tool*. Proceedings of 23nd Conference on Passive and Low Energy Architecture (2006)
5. M. Leckner, R. Zmeureanu, Life cycle cost and energy analysis of a net zero energy house with solar combisystem. *Appl. Energy* **88**, 232–241 (2011)

6. S. Pogharian, J. Ayoub, J. A. Candanedo, A. K. Athienitis, in *Getting to a net zero energy lifestyle in canada: the Alstonvale net zero energy house*. Proceeding of the 3rd European PV Solar Energy Conference, pp. 3305–3311 (2008)
7. E. Musall, T. Weiss, A. Lenoir, K. Voss, F. Garde, M. Donn, in *Net zero energy solar buildings: an overview and analysis on worldwide building projects*. Proceeding of EuroSun Conference (2010)
8. J. Marszal, P. Heiselberg, J.S. Bourrelle, E. Musall, K. Voss, I. Sartori, A. Napolitano, Zero energy building—a review of definitions and calculation methodologies. *Energy Build.* **43**, 971–979 (2011)
9. I. Sartori, A. Napolitano, K. Voss, Net zero energy buildings: a consistent definition framework. *Energy Build.* **48**, 220–232 (2012)
10. S.A. Tabatabaei, D.J. Thilakarathne, J. Treur, in *Agent-based analysis of annual energy usages for domestic heating based on a heat pump*. Proceedings of the International Conference on ICT for Sustainability, ICT4S™14. Atlantis Press (2014)
11. I. Staffell, D. Brett, N. Brandom, A. Hawkesd, A review of domestic heat pumps. *Energy Environ. Sci.* **5**, 9291–9306 (2012)
12. C. Maatouk, A. Zoughaib, D. Clodic, in *New methodology of characterization of seasonal performance factor of an air-to-water heat pump*. International Refrigeration and Air Conditioning Conference (2010)
13. S.A. Tabatabaei, D.J. Thilakarathne, J. Treur, in *An analytical model for mathematical analysis of smart daily energy management for air to water heat pumps*. Proceedings of the International Conference on Technologies and Materials for Renewable Energy, Environment and Sustainability, TMREES™14. Energy Procedia, Elsevier (2014)
14. A. Omar, S. Bo, Cold climates heat pump design optimization. *ASHRAE Trans.* **118**(1), 34–41 (2012)
15. J. Treur, in *On the use of agent-based simulation for efficiency analysis of domestic heating using photovoltaic solar energy production combined with a heatpump*. Proceedings of the International Conference on Energy Efficiency and Energy-Related Materials, ENEFM™13. Springer Proceedings in Physics, vol. 155 (2014)
16. J. Treur, in *A computational analysis of smart timing decisions for heating based on an air-to-water heatpump*. Proceedings of the European Conference on Smart Energy Research at the Crossroads of Engineering, Economics and Computer Science, SmartER Europe 2014, E-World Energy and Water (2014)
17. T.F. Coleman, Y. Li, An interior, trust region approach for nonlinear minimization subject to bounds. *SIAM J. Optim.* **6**, 418–445 (1996)
18. T.F. Coleman, Y. Li, On the convergence of reflective newton methods for large-scale nonlinear minimization subject to bounds. *Math. Program.* **67**(2), 189–224 (1994)

The Method of Determining Certain Parameters of Energy Absorption in Materials Under Complex Dynamic Excitations

Miroslaw Bocian, Krzysztof Jamroziak, Maciej Kulisiewicz
and Stanislaw Piesiak

Abstract The paper presents the method to identify the dissipative properties of the materials with a clear hysteresis loop under the quasi-static loads. Because of the fact that for low values of velocity, the resisting forces related to the speed are minimal, it is not possible to determine these forces as the functions of velocity in the quasi-static deformations. It results in the need to develop such methods for identification, which use the responses of the tested system to the cyclic loading with a high frequency. This paper presents such a method. Its application may be useful in the area of constructing the effective and modern ballistic shields.

1 Introduction

The phenomenon of the energy dissipation in deformable materials is important in the area of designing modern ballistic shields. In such cases, the primary purpose of the material is to quickly dissipate the impact energy. This dissipation is carried under the large changes of the material deformation and large changes of the speed

M. Bocian · M. Kulisiewicz

Department of Mechanics, Materials Science and Engineering, Wroclaw University of Technology, Smoluchowskiego 25, 50-370 Wroclaw, Poland
e-mail: miroslaw.bocian@pwr.edu.pl

M. Kulisiewicz
e-mail: maciej.kulisiewicz@pwr.edu.pl

K. Jamroziak (✉)
General Tadeusz Kosciuszko Military Academy of Land Forces,
Czajkowskiego 109, 51-150 Wroclaw, Poland
e-mail: krzysztof.jamroziak@wso.wroc.pl

S. Piesiak
The Lower Silesian University of Entrepreneurship and Technology,
Skalnikow 6b, 59-101 Polkowice, Poland
e-mail: s.piesiak@dwpst.pl

of deformation of the material. Such situation is also frequent in the case of dynamic loads of various elements of the machine constructed with modern and lightweight composite materials. In the case of large ranges of the deformation changes, the linear Hooke's law, even in the range of reversible deformation (elastic deformation), very inaccurately describes the relationship load-deformation not only for loads slowly growing (so-called quasi-static), but above all in case of quick dynamical loads (e.g. impact loads or load generating cyclic fatigue phenomena). Such materials are characterized by a high tendency to dissipate the energy. It is opposite to the metallic materials, mainly steel, for which the dissipation of the energy (in civil engineering applications) is generally omitted or described only by a single damping parameter associated with viscous Kelvin linear model. From the point of view of determining the life-time of the dissipative-elastic elements made of the modern materials, the size of the dissipated energy is very important. This implies the need to develop the more accurate model of identification, especially for more complex and precise models, like highly nonlinear models [1–5].

This paper presents a method to identify the dissipative properties of such materials for which there is a clear hysteresis loop under quasi-static loads. This is the loads which cause the deformations with a constant and possibly low velocity. Such situation exists, for example, during the common tests of static tension and compression of the samples of the tested material. However, for low values of the speed, the resisting forces related to the speed are negligible. So, in such conditions it is not possible to determine the forces as specific functions of the deformation velocity. Hence the need to develop such methods of identification, which use the system responses to cyclic loading with high frequency. Such methods may be useful in the field of constructing the effective and modern energy-consuming shields (ballistic shields) [6, 7].

In this study it has been assumed that the forces S of the material's response depend nonlinearly on the deformation x and the speed of deformation v :

$$S(x, v) = c_1 x + c_3 x^3 + h(x) \cdot \text{sgn}(v) + k v \quad (1)$$

where c_1, c_3, k —are the positive constants while $h(x)$ —the dry friction coefficient which is depend on the level of deformation of x :

$$h(x) = h_0 \cos\left(\frac{x\pi}{2A}\right) \quad (2)$$

where A is the range of the deformation change ($-A < x < +A$).

For such model the so-called energy balance equation was derived. Based on this equation, the method to determine the parameters k, h_0 was created. These parameters allow to precisely calculating the energy absorption under the condition of complex dynamic loads. The method has been tested experimentally by computer simulation technique.

2 Mathematical Description of the Model

It has been assumed that the dynamic system consist of the concentrated mass m fixed to the motionless reference system π (Fig. 1) by the component made of the tested material. The mass m is under the influence of the dynamic periodical excitations $p(t)$ which are not necessarily sinusoidal. Under the influence of this forces the movement of the mass m is usually periodical and has a period of T .

If we would assume that the influence of the force of the tested element on the mass m has the form (1), then the differential equation of motion of the mass m takes the form of:

$$m\ddot{x} + k\dot{x} + c_1x + c_3x^3 + h_0 \cos\left(\frac{x}{A} \cdot \frac{\pi}{2}\right) \cdot \operatorname{sgn} \dot{x} = p(t) \quad (3)$$

its solution $x(t)$ describes the deformation of the tested element and may physically mean both its compression/tension as well as its torsion or shearing, depending on the construction of the test stand in the practical applications.

In the case of the quasi-static tests, so when the specifically controlled forces $p(t)$ are being used, such that:

$$x(t) = v_0t + x_0 \quad (4)$$

where v_0 is a small, constant velocity given in the strength tests, and x_0 is any initial position, we have:

$$\ddot{x}(t) = 0, \dot{x}(t) = v_0 \quad (5)$$

which on the basis of the (3) gives the relation of the characteristics:

$$p = c_1x + c_3x^3 + h(x) \cdot \operatorname{sgn} v + kv_0 \quad (6)$$

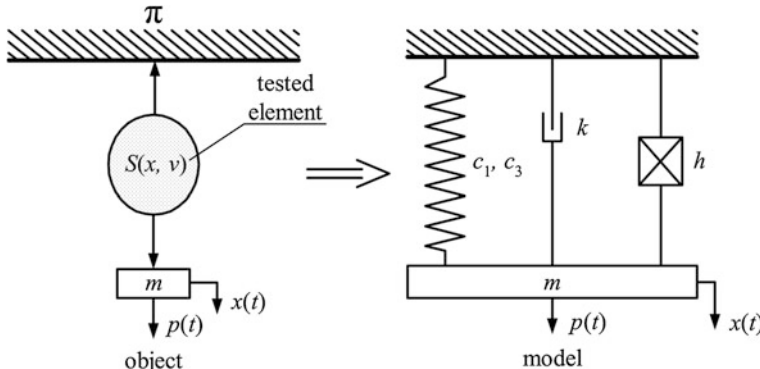
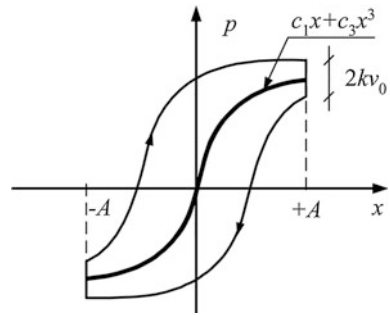


Fig. 1 Diagram of the analyzed system

Fig. 2 The shape of the static hysteresis loop of the adopted model



This relation represents the mathematical form of so-called static hysteresis loop which shape for the adopted model is shown in the Fig. 2.

In the case of the rapidly changing dynamic excitations, the dependence $p(x)$ is difficult to define mathematically for a nonlinear system. However, an energy balance equation can be introduced for this system [8, 9]. Such equation can be introduced in the case of periodic vibrations of any shape. The procedures stem from multiplication of the differential equation of the vibrations for elementary displacement dx and integrating it within the period of T .

3 Energy Balance Equation

The energy balance equation can be obtained assuming that the vibrations of the mass m are described by any form of the function which meets the condition:

$$x(t + T) = x(t) \quad (7)$$

where T is the period of the vibrations. By multiplying the differential equation (3) by the elementary displacement dx and integrating within the limits of $t = 0$ to $t = T$ it can be seen that:

$$\int_0^T \ddot{x} dx = \int_0^T \dot{v} v dt = \int_{v(0)}^{v(T)} v dv = \frac{v^2}{2} \Big|_0^T = 0 \quad (8)$$

$$\int_{x(0)}^{x(T)} x dx = \frac{x^2}{2} \Big|_0^T = 0 \quad (9)$$

$$\int_{x(0)}^{x(T)} x^3 dx = \frac{x^4}{4} \Big|_0^T = 0 \quad (10)$$

$$\int_0^T \dot{x} dx = \int_{x(0)}^{x(T)} v dx = \alpha_x^v \quad (11)$$

$$\int_{x(0)}^{x(T)} p dx = \alpha_x^p \quad (12)$$

where α_x^v is equal to the field contained within the closed loop of the phase trajectory of the determined oscillation and α_x^p is the field contained within a dynamic hysteresis loop (see Fig. 3).

In the case of the function $f(x, v)$ of the form:

$$f(x, v) = \cos \frac{x\pi}{2A} \cdot \operatorname{sgn} v \quad (13)$$

which chart is shown in the Fig. 4, similar procedure gives the result:

$$\begin{aligned} \int_{x(0)}^{x(T)} f(x, v) dx &= \alpha_x^f = \int_{-B}^{+B} \cos \frac{x\pi}{2A} \cdot \operatorname{sgn} v dx + \int_{+B}^{-B} \cos \frac{x\pi}{2A} \cdot \operatorname{sgn} v dx \\ &= \int_{-B}^B \cos \frac{x\pi}{2A} dx + \int_B^{-B} -\cos \frac{x\pi}{2A} dx = \frac{8A}{\pi} \cdot \sin \frac{B\pi}{2A} \end{aligned} \quad (14)$$

where $B = x_{\max}$

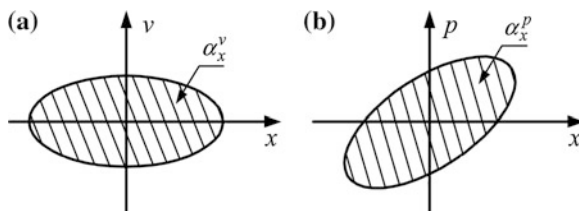
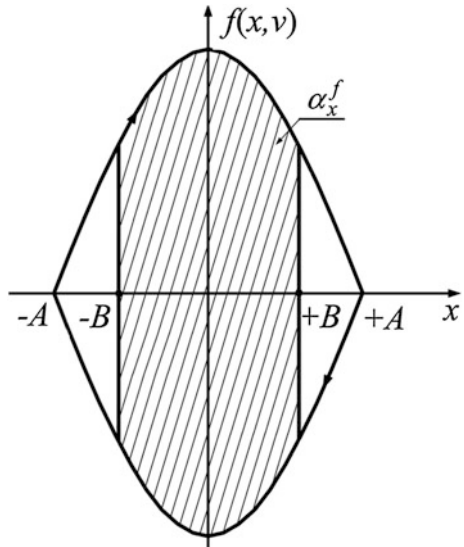


Fig. 3 Physical interpretation of the α variables: **a** phase portrait, **b** dynamic hysteresis loop

Fig. 4 Graph of the function $f(x, v)$ of the form (13) with an indication of the field of integration



Taking into account the results (8)–(12) and (14) the energy balance equation for the differential (3) takes the form:

$$k\alpha_x^v + h_0 \frac{8A}{\pi} \cdot \sin\left(\frac{B\pi}{2A}\right) = \alpha_x^p \quad (15)$$

Equation (15) is satisfied for the symmetric vibrations that satisfy the condition:

$$|x_{\min}| = |x_{\max}| = B \quad (16)$$

In the case of asymmetric vibrations it is necessary to directly measure the variable α_x^f by the numerical integration of the integral (14). In this case, the energy balance equation takes the form:

$$k\alpha_x^v + h_0 \alpha_x^f = \alpha_x^p \quad (17)$$

4 A Method of Identification. The Numerical Example

The method to determine the constant parameters describing the energy of dissipation (values of the constants k and h_0) is based on the use of the regression analysis of the energy balance equation of the form (16) and/or (17). To use this method in the case of the real system it is necessary to:

- build the test stand of the system in accordance with the diagram shown in the Fig. 1,
- determine the range of displacements of the mass m in which the system would be identified (the value of the number A),
- determine the types of the forcing forces $p(t)$ so that the response of the tested system were periodical and within the defined range that does not exceed the given number A (e.g. in the case of the sinusoidal excitations one should determine the range of the frequency and amplitude),
- for each excitation that meets the above conditions, to calculate the corresponding variables α that appear in the equation (15) or/and (17), and to calculate the value of the variable u_2 that appears next to the constant h_0 of the form:

$$u_2 = \frac{8A}{\pi} \sin\left(\frac{B\pi}{2A}\right) \quad (18)$$

- the optimal values of the parameters k and h_0 should be determined by the regression analysis according to the equation of the form:

$$ku_1 + h_0u_2 = y \quad (19)$$

where:

$$u_1 = \alpha_x^v, y = \alpha_x^p \quad (20)$$

The above procedure was initially verified based on the example of the numerical system. In this system, the following values of constants have been assumed:

$$m = 60 \text{ kg}, c_1 = 40 \times 10^3 \text{ Nm}^{-1}, c_3 = 25 \times 10^6 \text{ Nm}^{-3}, h_0 = 120 \text{ N}, \quad (21)$$

$$k = 308 \text{ kgs}^{-1}$$

This system has been modeled in Simulink software in the test scope of $A = 0.01$ m. For this range a sinusoidal excitations have been applied with different frequencies and amplitudes. A total of 120 different excitations have been introduced that gave the clearly non-sinusoidal periodic responses (see Fig. 5).

Example of the loop of the dependence α has been shown in the Fig. 6. As a result of the program of the regression analysis, the following values of the estimators were obtained: $k = 308.3 \pm 0.04 \text{ kgs}^{-1}$, $h_0 = 119.96 \pm 0.004 \text{ N}$.

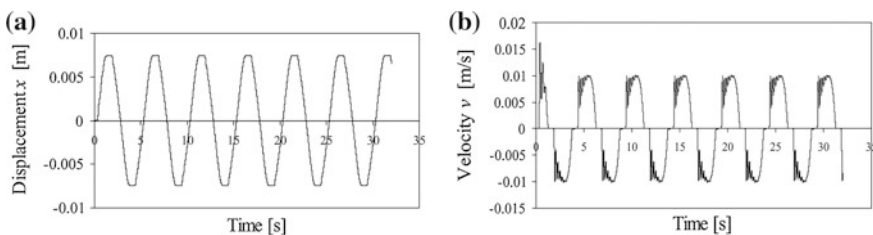


Fig. 5 Example of system's response (frequency 0.2 Hz): **a** displacement, **b** velocity

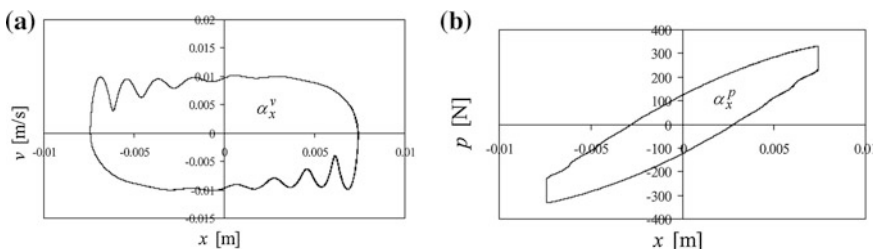


Fig. 6 Example of the loop α (frequency 0.2 Hz)

5 Conclusion

The paper presents a new method to determine the constants describing the energy dissipation in the materials subjected to the fast and cyclic loads. It presents the dynamic model with a hysteresis loop. This method allows identifying the system with a wide range of velocity change and can be used for a variety of dynamic excitations. The numerical tests of this method confirm its functioning.

References

1. J. Awrejcewicz, *Bifurcation and Chaos*. (© Springer, Berlin, 1995)
2. A. Buchacz et al., Control of characteristic of mechatronic systems. *J. Theor. Appl. Mech.* **51** (1), 225–234 (2013)
3. Bocian et al., An identification of nonlinear dissipative properties of constructional materials at dynamical impact loads conditions. *Meccanica* **49**(8), 1955–1965 (2014)
4. S. Lenci, Elastic and damage longitudinal shear behaviour of highly concentrated long fibre composites. *Meccanica* **39**, 415–439 (2004)
5. J. Warminsky et al., *Nonlinear Dynamics Phenomena in Mechanics* (Springer GmbH, Berlin, 2011)
6. T. Kang, C. Kim, Impact energy absorption mechanism of largely deformable composites with different reinforcing structures. *Fibers Polym.* **1**(1), 45–54 (2000)
7. V. Sanchez-Galvez et al., *Computational Ballistics II* (WIT Press Southampton, Boston, 2005)

8. M. Kulisiewicz, *Modeling and Identification of Nonlinear Mechanical Systems under Dynamic Complex Loads* (University of Technology Publishing House, Wroclaw, 2005)
9. K. Jamroziak, *An Identification of the Material Properties in the Terminal Ballistic* (University of Technology Publishing House, Wroclaw, 2013)

Erratum to: Tensile and Torsional Loads Stress Distribution Along the Drill String for Deep Wells

Lallia Belkacem, Noureddine Abdelbaki, Mohamed Gaceb, Elahmoun Bouali, Hedjaj Ahmed and Mourad Bettayeb

Erratum to:

Chapter ‘Tensile and Torsional Loads Stress Distribution Along the Drill String for Deep Wells’ in: A.Y. Oral et al. (eds.), 2nd International Congress on Energy Efficiency and Energy Related Materials (ENEFM2014), Springer Proceedings in Energy,
DOI [10.1007/978-3-319-16901-9_70](https://doi.org/10.1007/978-3-319-16901-9_70)

The author’s affiliation was swapped each other. The corrected affiliation should be cited as follows:

L. Belkacem, M. Gaceb, E. Bouali, H. Ahmed and M. Bettayeb
Laboratory of Petroleum Equipments Reliability and Materials, Faculty of Hydrocarbons and Chemistry Independence Street, University Mohamed Bougara, Boumerdes, 35000 Bougara, Algeria
e-mail: lallia.belkacem@gmail.com

N. Abdelbaki
University Akli Mohand Oulhadj, 10000 Bouira, Algeria
e-mail: lfep@umbb.dz

The online version of the original chapter can be found under
DOI [10.1007/978-3-319-16901-9_70](https://doi.org/10.1007/978-3-319-16901-9_70)

L. Belkacem (✉) · M. Gaceb · E. Bouali · H. Ahmed · M. Bettayeb
Laboratory of Petroleum Equipments Reliability and Materials,
Faculty of Hydrocarbons and Chemistry Independence Street,
University Mohamed Bougara, Boumerdes, 35000 Bougara, Algeria
e-mail: lallia.belkacem@gmail.com

N. Abdelbaki
University Akli Mohand Oulhadj, 10000 Bouira, Algeria
e-mail: lfep@umbb.dz